EXPERIMENTAL CONSTRAINTS ON THE GEOCHEMICAL PROCESSING OF PLANETARY INTERIORS: NOBLE GASES AND SPINEL SPECTROSCOPY

BY

COLIN R.M. JACKSON
B.S., EARTH SCIENCES, UNIVERSITY OF CALIFORNIA, SANTA CRUZ, 2008
SC.M., GEOLOGICAL SCIENCES, BROWN UNIVERSITY, 2012

A DISSERTATION SUBMITTED IN PARTIAL FULFILLMENT OF THE REQUIREMRENTS FOR THE DEGREE OF DOCTOR OF PHILOSOPHY IN THE DEPARTMENT OF GEOLOGICAL SCIENCES AT BROWN UNIVERSITY

PROVIDENCE, RHODE ISLAND
MAY 2014

This dissertation by Colin R.M. Jackson is accepted in its present form by the Department of Geological Sciences as satisfying the dissertation requirement for the degree of Doctor of Philosophy.

Date_____ _____
Stephen W. Parman, Ph.D, Advisor

Recommended to the Graduate Council

Date_____ _____
Reid F. Cooper, Ph.D., Reader

Date_____ _____
Greg Hirth, Ph.D., Reader

Date_____ _____
Sujoy Mukhopadhyay, Ph.D., Reader

Date_____ _____
E. Marc Parmentier, Ph.D., Reader

Date_____ _____
Alberto Saal, Ph.D., Reader

Approved by the Graduate Council

Date_____ _____
Peter M. Weber
Dean of the Graduate School

Vitae-Colin Robert Miller Jackson

Interest: Experimental investigations of terrestrial materials under elevated pressure and temperature

Education:

2009-: Brown University, Doctoral Program, Graduate Student (expected: May 2014)
2011: Brown University, Providence, M.Sc, Geological Sciences
2008: University of California, Santa Cruz, B.S., Earth Science
Thesis: "Partitioning of Ni between Olivine and an Iron-Rich Basalt: Experiments, Partition Models, and Planetary Implications"

Research Experience:

2009-: Research Assistant: Experimental Petrology Lab, Brown University
2008-2009: Research Assistant: USGS, Geophysics Unit of Menlo Park, CA
Assisted in paleomagnetic and gravity field measurement fieldwork. Sample preparation/analysis
2007: Summer Intern, Lunar and Planetary Institute, Houston, TX
Conducted experimental investigation of Ni partitioning with application to Mg-Suite petrogenesis

Manuscripts:

-**C.R.M. Jackson,** L. B. Ziegler, H. Zhang, M.G. Jackson, D. R. Stegman (2014) A geochemical evaluation of potential magma ocean dynamics using a parameterized model for perovskite crystallization, Earth and Planetary Science Letters, 392, 154-165

-**C. R. M. Jackson,** S.W. Parman, S.P. Kelley, R.F. Cooper (2013) Constraints on light noble gas partitioning at the conditions of spinel peridotite melting, Earth and Planetary Science Letters, 384, 178-187

-**C. R. M. Jackson,** S.W. Parman, S.P. Kelley, R.F. Cooper (2013) Noble gas transport into the mantle facilitated by high solubility in amphibole, Nature Geoscience, 6, 562-565

-Donaldson Hanna, K. L., I. R. Thomas, N. E. Bowles, B. T. Greenhagen, C. M. Pieters, J. F. Mustard, **C. R. M. Jackson**, and M. B. Wyatt (2012), Laboratory emissivity measurements of the plagioclase solid solution series under varying environmental conditions, Journal of Geophysical Research, Vol 117, Issue E11

-J. Filiberto, **C. Jackson,** L. Le., and A.H. Treiman (2009) Partitioning of Ni between Olivine and an Iron-Rich Basalt: Experiments, Partition Models, and Planetary Implications. American Mineralogist 94, 256-261

-**C. Jackson,** L. Cheek, K. Williams, K. Donaldson-Hanna, C. Pieters, S. Parman, R. Cooper, M. Dyar, M. Nelms, and M. Salvatore; Visible-Infrared Spectral Properties of Iron-bearing Aluminate Spinel Under Lunar-Like Redox Conditions, in revision, American Mineralogist

-T.C. Prissel, S.W. Parman, **C.R.M. Jackson**, M.J. Rutherford, P.C. Hess, J.W. Head, L. Cheek, D. Dhingra, and C.M. Pieters; Pink Moon: The Petrogenesis of Pink Spinel Anorthosites and Implications Concerning Mg-suite Magmatism, under review, Earth and Planetary Science Letters

-C. Pieters, K. Donaldson Hanna, L. Cheek, D. Dhingra, T. Prissel, **C. Jackson**, D. Moriarty, S. Parman, and L. Taylor; The distribution and origin of Mg-spinel on the Moon, in revision, American Mineralogist

Abstracts (selected):

-**C. Jackson**, SW Parman SP Kelley, RF Cooper (2013) Applicability of Henry's Law to helium solubility in olivine, AGU Fall Meeting, V33A-2729

-**C. Jackson**, SW Parman SP Kelley, RF Cooper (2013) Noble Gas Recycling and He-Ne-Ar Solubility in Ring Structure-Bearing Minerals, Goldschmidt Conference 2013, Florence

-K.B. Williams, **C.R.M. Jackson**, L.C. Cheek, T.C. Prissel, S.W. Parman, C.M. Pieters (2012) The effect of Cr content of the reflectance properties of Mg-Spinel, AGU Fall Meeting, P42A-1905

-**C. Jackson**, SW Parman SP Kelley, RF Cooper, (2012) Helium solubility in mica and mechanisms for deep transport of noble gases in subduction zones, AGU Fall Meeting, DI13D-2453

Honors/Awards:

-Dissertation Fellowship, Brown University, 2013
-Lunar Science Forum, Poster Award, 1st Place, 2013
-Outstanding Student Paper Award, AGU Fall Meeting 2013, VGP Section
-First Year Fellowship, Brown University, 2009-10
-Dean's Research Award, UCSC, 2007-08
-Departmental and Thesis Honors, Dept. of Earth Science, UCSC

Teaching Experience:

2014, Spring: Teaching Assistant: Introduction to Geochemistry (GEO 0230)
In progress
2010, Fall: Teaching Assistant: Physical Processes in Geology (GEO 0220)
Co-taught lab sections. Led field trip groups. Grading.

Invited Presentations:

-Post-AGU CIDER Workshop, UC Berkeley, Chemical consequences of perovskite fractionation from an ultramafic liquid with application to the evolving composition of a basal magma ocean, Dec. 2012 (with L Ziegler, H Zhang, M Jackson, D Stegman)
-Solid Earth Seminar, Boston University, Experimental constraints on the mantle noble gas cycle, Oct. 2011, (with SW Parman, SP Kelley, RF Cooper)
-Gordon Research Seminar, Mt. Holyoke, MA, Chemical consequences of perovskite fractionation from an ultramafic liquid with application to the evolving composition of a basal magma ocean, June. 2013 (with L Ziegler, H Zhang, M Jackson, D Stegman)

Professional Service and Synergistic Activities:

-Geological Sciences Graduate Student Representative to Faculty, 2012-2013
-Participant, CIDER Summer Workshop, Deep Time: How did early Earth become our modern world?, July-August 2012, Santa Barbara, CA, USA
-Participant, Gordon Research Conference, Interior of the Earth, June 2013, Mt Holyoke, MA, USA
-Participant, Gordon Research Conference, Interior of the Earth, June 2011, Mt Holyoke, MA, USA

Outreach and Advising:

-Volunteer science teacher, Vartan-Gregorian Elementary School, Providence, RI
-Mentored undergraduate Kelsey B Williams, NLSI internship (with Leah C. Cheek)
-Guest lectured on geologic material properties, Brown Summer School, 2013

Acknowledgements

Many people have contributed to the ideas, work, and spirit of this thesis. Some of my earliest exposure to science came from my grandfather. In his retirement, he was a docent at the Lawrence Hall of Science in Berkeley and took me there with him many times growing up. I can remember him trying to teach my brother and me about the nucleobases in DNA and how they created a pattern unique to every organism. I can remember deconstructing my grandmother's broken hairdryer to diagnose what had malfunctioned and actually fixing it! He helped cultivate a curiosity for how our world works and a sense that we could actively seek to understand it. I've been told by my dad that I asked many questions about the world growing up, and he assures me that he fielded the brunt of them. Despite my foggy memory of this period, I believe him. So, thank you, dad, for answering these questions and for your patience throughout the learning process. I have always enjoyed our discussions about stuff, where "stuff" can mean really almost anything. It is clear that we both enjoy arguing, usually about things that we only half know about, but you have always demanded logic and an awareness of the counterpoints to your own argument. You continue to be a source of "knowledge coming down" and will always remind me to pursue passions. My mom has helped guide and support me in different ways. You are my strongest advocate and were instrumental in navigating the year between college and graduate school. Your suggestion to move back home, although from one prospective might seem self-motivated and a tough sell to kid freshly out of college, was spot on and set me on the path I am still following today. You carefully listen to me and help me think things through. Your grace is an inspiration. I appreciate you and Tony bringing back rocks or books about rocks from

your travels. They don't let us out of the basement too often here and it's always nice to some natural rocks, rather than the synthetic ones we toil over. A shout out to my brother, Kirsten, and Roy. You guys rock and I'm sorry for nerding out from time to time. Big ups to Emma.

My formal introduction into geology has come from many teachers and advisors. Jim Gill and his Magma and Volcanoes class really got me going on solid Earth geochemistry and petrology, and he skillfully guided me through writing my undergraduate thesis. I have learned a great deal from each one of the GMP professors at Brown. I'm pretty sure Reid's phase equilibria class was challenging to us all our first year here, but Reid threw himself into the class and it was great. What we learned in that class has proved useful time and time again, both in terms of thermodynamics and the importance of rhetoric. I have always enjoyed sitting down with Reid to think a problem through. The main challenge here has always been remembering what the original question was. I was lucky enough to share a wall with Liang, the renaissance geologist. Indeed, I have learned aspects of experimental methods, computational methods, kinetics, geochemistry, and the geologic history of the Moon through Liang. Peter's isotope geochemistry class is foundational in my geologic knowledge, and he always had constructive feedback and thoughtful questions for the lunch bunches. I can remember sitting down for Alberto's trace element boot camp the summer before my first semester. He took me in like I was his own student and tossed us all into the deep end, or at least it seemed deep at the time. His expectations for us have always been high, but he has also broken his back to help us realize those expectations. I have often sought Alberto's advice, and he always provides a thoughtful response that cuts through "the shit," to steal

his words. I have truly enjoyed getting to know and learning from Alberto. Steve has been a wonderful advisor. One of the most valuable things I have learned from Steve is how to approach problems: find things that go counter to your intuition and study them. Data and your model should cross at 90 degrees, at least to start a project. He has allowed me extraordinary freedom to pursue my own ideas from a very early point in graduate school. This can be a scary prospect but also a rewarding one in the end. We have spent many hours in his office together mostly discussing geology, but really a little bit of most things. Similar to my father, Steve has always demanded logical thought in our discussions, and I have always enjoyed the back and forth.

To the geophysically-minded members of my committee, Greg and Marc. Marc, I appreciate you sitting down with me and thinking about the various box models I've attempted to put together and your attempts to joke with me. I'll keep working on my end of the bargain. Greg, your excitement and positive nature have made graduate school more fun. Thank you for being on my committee (despite your occasional slips regarding remembering membership).

Joe, thank you for all your help on the probe. I respect your commitment to acquiring high-quality data. Bill Collins, despite perpetuating the notion that "Colin" should be spelled with two L's, I want to thank you for everything you've done, but in particular, thank you for organizing summer softball. I had a blast playing. Gloria, you have been a huge help to me and have always made it easy to get things done in the front office. Thank you very much.

I've had the pleasure on going through graduate school with a uniformly great body of graduate students, minus Mark Salvatore. I got stuck living with him for four

years and he refused to let me be the best at anything. Stop practicing golf already and let me have it. Shannon is loads of fun and kept many of us balanced human beings, and I am no exception to this. I've drawn lots of support from my cohort in the basement, including Diane, Lijing, Amanda, Mary, and Nick. We went through a lot together and I've enjoyed *almost* every bit. It's been a particular pleasure sharing an office with Chen and a corner with Nick. I'll miss our impromptu discussions and having you guys around during the postdoc application gauntlet helped a lot. Chen, I'm sorry for constantly brewing more coffee. I'm sure you are tired of the smell by now. Tabb, #bestlabmateever. Kelsey, #2wise4youryears. Leah, #we'rebarelyholdingittogetherwithoutyou. #teamspinel. Tim, thank you for introducing me to hockey and manners. ESHes, Aron, both Wills, Steph, Sam, Marc, thank you for hanging with me. Chris, I enjoyed our year living together. I'm still trying to master the soccer shot off the outside edge of the foot that you've perfected. Ben, Kei, Boda, Tess, Taka, Brooks, Sicheng, basement solidarity! Jenny, if you'll recall, things got off to rough start, but I think we've found our groove since.

TABLE OF CONTENTS

Introduction

Geology is commonly introduced to students as a forensic science, where nature has run her experiment and the geologist is tasked with deducing what the experiment was. This thesis doesn't follow from that introduction. Rather, a series of synthetic experiments have been completed under known conditions to document the properties of matter. Pressure and temperature were set. The initial chemistry of the system was fixed. Durations were dictated. The exchange of matter into or out of the experimental system was controlled for. Experiments were repeated. Samples amenable to analysis were produced and interrogated.

This is the forward approach to geology: work from inputs to outputs. It's an unconventional approach, in part, because it goes against what draws most people to geology: getting outside and experiencing the natural world in its full glory. As experimentalists, we toil indoors, often in windowless basements, and we seek to simplify natural systems. We sometimes intentionally stray from nature to make experiments feasible or to isolate the effects of individual variables. We seek to understand the equilibrium state of a system but also the kinetics associated with the system approaching the equilibrium state. The experimental approach is a valuable approach to geology and to science in general. Experiments provide a framework to interpret observations of natural phenomena. They allow processes to be connected to observations. They provide benchmarks for models.

This thesis acts to expand the experimental framework. From the work communicated in this thesis, knowledge of the physical and chemical properties of

geological materials has increased, but the expansion of knowledge here is not uniform, far from it. Instead, it is concentrated in two general areas: the solubility of noble gases in geologic materials and the spectral properties of aluminate spinels. These additions of knowledge have been generally applied to understanding how noble gases cycle through the Earth and the early magmatic history of the Moon. A detailed introduction to each chapter and ideas for future research are provided below.

Chapters 1-3: experiments on the deep noble gas cycle

Chapter 1 presents a manuscript titled "Constraints on light noble gas partitioning at the conditions of spinel-peridotite melting," published in *Earth and Planetary Science Letters* (link here). In this manuscript we provide constraints for how light noble gases (helium-neon-argon) are partitioned between minerals and basalt and, for the first time, helium partitioning is determined for all the major minerals in spinel peridotite up to the pressure and temperature conditions associated with partial melting of the mantle. The bulk partition coefficient for helium is shown to be extremely low, 10^{-4}. Moreover, helium solubility is shown to be insensitive to the availability of common point defects, implying an interstitial dissolution mechanism dominates helium solubility in peridotite minerals, at least at high helium fugacity. Compared to U+Th, helium appears to be more incompatible, implying the partial melting process will impart lowered U+Th/He for the mantle that is residual to the melting process. Upper limits of neon and argon partitioning are also reported for olivine, and these limits are consistent with neon and argon being similarly incompatible as helium.

The second chapter presents a manuscript titled "Noble gas transport into the mantle facilitated by high solubility in amphibole," published in *Nature Geoscience* (link

here). This manuscript presents measurements of helium and neon solubility in a variety of amphiboles. We find that helium and neon are highly soluble in amphibole, extending up to ~1000× the solubility of helium in olivine. Further, we demonstrate that noble gas solubility in amphibole correlates with the concentration of unoccupied ring structures, providing evidence for noble gases partitioning onto a specific site in a mineral. Amphibole is a common product of hydrothermal alteration in oceanic crust and, correspondingly, may facilitate the transport of atmospheric noble gases deep into subduction zones.

The third chapter presents a manuscript titled "Light noble gas dissolution into ring structure-bearing materials and mineralogic influences on noble gas recycling," in preparation for submission to *Geochimica et Cosmochima Acta*. This manuscript expands upon the experiments presented in *Chapter 2* by exploring the solubility of light noble gases on a variety of ring structure-bearing minerals: beryl, cordierite, tourmaline, antigorite, muscovite, and F-phlogopite. Helium solubility in these ring structure-bearing minerals is relatively high but variable, ~100-100,000× the solubility of helium in olivine. The variation of helium solubility is explored in the context of ring structure topology (the geometry of cation polyhedra local to the ring structure). We show that minerals with similar topologies about their ring sites also share similar He solubilties, supporting the inference that ring structures strongly influence the solubilities of noble gases in minerals. Limited measurements of neon and argon solubility in minerals with ring structures suggest a general preference of ring structures for lighter noble gases. Interestingly, the elemental pattern of noble gases recycled into the mantle is not enriched in lighter noble gases. There is evidence that heavier noble gases are preferentially

recycled compared to lighter noble gases (Holland and Ballentine, 2006), opposite to the solubility measurements for noble gases in ring structure-bearing minerals. Thus, it seems that factors other than the solubility of noble gases in ring structure-bearing materials must be active to balance the integrated pattern of recycled noble gases. Possible balancing factors are briefly discussed in this chapter, including sediments, which are strongly enriched in heavier noble gases, and secondary phases in serpentine.

Future directions for experiments on the deep cycling of noble gases:

Early measurements of mantle mineral-basalt partition coefficients generally yielded high values, approaching compatible behavior for all gases (Broadhurst et al., 1992, 1996; Hiyagon and Ozima, 1982, 1986; Shibata et al. 1994). With time, it was recognized that secondary phases, particularly fluid inclusions, could strongly affect the apparent solubility of noble gases in minerals (e.g. Heber et al., 2007). With this recognition, reported noble gas partition coefficients have generally come down, helped in large part by UV laser ablation-mass spectrometry techniques (e.g. Brooker et al., 1998). The helium partition coefficients reported in *Chapter 1* are extremely low, $\sim 10^{-4}$, and thus, continue in the vein of UV laser ablation-mass spectrometry based measurements yielding low partition coefficients. Modern attempts to measure helium solubility in gem-quality olivine via crush-melt analysis, however, yield higher partition coefficients of $\sim 5 \times 10^{-3}$ (Parman et al., 2005). Importantly, the Parman et al. (2005) experiments were conducted at lower helium fugacities compared to the experiments reported in *Chapter 1* or in Heber et al. (2007), suggesting that helium solubility in olivine is non-Henrian, even at low helium concentrations (~10 ppb). Preliminary UV laser ablation-mass spectrometry based determinations of helium solubility in olivine at

lower helium fugacity (~50 bar) are consistent with lower partition coefficients (~10^{-4}) and Henrian solution behavior, but additional experiments are required at very low helium fugacity (< 10 bar) to determine naturally applicable partition coefficients. These preliminary data are included in *Appendix 1* and were reported at AGU Fall Meeting 2013. Similarly, at low noble gas fugacities, large radius, low abundance defects, such as oxygen vacancies, dislocations, and grain boundaries, are potentially significant hosts for noble gases in solids. Experiments that explicitly isolate the effect of these defects will allow for more accurate predictions for how noble gases are distributed in rocks.

There are relatively few data pertaining to the partitioning of heavier noble gases during mantle melting. Additional experiments are clearly needed here, as considerable scatter is present in the most current heavy noble gas partitioning datasets (c.f. Heber et al., 2007). Experiments similar to those run by Heber et al., 2007, but analyzed by state of the art mass spectrometers and 193 nm UV lasers should yield increased precision in heavy noble gas partition coefficient measurements.

An alternative approach to measuring heavy noble gas solubility in mantle minerals is to run in-diffusion experiments similar to those run in the EHPV (externally-heated pressure vessel) series of *Chapter 1*. Because heavy noble gases diffuse slowly, only the shallowest depths of minerals would equilibrate with the heavy noble gases from the pressure medium. Shallow equilibration depths cause two problems. First, there is very little material to analyze. Second, it is difficult to accurately measure the volume of large radius, shallow depth ablation pits. These problems can be addressed by adapting the methods applied in the EHPV series. The internally-heated pressure vessel at Brown can achieve higher temperatures than the externally-heated pressure vessel, which would

cause more rapid equilibration between the pressure medium and mineral, although there is some indication that high temperatures cause "frosted" appearances on mineral surfaces (see *Chapter 1*). The reason behind the "frosting" is unknown. Shallow pits on extremely flat surfaces are easier to measure for volume, but flat polished surfaces are difficult to prepare using the facilities of a typical experimental lab. Purchased sections of industrially polished olivine would be a substantial improvement in surface flatness and, thus, accuracy in pit volume measurement. A final adaptation for would be to use noble gases produced by irradiation as internal standards. Provided the concentration of the irradiated gas is known, the ratio of the irradiated gas to the experimental noble gas yields the concentration of the experimental gas in the absence of a volume measurement. Using noble gases produced by irradiation as internal standards may also facilitate the study noble gases on grain boundaries and other potentially gas-rich secondary phases.

Exotic mantle liquids, such as sulfide and carboniaite liquids, also merit investigation as liquids tend to strongly partition noble gases over solids at relatively moderate pressure conditions. If high noble gas solubility in exotic mantle liquids can be verified by experiment, it raises the possibility that small degree carbonatite, and potentially sulfide, liquids host the bulk of the upper mantle noble gas budget. A single study on noble gas solubility in carbonatite liquid suggests that He and Ar are similarly soluble in carbonatite and silicate liquids (Burnard et al., 2010), which could act to physically decouple noble gas isotopes from other lithophile radiogenic systems (Hofmann et al., 2010).

For noble gas recycling (*Chapters 2 and 3*), it is clearly a simplification to only consider ring structure-bearing minerals in the transport of noble gases in subduction

zones. This is emphasized by the He-Ne-Ar measurements on the antigorite presented in *Chapter 3*, where a secondary phase has a clear and strong influence on Ar and to a lesser extent Ne. There is a need to measure noble gas solubility in secondary phases, grain boundaries, and saline fluids (H_2O- and CO_2-rich) at high temperature. Adsorption also appears to be an important process for determining the abundance and pattern of noble gases in seafloor sediments (e.g. Fanale and Cannon, 1971; Podosek et al., 1981). Work is needed to determine adsorptive affinity of aqueous noble gases for different minerals in seafloor sediments and hydrothermal environments. The few studies that have experimentally investigated adsorption of noble gases on sedimentary materials have focused on shales and adsorption from a noble gas-bearing vapor (not aqueous solution) (Fanale and Cannon, 1971; Podosek et al. 1981).

Chapters 2 and 3 focus on determining the solubility of He-Ne-Ar in ring structure-bearing materials because these experiments could be run over relatively short durations, allowing for a reconnaissance of many different minerals. Additional ring structure minerals remain unexplored and should be the focus of future experiments. This list includes talc, chlorite, clays, and lower temperature polymorph of serpentine.

For the minerals where He-Ne-Ar reconnaissance has been completed, the focus should be on expanding measurements to include Kr and Xe. Including these gases in future experiments will be particularly useful because Kr and Xe provide many of the observational constraints on noble gas recycling. Kinetics of equilibration, particularly for the antigorite of *Chapter 3*, are sufficiently rapid that in-diffusion (noble gas uptake for a noble gas pressure medium) experiments for Kr and Xe are feasible. Similarly, it should be possible to run in-diffusion experiments on amphibole that equilibrates

sufficient material with Ar for analysis, which would extend the current amphibole data toward heavier noble gases without significant methods development. However, growth of amphibole from a He-, Ne-, Ar-, Kr-, and Xe-bearing silicate melt is likely required to define the full spectrum of noble gas solubility, as noble gas diffusion kinetics in amphibole are relatively sluggish.

A significant amount of noble gas solubility data collected together with the data included in *Chapters 1, 2, and 3* remains unpublished. The several noteworthy results are contained in this unpublished data. First, there is a compilation of helium solubility measurements in minerals with a wide range of ionic porosity. Only a weak correlation exists between ionic porosity and helium solubility, suggesting that other factors, such as topology of porosity, strongly influence helium solubility in minerals. Second, a test of Henry's Law in San Carlos olivine has been completed, and the results of consistent with Henrian solution behavior between 50 and 2000 bar helium fugacity (Appendix Figures 2 and 3). Limited He-Ne-Ar data have been collected for framework silicates (scapolite, K-spar, and plagioclase) and prehnite (sheet silicate) (Appendix Figure 4). These data are consistent with minerals having a general preference for smaller radii noble gases, which is in-line with He-Ne-Ar solubility data collected for ring structure-bearing minerals *(Chapter 3)*. These data will be incorporated into a manuscript in the near future.

Chapter 4: spectra of Al,Mg-rich spinel under lunar-like conditions

Chapter 4 marks a departure from the remainder of work presented in this thesis. The lunar reading seminars conducted during my time at Brown along with the recent identification of spinel-rich deposits on the lunar surface (Dhingra et al., 2011; Pieters et

al., 2011) motivated this chapter. Essentially, Leah Cheek and I were skeptical of the initial compositional estimates made for the remotely-detected lunar spinels, and we struck out to provide a more robust estimate. Many other people became involved in the project as it evolved.

Here, we explore the factors that control the visible-near infrared (V-NIR, 500 – 3000 nm) spectra of $(Mg,Fe)Al_2O_4$ (aluminate spinel). This chapter is currently under review for publication in the Lunar Highlands special issue in *American Mineralogist*. Specifically, we synthesized a series of aluminate spinels with varying Fe# to document the effect of Fe on spinel spectra at lunar-like fO_2. Controlling for fO_2 is crucial because many absorption bands in the V-NIR are related to the presence of Fe^{+3}, and the Moon is a relatively reduced system compared to the Earth. Particular attention is paid to the controls on spectral features at ~1000 nm because these features conspicuously absent in the observations of lunar spinel (Pieters et al., in review) but common in terrestrial, Fe-rich spinels (Cloutis et al., 2004). Compilations of terrestrial spinel spectra demonstrate a rough correlation between the bulk abundance of iron and the strength of ~1000 nm bands in spinel (Cloutis et al., 2004), which led to the early conclusion that the remotely detected lunar spinel were very Mg-rich (<5 wt. % FeOt, Pieters et al., 2011). The scatter in the correlation between bulk iron and the strength of ~1000 bands, however, suggested that other factors affect the strength of ~1000 nm bands in spinel. Indeed, we show that ~1000 nm bands are particularly sensitive to the abundance of octahedral ferrous iron, which is related to the degree of disordering in spinel. The degree of disordering in aluminate spinel is a primarily a function of cooling rate, implying that cooling rate must be accounted for when deriving compositional constraints for remotely-sensed spinels.

Toward this end, we apply order-disorder models for spinels to quantify the spectral sensitivity to cooling rate and derive Fe# constraints for lunar spinels. The results from this modeling support the lunar spinels being very Mg-rich (<12 Fe# or <6 wt. % FeOt) and imply a relation between lunar spinels and Mg-suite magmatism. Our results are further applied to the more recently observed spinels associated with the pyroclastic deposits at Sinus Aestuum (Sunshine et al., 2010; Yamamoto et al., 2013). Here, we demonstrate that either very rapid cooling rates or high ferric iron abundances are required to produce the relative strengths of the 1000 and 2000 nm bands associated with the Sinus Aestuum spinels. Rapid cooling rates would imply cooling in the absence of an extensive vapor cloud, which is supported by the lack of hydration features associated with the Sinus Aestuum spinel deposits (Li and Milliken, 2014). This contrasts with the cooling rates determined for the relatively volatile-rich picritic glass pyroclastic deposits returned during the Apollo missions (Saal et al., 2008).

Future directions for studies on lunar spinel:

Additional work is required to quantify the effect of ferric iron and chromium on spinel spectra. Ferric iron is relatively stable in spinel. Even at IW-1, ~5-10 % of total iron is ferric in aluminate spinel. Correspondingly, variations in ferric iron can cause significant spectral variability in lunar spinel. A better understanding of the effects of ferric iron in spinel may allow the effects of cooling rate and redox state to be deconvolved for the Sinus Aestuum spinels. Chromium is also relatively stable in spinel and is spectrally active in the V-NIR spectral range. Experiments calibrating the effect of chromium should allow for Cr# constraints to be placed on remotely sensed lunar spinels. Work on chromium-bearing spinel is currently underway and headed by K.B. Williams.

Twenty identifications of Mg-rich spinel have been made to date on the lunar surface. These identifications are almost exclusively found on the near-side of the Moon (17 near-side, 3 far-side. Pieters et al., in review). Accounting for the obscuring effects of mare basalt and thick crust, preliminarily analysis of the spinel distribution imply the Mg-rich deposits are anomalously concentrated on the near-side. Importantly, the Mg-rich spinel deposits on the near-side are nearly equally distributed between the northern and southern hemisphere, implying their presence is not related to the mare basalts, which are concentrated in the northern hemisphere. If Mg-rich spinel is taken as a proxy for the location of Mg-suite plutonism, then the distribution of spinel implies the Mg-suite is predominately a near-side product. The ramifications of the Mg-suite being a primarily near-side lithology are currently being considered within our research group, but continued analysis of Mg-rich spinel distribution promises to be an interesting line of inquiry. For example, current models for the petrogenesis of the Mg-suite invoke the remelting the earliest cumulates of the lunar magma ocean to explain the extremely magnesium compositions of Mg-suite olivines and pyroxenes (Elardo et al., 2011). Following these models, this would imply that early magma ocean cumulates were preferentially fluxed to the near-side of the Moon, providing an additional constraint for lunar magma ocean overturn. We intend to fully develop the ramifications of Mg-rich spinel distribution this summer.

References**:**

Broadhurst, C.L., Drake, M.J., Hagee, B.E., Bernatowicz, T.J., 1990. Solubility and partitioning of Ar in anorthite, diopside, forsterite, spinel, and synthetic basaltic liquids. Geochimica Et Cosmochimica Acta 54, 299-309.

Broadhurst, C.L., Drake, M.J., Hagee, B.E., Bernatowicz, T.J., 1992. Solubility and partitioning of Ne, Ar, Kr, and Xe in minerals synthetic basaltic melts. Geochimica Et Cosmochimica Acta 56, 709-723.

Brooker, R.A., Wartho, J.A., Carroll, M.R., Kelley, S.P., Draper, D.S., 1998. Preliminary UVLAMP determinations of argon partition coefficients for olivine and clinopyroxene grown from silicate melts. Chemical Geology 147, 185-200.

Burnard, P., Toplis, M.J., Medynski, S., 2010. Low solubility of He and Ar in carbonatitic liquids: Implications for decoupling noble gas and lithophile isotope systems. Geochimica Et Cosmochimica Acta 74, 1672-1683.

Cloutis, E.A., Sunshine, J.M., Morris, R.V., 2004. Spectral reflectance-compositional properties of spinels and chromites: Implications for planetary remote sensing and geothermometry. Meteoritics & Planetary Science 39, 545-565.

Dhingra, D., Pieters, C.M., Boardman, J.W., Head, J.W., Isaacson, P.J., Taylor, L.A., 2011. Compositional diversity at Theophilus Crater: Understanding the geological context of Mg-spinel bearing central peaks. Geophysical Research Letters 38, L11201.

Elardo, S.M., Draper, D.S., and Shearer Jr, C.K. (2011) Lunar Magma Ocean crystallization revisited: Bulk composition, early cumulate mineralogy, and the

source regions of the highlands Mg-suite. Geochimica et Cosmochimica Acta, 75, 3024-3045.

Fanale, F.P., Cannon, W.A., 1971. Physical Adsorption of rare gas on terrigenous sediments. Earth and Planetary Science Letters 11, 362-368.

Heber, V.S., Brooker, R.A., Kelley, S.P., Wood, B.J., 2007. Crystal-melt partitioning of noble gases (helium, neon, argon, krypton, and xenon) for olivine and clinopyroxene. Geochimica Et Cosmochimica Acta 71, 1041-1061.

Hiyagon, H., Ozima, M., 1982. Noble gas distribution between basalt melt and crystals. Earth and Planetary Science Letters 58, 255-264

Hiyagon, H., Ozima, M., 1986. Partition of noble gases between olivine and basalt melt. Geochimica Et Cosmochimica Acta 50, 2045-2057.

Hofmann, A.W., Farnetani, C.G., Spiegelman, M., Class, C., 2011. Displaced helium and carbon in the Hawaiian plume. Earth and Planetary Science Letters 312, 226-236.

Holland, G., Ballentine, C.J., 2006. Seawater subduction controls the heavy noble gas composition of the mantle. *Nature* 441, 186-191.

Li, S., Milliken, R, 2014, Quantitative mapping of hydration in lunar pyroclastic deposits: insightst into water from the lunar interior, Lunar Planetary Science Conference Abstracts, p. 2012.

Parman, S.W., Kurz, M.D., Hart, S.R., Grove, T.L., 2005. Helium solubility in olivine and implications for high $^{3}He/^{4}He$ in ocean island basalts. Nature 437, 1140-1143.

Pieters, C.M., Besse, S., Boardman, J., Buratti, B., Cheek, L., Clark, R.N., Combe, J.P., Dhingra, D., Goswami, J.N., Green, R.O., Head, J.W., Isaacson, P., Klima, R.,

Kramer, G., Lundeen, S., Malaret, E., McCord, T., Mustard, J., Nettles, J., Petro, N., Runyon, C., Staid, M., Sunshine, J., Taylor, L.A., Thaisen, K., Tompkins, S., Whitten, J., 2011. Mg-spinel lithology: A new rock type on the lunar farside. Journal of Geophysical Research-Planets 116, E00G08.

Pieters, C.M., Donaldson Hanna, Kerri, Cheek, L, Dhingra, D, Prissel, T, Jackson, C, Moriarty, D, Parman, S, Taylor, L.A. The Distribution and Origin of Mg-Spinel on the Moon. In review, American Mineralogist, lunar highlands special issue

Podosek, F.A., Bernatowicz, T.J., Kramer, F.E., 1981. Adsorption and xenon and krypton on shales. Geochimica Et Cosmochimica Acta 45, 2401-2415.

Podosek, F.A., Honda, M., Ozima, M., 1980. Sedimentary noble gases. Geochimica Et Cosmochimica Acta 44, 1875-1884.

Shibata, T., Takahashi, E., Ozima, M., 1994. Noble gas partition between basaltic melt and olivine crystals at high pressures. Noble gas Geochemistry and Cosmochemistry, Terra Scientific Publishing Company, Tokyo, 343-354.

Sunshine, J., Besse, S., Petro, N., Pieters, C., Head, J., Taylor, L., Klima, R., Isaacson, P., Boardman, J., Clark, R., 2010. Hidden in plain sight: Spinel-rich deposits on the nearside of the Moon as revealed by Moon Mineralogy Mapper (M^3), Lunar and Planetary Institute Science Conference Abstracts, p. 1508.

Yamamoto, S., Nakamura, R., Matsunaga, T., Ogawa, Y., Ishihara, Y., Morota, T., Hirata, N., Ohtake, M., Hiroi, T., Yokota, Y., 2013. A new type of pyroclastic deposit on the Moon containing Fe-spinel and chromite. Geophysical Research Letters 40, 4549–4554.

CHAPTER 1: Constraints on light noble gas partitioning at the conditions of spinel-peridotite melting

Colin R.M. Jackson[1], Stephen W. Parman[1], Simon P. Kelley[2], Reid F. Cooper[1]

1 Geological Sciences, Brown University, Providence, RI 02912
2 Department of Environment, Earth and Ecosystems, The Open University, Milton Keynes, United Kingdom

Submitted to:
Earth and Planetary Science Letters
December 19, 2013

Revised:
September 11, 2013

Accepted:
September 28, 2013

Title: Constraints on Light Noble Gas Partitioning at the Conditions of Spinel-Peridotite Melting

Authors: Colin RM Jackson, Stephen W Parman, Simon P Kelley, Reid F Cooper

Abstract: Helium partitioning between olivine, orthopyroxene, clinopyroxene, and spinel and basaltic melt has been experimentally determined under upper mantle melting conditions (up to 20 kbar and 1450 °C). Under the conditions explored, helium partition coefficients are similar in all minerals investigated ($K_d^{He} \sim 10^{-4}$), suggesting He is evenly distributed between the minerals of spinel peridotite. This is in contrast to most incompatible elements, which are concentrated in clinopyroxene in spinel peridotite. The studied minerals have different concentrations of point defects, but similar He solubility, providing no evidence for He partitioning onto specific defects sites (e.g. cation vacancies). Upper limits on the partition coefficients for Ne and Ar have also been determined, constraining these elements to be moderately to highly incompatible in olivine at the conditions of spinel peridotite melting ($<10^{-2}$ and $<10^{-3}$, respectively). Helium partitioning in peridotite minerals varies little within the range of temperatures, pressures, and mineral compositions explored in this study. Reported partition coefficients, in combination with previous work, suggest that moderate to high degrees of mantle melting is not an efficient mechanism for increasing (U+Th)/He, (U+Th)/Ne, or K/Ar of the depleted mantle (DMM) through time, and consequently, supports the argument that recycling of oceanic crust is largely responsible for the relatively strong radiogenic noble gas signatures in the depleted mantle. Mantle residues with lowered

(U+Th)/He, (U+Th)/Ne, and K/Ar may be produced through large extents of melting, but concentrations of noble gases will be low, unless noble gas solubility in solids deviate from Henry's Law at high fugacity.

1.0 Introduction:

Noble gas isotope and elemental variations in mantle-derived material are records of the Earth's volatile element evolution. Interpreting this record requires an understanding of noble gas behavior at conditions relevant to upper mantle melting. Given the inert nature of noble gases, models of noble gas evolution often assume that they are perfectly incompatible ($C_i^{\alpha}/C_i^{liq} = 0$) during mantle melting, resulting in rapid and uniform extraction from the residue (e.g. Allegre et al., 1996; Onions and Oxburgh, 1983). Early experimental work, however, did not support these predictions. Multiple studies have reported compatible ($C_i^{\alpha}/C_i^{liq} > 1$) behavior, especially for heavier noble gases (Broadhurst et al., 1990, 1992; Hiyagon and Ozima, 1982, 1986; Shibata et al., 1994).

Refinements in experimental and analytical methods have generally yielded lower noble gas partition coefficients, although with variable accuracy and precision. Significantly, the development of combined UV laser ablation and noble gas mass spectrometry allows for analysis of small volumes of material with fine spatial control (Brooker et al., 1998). This approach limits the inadvertent incorporation of secondary, gas-rich phases that can produce apparently high noble gas solubilities for solids. A series of studies utilizing simple system compositions (formulated to reduce the density

of fluid inclusions in synthesized crystals and co-existing glasses) and UV laser analysis yielded noble gas (He-Xe) partition coefficients between 10^{-3} and 10^{-4} for olivine and clinopyroxene (Brooker et al., 2003; Brooker et al., 1998; Chamorro et al., 2002; Heber et al., 2007). Somewhat higher (~10×) partition coefficients for He have been reported by Parman et al. (2005) using an alternative approach. This study prepared samples by gas-soaking cubes of olivine in 0.5 bar of He using a 1-atmosphere furnace. These cubes of olivine were then crushed and melted in the extraction line of a mass spectrometer. Partition coefficients were calculated only using the gas extracted by melting.

In contrast, more recent work utilizing Rutherford Backscattering (RBS) analysis suggests that Ar is highly compatible in both olivine and pyroxene, with partition coefficients up to ~10^4 (assuming literature values for noble gas solubility in melts, Watson et al., 2007; Thomas et al., 2008). These studies employed a constant source diffusion approach to defining Ar solubility in minerals, using Ar as the pressure medium and ranging Ar fugacity (fAr) between ~1 and 10^4 bar. Over the duration of the experiments Ar diffused into the minerals, producing concentration profiles. These profiles were relatively short (~100 nm). Results using this approach are in stark contrast to other experimentally determined Ar partition coefficients and diffusivities, though similar to the values found in early studies (Broadhurst et al., 1990, 1992; Shibata et al., 1994) at high fAr. The disagreement in experimental values casts large uncertainties on how noble gases behave (partitioning and diffusion) in the mantle and during melting.

In the present study, we report the results from two complimentary series of experiments aimed at better constraining noble gases partition during MORB (mid-oceanic ridge basalt) genesis. Most existing partitioning data were measured at pressures

below 2 kbar (e.g. Heber et al., 2007; Parman et al., 2005), much lower than the pressures at which MORB production occurs (10-30 kbar). Our experiments were performed up to 20 kbar to explore the effect of pressure on noble gas partitioning. The experiments are designed to maximize the amount of inclusion-free crystal available for analysis after the experiments. Lower pressure experiments (750 to 1150°C and 0.75 to 2 kbar) were conducted in an externally heated pressure vessel (EHPV), and higher pressure experiments were conducted in a piston cylinder (PC) apparatus (1380 to 1450°C and 20 kbar). For this work, we focused on determining He partitioning. However, adsorbed Ar was present in the all PC series experiments and Ne was present in a single PC series experiment, allowing for some inter-noble gas comparison. Combined, He partition coefficients for olivine, orthopryoxene, clinopyroxene, and spinel have been determined over a range of pressures and temperatures that are directly applicable to MORB genesis (~1400°C and 20 kbar). The reported dataset allows for the quantitative evaluation of how partial melting in the upper mantle redistributes He and provides insight into the solution mechanisms for noble gases in geologically relevant solids.

2.0 Methods:

A brief description of the experimental and analytical methods is provided below. For a complete description of the methods, see the Supplementary Material.

2.1 PC Series Approach:

The PC series utilized a piston cylinder apparatus (Brown University) and experiments were run at 20 kbar and 1380-1450°C. Noble gases were introduced by gas-loading the capsules using a method similar to that described by Boettcher et al. (1989). There were two inner graphite capsules in each PC series experiment; one containing a pair of polished, gem quality minerals, and the other containing a silicate liquid with basaltic composition (Figure 1a). Over the duration of the experiment both the mineral and melt diffusively equilibrated with the imposed partial pressure of noble gases in the Pt outer capsule. Partition coefficients were calculated as the ratio of noble gas concentration in the crystal to that determined for the silicate melt run in the same experiment. This approach does not require an a priori estimate for P_{He} for calculating partition coefficients.

2.2 EHPV Series Approach:

The EHPV series utilized an externally heated pressure vessel (Brown University), using He as the pressure medium. For each experiment, three polished, gem quality minerals were loaded into the hotspot of the pressure vessel in individual capsules where they diffusively equilibrated with the imposed partial pressure of He (Figure 1b). Partition coefficients were calculated as the ratio of the measured [He] in the mineral to the [He] in a basaltic liquid in equilibrium with the same P_{He} (Iacono-Marziano et al. 2010). See Table A.1 for values of [He] calculated for basaltic liquids.

2.3 Noble Gas Analysis:

Noble gas concentrations of the experimental run products were determined using a 193 nm laser ablation-noble gas mass spectrometer system at the Open University (UK). Because no internal standard is present in the analyzed samples, noble gas concentrations were calculated as the ratio moles of noble gas released during an ablation and the total mass of material ablated. The total volume of material ablated was determined by imaging each ablation pit using a white light interferometer, and volume was converted by mass by applying estimated densities. Analytical blanks are calculated each day as the average of the individual blanks run for a port. The detection limit for a given day and port is defined as 3σ of the blank mean. Analytical blanks are provided in Table A.1.

Confidence limits for each data point include the analytical uncertainty on the crystal analysis (regression and blank variability, typically <10%), crystal pit volume uncertainty (estimated to be 33%), and glass pit volume uncertainty (estimated to be 10%). All uncertainties are propagated as independent and Gaussian. A complete listing of noble gas concentration measurements, associated uncertainties, experimental conditions, and He partition coefficients are given in Table A.1 for both the PC and EHPV series. Minerals compositions and provenance are provided in Table A.2.

3.0 Results:

No melts were present in the EHPV series experiments. For a given P_{He}, the equilibrium concentration of He in a basaltic liquid has been calculated from published

solubility data (Iacono-Marziano et al. 2010), allowing for the determination of the corresponding partition coefficient. Not requiring an equilibrium melt phase to determine a partition coefficient allows for a wider range of temperatures to be explored and greater quantification of temperature dependence on He partitioning. The temperature dependence of He solubility in basaltic liquids is modest (e.g. Jambon et al., 1986; Lux, 1987), allowing for extrapolation of He solubility in melts to the relatively low temperatures of the EHPV series. Partition coefficients for the PC series experiments are calculated by ratioing [He] measured for the mineral and [He] measured for the glass from the same experiment.

3.1 Equilibrium Considerations:

Several lines of evidence suggest the He concentrations measured for this study closely approach equilibrium values. First, run products were depth profiled to explore for surface enrichments or concentration gradients. Depth profiling for He was accomplished by ablating separate pits to variable depths, effectively averaging different depth ranges in different ablation pits. No significant correlation between average pit depth and apparent K_d^{He} is observed (Figure 2), indicating the measured He was not confined to a surficial layer associated with mineral preparation. Average pit depth is defined as the average depth of pixels summed together during the volume analysis of a single ablation pit. A more detailed description of the volume analysis procedure is provided in the Supplemental Methods. Further, no significant correlation between duration and apparent K_d^{He} is observed (Figure 2). This observation, in combination with

the lack of correlation between average pit depth and apparent K_d^{He}, suggests the measured concentrations closely approach solubility. We define solubility as the concentration of He dissolved in a mineral in equilibrium with a given P_{He}, where P_{He} is not necessarily equal to confining pressure, as is the case for the PC series.

Given the uncertainties in He diffusivity, it is possible that some of the material analyzed in the shortest duration and lowest temperature experiments was not fully equilibrated. For example, the parameters for He ‖ b diffusion in olivine reported by Cherniak and Watson (2012) predict an e-folding distance for EHPV series experiment 3 (72 hours, 700 °C) of 25 μm (e-folding distance = distance over which the surface concentration is reduced by a factor of e). However, the net effect of this disequilibrium would be relatively small, if present at all, as the average pit depth in EHPV experiment 3 only approaches 20 μm. In this case, the measured concentration will be a factor of two lower than the true solubility and well within the variability of the data. Other recently reported He diffusion parameters predict longer e-folding distances, making this analysis an upper limit.

The fact that the PC and EHPV series yield overlapping estimates for He partition coefficients, despite significantly different experimental methodologies, also indicates equilibrium was closely approached.

All run products were carefully inspected before and after the experiment, and all reported data are from minerals with no indication of decomposition. Two high temperature (1150°C) olivine EHPV run products developed a frosted appearance during the experiment. The frosted surfaces contained greater quantities (~10×) of He as

compared to the clear surfaces, and consequently these data are not reported here. It is unclear what process led to the frosted appearance of minerals run at high temperatures.

A traverse of the glass from a representative experiment (PC series experiment 13) shows no resolvable He concentration gradient from the center to the rim of the melt (Figure 4). Although the center-most data point is higher than the remainder, diffusive loss would generate a concave down profile, rather than the observed concave up profile. The lack of a He concentration gradient demonstrates a close approach to equilibrium between the silicate melt and noble gas-bearing vapor present in the PC series experiment. It also suggests that He was not rapidly lost from PC series experiments.

3.2 Helium in olivine:

The median of all olivine partition coefficients is 2×10^{-4}, and the variability for individual calculations ranges from 2.2×10^{-5} to 5.7×10^{-4} (Table A.1, column Y). This median and range excludes PC experiment 7 (due to low precision) and analyses with signals lower than blank (single analysis). The total range of [He] measured in olivine is; -4.10×10^{-12} -2.64×10^{-8} mol g^{-1} (Table A.1, column Q). No significant correlations exist between the solubility of He in olivine (or the partition coefficient) and ablation pit depth, duration, pressure, P_{He}, and temperature at current analytical precision. The partition coefficients determined from experiment 7 of the PC series cluster higher ($\sim10^{-2}$) than the remainder of data for olivine but are uniformly within error of zero because of the small volume ablation pit volumes and consequently low signal. Fe-bearing olivines (OL_Fe,

San Carlos olivine) have similar He solubility compared to Fe-free olivine (OL ,synthetic).

3.3 Helium in pyroxene:

The partition coefficients for all pyroxenes are similar. The median of all orthopyroxene partition coefficients is 1.5×10^{-4}, and the variability for individual measurements ranges from 5.2×10^{-5} to 1.5×10^{-3} (Table A.1, column Y). The median of all clinopyroxene partition coefficients is 1.4×10^{-4}, and the variability for single calculations ranges from 1.2×10^{-5} to 4.2×10^{-4} (Table A.1, column Y). The total range of [He] measured in all pyroxenes is 5.18×10^{-10} to 2.63×10^{-8} mol g^{-1} (Table A.1, column Q). No significant correlations exist between the solubility of He in pyroxene (or the partition coefficient) and ablation pit depth, duration, pressure, P_{He}, and temperature. The OPX data from the PC series are shifted to slightly higher values compared to the OPX data from the EHPV series. The mean of the OPX PC series partition coefficients, however, is not significantly higher that the mean of the OPX EHPV series data (95% confidence). The different clinopyroxenes and orthopyroxenes studied have similar He solubility, and pyroxenes with different major element chemistry also have similar He solubility. Improvement in analytical precision may allow more subtle correlations to be evident.

3.4 Helium in spinel:

The average of all spinel partition coefficients is 2.6×10^{-4}, and the variability for individual calculations ranges from 4.2×10^{-6} to 3.8×10^{-4} (Table A.1, column Y). This average neglects analyses with signals lower than blank (single analysis). The total range of [He] measured in spinel is -1.10×10^{-7} to 1.14×10^{-8} mol g^{-1} (Table A.1, column Q). No significant correlations exist between either the solubility of He in spinel (or the partition coefficient) and ablation pit depth, duration, pressure, P_{He}, and temperature. The Cr-bearing aluminate spinel (SP_Cr) data from the PC series are shifted to lower values compared to the SP_Cr data from the EHPV series. The mean of the SP_Cr PC series partition coefficients is significantly lower that the mean of the EHPV series data (95% confidence). The magnitude of the different, however, is small: 4×10^{-5} for SP_Cr and 3×10^{-4} for the remainder of spinels. Thus, the data indicate that spinels with different major element compositions have similar He solubility, albeit with some minor differences.

3.5 Argon and Neon in PC Series

Argon concentrations in the PC series minerals are more variable compared to He (Table A.1). This variation likely stems from the incorporation of small amounts of residual graphite in the analyzed volume. In a preliminary series of experiments that were loaded with He-Ne-Ar gas, a correlation was observed between the density of residual graphite included in an analysis and Ar and to a lesser extent Ne (not He) concentrations, suggesting graphite contamination leads to apparently high solubilities for heavier noble gases. Surrounding the polished mineral faces with glassy carbon

significantly reduces the amount of residual graphite but does not completely eliminate it. Consequently, the reported Ar and Ne concentrations for PC series experiments 10-13 are not accurate measures of solubility. Special care was taken in PC series experiment 7 to analyze the shallow region of a crystal with minimal adhering carbon and this experiment provides are best constraints of Ar and Ne solubility in olivine at the conditions of MORB genesis (see Discussion 4.5).

3.6 Major Elements

Major element oxide for crystals and melts (PC series only) are reported in Table A.2 and A.3, respectively. Sums for the melts are consistently ~3 wt. % low (Table A.3). PC series capsules contain large amounts of graphite and head space. Both qualities make these experiments prone to the incorporation of atmospheric gases, such as water, O_2 (converted to CO_2 during experiment), N_2, and Ar. Based on the consistency of the EHPV series results and PC series results, the presence of these other volatiles does not have a large effect on noble gas partitioning, although it has been suggested that water in silicate liquid acts to increase the solubility of He in melts (addition of 3 wt. % H_2O causes a factor of 3 increase, Paonita et al., 2000).

4.0 Discussion:

4.1 Comparison with Previous Work:

Previously reported noble gas partition coefficients vary widely. For example, different studies have yielded Ar partition coefficients that range from ~10^{4} to ~10^{-4} (i.e. Thomas et al, 2008; Heber et al. 2007). Reported He partition coefficients also display large variance, ranging from nearly compatible to ~10^{-4} (i.e. Shibata et al., 1994; Heber et al. 2007). In comparison to this variance, the He partitioning data reported here are in general agreement (order of magnitude) with the most recently reported partitioning data (Heber et al., 2007; Parman et al., 2005, Figure 5). It is important to note that these two earlier studies used different methods compared to the present study. Heber et al. (2007) grew crystals directly from noble gas-bearing melts (simple systems) and analyzed the run products using a UV (213 nm) laser. Parman et al. (2005) gas-soaked large grains of olivine and analyzed them using a crush-melt degassing method. This study utilizes a hybrid approach of gas soaking polished mineral grains and UV (193 nm) laser ablation analysis. There is some indication that experiments conducted at lower P_{He} (Parman et al., 2005) yield higher He partition coefficients compared to experiments conducted at higher P_{He} (this study, Heber et al., 2007). The difference in partition coefficient between these most recent studies, however, is small when compared to the range from earlier, bulk degassing studies (Broadhurst et al., 1990, 1992; Hiyagon and Ozima, 1982, 1986; Shibata et al., 1994).

4.2 Henry's Law and the effect of P_{He}:

Experiments were conducted at noble gas partial pressures that are unnaturally high in order to achieve precise analyses. As such, the applicability of Henry's Law must

be evaluated before partition coefficients can be used to model noble gas behavior. For Henry's Law to apply to He partitioning, the partition coefficient must be independent of P_{He}, i.e. the solubility of He in mineral and melts are both linearly proportional to P_{He}. For melts, the solubility of noble gases have been demonstrated obey Henry's Law (e.g. Carroll and Stolper, 1993; Chamorro-Perez et al., 1998; White et al., 1989, Jambon et al. 1986, Paonita et al. 2000). An equivalent demonstration has not been made for noble gas dissolution into upper mantle minerals. However, the range of P_{He} in the present study is too small and variability in measured He solubilities too large to adequately evaluate the applicability of Henry's Law.

To expand the range of P_{He} for comparison, we compiled published studies of He partitioning (Heber et al., 2007; Parman et al., 2005). Total confining pressure, temperature, and composition are not constant across this compilation, making this comparison not a strict evaluation of Henry's Law. However, the results of this study suggest the effect of these variables on He solubility is small (Figure 3). We note that noble gas solubility is linearly correlated with pressure up to moderate pressures (<1 kbar) at elevated temperatures when confining pressure, noble gas partial pressure, and noble gas fugacity are sub-equal. This indicates ΔV associated with noble gas dissolution is small, and equivalently, that the effect of confining pressure on noble gas solubility is also small in the EHPV series (e.g. Carroll et al., 1994). Although a wide range of methods were employed, the He partition coefficients range between $\sim 10^{-3}$ and 10^{-4}, while spanning more than three orders of magnitude (0.5 to 2000 bar) in P_{He} (Figure 5). It is clear that He solubility in olivine increases with P_{He}, but the variability in the data makes it uncertain if the correlation is linear or non-linear.

For Henry's Law to be applicable to He dissolution in olivine, the data compiled in Figure 5 should plot along a single line. The lowest partition coefficients of Parman et al. (2005) do overlap with the highest partition coefficients determined here, which is broadly consistent with Henry's Law. However, there is some evidence that partition coefficients determined at low P_{He} are higher than partition coefficients determined at high P_{He}. This may reflect He solubility in olivine not obeying Henry's Law at higher P_{He} (~1 kbar) or a difference associated with the different experimental and analytical methods employed at low P_{He} and high P_{He}.

If He solubility in mantle minerals departs negatively from Henry's Law at high P_{He}, the experiments run at low P_{He} (i.e. Parman et al., 2005) will be most applicable modeling the behavior of He in the upper mantle. Undegassed MORB melt contains ~10 ppb He (Javoy and Pineau, 1991; Moreira et al., 1998), which requires ~0.1 bar P_{He} using He solubility data for basalts from Lux (1987). This simple analysis predicts a He partition coefficient ~10^{-2} at natural partial pressure for the most extreme non-Henrian behavior consistent with current data. Estimates of upper limit He partition coefficients (olivine-melt) determined using natural samples (low P_{He} environment) range between 5.8×10^{-3} and ~10^{-1} (Kurz, 1993; Marty and Lussiez, 1993; Valbracht et al., 1994). Further improvements in the precision of the measurements at low concentrations are needed to resolve the applicability of Henry's Law to He dissolution into mantle minerals.

4.3 Confining Pressure, Temperature, fO_2, and Compositional Effects:

4.3.1 Confining Pressure:

The high-pressure data from the PC series are within the uncertainty of low-pressure EHPV series data, indicating confining pressure has, at most, a modest effect on He partitioning up to 20 kbar (Figure 3). Chamorro et al. (2002) conducted a similar series of experiments, exploring the partitioning systematics of Ar (and K) between clinopyroxene and albite-diopside melts up to 8 GPa. Both the $Albite_{20}Diopside_{80}$ and $Albite_{80}Diopside_{20}$ melt series do not show any resolvable pressure effect, consistent with the current findings for He. Combined, these observations suggest the effect of confining pressure on noble gas solubility in upper mantle minerals is small. Experimental and theoretical arguments suggest noble gas solubility in silicate melts deviates from Henry's Law at high pressures, likely due to structural changes in melt structure upon compression (e.g. Chamorro-Perez et al., 1998; Guillot and Sator, 2012). It is expected that the light noble gases will deviate at relatively high pressures while heavier noble gases may deviate at pressures associated with MORB and OIB genesis. This is because heavier noble gases require large voids in the silicate liquid structure, and these large voids are more prone to collapse with pressure compared to the smaller voids that facilitate the dissolution of lighter noble gases (Guillot and Sator, 2012). If the solubilities of noble gases in minerals are insensitive to confining pressure, heavy noble gas partition coefficients may shift to higher values at pressures applicable to upper mantle melting due to their decreased melt solubility.

4.3.2 Temperature, Composition, and fO_2:

No temperature dependence on He partitioning is observed over the conditions explored in the PC and EHPV series. A small temperature dependence for He partitioning is consistent with the weak bonds (Van der Waals) noble gases form in materials. However, it is possible that a modest dependence on temperature is obscured by the variability in the reported data (factor of ~10). Figure 3 shows He partition coefficients as a function of temperature for the suite of minerals investigated. The lack of obvious temperature dependence for He partitioning by olivine, pyroxene, and spinel, combined with the modest temperature dependence for He solubility in silicate melts (Jambon et al., 1986; Lux, 1987), provides a basis of extrapolation of measured partition coefficients to more extreme temperatures.

To explore the effects of composition and fO_2 on noble gas solubility in silicates, He solubility has been determined for range of olivines, pyroxenes, and spinels with variable compositions and point defect populations. For olivine and pyroxene, fO_2 and Fe content primarily affect the concentration of octahedral site vacancies according to the following reaction:

$$3Fe_M^X + \frac{1}{2}O_2 = 2Fe_M^{\cdot} + V_M^{''} + FeO \quad [1]$$

where subscripted M refers to the octahedral site in olivine and V refers to a lattice vacancy. The presence of graphite constrains the fO_2 of the PC series experience to below GCO (~QFM-2 at 20 kbar) and the nearly pure Mo metal in the pressure vessel constrains the fO_2 of the EHPV series to at or below MMO, or ~IW. Unoccupied sites or

lattice vacancies may be important hosts for noble gases in solids because charge neutrality is not upset by the incorporation of neutral atoms onto these sites (Shcheka and Keppler, 2012; Jackson et al., 2013). Importantly, the majority disorder for ferromagnesian olivine is the oxygen activity disorder described by reaction [1] (Hirsch and Shankland, 1993).

Higher concentrations of Fe and higher fO_2 result in higher concentrations of extrinsic octahedral site vacancies ($V_M^{''}$ in reaction [1]), for a given $aSiO_2$. The observation that He is equally soluble in pure forsterite (experiments conducted with OL, Fe-free) and San Carlos olivine (experiments conducted with OL_Fe, Fe-bearing) suggests $V_M^{''}$ are not the dominant hosts for He in olivine. A similar conclusion can be drawn for pyroxene, as He partitions equally (to current precision) into all four pyroxenes investigated (Figure 2 and 3), although the range is Fe content in the experimental pyroxenes is relatively narrow (Table A.2). This suggests changes in mantle Fe content and fO_2 do not have a large effect on the partitioning of He by peridotite minerals. This finding is consistent with the previously reported results for Sc-doped olivine (Heber et al., 2007) but is inconsistent with proposed solution mechanisms for Ar in olivine and pyroxene (Thomas et al., 2008).

Helium solubility in a stoichiometric and Al_2O_3-rich spinel was also measured. Excess Al_2O_3 in the spinel structure is accommodated via the generation tetrahedral and/or octahedral vacancies (e.g. Ting and Lu, 1999):

$$Al_2O_3 + 3Mg_{IV}^{X} = 2Al_{IV} + V_{IV}^{''} + 3MgO \quad (2)$$

$$3Al_2O_3 + 6Mg_{iv}^{X} + 2Al_{vi}^{X} = 6Al_{iv} + 2V_{vi}^{'''} + MgAl_2O_4 + 5MgO \quad (3)$$

The magnitude of excess Al_2O_3 in the spinel investigated is large (Table A.2), generating a high density of cation vacancies compared to the Fe-bearing olivine and pyroxene. Despite the highly contrasting density of vacancies in the three investigated spinels, there is no significant variation in He partitioning (Figure 2 and 3). The radius of the tetrahedral site in spinel is similar to the octahedral site in olivine, supporting the inference that Mg-Fe vacancies in olivine and pyroxene are not major hosts for He.

The diopside and forsterite studied here are synthetic and stoichometric, indicating the majority disorder will be the intrinsic type defects in these minerals. Intrinsic point defect concentrations are highly temperature dependent due to the strong increase in configurational entropy associated with their presence. For stoichometric forsterite, the majority intrinsic disorder is likely Frenkel (Smyth and Stocker, 1975), where a lattice magnesium ion occupies an interstitial site, creating, too, a $V_M^{''}$. Frenkel equilibrium is homogenous, and therefore, is rapidly established. The fact that temperature does not strongly correlate with K_d^{He} for forsterite or diopside supports the inference that octahedral vacancies are not significant hosts of He in mantle silicates. More precise analysis of He solubility may reveal more subtle correlations.

Oxygen vacancies ($V_O^{\cdot}$) are large radius, zero charge sites, and therefore, may be energetically favorable locations for noble gas dissolution (Shcheka and Keppler, 2012). However, $V_O^{\cdot}$ are minority defects in olivine. Consequently, their abundance is extremely low and varies inversely to Fe content and fO_2 under the P-type regime. Thus, the

similarity of He solubility in San Carlos olivine (OL_Fe) and forsterite (OL) suggests $V_O^{\cdot\cdot}$ are not the dominant hosts for He in olivine.

The similarity of He solubility across different minerals types with different point defect populations suggests that interstitial sites are important hosts for He in mantle minerals. This suggestion is consistent with atomistic simulations of He incorporation into jadeite and periclase (Brooker et al., 2003; Tsuchiyama and Kawamura, 1994), although larger radius or more polarized sites may be more important for the dissolution of heavier (larger radii and more polarizable) noble gases (Brooker et al., 2003; Shcheka and Keppler, 2012; Thomas et al., 2008; Tsuchiyama and Kawamura, 1994).

4.4 Helium Diffusivity Constraints:

Many methods have been used to quantify kinetic behavior of helium diffusion in olivine. The bulk of studies report activation energies of ~125 kJ mol^{-1} (Blard et al., 2008; Cassata et al., 2011; Cherniak and Watson, 2012; Futagami et al., 1993; Shuster et al., 2004; Tolstikhin et al., 2010; Trull et al., 1991), while two studies report relatively high activation energies of ~450 kJ mol^{-1} (Hart, 1984; Trull and Kurz, 1993). High activation energies lead to slow predicted diffusivities at low temperatures and correspondingly small amounts of equilibrated material. For example, application of the diffusion parameters of from Hart (1984) or Trull and Kurz (1993) predict He diffusive length scales of <<1 μm (e-folding distance) for EHPV series experiment 3 (700°C, 72 hrs.). Application of diffusion parameters from the remaining studies with lower activation energies predict >10 μm diffusive length scales (Blard et al., 2008; Cassata et

al., 2011; Cherniak and Watson, 2012; Futagami et al., 1993; Shuster et al., 2004; Tolstikhin et al., 2010; Trull et al., 1991). No correlation between ablation pit average depth and He concentration is observed, even at low temperatures, indicating measureable quantities of He diffused >>1 μm (Figure 2) and supporting the use of the lower activation energies in He diffusion calculations. Importantly, in this study He diffusion occurred through a relatively undamaged olivine lattice that is similar to olivine under mantle conditions.

4.5 Partitioning Constraints for Ar and Ne:

Watson et al. (2007) and Thomas et al. (2008) highlight the potential geologic importance of low activation energy, high solubility mechanisms for Ar in a variety of minerals, including olivine and pyroxene. Although no Ar was intentionally loaded into the PC series capsules, except for PC experiment 7, all of these experiments did contain measureable concentrations of Ar, presumably present initially as adsorbed gas on the graphite capsules and starting materials (Table A.1). Results from PC series experiment 7 are compared to the results reported by the RPI group because the crystal run products from this experiment were most finely depth profiled and the duration was 8 hours longer than the other in the PC series. Both of these qualities increase the likelihood that we would observe the low activation energy, high solubility mechanism, if present in the PC series.

For the conditions of PC series experiment 7 (10 hrs, 1450°C, San Carlos olivine), the diffusion parameters reported by Thomas et al. (2008) for forsterite predict a ~20 nm

diffusive length scale for Ar. While these profiles are shorter than the maximum depth resolution of the 193 nm laser used in this study (~50 nm, Clay et al., 2010), the predicted concentrations are high enough to be detectable. To calculate the expected concentration for a given analysis, we assume a 2.5×10^{-5} mol g^{-1} (1000 ppm) Ar solubility, which is a lower limit given the results of Thomas et al. (2008) for Fe-bearing olivine. We then integrate the one-dimensional, concentration-independent expression for diffusion into a semi-infinite medium from a constant source to obtain the predicted Ar concentration given the depth of ablation for a particular analysis. Figure 6 compares the predicted Ar concentration for the first analysis of the depth profile if the low activation energy, high solubility mechanism were operable to the concentrations measured during the depth profile. In this experiment, the olivine was depth profiled in the conventional sense (as opposed to the depth profiling completed on the remainder of minerals), where material from one spot was analyzed at sequentially deeper horizons. Figure 6 also compares the predicted Ar concentration for a deeper, single step ablation pit to the actual measured value. In both cases, measured [Ar] is substantially lower than predicted if the low activation energy, high solubility mechanism was operating in a similar fashion to that reported by Thomas et al. (2008) in olivine. It is worth noting that all Ar analyses for PC series experiment 7 are within analytical (not accounting for pit volume uncertainties) error of zero. Changes in pressure, temperature, and fO_2 do not appear to substantially affect the properties of the low activation energy, high Ar solubility mechanism (Thomas et al., 2008), suggesting its absence is not simply the result of the higher temperatures and pressures of the PC series. From this single PC Series experiment, is it unclear why the low activation energy, high solubility mechanism was not observed. We note that in on-

going, long duration, high temperature experiments on San Carlos olivine using an EHPV and a He-Ne-Ar pressure medium, we do observe relatively high concentrations of Ar in the shallowest analyses. This may be consistent with the results of Watson et al. (2007) and Thomas et al. (2008). However, He and Ne are not anomalously concentrated in the shallowest analyses. More work is needed to understand when the low activation energy, high solubility mechanism controls the behavior of Ar in geological systems.

The data from PC series experiment 7 can be used to place constraints on Ne and Ar partitioning under mantle conditions. No measurement of Ne or Ar concentration exceeded the nominal session detection limit (3σ above blank). Assuming solubility is below the detection limit, upper limit partition coefficients are determined by ratioing the Ne and Ar detection limits to their respective concentration in the melt. This approach yields olivine-melt partition coefficients of $<10^{-2}$ for Ne and $<10^{-3}$ for Ar. It is implicit in this analysis that the material analyzed in the crystal equilibrated with Ne and Ar. We believe these upper-limit partition coefficients are valid since they are corroborated by the lack of evidence for the low activation energy, high Ar solubility mechanism in PC Series experiment 7 and the relatively rapid rates for Ar diffusion reported for mantle silicates by other researchers at magmatic temperatures (e.g. Cassata et al., 2011). The melt noble gas concentrations in PC series experiment 7 are repeatable, implying equilibrium was closely approached between the noble gas-bearing vapor and the silicate liquid.

4.6 (U+Th)/He Fractionation During MORB Genesis:

Current data demonstrates light noble gases (He-Ar) are moderately to highly incompatible in the minerals present during MORB genesis under appropriate mantle conditions. Given the currently available partitioning data for spinel-peridotite minerals, there are three basic scenarios for (U+Th)/He fractionation during MORB genesis (Figure 7). These scenarios will produce different outcomes for He isotope variations during partial melting of the mantle. The field of partition coefficients for $U+Th_{avg.}$ in the following model is sourced directly from the published range (Supplementary References).

1) Helium partitions according to the median of the results from the present study, $\sim 2\times10^{-4}$, under natural conditions. This is our preferred set of naturally applicable partition coefficients (Table 1), and these partition coefficients are similar to those determined by Heber et al. (2007). Application of these partition coefficients to natural systems assumes Henry's Law applies to He solubility in olivine and pyroxene. In this scenario, He is preferentially extracted from the mantle compared to U+Th until near clinopyroxene exhaustion (cpx-out). Moderate degrees of melting should preferentially extract He, but high degrees of melting, associated with hotter mantle, should result in lower (U+Th)/He and low [He] for the melting residue.

2) Helium partitions between minerals and silicate melts according to the lower end of variability because higher values are due to unseen melt or fluid inclusions, $\sim 2\times10^{-5}$, under natural conditions. In this scenario, He is preferentially extracted from the mantle until melting approaches the opx-out

point. Under these conditions, melting residues should always possess elevated (U+Th)/He for F <0.35.

3) Helium solubility in olivine and pyroxene deviates negatively from Henry's Law at high P_{He} (i.e. solubility at low P_{He} is higher than predicted by high P_{He} experiments) and the naturally applicable partition coefficient is ~10^{-2}. In this scenario, He, U, and Th have similar partition coefficients for clinopyroxene, but He is more compatible in orthopyroxene and olivine. This results in preferential retention of He relative to U+Th under all degrees of melting. Following this, melting residues will have depressed (U+Th)/He compared to the initial source values, and the concentrations of these elements can be high relatively high. This is especially true if the melting residues are formed early in Earth history, when less mantle degassing had occurred.

DMM is marked by $^4He/^3He$ that is relatively homogenous and higher than many OIB, implying OIB sources have lower time-integrated $(U+Th)/^3He$ than DMM. In scenarios 1 and 3, typical degrees of melting produces residues of melting with $(U+Th)/^3He$ that is similar to or less than the initial source value, making back-mixing of depleted peridotite (via subduction or delamination) an inefficient mechanism for preferentially increasing $(U+Th)/^3He$ of DMM through time. Oceanic crust is a high $(U+Th)/^3He$ reservoir (due to the degassed nature of oceanic crust), and it is well established that large volumes have been recycled back into the mantle through subduction. Therefore, the higher $^4He/^3He$ of DMM likely reflects extensive recycling of

oceanic crust back into DMM, rather than preferential loss of He over U+Th during melting (e.g. Gonnermann and Mukhopadhyay, 2009).

5.0 Conclusions:

We report He partitioning in peridotite minerals (ol, opx, cpx, spinel) at the conditions applicable to MORB genesis. Helium is moderately (non-Herian solution behavior) to highly (low end of variability) incompatible in the minerals present during MORB genesis. Confining pressure, temperature, and composition do not have significant effects on He solubility in peridotite minerals up to 20 kbar and 1400°C, suggesting the use of constant partition coefficients is warranted and that noble gases are evenly distributed between the upper mantle minerals. Helium solubility systematics suggest interstitial sites are important hosts for He in olivine, pyroxene, and spinel. Melting scenarios derived from current data partitioning data suggest partial melting of peridotite is not an efficient mechanism for raising $(U+Th)/^{3}He$ of DMM relative to low $^{4}He/^{3}He$ OIB mantle domains. Limited data on Ne and Ar suggest they have similar incompatibilities as He during peridotite melting.

References:

Allegre, C.J., Hofmann, A., Onions, K., 1996. The Argon constraints on mantle structure. Geophysical Research Letters 23, 3555-3557.

Ballentine, C.J., Marty, B., Lollar, B.S., Cassidy, M., 2005. Neon isotopes constrain convection and volatile origin in the Earth's mantle. Nature 433, 33-38.

Blard, P.H., Puchol, N., Farley, K.A., 2008. Constraints on the loss of matrix-sited helium during vacuum crushing of mafic phenocrysts. Geochimica Et Cosmochimica Acta 72, 3788-3803.

Boettcher, S.L., Guo, Q., Montana, A., 1989. A simple device for loading gases in high-pressure experiments. American Mineralogist 74.

Broadhurst, C.L., Drake, M.J., Hagee, B.E., Bernatowicz, T.J., 1990. Solubility and partitioning and Ar in anorthite, diopside, forsterite, spinel, and synthetic basaltic liquids. Geochimica Et Cosmochimica Acta 54.

Broadhurst, C.L., Drake, M.J., Hagee, B.E., Bernatowicz, T.J., 1992. Solubility and partitioning of Ne, Ar, Kr, and Xe in minerals and synthetic basaltic melts. Geochimica Et Cosmochimica Acta 56.

Brooker, R.A., Du, Z., Blundy, J.D., Kelley, S.P., Allan, N.L., Wood, B.J., Chamorro, E.M., Wartho, J.A., Purton, J.A., 2003. The 'zero charge' partitioning behaviour of noble gases during mantle melting. Nature 423, 738-741.

Brooker, R.A., Wartho, J.A., Carroll, M.R., Kelley, S.P., Draper, D.S., 1998. Preliminary UVLAMP determinations of argon partition coefficients for olivine and clinopyroxene grown from silicate melts. Chemical Geology 147.

Carroll, M.R., Draper, D.S., Brooker, R.A., Kelley, S., 1994. Noble gas solubilities in melts and crystals. Noble Gas Geochemistry and Cosmochemistry. Terra Scientific Publications, 325-341.

Carroll, M.R., Stolper, E.M., 1993. Noble gas solubilities in silicate melts and glasses: New experimental results for argon and the relationship between solubility and ionic porosity. Geochimica et Cosmochimica Acta 57, 5039-5051.

Cassata, W.S., Renne, P.R., Shuster, D.L., 2011. Argon diffusion in pyroxenes: Implications for thermochronometry and mantle degassing. Earth and Planetary Science Letters 304.

Chamorro, E.M., Brooker, R.A., Wartho, J.A., Wood, B.J., Kelley, S.P., Blundy, J.D., 2002. Ar and K partitioning between clinopyroxene and silicate melt to 8 GPa. Geochimica Et Cosmochimica Acta 66.

Chamorro-Perez, E., Gillet, P., Jambon, A., Badro, J., McMillan, P., 1998. Low argon solubility in silicate melts at high pressure. Nature 393.

Cherniak, D., Watson, E., 2012. Diffusion of helium in olivine at 1atm and 2.7 GPa. Geochimica Et Cosmochimica Acta.

Clay, P.L., Baxter, E.F., Cherniak, D.J., Kelley, S.P., Thomas, J.B., Watson, E.B., 2010. Two diffusion pathways in quartz: A combined UV-laser and RBS study. Geochimica Et Cosmochimica Acta 74.

Futagami, T., Ozima, M., Nagai, S., Aoki, Y., 1993. Experiments on thermal release of implanted noble gases from minerals and their implications for noble gases in lunar soil grains. Geochimica Et Cosmochimica Acta 57, 3177-3194.

Gonnermann, H.M., Mukhopadhyay, S., 2009. Preserving noble gases in a convecting mantle. Nature 459, 560-U588.

Guillot, B., Sator, N., 2012. Noble gases in high-pressure silicate liquids: A computer simulation study. Geochimica Et Cosmochimica Acta 80, 51-69.

Hart, S.R., 1984. He diffusion in olivine. Earth and Planetary Science Letters 70.

Heber, V.S., Brooker, R.A., Kelley, S.P., Wood, B.J., 2007. Crystal-melt partitioning of noble gases (helium, neon, argon, krypton, and xenon) for olivine and clinopyroxene. Geochimica Et Cosmochimica Acta 71, 1041-1061.

Hirsch, L.M., Shankland, T.J., 1993. Quantitative olivine defect chemical model – insights on electrical conduction, diffusion, and the role of Fe content. Geophysical Journal International 114, 21-35.

Hiyagon, H., Ozima, M., 1982. Noble gas distribution between basalt melt and crystals. Earth and Planetary Science Letters 58.

Hiyagon, H., Ozima, M., 1986. Parition of noble gases between olivine and basalt melt. Geochimica Et Cosmochimica Acta 50.

Iacono-Marziano, G., Paonita, A., Rizzo, A., Scaillet, B., Gaillard, F., 2010. Noble gas solubilities in silicate melts: New experimental results and a comprehensive model of the effects of liquid composition, temperature and pressure. Chemical Geology 279, 145-157.

Jackson, C.R.M, Parman, S.W., Kelley, S.P., Cooper, R.F., 2013, Noble gas transport into the mantle facilitated by high solubility in amphibole. Nature Geoscience 6, 562-565.

Jambon, A., Weber, H., Braun, O., 1986. Solubility of He, Ne, Ar, Kr, and Xe in a basalt melt in the range of 1250-1600 degrees C. Geochimica Et Cosmochimica Acta 50, 401-408.

Kurz, M.D., 1993. Mantle Heterogeneity beneath oceanic islands – some inferences from isotopes. Philosophical Transactions of the Royal Society of London Series a-Mathematical Physical and Engineering Sciences 342, 91-103.

Lux, G., 1987. The behavior of noble gases in silicate liquids – solution, diffusion, bubbles, and surface effects, with applications to natural samples. Geochimica Et Cosmochimica Acta 51, 1549-1560.

Marty, B., Lussiez, P., 1993. Constraints on rare gas partition coefficients from analysis of olivine-glass from a picritic mid-ocean ridge basalt. Chemical Geology 106, 1-7.

Moreira, M., Kunz, J., Allegre, C., 1998. Rare gas systematics in popping rock: Isotopic and elemental compositions in the upper mantle. Science 279, 1178-1181.

Nuccio, P., Paonita, A., 2000. Investigation of the noble gas solubility in H_2O-CO_2 bearing silicate liquids at moderate pressure II: the extended ionic porosity (EIP) model. Earth and Planetary Science Letters 183, 499-512.

Paonita A., Gigli G., Gozzi D., Nuccio P.M., Trigila R., 2000, Investigations of the He solubility in H_2O-CO_2 bearing silicate liquids at moderate pressure: a new experimental method. Earth and Planetary Science Letters 181, 595-604

Onions, R.K., Oxburgh, E.R., 1983. Heat and helium in the earth. Nature 306.

Parman, S.W., Grove, T.L., 2004. Harzburgite melting with and without H2O: Experimental data and predictive modeling. Journal of Geophysical Research-Solid Earth 109.

Parman, S.W., Kurz, M.D., Hart, S.R., Grove, T.L., 2005. Helium solubility in olivine and implications for high (3)He/(4)He in ocean island basalts. Nature 437, 1140-1143.

Robinson, J.A.C., Wood, B.J., Blundy, J.D., 1998. The beginning of melting of fertile and depleted peridotite at 1.5 GPa. Earth and Planetary Science Letters 155.

Shcheka, S.S., Keppler, H., 2012. The origin of the terrestrial noble-gas signature. Nature 490.

Shibata, T., Takahashi, E., Ozima, M., 1994. Noble gas partition between basaltic melt and olivine crystals at high pressures. Noble gas Geochemistry and Cosmochemistry, Terra Scientific Publishing Company, Tokyo, 343-354.

Shuster, D.L., Farley, K.A., Sisterson, J.M., Burnett, D.S., 2004. Quantifying the diffusion kinetics and spatial distributions of radiogenic He-4 in minerals containing proton-induced He-3. Earth and Planetary Science Letters 217, 19-32.

Smyth, D.M., Stocker, R.L., 1975. Point defects and nonstoichimetry in forsterite. Physics of the Earth and Planetary Interiors 10.

Thomas, J.B., Cherniak, D.J., Watson, E.B., 2008. Lattice diffusion and solubility of argon in forsterite, enstatite, quartz and corundum. Chemical Geology 253, 1-22.

Ting, C.J., Lu, H.Y., 1999. Defect reactions and the controlling mechanism in the sintering of magnesium aluminate spinel. Journal of the American Ceramic Society 82.

Tolstikhin, I., Kamensky, I., Tarakanov, S., Kramers, J., Pekala, M., Skiba, V., Gannibal, M., Novikov, D., 2010. Noble gas isotope sites and mobility in mafic rocks and olivine. Geochimica Et Cosmochimica Acta 74, 1436-1447.

Trull, T.W., Kurz, M.D., 1993. Experimental measuremetns of ^{3}He and ^{4}He mobilty in olivine and clinopyroxene at magatic temperatures. Geochimica Et Cosmochimica Acta 57.

Trull, T.W., Kurz, M.D., Jenkins, W.J., 1991. Diffusion and cosmogenic ^{3}He in olivine and quartz – implications for surface exposure dating. Earth and Planetary Science Letters 103.

Tsuchiyama, A., Kawamura, K., 1994. Sites and behaviors of noble gas atoms in MgO crystal simulated by the molecular dynamics (MD) method. Noble Gas Geochemistry and Cosmochemistry, Terra Scientific Publishing, Tokyo, 315-323.

Valbracht, P., Honda, M., Staudigel, H., McDougall, I., Trost, A., 1994. Noble gas partitioning in natural samples: results from coexisting glass and olivine phenocrysts in four Hawaiian submarine basalts. Noble Gas Geochemistry and Cosmochemistry. Terra Scientific, Tokyo, 373-381.

Watson, E.B., Thomas, J.B., Cherniak, D.J., 2007. Ar-40 retention in the terrestrial planets. Nature 449.

White, B.S., Brearley, M., Montana, A., 1989. Solubility of argon in silicate liquids at high pressures. American Mineralogist 74, 513-529.

.

Figure Captions:

Figure 1: Experimental design for PC Series (A) and EHPV Series (B). A) Cross-sectional view of sample capsule used in PC Series. Crystals and silicate melt equilibrate with a common noble gas-rich vapor while remaining physically separated. This approach allows for a substantial improvement in analytical precision in determining noble gas partition coefficients B) Cross-sectional view of assembly used in EHPV series. Three capsules are loaded into the hotspot of a TZM pressure vessel and the pressure medium is pure He, allowing for precise external measurement of P_{He} over the duration of the experiment.

Figure 2: Demonstrations of equilibrium for minerals: K_d^{He} plotted against experimental duration (top row) and average pit depth (bottom row). Each data point is an individual analysis of a crystal ratioed to the either the average He concentration in the corresponding silicate glass phase (PC Series) or the calculated He solubility in basaltic melt (EHPV Series). Pit depth is calculated as the average depth of pixels summed in volume calculations. See Supplemental Information for more detail. K_d^{He} does not correlate with duration, indicating solubility is closely approached. There is no correlation between K_d^{He} and average pit depth, indicating uniform concentrations of He diffused into the interior of minerals during experiments and that solubility is closely approached for a given P_{He}, pressure, and temperature. Partition coefficients from PC Series experiment 7 are uniformly within error of 0, and consequently are not plotted. For plotting clarity, data below 10^{-5} are not plotted (3 values).

Figure 3: Effect of temperature (top row) and pressure (bottom row) on partitioning: Each data point is an individual analysis of a crystal ratioed to the either the average He concentration in the corresponding silicate glass phase (PC Series) or the calculated He solubility in basaltic melt (EHPV Series). Both the experimental pressure and temperature do not correlate with He partition coefficient. The variability in the data is substantial, but the present data suggest the effect of temperature and pressure is not large. Partition coefficients from PC Series experiment 7 are uniformly within error of 0, and consequently are not plotted. For plotting clarity, data below 10^{-5} are not plotted (3 values).

Figure 4: Demonstrations of equilibrium for melts: [He] measured in silicate glass of PC Series experiment 12 plotted against distance from center of capsule. Each data point is an individual analysis of the glass phase. There is no correlation between [He] and distance from center of capsule indicating the entire melt phase equilibrated with a single P_{He}.

Figure 5: Henry's Law comparison: Experimental determinations of He solubility have been compiled and plotted with the currently reported data. Data collected at high P_{He} (~1 kbar) cluster between 10^{-11} and 10^{-12} mol g^{-1} bar^{-1} but considerable variability is present. Lower P_{He} data cluster above 10^{-11} mol g^{-1} bar^{-1} (Parman et al., 2005). Given the variability in recently reported He solubility measurements, it remains uncertain whether Henry's Law is satisfied up to 1 kbar P_{He} or if the higher P_{He} data negatively deviate from Henry's Law. Data from Parman et al. (2005) were collected by crush-melt analysis of

olivine crystals equilibrated with 0.5 bar He. Heber et al. (2007) datum is calculated from their preferred solubility summary. No data from the PC Series were included in this comparison.

Figure 6: Argon Comparison: Ar concentrations measured olivine exposed to Ar-rich vapor. Each green point is an individual analysis. All plotted values are below the detection limit (3σ above blank) and within error of zero. In comparison, the diffusion parameters and Ar solubilities of Thomas et al. (2008) predict [Ar] >10× the detection limit.

Figure 7: Comparison of He and $U+Th_{avg}$ partitioning during upper mantle melting: current partition coefficients suggest He is evenly distributed among the minerals of spinel-peridotite. In contrast, U+Th are concentrated in clinopyroxene. As clinopyroxene is preferentially melted out, U+Th become increasingly incompatible, where as He partitions at nearly the same value. If the dissolution of He into olivine and pyroxene deviates negatively from Henry's Law at high P_{He}, this behavior can result in residues of melting with depressed (U+Th)/He at only moderate degrees of melting. If Henry's Law applies to the current dataset, typical degrees of melting impart have relatively small changes to (U+Th)/He of melting residues. More incompatible behavior for He will tend to impart melting residues with elevated (U+Th)/He unless significant melting of harzburgite occurs. The melting reaction for lherzolite is from (Robinson et al., 1998). The melting reaction for harzburgite is taken to be 1 opx = 1 melt, which is

similar to experimentally derived harzburgite melting reaction at moderate pressure (Parman and Grove, 2004).

Table 1: Preferred Helium Partition Coefficients: The preferred He partition coefficients are calculated as the median value for all analyses of a single mineral type, e.g. olivine, neglecting data that are below blank and the data from PC Series experiment 7. The medians are preferred to the averages because the data are skewed to the right. Uncertainties are reported as 25-75% quartile values, providing lower and upper bounds, respectively.

Chapter 1, Figure 1

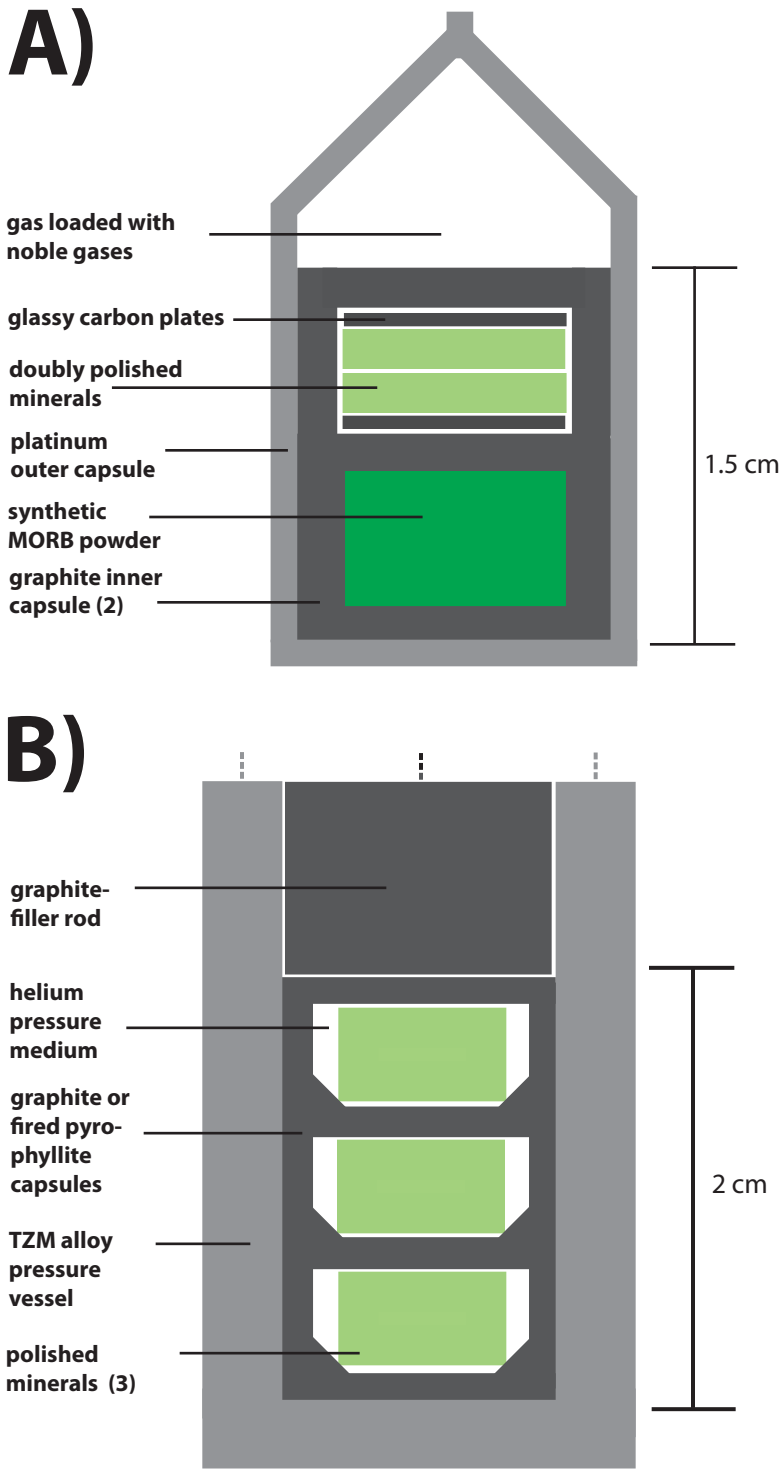

Chapter 1, Figure 2

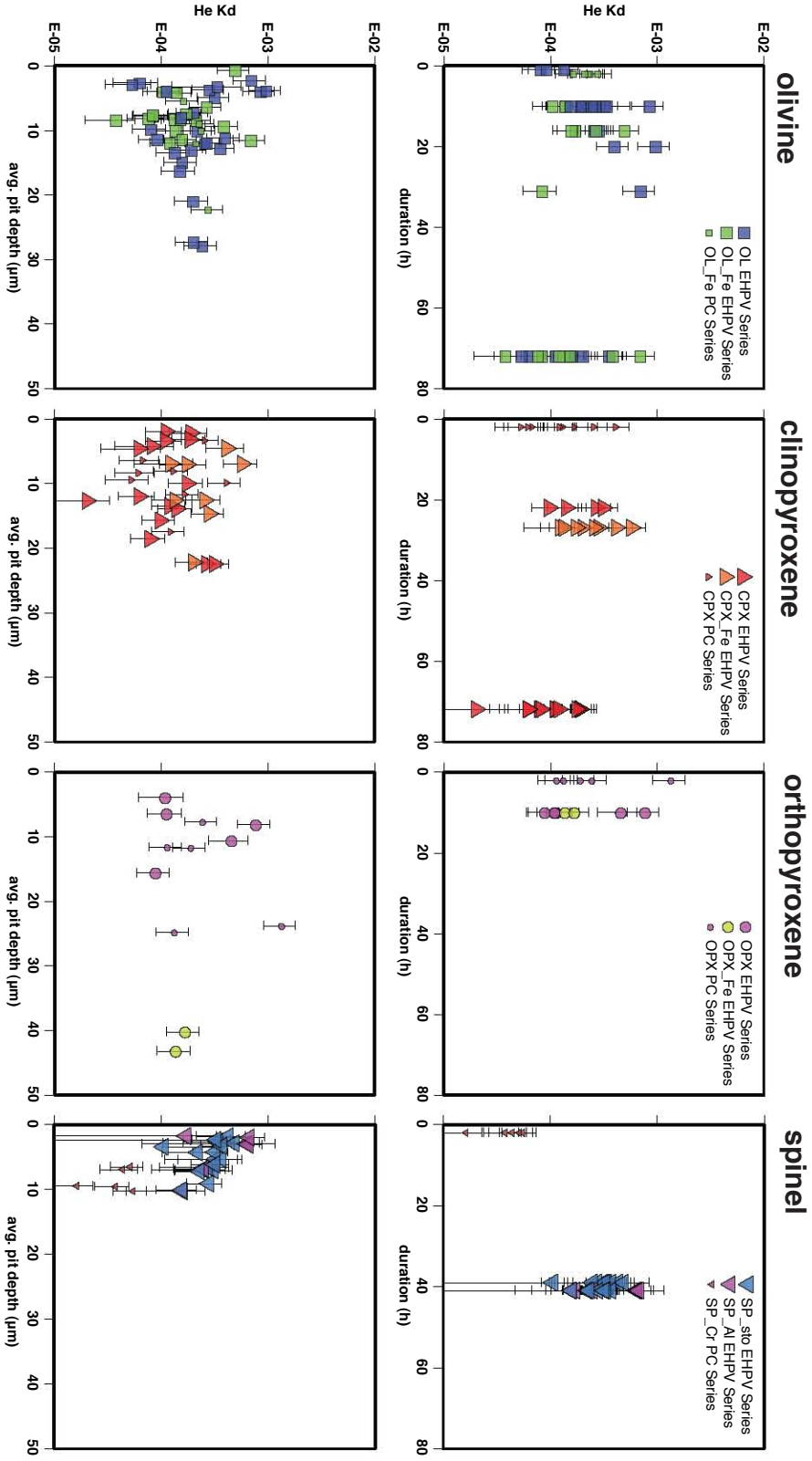

Chapter 1, Figure 3

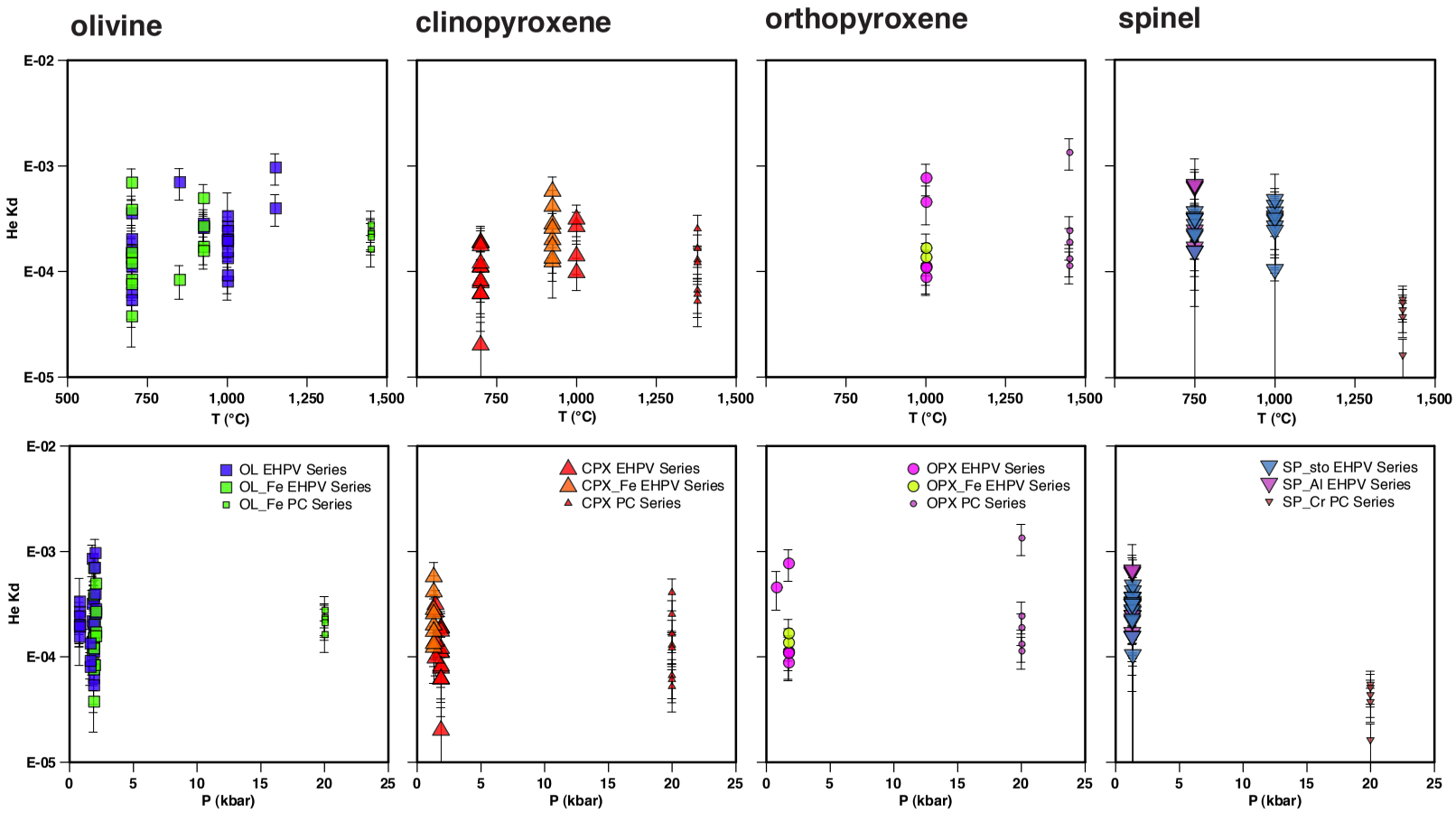

Chapter 1, Figure 4

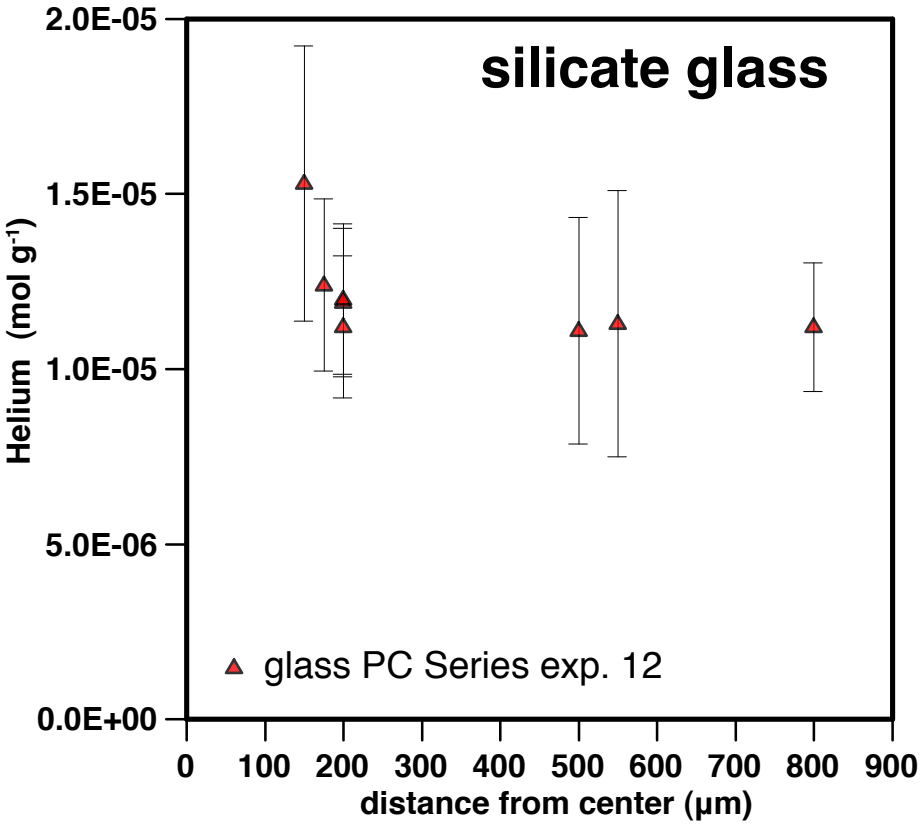

Chapter 1, Figure 5

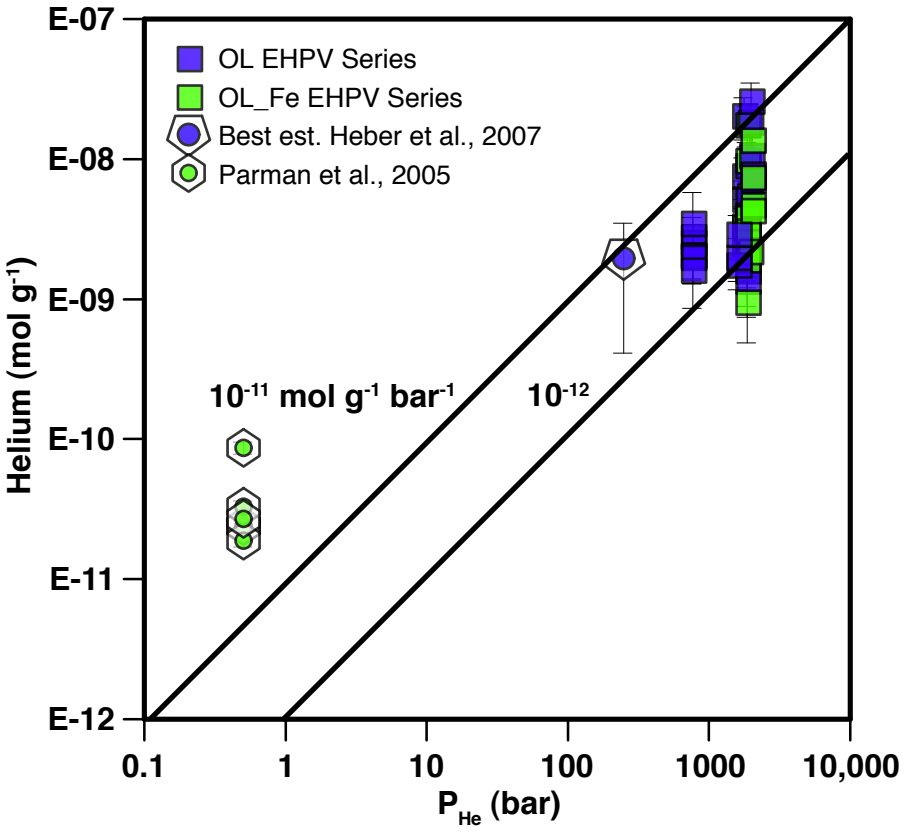

Chapter 1, Figure 6

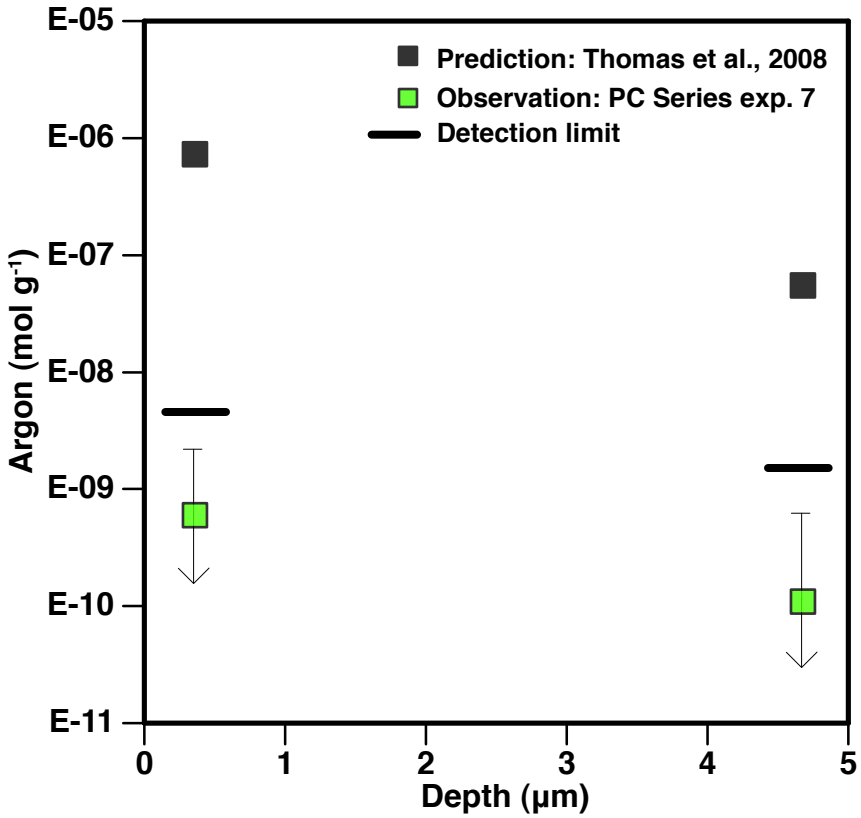

Chapter 1, Figure 7

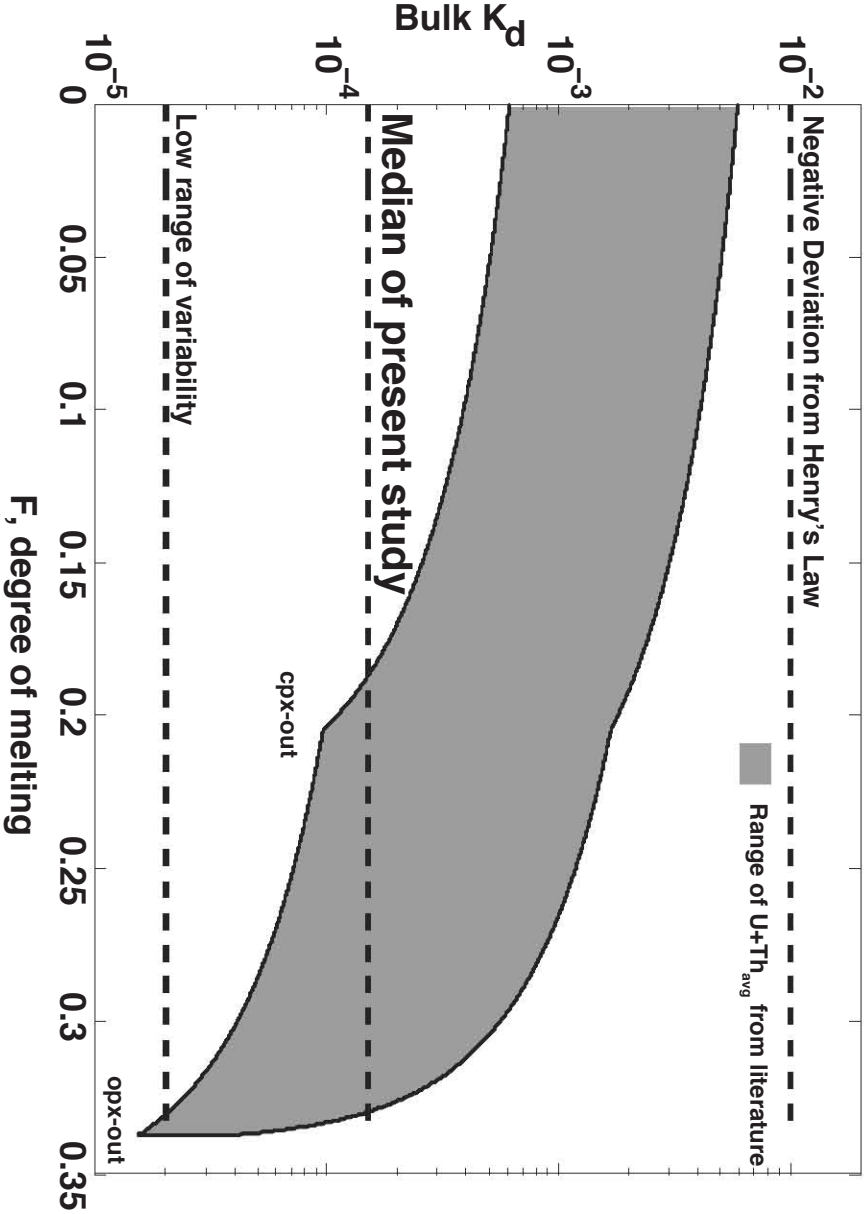

Table 1: Preferred Set of Helium Partition Coefficients

	Olivine	OPX	CPX	Spinel
Kd He	2.0E-04	1.5E-04	1.4E-04	2.6E-04
upper bound	2.8E-04	3.0E-04	2.3E-04	3.3E-04
lower bound	1.4E-04	1.1E-04	9.2E-05	1.5E-04

Supplementary Information for "Constraints on Light Noble Gas Partitioning at the Conditions of Spinel-Peridotite Melting"

1.0 Supplementary Methods:

1.1 Starting Materials:

Gem quality crystals were used as the solid phases in the experiments. This approach was taken to reduce the number of secondary, gas-rich phases and to provide large crystals for analysis, improving noble gas analytical precision. Mineral compositions are given in Table A.2. Bulk crystals were sectioned into sizes appropriate for the experiments, approximately 2 x 2 x 1 mm, using a low speed saw and diamond encrusted wafering blade. No attempt was made to crystallographically orient the sample during sectioning. Two parallel faces of each sectioned crystal were mechanically polished, finishing with 0.05 μm alumina grit. These faces were then chemically polished using colloidal silica for >6 hours. The preparation of the minerals follows the method outlined by (Thomas et al., 2008) and is designed to minimize any lattice damage induced by the cutting and mechanical polishing procedure. Once polished, but prior to analysis, the crystals were mapped for inclusions using a 120x stereoscope. Any areas affected by inclusions were avoided during analysis.

1.2 Experimental Methods:

1.2.1 PC (Piston Cylinder) Series:

PC series sample geometry is given in Figure 1a. Two graphite inner capsules were used for each experiment. The upper capsule contains two doubly polished, compositionally identical minerals faced against polished plates of glassy carbon. Glassy carbon was used because it does not leave a residue on the mineral face, whereas graphite tends to adhere to the polished mineral faces. Two minerals were loaded into the upper capsule to compare the analytical results for a mineral faced against glassy carbon and a mineral faced against an identical mineral. However, the mineral-mineral interfaces tended to become impregnated with graphite from the surrounding capsule during the experimental run, and consequently, only the mineral faces that were juxtaposed against glassy carbon were analyzed.

The lower capsule in the PC series was packed with a synthetic primitive MORB powder (Figure 1a). This allows for direct calculation of the partitioning of noble gases between the crystal and melt, without knowing the precise P_{He} in the experiment (assumed to be equal to fHe at high temperature and relatively low pressures). Because the solid and liquid phases are physically separated, only volatile elements equilibrated between the two phases and some major element disequilibrium was present. The basaltic liquid composition used in this study, however, is in equilibrium with a mantle assemblage (modeled after composition 62a, Hirschmann et al., 1998), suggesting disequilibrium is not large and that measured partition coefficients provide good estimates for naturally applicable values. The compositions of the melts in all PC series experiments are given in Table A.3. The powder was prepared using reagent grade

oxides (SiO_2, TiO_2, Al_2O_3, Cr_2O_3, MgO, MnO, Fe_2O_3) and carbonates ($CaCO_3$, Na_2CO_3, K_2CO_3). The mixture of these compounds was ground under ethanol using an agate mortar and pestle and then decarbonated at ~IW+1 and 900°C for several hours in a horizontal furnace.

All experimental materials for the PC series were stored in a 150°C drying oven for >6 hours prior to gas loading of He (or equal volume He-Ne-Ar for PC series experiment 7). Gas loading was accomplished using an apparatus similar to that detailed by (Boettcher et al., 1989). A ~0.1 bar vacuum was drawn on the sample before it was loaded with ~60 bar of noble gas. After ensuring that there were no leaks, a second ~0.1 bar vacuum was drawn on the sample. Once the maximum vacuum was obtained, the sample was loaded again with 60 bar of pure noble gas. The Pt outer capsule was then crimped ~5 mm below its top using a pair tapered steel plates attached to a vise. This crimp effectively isolates the portion of the Pt outer capsule containing the two graphite capsules in an atmosphere of pressurized gas. After spot welding, the single crimp was shaped so it could fit in a hollowed MgO sleeve. Gaps between the Pt capsule and the hollowed MgO sleeve were filled using hand crafted, solid MgO spacers. Temperature was monitored using type-D thermocouple (3WRe/25WRe) housed in a four-hole alumina rod. The thermocouple was positioned directly above the sample and was separated from the Pt outer capsule by a 1 mm solid MgO disc. The top and bottom MgO spacers were cut to position the melt and crystal capsules in the center of the hotspot. The sample assembly was housed in a straight walled graphite furnace and temperature was controlled using a PID controller (Eurotherm 2404). A pyrex© sleeve and salt cells

were used as the pressure medium and the entire experimental assembly was wrapped in Pb foil before being loaded into the piston cylinder.

Experiments were cold pressurized to 20 kbar in an end-loaded piston cylinder apparatus (Rockland Research). Sample temperatures were increased at a rate of 75°C per minute to the desired run temperature. The final pressure was reached using a hot-piston-in approach. Samples were quenched by cutting the power while maintaining pressure. Over the duration of the experiment, the liquid and solid phases equilibrated with a common, noble gas-rich vapor. Although Ar was not gas loaded (excluding PC series experiment 7), the silicate glasses contain significant concentrations of Ar. We suspect Ar was introduced as an adsorbed gas associated with the graphite capsules. All of the PC experiments were conducted at superliquidus temperatures for the melt composition, verified by the lack of solid phases in the glass after quench.

1.2.2 EHPV (Externally Heated Pressure Vessel) Series:

Each EHPV experiment consists of three polished crystals loaded into separate capsules (graphite or fired pyrophyllite). The sample geometry and dimensions of this series are given in Figure 1b. The capsules were machined so that all three crystals were contained within the hotspot, as determined by the temperature calibration of the pressure vessel assembly. Once fired, the pyrophyllite breaks down to an assemblage of mullite, silica, and sillimanite; all can be considered inert at the relatively low temperatures and over the relatively short durations of the EHPV experiments. Given the subliquidus temperatures (basaltic) of the EHPV series, no liquid phase was included in this series of

experiments. Partition coefficients are calculated as the ratio of the He solubility observed in the solid phase and the He solubility calculated for a basalt at the same P_{He} (Iacono-Marziano et al., 2010).

Pure He gas was used as the pressure medium for all the EHPV series experiments allowing for precise and sustained control of P_{He}. Typical leakage of the gas pressure was <5% over the run duration with a maximum observed leakage of 10%. Temperatures ranged from 750° to 1150°C and pressures ranged from 0.75 to 2 kbar. Convection within the pressure vessel was suppressed using graphite filler rods that extend the length of the pressure vessel above the sample capsules.

Three minerals per experiment were placed into separate capsules and loaded into the pressure vessel. A ~0.1 bar vacuum was drawn on the entire assembly before it was pressurized. The samples were brought to temperature by placing the pressure vessel into a vertical Deltech furnace. Experiments were quenched by removing the pressure vessel from the furnace and allowing it to cool against air. The vessel cooled to ~50°C in 20 minutes. At this point the pressure vessel was rapidly depressurized and unloaded.

1.3 Analytical Approach and Data Processing:

1.3.1 Major Element Analysis:

Major element compositions of minerals and glasses were determined using an electron microprobe (Cameca SX-100, Brown University). Analyses were completed using wavelength dispersive spectrometry, and the PAP correction was applied. For

minerals, the analytical parameters were 15 kV, 20 nA, and a focused beam, and for glasses the analytical parameters were 15 kV, 20 nA, and a 5 μm diameter beam. Counting times on all elements were 45 seconds, excepting Na, Mn, and Cr in glass (30 seconds) and Fe in both minerals and glass (90 seconds).

1.3.2 Noble Gas Analysis:

Noble gas concentrations of the experimental run products were determined using a UV laser ablation-noble gas mass spectrometer system at the Open University (UK). A 193 nm NeF excimer laser was used to ablate all materials. Three SAES AP-10 getters in the extraction system removed active gases released during ablation before introduction into a MAP215-50 mass spectrometer. ^{4}He, ^{22}Ne and ^{40}Ar were measured by an electron multiplier in peak hopping mode. The sensitivity of the mass spectrometer was determined by gas pipetting a known volume of noble gases with elemental ratios designed to allow measurement without separation and atmospheric isotopic ratios into the mass spectrometer. Further details regarding the basic laser ablation technique can be found in (Kelley et al., 1994).

Because minerals and glasses are physically separated in the experiments, these phases could be analyzed during separate sessions. This approach provided a low and repeatable blank for the low concentration minerals without heat soaking the sample prior to mineral analysis, as is required when minerals are grown directly from melts (cf. Heber et al., 2007). PC series glasses were analyzed using smaller diameter (<100 μm), single spots. Pit depths for glasses were ~10 μm. The minerals from the PC and EHPV series

were analyzed using a combination of large diameter (150-400 μm) spots and single-line rasters. Average pit depth for minerals ranged up to ~45 μm. The gem quality crystals used in this study are large and contain few inclusions compared to minerals grown directly from silicate melts. These qualities allow for the ablation of large volume pits that are unaffected by microscopic inclusions. In general, the pit volumes ablated for this study are >10x times larger than those ablated in similar studies (Heber et al., 2007), providing a substantial improvement in analytical precision. Blanks were typically run before and after an analysis. A session blank was calculated as the mean of the blanks for a particular session (defined as a single day of analysis on a single port) and the blank standard deviation is calculated as the standard deviation on the mean. The detection limit is defined as three standard deviations above the mean blank.

Pits volumes were measured using a white light interferometer (Zygo Instruments, New View 6000 Series, Brown University). This device provides an image of the ablated surface that requires minimal interpolation of pixels with unknown values. A surface continuum is calculated by masking out the ablated area of the interferometer image and interpolating across the masked region. The inpainted interferometer image is subtracted from the surface continuum, isolating the relief associated with the ablation pit. To calculate the pit volume, the individual volumes of pixels are summed assuming rectangular prism geometry for each pixel. Uncertainties associated with mineral ablation pits tend to be larger than those associated with glass ablation pits because interpolation across mineral ablation pits involves larger distances and more complex surface curvatures. A small ring of vapor deposition forms along the circumference of the pits, creating a halo of pixels with negative depth. We avoid including these pixels in

the volume determination by only summing pixels with positive depths. In general, >30,000 pixels are summed for a glass pit and >100,000 pixels are summed for a mineral pit. In total each topographic image contains 307,200 pixels (480 x 640).

All minerals were carbon coated prior to imaging. This significantly improved the return signal for clear minerals, reducing the amount of interpolation required for pit volume determinations. Carbon coat thickness was not measured directly, but based on distance from source and coating time, the thickness is ~20 nm.

The density of the glass and minerals must be estimated in order to calculate the mass of material ablated. The densities of the minerals were taken from (Deer et al., 1996), assuming a linear increase in density from Mg to Fe endmembers. The glass density was estimated using the data from (Lange and Carmichael, 1987).

2.0 Role of Extended Defects in Helium Dissolution

This study has focused on determining He solubility in the minerals present during MORB genesis. It is possible that the energetics associated with He partitioning between solid and melt are dominated by extended defects. If true, bulk partition coefficients that neglect the effects grain boundaries, subgrain boundaries, and "free" dislocations (not associated with a subgrain boundary) will be systematically low. Studies regarding noble gas solubility in extended defects are few, but limited data and modeling suggests that grain boundaries can host significant quantities of noble gases (Baxter et al., 2007; Pinilla et al., 2012). U+Th are also likely enriched within grain

boundaries, leaving the net effect of grain boundaries on (U+Th)/He during partial melting unclear.

Although the analytical precision of this study is substantially improved compared to earlier efforts, a considerable amount of variability remains in the individual measurements of [He]. No full grain boundaries were present in the minerals analyzed, ruling out this type of defect structure as a cause of the variability. Additionally, no correlation was observed between average pit depth and [He], arguing against variability being associated with a thin (~200 nm), defect-rich surface layer produced during mineral preparation (Pinilla et al., 2012).

Helium solubility was determined for both San Carlos olivine (OL_Fe) and synthetic forsterite. Because San Carlos is a mantle olivine, it contains relatively high concentrations of "free" dislocations and dislocations stored in subgrain boundaries. The synthetic forsterite was grown by the Czochalski method, and thus, should have a lower concentration of dislocations. There is no significant difference in averages of measured He solubility mantle and synthetic olivine, supporting the hypothesis that the variability is not related to varying concentrations of dislocations in different volumes of analyzed material. The location of several subgrain boundaries within the San Carlos olivine starting materials were mapped and then preferentially ablated (Supplemental Figure 1). Analyses of [He] that include subgrain boundaries are not significantly higher than those that do not. This also supports the hypothesis that dislocations are not large contributors to the variability in [He]. These comparisons do not rule out dislocations or subgrain boundaries as hosts for He in natural systems because it is possible that He originally hosted in these fast-path features diffused out of structure prior to analysis. Rather, these

comparisons argue against "free" dislocations and subgrain boundaries being a major source of variability in the present data set.

Nano-scale inclusions in crystals may facilitate the incorporation of noble gases, and it is difficult to dismiss this as a cause of [He] variability. Indeed, the data are right skewed when plotted as a histogram of partition coefficients. This may indicate the data are variably affected by relatively high concentration regions in the minerals. The potential nature of these regions, however, remains unclear. The minerals investigated have very different grown histories, i.e. mantle minerals and synthetic minerals, yet all minerals show similar median [He] and variability of [He], possibly excepting SP_Cr. Attributing the majority of variability to nano-scale inclusion would suggest a similar density and distribution of nano-scale inclusions across all minerals investigated despite their diverse formation history.

The absolute number of atoms released during ablation of the minerals is small ($\sim 1 \times 10^{-14}$ mol), so a large component of [He] variation ultimately reflects the precision of the analysis and pit volume measurements.

Supplementary References:

Boettcher, S.L., Guo, Q., Montana, A., 1989. A simple device for loading gases in high pressure experiments. American Mineralogist 74.

Deer, W.A., Howie, R.A., Zussman, J., 1996. An Introduction to the Rock-Forming Minerals, 2nd Edition ed. Prentice Hall.

Heber, V.S., Brooker, R.A., Kelley, S.P., Wood, B.J., 2007. Crystal-melt partitioning of noble gases (helium, neon, argon, krypton, and xenon) for olivine and clinopyroxene. Geochimica Et Cosmochimica Acta 71, 1041-1061.

Hirschmann, M.M., Baker, M.B., Stolper, E.M., 1998. The effect of alkalis on the silica content of mantle-derived melts. Geochimica Et Cosmochimica Acta 62, 883-902.

Iacono-Marziano, G., Paonita, A., Rizzo, A., Scaillet, B., Gaillard, F., 2010. Noble gas solubilities in silicate melts: New experimental results and a comprehensive model of the effects of liquid composition, temperature and pressure. Chemical Geology 279, 145-157.

Kelley, S.P., Arnaud, N.O., Turner, S.P., 1994. High spatial resolution $^{40}Ar/^{39}Ar$ investigations using an ultra violet laser probe extraction technique. Geochimica Et Cosmochimica Acta 58, 3519-3525.

Lange, R.A., Carmichael, I.S.E., 1987. Densities of Na_2O-K_2O-CaO-MgO-FeO-Fe_2O_3-Al_2O_3-TiO_2-SiO_2 liquds - new measurements and derived partial molar properties. Geochimica Et Cosmochimica Acta 51.

Thomas, J.B., Cherniak, D.J., Watson, E.B., 2008. Lattice diffusion and solubility of argon in forsterite, enstatite, quartz and corundum. Chemical Geology 253, 1-22.

Supplementary Figure Captions:

Supplementary Figure 1: Subgrain boundaries and [He]: A) An image showing the different extinction angles associated with different domains within starting material for EHPV Series experiment 3 (OL_Fe, San Carlos olivine). Each domain is separated by a subgrain boundary. B) An image showing the locations of analyses. In total, three different line rasters ablated into material containing subgrain boundaries as evidenced; the upper right line, the lower left line, and the line diagonal running line. Subgrain boundaries contain elevated concentrations of dislocations, which are potential hosts for noble gases in crystals due to their relatively open structure. This image also gives an example of the run products of EHPV experiments. Examples of PC Series run products are provided in the Supplement. The residue that is concentrated near the center of the grain is a carbon coat that was applied to aid the pit volume measurements. C) A graph comparing the measured [He] of the individual analyses. Analyses that ablated into material contain subgrain boundaries are highlighted box a transparent black box. The analyses contains subgrain boundaries are not anomalously high, indicating dislocations are not the dominant host for He in these experiments and are not a major source of [He] variability.

Supplementary Figure 2:

PC Series expt. 10:

A) Doubly polished olivine plates with polished glassy carbon plates (lower left).

B) Mineral capsule geometry after completion of experiment.

C) Image of mineral surface following extraction from experiment.

D) Examples of line rasters completed on mineral surface. Note, the mineral fractured when it was being remounted in indium following analysis.

PC Series expt. 7:

E) Image of mineral surface following extraction from experiment. Note the use of smaller radius glassy carbon plate.

F) Image of spot analyses (2) of PC Series expt. 7. Left analysis is deeper and smaller diameter compared to right analysis.

Chapter 1, Supplementary Figure 1

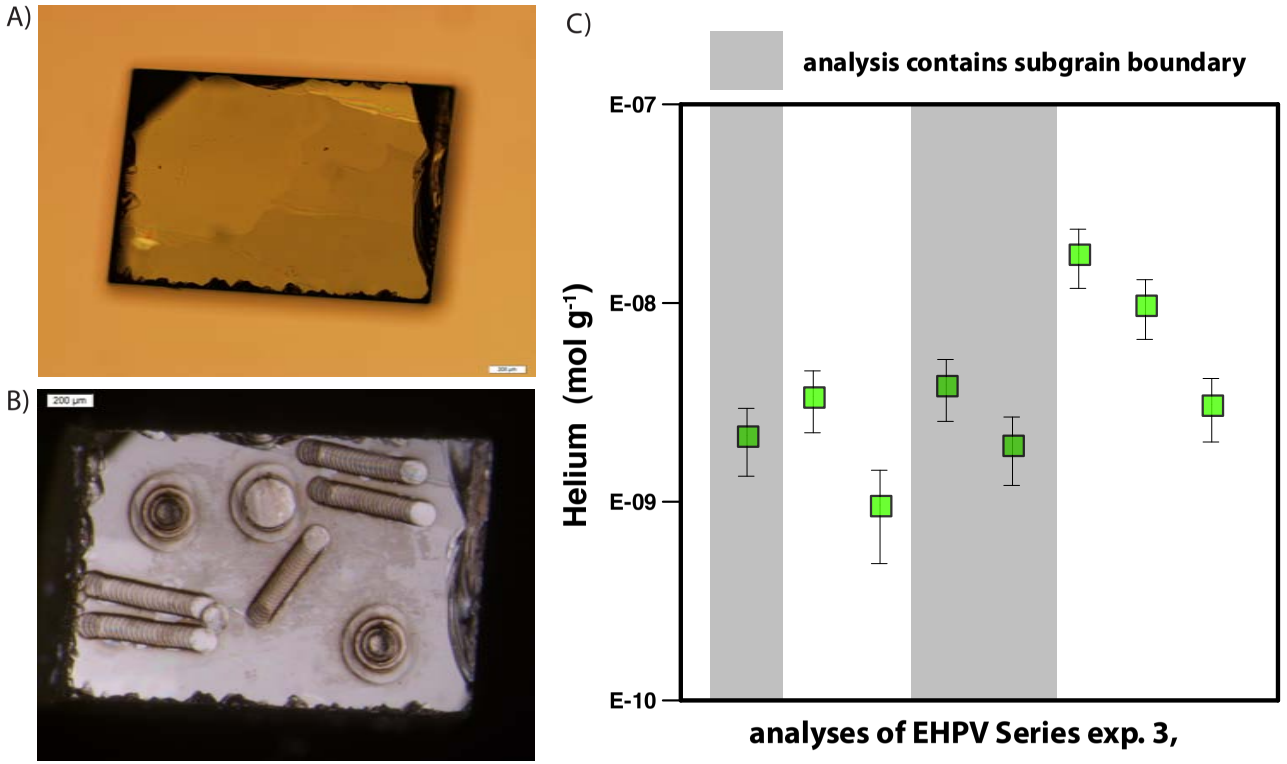

Chapter 1, Supplementary Figure 2

Example images of PC Series run products:

PC Series expt. 10

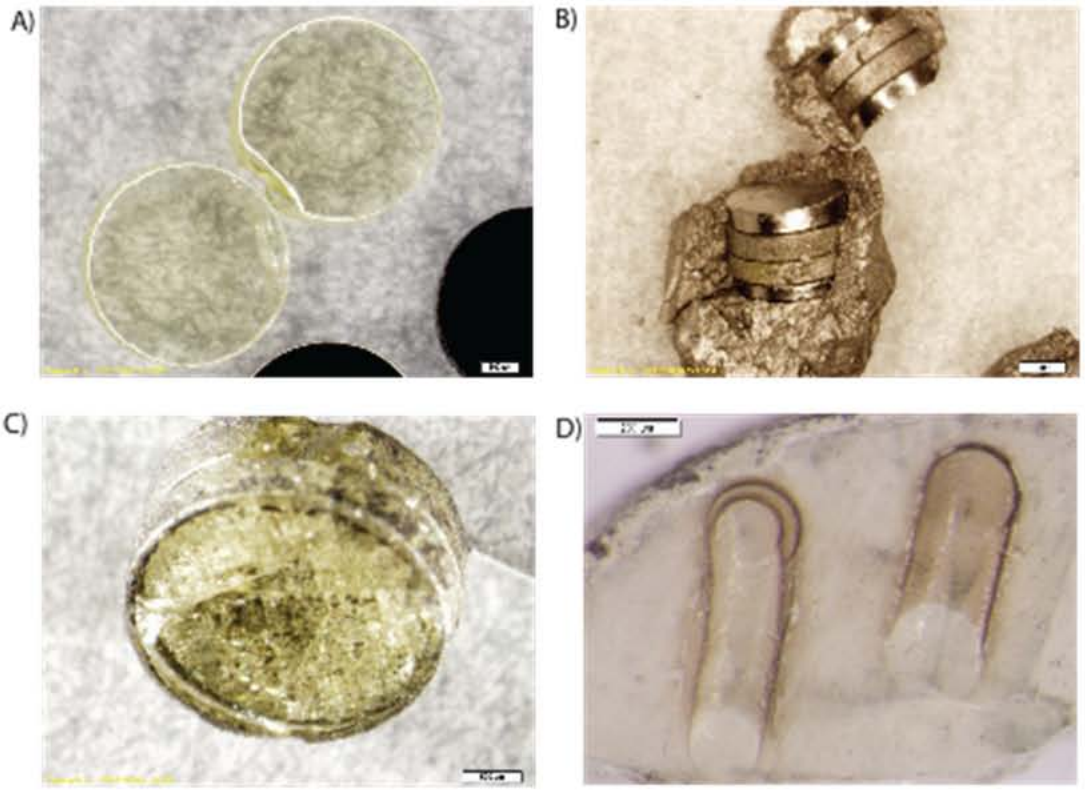

PC Series expt. 7

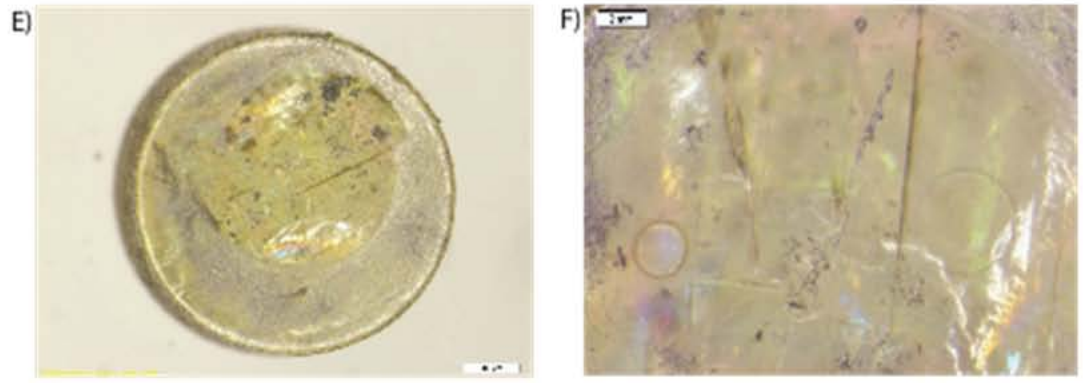

Supplementary Table 1: Noble gas Analyses

series	exp #	P (kbar)	T (C)	duration (hr)	phase	pit type*	pit volume** (um^3)	pit volume uncert.	avg. pit depth (um)	He (mol)	He uncert.	Ne (mol)	Ne uncert.	Ar (mol)	Ar uncert.	He (mol/g)	He uncert.	Ne (mol/g)	Ne uncert.	Ar (mol/g)	Ar uncert.	calc. He sol., melt*** (mol/g)	avg. He conc., melt (mol/g)	He Kd	He Kd uncert.	He blank (mol)	He blank uncert.	Ne blank (mol)	Ne blank uncert.	Ar blank (mol)	Ar blank uncert.
EHPV	1	1.77	1000	10	OL	raster line	9.14E+05	3.01E+05	4.91E+00	2.26E-14	9.25E-16	NR	NR	NR	NR	7.68E-09	2.55E-09	NR	NR	NR	NR	2.39E-05	NA	3.22E-04	1.07E-04	2.66E-15	1.54E-16	NR	NR	NR	NR
EHPV	1	1.77	1000	10	OL	raster line	9.31E+05	3.07E+05	3.96E+00	6.16E-14	1.61E-15	NR	NR	NR	NR	2.05E-08	6.80E-09	NR	NR	NR	NR	2.39E-05	NA	8.61E-04	2.85E-04	2.66E-15	1.54E-16	NR	NR	NR	NR
EHPV	1	1.77	1000	10	OL	terraced pit	1.10E+06		1.01E+01	1.86E-14	1.15E-15	NR	NR	NR	NR	5.24E-09	1.76E-09	NR	NR	NR	NR	2.39E-05	NA	2.20E-04	7.38E-05	3.35E-15	1.19E-16	NR	NR	NR	NR
EHPV	1	1.77	1000	10	OL_Fe	raster line	7.18E+05	2.37E+05	3.99E+00	6.04E-15	9.34E-16	NR	NR	NR	NR	2.52E-09	9.17E-10	NR	NR	NR	NR	2.39E-05	NA	1.06E-04	3.85E-05	2.66E-15	1.54E-16	NR	NR	NR	NR
EHPV	1	1.77	1000	10	OL_Fe	raster line	7.24E+05	2.39E+05	4.17E+00	8.14E-15	1.04E-15	NR	NR	NR	NR	3.37E-09	1.19E-09	NR	NR	NR	NR	2.39E-05	NA	1.41E-04	4.99E-05	2.66E-15	1.54E-16	NR	NR	NR	NR
EHPV	1	1.77	1000	10	OL_Fe	terraced pit	9.78E+05	3.23E+05	1.00E+01	1.08E-14	1.13E-15	NR	NR	NR	NR	3.30E-09	1.14E-09	NR	NR	NR	NR	2.39E-05	NA	1.38E-04	4.79E-05	3.35E-15	1.19E-16	NR	NR	NR	NR
EHPV	2	1.93	1150	10	OL_Fe	terraced pit	1.06E+06	3.50E+05	8.43E+00	1.98E-14	1.17E-15	NR	NR	NR	NR	5.60E-09	1.88E-09	NR	NR	NR	NR	2.60E-05	NA	2.15E-04	7.22E-05	3.35E-15	1.19E-16	NR	NR	NR	NR
EHPV	3	1.87	700	72	OL	raster line	5.53E+05	1.82E+05	2.63E+00	2.87E-15	8.66E-16	NR	NR	NR	NR	1.61E-09	7.20E-10	NR	NR	NR	NR	2.52E-05	NA	6.39E-05	2.86E-05	2.66E-15	1.54E-16	NR	NR	NR	NR
EHPV	3	1.87	700	72	OL	raster line	6.15E+05	2.03E+05	2.88E+00	2.72E-15	8.62E-16	NR	NR	NR	NR	1.37E-09	6.28E-10	NR	NR	NR	NR	2.52E-05	NA	5.45E-05	2.49E-05	2.66E-15	1.54E-16	NR	NR	NR	NR
EHPV	3	1.87	700	72	OL	raster line	2.37E+05	7.83E+04	1.03E+00	bb	bb	NR	NR	NR	NR	bb	bb	NR	NR	NR	NR	2.52E-05	NA	BB	BB	2.66E-15	1.54E-16	NR	NR	NR	NR
EHPV	3	1.87	700	72	OL	raster line	1.40E+06	4.61E+05	7.25E+00	2.34E-14	9.15E-16	NR	NR	NR	NR	5.18E-09	1.72E-09	NR	NR	NR	NR	2.52E-05	NA	2.05E-04	6.83E-05	2.66E-15	1.54E-16	NR	NR	NR	NR
EHPV	3	1.87	700	72	OL	raster line	1.07E+06	3.52E+05	3.94E+00	9.85E-15	9.03E-16	NR	NR	NR	NR	2.86E-09	9.79E-10	NR	NR	NR	NR	2.52E-05	NA	1.13E-04	3.88E-05	2.66E-15	1.54E-16	NR	NR	NR	NR
EHPV	3	1.87	700	72	OL	terraced pit	1.02E+06	3.35E+05	1.28E+01	2.99E-14	1.44E-15	NR	NR	NR	NR	9.11E-09	3.04E-09	NR	NR	NR	NR	2.52E-05	NA	3.61E-04	1.20E-04	4.65E-15	1.62E-16	NR	NR	NR	NR
EHPV	3	1.87	700	72	OL	terraced pit	1.55E+06	5.12E+05	1.49E+01	2.01E-14	1.51E-15	NR	NR	NR	NR	4.03E-09	1.36E-09	NR	NR	NR	NR	2.52E-05	NA	1.60E-04	5.41E-05	4.65E-15	1.62E-16	NR	NR	NR	NR
EHPV	3	1.87	700	72	OL	terraced pit	1.70E+06	5.61E+05	1.63E+01	2.09E-14	1.71E-15	NR	NR	NR	NR	3.82E-09	1.30E-09	NR	NR	NR	NR	2.52E-05	NA	1.52E-04	5.15E-05	4.65E-15	1.62E-16	NR	NR	NR	NR
EHPV	3	1.87	700	72	OL_Fe	raster line	7.89E+05	2.60E+05	7.79E+00	5.66E-15	1.01E-15	NR	NR	NR	NR	2.15E-09	8.05E-10	NR	NR	NR	NR	2.52E-05	NA	8.52E-05	3.20E-05	2.66E-15	1.54E-16	NR	NR	NR	NR
EHPV	3	1.87	700	72	OL_Fe	raster line	8.10E+05	2.67E+05	8.27E+00	9.18E-15	9.40E-16	NR	NR	NR	NR	3.39E-09	1.17E-09	NR	NR	NR	NR	2.52E-05	NA	1.35E-04	4.65E-05	2.66E-15	1.54E-16	NR	NR	NR	NR
EHPV	3	1.87	700	72	OL_Fe	raster line	7.38E+05	2.44E+05	8.44E+00	2.37E-15	8.69E-16	NR	NR	NR	NR	9.61E-10	4.74E-10	NR	NR	NR	NR	2.52E-05	NA	3.81E-05	1.88E-05	2.66E-15	1.54E-16	NR	NR	NR	NR
EHPV	3	1.87	700	72	OL_Fe	raster line	7.48E+05	2.47E+05	8.33E+00	9.64E-15	9.43E-16	NR	NR	NR	NR	3.86E-09	1.33E-09	NR	NR	NR	NR	2.52E-05	NA	1.53E-04	5.27E-05	2.66E-15	1.54E-16	NR	NR	NR	NR
EHPV	3	1.87	700	72	OL_Fe	raster line	7.43E+05	2.45E+05	8.14E+00	4.81E-15	8.80E-16	NR	NR	NR	NR	1.94E-09	7.31E-10	NR	NR	NR	NR	2.52E-05	NA	7.69E-05	2.90E-05	2.66E-15	1.54E-16	NR	NR	NR	NR
EHPV	3	1.87	700	72	OL_Fe	terraced pit	1.16E+06	3.82E+05	1.15E+01	6.86E-14	1.72E-15	NR	NR	NR	NR	1.77E-08	5.86E-09	NR	NR	NR	NR	2.52E-05	NA	7.03E-04	2.33E-04	4.65E-15	1.62E-16	NR	NR	NR	NR
EHPV	3	1.87	700	72	OL_Fe	terraced pit	9.18E+05	3.03E+05	9.34E+00	3.01E-14	1.45E-15	NR	NR	NR	NR	9.82E-09	3.27E-09	NR	NR	NR	NR	2.52E-05	NA	3.89E-04	1.30E-04	4.65E-15	1.62E-16	NR	NR	NR	NR
EHPV	3	1.87	700	72	OL_Fe	terraced pit	1.21E+06	3.98E+05	1.19E+01	1.25E-14	1.57E-15	NR	NR	NR	NR	3.09E-09	1.09E-09	NR	NR	NR	NR	2.52E-05	NA	1.22E-04	4.33E-05	4.65E-15	1.62E-16	NR	NR	NR	NR
EHPV	3	1.87	700	72	CPX	raster line	2.84E+05	9.36E+04	2.14E+00	4.45E-15	9.05E-16	NR	NR	NR	NR	4.87E-09	1.89E-09	NR	NR	NR	NR	2.52E-05	NA	1.93E-04	7.48E-05	2.66E-15	1.54E-16	NR	NR	NR	NR
EHPV	3	1.87	700	72	CPX	raster line	6.42E+05	2.12E+05	3.22E+00	9.94E-15	8.88E-16	NR	NR	NR	NR	4.81E-09	1.64E-09	NR	NR	NR	NR	2.52E-05	NA	1.91E-04	6.52E-05	2.66E-15	1.54E-16	NR	NR	NR	NR
EHPV	3	1.87	700	72	CPX	raster line	6.00E+05	1.98E+05	1.92E+00	5.49E-15	9.03E-16	NR	NR	NR	NR	2.84E-09	1.05E-09	NR	NR	NR	NR	2.52E-05	NA	1.13E-04	4.16E-05	2.66E-15	1.54E-16	NR	NR	NR	NR
EHPV	3	1.87	700	72	CPX	raster line	6.14E+05	2.03E+05	3.39E+00	5.60E-15	8.86E-16	NR	NR	NR	NR	2.83E-09	1.04E-09	NR	NR	NR	NR	2.52E-05	NA	1.12E-04	4.11E-05	2.66E-15	1.54E-16	NR	NR	NR	NR
EHPV	3	1.87	700	72	CPX	terraced pit	1.67E+06	5.52E+05	1.86E+01	1.09E-14	1.49E-15	NR	NR	NR	NR	2.02E-09	7.22E-10	NR	NR	NR	NR	2.52E-05	NA	8.01E-05	2.86E-05	4.65E-15	1.62E-16	NR	NR	NR	NR
EHPV	3	1.87	700	72	CPX	terraced pit	8.32E+05	2.75E+05	1.00E+01	1.21E-14	1.55E-15	NR	NR	NR	NR	4.51E-09	1.60E-09	NR	NR	NR	NR	2.52E-05	NA	1.79E-04	6.33E-05	4.65E-15	1.62E-16	NR	NR	NR	NR
EHPV	3	1.87	700	72	CPX	terraced pit	4.42E+05	1.46E+05	4.19E+00	3.00E-15	1.35E-15	NR	NR	NR	NR	2.11E-09	1.18E-09	NR	NR	NR	NR	2.52E-05	NA	8.36E-05	4.66E-05	4.65E-15	1.62E-16	NR	NR	NR	NR
EHPV	3	1.87	700	72	CPX	terraced pit	1.36E+06	4.48E+05	1.35E+01	1.36E-14	1.32E-15	NR	NR	NR	NR	3.10E-09	1.07E-09	NR	NR	NR	NR	2.52E-05	NA	1.23E-04	4.23E-05	4.65E-15	1.62E-16	NR	NR	NR	NR
EHPV	3	1.87	700	72	CPX	terraced pit	4.93E+05	1.63E+05	4.59E+00	2.51E-15	1.16E-15	NR	NR	NR	NR	1.58E-09	8.96E-10	NR	NR	NR	NR	2.52E-05	NA	6.27E-05	3.56E-05	3.35E-15	1.19E-16	NR	NR	NR	NR
EHPV	3	1.87	700	72	CPX	terraced pit	1.08E+06	3.56E+05	1.20E+01	5.53E-15	9.20E-16	NR	NR	NR	NR	1.59E-09	5.87E-10	NR	NR	NR	NR	2.52E-05	NA	6.31E-05	2.33E-05	2.66E-15	1.54E-16	NR	NR	NR	NR
EHPV	3	1.87	700	72	CPX	terraced pit	1.12E+06	3.70E+05	1.27E+01	1.86E-15	9.56E-16	NR	NR	NR	NR	5.17E-10	3.15E-10	NR	NR	NR	NR	2.52E-05	NA	2.05E-05	1.25E-05	2.66E-15	1.54E-16	NR	NR	NR	NR
EHPV	4	1.95	850	31	OL	raster line	5.84E+05	1.93E+05	2.24E+00	3.50E-14	1.05E-15	NR	NR	NR	NR	1.86E-08	6.17E-09	NR	NR	NR	NR	2.63E-05	NA	7.09E-04	2.35E-04	2.66E-15	1.54E-16	NR	NR	NR	NR
EHPV	4	1.95	850	31	OL_Fe	pit	3.52E+06	1.16E+06	7.59E+00	2.61E-14	3.07E-15	NR	NR	NR	NR	2.22E-09	7.77E-10	NR	NR	NR	NR	2.63E-05	NA	8.44E-05	2.96E-05	2.61E-14	4.41E-16	NR	NR	NR	NR
EHPV	5	1.98	1150	20	OL	raster line	8.25E+05	2.72E+05	3.84E+00	6.95E-14	9.97E-16	NR	NR	NR	NR	2.62E-08	8.64E-09	NR	NR	NR	NR	2.67E-05	NA	9.80E-04	3.24E-04	2.66E-15	1.54E-16	NR	NR	NR	NR
EHPV	5	1.98	1150	20	OL	terraced pit	1.10E+06	3.62E+05	1.12E+01	3.80E-14	1.10E-15	NR	NR	NR	NR	1.07E-08	3.55E-09	NR	NR	NR	NR	2.67E-05	NA	4.01E-04	1.33E-04	3.35E-15	1.19E-16	NR	NR	NR	NR
EHPV	6	2.04	925	16	OL	raster line	8.14E+05	2.69E+05	3.72E+00	2.07E-14	8.92E-16	NR	NR	NR	NR	7.91E-09	2.63E-09	NR	NR	NR	NR	2.75E-05	NA	2.88E-04	9.57E-05	2.66E-15	1.54E-16	NR	NR	NR	NR
EHPV	6	2.04	925	16	OL	terraced pit	1.06E+06	3.49E+05	1.20E+01	2.45E-14	1.26E-15	NR	NR	NR	NR	7.19E-09	2.40E-09	NR	NR	NR	NR	2.75E-05	NA	2.61E-04	8.73E-05	3.35E-15	1.19E-16	NR	NR	NR	NR
EHPV	6	2.04	925	16	OL_Fe	raster line	1.04E+06	3.43E+05	7.36E+00	1.66E-14	8.73E-16	NR	NR	NR	NR	4.79E-09	1.60E-09	NR	NR	NR	NR	2.75E-05	NA	1.74E-04	5.82E-05	2.66E-15	1.54E-16	NR	NR	NR	NR
EHPV	6	2.04	925	16	OL_Fe	raster line	8.97E+05	2.96E+05	6.44E-01	4.13E-14	1.71E-15	NR	NR	NR	NR	1.38E-08	4.58E-09	NR	NR	NR	NR	2.75E-05	NA	5.01E-04	1.67E-04	2.66E-15	1.54E-16	NR	NR	NR	NR
EHPV	6	2.04	925	16	OL_Fe	raster line	8.97E+05	2.96E+05	6.36E+00	2.24E-14	8.67E-16	NR	NR	NR	NR	7.47E-09	2.48E-09	NR	NR	NR	NR	2.75E-05	NA	2.72E-04	9.03E-05	2.66E-15	1.54E-16	NR	NR	NR	NR
EHPV	6	2.04	925	16	OL_Fe	terraced pit	9.70E+05	3.20E+05	1.14E+01	1.41E-14	1.05E-15	NR	NR	NR	NR	4.36E-09	1.48E-09	NR	NR	NR	NR	2.75E-05	NA	1.59E-04	5.37E-05	3.35E-15	1.19E-16	NR	NR	NR	NR
EHPV	9	1.71	1000	10	OPX	raster line	1.11E+06	3.67E+05	8.10E+00	6.41E-14	2.51E-15	NR	NR	NR	NR	1.80E-08	5.98E-09	NR	NR	NR	NR	2.30E-05	NA	7.80E-04	2.59E-04	1.51E-14	2.79E-16	NR	NR	NR	NR
EHPV	9	1.71	1000	10	OPX	raster line	1.51E+06	4.99E+05	6.43E+00	1.28E-14	1.41E-15	NR	NR	NR	NR	2.63E-09	9.16E-10	NR	NR	NR	NR	2.30E-05	NA	1.14E-04	3.98E-05	1.51E-14	2.79E-16	NR	NR	NR	NR
EHPV	9	1.71	1000	10	OPX	raster line	4.47E+06	1.48E+06	1.56E+01	2.95E-14	1.50E-15	NR	NR	NR	NR	2.06E-09	6.86E-10	NR	NR	NR	NR	2.30E-05	NA	8.92E-05	2.98E-05	1.51E-14	2.79E-16	NR	NR	NR	NR
EHPV	9	1.71	1000	10	OPX	raster line	4.91E+05	1.62E+05	3.91E+00	4.01E-15	1.18E-15	NR	NR	NR	NR	2.54E-09	1.13E-09	NR	NR	NR	NR	2.30E-05	NA	1.10E-04	4.88E-05	1.51E-14	2.79E-16	NR	NR	NR	NR
EHPV	9	1.71	1000	10	OPX_Fe	raster line	5.53E+06	1.82E+06	4.32E+01	5.80E-14	4.28E-15	NR	NR	NR	NR	3.19E-09	1.08E-09	NR	NR	NR	NR	2.30E-05	NA	1.38E-04	4.68E-05	2.56E-14	1.25E-16	NR	NR	NR	NR
EHPV	9	1.71	1000	10	OPX_Fe	raster line	5.64E+06	1.86E+06	4.02E+01	7.22E-14	4.45E-15	NR	NR	NR	NR	3.89E-09	1.31E-09	NR	NR	NR	NR	2.30E-05	NA	1.69E-04	5.67E-05	2.56E-14	1.25E-16	NR	NR	NR	NR
EHPV	10	1.61	1000	1	OL	raster line	1.82E+06	6.02E+05	9.83E+00	1.04E-14	9.78E-16	NR	NR	NR	NR	1.77E-09	6.07E-10	NR	NR	NR	NR	2.17E-05	NA	8.15E-05	2.80E-05	2.13E-15	4.06E-17	NR	NR	NR	NR
EHPV	10	1.61	1000	1	OL	raster line	1.81E+06	5.98E+05	1.14E+01	1.18E-14	8.93E-16	NR	NR	NR	NR	2.02E-09	6.85E-10	NR	NR	NR	NR	2.17E-05	NA	9.32E-05	3.15E-05	2.13E-15	4.06E-17	NR	NR	NR	NR
EHPV	10	1.61	1000	1	OL	terraced pit	1.19E+06	3.91E+05	1.34E+01	1.13E-14	1.11E-15	NR	NR	NR	NR	2.95E-09	1.02E-09	NR	NR	NR	NR	2.17E-05	NA	1.36E-04	4.68E-05	3.35E-15	1.19E-16	NR	NR	NR	NR
EHPV	19	0.77	1000	10	OPX	raster line	1.47E+06	4.86E+05	1.06E+01	2.26E-14	5.05E-15	NR	NR	NR	NR	4.78E-09	1.91E-09	NR	NR	NR	NR	1.04E-05	NA	4.61E-04	1.84E-04	6.27E-14	9.95E-16	NR	NR	NR	NR
EHPV	19	0.77	1000	10	OL	raster line	2.42E+06	7.97E+05	1.19E+01	2.19E-14	2.99E-15	NR	NR	NR	NR	2.81E-09	1.00E-09	NR	NR	NR	NR	1.04E-05	NA	2.71E-04	9.67E-05	2.61E-14	4.41E-16	NR	NR	NR	NR
EHPV	19	0.77	1000	10	OL	raster line	5.34E+06	1.76E+06	2.79E+01	4.40E-14	2.86E-15	NR	NR	NR	NR	2.56E-09	8.60E-10	NR	NR	NR	NR	1.04E-05	NA	2.46E-04	8.29E-05	2.61E-14	4.41E-16	NR	NR	NR	NR
EHPV	19	0.77	1000	10	OL	raster line	5.36E+06	1.77E+06	2.10E+01	3.62E-14	3.35E-15	NR	NR	NR	NR	2.09E-09	7.18E-10	NR	NR	NR	NR	1.04E-05	NA	2.02E-04	6.92E-05	2.61E-14	4.41E-16	NR	NR	NR	NR
EHPV	19	0.77	1000	10	OL	raster line	6.12E+06	2.02E+06	2.73E+01	4.15E-14	3.15E-15	NR	NR	NR	NR	2.11E-09	7.13E-10	NR	NR	NR	NR	1.04E-05	NA	2.03E-04	6.87E-05	2.61E-14	4.41E-16	NR	NR	NR	NR
EHPV	19	0.77	1000	10	OL	raster line	3.39E+06	1.12E+06	1.30E+01	2.19E-14	3.02E-15	NR	NR	NR	NR	2.01E-09	7.18E-10	NR	NR	NR	NR	1.04E-05	NA	1.94E-04	6.92E-05	2.61E-14	4.41E-16	NR	NR	NR	NR
EHPV	19	0.77	1000	10	OL	raster line	4.69E+05	1.55E+05	3.18E+00	5.33E-15	2.90E-15	NR	NR	NR	NR	3.53E-09	2.25E-09	NR	NR	NR	NR	1.04E-05	NA	3.40E-04	2.16E-04	2.61E-14	4.41E-16	NR	NR	NR	NR

EHPV	19	0.77	1000	10	OL	raster line	1.65E+06	5.46E+05	8.01E+00	8.64E-15	2.93E-15	NR	NR	NR	NR	1.63E-09	7.69E-10	NR	NR	NR	NR	1.04E-05	NA	1.57E-04	7.41E-05	2.61E-14	4.41E-16	NR	NR	NR	NR
EHPV	22	1.45	1000	22	CPX	raster line	4.40E+06	1.45E+06	2.25E+01	7.50E-14	2.89E-15	NR	NR	NR	NR	5.31E-09	1.76E-09	NR	NR	NR	NR	1.95E-05	NA	2.72E-04	9.03E-05	2.61E-14	4.41E-16	NR	NR	NR	NR
EHPV	22	1.45	1000	22	CPX	raster line	6.92E+06	2.28E+06	1.57E+01	4.32E-14	3.12E-15	NR	NR	NR	NR	1.95E-09	6.58E-10	NR	NR	NR	NR	1.95E-05	NA	9.96E-05	3.37E-05	2.61E-14	4.41E-16	NR	NR	NR	NR
EHPV	22	1.45	1000	22	CPX	raster line	4.39E+06	1.45E+06	2.25E+01	8.81E-14	2.78E-15	NR	NR	NR	NR	6.25E-09	2.07E-09	NR	NR	NR	NR	1.95E-05	NA	3.20E-04	1.06E-04	2.61E-14	4.41E-16	NR	NR	NR	NR
EHPV	22	1.45	1000	22	CPX	raster line	3.43E+06	1.13E+06	1.39E+01	3.11E-14	3.63E-15	NR	NR	NR	NR	2.82E-09	9.88E-10	NR	NR	NR	NR	1.95E-05	NA	1.44E-04	5.06E-05	2.61E-14	4.41E-16	NR	NR	NR	NR
EHPV	40	1.3	925	27	CPX_Fe	spot	5.75E+05	1.90E+05	4.57E+00	1.37E-14	2.73E-15	NR	NR	NR	NR	7.41E-09	2.86E-09	NR	NR	NR	NR	1.75E-05	NA	4.23E-04	1.63E-04	3.51E-14	3.13E-16	NR	NR	NR	NR
EHPV	40	1.3	925	27	CPX_Fe	spot	1.85E+06	6.11E+05	1.47E+01	3.00E-14	2.74E-15	NR	NR	NR	NR	5.03E-09	1.72E-09	NR	NR	NR	NR	1.75E-05	NA	2.87E-04	9.83E-05	3.51E-14	3.13E-16	NR	NR	NR	NR
EHPV	40	1.3	925	27	CPX_Fe	spot	2.79E+06	9.22E+05	2.22E+01	3.22E-14	2.92E-15	NR	NR	NR	NR	3.58E-09	1.22E-09	NR	NR	NR	NR	1.75E-05	NA	2.04E-04	6.99E-05	3.51E-14	3.13E-16	NR	NR	NR	NR
EHPV	40	1.3	925	27	CPX_Fe	spot	1.58E+06	5.22E+05	1.26E+01	2.33E-14	3.00E-15	NR	NR	NR	NR	4.57E-09	1.62E-09	NR	NR	NR	NR	1.75E-05	NA	2.61E-04	9.23E-05	3.51E-14	3.13E-16	NR	NR	NR	NR
EHPV	40	1.3	925	27	CPX_Fe	spot	8.73E+05	2.88E+05	6.95E+00	2.89E-14	2.71E-15	NR	NR	NR	NR	1.03E-08	3.52E-09	NR	NR	NR	NR	1.75E-05	NA	5.86E-04	2.01E-04	3.51E-14	3.13E-16	NR	NR	NR	NR
EHPV	40	1.3	925	27	CPX_Fe	spot	8.70E+05	2.87E+05	6.92E+00	6.21E-15	2.76E-15	NR	NR	NR	NR	2.22E-09	1.23E-09	NR	NR	NR	NR	1.75E-05	NA	1.26E-04	7.00E-05	3.51E-14	3.13E-16	NR	NR	NR	NR
EHPV	40	1.3	925	27	CPX_Fe	spot	1.58E+06	5.21E+05	1.26E+01	1.22E-14	3.00E-15	NR	NR	NR	NR	2.39E-09	9.86E-10	NR	NR	NR	NR	1.75E-05	NA	1.37E-04	5.63E-05	3.51E-14	3.13E-16	NR	NR	NR	NR
EHPV	40	1.3	925	27	CPX_Fe	spot	8.90E+05	2.94E+05	7.08E+00	8.96E-15	2.82E-15	NR	NR	NR	NR	3.13E-09	1.43E-09	NR	NR	NR	NR	1.75E-05	NA	1.78E-04	8.14E-05	3.51E-14	3.13E-16	NR	NR	NR	NR
EHPV	41	1.35	1000	39	SP_sto	raster line	8.37E+05	2.76E+05	1.79E+00	2.22E-14	7.73E-15	NR	NR	NR	NR	7.49E-09	3.59E-09	NR	NR	NR	NR	1.82E-05	NA	4.12E-04	1.97E-04	3.96E-14	2.45E-16	NR	NR	NR	NR
EHPV	41	1.35	1000	39	SP_sto	raster line	9.53E+05	3.15E+05	2.66E+00	2.01E-14	7.65E-15	NR	NR	NR	NR	5.95E-09	3.00E-09	NR	NR	NR	NR	1.82E-05	NA	3.27E-04	1.65E-04	3.96E-14	2.45E-16	NR	NR	NR	NR
EHPV	41	1.35	1000	39	SP_sto	spot	2.99E+05	9.85E+04	2.38E+00	1.41E-16	7.62E-15	NR	NR	NR	NR	1.33E-10	7.19E-09	NR	NR	NR	NR	1.82E-05	NA	7.30E-06	3.95E-04	3.96E-14	2.45E-16	NR	NR	NR	NR
EHPV	41	1.35	1000	39	SP_sto	spot	8.86E+05	2.92E+05	7.05E+00	1.72E-14	7.58E-15	NR	NR	NR	NR	5.46E-09	3.01E-09	NR	NR	NR	NR	1.82E-05	NA	3.00E-04	1.65E-04	3.96E-14	2.45E-16	NR	NR	NR	NR
EHPV	41	1.35	1000	39	SP_sto	spot	6.76E+05	2.23E+05	5.38E+00	1.56E-14	7.65E-15	NR	NR	NR	NR	6.48E-09	3.84E-09	NR	NR	NR	NR	1.82E-05	NA	3.56E-04	2.11E-04	3.96E-14	2.45E-16	NR	NR	NR	NR
EHPV	41	1.35	1000	39	SP_sto	spot	8.31E+05	2.74E+05	6.61E+00	1.42E-14	7.64E-15	NR	NR	NR	NR	4.81E-09	3.04E-09	NR	NR	NR	NR	1.82E-05	NA	2.64E-04	1.67E-04	3.96E-14	2.45E-16	NR	NR	NR	NR
EHPV	41	1.35	1000	39	SP_sto	spot	4.28E+05	1.41E+05	3.41E+00	2.81E-15	7.58E-15	NR	NR	NR	NR	1.85E-09	5.03E-09	NR	NR	NR	NR	1.82E-05	NA	1.02E-04	2.76E-04	3.96E-14	2.45E-16	NR	NR	NR	NR
EHPV	41	1.35	1000	39	SP_sto	spot	6.79E+05	2.24E+05	5.40E+00	1.37E-14	7.69E-15	NR	NR	NR	NR	5.67E-09	3.70E-09	NR	NR	NR	NR	1.82E-05	NA	3.12E-04	2.03E-04	3.96E-14	2.45E-16	NR	NR	NR	NR
EHPV	41	1.35	1000	39	SP_sto	spot	8.69E+05	2.87E+05	6.91E+00	1.34E-14	7.67E-15	NR	NR	NR	NR	4.36E-09	2.87E-09	NR	NR	NR	NR	1.82E-05	NA	2.40E-04	1.58E-04	3.96E-14	2.45E-16	NR	NR	NR	NR
EHPV	41	1.35	1000	39	SP_sto	spot	3.60E+05	1.19E+05	2.87E+00	1.09E-14	7.64E-15	NR	NR	NR	NR	8.49E-09	6.60E-09	NR	NR	NR	NR	1.82E-05	NA	4.67E-04	3.63E-04	3.96E-14	2.45E-16	NR	NR	NR	NR
EHPV	44	1.3	750	41	SP_Al	raster line	2.40E+05	7.92E+04	2.92E+00	9.17E-15	7.59E-15	NR	NR	NR	NR	1.08E-08	9.59E-09	NR	NR	NR	NR	1.75E-05	NA	6.14E-04	5.47E-04	3.96E-14	2.45E-16	NR	NR	NR	NR
EHPV	44	1.3	750	41	SP_Al	raster line	8.03E+05	2.65E+05	1.74E+00	8.28E-15	7.65E-15	NR	NR	NR	NR	2.91E-09	2.85E-09	NR	NR	NR	NR	1.75E-05	NA	1.66E-04	1.63E-04	3.96E-14	2.45E-16	NR	NR	NR	NR
EHPV	44	1.3	750	41	SP_Al	raster line	1.62E+06	5.36E+05	6.80E+00	2.44E-14	7.68E-15	NR	NR	NR	NR	4.23E-09	1.93E-09	NR	NR	NR	NR	1.75E-05	NA	2.41E-04	1.10E-04	3.96E-14	2.45E-16	NR	NR	NR	NR
EHPV	44	1.3	750	41	SP_Al	raster line	1.02E+06	3.38E+05	3.07E+00	4.01E-14	7.83E-15	NR	NR	NR	NR	1.10E-08	4.22E-09	NR	NR	NR	NR	1.75E-05	NA	6.29E-04	2.41E-04	3.96E-14	2.45E-16	NR	NR	NR	NR
EHPV	44	1.3	750	41	SP_Al	raster line	7.36E+05	2.43E+05	1.96E+00	2.96E-14	7.60E-15	NR	NR	NR	NR	1.13E-08	4.74E-09	NR	NR	NR	NR	1.75E-05	NA	6.48E-04	2.71E-04	3.96E-14	2.45E-16	NR	NR	NR	NR
EHPV	44	1.3	750	41	SP_Al	spot	1.30E+06	4.29E+05	1.03E+01	1.23E-14	7.57E-15	NR	NR	NR	NR	2.67E-09	1.86E-09	NR	NR	NR	NR	1.75E-05	NA	1.53E-04	1.06E-04	3.96E-14	2.45E-16	NR	NR	NR	NR
EHPV	44	1.3	750	41	SP_sto	raster line	1.21E+06	3.98E+05	4.24E+00	2.32E-14	2.88E-15	NR	NR	NR	NR	5.42E-09	1.91E-09	NR	NR	NR	NR	1.75E-05	NA	3.09E-04	1.09E-04	3.51E-14	3.13E-16	NR	NR	NR	NR
EHPV	44	1.3	750	41	SP_sto	raster line	1.11E+06	3.65E+05	3.28E+00	2.47E-14	2.83E-15	NR	NR	NR	NR	6.28E-09	2.19E-09	NR	NR	NR	NR	1.75E-05	NA	3.59E-04	1.25E-04	3.51E-14	3.13E-16	NR	NR	NR	NR
EHPV	44	1.3	750	41	SP_sto	raster line	7.12E+05	2.35E+05	2.35E+00	1.41E-14	2.83E-15	NR	NR	NR	NR	5.59E-09	2.16E-09	NR	NR	NR	NR	1.75E-05	NA	3.19E-04	1.23E-04	3.51E-14	3.13E-16	NR	NR	NR	NR
EHPV	44	1.3	750	41	SP_sto	spot	4.34E+04	1.43E+04	3.46E-01	bb	bb	NR	NR	NR	NR	bb	bb	NR	NR	NR	NR	1.75E-05	NA	BB	BB	3.51E-14	3.13E-16	NR	NR	NR	NR
EHPV	44	1.3	750	41	SP_sto	spot	1.14E+06	3.76E+05	9.08E+00	1.93E-14	2.90E-15	NR	NR	NR	NR	4.77E-09	1.73E-09	NR	NR	NR	NR	1.75E-05	NA	2.72E-04	9.87E-05	3.51E-14	3.13E-16	NR	NR	NR	NR
EHPV	44	1.3	750	41	SP_sto	spot	7.75E+05	2.56E+05	6.17E+00	1.49E-14	2.77E-15	NR	NR	NR	NR	5.41E-09	2.05E-09	NR	NR	NR	NR	1.75E-05	NA	3.09E-04	1.17E-04	3.51E-14	3.13E-16	NR	NR	NR	NR
EHPV	44	1.3	750	41	SP_sto	spot	1.27E+06	4.19E+05	1.01E+01	1.20E-14	2.84E-15	NR	NR	NR	NR	2.66E-09	1.08E-09	NR	NR	NR	NR	1.75E-05	NA	1.52E-04	6.17E-05	3.51E-14	3.13E-16	NR	NR	NR	NR
EHPV	44	1.3	750	41	SP_sto	spot	5.39E+05	1.78E+05	4.29E+00	7.17E-15	2.93E-15	NR	NR	NR	NR	3.75E-09	1.97E-09	NR	NR	NR	NR	1.75E-05	NA	2.14E-04	1.12E-04	3.51E-14	3.13E-16	NR	NR	NR	NR
EHPV	44	1.3	750	41	SP_sto	spot	9.02E+05	2.98E+05	7.18E+00	1.25E-14	2.83E-15	NR	NR	NR	NR	3.90E-09	1.56E-09	NR	NR	NR	NR	1.75E-05	NA	2.22E-04	8.91E-05	3.51E-14	3.13E-16	NR	NR	NR	NR
PC	7	20	1450	10	glass	spot	2.79E+05	2.79E+04	1.17E+02	1.32E-13	9.28E-16	2.28E-12	2.23E-14	3.04E-12	5.99E-15	1.78E-07	1.78E-08	3.07E-06	3.08E-07	4.09E-06	4.09E-07	NA	1.89E-07	NA	NA	4.71E-16	2.53E-17	3.32E-14	2.42E-15	1.42E-14	1.30E-16
PC	7	20	1450	10	glass	spot	1.81E+04	1.81E+03	7.63E+00	1.02E-14	2.78E-16	1.83E-13	1.65E-14	2.63E-13	5.58E-15	2.10E-07	2.18E-08	3.77E-06	5.09E-07	5.43E-06	5.55E-07	NA	1.89E-07	NA	NA	4.71E-16	2.53E-17	3.32E-14	2.42E-15	1.42E-14	1.30E-16
PC	7	20	1450	10	glass	spot	1.81E+04	1.81E+03	7.63E+00	9.00E-15	3.02E-16	1.74E-13	1.82E-14	2.07E-13	5.60E-15	1.86E-07	1.96E-08	3.60E-06	5.21E-07	4.28E-06	4.43E-07	NA	1.89E-07	NA	NA	4.71E-16	2.53E-17	3.32E-14	2.42E-15	1.42E-14	1.30E-16
PC	7	20	1450	10	glass	spot	1.84E+04	1.84E+03	7.74E+00	8.76E-15	2.68E-16	1.69E-13	1.64E-14	2.10E-13	5.58E-15	1.78E-07	1.87E-08	3.45E-06	4.80E-07	4.28E-06	4.43E-07	NA	1.89E-07	NA	NA	4.71E-16	2.53E-17	3.32E-14	2.42E-15	1.42E-14	1.30E-16
PC	7	20	1450	10	glass	spot	1.63E+04	1.63E+03	6.85E+00	8.05E-15	2.65E-16	1.70E-13	1.67E-14	2.14E-13	5.61E-15	1.85E-07	1.95E-08	3.90E-06	5.47E-07	4.93E-06	5.10E-07	NA	1.89E-07	NA	NA	4.71E-16	2.53E-17	3.32E-14	2.42E-15	1.42E-14	1.30E-16
PC	7	20	1450	10	OL_Fe	spot	1.35E+05	1.35E+04	4.67E+00	2.04E-16	2.40E-16	2.18E-15	1.66E-15	5.07E-17	2.28E-16	4.53E-10	5.54E-10	4.83E-09	4.00E-09	1.12E-10	5.07E-10	NA	1.89E-07	2.40E-03	2.93E-03	1.37E-16	2.89E-17	1.65E-15	1.59E-16	8.10E-16	1.91E-17
PC	7	20	1450	10	OL_Fe	spot profile	4.36E+04	1.44E+04	3.50E-01	1.51E-16	2.42E-16	bb	bb	8.98E-17	2.28E-16	1.04E-09	1.70E-09	bb	bb	6.17E-10	1.58E-09	NA	1.89E-07	5.49E-03	9.00E-03	1.37E-16	2.89E-17	1.65E-15	1.59E-16	8.10E-16	1.91E-17
PC	7	20	1450	10	OL_Fe	spot profile	4.36E+04	1.44E+04	7.00E-01	1.91E-16	2.37E-16	1.38E-16	1.64E-15	bb	bb	1.31E-09	1.68E-09	9.49E-10	1.13E-08	bb	bb	NA	1.89E-07	6.95E-03	8.93E-03	1.37E-16	2.89E-17	1.65E-15	1.59E-16	8.10E-16	1.91E-17
PC	7	20	1450	10	OL_Fe	spot profile	4.36E+04	1.44E+04	1.05E+00	1.91E-16	2.37E-16	1.33E-15	1.66E-15	bb	bb	1.31E-09	1.68E-09	9.12E-09	1.18E-08	bb	bb	NA	1.89E-07	6.95E-03	8.93E-03	1.37E-16	2.89E-17	1.65E-15	1.59E-16	8.10E-16	1.91E-17
PC	7	20	1450	10	OL_Fe	spot profile	4.36E+04	1.44E+04	1.40E+00	2.65E-16	2.33E-16	bb	bb	bb	bb	1.82E-09	1.71E-09	bb	bb	bb	bb	NA	1.89E-07	9.63E-03	9.07E-03	1.37E-16	2.89E-17	1.65E-15	1.59E-16	8.10E-16	1.91E-17
PC	7	20	1450	10	OL_Fe	spot profile	4.36E+04	1.44E+04	1.75E+00	1.84E-16	2.47E-16	bb	bb	bb	bb	1.27E-09	1.75E-09	bb	bb	bb	bb	NA	1.89E-07	6.71E-03	9.25E-03	1.37E-16	2.89E-17	1.65E-15	1.59E-16	8.10E-16	1.91E-17
PC	10	20	1450	2	glass	spot	1.28E+04	1.28E+03	5.39E+00	1.00E-12	3.66E-14	bb	bb	2.69E-14	8.44E-16	2.93E-05	3.12E-06	bb	bb	7.87E-07	8.25E-08	NA	2.74E-05	NA	NA	3.73E-13	5.55E-15	9.40E-14	7.73E-16	7.97E-15	6.09E-17
PC	10	20	1450	2	glass	spot	1.28E+04	1.28E+03	5.37E+00	8.50E-13	3.58E-14	bb	bb	2.47E-14	9.23E-16	2.49E-05	2.70E-06	bb	bb	7.23E-07	7.72E-08	NA	2.74E-05	NA	NA	3.73E-13	5.55E-15	9.40E-14	7.73E-16	7.97E-15	6.09E-17
PC	10	20	1450	2	glass	spot	1.20E+04	1.20E+03	5.04E+00	8.59E-13	3.63E-14	1.44E-14	1.03E-14	2.81E-14	8.71E-16	2.68E-05	2.91E-06	4.48E-07	3.24E-07	8.77E-07	9.18E-08	NA	2.74E-05	NA	NA	3.73E-13	5.55E-15	9.40E-14	7.73E-16	7.97E-15	6.09E-17
PC	10	20	1450	2	glass	spot	1.28E+04	1.28E+03	5.38E+00	9.77E-13	3.59E-14	bb	bb	2.85E-14	8.86E-16	2.86E-05	3.05E-06	bb	bb	8.33E-07	8.73E-08	NA	2.74E-05	NA	NA	3.73E-13	5.55E-15	9.40E-14	7.73E-16	7.97E-15	6.09E-17
PC	10	20	1450	2	OL_Fe	raster line	1.48E+06	4.90E+05	5.44E+00	2.23E-14	1.07E-15	bb	bb	2.53E-14	5.73E-15	4.51E-09	1.50E-09	bb	bb	5.12E-09	2.05E-09	NA	2.74E-05	1.65E-04	5.49E-05	1.34E-15	2.12E-16	1.07E-15	1.70E-16	2.79E-15	2.38E-17
PC	10	20	1450	2	OL_Fe	raster line	1.64E+06	5.41E+05	1.00E+01	3.59E-14	9.72E-16	bb	bb	1.12E-14	5.73E-15	6.55E-09	2.17E-09	bb	bb	2.04E-09	1.25E-09	NA	2.74E-05	2.39E-04	7.92E-05	1.34E-15	2.12E-16	1.07E-15	1.70E-16	2.79E-15	2.38E-17
PC	10	20	1450	2	OL_Fe	raster line	3.23E+06	1.07E+06	2.23E+01	8.29E-14	8.85E-16	bb	bb	1.83E-15	5.73E-15	7.69E-09	2.54E-09	bb	bb	1.70E-10	5.34E-10	NA	2.74E-05	2.81E-04	9.26E-05	1.34E-15	2.12E-16	1.07E-15	1.70E-16	2.79E-15	2.38E-17
PC	10	20	1450	2	OL_Fe	raster line	1.99E+06	6.55E+05	9.01E+00	4.21E-14	1.10E-15	4.63E-15	1.25E-15	6.62E-16	5.73E-15	6.34E-09	2.10E-09	6.97E-10	2.97E-10	9.96E-11	8.63E-10	NA	2.74E-05	2.31E-04	7.66E-05	1.34E-15	2.12E-16	1.07E-15	1.70E-16	2.79E-15	2.38E-17
PC	10	20	1450	2	OL_Fe	raster line	1.70E+06	5.63E+05	1.20E+01	3.32E-14	9.32E-16	bb	bb	7.53E-16	5.73E-15	5.85E-09	1.94E-09	bb	bb	1.33E-10	1.01E-09	NA	2.74E-05	2.14E-04	7.07E-05	1.34E-15	2.12E-16	1.07E-15	1.70E-16	2.79E-15	2.38E-17
PC	11	20	1450	2	glass	spot	9.62E+03	9.62E+02	1.36E+01	4.78E-13	4.53E-15	bb	bb	2.69E-14	9.36E-15	1.86E-05	1.87E-06	bb	bb	1.05E-06	3.79E-07	NA	1.92E-05	NA	NA	1.20E-14	1.24E-16	8.64E-16	4.01E-17	5.83E-15	3.90E-17
PC	11	20	1450	2	glass	spot	8.93E+03	8.93E+02	1.26E+01	5.09E-13	5.35E-15	bb	bb	2.66E-14	9.36E-15	2.13E-05	2.15E-06	bb	bb	1.11E-06	4.08E-07	NA	1.92E-05	NA	NA	1.20E-14	1.24E-16	8.64E-16	4.01E-17	5.83E-15	3.90E-17
PC	11	20	1450	2	glass	spot	8.53E+03	8.53E+02	1.21E+01	5.11E-13	4.10E-15	bb	bb	2.67E-14	9.36E-15	2.24E-05	2.25E-06	bb	bb	1.17E-06	4.27E-07	NA	1.92E-05	NA	NA	1.20E-14	1.24E-16	8.64E-16	4.01E-17	5.83E-15	3.90E-17
PC	11	20	1450	2	glass	spot	1.29E+04	1.29E+03	5.41E+00	5.41E-13	4.19E-15	1.35E-15	8.80E-16	2.63E-14	9.37E-15	1.57E-05	1.58E-06	3.91E-08	2.58E-08	7.63E-07	2.82E-07	NA	1.92E-05	NA	NA	1.20E-14	1.24E-16	8.64E-16	4.01E-17	5.83E-15	3.90E-17
PC	11	20	1450	2	glass	spot	1.02E+04	1.02E+03	4.27E+00	5.65E-13	3.98E-15	1.43E-15	9.62E-16	2.68E-14	9.36E-15	2.07E-05	2.08E-06	5.26E-08	3.57E-08	9.83E-07	3.58E-07	NA	1.92E-05	NA	NA	1.20E-14	1.24E-16	8.64E-16	4.01E-17	5.83E-15	3.90E-17
PC	11	20	1450	2	glass	spot	1.20E+04	1.20E+03	5.07E+00	5.31E-13	4.30E-15	4.11E-16	8.80E-16	2.78E-14	9.37E-15	1.66E-05	1.66E-06	1.28E-08	2.75E-08	8.68E-07	3.05E-07	NA	1.92E-05	NA	NA	1.20E-14	1.24E-16	8.64E-16	4.01E-17	5.83E-15	3.90E-17
PC	11	20	1450	2	OPX	raster line	1.22E+06	4.02E+05	7.70E+00	1.87E-14	8.62E-16	5.74E-15	1.33E-15	1.39E-14	5.73E-15	4.77E-09	1.59E-09	1.46E-09	5.91E-10	3.56E-09	1.88E-09	NA	1.92E-05	2.48E-04	8.27E-05	1.34E-15	2.12E-16	1.07E-15	1.70E-16	2.79E-15	2.38E-17
PC	11	20	1450	2	OPX	raster line	2.06E+06	6.79E+05	1.16E+01	1.46E-14	8.46E-16	7.31E-15	1.23E-15	bb	bb	2.20E-09	7.38E-10	1.10E-09	4.09E-10	bb	bb	NA	1.92E-05	1.15E-04	3.84E-05	1.34E-15	2.12E-16	1.07E-15	1.70E-16	2.79E-15	2.38E-17
PC	11	20	1450	2	OPX	raster line	1.87E+06	6.17E+05	2.48E+01	1.55E-14	8.66E-16	3.73E-15	1.16E-15	bb	bb	2.58E-09	8.63E-10	6.22E-10	2.82E-10	bb	bb	NA	1.92E-05	1.34E-04	4.49E-05	1.34E-15	2.12E-16	1.07E-15	1.70E-16	2.79E-15	2.38E-17
PC	11	20	1450	2	OPX	raster line	4.64E+06	1.53E+06	1.17E+01	5.50E-14	1.17E-15	bb	bb	1.73E-14	5.73E-15	3.69E-09	1.22E-09	bb	bb	1.16E-09	5.43E-10	NA	1.92E-05	1.92E-04	6.35E-05	1.34E-15	2.12E-16	1.07E-15	1.70E-16	2.79E-15	2.38E-17
PC	11	20	1450	2	OPX	raster line	3.28E+06	1.08E+06	2.38E+01	2.75E-13	1.34E-15	bb	bb	3.14E-13	6.10E-15	2.61E-08	8.62E-09	bb	bb	2.98E-08	9.86E-09	NA	1.92E-05	1.36E-03	4.48E-04	1.34E-15	2.12E-16	1.07E-15	1.70E-16	2.79E-15	2.38E-17
PC	12	20	1380	2	glass	spot	4.20E+03	4.20E+02	1.77E+00	1.72E-13	4.06E-14	3.68E-15	4.09E-15	2.87E-14	7.55E-16	1.53E-05	3.93E-06	3.28E-07	3.66E-07	2.56E-06	2.64E-07	NA	1.21E-05	NA	NA	4.14E-13	6.17E-15	3.37E-14	2.77E-16	6.95E-15	5.31E-17
PC	12	20	1380	2	glass	spot	7.03E+03	7.03E+02	2.96E+00	2.33E-13	3.99E-14	bb	bb	4.71E-14	7.41E-16	1.24E-05	2.46E-06	bb	bb	2.51E-06	2.54E-07	NA	1.21E-05	NA	NA	4.14E-13	6.17E-15	3.37E-14	2.77E-16	6.95E-15	5.31E-17
PC	12	20	1380	2	glass	spot	8.78E+03	8.78E+02	3.70E+00	2.63E-13	3.97E-14	bb	bb	5.97E-14	7.54E-16	1.12E-05	2.03E-06	bb	bb	2.55E-06	2.57E-07	NA	1.21E-05	NA	NA	4.14E-13	6.17E-15	3.37E-14	2.77E-16	6.95E-15	5.31E-17
PC	12	20	1380	2	glass	spot	8.51E+03	8.51E+02	3.58E+00	2.70E-13	4.00E-14	bb	bb	6.74E-14	7.58E-16	1.19E-05	2.12E-06	bb	bb	2.96E-06	2.98E-07	NA	1.21E-05	NA	NA	4.14E-13	6.17E-15	3.37E-14	2.77E-16	6.95E-15	5.31E-17

PC	12	20	1380	2	glass	spot	8.38E+03	8.38E+02	3.53E+00	2.67E-13	3.97E-14	5.42E-15	4.20E-15	6.47E-14	7.63E-16	1.20E-05	2.14E-06	2.42E-07	1.89E-07	2.89E-06	2.91E-07	NA	1.21E-05	NA	NA	4.14E-13	6.17E-15	3.37E-14	2.77E-16	6.95E-15	5.31E-17
PC	12	20	1380	2	glass	spot	4.90E+03	4.90E+02	3.90E+00	1.45E-13	3.98E-14	bb	bb	4.52E-14	7.40E-16	1.11E-05	3.24E-06	bb	bb	3.45E-06	3.50E-07	NA	1.21E-05	NA	NA	4.14E-13	6.17E-15	3.37E-14	2.77E-16	6.95E-15	5.31E-17
PC	12	20	1380	2	glass	spot	4.09E+03	4.09E+02	3.25E+00	1.24E-13	3.97E-14	bb	bb	3.99E-14	7.40E-16	1.13E-05	3.80E-06	bb	bb	3.66E-06	3.72E-07	NA	1.21E-05	NA	NA	4.14E-13	6.17E-15	3.37E-14	2.77E-16	6.95E-15	5.31E-17
PC	12	20	1380	2	glass	spot	1.03E+04	1.03E+03	4.32E+00	3.09E-13	3.99E-14	bb	bb	7.26E-14	7.69E-16	1.12E-05	1.84E-06	bb	bb	2.64E-06	2.66E-07	NA	1.21E-05	NA	NA	4.14E-13	6.17E-15	3.37E-14	2.77E-16	6.95E-15	5.31E-17
PC	12	20	1380	2	CPX	raster line	1.89E+06	6.22E+05	9.91E+00	3.12E-14	9.72E-16	9.89E-16	4.20E-16	5.25E-14	5.00E-15	4.95E-09	1.64E-09	1.57E-10	8.43E-11	8.32E-09	2.86E-09	NA	1.21E-05	4.10E-04	1.36E-04	1.49E-15	2.36E-16	3.82E-16	6.08E-17	2.44E-15	2.07E-17
PC	12	20	1380	2	CPX	raster line	1.64E+06	5.40E+05	8.10E+00	8.61E-15	9.03E-16	1.05E-16	4.37E-16	5.45E-14	5.00E-15	1.57E-09	5.44E-10	1.93E-11	8.01E-11	9.96E-09	3.41E-09	NA	1.21E-05	1.30E-04	4.51E-05	1.49E-15	2.36E-16	3.82E-16	6.08E-17	2.44E-15	2.07E-17
PC	12	20	1380	2	CPX	raster line	1.20E+06	3.97E+05	3.33E+00	1.23E-14	9.13E-16	bb	bb	5.58E-14	5.00E-15	3.07E-09	1.04E-09	bb	bb	1.39E-08	4.76E-09	NA	1.21E-05	2.55E-04	8.62E-05	1.49E-15	2.36E-16	3.82E-16	6.08E-17	2.44E-15	2.07E-17
PC	12	20	1380	2	CPX	raster line	1.76E+06	5.82E+05	1.17E+01	1.18E-14	9.07E-16	7.76E-16	4.11E-16	1.76E-13	5.02E-15	2.00E-09	6.78E-10	1.32E-10	8.24E-11	2.99E-08	9.90E-09	NA	1.21E-05	1.66E-04	5.62E-05	1.49E-15	2.36E-16	3.82E-16	6.08E-17	2.44E-15	2.07E-17
PC	12	20	1380	2	CPX	raster line	1.45E+06	4.78E+05	6.43E+00	3.91E-15	8.94E-16	bb	bb	5.27E-14	5.00E-15	8.07E-10	3.24E-10	bb	bb	1.09E-08	3.73E-09	NA	1.21E-05	6.70E-05	2.69E-05	1.49E-15	2.36E-16	3.82E-16	6.08E-17	2.44E-15	2.07E-17
PC	12	20	1380	2	CPX	raster line	1.66E+06	5.48E+05	8.37E+00	4.10E-15	9.35E-16	bb	bb	6.29E-14	5.00E-15	7.40E-10	2.97E-10	bb	bb	1.13E-08	3.85E-09	NA	1.21E-05	6.14E-05	2.46E-05	1.49E-15	2.36E-16	3.82E-16	6.08E-17	2.44E-15	2.07E-17
PC	12	20	1380	2	CPX	raster line	1.56E+06	5.16E+05	9.48E+00	3.32E-15	9.17E-16	bb	bb	6.67E-14	5.00E-15	6.36E-10	2.74E-10	bb	bb	1.28E-08	4.33E-09	NA	1.21E-05	5.28E-05	2.27E-05	1.49E-15	2.36E-16	3.82E-16	6.08E-17	2.44E-15	2.07E-17
PC	12	20	1380	2	CPX	raster line	3.19E+06	1.05E+06	1.75E+01	1.57E-14	9.17E-16	bb	bb	2.54E-13	5.01E-15	1.47E-09	4.93E-10	bb	bb	2.39E-08	7.89E-09	NA	1.21E-05	1.22E-04	4.09E-05	1.49E-15	2.36E-16	3.82E-16	6.08E-17	2.44E-15	2.07E-17
PC	13	20	1400	2	glass	spot	9.64E+04	9.64E+03	1.62E+00	3.25E-12	3.61E-14	bb	3.08E-14	1.96E-13	1.46E-15	1.26E-05	1.27E-06	bb	bb	7.60E-07	7.63E-08	NA	1.51E-05	NA	NA	2.20E-13	1.61E-15	2.40E-14	4.82E-15	1.08E-14	8.41E-17
PC	13	20	1400	2	glass	spot	9.91E+04	9.91E+03	5.61E+00	3.54E-12	2.42E-14	2.48E-14	2.81E-14	2.22E-13	1.26E-15	1.34E-05	1.34E-06	9.38E-08	1.06E-07	8.39E-07	8.41E-08	NA	1.51E-05	NA	NA	2.20E-13	1.61E-15	2.40E-14	4.82E-15	1.08E-14	8.41E-17
PC	13	20	1400	2	glass	spot	8.93E+04	8.93E+03	5.05E+00	3.74E-12	2.46E-14	2.08E-14	2.83E-14	2.20E-13	1.24E-15	1.57E-05	1.57E-06	8.74E-08	1.19E-07	9.23E-07	9.24E-08	NA	1.51E-05	NA	NA	2.20E-13	1.61E-15	2.40E-14	4.82E-15	1.08E-14	8.41E-17
PC	13	20	1400	2	glass	spot	4.54E+04	4.54E+03	2.57E+00	1.94E-12	3.27E-14	bb	2.91E-14	1.16E-13	1.20E-15	1.60E-05	1.62E-06	bb	bb	9.60E-07	9.65E-08	NA	1.51E-05	NA	NA	2.20E-13	1.61E-15	2.40E-14	4.82E-15	1.08E-14	8.41E-17
PC	13	20	1400	2	glass	spot	4.65E+04	4.65E+03	2.63E+00	1.93E-12	2.93E-14	6.76E-14	2.84E-14	1.16E-13	1.27E-15	1.56E-05	1.58E-06	5.44E-07	2.35E-07	9.38E-07	9.44E-08	NA	1.51E-05	NA	NA	2.20E-13	1.61E-15	2.40E-14	4.82E-15	1.08E-14	8.41E-17
PC	13	20	1400	2	glass	spot	3.02E+04	3.02E+03	1.71E+00	1.36E-12	2.39E-14	3.23E-14	2.95E-14	8.14E-14	1.21E-15	1.69E-05	1.71E-06	4.00E-07	3.67E-07	1.01E-06	1.02E-07	NA	1.51E-05	NA	NA	2.20E-13	1.61E-15	2.40E-14	4.82E-15	1.08E-14	8.41E-17
PC	13	20	1400	2	glass	spot	3.27E+04	3.27E+03	1.85E+00	1.37E-12	2.44E-14	3.09E-14	2.76E-14	8.31E-14	1.19E-15	1.56E-05	1.59E-06	3.53E-07	3.18E-07	9.51E-07	9.61E-08	NA	1.51E-05	NA	NA	2.20E-13	1.61E-15	2.40E-14	4.82E-15	1.08E-14	8.41E-17
PC	13	20	1400	2	SP_Cr	raster line	2.16E+06	7.14E+05	1.03E+01	6.32E-15	6.67E-16	bb	bb	bb	bb	8.23E-10	2.85E-10	bb	bb	bb	bb	NA	1.51E-05	5.44E-05	1.89E-05	2.04E-15	9.12E-17	1.33E-15	1.37E-16	3.65E-15	7.53E-17
PC	13	20	1400	2	SP_Cr	raster line	1.41E+06	4.64E+05	6.94E+00	3.27E-15	6.52E-16	bb	bb	bb	bb	6.55E-10	2.53E-10	bb	bb	bb	bb	NA	1.51E-05	4.34E-05	1.67E-05	2.04E-15	9.12E-17	1.33E-15	1.37E-16	3.65E-15	7.53E-17
PC	13	20	1400	2	SP_Cr	raster line	2.93E+06	9.67E+05	9.44E+00	2.55E-15	6.64E-16	bb	bb	bb	bb	2.45E-10	1.03E-10	bb	bb	bb	bb	NA	1.51E-05	1.62E-05	6.82E-06	2.04E-15	9.12E-17	1.33E-15	1.37E-16	3.65E-15	7.53E-17
PC	13	20	1400	2	SP_Cr	raster line	2.40E+06	7.93E+05	9.56E+00	4.79E-15	6.57E-16	bb	bb	bb	bb	5.61E-10	2.01E-10	bb	bb	bb	bb	NA	1.51E-05	3.72E-05	1.33E-05	2.04E-15	9.12E-17	1.33E-15	1.37E-16	3.65E-15	7.53E-17
PC	13	20	1400	2	SP_Cr	raster line	2.92E+06	9.64E+05	6.51E+00	7.96E-15	6.57E-16	bb	bb	bb	bb	7.67E-10	2.61E-10	bb	bb	bb	bb	NA	1.51E-05	5.07E-05	1.73E-05	2.04E-15	9.12E-17	1.33E-15	1.37E-16	3.65E-15	7.53E-17

NR = not reported
NA = field not applicable to particular analysis
BB = voltage of analysis below blank for session
Reported number of moles released are corrected for blanks
*pit type:
spot = ablation into single spot with constant appeature
spot profile = ablation into single spot with constant apeature where gas is collected and analyzed at intermediate stages
raster line = ablation along a line with constant aperture
terraced pit = ablation into one spot with a step(s) in aperture radius
** pit volume:
Pit volumes are calculated using white light interferometer. See text for more detail.
*** calculated He solubilty, melt:
The solublity of He in basaltic melt is calculated using the noble gas solublity model of Iacono-Marziano et al. (2010). See text for more detail.

Supplementary Table 2: Major element analyses of minerals

phase	Provenance		SiO2	TiO2	Al2O3	Cr2O3	FeO	MnO	MgO	CaO	Na2O	Total
OPX	Chandrika Wewa Reservoir, Embilipitiya, Sri Lanka, Harvard Mineral Museum # 132059C	avg.	58.58	0.02	1.96	0.00	0.29	0.00	39.01	0.13	bd	99.99
		avg. (norm. 100%)	58.59	0.02	1.96	0.00	0.29	0.00	39.02	0.13	bd	100.00
		stdev.	0.09	0.01	0.02	0.01	0.03	0.01	0.11	0.01	0.01	
OPX_Fe	Gairo, Tanzania, Harvard Mineral Museum # 132059C	avg.	58.30	0.03	1.44	0.00	1.34	0.08	38.66	0.11	0.03	100.00
		avg. (norm. 100%)	58.30	0.03	1.44	0.00	1.34	0.08	38.66	0.11	0.03	100.00
		stdev.	0.02	0.01	0.01	0.01	0.04	0.01	0.05	0.01	0.01	
CPX	synthetic, Sneeringer, M.A., PhD thesis, MIT, 1981	avg.	55.63	0.00	0.00	0.00	0.01	0.00	20.01	24.33	bd	99.98
		avg. (norm. 100%)	55.64	0.00	0.00	0.00	0.01	0.00	20.02	24.33	bd	100.00
		stdev.	0.03	0.01	0.01	0.01	0.02	0.01	0.05	0.05	bd	
CPX_Fe	natural, unknown	avg.	55.10	0.06	0.21	0.51	1.07	0.04	17.98	24.70	0.32	100.00
		avg. (norm. 100%)	55.10	0.06	0.21	0.51	1.07	0.04	17.98	24.70	0.32	100.00
		stdev.	0.04	0.01	0.01	0.03	0.03	0.01	0.02	0.03	0.03	
OL	synthetic, Morion Corp. Czochralski	avg.	42.79	0.00	0.00	0.01	bd	bd	57.19	0.00	0.00	99.99
		avg. (norm. 100%)	42.79	0.00	0.00	0.01	bd	bd	57.20	0.00	0.00	100.00
		stdev.	0.03	0.00	0.01	0.01	bd	bd	0.05	0.01	0.01	
OL_Fe	San Carlos	avg.	40.07	0.01	0.02	0.02	12.59	0.16	47.05	0.07	0.00	99.99
		avg. (norm. 100%)	40.08	0.01	0.02	0.02	12.59	0.16	47.05	0.07	0.00	100.00
		stdev.	0.07	0.00	0.01	0.01	0.10	0.01	0.09	0.00	0.03	
SP_Al	synthetic, non-sto.(Al-rich), unknown method	avg.	0.02	0.01	88.23	0.00	bd	0.01	11.71	0.00	0.00	99.97
		avg. (norm. 100%)	0.02	0.01	88.25	0.00	bd	0.01	11.71	0.00	0.00	100.00
		stdev.	0.01	0.00	0.05	0.01	bd	0.01	0.03	0.00	0.02	
SP_Cr	Sri Lanka, Harvard Mineral Museum #88346	avg.	0.03	0.24	68.32	2.72	0.05	0.01	28.62	0.00	bd	99.99
		avg. (norm. 100%)	0.03	0.24	68.32	2.72	0.05	0.01	28.62	0.00	bd	100.00
		stdev.	0.00	0.02	0.30	0.29	0.04	0.01	0.08	0.00	bd	
SP	synthetic, MTI corp., Czochralski	avg.	0.03	0.00	71.55	0.00	0.01	0.01	28.39	0.00	0.00	99.98
		avg. (norm. 100%)	0.03	0.00	71.57	0.00	0.01	0.01	28.39	0.00	0.00	100.00
		stdev.	0.01	0.01	0.05	0.01	0.04	0.01	0.02	0.00	0.02	

Supplementary Table 3: Major element analyses of melts

Experiment		SiO2	TiO2	Al2O3	Cr2O3	MnO	FeO	MgO	CaO	Na2O	K2O	Total
PC_EXP7	avg.	48.51	0.50	14.56	0.22	0.11	6.48	12.80	12.11	1.63	0.07	96.99
	avg. (norm. 100%)	50.01	0.52	15.01	0.23	0.11	6.68	13.20	12.48	1.68	0.07	100.00
	stdev.	0.09	0.00	0.07	0.01	0.03	0.06	0.03	0.03	0.04	0.00	
PC_EXP10	avg.	49.47	0.47	14.43	0.23	0.09	6.38	12.83	11.96	1.61	0.06	97.55
	avg. (norm. 100%)	50.71	0.48	14.80	0.23	0.10	6.54	13.16	12.26	1.65	0.06	100.00
	stdev.	0.05	0.01	0.06	0.02	0.01	0.07	0.06	0.04	0.07	0.00	
PC_EXP11	avg.	49.12	0.47	14.45	0.23	0.10	6.37	12.67	11.95	1.54	0.06	96.99
	avg. (norm. 100%)	50.65	0.49	14.90	0.24	0.11	6.57	13.07	12.32	1.59	0.07	100.00
	stdev.	0.11	0.01	0.07	0.01	0.02	0.08	0.03	0.03	0.05	0.00	
PC_EXP12	avg.	48.23	0.45	14.52	0.21	0.10	6.42	12.96	12.38	1.56	0.06	96.89
	avg. (norm. 100%)	49.78	0.47	14.98	0.22	0.10	6.63	13.37	12.78	1.61	0.06	100.00
	stdev.	0.08	0.01	0.03	0.03	0.01	0.07	0.04	0.03	0.06	0.00	
PC_EXP13	avg.	48.39	0.44	14.51	0.24	0.10	6.42	12.81	12.27	1.53	0.06	96.78
	avg. (norm. 100%)	50.01	0.46	14.99	0.25	0.10	6.64	13.23	12.68	1.58	0.07	100.00
	stdev.	0.06	0.02	0.03	0.02	0.02	0.07	0.03	0.04	0.05	0.00	

References used to determine $U+Th_{avg}$

Adam, J., Green, T., 2003. The influence of pressure, mineral composition and water on trace element partitioning between clinopyroxene, amphibole and basanitic melts. European Journal of Mineralogy 15, 831-841.

Adam, J., Green, T., 2006. Trace element partitioning between mica- and amphibole-bearing garnet lherzolite and hydrous basanitic melt: 1. Experimental results and the investigation of controls on partitioning behaviour. Contributions to Mineralogy and Petrology 152, 1-17.

Blundy, J., Wood, B., 2003. Mineral-Melt Partitioning of Uranium, Thorium and Their Daughters. Reviews in Mineralogy and Geochemistry 52, 59-123.

Frei, D., Liebscher, A., Franz, G., Wunder, B., Klemme, S., Blundy, J., 2009. Trace element partitioning between orthopyroxene and anhydrous silicate melt on the lherzolite solidus from 1.1 to 3.2 GPa and 1,230 to 1,535 degrees C in the model system Na2O-CaO-MgO-Al2O3-SiO2. Contributions to Mineralogy and Petrology 157.

Gaetani, G.A., Kent, A.J.R., Grove, T.L., Hutcheon, I.D., Stolper, E.M., 2003. Mineral/melt partitioning of trace elements during hydrous peridotite partial melting. Contributions to Mineralogy and Petrology 145.

Green, T.H., Blundy, J.D., Adam, J., Yaxley, G.M., 2000. SIMS determination of trace element partition coefficients between garnet, clinopyroxene and hydrous basaltic liquids at 2-7.5 GPa and 1080-1200 degrees C. Lithos 53, 165-187.

Hill, E., Wood, B.J., Blundy, J.D., 2000. The effect of Ca-Tschermaks component on trace element partitioning between clinopyroxene and silicate melt. Lithos 53.

Lundstrom, C.C., Shaw, H.F., Ryerson, F.J., Williams, Q., Gill, J., 1998. Crystal chemical control of clinopyroxene-melt partitioning in the Di-Ab-An system: Implications for elemental fractionations in the depleted mantle. Geochimica Et Cosmochimica Acta 62.

McDade, P., Blundy, J.D., Wood, B.J., 2003a. Trace element partitioning between mantle wedge peridotite and hydrous MgO-rich melt. American Mineralogist 88.

McDade, P., Blundy, J.D., Wood, B.J., 2003b. Trace element partitioning on the Tinaquillo Lherzolite solidus at 1.5 GPa. Physics of the Earth and Planetary Interiors 139.

Salters, V.J.M., Longhi, J., 1999. Trace element partitioning during the initial stages of melting beneath mid-ocean ridges. Earth and Planetary Science Letters 166.

Salters, V.J.M., Longhi, J.E., Bizimis, M., 2002. Near mantle solidus trace element partitioning at pressures up to 3.4 GPa. Geochemistry Geophysics Geosystems 3.

Tuff, J., Gibson, S.A., 2007. Trace-element partitioning between garnet, clinopyroxene and Fe-rich picritic melts at 3 to 7 GPa. Contributions to Mineralogy and Petrology 153.

van Kan Parker, M., Liebscher, A., Frei, D., van Sijl, J., van Westrenen, W., Blundy, J., Franz, G., 2010. Experimental and computational study of trace element distribution between orthopyroxene and anhydrous silicate melt: substitution mechanisms and the effect of iron. Contributions to Mineralogy and Petrology 159.

van Kan Parker, M., Mason, P.R.D., van Westrenen, W., 2011. Experimental study of trace element partitioning between lunar orthopyroxene and anhydrous silicate melt: Effects of lithium and iron. Chemical Geology 285.

van Westrenen, W., Blundy, J.D., Wood, B.J., 2000. Effect of Fe2+ on garnet-melt trace element partitioning: experiments in FCMAS and quantification of crystal-chemical controls in natural systems. Lithos 53.

Wood, B.J., Blundy, J.D., Robinson, J.A.C., 1999. The role of clinopyroxene in generating U-series disequilibrium during mantle melting. Geochimica Et Cosmochimica Acta 63.

CHAPTER 2: Noble gas transport into the mantle facilitated by high solubility in amphibole

Colin R.M. Jackson[1], Stephen W. Parman[1], Simon P. Kelley[2], Reid F. Cooper[1]

1 Geological Sciences, Brown University, Providence, RI 02912
2 Department of Environment, Earth and Ecosystems, The Open University, Milton Keynes, United Kingdom

Submitted to:
Nature Geoscience
October 5, 2012

Accepted:
May 13, 2013

Title: Noble gas transport into the mantle facilitated by high solubility in amphibole

Authors: Colin R.M. Jackson, Stephen W. Parman, Simon P. Kelley, Reid F. Cooper

Noble gases trace the chemical evolution of both the Earth's atmosphere and mantle [1-5]. A key aspect is the balance between the flux of noble gases leaving Earth's interior through magmatism and the flux of noble gases back into the mantle via recycling at subduction zones. It is traditionally assumed that recycling of noble gases is negligible [e.g.1]. However, analyses of natural samples suggest that the inward flux of noble gases is more significant than previously recognized [e.g.6-8]. The mechanisms (e.g. fluid encapsulation or mineral dissolution) responsible for returning noble gases to the mantle, however, remain unclear. Here we report high-pressure experimental measurements of noble gas solubility in amphibole, which is an important hydrous mineral in altered-oceanic crust (AOC) [9-11]. Noble gases are very soluble in amphibole (up to $1x10^{-8}$ mol g^{-1} bar^{-1}, helium), and solubility correlates with the concentration of unoccupied A-sites present. These correlations provide strong evidence that A-sites are energetically favorable locations for noble gas dissolution in amphibole. Thus, subduction of AOC provides a potential mechanism for recycling noble gases. Many hydrous minerals present in subducting slabs have lattice structures similar to the A-site in amphibole (serpentine & chlorite) and may provide even larger recycling pathways [7,11].

The analysis of noble gases in basaltic materials derived from the mantle is complicated by ubiquitous atmospheric contamination [e.g.12]. The prevalence of these modern atmospheric contaminants make it difficult to confidently determine if different

mantle reservoirs contain an intrinsic recycled component that is ultimately derived from Earth's paleo-atmosphere. However, it is well established that radiogenic, and to a lesser degree non-radiogenic [13], noble gas heterogeneity exists between different mantle reservoirs and between the atmosphere and mantle [e.g.5,6,13-18]. The fact that this heterogeneity exists requires long time scales for mixing noble gases within the solid Earth and for mixing atmospheric noble gases into the mantle. At the same time, high-precision noble gas measurements of materials derived from the mantle now raise the possibility that substantial quantities of atmospheric noble gases have been recycled back into the mantle [6-8,13-18]. The proposed recycling of chemically inert noble gases met resistance, in part because noble gas solubility in geologically relevant minerals was thought to be low. However, data relevant to the transport of noble gases in subduction zones are scarce [e.g.7,8,19-21], leaving potential transport mechanisms for noble gases into subduction zones and the convecting mantle unclear [e.g.6,7].

This study seeks to clarify the possible role of hydrothermally altered-oceanic crust (AOC) in noble gas recycling by measuring the solubility of noble gases (He and Ne) in amphibole (Figure 1), a common mineral in AOC. Amphibole comprises 1.5-12 % of bulk basaltic crust and can locally occupy 50% of AOC [9,10]. As amphibole is a major volatile-bearing component of subducted crust, it has the potential to recycle noble gases and other volatile elements (e.g. H_2O, F, Cl). High solubility would imply that noble gases could be recycled via AOC (at least to the depth of amphibole breakdown, ~100 km) along with other volatiles, while low solubility would imply that amphibole is not a major carrier of noble gases.

Helium and neon solubilities were measured in six amphiboles that span a range of compositions (Supplementary Information, Table 1). The experiments consisted of gem-quality crystals that were equilibrated with He-Ne-Ar gas mixtures at pressures up to 1.7 kbar and temperatures up to 875^{o}C in an externally-heated, gas-pressure device. The crystals were then measured for noble gas concentration with a laser-ablation noble gas mass spectrometer (see Supplementary Information for detailed methods).

The solubility of He and Ne in amphibole is high relative to other silicates, and varies with amphibole composition. Pargasite and richterite have Henry's constants for He of 0.3-1x10^{-9} (mol g^{-1} bar^{-1}), while actinolite (1-8x10^{-9}) and tremolite (1x10^{-8}) have significantly higher solubilities (Figure 2). The Henry's constants for He in amphibole are up to four orders of magnitude greater than in other Fe-Mg bearing silicates, such as olivine and pyroxene [22,23] (assuming Henry's Law applies). Measured He solubilities are independent of temperature, run duration, and ablation pit depth, with the exception of two low temperature, short duration experiments (Supplementary Information, Figure 1). These findings demonstrate a close approach to equilibrium was achieved for He, and so diffusional disequilibrium effects do not appear to have influenced the measured concentrations. The lack of temperature dependence of He solubility indicates He dissolution in amphibole has a relatively small associated enthalpy. This allows for simple extrapolation of solubilites to higher (magmatic) or lower temperatures (hydrothermal). Likewise, Henry's constants for He are independent of P_{He} over the range explored here. This allows Henry's constants to be extrapolated to natural conditions.

Neon diffuses more slowly than He and so diffusional equilibrium was not obtained during the experiments (Supplementary Information, Figure 2). The solubility of Ne, however, can be quantified by extrapolating diffusion profiles of Ne to the surface of the crystal (assumed to be at equilibrium with the pressure medium). Due to analytical interferences and the extrapolation to the surface, uncertainties in Ne solubility are substantially greater than those for He. However, the extrapolated results show, like He, Ne solubility is high, with actinolite having higher solubilities than pargasite and richterite. (Figure 3) The best-fit Henry's constants for Ne are $1x10^{-10}$ (mol g^{-1} bar^{-1}) for richterite, $1x10^{-9}$ for amber pargasite, and $3\text{-}4x10^{-9}$ for the actinolites (Figure 3a).

The higher precision of the new experimental data allows a range of outstanding questions to be addressed. Chief amongst these is where noble gases are located in silicate mineral structures. The variation in both He and Ne solubility between the amphiboles can be understood by considering the A-site, or ring site, in amphibole. This site is constituted by a pair of opposing six member $(Si,Al)O_4^{-4,-5}$ tetrahedra rings (Figure 1). These ring sites host large ion lithophile elements (large radius), but are unoccupied (uncharged) when other cations within the amphibole structure satisfy charge balance. Following lattice strain theory, ring sites are energetically favorable locations for noble gases (large radius, uncharged elements) in mineral structures. Figure 2a shows that He solubility does not correlate with the concentration of ring sites present, which is similar for all of amphiboles. But He solubility does show an excellent correlation with the concentration of *unoccupied* ring sites in the amphiboles (Figure 2b). This correlation strongly implies that He partitions readily into the unoccupied (and uncharged) ring sites in amphibole. The affinity of He for these sites has substantial implications for recycling

of noble gases, as similar ring sites (with variable occupancy) are present in a wide range of hydrous minerals.

Though analytical uncertainties are greater, Ne solubility also correlates with unoccupied ring concentration (Figure 3a). For actinolite and richterite, He is approximately twice as soluble as Ne, while He is marginally more soluble in pargasite (Figure 3b). Since noble gases do not have net charges, one way they can form bonds is for their electrons to localize in a polarized environment, enabling the formation of dipole-induced dipole bonds. Noble gas polarizability correlates with atomic radius, and consequently, Ne is more polarizable than He. The fact that Ne is not more soluble than He implies that, while polarizability may play a role in noble gas solubility, it likely competes with other factors in determining solubility associated with the ring site.

The affinity of noble gases for ring sites is consistent with previous analyses of natural and experimental ring site-bearing materials. High concentrations of noble gases have been observed in a wide range of ring site-bearing minerals, such as beryl, cordierite, tourmaline, and amphibole [24,25]. High concentrations of mantle-derived helium have been correlated with the presence of tremolitic (unoccupied ring site-rich) amphibole in AOC [26], consistent with the present experimental results. High concentrations of noble gases have also been observed in serpentinite [7]. Further, the ring site in leucite transforms from highly distorted to symmetrical with temperature, and this transformation is associated with a substantial increase in the Ar Henry's constant [27]. Determinations of Ar solubility in melts suggest unoccupied (Si,Al)-O ring structures host noble gases in silicate liquids, and that ring structure collapse at high pressure is associated with a discontinuous drop in noble gas solubility [28]. Combined, these

observations suggest all noble gases may have a high affinity for unoccupied ring sites, regardless of the structure of the material surrounding the ring.

Despite the high capacity for noble gases, it is not necessary that noble gases are recycled via amphibole in AOC. Recycling can be broken into two factors: abundance input into a subduction zone and percentage lost before slab material is transported to the convecting mantle. Thus, the flux of noble gases recycled via hydrothermal minerals primarily depends on two parameters: 1) the product of noble gas fugacity present during mineral equilibration (supplied by brines derived from seawater or fluids generated by mineral decomposition) and noble gas Henry's constants for the applicable minerals, and 2) the depth at which noble gases are released from the slab during subduction (i.e. fore-arc, arc, or back-arc). The high solubility of noble gases in amphibole indicates that AOC has the *potential* to input large quantities noble gases, H_2O, Cl, and F into subduction zones. Amphibole alone is capable of transporting volatiles to ~100 km depth. Deeper transport may be facilitated by other ring-bearing minerals, like mica or antigorite, or a free fluid phase trapped within subducting materials. It is important to note that noble gas diffusion through minerals, including amphibole, is an inefficient transport mechanism. For example, using the fastest diffusion coefficient for Ne from this study, (Supplementary Information) the characteristic diffusion length scale is ~0.35 m in 100 Ma. Significant loss of noble gases from AOC likely requires advection via a fluid phase.

Elemental patterns of noble gases derived from the mantle suggest heavier noble gases are recycled in ratios in excess of seawater [6]. This important observation can be used to investigate the materials responsible for noble gas recycling.

Helium appears to be more soluble than Ne in amphibole (Figure 3b); suggesting amphibole could facilitate preferential the subduction of light, rather than heavy, noble gases. Alone, this observation argues against AOC being a major contributor to noble gas recycling. Alternatively, AOC may contribute to noble gas recycling if other factors counter the apparent preference of amphibole for lighter noble gases. Factors may include preferential diffusive loss of lighter noble gases during the early stages of subduction or noble gas fractionations associated with amphibole breakdown and stabilization of deeper hydrous minerals. It is also possible that AOC can preferentially recycle light noble gases if the integrated recycling flux is dominated by other materials (minerals, defect structures, fluids) that preferentially recycle heavy noble gases. Indeed, there is experimental and observational evidence that serpentine has a greater affinity for heavier noble gases [7,20]. In either case, the high solubility of noble gases associated with unoccupied ring sites in amphibole demonstrates that minerals can transport significant amounts of noble gases in subduction zones and that minerals can induce strong inter-noble gas fractionations.

In addition to transporting seawater-derived noble gases into subduction zones, amphibole offers a mechanism to trap mantle-derived noble gases in the lithosphere. Low degree melts that infiltrate lithospheric mantle stabilize hydrous minerals, like amphibole [29]. These amphibole-bearing lithologies, once subducted or delaminated, may be noble gas-rich and contribute to the heterogeneity of radiogenic and non-radiogenic noble gases observed within the mantle [e.g.13,17,18]. Combining experimentally determined silicate melt solubility data [30] with the present dataset, we predict a He and Ne partition coefficient (amphibole-basaltic melt) for amphibole near 0.25 for an amphibole in equilibrium with

peridotite (50% unoccupied rings) [29]. This relatively high partition coefficient indicates amphibole can be a significant host of noble gases in lithospheric mantle environments.

An increasing number of observations suggest atmospheric noble gas isotopes of Ar, Kr, and Xe are recycled in significant quantities. Our new experimental measurements demonstrate that He and Ne are highly soluble in amphibole and that this solubility is associated with unoccupied ring sites. Similar sites exist in other hydrous minerals present in subducting lithosphere, potentially providing a range of transport mechanisms for noble gases both into subduction zones and the convecting mantle. Further work is now required to establish the extent to which noble gas recycling is coupled to recycling of water and other volatiles during subduction, and therefore, to determine if noble gases can be used as tracers of volatile cycling in general.

References:

Allegre, C. J., Hofmann, A. & Onions, K. The Argon constraints on mantle structure. *Geophysical Research Letters* **23**, 3555-3557, (1996).

Kurz, M. D., Jenkins, W. J. & Hart, S. R. Helium isotopic systematics of oceanic island and mantle heterogeneity. *Nature* **297**, 43-47, (1982).

Ballentine, C. J., Marty, B., Lollar, B. S. & Cassidy, M. Neon isotopes constrain convection and volatile origin in the Earth's mantle. *Nature* **433**, 33-38

Pujol, M., Marty, B. & Burgess, R. Chondritic-like xenon trapped in Archean rocks: A possible signature of the ancient atmosphere. *Earth and Planetary Science Letters* **308**, 298-306, (2011).

Moreira, M., Kunz, J. & Allegre, C. Rare gas systematics in popping rock: Isotopic and elemental compositions in the upper mantle. *Science* **279**, 1178-1181, (1998).

Holland, G. & Ballentine, C. J. Seawater subduction controls the heavy noble gas composition of the mantle. *Nature* **441**, 186-191, (2006).

Kendrick, M. A., Scambelluri, M., Honda, M. & Phillips, D. High abundances of noble gas and chlorine delivered to the mantle by serpentinite subduction. *Nature Geosci* **4**, 807-812, (2011).

Sumino, H. *et al.* Seawater-derived noble gases and halogens preserved in exhumed mantle wedge peridotite. *Earth and Planetary Science Letters* **294**, 163-172, 029 (2010).

Ito, E., Harris, D. M. & Anderson, A. T. Alteration of oceanic crust and geologic cycling of chlorine and water. *Geochimica Et Cosmochimica Acta* **47**, 1613-1624 (1983).

Carlson, R. L. Bound water content of the lower oceanic crust estimated from modal analyses and seismic velocities of oceanic diabase and gabbro. *Geophysical Research Letters* **30**, (2003).

Hacker, B. R. H_2O subduction beyond arcs. *Geochemistry Geophysics Geosystems* **9**, 24, (2008).

Ballentine, C. J. & Barfod, D. N. The origin of air-like noble gases in MORB and OIB. *Earth and Planetary Science Letters* **180**, 39-48, (2000).

Mukhopadhyay, S. Early differentiation and volatile accretion recorded in deep-mantle neon and xenon. *Nature* **486**, (2012).

Caffee, M. W. *et al.* Primordial noble cases from Earth's mantle: Identification of a primitive volatile component. *Science* **285**, 2115-2118, (1999).

Trieloff, M., Kunz, J., Clague, D. A., Harrison, D. & Allegre, C. J. The nature of pristine noble gases in mantle plumes. *Science* **288**, 1036-1038, (2000).

Holland, G., Cassidy, M. & Ballentine, C. J. Meteorite Kr in Earth's Mantle Suggests a Late Accretionary Source for the Atmosphere. *Science* **326**, 1522-1525, (2009).

Parai, R., Mukhopadhyay, S. & Standish, J. Heterogeneous upper mantle Ne, Ar and Xe isotopic compositions and a possible Dupal noble gas signature recorded in basalts from the Southwest Indian Ridge. *Earth and Planetary Science Letters* **359**, 227-239 (2012).

Tucker, J. M., Mukhopadhyay, S. & Schilling, J. G. The heavy noble gas composition of the depleted MORB mantle (DMM) and its implications for the preservation of heterogeneities in the mantle. *Earth and Planetary Science Letters* **355**, 244-254 (2012).

Moreira, M. *et al.* He and Ne isotopes in oceanic crust: implications for noble gas recycling in the mantle. *Earth and Planetary Science Letters* **216**, 635-643, (2003).

Zaikowski, A. & Schaeffer, O. A. Solubilty of Noble Gases in Serpentine – Implications for Meteoritic Noble Gas Abundances. *Earth and Planetary Science Letters* **45**, 141-154 (1979).

Staudacher, T. & Allegre, C. J. Recycling of oceanic crust and sediments-the noble gas subduction barrier. *Earth and Planetary Science Letters* **89**, 173-183, (1988).

Heber, V. S., Brooker, R. A., Kelley, S. P. & Wood, B. J. Crystal-melt partitioning of noble gases (helium, neon, argon, krypton, and xenon) for olivine and clinopyroxene. *Geochimica Et Cosmochimica Acta* **71**, 1041-1061, (2007).

Parman, S. W., Kurz, M. D., Hart, S. R. & Grove, T. L. Helium solubility in olivine and implications for high $^{3}He/^{4}He$ in ocean island basalts. *Nature* **437**, 1140-1143, (2005).

Kelley, S. Excess argon in K-Ar and Ar-Ar geochronology. *Chemical Geology* **188**, 1-22, (2002).

Damon, P. E. & Kulp, J. L. Excess helium and argon in beryl and other minerals. *American Mineralogist* **43**, 433-459 (1958).

Kumagai, H., Dick, H. J. B. & Kaneoka, I. Noble gas signatures of abyssal gabbros and peridotites at an Indian Ocean core complex. *Geochemistry Geophysics Geosystems* **4**, (2003).

Wartho, J. A., Kelley, S. P. & Elphick, S. C. Estimates of Ar diffusion and solubility in leucite and nepheline: Electron microprobe imaging of Ar distribution in a mineral. *American Mineralogist* **90**, 954-962, (2005).

Chamorro-Perez, E., Gillet, P., Jambon, A., Badro, J. & McMillan, P. Low argon solubility in silicate melts at high pressure. *Nature* **393,** 352-355 (1998).

Green, D. H., Hibberson, W. O., Kovacs, I. & Rosenthal, A. Water and its influence on the lithosphere-asthenosphere boundary. *Nature* **467**, 448-U497, (2010).

Lux, G. The Behavior of noble gases in silicate liquids – Solution, diffusion, bubbles, and surface effects, with applications to natural samples. *Geochimica Et Cosmochimica Acta* **51**, 1549-1560, (1987).

Figure Captions:

Figure 1: Amphibole lattice structure. The A-site, or ring site, in amphibole is constituted by an opposing pair of tetrahedral rings bound in a hexagonal pattern. It is a large site and unoccupied when charge balance is satisfied by the other cations in amphibole. The ring site location is marked by larger black dots. The M4 site is marked by smaller grey dots. Noble gases are large radius, zero charged elements, and following lattice-strain theory, should partition into ring-sites.

Figure 2: Helium Henry's constants in amphiboles plotted against ring site concentration (mol g^{-1}) (A) and unoccupied ring site concentration (B). Helium solubility is high compared to mantle minerals and correlates with the concentration of unoccupied ring-sites rather the concentration of total ring-sites. This correlation provides experimental support for the hypothesis that noble gases partition strongly onto ring sites. Ring site-bearing lithologies have the potential to deliver significant quantities of noble gases, water, and halogens to subduction zones. Thus, atmospheric noble gas isotopes may be useful tracers of volatile element recycling. Error bars are one standard deviation of replicate analyses.

Figure 3: Neon Henry's constants in amphiboles plotted against unoccupied ring site concentration (A) and He/Ne (solubility ratio) (B). Data in (A) are fit from Ne concentration profiles using a diffusion model (Supplementary Information). Similar to He, Ne solubility is high compared to mantle minerals and correlates with the

concentration of unoccupied ring sites rather the concentration of total ring sites (A). The ring site in amphibole appears to favor He over Ne (B), suggesting lighter noble gases have a greater affinity for this site compared to heavier noble gases. Error bars are one standard deviation. Dashed error bars indicate uncertainty is undefined.

Chapter 2, Figure 1

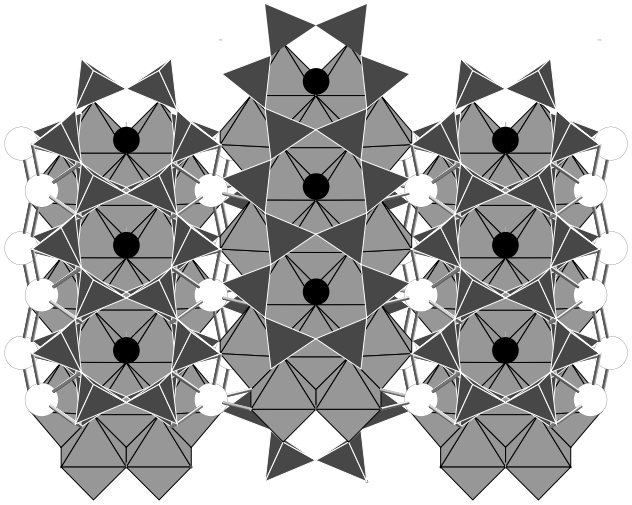

Chapter 2, Figure 2

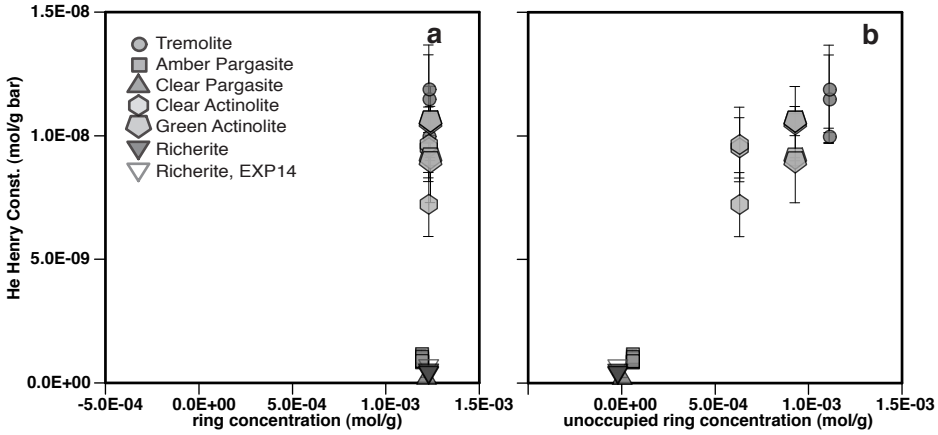

Chapter 2, Figure 3

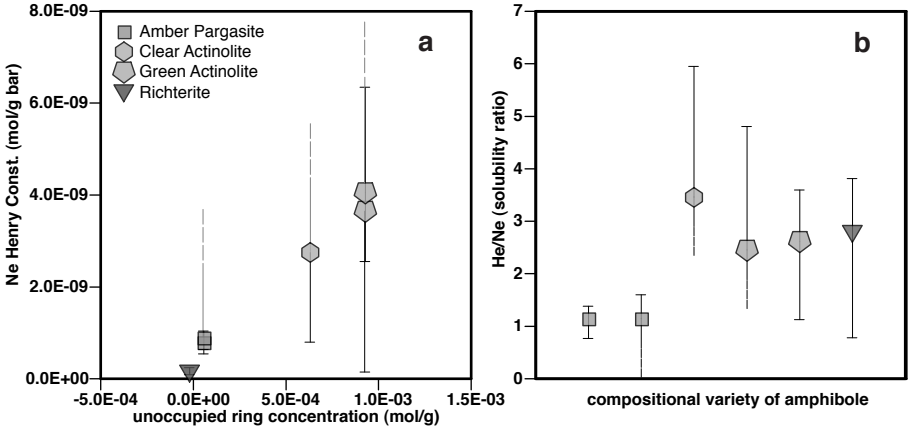

Supplementary Information for "Noble gas transport into the mantle facilitated by high solubility in amphibole"

1.0 Methods:

1.1 Starting Materials:

Starting materials were gem quality amphibole. Major element compositions were determined by electron microprobe at MIT (WDS, 10 nA and 15 kV accelerating voltage) and are given in Supplementary Table 1. A focused beam was used and the raw data were corrected using CITZAF [35]. Bulk crystals were sectioned into appropriate sizes (2 x 2 x 0.5 mm) using either a low speed diamond blade wafering saw or by cleaving. Cut faces were polished using alumina (0.05 um) and colloidal silica. Cleaved faced were not prepared further. Once prepared, but prior to analysis, the crystals were mapped for inclusions using a 120x stereoscope. Any areas affected by inclusions were avoided during analysis.

Amphibole A-site, or ring site, occupancy was calculated by assigning all Ca to the M4 site. Additional Na was added to the M4 site to achieve two cations per formula unit. The remainder of Na and K were partitioned on to the A site, defining the occupancy. Density was estimated by assuming a constant unit cell volume of 900 μm^3 and applying the mass of the formula unit as calculated from the stoichiometry. Compositional and associated data are given in Supplementary Table 1.

1.2 Experimental and Analytical Methods:

We dissolved noble gases into amphibole using a TZM-type externally-heated pressure vessel apparatus. Either pure He or an equal mixture of He-Ne-Ar gas was used as the pressure medium for all experiments, allowing for precise and sustained control of noble gas fugacity. Typical change of the gas pressure was ~1% over the run duration with a maximum observed leakage of 10%. Reported pressures are those recorded directly before quench. Temperatures ranged from 680° to 875°C and pressures ranged from 0.7 to 1.7 kbar. Convection within the pressure vessel was suppressed using graphite filler rods that extend the length of the pressure vessel above the capsules. Run conditions are given in Supplementary Table 2.

All experiments consisted of three separate crystals loaded into graphite capsules, excepting experiments 7, 8, and 14, where fired pyrophyllite capsules were used. Capsule type does not have a significant effect on the He solubility results, and there was no apparent reaction between crystals and capsule. A capsule loaded with brucite, MgO, and H_2O was placed directly above the third capsule to generate a small water fugacity. All three crystals were contained within the hotspot, as determined by temperature calibration of the pressure vessel assembly.

Experiments were quenched by removing the TZM vessel from the furnace and allowing it to cool against air. The vessel cooled to ~50°C in 20 minutes. At this point the pressure vessel was rapidly depressurized and unloaded. Essentially, the experimental method was a constant source diffusion approach.

Noble gas concentrations of the experimental run products were determined using a UV laser ablation-mass spectrometer system at the Open University. A 193 nm NeF excimer laser was used to ablate all minerals. Laser power varied between 10 and 40 % (200 mJ pulse^{-1} at 20 Hz and 100% power), and laser pulse frequency was varied between 1 and 20 Hz to achieve desired ablation pit volumes and depths (200 mJ pulse^{-1} at 20 Hz and 100% power). Three SAES AP-10 getters removed active gases released during ablation before introduction into a MAP215-50 mass spectrometer. ^{4}He, ^{22}Ne and ^{40}Ar were measured by a multiplier collector in peak hopping mode. The sensitivity of the mass spectrometer was determined by gas pipetting a known volume of noble gases with atmospheric isotopic ratios into the mass spectrometer. A session blank was calculated as the mean of the all the blanks for a particular session (defined as a single day of analysis on a single port). No significant trends were present. Further details regarding the basic laser ablation technique can be found in [36].

The volume of ablation pits were measured using a white light interferometer (Zygo Instruments, Brown University). This device provides an image of the ablated surface that requires minimal "inpainting" (interpolation of pixels with unknown values). A surface continuum is calculated by masking out the ablated area of the interferometer image and interpolating across the masked region. The inpainted interferometer image is subtracted from the surface continuum, creating a positive relief topographic image that has been rotated into a horizontal plane. To calculate the pit volume, the individual volumes of all remaining pixels are summed assuming rectangular prism geometry for each pixel. A small ring of high topography was occasionally observed along the circumference of the pits, creating a halo of negative volume after continuum correction.

We avoid including the negative volume halo in the volume calculation by only summing the pixels with positive depths. There is additional scatter in data from shallow pits and pits with more complex surrounding surface geometry. Both qualities make it more difficult to precisely determine a surface continuum and to accurately determine pit volumes. Using multiple interpolation methods we estimate a ±15% uncertainty in the pit volume calculation.

All minerals were carbon coated prior to imaging with the white light interferometer to improve reflectivity. More reflective minerals provide an image with greater returned signal and require less "inpainting." This is particularly beneficial in imaging clear minerals.

1.3 Uncertainties:

Uncertainty in noble gas concentration is a product of analytical and ablation pit volume uncertainties. Reported uncertainties include the following sources and are propagated assuming that they are independent from each other and random: 1) Statistical uncertainty associated with blank variability and noble gas analysis regressions (typically ~1% for ^{4}He and ~15% for ^{22}Ne from experiment 34 and 36, but can be >100% for very low-voltage analyses), 2) Pit volume determination. Volume uncertainty is greatest for very shallow pits (<1 μm) and pits with complexly curved surrounding surfaces. Using various interpolation and masking methods on very shallow pits with complex shaped surrounding surfaces we observe ±~15% variability in volume calculations, and we take this as a reasonable high-end uncertainty. We ignore any uncertainty associated with

density calculations (~3%, estimated from variability in amphibole unit cell volume and molar mass calculation) and composition of calibration gas (~1%) [23]. The calibration gas contains atmospheric ratios of noble gas isotopes but the elemental abundances are non-atmospheric to facilitate analysis. Helium measurements are generally >10x the absolute value of the He blank but can approach 2x for small volume analyses on low solubility amphiboles (e.g. richterite). Neon measurements are generally >5x the absolute value of the Ne blank but approach for the blank small volume analyses on low solubility amphiboles. All uncertainties are one standard deviation.

2.0 Results:

2.1 Evidence for Measurement of Solubility:

Henry's constants for He dissolved into amphibole are plotted against P_{He}, duration, depth, and temperature in Supplementary Figure 1 A, B, C, and D respectively. No obvious systematics are present. Fact the Henry's constants do not vary with P_{He} indicates that Henry's Law applies for the experimental conditions explored (P_{He}<1.5 kbar) and that reported Henry's constants are applicable to systems with natural (lower) noble gas fugacities. The lack of temperature or duration dependence for He solubility strongly argues for a close approach to equilibrium that is unaffected by decomposition of the amphibole. Importantly, the insignificant temperature dependence for He solubility supports extrapolation of results to both hydrothermal and magmatic systems.

Depth profiling was accomplished by ablating sequentially deeper pits at different locations on the mineral surface, effectively increasing the average depth of material sampled in a single analysis (Supplementary Figure 1C, 2, 3, and 4). In general, no systematic He gradients (plotted as apparent Henry's Law constants) were observed, providing supporting evidence for a close approach to equilibrium for a given experiment. The notable exceptions are actinolites from experiments 29 and 30. These experiments are relatively cool (680°C) and short duration experiments (17 and 40 hrs, respectively), suggesting the profiles are diffusion gradients. However, depth profiling of other amphibole run at similar conditions or conditions less conducive to obtaining near surface equilibrium do not reveal He concentration gradients. It has been argued that Ar diffusion in amphibole is more rapid when the ring sites are unoccupied [37]. Current observations support the notion that He diffusion is affected by amphibole composition but the correlation does not appear to be a simple positive relationship to unoccupied ring site concentration. No attempt was made to orient the samples, and it is possible anisotropy could cause some of the variability in the data.

Helium solubility is calculated as the uncertainty-weighted mean of the individual measurements for a single phase, unless there were clear concentration gradients, as noted for actinolites in experiment 29 and 30. The solubility for experiments with concentration gradients is estimated by applying a diffusion model to the data and fitting for diffusivity and surface concentration. Surface concentrations are assumed to be solubility. This method is discussed further below.

Helium data from richterite in experiment 14 are significantly higher than the other three richterite experiments conducted (experiment 23, 33, and 34). Given the close

agreement in the later experiments, we consider experiment 14 an outlier. No other amphibole was run in experiment 14, so it is unclear if the apparent high He solubility is the result of an experimental or starting material artifact. Nonetheless, the shift is relatively small and does not affect the conclusions of this work.

2.2 Calculation of Solubility and Diffusivity from Concentration Profiles:

Neon solubility in amphibole can be estimated using either near-surface depth profiling or by using He as an internal standard. These approaches allow for solubility estimations of slower diffusing noble gases that only equilibrate with the near-surface of the mineral. In Supplementary Figure 2, Ne/He (molar ratio) is plotted against pit depth for the longest duration, highest temperature experiments where Ne was present (34 and 36).

Higher Ne/He is observed for progressively shallower pits, as expected for a system where Ne is less equilibrated than He. To quantify solubility and diffusivity, a one-dimensional, semi-infinite medium, constant source diffusion model is fit to the concentration-depth data. Because the reported concentrations are depth averages rather than concentrations at discrete depths, the model calculates the predicted depth-averaged concentration for each pit depth and fits for a least squares solution for diffusivity and surface concentration (solubility, Supplementary Figure 3). Uncertainty envelopes (Supplementary Figure 3) are calculated using an F-Test and show a negative correlation between solubility and diffusivity. Often this correlation results in extreme uncertainty towards high solubility and low diffusivity, but some (3) experiments yield reasonable

uncertainty limits for solubility and diffusivity. There is good agreement between calculated Ne solubility for the same phase run in different experiments despite large calculated uncertainties, and Ne solubility correlates with He solubility. Both of these observations suggest that Ne solubility estimations are accurate. In addition to the depth profiling, a series of very shallow trenches were ablated on the green actinolite from experiment 36. The geometry of these trenches is not amenable to precise volume determinations, but the Ne/He ratio can quantified nonetheless. These data are plotted as larger symbols at 0 μm depth (Supplementary Figure 2) and represent lower bounds for the solubility ratio of Ne to He. Uncertainty on Ne/He for trenches is propagated as independent and random error associated with the noble gas analysis and does not include error in the pit volume. Actual average depths for trenches are ~0.25 μm but poorly known and variable. The absolute noble gas concentrations of these trenches are not reported because the volume calculations are deemed unreliable.

Comparison of Ne and He data indicates Ne is approximately half as soluble on a molar basis (Figure 3, Supplementary Figure 2). Notably, Ne solubility also correlates with the density of unoccupied rings, indicating unoccupied ring sites host noble gases heavier than He. Uncertainty in fitted Ne solubility and diffusivity is considerable, but to a first order, the data scatter around a diffusion coefficient of $5x10^{-17}$ m^2 s^{-1} for a temperature of 850-875 °C. This value is faster (50x) than predicted Ar diffusion coefficients for the same conditions based on aggregate stepped heating experiments, where radiogenic Ar was degassed [38]. Based on the diffusion parameters for Ar determined by stepped heating experiments, the characteristic Ar diffusive length scale for experiment 36 (92 hr duration) is ~1 μm, which is resolvable by the 193 nm laser used

in this study. The lack of a concentration profile suggests that Ar uptake from the pressure medium is slower than outgassing of radiogenic Ar, but more work is needed to verify this initial observation.

Neon was present in experiment 33 but concentrations were too low to allow for any estimation for the surface concentration or diffusivity. Argon was present in experiments 33, 34, and 36. As with Ne in experiment 33, the concentrations were too low for solubility or diffusivity estimations, although the highest concentrations come from the shallowest pits measured for this experiment.

Supplementary References:

Futagami, T., Ozima, M., Nagai, S. & Aoki, Y. Experiments on thermal release of implanted noble gases from minerals and their implications for noble gases in lunar soil grains. *Geochimica Et Cosmochimica Acta* 57, 3177-3194, (1993).

Gourbet, L. *et al.* Neon diffusion kinetics in olivine, pyroxene and feldspar: Retentivity of cosmogenic and nucleogenic neon. *Geochimica Et Cosmochimica Acta* 86, 21-36, (2012).

Shuster, D. L., Farley, K. A., Sisterson, J. M. & Burnett, D. S. Quantifying the diffusion kinetics and spatial distributions of radiogenic He-4 in minerals containing proton-induced He-3. *Earth and Planetary Science Letters* 217, 19-32, (2004).

Blard, P. H., Puchol, N. & Farley, K. A. Constraints on the loss of matrix-sited helium during vacuum crushing of mafic phenocrysts. *Geochimica Et Cosmochimica Acta* 72, 3788-3803, (2008).

Armstrong, J. T. CITZAF – A package of correctino programs for the quantitative electron microbeam x-ray analysis of thick polished materials, thin films, and particles. *Microbeam Analysis* 4, 177-200 (1995).

Kelley, S. P., Arnaud, N. O. & Turner, S. P. High spatial resolution Ar-40 Ar-39 investigations using an ultra-violet laser probe extraction technique. *Geochimica Et Cosmochimica Acta* 58, 3519-3525, (1994).

Dahl, P. S. The effects of composition on retentivity of argon and oxygen in hornblende and related amphiboles: A field-tested empirical model. *Geochimica Et Cosmochimica Acta* 60, 3687-3700, (1996).

Harrison, T. M. Diffusion of Ar-40 in hornblende. *Contributions to Mineralogy and Petrology* 78, 324-331 (1981).

Supplementary Figure Captions:

Supplementary Figure 1: Henry's constants for He plotted as function of P_{He} (A), duration (B), depth (C), and temperature (D) for amphibole. Each point is an individual analysis. In general, trends are horizontal, indicating close approaches to equilibrium and applicability to natural systems. Exceptions are plotted as open symbols (see text). Henry's constants do not correlate with P_{He} (A), indicating Henry's Law applies over the range of P_{He} explored (1.7 kbar) and that data are applicable to natural systems with significantly lower noble gas fugacities. Henry's constants do not vary with duration or depth (B and C). This strongly argues for a close approach to equilibrium that is unaffected by surfical phenomena. Henry's constants are not measurably sensitive to changes in temperature between 680 and 875° C (D), allowing for simple extrapolation of results to hydrothermal or magmatic systems. Open symbols labeled "kinetic" are data from relatively low temperature, short duration experiments that have near-surface concentration profiles. Helium solubilities are determined for these experiments by fitting diffusion models (Supplementary Figure 4). Error bars are one standard deviation.

Supplementary Figure 2: Ne/He (molar) plotted as function of depth (μm) for longest duration, highest temperature experiments with Ne present (experiments 34 and 36). Each data point is an individual analysis. Data show decreasing Ne/He with increasing pit depth, consistent with decreasing degrees of equilibration for Ne with respect to He. Data for pentagons were acquired by slowly ablating along a line, generating a very shallow (~0.25 μm but highly variable) trench. We report only Ne/He for these pits

because the precision on volume calculations for this geometry type is poor. At shallowest depths, data trend towards a Ne/He ~ 0.5, indicating Ne is approximately half as soluble in amphibole as He.

Supplementary Figure 3: Expanded views of data from experiment 34 and 36 (Supplementary Figure3) showing resolvable Ne concentration gradients with fitted diffusion curves. Boxes (left plots) are individual data points acquired by ablating different locations on a crystal face to variable depths. Black curves (left plots) are the best-fit solution for a depth-averaged diffusion model based on the box data points. See the supplementary text below for a more detailed description of the diffusion model. Dashed grey curves (left plots) are the standard complimentary error function for the given set of fitted parameters. Uncertainty envelopes (black shapes, right plots) fail to define useful limits in some cases (B, D, & E), although there is good agreement between the various best-fit Ne diffusivities. Black circles (right plots) are the best-fit solution. For comparison, neon diffusivity in amphibole is similar at 850-875° C to values reported for olivine by [31](black diamond) but 1000x slower than reported by [32] (black square). Neon solubility in olivine is taken from [23]. Error bars are one standard deviation and no error is associated with the depth measurement.

Supplementary Figure 4: Expanded views of data from experiment 29 and 30 showing resolvable He concentration gradients ("kinetic" in Supplementary Figure1) with fitted diffusion curves. Boxes (left plots) are individual data points acquired by ablating different locations on a crystal face to variable depths. Black curves (left plots) are the

best-fit solution for a depth-averaged diffusion model based on the box data points. See the supplementary text below for a more detailed description of the diffusion model. Dashed grey curves (left plots) are the standard complimentary error function for the given set of fitted parameters. Uncertainty envelopes (black shapes, right plots) are relatively tight compared to Ne diffusion models. Both green actinolite fitted He diffusion coefficients and solubilities agree well and are marginally slower than the values fit for the clear actinolite, although their confidence envelopes overlap. Black circle on right plots is the best fit solution. Compared to He diffusion in olivine, He diffusion in these amphiboles is 10-1000x slower at 680°C [e.g.33,34] (black diamond and square, following reference order). Helium solubility in olivine taken from [23]. It should be noted, however, that other amphiboles have more He equilibrated profiles for equivalent conditions or conditions less conducive to diffusion, suggesting composition may have a significant effect on noble gas diffusion in amphibole. Error bars are one standard deviation and no error is associated with the depth measurement.

Chapter 2,
Supplementary Fig. 1

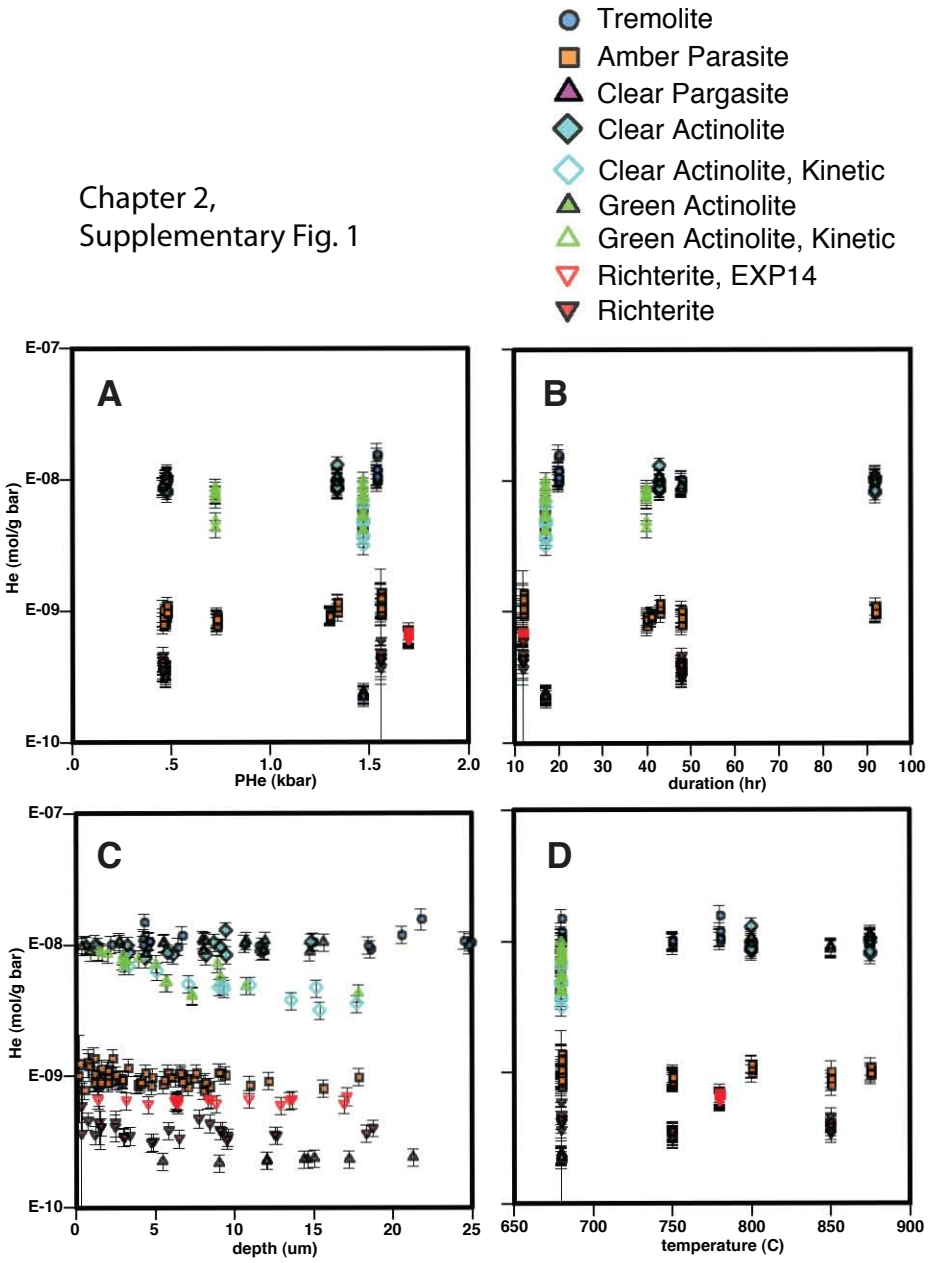

Chapter 2,
Supplementary Fig. 2

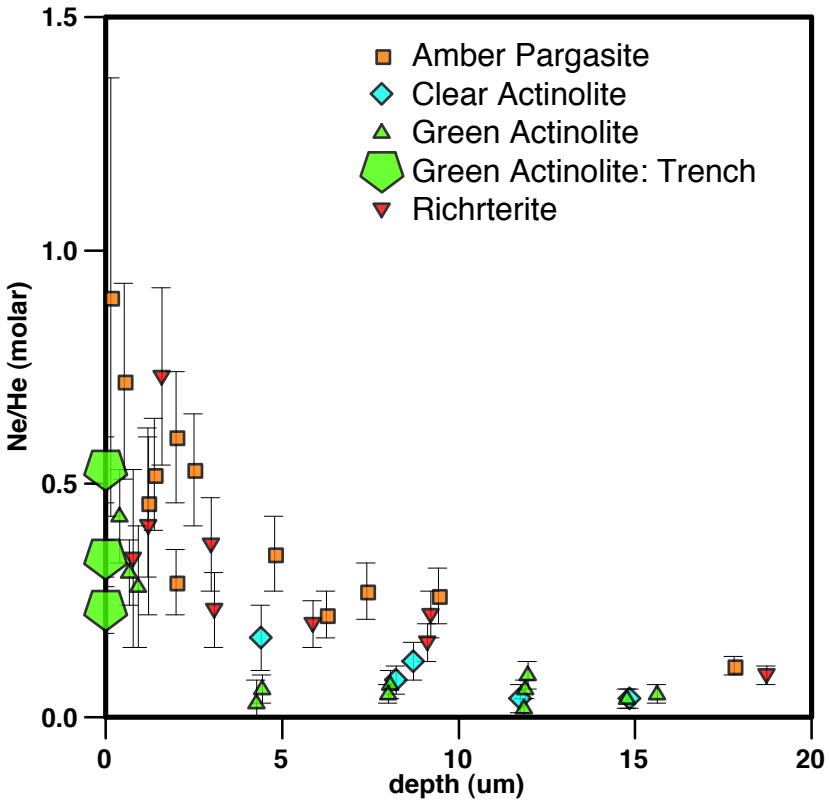

Chapter 2,
Supplementary Fig. 3a

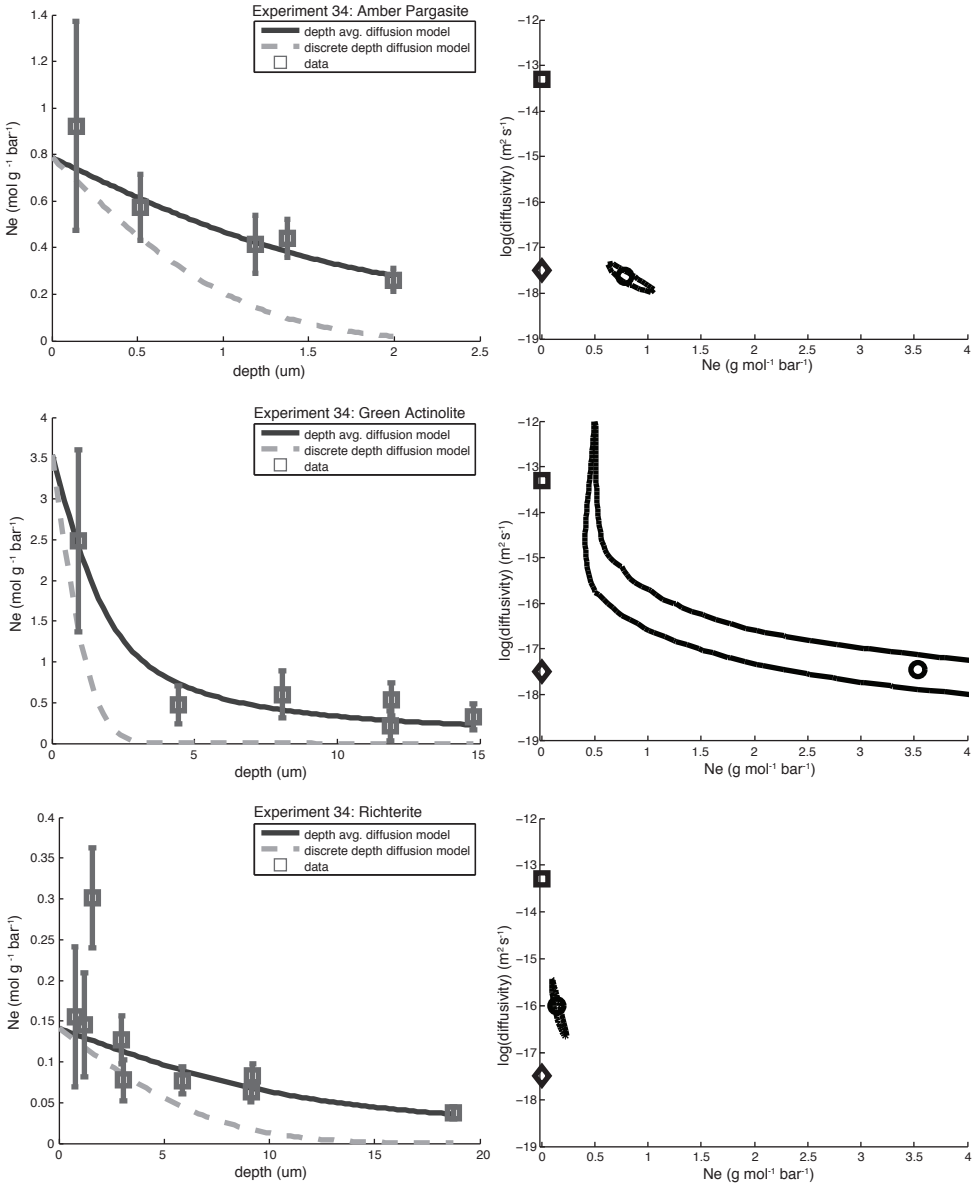

Chapter 2,
Supplementary Fig. 3b

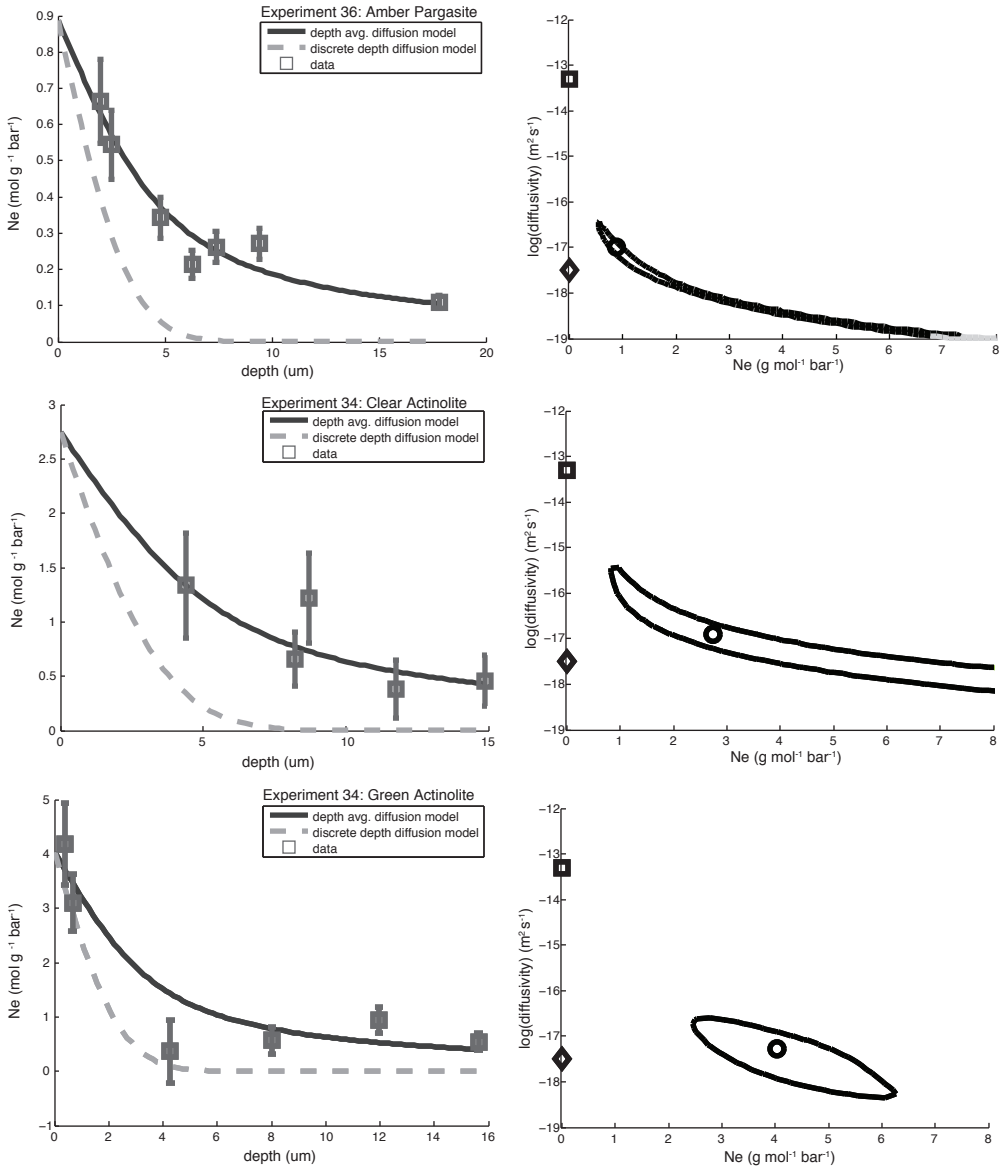

Chapter 2,
Supplementary Fig. 4

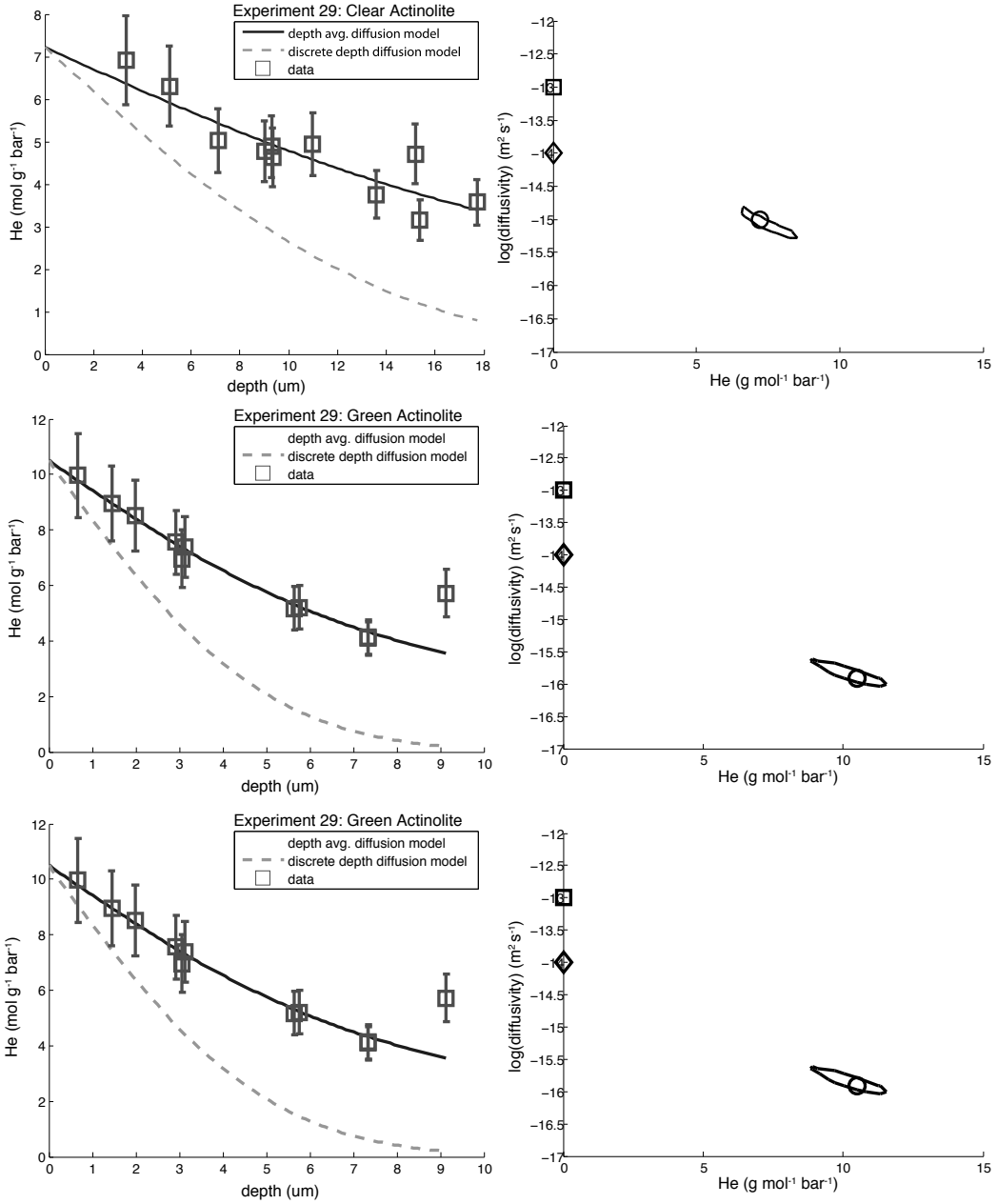

Supplementary Table 1: Major Element Compositions of Amphiboles

phase					SiO2	Al2O3	TiO2	Cr2O3	MnO	FeO	MgO	CaO	ZnO	Na2O	K2O	Cl	F	Total
Pargasite (amber)		total ring site density (mol/g)	1.2E-03		45.31	16.02	1.11	0.00	0.03	0.54	19.16	12.45	0.00	2.96	1.67	0.08	0.68	100.01
density (g/cm^3)	3.11	avg. ring site vacancy density (mol/g)	5.6E-05		45.02	16.10	1.11	0.00	0.04	0.55	19.30	12.50	0.01	2.94	1.65	0.10	0.70	100.00
formula unit mass (g)	842.7	ring site vacancy density std. dev. (mol/g)	4.5E-06		45.32	16.09	1.10	0.00	0.04	0.53	19.20	12.52	0.00	2.97	1.68	0.10	0.69	100.24
					45.31	16.04	1.11	0.00	0.03	0.53	19.28	12.55	0.00	2.97	1.63	0.09	0.75	100.29
					45.27	16.10	1.09	0.00	0.03	0.54	19.26	12.58	0.01	2.92	1.67	0.09	0.71	100.26
				average	45.25	16.07	1.10	0.00	0.03	0.53	19.24	12.52	0.00	2.95	1.66	0.09	0.71	100.16
				std dev.	0.13	0.04	0.01	0.00	0.01	0.01	0.06	0.05	0.00	0.02	0.02	0.01	0.03	0.14
Pargasite (clear)		total ring site density (mol/g)	1.2E-03		48.49	11.89	0.12	0.01	0.00	0.20	21.58	12.01	0.00	4.14	0.53	0.01	1.23	100.20
density (g/cm^3)	3.02	avg. ring site vacancy density (mol/g)	4.5E-06		48.01	11.91	0.12	0.00	0.00	0.21	21.58	11.87	0.00	4.17	0.51	0.01	1.22	99.62
formula unit mass (g)	819.4	ring site vacancy density std. dev. (mol/g)	2.0E-05		47.94	11.90	0.10	0.00	0.00	0.21	21.64	11.92	0.01	4.11	0.51	0.01	1.23	99.59
					47.70	11.91	0.10	0.00	0.00	0.21	21.75	11.98	0.00	4.16	0.51	0.01	1.23	99.56
					47.33	11.90	0.10	0.01	0.00	0.21	21.71	12.01	0.00	4.14	0.50	0.01	1.22	99.14
				average	47.89	11.90	0.11	0.00	0.00	0.21	21.65	11.96	0.00	4.14	0.51	0.01	1.23	99.62
				std dev.	0.43	0.01	0.01	0.01	0.00	0.01	0.08	0.06	0.00	0.02	0.01	0.00	0.01	0.38
Richterite		total ring site density (mol/g)	1.2E-03		58.08	1.52	0.15	0.00	0.04	0.10	24.05	7.73	0.03	5.79	1.93	0.01	0.92	100.35
density (g/cm^3)	2.99	avg. ring site vacancy density (mol/g)	-2.1E-05		57.97	1.52	0.15	0.01	0.04	0.10	24.00	7.75	0.00	5.83	1.94	0.02	0.91	100.23
formula unit mass (g)	810.7	ring site vacancy density std. dev. (mol/g)	-1.3E-05		57.86	1.54	0.15	0.00	0.05	0.08	24.04	7.69	0.01	5.83	1.93	0.01	0.91	100.11
					57.89	1.65	0.13	0.01	0.04	0.09	24.00	7.74	0.00	5.80	1.94	0.01	0.90	100.20
					57.73	1.67	0.14	0.01	0.04	0.10	23.95	7.73	0.02	5.85	1.94	0.00	0.91	100.10
				average	57.91	1.58	0.15	0.01	0.04	0.09	24.01	7.73	0.01	5.82	1.94	0.01	0.91	100.20
				std dev.	0.13	0.08	0.01	0.00	0.00	0.01	0.04	0.02	0.01	0.02	0.01	0.01	0.01	0.10
Actinolite (clear)		total ring site density (mol/g)	1.2E-03		57.39	1.44	0.04	0.01	0.09	0.68	23.82	11.94	0.04	2.11	0.83	0.01	1.89	100.28
density (g/cm^3)	2.99	avg. ring site vacancy density (mol/g)	6.3E-04		55.20	1.34	0.05	0.01	0.08	0.96	23.92	12.49	0.02	1.61	0.75	0.01	1.64	98.08
formula unit mass (g)	810.9	ring site vacancy density std. dev. (mol/g)	4.1E-05		55.37	1.38	0.04	0.00	0.08	0.61	23.85	11.93	0.04	2.09	0.82	0.01	1.82	98.04
					54.72	1.39	0.04	0.01	0.08	0.76	23.87	11.91	0.05	2.03	0.82	0.02	1.80	97.49
					56.97	1.45	0.04	0.01	0.11	1.04	23.55	12.06	0.04	1.96	0.80	0.01	1.73	99.78
				average	55.93	1.40	0.04	0.01	0.09	0.81	23.80	12.07	0.04	1.96	0.80	0.01	1.78	98.73
				std dev.	1.18	0.05	0.00	0.00	0.01	0.18	0.15	0.24	0.01	0.20	0.03	0.00	0.10	1.22
Actinolite (green)		total ring site density (mol/g)	1.2E-03		54.71	5.75	0.24	0.06	0.10	0.04	22.39	13.43	0.00	0.68	0.52	0.00	0.65	98.57
density (g/cm^3)	2.97	avg. ring site vacancy density (mol/g)	9.3E-04		54.64	5.80	0.24	0.05	0.10	0.05	22.46	13.38	0.00	0.68	0.56	0.00	0.66	98.61
formula unit mass (g)	804.3	ring site vacancy density std. dev. (mol/g)	1.1E-05		55.03	5.81	0.24	0.05	0.11	0.04	22.39	13.39	0.00	0.68	0.53	0.00	0.65	98.93
					54.50	5.80	0.24	0.05	0.10	0.05	22.36	13.44	0.00	0.68	0.55	0.00	0.67	98.44
					54.86	5.84	0.23	0.05	0.09	0.04	22.48	13.46	0.00	0.68	0.54	0.00	0.63	98.91
				average	54.75	5.80	0.24	0.05	0.10	0.04	22.42	13.42	0.00	0.68	0.54	0.00	0.65	98.69
				std dev.	0.20	0.03	0.00	0.00	0.01	0.00	0.05	0.03	0.00	0.00	0.01	0.00	0.01	0.22
Tremolite (green)		total ring site density (mol/g)	1.2E-03		58.58	0.67	0.06	0.01	0.10	3.53	22.39	13.12	0.02	0.44	0.14	0.02	0.21	99.28
density (g/cm^3)	3.02	avg. ring site vacancy density (mol/g)	1.1E-03		58.01	0.59	0.05	0.01	0.09	3.32	22.56	13.18	0.01	0.43	0.13	0.03	0.20	98.60
formula unit mass (g)	810.1	ring site vacancy density std. dev. (mol/g)	4.0E-05		58.12	0.53	0.07	0.01	0.09	2.84	22.95	13.19	0.04	0.42	0.12	0.02	0.26	98.67
					57.46	0.78	0.08	0.01	0.08	2.79	22.85	13.06	0.00	0.56	0.19	0.03	0.33	98.22
					57.34	0.79	0.08	0.01	0.08	2.76	22.90	13.10	0.00	0.61	0.20	0.02	0.41	98.29
				average	57.90	0.67	0.07	0.01	0.09	3.05	22.73	13.13	0.01	0.49	0.15	0.02	0.28	98.61
				std dev.	0.51	0.12	0.01	0.00	0.01	0.35	0.24	0.05	0.02	0.09	0.04	0.00	0.09	0.42

Supplementary Table 2: Noble gas analyses of amphibole and experimental run conditions

Depth (um)	Volume (um^3)	He (mol/g)	He uncert. (mol/g)	Ne (mol/g)	Ne uncert. (mol/g)	Ar (mol/g)	Ar uncert. (mol/g)	avg. He Henry Const. (mol/g bar)	std. He Henry Const. (mol/g bar)	pressure (kbar)	temp (cent.)	duration (hr)	PHe (kbar)	PNe (kbar)	PAr (kbar)	Ne/He (molar)	Ne/He uncert.	Ne Henry Const. (mol/g bar)	Ne Henry const. +uncert. (mol/g bar)	Ne Henry const. -uncert. (mol/g bar)
Tremolite																				
EHPV_NG_EXP7_trem																				
6.70	1.18E+05	1.83E-05	2.74E-06	1.39E-09	4.78E-10	-2.23E-11	5.16E-11			1.54	680	20	1.54	0	0	0.00	0.00			
4.56	8.05E+04	1.66E-05	2.50E-06	8.52E-09	3.56E-09	1.53E-09	7.83E-10			1.54	680	20	1.54	0	0	0.00	0.00			
4.59	8.11E+04	1.64E-05	2.47E-06	5.69E-09	3.29E-09	1.81E-09	7.94E-10			1.54	680	20	1.54	0	0	0.00	0.00			
4.64	8.19E+04	1.66E-05	2.50E-06	8.72E-09	3.52E-09	7.32E-10	7.48E-10			1.54	680	20	1.54	0	0	0.00	0.00			
4.31	7.62E+04	2.31E-05	3.47E-06	1.62E-09	3.38E-09	7.22E-09	1.35E-09			1.54	680	20	1.54	0	0	0.00	0.00			
4.51	7.97E+04	1.48E-05	2.23E-06	7.91E-09	3.29E-09	-3.46E-10	7.71E-10			1.54	680	20	1.54	0	0	0.00	0.00			
4.24	7.50E+04	1.56E-05	2.35E-06	5.77E-09	3.37E-09	1.89E-09	8.52E-10			1.54	680	20	1.54	0	0	0.00	0.00			
								1.15E-08	1.77E-09	1.54	680	20	1.54	0	0			NA	NA	NA
EHPV_NG_EXP8_trem																				
24.84	9.56E+04	1.62E-05	2.43E-06	6.80E-09	4.64E-09	8.15E-09	1.68E-09			1.54	780	20	1.54	0	0	0.00	0.00			
24.95	9.60E+04	1.62E-05	2.43E-06	3.26E-10	5.24E-09	7.55E-09	1.63E-09			1.54	780	20	1.54	0	0	0.00	0.00			
24.50	9.43E+04	1.66E-05	2.49E-06	-8.63E-10	5.03E-09	8.56E-09	1.74E-09			1.54	780	20	1.54	0	0	0.00	0.00			
24.79	9.54E+04	1.54E-05	2.31E-06	7.41E-09	4.85E-09	5.91E-09	1.45E-09			1.54	780	20	1.54	0	0	0.00	0.00			
14.98	3.56E+04	1.64E-05	2.46E-06	6.42E-09	1.24E-08	2.07E-09	3.17E-09			1.54	780	20	1.54	0	0	0.00	0.00			
20.54	4.88E+04	1.84E-05	2.77E-06	-8.01E-09	9.31E-09	2.74E-09	2.30E-09			1.54	780	20	1.54	0	0	0.00	0.00			
21.79	5.18E+04	2.44E-05	4.45E-06	-2.66E-09	8.36E-09	-2.31E-09	2.87E-09			1.54	780	20	1.54	0	0	0.00	0.00			
								1.19E-08	1.77E-09	1.54	780	20	1.54	0	0			NA	NA	NA
EHPV_NG_EXP33_trem																				
6.44	5.06E+04	4.58E-06	6.90E-07	3.81E-08	2.19E-08	1.28E-08	3.78E-09			1.4	750	48	0.47	0.47	0.47	0.01	0.00			
2.22	3.93E+04	4.77E-06	7.17E-07	1.93E-07	3.97E-08	9.19E-08	1.45E-08			1.4	750	48	0.47	0.47	0.47	0.04	0.01			
1.38	4.34E+04	4.63E-06	6.97E-07	7.84E-08	2.57E-08	2.00E-08	4.95E-09			1.4	750	48	0.47	0.47	0.47	0.02	0.01			
1.20	3.76E+04	4.85E-06	7.30E-07	6.36E-07	1.08E-07	3.68E-07	5.57E-08			1.4	750	48	0.47	0.47	0.47	0.13	0.03			
0.59	3.48E+04	4.76E-06	7.18E-07	7.82E-08	3.25E-08	9.82E-09	4.98E-09			1.4	750	48	0.47	0.47	0.47	0.02	0.01			
18.59	1.46E+05	4.40E-06	6.60E-07	-5.70E-09	6.56E-09	1.30E-09	1.22E-09			1.4	750	48	0.47	0.47	0.47	0.00	0.00			
18.46	1.45E+05	4.67E-06	7.00E-07	2.66E-08	7.81E-09	1.06E-09	1.15E-09			1.4	750	48	0.47	0.47	0.47	0.01	0.00			
10.64	1.88E+05	4.79E-06	7.19E-07	3.16E-08	7.34E-09	1.77E-09	9.17E-10			1.4	750	48	0.47	0.47	0.47	0.01	0.00			
								1.00E-08	3.11E-10	1.4	750	48	0.47	0.47	0.47			NA	NA	NA
Amber Pargasite																				
EHPV_NG_EXP23_amber_par																				
2.29	1.36E+05	2.16E-06	3.46E-07	1.51E-10	3.58E-09	1.83E-09	3.67E-10			1.56	680	12	1.56	0	0	0.00	0.00			
6.65	3.95E+05	1.59E-06	2.43E-07	3.93E-09	1.51E-09	1.99E-09	3.08E-10			1.56	680	12	1.56	0	0	0.00	0.00			
2.44	1.45E+05	1.47E-06	2.48E-07	-3.06E-09	3.33E-09	1.63E-09	3.22E-10			1.56	680	12	1.56	0	0	0.00	0.00			
1.11	6.60E+04	2.16E-06	4.09E-07	2.02E-08	7.62E-09	1.57E-09	5.42E-10			1.56	680	12	1.56	0	0	0.01	0.00			
0.74	4.37E+04	2.01E-06	4.82E-07	-8.29E-09	1.08E-08	7.15E-10	7.07E-10			1.56	680	12	1.56	0	0	0.00	-0.01			
1.27	7.56E+04	1.52E-06	3.15E-07	4.61E-09	6.14E-09	1.28E-09	4.47E-10			1.56	680	12	1.56	0	0	0.00	0.00			
1.19	7.08E+04	1.63E-06	3.37E-07	2.61E-09	6.53E-09	1.52E-09	5.00E-10			1.56	680	12	1.56	0	0	0.00	0.00			
2.04	1.21E+05	1.78E-06	3.00E-07	2.65E-09	3.91E-09	1.92E-09	3.95E-10			1.56	680	12	1.56	0	0	0.00	0.00			
0.80	4.74E+04	1.88E-06	4.47E-07	-1.86E-08	1.05E-08	8.79E-10	6.88E-10			1.56	680	12	1.56	0	0	-0.01	-0.01			
5.79	3.44E+05	1.66E-06	2.54E-07	1.17E-09	1.49E-09	1.65E-09	2.70E-10			1.56	680	12	1.56	0	0	0.00	0.00			
0.22	1.33E+04	1.96E-06	1.27E-06	2.21E-08	3.61E-08	2.87E-09	2.34E-09			1.56	680	12	1.56	0	0	0.01	0.02			
								1.19E-09	1.59E-10	1.56	680	12	1.56	0	0			NA	NA	NA
EHPV_NG_EXP30_amber_par																				
15.59	9.26E+05	5.94E-07	8.91E-08	1.20E-09	8.85E-10	1.35E-09	2.72E-10			0.725	680	40	0.73	0	0	0.00	0.00			
5.47	3.25E+05	6.36E-07	9.55E-08	4.68E-09	2.48E-09	3.40E-09	7.00E-10			0.725	680	40	0.73	0	0	0.01	0.00			
2.86	1.70E+05	6.51E-07	9.80E-08	2.35E-09	4.50E-09	1.91E-09	1.03E-09			0.725	680	40	0.73	0	0	0.00	0.01			
8.05	4.78E+05	5.67E-07	8.52E-08	3.24E-09	1.69E-09	2.33E-09	4.87E-10			0.725	680	40	0.73	0	0	0.01	0.00			
2.24	1.33E+05	6.79E-07	1.02E-07	3.00E-09	5.98E-09	3.38E-09	1.29E-09			0.725	680	40	0.73	0	0	0.00	0.01			
8.42	5.00E+05	6.12E-07	9.18E-08	-2.54E-09	1.62E-09	3.56E-09	6.19E-10			0.725	680	40	0.73	0	0	0.00	0.00			
3.87	2.30E+05	6.34E-07	9.54E-08	2.81E-09	3.36E-09	2.49E-09	7.96E-10			0.725	680	40	0.73	0	0	0.00	0.01			
8.03	4.77E+05	6.40E-07	9.60E-08	8.94E-10	1.67E-09	2.19E-09	4.67E-10			0.725	680	40	0.73	0	0	0.00	0.00			
								8.67E-10	2.00E-10	0.725	680	40	0.73	0	0			NA	NA	NA
EHPV_NG_EXP33_amber_par																				
7.05	4.19E+05	3.91E-07	5.90E-08	1.95E-08	4.24E-09	5.68E-09	9.34E-10			1.4	750	48	0.47	0.47	0.47	0.05	0.01			
7.07	4.20E+05	4.51E-07	6.79E-08	1.52E-07	2.34E-08	2.87E-08	4.33E-09			1.4	750	48	0.47	0.47	0.47	0.34	0.07			
2.00	2.51E+05	4.62E-07	6.99E-08	8.69E-08	1.44E-08	1.36E-08	2.14E-09			1.4	750	48	0.47	0.47	0.47	0.19	0.04			
4.02	2.39E+05	4.16E-07	6.32E-08	4.53E-08	8.14E-09	1.59E-08	2.48E-09			1.4	750	48	0.47	0.47	0.47	0.11	0.03			
10.96	6.51E+05	4.05E-07	6.09E-08	2.17E-08	4.08E-09	1.15E-08	1.75E-09			1.4	750	48	0.47	0.47	0.47	0.05	0.01			
4.73	2.81E+05	4.03E-07	6.10E-08	1.41E-08	3.83E-09	2.91E-09	7.43E-10			1.4	750	48	0.47	0.47	0.47	0.03	0.01			
6.70	3.98E+05	4.28E-07	6.45E-08	3.16E-08	7.06E-09	2.91E-08	4.38E-09			1.4	750	48	0.47	0.47	0.47	0.07	0.02			
								9.08E-10	5.57E-11	1.4	750	48	0.47	0.47	0.47			NA	NA	NA
EHPV_NG_EXP34_amber_par																				
1.99	2.51E+05	4.13E-07	6.21E-08	1.20E-07	2.27E-08	9.55E-09	1.94E-09			1.38	850	48	0.46	0.46	0.46	0.29	0.07			
1.37	1.73E+05	3.91E-07	5.89E-08	2.03E-07	3.79E-08	3.28E-08	5.28E-09			1.38	850	48	0.46	0.46	0.46	0.52	0.12			
0.52	6.50E+04	3.65E-07	5.64E-08	2.64E-07	6.56E-08	8.63E-08	1.39E-08			1.38	850	48	0.46	0.46	0.46	0.72	0.21			
0.14	1.77E+04	4.69E-07	8.66E-08	4.24E-07	2.06E-07	8.58E-08	2.26E-08			1.38	850	48	0.46	0.46	0.46	0.90	0.47			
1.19	7.06E+04	4.13E-07	6.40E-08	1.90E-07	5.79E-08	1.59E-08	5.28E-09			1.38	850	48	0.46	0.46	0.46	0.46	0.16			
								9.04E-10	8.28E-11	1.38	850	48	0.46	0.46	0.46			**7.90E-10**	**2.50E-10**	**1.50E-10**
EHPV_NG_EXP36_amber_par																				
7.40	4.39E+05	4.63E-07	6.95E-08	1.25E-07	2.05E-08	2.67E-09	8.57E-10			1.44	875	92	0.48	0.48	0.48	0.27	0.06			
2.50	1.49E+05	4.94E-07	7.45E-08	2.61E-07	4.58E-08	3.21E-09	2.26E-09			1.44	875	92	0.48	0.48	0.48	0.53	0.12			
9.42	5.59E+05	4.94E-07	7.41E-08	1.30E-07	2.06E-08	4.10E-09	8.50E-10			1.44	875	92	0.48	0.48	0.48	0.26	0.06			
4.79	2.85E+05	4.74E-07	7.12E-08	1.64E-07	2.75E-08	5.55E-09	1.43E-09			1.44	875	92	0.48	0.48	0.48	0.35	0.08			
17.81	1.06E+06	4.76E-07	7.14E-08	5.27E-08	8.54E-09	2.03E-09	4.38E-10			1.44	875	92	0.48	0.48	0.48	0.11	0.02			
6.26	3.72E+05	4.72E-07	7.09E-08	1.03E-07	1.83E-08	2.47E-09	9.56E-10			1.44	875	92	0.48	0.48	0.48	0.22	0.05			
1.98	1.18E+05	5.31E-07	8.00E-08	3.19E-07	5.58E-08	6.57E-09	3.00E-09			1.44	875	92	0.48	0.48	0.48	0.60	0.14			
								1.02E-09	4.74E-11	1.44	875	92	0.48	0.48	0.48			**8.90E-10**	**NR**	**3.50E-10**
EHPV_NG_EXP38_amber_par																				
5.96	3.54E+05	1.32E-06	1.99E-07	3.45E-09	2.57E-09	1.87E-09	5.28E-10			1.34	800	43	1.34	0	0	0.00	0.00			
7.56	4.49E+05	1.42E-06	2.13E-07	1.81E-09	2.02E-09	1.74E-09	4.47E-10			1.34	800	43	1.34	0	0	0.00	0.00			
1.58	9.36E+04	1.54E-06	2.32E-07	-3.00E-09	9.92E-09	4.54E-09	1.83E-09			1.34	800	43	1.34	0	0	0.00	-0.01			
4.37	2.60E+05	1.43E-06	2.15E-07	6.29E-09	3.60E-09	2.21E-09	7.03E-10			1.34	800	43	1.34	0	0	0.00	0.00			
6.56	3.89E+05	1.42E-06	2.13E-07	2.62E-10	2.33E-09	1.58E-09	4.72E-10			1.34	800	43	1.34	0	0	0.00	0.00			
9.11	5.41E+05	1.44E-06	2.15E-07	-2.66E-10	1.69E-09	1.90E-09	4.11E-10			1.34	800	43	1.34	0	0	0.00	0.00			
9.01	5.35E+05	1.44E-06	2.17E-07	5.99E-10	1.75E-09	1.58E-09	3.84E-10			1.34	800	43	1.34	0	0	0.00	0.00			
3.27	1.94E+05	1.56E-06	2.35E-07	2.21E-09	4.71E-09	2.14E-09	9.20E-10			1.34	800	43	1.34	0	0	0.00	0.00			
								1.08E-09	5.56E-11	1.34	800	43	1.34	0	0			NA	NA	NA
EHPV_NG_EXP44_amber_par																				
4.08	2.42E+05	1.18E-06	1.77E-07	-3.11E-09	1.00E-08	9.44E-10	5.54E-09			1.3	750	41	1.30	0	0	0.00	-0.01			
8.16	4.85E+05	1.18E-06	1.76E-07	5.33E-09	5.15E-09	5.11E-10	2.78E-09			1.3	750	41	1.30	0	0	0.00	0.00			
2.90	1.72E+05	1.24E-06	1.87E-07	-1.68E-08	1.48E-08	5.41E-11	7.81E-09			1.3	750	41	1.30	0	0	-0.01	-0.01			
1.49	8.86E+04	1.23E-06	1.87E-07	-5.39E-08	2.87E-08	-1.93E-09	1.52E-08			1.3	750	41	1.30	0	0	-0.04	-0.02			
5.57	3.31E+05	1.22E-06	1.84E-07	7.81E-09	7.43E-09	5.28E-10	4.07E-09			1.3	750	41	1.30	0	0	0.01	0.01			
2.92	1.73E+05	1.22E-06	1.84E-07	6.38E-09	1.32E-08	1.17E-09	7.76E-09			1.3	750	41	1.30	0	0	0.01	0.01			
1.55	9.19E+04	1.17E-06	1.78E-07	1.02E-09	2.61E-08	5.47E-09	1.46E-08			1.3	750	41	1.30	0	0	0.00	0.02			
12.13	7.20E+05	1.20E-06	1.80E-07	-8.19E-10	3.35E-09	8.68E-10	1.87E-09			1.3	750	41	1.30	0	0	0.00	0.00			
								9.27E-10	2.16E-11	1.3	750	41	1.30	0	0			NA	NA	NA
Clear Pargasite																				
EHPV_NG_EXP29_clear_pargasite																				
14.61	2.58E+05	3.43E-07	5.18E-08	3.93E-10	3.03E-09	8.74E-10	6.35E-10			1.47	680	17	1.47	0	0	0.00	0.01			
15.04	2.66E+05	3.49E-07	5.26E-08	6.99E-10	3.15E-09	8.46E-10	6.12E-10			1.47	680	17	1.47	0	0	0.00	0.01			
9.04	2.84E+05	3.21E-07	4.83E-08	4.32E-09	3.23E-09	-3.42E-11	5.93E-10			1.47	680	17	1.47	0	0	0.01	0.01			
12.06	3.79E+05	3.37E-07	5.07E-08	2.72E-09	2.27E-09	3.17E-10	4.31E-10			1.47	680	17	1.47	0	0	0.01	0.01			
12.04	3.78E+05	3.35E-07	5.03E-08	1.68E-09	2.08E-09	4.87E-10	4.35E-10			1.47	680	17	1.47	0	0	0.01	0.01			
21.27	3.76E+05	3.56E-07	5.36E-08	4.19E-10	2.15E-09	1.70E-10	4.29E-10			1.47	680	17	1.47	0	0	0.00	0.01			
14.41	4.53E+05	3.43E-07	5.15E-08	3.08E-09	1.79E-09	-6.19E-11	3.62E-10			1.47	680	17	1.47	0	0	0.01	0.01			
17.26	5.42E+05	3.43E-07	5.15E-08	2.39E-10	1.61E-09	-1.09E-10	3.05E-10			1.47	680	17	1.47	0	0	0.00	0.00			
5.47	3.25E+05	3.33E-07	5.01E-08	-1.21E-10	2.49E-09	2.73E-10	4.99E-10			1.47	680	17	1.47	0	0	0.00	-0.01			
								2.31E-10	6.88E-12	1.47	680	17	1.47	0	0			NA	NA	NA
Clear Actinolite																				
EHPV_NG_EXP29_clear_act																				
9.30	7.31E+04	7.18E-06	1.08E-06	2.24E-08	1.15E-08	3.99E-09	2.30E-09			1.47	680	17	1.47	0	0	0.00	0.00			
9.02	7.08E+04	7.02E-06	1.05E-06	5.06E-09	1.16E-08	3.85E-09	2.38E-09			1.47	680	17	1.47	0	0	0.00	0.00			
9.34	7.33E+04	6.81E-06	1.02E-06	1.78E-09	1.10E-08	-2.65E-11	2.21E-09			1.47	680	17	1.47	0	0	0.00	0.00			
13.59	1.07E+05	5.53E-06	8.29E-07	2.29E-09	7.48E-09	3.63E-09	1.61E-09			1.47	680	17	1.47	0	0	0.00	0.00			
5.11	4.02E+04	9.27E-06	1.39E-06	2.66E-08	2.03E-08	2.66E-09	4.22E-09			1.47	680	17	1.47	0	0	0.00	0.00			
17.73	1.39E+05	5.26E-06	7.89E-07	3.80E-09	5.80E-09	4.94E-09	1.39E-09			1.47	680	17	1.47	0	0	0.00	0.00			
7.10	5.58E+04	7.39E-06	1.11E-06	1.81E-08	1.46E-08	4.78E-09	2.98E-09			1.47	680	17	1.47	0	0	0.00	0.00			
10.98	8.62E+04	7.25E-06	1.09E-06	-1.78E-09	9.39E-09	1.18E-09	1.91E-09			1.47	680	17	1.47	0	0	0.00	0.00			
15.18	1.19E+05	6.93E-06	1.04E-06	-2.00E-09	6.74E-09	3.18E-09	1.47E-09			1.47	680	17	1.47	0	0	0.00	0.00			
15.38	1.21E+05	4.65E-06	6.97E-07	3.20E-09	7.01E-09	3.07E-09	1.47E-09			1.47	680	17	1.47	0	0	0.00	0.00			
3.33	2.62E+04	1.02E-05	1.53E-06	2.02E-08	3.08E-08	7.68E-09	6.35E-09			1.47	680	17	1.47	0	0	0.00	0.00			
								7.22E-09	**1.30E-09**	1.47	680	17	1.47	0	0			NA	NA	NA

EHPV_NG_EXP36_clear_act																				
11.76	2.79E+04	4.70E-06	7.06E-07	1.83E-07	1.30E-07	-4.47E-09	1.23E-08			1.44	875	92	0.48	0.48	0.48	0.04	0.03			
8.72	2.07E+04	5.01E-06	7.53E-07	5.86E-07	1.98E-07	4.17E-08	1.77E-08			1.44	875	92	0.48	0.48	0.48	0.12	0.04			
14.86	3.53E+04	5.04E-06	7.57E-07	2.21E-07	1.13E-07	-5.13E-09	9.68E-09			1.44	875	92	0.48	0.48	0.48	0.04	0.02			
4.40	1.69E+04	3.79E-06	5.71E-07	6.41E-07	2.32E-07	6.00E-08	2.22E-08			1.44	875	92	0.48	0.48	0.48	0.17	0.07			
8.23	3.17E+04	3.98E-06	5.98E-07	3.16E-07	1.21E-07	5.11E-09	1.08E-08			1.44	875	92	0.48	0.48	0.48	0.08	0.03			
								9.51E-09	1.22E-09	1.44	875	92	0.48	0.48	0.48			**2.75E-09**	**NR**	**1.95E-09**
EHPV_NG_EXP38_clear_act																				
6.15	2.37E+04	1.13E-05	1.70E-06	-2.20E-08	4.00E-08	9.00E-09	7.21E-09			1.34	800	43	1.34	0	0	0.00	0.00			
11.73	4.51E+04	1.20E-05	1.80E-06	-2.69E-09	2.14E-08	3.30E-09	3.70E-09			1.34	800	43	1.34	0	0	0.00	0.00			
9.47	3.64E+04	1.12E-05	1.68E-06	-1.74E-08	2.57E-08	1.01E-08	4.91E-09			1.34	800	43	1.34	0	0	0.00	0.00			
3.36	1.29E+04	1.16E-05	1.75E-06	1.16E-07	7.95E-08	1.14E-08	1.29E-08			1.34	800	43	1.34	0	0	0.01	0.01			
9.48	3.65E+04	1.73E-05	2.60E-06	-1.11E-08	2.67E-08	4.34E-09	4.57E-09			1.34	800	43	1.34	0	0	0.00	0.00			
9.13	3.51E+04	1.29E-05	1.94E-06	-1.48E-08	2.65E-08	4.25E-09	4.95E-09			1.34	800	43	1.34	0	0	0.00	0.00			
5.80	2.23E+04	1.16E-05	1.74E-06	4.93E-08	4.35E-08	1.09E-08	7.88E-09			1.34	800	43	1.34	0	0	0.00	0.00			
3.28	1.26E+04	1.33E-05	2.01E-06	2.41E-08	7.87E-08	1.32E-08	1.34E-08			1.34	800	43	1.34	0	0	0.00	0.01			
								9.65E-09	1.51E-09	1.34	800	43	1.34	0	0			NA	NA	NA
Green Actinolite																				
EHPV_NG_EXP_29_green_act																				
9.13	7.17E+04	8.42E-06	1.26E-06	6.39E-10	1.10E-08	-2.45E-09	2.31E-09			1.47	680	17	1.47	0	0	0.00	0.00			
5.77	4.53E+04	7.66E-06	1.15E-06	-1.54E-08	2.17E-08	3.58E-09	3.62E-09			1.47	680	17	1.47	0	0	0.00	0.00			
5.65	4.44E+04	7.60E-06	1.14E-06	-4.16E-08	2.25E-08	1.13E-09	3.70E-09			1.47	680	17	1.47	0	0	-0.01	0.00			
7.34	5.77E+04	6.09E-06	9.15E-07	2.26E-08	1.47E-08	2.93E-09	2.86E-09			1.47	680	17	1.47	0	0	0.00	0.00			
7.34	5.77E+04	6.01E-06	9.02E-07	-5.66E-09	1.42E-08	-5.65E-10	2.87E-09			1.47	680	17	1.47	0	0	0.00	0.00			
2.93	2.30E+04	1.11E-05	1.67E-06	9.46E-09	3.49E-08	5.19E-09	7.20E-09			1.47	680	17	1.47	0	0	0.00	0.00			
3.13	2.46E+04	1.09E-05	1.63E-06	4.19E-09	3.46E-08	6.17E-09	6.68E-09			1.47	680	17	1.47	0	0	0.00	0.00			
1.99	1.56E+04	1.25E-05	1.88E-06	8.91E-08	5.49E-08	-1.81E-09	1.05E-08			1.47	680	17	1.47	0	0	0.01	0.00			
1.44	1.13E+04	1.32E-05	1.98E-06	6.22E-08	7.32E-08	-9.37E-09	1.48E-08			1.47	680	17	1.47	0	0	0.00	0.01			
0.67	5.25E+03	1.46E-05	2.21E-06	1.34E-07	1.54E-07	7.58E-09	3.12E-08			1.47	680	17	1.47	0	0	0.01	0.01			
3.07	2.41E+04	1.02E-05	1.53E-06	2.33E-08	3.30E-08	-4.37E-09	6.85E-09			1.47	680	17	1.47	0	0	0.00	0.00			
								1.05E-08	**1.50E-09**	1.47	680	17	1.47	0	0			NA	NA	NA
EHPV_NG_EXP_30_green_act																				
8.96	7.04E+04	5.25E-06	7.88E-07	-1.79E-09	1.13E-08	5.68E-10	2.36E-09			0.725	680	40	0.725	0	0	0.00	0.00			
17.83	1.40E+05	2.10E-06	4.64E-07	7.28E-09	5.84E-09	2.37E-10	1.18E-09			0.725	680	40	0.725	0	0	0.00	0.00			
5.05	3.97E+04	5.19E-06	7.80E-07	-1.98E-08	2.11E-08	2.50E-09	4.20E-09			0.725	680	40	0.725	0	0	0.00	0.00			
2.99	2.35E+04	6.01E-06	9.03E-07	1.41E-08	3.39E-08	-5.67E-09	7.39E-09			0.725	680	40	0.725	0	0	0.00	0.01			
3.97	3.12E+04	5.70E-06	8.56E-07	-1.23E-08	2.64E-08	2.48E-09	5.23E-09			0.725	680	40	0.725	0	0	0.00	0.00			
10.76	8.45E+04	3.53E-06	5.31E-07	-1.49E-09	1.01E-08	-2.43E-09	2.05E-09			0.725	680	40	0.725	0	0	0.00	0.00			
1.63	5.13E+04	6.35E-06	9.53E-07	2.88E-08	1.66E-08	3.23E-09	3.30E-09			0.725	680	40	0.725	0	0	0.00	0.00			
3.15	9.89E+04	5.55E-06	8.32E-07	1.33E-09	8.60E-09	1.97E-10	1.66E-09			0.725	680	40	0.725	0	0	0.00	0.00			
								9.10E-09	**1.80E-09**	0.725	680	40	0.725	0	0			NA	NA	NA
EHPV_NG_EXP_34_green_act																				
0.92	7.21E+03	4.10E-06	6.29E-07	1.14E-06	5.13E-07	-2.72E-08	4.84E-08			1.38	850	48	0.46	0.46	0.46	0.28	0.13			
11.89	4.57E+04	4.14E-06	6.21E-07	2.48E-07	9.26E-08	-2.98E-09	7.51E-09			1.38	850	48	0.46	0.46	0.46	0.06	0.02			
14.78	5.69E+04	4.08E-06	6.13E-07	1.50E-07	7.20E-08	3.10E-09	6.37E-09			1.38	850	48	0.46	0.46	0.46	0.04	0.02			
8.07	3.10E+04	4.18E-06	6.28E-07	2.75E-07	1.33E-07	-3.29E-09	1.13E-08			1.38	850	48	0.46	0.46	0.46	0.07	0.03			
4.43	3.48E+04	3.98E-06	5.98E-07	2.19E-07	1.07E-07	7.29E-11	9.99E-09			1.38	850	48	0.46	0.46	0.46	0.06	0.03			
11.86	4.56E+04	4.20E-06	6.30E-07	9.73E-08	8.51E-08	5.57E-09	7.58E-09			1.38	850	48	0.46	0.46	0.46	0.02	0.02			
								8.95E-09	1.68E-10	1.38	850	48	0.46	0.46	0.46			**3.65E-09**	**NR**	**3.50E-09**
EHPV_NG_EXP_36_green_act																				
0.67	3.95E+04	4.79E-06	7.19E-07	1.49E-06	2.50E-07	3.77E-08	1.05E-08			1.44	875	92	0.48	0.48	0.48	0.31	0.07			
11.96	4.60E+04	5.17E-06	7.77E-07	4.54E-07	1.17E-07	-8.57E-10	7.46E-09			1.44	875	92	0.48	0.48	0.48	0.09	0.03			
8.02	3.09E+04	5.30E-06	7.95E-07	2.74E-07	1.20E-07	-3.79E-09	1.11E-08			1.44	875	92	0.48	0.48	0.48	0.05	0.02			
4.27	1.65E+04	5.41E-06	8.14E-07	1.74E-07	2.75E-07	6.84E-10	2.08E-08			1.44	875	92	0.48	0.48	0.48	0.03	0.05			
15.63	6.02E+04	5.06E-06	7.60E-07	2.61E-07	7.76E-08	4.94E-09	5.76E-09			1.44	875	92	0.48	0.48	0.48	0.05	0.02			
0.39	2.30E+04	4.68E-06	7.04E-07	2.01E-06	3.61E-07	1.56E-08	1.52E-08			1.44	875	92	0.48	0.48	0.48	0.43	0.10			
Trench 1										1.44	875	92	0.48	0.48	0.48	0.34	0.04			
Trench 2										1.44	875	92	0.48	0.48	0.48	0.53	0.07			
Trench 3										1.44	875	92	0.48	0.48	0.48	0.23	0.05			
								1.06E-08	5.94E-10	1.44	875	92	0.48	0.48	0.48			**4.05E-09**	**2.30E-09**	**1.50E-09**
EHPV_NG_EXP_38_green_act																				
8.06	3.10E+04	1.43E-05	2.15E-06	-2.10E-09	3.08E-08	4.62E-09	5.40E-09			1.34	800	43	1.34	0	0	0.00	0.00			
10.78	4.15E+04	1.44E-05	2.16E-06	3.71E-08	2.32E-08	2.07E-09	4.06E-09			1.34	800	43	1.34	0	0	0.00	0.00			
5.60	2.15E+04	1.41E-05	2.12E-06	5.41E-08	4.51E-08	1.36E-09	7.71E-09			1.34	800	43	1.34	0	0	0.00	0.00			
5.52	2.12E+04	1.38E-05	2.08E-06	3.68E-09	4.76E-08	1.50E-08	8.13E-09			1.34	800	43	1.34	0	0	0.00	0.00			
2.77	1.07E+04	1.39E-05	2.09E-06	2.08E-08	8.86E-08	8.90E-09	1.62E-08			1.34	800	43	1.34	0	0	0.00	0.01			
10.67	4.11E+04	1.38E-05	2.07E-06	2.60E-09	2.33E-08	-1.17E-09	4.62E-09			1.34	800	43	1.34	0	0	0.00	0.00			
8.22	3.16E+04	1.44E-05	2.17E-06	4.77E-08	3.05E-08	6.24E-09	5.43E-09			1.34	800	43	1.34	0	0	0.00	0.00			
2.77	1.07E+04	1.43E-05	2.16E-06	6.64E-08	8.97E-08	-1.80E-08	1.58E-08			1.34	800	43	1.34	0	0	0.00	0.01			
								1.06E-08	2.10E-10	1.34	800	43	1.34	0	0			NA	NA	NA
Richterite																				
EHPV_NG_EXP14_rich																				
8.48	2.66E+05	1.14E-06	1.71E-07	3.06E-09	1.20E-09	2.88E-10	9.95E-10			1.7	780	12	1.7	0	0	0.00	0.00			
17.12	6.59E+04	1.19E-06	1.83E-07	1.50E-08	4.73E-09	-1.23E-09	4.03E-09			1.7	780	12	1.7	0	0	0.01	0.00			
16.94	5.32E+05	1.04E-06	1.56E-07	1.37E-09	6.20E-10	1.85E-11	4.95E-10			1.7	780	12	1.7	0	0	0.00	0.00			
12.91	4.06E+05	1.02E-06	1.54E-07	1.73E-09	7.76E-10	-7.99E-10	6.77E-10			1.7	780	12	1.7	0	0	0.00	0.00			
8.83	2.77E+05	1.05E-06	1.58E-07	1.30E-09	1.01E-09	-3.68E-10	9.51E-10			1.7	780	12	1.7	0	0	0.00	0.00			
4.56	1.43E+05	1.04E-06	1.57E-07	-2.64E-09	1.90E-09	-1.22E-09	1.87E-09			1.7	780	12	1.7	0	0	0.00	0.00			
6.34	1.12E+05	1.09E-06	1.63E-07	-9.96E-10	4.64E-09	1.04E-09	7.77E-10			1.7	780	12	1.7	0	0	0.00	0.00			
6.43	1.14E+05	1.11E-06	1.68E-07	5.77E-09	4.54E-09	1.41E-10	6.20E-10			1.7	780	12	1.7	0	0	0.01	0.00			
6.43	1.14E+05	1.04E-06	1.57E-07	-8.24E-09	4.89E-09	4.50E-11	6.55E-10			1.7	780	12	1.7	0	0	-0.01	0.00			
6.26	1.11E+05	1.09E-06	1.64E-07	1.30E-09	4.58E-09	1.40E-09	7.00E-10			1.7	780	12	1.7	0	0	0.00	0.00			
6.32	1.12E+05	1.13E-06	1.69E-07	-7.62E-09	4.64E-09	6.01E-10	7.45E-10			1.7	780	12	1.7	0	0	-0.01	0.00			
6.37	1.13E+05	1.07E-06	1.61E-07	5.07E-09	4.62E-09	-4.56E-10	6.53E-10			1.7	780	12	1.7	0	0	0.00	0.00			
13.51	1.06E+05	1.11E-06	1.66E-07	-2.93E-09	4.91E-09	-4.96E-12	6.71E-10			1.7	780	12	1.7	0	0	0.00	0.00			
13.66	1.07E+05	1.13E-06	1.70E-07	1.88E-09	4.73E-09	6.45E-11	6.81E-10			1.7	780	12	1.7	0	0	0.00	0.00			
3.18	9.98E+04	1.11E-06	1.67E-07	1.73E-09	5.14E-09	-4.09E-10	7.27E-10			1.7	780	12	1.7	0	0	0.00	0.00			
8.34	2.62E+05	1.13E-06	1.69E-07	1.17E-10	1.93E-09	5.01E-10	2.89E-10			1.7	780	12	1.7	0	0	0.00	0.00			
1.40	4.41E+04	1.12E-06	1.69E-07	-1.41E-08	1.18E-08	-3.93E-11	1.62E-09			1.7	780	12	1.7	0	0	-0.01	-0.01			
10.92	3.43E+05	1.14E-06	1.71E-07	1.66E-09	1.50E-09	2.45E-10	2.22E-10			1.7	780	12	1.7	0	0	0.00	0.00			
								6.46E-10	2.67E-11	1.7	780	12	1.7	0	0			NA	NA	NA
EHPV_NG_EXP23_rich																				
0.35	2.05E+04	9.18E-07	8.45E-07	1.49E-08	2.71E-08	3.86E-10	1.83E-09			1.56	680	12	1.56	0	0	0.02	0.03			
0.36	2.13E+04	5.70E-07	8.08E-07	7.17E-08	2.49E-08	-1.96E-09	1.61E-09			1.56	680	12	1.56	0	0	0.13	0.18			
1.55	9.19E+04	6.42E-07	2.10E-07	3.95E-09	5.65E-09	-5.41E-10	4.07E-10			1.56	680	12	1.56	0	0	0.01	0.01			
1.45	8.62E+04	6.94E-07	2.24E-07	3.21E-09	6.01E-09	-1.09E-11	3.69E-10			1.56	680	12	1.56	0	0	0.00	0.01			
2.50	1.49E+05	6.91E-07	1.55E-07	-1.20E-09	3.41E-09	2.48E-10	2.53E-10			1.56	680	12	1.56	0	0	0.00	0.00			
2.48	1.47E+05	6.44E-07	1.51E-07	2.85E-09	3.31E-09	3.31E-10	2.47E-10			1.56	680	12	1.56	0	0	0.00	0.01			
7.75	4.60E+05	7.39E-07	1.17E-07	1.59E-09	1.20E-09	9.85E-11	7.06E-11			1.56	680	12	1.56	0	0	0.00	0.00			
8.45	5.02E+05	6.81E-07	1.08E-07	2.65E-09	1.03E-09	2.25E-10	7.17E-11			1.56	680	12	1.56	0	0	0.00	0.00			
								4.63E-10	6.53E-11	1.56	680	12	1.56	0	0			NA	NA	NA
EHPV_NG_EXP33_rich																				
12.69	7.54E+05	1.66E-07	2.51E-08	4.67E-09	1.43E-09	2.92E-10	2.23E-10			1.4	750	48	0.47	0.47	0.47	0.03	0.01			
4.89	6.14E+05	1.49E-07	2.27E-08	1.38E-08	2.81E-09	1.02E-10	2.69E-10			1.4	750	48	0.47	0.47	0.47	0.09	0.02			
9.58	5.69E+05	1.62E-07	2.46E-08	8.18E-09	2.13E-09	7.99E-11	2.92E-10			1.4	750	48	0.47	0.47	0.47	0.05	0.02			
9.53	5.66E+05	1.53E-07	2.33E-08	7.57E-09	2.02E-09	2.22E-10	2.94E-10			1.4	750	48	0.47	0.47	0.47	0.05	0.02			
18.35	1.09E+06	1.72E-07	2.59E-08	4.01E-09	1.24E-09	3.08E-10	1.60E-10			1.4	750	48	0.47	0.47	0.47	0.02	0.01			
12.54	7.45E+05	1.68E-07	2.54E-08	7.39E-09	1.67E-09	1.09E-10	2.21E-10			1.4	750	48	0.47	0.47	0.47	0.04	0.01			
6.53	3.88E+05	1.58E-07	2.44E-08	1.26E-08	3.44E-09	2.88E-10	4.27E-10			1.4	750	48	0.47	0.47	0.47	0.08	0.03			
4.78	2.84E+05	1.47E-07	2.34E-08	3.19E-08	5.84E-09	3.89E-09	8.24E-10			1.4	750	48	0.47	0.47	0.47	0.22	0.05			
3.42	2.03E+05	1.66E-07	2.74E-08	3.39E-08	7.22E-09	6.36E-09	1.26E-09			1.4	750	48	0.47	0.47	0.47	0.20	0.06			
								3.44E-10	1.91E-11	1.4	750	48	0.47	0.47	0.47			NA	NA	NA
EHPV_NG_EXP34_rich																				
0.77	9.63E+04	2.11E-07	3.30E-08	7.15E-08	3.93E-08	8.02E-09	3.77E-09			1.38	850	48	0.46	0.46	0.46	0.34	0.19			
18.74	2.35E+06	1.85E-07	2.77E-08	1.73E-08	3.23E-09	5.68E-10	1.69E-10			1.38	850	48	0.46	0.46	0.46	0.09	0.02			
9.21	1.16E+06	1.76E-07	2.65E-08	3.81E-08	6.97E-09	7.39E-10	3.15E-10			1.38	850	48	0.46	0.46	0.46	0.22	0.05			
5.87	7.37E+05	1.79E-07	2.69E-08	3.55E-08	7.56E-09	9.01E-10	4.84E-10			1.38	850	48	0.46	0.46	0.46	0.20	0.05			
2.99	3.76E+05	1.59E-07	2.40E-08	5.86E-08	1.36E-08	1.14E-09	9.53E-10			1.38	850	48	0.46	0.46	0.46	0.37	0.10			
3.07	3.85E+05	1.58E-07	2.39E-08	3.56E-08	1.17E-08	6.10E-10	8.88E-10			1.38	850	48	0.46	0.46	0.46	0.23	0.08			
1.59	2.00E+05	1.89E-07	2.88E-08	1.38E-07	2.81E-08	3.64E-08	5.73E-09			1.38	850	48	0.46	0.46	0.46	0.73	0.19			
1.21	1.52E+05	1.65E-07	2.54E-08	6.69E-08	2.93E-08	2.00E-09	2.26E-09			1.38	850	48	0.46	0.46	0.46	0.41	0.19			
9.12	1.15E+06	1.78E-07	2.68E-08	2.88E-08	5.55E-09	5.22E-11	3.00E-10			1.38	850	48	0.46	0.46	0.46	0.16	0.04			
								3.90E-10	3.62E-11	1.38	850	48	0.46	0.46	0.46			**1.40E-10**	**1.00E-10**	**5.00E-11**

BOLD = values determined by concentration profiles
NR = none reported
NA = not applicable to particular experiment

Supplemental Table 3: Noble gas diffusion parameters for amphibole

experiment	phase	D He (m^2/s)	D He + uncert.	D He - uncert.	Temp. (˚C)
EHPV_NG_EXP29	green act	1.3E-16	1.4E-16	3.3E-17	680
EHPV_NG_EXP29	clear act	1.0E-15	5.8E-16	5.0E-16	680
EHPV_NG_EXP30	green act	3.6E-16	2.8E-16	1.0E-16	680
experiment	phase	D Ne (m^2/s)	D Ne + uncert.	D Ne - uncert.	Temp. (˚C)
EHPV_NG_EXP34	green act	3.5E-18	1.0E-12	NR	850
EHPV_NG_EXP34	amber par	2.3E-18	2.8E-18	1.2E-18	850
EHPV_NG_EXP34	richterite	1.0E-16	3.0E-16	7.8E-17	850
EHPV_NG_EXP 36	green act	6.3E-18	1.9E-17	5.8E-18	875
EHPV_NG_EXP 36	clear act	1.3E-17	3.9E-16	NR	875
EHPV_NG_EXP 36	amber par	1.1E-17	3.0E-17	NR	875

NR = none reported

CHAPTER 3: Light noble gas dissolution into ring structure-bearing materials and mineralogic influences on noble gas recycling

Colin R.M. Jackson[1], Stephen W. Parman[1], Simon P. Kelley[2], Reid F. Cooper[1]

1 Geological Sciences, Brown University, Providence, RI 02912
2 Department of Environment, Earth and Ecosystems, The Open University, Milton Keynes, United Kingdom

For submission to:
Geochimica et Cosmochimica Acta

Title: Light noble gas dissolution into ring structure-bearing materials and mineralogic influences on noble gas recycling

Authors: Colin R.M. Jackson, Stephen W. Parman, Simon P. Kelley, Reid F. Cooper

Abstract: Light noble gas (He-Ne-Ar) solubility has been experimentally determined in a range of materials with six-member, tetrahedral ring structures: beryl, cordierite, tourmaline, antigorite, muscovite, and F-phlogopite. Helium solubility in these materials is relatively high, 4×10^{-10} - 3×10^{-7} mol g^{-1} bar^{-1}, which is ~100 to 100,000× greater than He solubility in olivine, pyroxene, or spinel, assuming Henry's Law applies. Helium solubility and the topology of ring structures within different minerals are broadly correlated. Distinctive He-Ne-Ar solubility patterns are identified for different ring structure topologies. Combined, these observations suggest ring structures have a strong influence on noble gas solubility in materials and could facilitate the recycling of noble gases into the mantle. Measurements of Ne and Ar solubility in antigorite, however, are highly variable and correlated, suggesting multiple factors contribute the solubility of noble gases in serpentine-rich materials.

1.0 Introduction

Earth's mantle and atmosphere are distinct in both their elemental and isotopic noble gas compositions (Lupton and Craig, 1975; Staudacher and Allegre, 1982; Sarda et al., 1985; Sarda et al., 1988; Holland and Ballentine, 2006, Holland et al., 2009;

Mukhopadhyay, 2012). Isotopic heterogeneity between the atmosphere and mantle exists for long-lived radiogenic systems, short-lived radiogenic systems, and non-radiogenic systems. However, it is well-established that sediments and the upper-most oceanic crust contain relatively high concentrations of noble gases, and these materials deliver atmospheric noble gases to Earth's interior during subduction (Matsuda and Nagao, 1986, Podosek et al., 1980, Staudacher and Allegre, 1988). To maintain the observed noble gas isotope heterogeneity between the atmosphere and mantle it has been argued that devolatilization of subducted material is sufficiently efficient that subduction zones provide a near-complete barrier to noble gas recycling (Staudacher and Allegre, 1982).

The model of an extremely efficient barrier to noble gas recycling has since been challenged by a diverse set of observations. Deeper sections of exhumed slabs, which are correspondingly more difficult efficiently devolatilize, have been shown to host large quantities of seawater-derived noble gases (Kendrick et al., 2011, Kendrick et al., 2013). Peridotitic rocks interpreted to be exhumed from the mantle wedge have been overprinted by noble gases with elemental fractionations most consistent with a seawater origin (Sumino et al., 2010). Samples of metasomatized subcontinental lithospheric mantle show evidence for atmospheric Ar-rich fluids (Matsumoto et al. 2001; Matsumoto et al., 2002; Yamamoto et al., 2004; Gautheron et al., 2005; Matsumoto et al. 2005; Hopp and Ionov, 2011). Measurements of Xe isotopes derived from both ridge and plume environments seem to require the coexistence of an atmospheric and primordial Xe component in their mantle source, and the atmospheric component has been linked to noble gas recycling (Mukhopadhyay, 2012; Parai et al., 2012; Tucker et al., 2012, Peto et al., 2013). Measurements of Kr and Xe from well gases that contain mantle-derived

volatiles also provide evidence for the coexistence of atmospheric and primordial noble gases in the mantle (Caffee et al., 1999, Holland and Ballentine, 2006, Holland et al., 2009). Thus, many lines of evidence suggest that large volumes of the mantle have interacted with the noble gases from Earth's atmosphere, yet the recycling process is sufficiently inefficient that very early-forming mantle-atmosphere heterogeneities persist to the present day.

Despite the mounting evidence for the large scale recycling, the responsible carrier phases remain poorly understood. Here, we seek to understand the materials that are capable of transporting noble gases into and through subduction zones. We specifically focus on exploring the role of ring structure-bearing minerals. Ring structures are constituted by six $(Si,Al)O_4^{-4,-5}$ tetrahedral units bound in a hexagonal pattern (Figure 1). They are large radius structures and are commonly unoccupied. Noble gases are large radius, neutrally charged elements. Following lattice strain theory, unoccupied ring structures are predicted to be energetically favorable locations for noble gas dissolution in minerals (Damon and Kulp, 1958). Experiments corroborate this prediction (Smith and Schreyer, 1962; Wartho et al., 2005; Jackson et al., 2013a), suggesting minerals with ring structures are capable of the transporting significant quantities of noble gases in subduction zones.

The geometry of the ring structure hexagon (Figure 1) and the distribution of cation polyhedra local to the ring structure (combined, ring structure topology) vary between minerals. The topology of a ring structure will have a characteristic polarizability and size which, in turn, should affect the solubility of noble gases in the mineral that hosts the ring structure. To test this hypothesis, we experimentally quantify

the solubility of light noble gases in materials that possess a range of ring structure topologies.

2.0 Methods

2.1 Starting Materials

Large specimens of beryl, cordierite, tourmaline, antigorite, muscovite, and F-phlogopite materials were used as the starting materials in the experiments. Major element compositions are given in Table 1. Bulk materials of beryl, cordierite, tourmaline, and antigoritre were sectioned into sizes appropriate for the experiments, approximately 2 × 2 × 1 mm, using a low speed saw and diamond encrusted wafering blade. The large volume of the run products allows for repeated, high-precision measurements of noble gas contents in a particular material. No attempt was made to crystallographically orient samples during sectioning. A single face of each sectioned material was mechanically polished, finishing with 0.05 μ m alumina grit. Each mechanically polished face was then chemically polished using colloidal silica for >3 hours. This preparation is designed to minimize any lattice damage induced by the cutting and mechanical polishing procedure. Muscovite starting materials were purchased (SPI Supplies, V-1 grade) as cut and cleaved ~3 mm diameter discs (~50 μm height) and used as purchased. The F-phlogopite bulk material is synthetic and exists as inter-grown books. Starting materials were prepared by cleaving books from the bulk F-

phlogopite sample and cutting the cleaved books into appropriate sizes using a razor blade. Once prepared, but prior to the experiment, starting materials were mapped for secondary phases using a 120× stereoscope. All materials, except antigorite, are essentially devoid of observable secondary phases. The antigorite material contains both macro- and micro-scale magnetite as well as a separate fine-scale secondary phase (Figure 2). Macro-scale magnetite was avoided during analysis, but micro-scale and the fine-scale secondary phase were variably incorporated into the analyses of antigorite.

2.2 Noble Gas Solubility Experiments

Each experiment consists of three samples loaded into separate graphite capsules. The capsules were machined so that all three samples were contained within the hotspot, as determined by the temperature calibration of the pressure vessel assembly. A ~0.1 bar vacuum was drawn on the entire assembly before it was pressurized. The pressure medium was noble gases ± methane (He-Ne-Ar) for all experiments, allowing for precise and sustained control of noble gas fugacity over the duration of the experiment. Methane was included in some initial experiments to provide a small fugacity of H_2O (f_{H_2O}) in order to prevent mineral decomposition but was found to be unnecessary and was not used for later experiments. Leakage of the gas pressure medium was <5% over the run duration. Temperatures were controlled by placing the molybdenum-hafnium-carbide alloy pressure vessel into a vertical furnace for EHPV (externally heated pressure vessel) series experiments or a horizontal furnace for CS (cold seal) series experiments. Temperatures ranged from 350 to 800°C and pressures ranged from 0.06 to 1.77 kbar.

Convection within the pressure vessel was suppressed using graphite filler rods that extend the length of the pressure vessel above the sample capsules. Experiments were quenched by removing the pressure vessel from the furnace and allowing it to cool against air. The vessel cooled to ~50°C in 20 minutes. At this point the pressure vessel was rapidly depressurized and unloaded.

2.3 Analytical Methods

2.3.1 Major Element Analysis

Major element compositions were determined using an electron microprobe (Cameca SX-100, Brown University). Analyses were completed using wavelength dispersive spectrometry, and the PAP correction was applied. Analytical parameters were 15 kV, 10 nA, and a 10 μm beam.

2.3.2 Noble Gas Analysis

Noble gas concentrations of the experimental run products were determined using a UV laser ablation-noble gas mass spectrometer system at the Open University (UK). A 193 nm NeF excimer laser was used to ablate all materials. Three SAES AP-10 getters in the extraction system removed active gases released during ablation before introduction into a MAP215-50 mass spectrometer. ^{4}He, ^{22}Ne and ^{40}Ar were measured by an electron multiplier in peak hopping mode. The sensitivity of the mass spectrometer was

determined by gas pipetting a known volume of noble gases with elemental ratios designed to allow for measurement without separation and atmospheric isotopic ratios into the mass spectrometer. A more detailed description of the noble gas analytical method can be found in Kelley et al. (1994).

Materials from each experiment were analyzed repeatedly for noble gas contents using a combination of large diameter (40-400 μm) spots and single-line rasters. Pit depths ranged up to ~33 μm (average depth of a single pit). Blanks were typically run as every fourth analysis. The blank for each analytical session was calculated as the mean of individual blanks over the duration of that particular session, and the blank standard deviation is calculated as the standard deviation on the blank mean. A session is defined as a single day of analysis on a single port. Systematic changes in blanks were not observed over a session.

No internal standard was available for noble gas analyses. To determine noble gas concentration, we ratio the number of noble gas moles released to the volume of the ablation pit. Pits volumes were measured using a white light interferometer (Zygo Instruments, New View 6000 Series, Brown University). This device provides an image of the ablated surface that requires minimal interpolation of pixels with unknown depth values. A surface continuum is calculated by masking out the ablated area of the interferometer image and interpolating across the masked region. The inpainted interferometer image is subtracted from the surface continuum, isolating the relief associated with the ablation pit. To calculate the pit volume, the individual volumes of pixels are summed assuming rectangular prism geometry for each pixel. Shallow pits, pits ablated into highly curved surfaces, and pits that require longer distances of

interpolation have greater uncertainties associated with their volume. We estimate an uncertainty of 15% on volume calculations. Although, as discussed below, this is likely an underestimate for some extremely shallow pits. A small ring of vapor deposition forms along the circumference of the pits, creating a halo of pixels with negative depth. We avoid including these pixels in the volume determination by only summing pixels with positive depths. In general, >100,000 pixels are summed for an ablation pit. In total each topographic image contains 307,200 pixels (480 × 640).

All materials were carbon coated prior to imaging for volume determinations. This significantly improved the return signal, reducing the amount of interpolation required for pit volume determinations. Carbon coat thickness was not measured directly, but based on distance from source and coating time, the thickness is estimated at 20 nm.

2.3.2.1 Noble Gas Data Processing

To convert pit volumes into mass, we apply densities from Deer et al. (1996), accounting for Mg-Fe exchange. The pit depth associated with each analysis is the average depth of pixels summed in the volume calculation. The ablation pits are not perfectly flat bottomed, and thus, pit depth is a spatially averaged value. Also, it should be stressed that noble gas-laser ablation mass spectrometry is a micro-sampling technique that analyzes the bulk contents of noble gases in an ablated volume. Noble gases are not analyzed from a strict depth horizon within the sample. Rather, the concentration of a

noble gas in an analysis is a depth-averaged value. Individual measurements of noble gas concentrations in experimental run products are reported in Supplementary Table 1.

Noble gases are not ideal gases. This is particularly true for heavier noble gases in higher pressure, lower temperature systems. To account for the non-ideality of Ne and Ar, we calculate their fugacity in a given pressure medium using a modified Redlich-Kwong equation of state for gas mixtures (Flowers, 1979). Helium is taken as an ideal gas across the range of conditions explored here.

The solubilites of Ne and Ar in beryl and cordierite are calculated using He as an internal standard, applying the He solubility relationships determined here. We take this approach because the majority of ablations pits completed to measure Ne and Ar solubility in beryl and cordierite are very shallow and prone to systematic underestimations of pit volume (detailed below). A more detailed explanation of Ne and Ar solubility calculations in beryl and cordierite are provided in the Supplementary Information.

3.0 Results and Discussion

3.1 Major Element Results

Major element compositions for all materials investigated are reported in Table 1. Cations are reported as oxide wt. %, which causes low totals on an oxide basis for minerals with significant F, Cl, and OH. Quality of analyses can be evaluated by stoichiometry. Stoichiometry is calculated assuming that no oxy-component is present

for hydrous minerals, i.e. OH sites host only F, Cl, and OH. Beryl contains stoichiometric Be, and tourmaline contains stoichiometric Li and B. Be, Li, and B were not analyzed, and so the abundances of these elements are assumed to be stoichiometric, i.e. three Be atoms per beryl formula unit, three B atoms per tourmaline formula unit, and 1.5 Li atoms per tourmaline formula unit. There is some uncertainty regarding the stoichiometric component of Li in tourmaline. We choose 1.5 atoms per formula unit because the chemistry of the tourmaline is close to the elbaite endmember. Changes in the assumed amount of Li in tourmaline do not have a significant effect on stoichiometry calculated for tourmaline. Electron mircoprobe analyses confirm that inclusions of magnetite are present the in antigorite material.

3.2. Noble Gas Results

3.2.1. Equilibrium Considerations: Depth Correlations

Several lines of evidence suggest the measured concentrations of He closely approach equilibrium values. Figure 3 plots all He analyses against the associated ablation pit depth. Helium concentrations are normalized to f_{He} of the experiment (yielding a Henry's constant for He, abbriviated He_{HC}, mol g^{-1} bar^{-1}). This approach is implemented to account for the variabilty in concentration directly related to changes noble gas fugacity and to allow the effects of other variables (e.g. depth) to be observed in inter-experiment comparisons. This approach is justified here because each investigated phase has been verified follow Henrian solution behavior for He (Figure 4b).

No correlation is observed between He_{HC} and pit depth, neglecting some very shallow pits and some experiments on muscovite and F-phlogopite. The general lack of correlation between He_{HC} and depth supports the argument that the measured He concentrations are equilibrium values and are not affected by lattice damage induced during sample preparation or the inclusion of secondary phases during analysis. Henry's constants for He are calculated for an experiment as equal-weight averages of the individual analyses on that experiment when no depth dependence for concentration is observed.

The high He concentrations associated with shallow pits (<0.33 μm) are likely artifacts. We argue these high concentrations result from systematic underestimations of the ablation pit volume. Ablation pits with large radius/depth ratios are difficult to measure accurately because small biases in the interpolation of the unablated surface can lead to relatively large errors in volume calculations. The interpolation algorithms used here tend to under-account for surface curvature, which results in systematic underestimates of volume when curvature is concave in the direction of ablation (down). All ablation pits on beryl, cordierite, tourmaline, antigorite were drilled into polished surfaces, and given the polishing techniques utilized here, these surfaces are typically concave down. Shallower pits are more prone to this systematic bias, and consequently, we only consider concentration data for ablation pits that are >0.33 μm deep as reliable. All analyses that are <0.33 μm deep are plotted as unfilled symbols. The volume bias is most obvious for the shallow analyses of beryl but is also observed for shallow analyses of tourmaline. Shallow pits of cordierite were also analyzed (Figure 3a), but no obvious volume bias is present, supporting the interpretation that the high concentration analyses

are apparent and not the result of He enrichment. Several spurious, high concentration analyses were observed deeper than 0.33 μm (also plotted as unfilled symbols). We interpret these analyses to reflect the inadvertent incorporation of a gas-rich secondary phase in the ablated volume. These data are not used in further analysis or calculations of Henry's constants as the remainder of data are comparatively repeatable.

Several lower temperature, shorter duration experiments on micas display clear He concentration gradients that extend several microns into the mineral interior (symbols labeled "diffusion fit," Figure 3b). The fact that concentration is depth dependent precludes calculating He Henry's constants as simple averages. For these experiments, we fit diffusion profiles (tracer diffusion into a semi-infinite medium from a reservoir of constant chemical potential) to quantify He diffusion kinetics and solubility (Supplementary Table 2). Solubility in this circumstance is taken as the modeled concentration of He at the surface. Note, however, that some micas run at similar temperatures and for similar durations do not show a clear concentration profile but yield similar He_{Hc} (see the muscovite and F-phlogopite from CS_NG_EXP2 and the F-phlogopite from CS_NG_EXP15). The reason for this discrepancy is unclear but may reflect that the diffusional length scale for these samples was not the grain size.

Helium diffusivities fit for muscovite and F-phlogopite vary between 2.48×10^{-15} and 1.71×10^{-17} m^2 s^{-1} at 500°C. The average of He diffusivities fit for muscovite is $9 \pm 5\times10^{-17}$ m^2 s^{-1}, and this value is ~100× slower than previous step-degassing based determinations of He diffusion in muscovite at 500°C (Lippolt and Weigel, 1988). Micas in this study were prepared as cleaved discs and were consequently ablated perpendicular to the 001 plane during analysis, far from grain edges. This analytical approach

effectively constrains diffusion to occur across, rather than parallel to, the interlayer structures. Thus, the slow He diffusivities measured here are consistent with noble gas diffusion being strongly anisotropic in mica, where diffusion preferentially occurs through interlayers. Similar observations have been made for Ar diffusion in mica (Giletti, 1974).

3.2.2. Equilibrium Considerations: Duration, f_{He}, and Temperature Correlations

Figure 4 plots the He_{Hc} determined for each experiment against the respective experimental duration, $f_{He,}$ and temperature. Where no concentration profile was observed in a run product, He_{Hc} is calculated as an equal-weight average of the population of individual analyses. Where a concentration profile was observed, He_{Hc} is calculated by fitting a diffusion profile and using the surface concentration as solubility. He_{Hc} values for each experiment are provided in Table 2 along with associated experimental parameters.

He_{Hc} values are independent of duration, $f_{He,}$ and temperature (Figure 4). Many of the minerals investigated here are hydrous and, thus, prone to decomposition under the imposed experimental conditions (i.e. high temperature, low f_{H_2O} systems). The lack of correlation between He_{Hc} and duration argues against H loss or decomposition affecting the concentrations of He measurements. Similarly, higher temperatures promote more rapid loss of H and decomposition. No correlation is observed between He_{Hc} and temperature, also arguing against H loss and decomposition affecting He concentrations. Moreover, the lack of correlation between He_{He} and temperature indicates that there is a

small enthalpy associated with the dissolution of He into the ring structure-bearing minerals explored here. This is consistent with the weak bonding between noble gases and their surroundings and allows for simple extrapolations to higher and lower temperatures.

Experiments were conducted at noble gas fugacities that are unnaturally high in order to achieve precise analyses. As such, the applicability of Henry's Law must be evaluated before solubility relationships can be applied to modeling the behavior of noble gases in natural systems. Henrian solution behavior requires that the concentration of an element dissolved into a phase is linearly proportional to the fugacity of that element in the system, or equivalently, the Henry's constant for an element is invariant with changes in the fugacity of that element. Figure 4b demonstrates the invariance of He_{Hc} over a range of f_{He}, indicting Henry's Law is obeyed. The repeatability of He_{Hc} across the range of f_{He} suggests the solubility relationships determined for He are robust and meaningful for natural systems.

At higher f_{He}, it is expected that the available ring structures approach complete occupancy, resulting in a non-linear relationship between f_{He} and He solubility, i.e. a Langmuir Isotherm. However, the occupancy of ring structures by noble gases, up to the highest f_{He} explored here, remains relatively small. Cordierite shows the strongest affinity for He, but only ~15% of available rings structures are occupied by He at f_{He} = 1.77 kbar (two ring sites per formula unit).

It is important to note that Figure 4b only demonstrates that Henry's Law is applicable for the dissolution mechanisms that dominate bulk solubility at relatively high f_{He}. It remains possible that separate dissolution mechanisms are important at lower f_{He},

but that these mechanisms saturate at higher f_{He}, leaving their contribution to bulk solubility in the present experiments small. In this case, the Henry's constants reported here will be lower limits for modeling natural systems, i.e. noble gases will have a stronger affinity for solids under natural conditions.

3.2.3. Correlations Between He_{Hc} and Ring Structure Topology

Ring structures tend to generate large radius interstices that are potential hosts for noble gases and other large radius, zero charge species, e.g. H_2 or N_2. However, the geometry of the ring structure hexagon (Figure 1) and the distribution of cation polyhedra local to the ring structure (combined, ring structure topology) are not constant between minerals (Figure 5). Thus, the solubility of noble gases in ring structure-bearing minerals may be sensitive to changes in ring structure topology.

Figure 5 plots He_{Hc} for the various ring structure-bearing minerals studied here, ordered in ascending He_{Hc}. He_{Hc} for olivine (Jackson et al. 2013b, calculated assuming Henrian behavior) is also plotted to provide a frame of reference. Compared to olivine, He is highly soluble in ring structure-bearing minerals, but the range in He_{Hc} is large, varying between ~100 to 100,000× olivine He_{Hc}. We seek here to understand the cause of this variability by considering variations in ring structure topology.

3.2.3.1. Mica He_{Hc}

Helium is the least soluble in muscovite and F-phlogopite (Figure 5). This low solubility supports the hypothesis that unoccupied ring structures enhance noble gas solubility in minerals, as the ring structures in mica are nominally occupied by K, or to a lesser extent, Na. The high occupancy of ring structures in micas suggests other locations are required to accommodate the observed noble gas uptake. Dioctehedral micas, such as muscovite, contain abundant unoccupied interstices in their octahedral sheets. These interstices provide additional porosity that is not available in trioctehedral micas, such as F-phlogopite. The similar values of He_{Hc} measured for muscovite and F-phlogopite, however, argue for the octahedral sheets being only minor hosts for He and, by extension, other noble gases in mica. This result is also supported by the similarity of He solubility measurements in pyroxene, olivine, and spinel with variable concentrations of Mg-site vacancies (Heber et al., 2007; Jackson et al., 2013b). The small solubility associated with octahedral vacancies suggests that noble gases are hosted in the mica interlayer despite the presence of cations in the ring structures. The strong diffusional anisotropy inferred for micas (Section 3.2.1) also supports the argument that the octahedral sheets are relatively high energy locations for noble gases. Stoichiometric calculations suggest that a small interlayer-deficiency (~10%) is present in the muscovite (Table 1), which manifests itself as unoccupied ring structures. A more complete characterization of the muscovite is needed to confirm this, but if true, this suggest that He is more soluble in F-phlogopite compared to muscovite in the absence of interlayer-deficiencies.

3.2.3.2. Antigorite and Tourmaline He_{Hc}

Antigorite and tourmaline have similar He_{Hc} and share similar topologies about their ring structures (Figure 5). Specifically, both minerals have groups of octahedra above and below a single ring, and the tetrahedral units in the ring are oriented with an apex pointed towards the upper octahedra. In tourmaline, the ring structure exists as an isolated unit and is commonly occupied by Na, and to a lesser extent, Ca. Each of the octahedra associated with the ring structure in tourmaline shares an oxygen with a trigonally coordinated B ion. Measured He_{Hc} in tourmaline have been extrapolated to zero occupancy of the ring structure for comparison purposes in Figure 5. The ring structure in antigorite is defined by an upper and lower octahedral sheet with a tetrahedral sheet of rings bound to the upper octahedra. Nominally, all the ring structures in antigorite are unoccupied. Compared to the other minerals with unoccupied ring structures, tourmaline and antigorite have the lowest associated $He_{Hc,}$ $\sim 1\times10^{-9}$ mol g^{-1} $bar^{-1,}$ suggesting He has the weakest affinity for this general topology.

3.2.3.3. Amphibole (actinolite) He_{Hc}

The ring structure in amphibole is constituted by an opposing pair of rings that are offset by distorted polyhedra of Ca and Na ions. Octahedral polyhedra border the pair of rings, both above and below. The ring structure in amphibole is commonly occupied by Na, and to a lesser degree, K. He_{Hc} values for amphibole are taken from Jackson et al. 2013a, and these values have been extrapolated to zero occupancy of the ring structure for comparison purposes in Figure 5. He_{Hc} for both amphiboles is $\sim 1\times10^{-8}$ mol g^{-1} bar^{-1},

suggesting He favors the amphibole ring structure topology compared to the topology present in antigorite and tourmaline.

3.2.3.4. Beryl and Cordierite He_{Hc}

Beryl and high-cordierite are isostructural, hexagonal minerals, but under most geologic conditions cordierite reverts to its low, orthorhombic form. The orthorhombic transition causes a small distortion to the ring in cordierite compared to beryl (see Figure 1c and 1d). Nonetheless, beryl and low-cordierite share a similar ring structure topology. The tetrahedra that comprise the rings in beryl and cordierite are oriented such that no apex is pointed normal the ring plane, and the rings are stacked continuously along the c-axis, forming "ring channels." A larger ring of tetrahedral and octahedral cations is positioned between the purely tetrahedral rings. The alternating channel structure creates two distinct environments: a larger radius interstice in the plane of the tetrahedral-octahedral ring and smaller radius interstice in the plane of the tetrahedral ring. Both locations have been shown to host large radius species such as alkali cations, Ar, and H_2O (Smith and Schreyer, 1962; Goldman et al., 1977). The present experiments on beryl and cordierite confirm that channel structures are also capable of hosting smaller radii noble gases. Indeed, He_{Hc} determined for beryl and cordierite is exceptionally high compared to other ring structure topologies: $\sim 1 \times 10^{-7}$ mol g^{-1} bar^{-1}. This suggests He has the strongest affinity for the topology of ring structures in beryl and cordierite compared to the other topologies considered here. Additional work is needed, however, to determine if He is primarily hosted in the larger or smaller radius ring structure.

3.2.4. He-Ne-Ar Solubility Patterns

Figure 6 plots determinations of He_{Hc}, Ne_{Hc}, and Ar_{Hc} for experiments where He-Ne-Ar solubility data were collected. He_{Hc} and Ne_{Hc} data for amphibole (actinolite) are taken from Jackson et al. 2013b and have been extrapolated to zero occupancy of the ring structure for comparison purposes. Ne and Ar data are normalized to f_{Ne} and f_{Ar}, respectively, for comparison purposes, but explicit demonstrations of Henry's Law applicability have not been made for these data.

To a first order, Ne_{Hc}, and Ar_{Hc} measurements are similar to He_{Hc} measurements made on the same material: He_{Hc}, Ne_{Hc}, and Ar_{Hc} are high for beryl and cordierite, intermediate for amphibole, and low for antigorite. However, distinctive He_{Hc}-Ne_{Hc}-Ar_{Hc} patterns are present between minerals that correlate with the different classes of ring structures. Beryl and cordierite both display a chevron He_{Hc}-Ne_{Hc}-Ar_{Hc} pattern, where He_{Hc} and Ar_{Hc} are lower than Ne_{Hc}. The ~3× difference between He_{Hc} for beryl and cordierite (Figure 5) remains similar for Ne_{Hc} and expands for Ar_{Hc}. A negative slope exists between He_{Hc} and Ne_{Hc} for both amphiboles, although He_{Hc} and Ne_{Hc} measurements on a Ti-rich, pargasitic amphibole show a more moderate, He_{Hc}-Ne_{Hc} slope (Jackson et al. 2013a). Antigorite displays an inverted chevron He_{Hc}-Ne_{Hc}-Ar_{Hc} pattern, opposite to the pattern observed for beryl and cordierite. The slope between He_{Hc} and Ne_{Hc} for antigorite is negative and steep compared to that observed for amphibole. There appears to be a reversal in slope between Ne_{Hc} and Ar_{Hc}, but considerable variability is present in both the Ne and Ar data for antigorite (Figure 6). Because of this variability,

we do not interpret the Ne_{Hc} and Ar_{Hc} data as simply being reflective of solubility in pure antigorite. The source for this variability is not immediately clear, as He_{Hc} data are highly reproducible. Possible root causes for this variability are explored below.

3.2.5. Ne_{Hc} and Ar_{Hc} Variability in Antigorite

The antigorite studied here is not a mono-mineralic sample. This contrasts with the other materials used here for He, Ne and Ar solubility determinations. Transmitted light images of a representative antigorite sample are provided in Figure 2. Multiple secondary phases are present. The most visually obvious secondary phase is magnetite, identified as opaque, black masses. Magnetite is mostly present as macro-scale inclusions. Micro-scale magnetite inclusions are also distributed throughout the sample. A separate secondary phase is also present throughout the antigorite. The nature of this separate secondary phase is more difficult to determine given its very fine scale, but on the sample-scale this phase causes a cloudy appearance and is heterogeneously concentrated (Figure 2a and 2b). The experimental antigorite samples were taken from the more translucent sections of the starting material, similar to material on the left side of Figure 2a, limiting the net effect of the clouding phase. However, the clouding phase is present throughout the antigorite and has the potential to affect the abundances of noble gases concentrated in the antigorite material.

Figure 7 correlates individual measurements of He_{Hc} and Ne_{Hc} against Ar_{Hc} in antigorite where a He-Ne-Ar pressure medium was used (CS_NG_21, 22, and 25). He_{Hc} measurements are repeatable, clustering near 1.5×10^{-9} mol g^{-1} bar^{-1}. Simultaneous

measurements of Ar_{Hc} are scattered in excess of analytical precision, ranging between 4.24×10^{-10} and 3.79×10^{-9} mol g^{-1} bar^{-1} (Figure 7a). Similarly, simultaneous measurements of Ne_{Hc} and Ar_{Hc} are correlated, with a slope of 0.12±0.03 1σ (Figure 7b), neglecting two data points with strongly negative Ne_{Hc}. The fact that Ar_{Hc} variability is not correlated with He_{Hc} variability, yet correlated with $Ne_{Hc,}$ suggests that a secondary, noble gas-rich phase was variably included in the analyses of antigorite samples. Given the relationships present in Figure 7, it appears this secondary phase prefers Ar, and to a lesser extent Ne, compared to He.

Micro-scale inclusions of magnetite and a fine-scale "clouding" phase are present throughout the sample, and these materials have likely been variably incorporated into the analyzed antigorite. The edge of a macro-scale magnetite inclusion was intentionally incorporated into the final analysis of the antigorite sample from experiment CS_NG_EXP30 (noted in Supplementary Table 1). A He-only pressure medium was used in CS_NG_EXP30, so the combined He-Ne-Ar effect of magnetite inclusions remains uncertain. However, the concentration of He in the final analysis was 2.05 ± 0.31×10^{-6} mol g^{-1}, and the average of the other analyses on antigorite in CS_NG_EXP30 is 1.49 ± 0.03×10^{-6} mol g^{-1}. From this single comparison it appears that magnetite inclusions or magnetite-antigorite grain boundaries are potentially noble gas-rich materials. More work is needed to confirm this result and extend the analysis to Ne and Ar. The effect of the clouding secondary phases has not been isolated, and thus, it also remains a potential source for the observed variability in Ne and Ar.

The general preference of the gas-rich secondary phase for heavy noble gases is consistent the properties of aqueous fluids. However, between 75˚C and the critical point

(374˚C), Ar is approximately twice as soluble as Ne in water (Potter and Clynne, 1978; Crovetto et al., 1982), and dissolved salts are expected to make Ar and Ne solubility converge (Smith and Kennedy, 1983). Given the relatively moderate slope of the Ne_{Hc}-Ar_{Hc} correlation (0.12 ± 0.03 1σ, Figure 7b), aqueous fluid inclusions alone do not appear to be the source of Ne and Ar variability.

Regardless of the source of Ne and Ar variability, several inferences can be drawn for the solubility of noble gases in pure antigorite (antigorite in the absence of gas-rich secondary phases). Ne_{Hc} is ~10× lower than He_{Hc}, despite the skew of Ne to higher concentrations. Several analyses of Ne_{Hc} are within error of or below zero, suggesting He_{Hc} in pure antigorite is more than 10× greater than Ne_{Hc}. Many simultaneous analyses of Ar_{Hc} and He_{Hc} have Ar_{Hc}/He_{Hc} ratios less than unity, suggesting $He_{Hc}>Ar_{Hc}$ in pure antigorite. Moreover, Ar_{Hc} analyses of antigorite from EHPV_NG_EXP53 and CS_NG_EXP18 are either within error of zero or low compared to the remainder of Ar_{Hc} analyses (Table 2). Applying the axiom that the highest Ar_{Hc} determinations reflect the strongest contribution from gas-rich secondary phases, the low Ar_{Hc} analyses also imply a low value of Ar_{Hc} and a low Ar_{Hc}/He_{Hc} ratio for pure antigorite. However, we do not adopt the low determinations of Ar_{Hc} from EHPV_NG_EXP53 and CS_NG_EXP18 as being necessarily representative of pure antigorite. Both EHPV_NG_EXP53 and CS_NG_EXP18 were run simultaneously and shared a pressure medium. Moreover, EHPV_NG_EXP53 and CS_NG_EXP18 were the only two experiments that had a methane + Ar pressure medium. Correlated experimental factors may have contributed to the low Ar_{Hc} measurements on EHPV_NG_EXP53 and CS_NG_EXP18. With the current data it is impossible to completely deconvolve the competing effects of gas-rich

secondary phases, pure antigorite, and systematic experimental factors in interpreting the concentrations of noble gases analyzed in antigorite. Nonetheless, it appears that in bulk antigorite, ring structures compete with secondary phases to determine bulk noble gas solubility. The relatively low noble gas solubility associated with ring structures in antigorite makes the bulk noble gas solubility in serpentinites more easily influenced by other factors.

4.0. Implications for Noble Gas Recycling

4.1 Effect of Noble Gas Solubility in Unoccupied Ring Structure-Bearing Minerals

Atmospheric noble gases are introduced into slab materials during hydrothermal alteration (Staudacher and Allegre, 1988, Kumagai et al., 2003; Moreira et al., 2003; Kendrick et al., 2011; Kendrick et al., 2013). Seawater is the ultimate source of hydrothermal fluids and, thus, it is expected that noble gases are initially introduced into the slab in elemental proportions equal to those found in seawater. Bulk seawater isotopically identical to the atmosphere but is elementally enriched in heavier noble gases compared to the atmosphere following noble gas solubility in saline water at surface temperatures (Potter and Clynne, 1978; Crovetto et al., 1982). If no fractionations occur during noble gas uptake and devolatilization of the slab, then noble gases should be recycled in seawater-like elemental proportions with atmospheric isotopic signatures.

Measurements of mantle-derived Ne indicate that less than 30% of non-nucleogenic Ne in the mantle is recycled (Moreira et al., 1998; Yokochi and Marty, 2004; Ballentine et al., 2005; Mukhopadhyay, 2012). Similarly, measurements of mantle-derived Xe indicate that ~85% of Xe in the mantle is recycled (Holland and Ballentine, 2006; Mukhopadhyay, 2012; Parai et al., 2012, Tucker et al., 2012; Peto et al., 2013). Using modern noble gas concentrations for the mantle and seawater (Holland and Ballentine, 2006), these measurements suggest that the Ne/Xe ratio associated with the flux of recycled noble gases is either close to that of seawater or favors preferential recycling of heavier noble gases. Elemental abundance measurements of noble gases derived from the mantle have also been argued to reflect preferential recycling of heavier noble gases compared to their proportions in seawater (Holland and Ballentine, 2006). Thus, available data suggest the recycling flux is not enriched in the light noble gases.

We have demonstrated that noble gases have a strong affinity for unoccupied ring structures and that ring structure topology influences the He_{Hc}-Ne_{Hc}-Ar_{Hc} pattern in minerals. However, none of the ring structure topologies studied here have a preference for larger radii, heavier noble gases (Figure 6 and 7). The minerals that are most relevant to noble gas recycling, antigorite in its pure form and amphibole, appear to favor He compared heavier noble gases. Simple extrapolation of amphibole and pure antigorite He_{Hc}-Ne_{Hc}-Ar_{Hc} patterns to heavier noble gases suggests that these minerals would preferentially facilitate the recycling of lighter noble gases, opposite to the inferred pattern for noble gas recycling. Other minerals with unoccupied ring structures are formed during hydrothermal alteration of slab materials, including talc, chlorite, clays, and the lower temperature polymorphs of antigorite, chrysotile and lizardite. All of these

minerals may contribute significantly to the flux of recycled noble gases. However, these minerals are all phyllosilicates, and thus, share a ring structure topology similar to antigorite. Correspondingly, these minerals do not offer an obvious balance to the preference of amphibole and antigorite for light noble gases.

If occupied ring structures are important noble gas recycling, then factors other than noble gas solubility appear to be required to maintain a flux of recycled noble gases that is not elementally enriched in lighter noble gases. Other factors may include elemental fractionations associated with slab devolatilzation, adsorption, hydrothermal fluids enriched in heavier noble gases, closed system incorporation of seawater noble gases, or a balancing flux of materials that have a preference for heavier noble gases. Noble gases in seafloor sediments are abundant and consistently fractioned to heavier gases, likely reflecting adsorption processes (Podosek et al., 1980, Matsuda and Nagao, 1986, Staudacher and Allegre, 1988). The enrichment of heavy noble gases in seafloor sediments is sufficiently strong that if sediments are a major contributor to noble gas recycling, a balancing flux of materials is required that is relatively enriched in lighter noble gases to match the elemental pattern of noble gases in the mantle (Holland and Ballentine, 2006). In this context, noble gas solubility in ring structure minerals and adsorption can combine to moderate the elemental fractionations associated with either process.

4.2 He-Ne-Ar Behavior in Bulk Antigorite

We have focused on determining He-Ne-Ar solubility in pure minerals in order to understand the mineralogic controls on noble gas recycling. However, recycled lithologies are an aggregate of minerals, grain boundaries, and fluid inclusions. It is the combined affinity of these materials for noble gases that act to determine the concentration of noble gases in a lithology following hydrothermal alteration, provided hydrothermal alternation occurs as an open system. The antigorite studied is multiphase and contains many grain boundaries, making it a more complete analog of recycled serpentinite.

When considered as bulk system and not a pure phase, antigorite has a strong affinity for Ar and for Ar compared to Ne. Measurements of Ar_{Hc} in antigorite are uniformly greater than Ne_{Hc} and commonly surpass He_{Hc} (Figure 7). These measurements suggest that serpentinites may act to preferentially incorporate Ar compared to Ne during their equilibration with hydrothermal fluids and that serpentinites may have a strong affinity for noble gases in general.

There is corroborating evidence for this behavior of Ne and Ar in natural serpentinites. Measurements of antigorite schists (serpentinites) that are inferred to be exhumed slab materials indicate that serpentinite can host high concentrations of seawater-derived noble gases, with ^{36}Ar abundances in serpentinite reaching ~100× the abundance of ^{36}Ar in the depleted mantle. Measured Ne/Ar ratios in slab serpentine are typically ~2× lower than seawater values, although considerable scatter is observed (Kendrick et al. 2011, Kendrick et al., 2013). This fractionation of Ne from Ar is consistent with the measurements of Ne_{Hc} and Ar_{Hc} in bulk antigorite. Previous experimental work defining noble gas solubility in bulk serpentine also supports Ne being

less soluble compared to Ar (Zaikowski and Schaeffer, 1979). Combined, these results are consistent with the solubility of noble gases in materials affecting the elemental patterns of noble gases associated with hydrothermally altered lithologies. Other processes, such as adsorption, can also cause low Ne/Ar ratios for materials and cannot be ruled out as the ultimate source of elemental fractionations observed in serpentinites given the current experimental data.

The kinetics of equilibration between bulk antigorite and the pressure medium have not been directly quantified here, but limits can be evaluated. Experiments on antigorite were conducted at temperatures ≤450˚C, which are low compared to the remainder of experiments. Despite the low temperatures, He_{Hc}, Ne_{Hc}, and Ar_{Hc} do not correlate with ablation pit depth, indicating that these gases equilibrated with the antigorite to at least a depth of 33 μm over the experimental durations (Supplementary Table 2). This is extremely rapid compared to the other materials investigated here, particularly for Ar. For example, Ar diffusion profiles in beryl and cordierite extended <1 μm deep after 41.5 hours at 800 ˚C (Supplementary Information). The rapid nature of noble gas uptake is consistent with observed degassing behaviors of serpentinites during step-degassing noble gas analysis, i.e. heating of 20-40 mg chips of serpentinite at 300˚C for 20 minutes typically extracts >20% of total ^{36}Ar from the sample (Kendrick et al, 2013). It is likely that grain boundaries and the relatively open sheet structures facilitate rapid diffusion of noble gases through sepentinites. Consequently, an equilibrium distribution of noble gases between serpentinite and hydrothermal fluids should be closely approached in natural systems, even at the relatively low temperature associated with serpentine stability. It is also worth noting that He, Ne, and Ar concentrations do

not decrease with decreasing pit depth in the experimental antigorite samples, indicating loss of noble gases prior to analysis in the present experiements is negligible.

4.3 Deep Recycling of Noble Gases and Alternative Recycling Environments

Micas, such as phengite, are stable to high pressures and temperatures compared to the majority of hydrous minerals in slabs. Consequently, mica is thought to be a relatively important mineral for the deep transport of water associated with crustal slab lithologies and may dominate the transport of water in relatively hot slabs (Hacker et al., 2008). Measurements of He_{Hc} in muscovite and F-phlogopite are similar to each other and somewhat lower compared to minerals with unoccupied ring structures (Figure 5). Nonetheless, He_{Hc} is ~100× higher compared to mantle minerals, such as olivine, which suggests that mica could be an important host for noble gases deeper in subduction zones, particularly for slabs where serpentine stability is small.

Mica and amphibole are also stable in the metasomatized, lithospheric mantle (e.g. Pilet et al., 2008; Green et al., 2010) and hydrated sections of lower continental crust (e.g. Rapp and Watson, 1995, Liu et al., 1996). Both of the lower crust and lithospheric mantle can become sufficiently dense that they are delaminated and returned to the convecting mantle (e.g. Bird, 1978, Ducea and Saleeby, 1996; Davidson et al., 2008, Jagoutz and Behn, 2013). Depending on physics of delamination, these recycled lithologies can retain significant amounts of their initial volatiles upon recycling (Elkins-Tanton, 2007). If enriched in mica and amphibole, these lithogies may also provide alternative environments for noble gas recycling. The noble gases hosted in these

delaminated lithologies can be either dominated by mantle noble gases or atmospheric noble gases depending on the ultimate origin for the hydrating fluid.

5.0 Conclusions

We have experimentally determined the solubility of noble gases in a series of materials that are broadly applicable to noble gas recycling. For pure minerals, the availability and topology of unoccupied ring structures has a strong control on the solubility of He. Distinctive He_{Hc}-Ne_{Hc}-Ar_{Hc} patterns for pure minerals have also been identified. These patterns correlate with ring structure topology and do not appear to favor dissolution of heavier noble gases. Secondary phases, such as those present in antigorite, can also strongly concentrate noble gases, and thus, affect the solubility of noble gases in bulk materials. This is particularly true for antigorite because He, Ne, and Ar are relatively insoluble the pure mineral. In contrast to ring structures, secondary phases may favor the uptake of heavier noble gases, and the variable presence secondary phases may contribute to local elemental fractionations and concentration variations in natural systems. Continued experimental work, particularly on a wider variety of recycled materials and heavier noble gases, is now needed to help understand the processes and lithologies that have resulted in the atmospheric component of noble gases present in the mantle.

References:

Ballentine, C.J., Marty, B., Lollar, B.S., Cassidy, M., 2005. Neon isotopes constrain convection and volatile origin in the Earth's mantle. *Nature* 433, 33-38.\

Bird, P., 1979. Continental delamination and the Colorado Plateau. *Journal of Geophysical Research* 84, 7561-7571.

Caffee, M.W., Hudson, G.U., Velsko, C., Huss, G.R., Alexander, E.C., Chivas, A.R., 1999. Primordial noble cases from Earth's mantle: Identification of a primitive volatile component. *Science* 285, 2115-2118.

Crovetto, R., Fernández-Prini, R., Japas, M.L., 1982. Solubilities of inert gases and methane in H_2O and in D_2O in the temperature range of 300 to 600 K. *The Journal of Chemical Physics* 76, 1077-1086.

Damon, P.E., Kulp, J.L., 1958. Excess helium and argon in beryl and other minerals. *American Mineralogist* 43, 433-459.

Davidson, J., Turner, S., Handley, H., Macpherson, C., Dosseto, A., 2007. Amphibole "sponge" in arc crust? *Geology* 35, 787-790.

Deer, W.A., Howie, R.A., Zussman, J., 1996. An Introduction to the Rock-Forming Minerals, 2nd Edition ed. Prentice Hall.

Ducea, M.N., Saleeby, J.B., 1996. Buoyancy sources for a large, unrooted mountain range, the Sierra Nevada, California: Evidence from xenolith thermobarometry. *Journal of Geophysical Research-Solid Earth* 101, 8229-8244.

Elkins-Tanton, L.T., 2007. Continental magmatism, volatile recycling, and a heterogeneous mantle caused by lithospheric gravitational instabilities. *Journal of Geophysical Research-Solid Earth* 112, B03405.

Fanale, F.P., Cannon, W.A., 1971. Physical Adsorption of rare gas on terrigenous sediments. *Earth and Planetary Science Letters* 11, 362-368

Flowers, G.C., 1979. Correction of Holloway's (1977) adaptation of the modified Redlick-Kwong equation of state for calculation of the fugacities of molecular species in super critical fluid of geologic interest. *Contributions to Mineralogy and Petrology* 69, 315-318.

Gautheron, C., Moreira, M., Allègre, C., 2005. He, Ne and Ar composition of the European lithospheric mantle. *Chemical Geology* 217, 97-112.

Giletti, B.J., 1974. Studies in diffusion I: argon in phlogopite mica. *Geochemical transport and kinetics* 634, 107-115.

Goldman, D.S., Rossman, G.R., Dollase, W.A., 1977. Channel constituents in cordierite. *American Mineralogist* 62, 1144-1157.

Green, D.H., Hibberson, W.O., Kovacs, I., Rosenthal, A., 2010. Water and its influence on the lithosphere-asthenosphere boundary. *Nature* 467, 448-451.

Heber, V.S., Brooker, R.A., Kelley, S.P., Wood, B.J., 2007. Crystal-melt partitioning of noble gases (helium, neon, argon, krypton, and xenon) for olivine and clinopyroxene. *Geochimica Et Cosmochimica Acta* 71, 1041-1061.

Holland, G., Ballentine, C.J., 2006. Seawater subduction controls the heavy noble gas composition of the mantle. *Nature* 441, 186-191.

Holland, G., Cassidy, M., Ballentine, C.J., 2009. Meteorite Kr in Earth's Mantle Suggests a Late Accretionary Source for the Atmosphere. *Science* 326, 1522-1525.

Hopp, J., Ionov, D.A., 2011. Tracing partial melting and subduction-related metasomatism in the Kamchatkan mantle wedge using noble gas compositions. *Earth and Planetary Science Letters* 302, 121-131.

Jackson, C.R.M., Parman, S., Kelley, S.P., Cooper, R.F., 2013a. Noble gas transport into the mantle facilitated by high solubility in amphibole. *Nature Geoscience* 6, 562-565.

Jackson, C.R.M., Parman, S.W., Kelley, S.P., Cooper, R.F., 2013b. Constraints on light noble gas partitioning at the conditions of spinel-peridotite melting. *Earth and Planetary Science Letters* 384, 178-187.

Jagoutz, O., Behn, M.D., 2013. Foundering of lower island-arc crust as an explanation for the origin of the continental Moho. *Nature* 504, 131-134.

Kelley, S. P., Arnaud, N. O. & Turner, S. P., 1994. High spatial resolution $^{40}Ar/^{39}Ar$ investigations using an ultra-violet laser probe extraction technique. *Geochimica Et Cosmochimica Acta* 58, 3519-3525.

Kendrick, M.A., Scambelluri, M., Honda, M., Phillips, D., 2011. High abundances of noble gas and chlorine delivered to the mantle by serpentinite subduction. *Nature Geoscience* 4, 807-812.

Kendrick, M.A., Honda, M., Pettke, T., Scambelluri, M., Phillips, D., Giuliani, A., 2013. Subduction zone fluxes of halogens and noble gases in seafloor and forearc serpentinites. *Earth and Planetary Science Letters* 365, 86-96.

Kumagai, H., Dick, H.J.B., Kaneoka, I., 2003. Noble gas signatures of abyssal gabbros and peridotites at an Indian Ocean core complex. *Geochemistry Geophysics Geosystems* 4, 9107.

Lippolt, H.J., Weigel, E., 1988. ^{4}He diffusion in ^{40}Ar-retentive minerals. *Geochimica Et Cosmochimica Acta* 52, 1449-1458.

Liu, J., Bohlen, S.R., Ernst, W.G., 1996. Stability of hydrous phases in subducting oceanic crust. *Earth and Planetary Science Letters* 143, 161-171.

Lupton, J.E., Craig, H., 1975. Excess ^{3}He in oceanic basalts: evidence for terrestrial primordial helium. *Earth and Planetary Science Letters* 26, 133-139.

Matsuda, J., Nagao, K., 1986. Noble gas abundances in a deep sea sediment core from eastern equatorial Pacific. *Geochemical Journal* 20, 71-80.

Matsumoto, T., Chen, Y., Matsuda, J.-i., 2001. Concomitant occurrence of primordial and recycled noble gases in the Earth's mantle. *Earth and Planetary Science Letters* 185, 35-47.

Matsumoto, T., Morishita, T., Matsuda, J.-i., Fujioka, T., Takebe, M., Yamamoto, K., Arai, S., 2005. Noble gases in the Finero phlogopite-peridotites, western Italian Alps. *Earth and Planetary Science Letters* 238, 130-145.

Matsumoto, T., Pinti, D.L., Matsuda, J., Umino, S., 2002. Recycled noble gas and nitrogen in the subcontinental lithospheric mantle: Implications from N-He-Ar in fluid inclusions of SE Australian xenoliths. *Geochemical Journal* 36, 209-217.

Moreira, M., Blusztajn, J., Curtice, J., Hart, S., Dick, H., Kurz, M.D., 2003. He and Ne isotopes in oceanic crust: implications for noble gas recycling in the mantle. *Earth and Planetary Science Letters* 216, 635-643.

Moreira, M., Kunz, J., Allegre, C., 1998. Rare gas systematics in popping rock: Isotopic and elemental compositions in the upper mantle. *Science* 279, 1178-1181.

Mukhopadhyay, S., 2012. Early differentiation and volatile accretion recorded in deep-mantle neon and xenon. *Nature* 486, 101-104.

Parai, R., Mukhopadhyay, S., Standish, J., 2012. Heterogeneous upper mantle Ne, Ar and Xe isotopic compositions and a possible Dupal noble gas signature recorded in basalts from the Southwest Indian Ridge. *Earth and Planetary Science Letters* 359, 227-239.

Peto, M.K., Mukhopadhyay, S., Kelley, K.A., 2013. Heterogeneities from the first 100 million years recorded in deep mantle noble gases from the Northern Lau Back-arc Basin. *Earth and Planetary Science Letters* 369, 13-23.

Pilet, S., Baker, M.B., Stolper, E.M., 2008. Metasomatized lithosphere and the origin of alkaline lavas. *Science* 320, 916-919.

Podosek, F.A., Honda, M., Ozima, M., 1980. Sedimentary noble gases. *Geochimica Et Cosmochimica Acta* 44, 1875-1884.

Potter, R.W., Clynne, M.A., 1978. Solublity of the noble gases He, Ne, Ar, Kr, and Xe in water up to the critical point. *Journal of Solution Chemistry* 7, 837-844.

Rapp, R.P., Watson, E.B., 1995. Dehydration melting of metabasalt at 8-32 kbar: Implications for continental growth and crust-mantle recycling. *Journal of Petrology* 36, 891-931.

Sarda, P., Staudacher, T., Allegre, C.J., 1988. Neon isotopes in submarine basalts. *Earth and Planetary Science Letters* 91, 73-88.

Sarda, P., Staudacher, T., Allègre, C.J., 1985. $^{40}Ar/^{36}Ar$ in MORB glasses: constraints on atmosphere and mantle evolution. *Earth and Planetary Science Letters* 72, 357-375.

Smith, J., Schreyer, W., 1962. Location of argon and water in cordierite. *Mineralogical Magazine* 33, 226-236.

Staudacher, T., Allegre, C.J., 1982. Terrestrial Xenology. *Earth and Planetary Science Letters* 60, 389-406.

Staudacher, T., Allegre, C.J., 1988. Recycling of oceanic crust and sediments: the noble gas subduction barrier. *Earth and Planetary Science Letters* 89, 173-183.

Sumino, H., Burgess, R., Mizukami, T., Wallis, S.R., Holland, G., Ballentine, C.J., 2010. Seawater-derived noble gases and halogens preserved in exhumed mantle wedge peridotite. *Earth and Planetary Science Letters* 294, 163-172.

Tucker, J.M., Mukhopadhyay, S., Schilling, J.G., 2012. The heavy noble gas composition of the depleted MORB mantle (DMM) and its implications for the preservation of heterogeneities in the mantle. *Earth and Planetary Science Letters* 355, 244-254.

Wartho, J.A., Kelley, S.P., Elphick, S.C., 2005. Estimates of Ar diffusion and solubility in leucite and nepheline: Electron microprobe imaging of Ar distribution in a mineral. *American Mineralogist* 90, 954-962.

Yamamoto, J., Kaneoka, I., Nakai, S., Kagi, H., Prikhod'ko, V.S., Arai, S., 2004. Evidence for subduction-related components in the subcontinental mantle from

low $^{3}He/^{4}He$ and $^{40}Ar/^{36}Ar$ ratio in mantle xenoliths from Far Eastern Russia. *Chemical Geology* 207, 237-259.

Yokochi, R., Marty, B., 2004. A determination of the neon isotopic composition of the deep mantle. *Earth and Planetary Science Letters* 225, 77-88.

Zaikowski, A., Schaeffer, O.A., 1979. Solubilty of noble gases in serpentine: implications for meteoritic noble gas abundances. *Earth and Planetary Science Letters* 45, 141-154

Figure Captions:

Figure 1: Different geometries of six-member, tetrahedral ring structures. A) Regular hexagon with apexes pointed normal to the plane of the ring. B) Distorted hexagon with apexes pointed normal to the plane of the ring. This geometry is similar to that found in tourmaline. C) Regular hexagon with apexes pointed oblique to the plane of the ring. This geometry is similar to that found in beryl and high-cordierite. D) Distorted hexagon with apxes pointed oblique to plane. This geometry is similar to that found in low-cordierite, which is the common form for geological samples.

Figure 2: Images of representative antigorite material. A) Large scale transmitted light mircograph. Note the presence of macro- and micro-scale inclusions of magnetite as well as a "clouding" phase that is concentrated on the right side of the image. The gap in material on the left is a partial cut of the antigorite using the wafering blades. B) Small scale transmitted light micrograph. Image is taken from boxed region in A).

Figure 3: He_{Hc} measurements versus ablation pit depth. Each data point is an individual measurement of He concentration normalized to f_{He} for the experiment. Error bars are 1σ and include analytical and pit volume determination uncertainties. Data for beryl, cordierite, antigorite, and tourmaline are plotted in A). Data for muscovite and F-phlogopite are plotted in B). Note the change in axis scales between A) and B). No correlations are observed between He_{Hc} and pit depth excepting shallow measurements

on beryl and tourmaline (A) and some experiments on micas (B). Data points not used for solubility determinations are plotted as open symbols.

Figure 4: He_{Hc} determinations for an experiment versus experimental A) duration, B) f_{He}, and C) temperature. He_{Hc} values are determined by either averaging individual measurements of He_{Hc} in an experiment or fitting diffusion profiles to individual measurements He_{Hc} in an experiment. Error bars are 1σ and are calculated as standard deviations of the mean or from diffusion profile fits. He_{Hc} is not correlated with experimental duration, *f*He, or temperature for all materials investigated.

Figure 5: He_{Hc} determinations for each material type plotted in ascending order, left to right. He_{Hc} values are determined by either averaging individual measurements of He_{Hc} in an experiment or fitting diffusion profiles to individual measurements He_{Hc} in an experiment. The cation polyhedra local to the ring structures (ring structure topology) in each mineral are provided along the x-axis below the respective He_{Hc} data. There is a broad correlation between the topology local to ring structures and He_{Hc}. He_{Hc} for olivine (Jackson et al., 2013b) is plotted to provide a frame of reference.

Figure 6: He_{Hc}-Ne_{Hc}-Ar_{Hc} determinations for materials where He-Ne-Ar data where collected. He_{Hc}-Ne_{Hc}-Ar_{Hc} values are determined by averaging individual measurement in an experiment. Distinctive patterns present for material types: beryl and cordierite display a chevron He_{Hc}-Ne_{Hc}-Ar_{Hc} pattern, amphibole displays a negative slope between

He_{Hc}-Ne_{Hc}, and antigorite displays an inverted chevron He_{Hc}-Ne_{Hc}-Ar_{Hc} pattern, although considerable variability is present in Ne_{Hc} and Ar_{Hc} determinations for antigorite.

Figure 7: Simultaneous measurements of A) He_{Hc} and Ar_{Hc} and B) Ne_{Hc} and Ar_{Hc} in antigorite. Each data point is an individual measurement of antigorite. Error bars are 1σ and include analytical and pit volume determination uncertainties. A) He_{Hc} measurements are repeatable, but Ar_{Hc} measurements are highly variable. B) Ar_{Hc} variability is correlated with $Ne_{Hc,}$ suggesting Ar_{Hc} and Ne_{Hc} variability are controlled by the same factor. Two data points from CS_NG_21, 22, and 25 are not included in the regression of Figure 7 because the Ne_{Hc} measurements are anomalously negative.

Chapter 3,
Figure 1

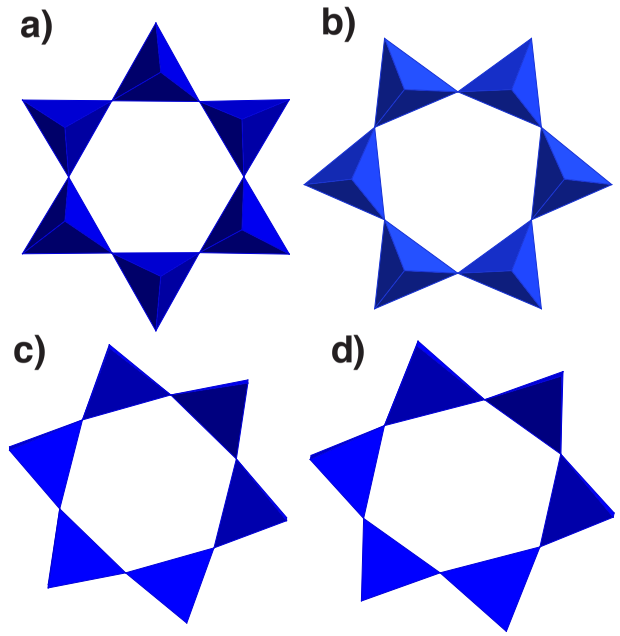

Chapter 3, Figure 2:

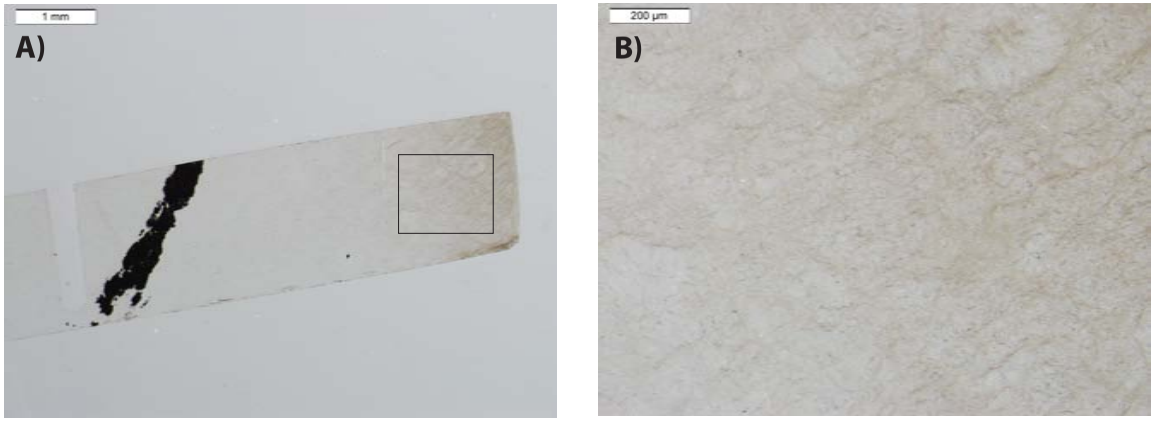

Chapter 3, Figure 3:

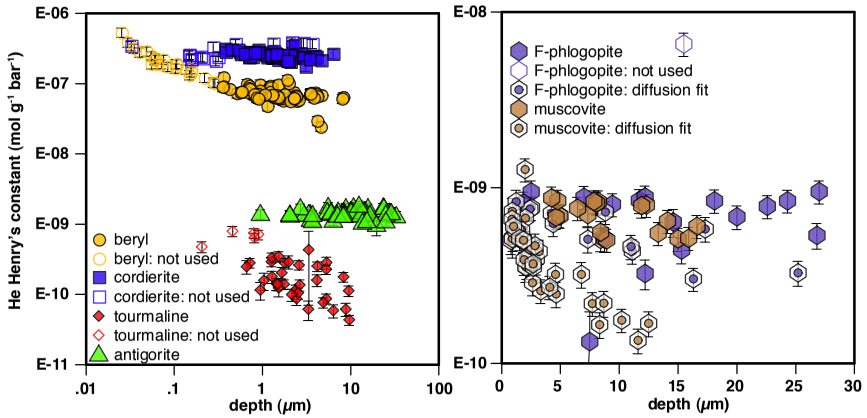

Chapter 3, Figure 4:

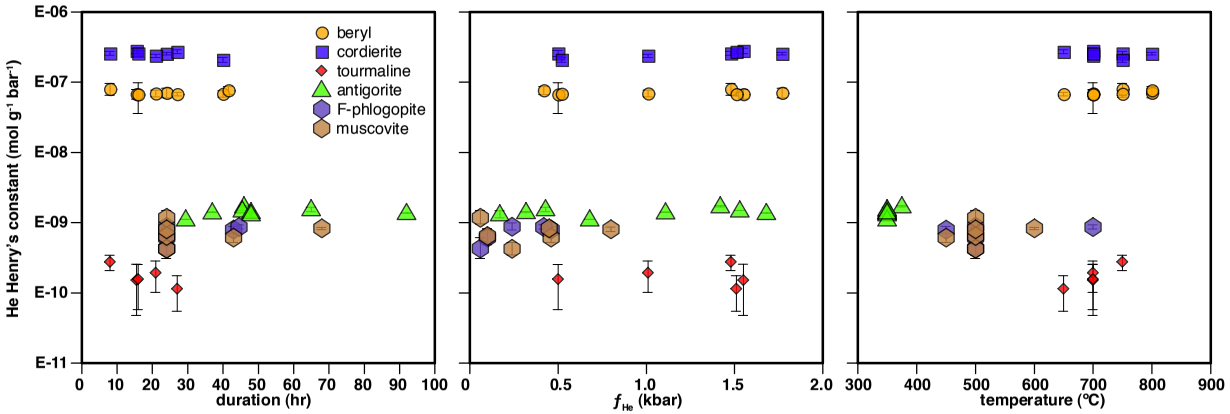

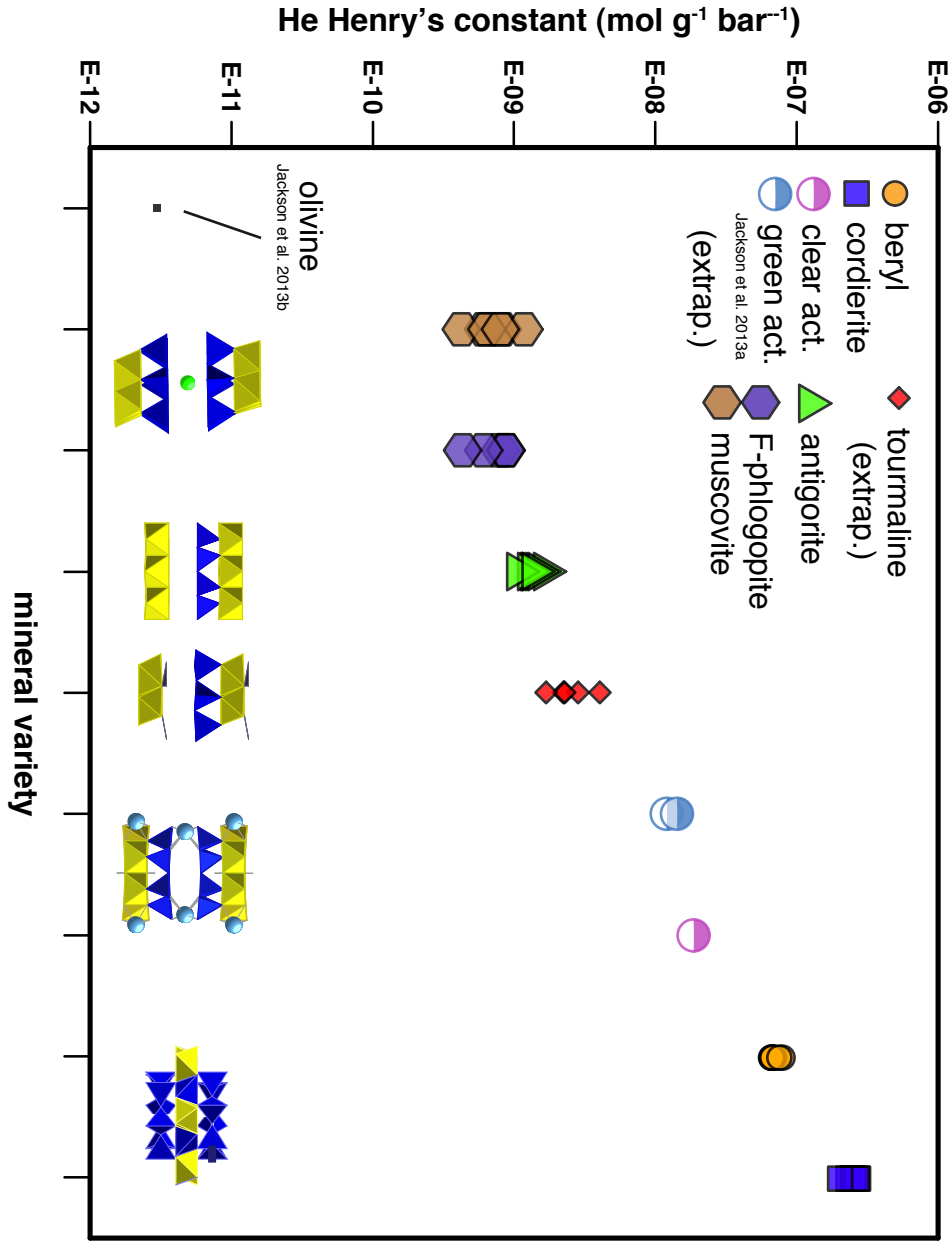
Chapter 3, Figure 5
He Henry's constant (mol g-1 bar-1)
E-06
E-07
E-08
E-09
E-10
E-11
E-12
beryl
cordierite
clear act.
green act.
Jackson et al. 2013a
(extrap.)
tourmaline
(extrap.)
antigorite
F-phlogopite
muscovite
olivine
Jackson et al. 2013b
mineral variety

Chapter 3, Figure 6:

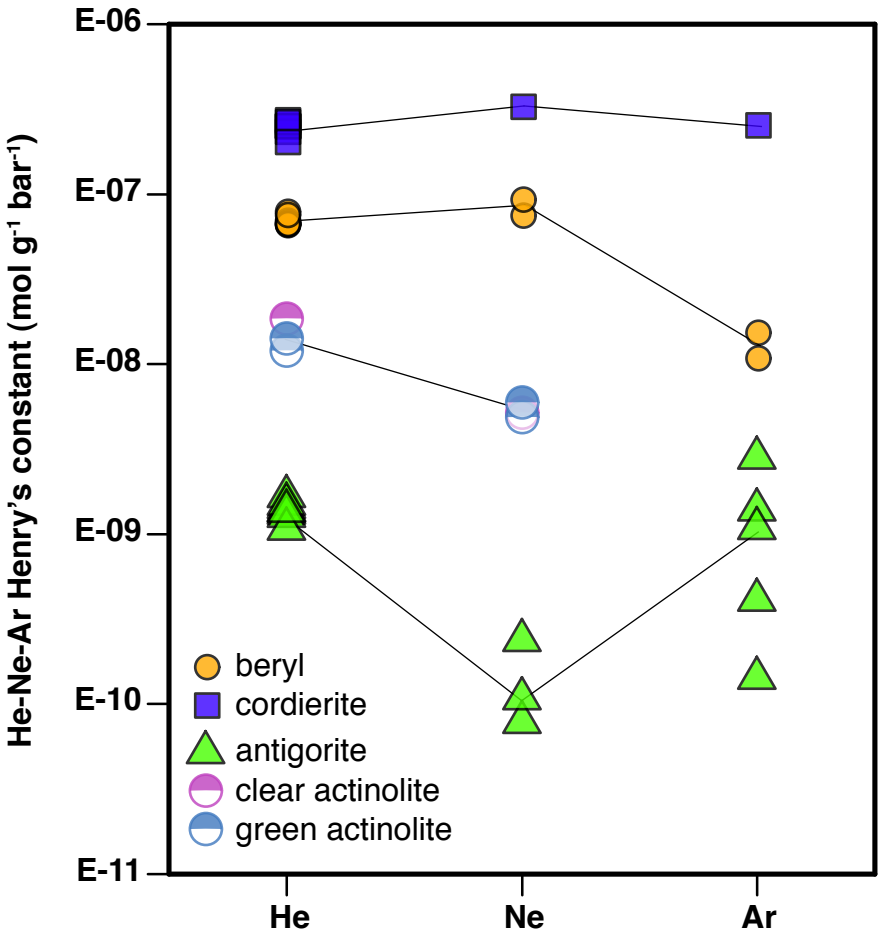

Chapter 3, Figure 7:

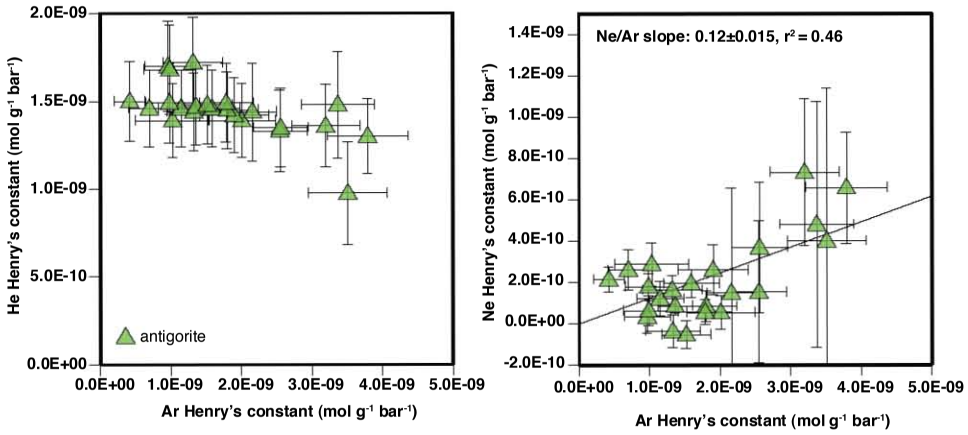

Table 1: Major element compositions

	beryl		cordierite		tourmaline		antigorite		muscovite		F-phlogopite	
	avg. (wt.%)	std. dev.										
SiO_2	67.24	0.39	50.36	0.31	37.63	0.05	44.15	0.30	46.20	0.30	43.17	0.70
Al_2O_3	18.85	0.06	34.55	0.09	39.41	0.13	0.92	0.15	35.28	0.12	12.48	0.35
TiO_2	0.00	0.00	0.00	0.00	0.04	0.01	0.01	0.02	0.53	0.02	0.01	0.02
MnO	0.00	0.00	0.02	0.00	2.93	0.02	0.04	0.01	0.01	0.02	-0.01	0.01
FeO	0.04	0.00	3.01	0.01	1.46	0.02	1.40	0.07	1.77	0.07	0.04	0.03
MgO	0.00	0.00	11.99	0.02	0.00	0.00	40.47	0.43	1.08	0.02	28.68	0.32
CaO	0.00	0.00	0.01	0.00	2.36	0.02	-0.01	0.01	0.00	0.01	-0.01	0.01
Na_2O	0.97	0.01	0.29	0.00	1.72	0.02	0.00	0.02	0.75	0.09	0.02	0.01
K_2O	0.04	0.00	0.01	0.00	0.02	0.00	0.00	0.00	9.61	0.29	10.88	0.11
Cl	0.00	0.00	0.00	0.00	0.00	0.00	0.00	0.00	0.01	0.00	0.00	0.00
F	0.00	0.00	0.00	0.00	1.36	0.01	NA	NA	NA	NA	11.02	0.28
Oxide total	87.15	0.39	100.23	0.36	85.58	0.14	86.97	0.61	95.23	0.33	95.25	0.99
	Cations per FU											
Si	5.98	0.01	4.97	0.01	5.84	0.01	2.04	0.01	3.07	0.01	3.00	0.02
Al	1.97	0.01	4.02	0.01	7.22	0.01	0.05	0.01	2.76	0.01	1.02	0.03
Ti	0.00	0.00	0.00	0.00	0.00	0.00	0.00	0.00	0.03	0.00	0.00	0.00
Mg	0.00	0.00	1.76	0.01	0.00	0.00	2.79	0.02	0.11	0.00	2.98	0.01
Fe_T	0.00	0.00	0.25	0.00	0.19	0.00	0.05	0.00	0.10	0.00	0.00	0.00
Mn	0.00	0.00	0.00	0.00	0.39	0.00	0.00	0.00	0.00	0.00	0.00	0.00
Ca	0.00	0.00	0.00	0.00	0.39	0.00	0.00	0.00	0.00	0.00	0.00	0.00
Na	0.17	0.00	0.06	0.00	0.52	0.01	0.00	0.00	0.10	0.01	0.00	0.00
K	0.00	0.00	0.00	0.00	0.00	0.00	0.00	0.00	0.82	0.03	0.97	0.01
Ring Vac. %	91.40	0.08	97.19	0.04	8.55	0.76	NA	NA	NA	NA	NA	NA
Note:	assume 3 Be				assume 3 B, 1.5 Li				possible ring vac.			

Table 2: Noble gas Henry's Constants

	He_{Hc}	He_{Hc} uncert. +	He_{Hc}. uncert. -	Ne_{Hc}	Ne_{Hc} uncert. +	Ne_{Hc} uncert. -	Ar_{Hc}	Ar_{Hc} uncert. +	Ar_{Hc} uncert. -	pressure (kbar)	temp. (°C)	duration (hr.)	f_{He} (kbar)	f_{Ne}	f_{Ar}
beryl															
EHPV_NG_EXP13	8.07E-08	1.58E-08	1.58E-08	-	-	-	-	-	-	1.48	750	8	1.48	0.00	0.00
EHPV_NG_EXP15	7.09E-08	1.13E-08	1.13E-08	-	-	-	-	-	-	1.77	800	24	1.77	0.00	0.00
EHPV_NG_EXP16	6.81E-08	1.09E-08	1.09E-08	-	-	-	-	-	-	1.55	700	15.5	1.55	0.00	0.00
EHPV_NG_EXP17	6.93E-08	7.59E-09	7.59E-09	-	-	-	-	-	-	1.01	700	21	1.01	0.00	0.00
EHPV_NG_EXP18	6.69E-08	3.11E-08	3.11E-08	-	-	-	-	-	-	0.50	700	16	0.50	0.00	0.00
EHPV_NG_EXP24	6.76E-08	3.95E-09	3.95E-09	-	-	-	-	-	-	1.51	650	27	1.51	0.00	0.00
EHPV_NG_EXP32	6.83E-08	6.99E-09	6.99E-09	*7.64E-08*	*9.84E-09*	*9.84E-09*	**1.56E-08**	**4.67E-10**	**6.23E-10**	1.55	750	40	0.52	0.66	0.76
EHPV_NG_EXP43	7.68E-08	1.01E-08	1.01E-08	*9.49E-08*	*1.30E-08*	*1.30E-08*	**1.10E-08**	**1.08E-09**	**1.87E-09**	1.27	800	41.5	0.42	0.50	0.56
cordierite															
EHPV_NG_EXP13	2.58E-07	1.71E-08	1.71E-08	-	-	-	-	-	-	1.48	750	8	1.48	0.00	0.00
EHPV_NG_EXP15	2.55E-07	1.19E-08	1.19E-08	-	-	-	-	-	-	1.77	800	24	1.77	0.00	0.00
EHPV_NG_EXP16	2.79E-07	2.40E-08	2.40E-08	-	-	-	-	-	-	1.55	700	15.5	1.55	0.00	0.00
EHPV_NG_EXP17	2.38E-07	1.24E-08	1.24E-08	-	-	-	-	-	-	1.01	700	21	1.01	0.00	0.00
EHPV_NG_EXP18	2.57E-07	2.61E-08	2.61E-08	-	-	-	-	-	-	0.50	700	16	0.50	0.00	0.00
EHPV_NG_EXP24	2.71E-07	1.71E-08	1.71E-08	-	-	-	-	-	-	1.51	650	27	1.51	0.00	0.00
EHPV_NG_EXP32	2.08E-07	1.69E-08	1.69E-08	*3.34E-07*	*4.65E-08*	*4.79E-08*	**2.58E-07**	**3.33E-08**	**3.62E-08**	1.55	750	40	0.52	0.66	0.76
tourmaline															
EHPV_NG_EXP13	2.75E-10	6.79E-11	6.79E-11	-	-	-	-	-	-	1.48	750	8	1.48	0.00	0.00
EHPV_NG_EXP16	1.52E-10	1.04E-10	1.04E-10	-	-	-	-	-	-	1.55	700	15.5	1.55	0.00	0.00
EHPV_NG_EXP17	1.93E-10	9.09E-11	9.09E-11	-	-	-	-	-	-	1.01	700	21	1.01	0.00	0.00
EHPV_NG_EXP18	1.56E-10	9.81E-11	9.81E-11	-	-	-	-	-	-	0.50	700	16	0.50	0.00	0.00
EHPV_NG_EXP24	1.15E-10	6.00E-11	6.00E-11	-	-	-	-	-	-	1.51	650	27	1.51	0.00	0.00
antigorite															
CS_NG_EXP17	1.72E-09	3.66E-11	3.66E-11	-	-	-	-	-	-	1.57	375	46	1.42	0.00	0.00
CS_NG_EXP18	helium detected	-	-	-	-	-	1.85E-10	3.59E-11	3.59E-11	1.57	350	48	0.00	0.00	2.27
CS_NG_EXP20	1.49E-09	1.87E-13	1.87E-13	-	-	-	-	-	-	1.53	350	45.5	1.53	0.00	0.00
CS_NG_EXP21	1.42E-09	3.49E-11	3.49E-11	8.06E-11	1.93E-10	1.93E-10	1.43E-09	4.78E-10	4.78E-10	0.97	350	48	0.32	0.41	0.44
CS_NG_EXP22	helium detected	-	-	-	-	-	4.24E-10	1.02E-10	1.02E-10	1.73	350	48	0.00	0.00	2.94
CS_NG_EXP23	1.37E-09	9.98E-14	9.98E-14	-	-	-	-	-	-	1.68	350	92	1.68	0.00	0.00
CS_NG_EXP24	1.55E-09	1.11E-10	1.11E-10	1.11E-10	1.00E-10	1.00E-10	1.12E-09	4.23E-10	4.23E-10	1.30	350	65	0.43	0.60	0.68
CS_NG_EXP25	1.32E-09	1.52E-10	1.52E-10	2.44E-10	5.40E-10	5.40E-10	2.90E-09	6.56E-10	6.56E-10	0.50	350	48	0.17	0.19	0.19
CS_NG_EXP29	1.11E-09	6.10E-14	6.10E-14	-	-	-	-	-	-	0.68	350	29.5	0.68	0.00	0.00
CS_NG_EXP30	1.41E-09	6.07E-13	6.07E-13	-	-	-	-	-	-	1.11	350	37	1.11	0.00	0.00
EHPV_NG_EXP53	helium detected	-	-	-	-	-	-2.71E-12	4.19E-12	4.19E-12	1.57	450	48	0.00	0.00	2.19
F-phlogopite															
CS_NG_EXP2	7.98E-10	8.86E-11	8.86E-11	-	-	-	-	-	-	1.38	450	43	0.46	0.62	0.71
CS_NG_EXP11	8.69E-10	5.95E-11	5.95E-11	-	-	-	-	-	-	1.27	700	44.5	0.42	0.52	0.58
CS_NG_EXP13	**8.74E-10**	**1.21E-10**	**8.40E-11**	-	-	-	-	-	-	0.24	500	24	0.24	0.00	0.00
CS_NG_EXP14	**6.10E-10**	**1.80E-10**	**1.21E-10**	-	-	-	-	-	-	0.10	500	24	0.10	0.00	0.00
CS_NG_EXP15	4.31E-10	1.79E-10	**1.20E-10**	-	-	-	-	-	-	0.06	500	24	0.06	0.00	0.00
muscovite															
CS_NG_EXP2	6.12E-10	9.05E-11	9.05E-11	-	-	-	argon detected	-	-	1.38	450	43	0.46	0.62	0.71
CS_NG_EXP7	8.27E-10	2.89E-11	2.89E-11	-	-	-	argon detected	-	-	1.36	600	68	0.45	0.58	0.66
CS_NG_EXP13	**4.23E-10**	**9.90E-11**	**7.40E-11**	-	-	-	-	-	-	0.24	500	24	0.24	0.00	0.00
CS_NG_EXP14	**6.45E-10**	**1.80E-10**	**1.10E-10**	-	-	-	-	-	-	0.10	500	24	0.10	0.00	0.00
CS_NG_EXP15	**1.17E-09**	**3.30E-10**	**2.10E-10**	-	-	-	-	-	-	0.06	500	24	0.06	0.00	0.00
CS_NG_EXP16	**8.02E-10**	**6.60E-11**	**5.40E-11**	-	-	-	-	-	-	0.80	500	24	0.80	0.00	0.00

Notes:
italics solubility calculated as the product of the Ne/He ratio and He solubility
bold solubility calculated by fitting diffusion profiles
noble gas fugacity calculated using modified Redlich-Kwong EOS (Flowers, 1979)
Henry's constant units: $mol\,g^{-1}\,bar^{-1}$

Supplementary Information for "Light noble gas dissolution into ring structure-bearing materials and mineralogic influences on noble gas recycling"

1.0 He solubility calculations for muscovite and F-phlogopite

Supplementary Figure 1 displays He concentrations profiles observed in mica fit with diffusion profiles. Profiles are calculated based on tracer diffusion from a reservoir of constant chemical potential into a semi-infinite medium. Solid curves are the depth-averaged model, where the He concentration at each depth is the average He concentration from that depth to the surface. Dashed curves are the corresponding modeled concentrations at each discrete depth. Error bars on data points are 1σ and include analytical and pit volume determination uncertainties. He solubility calculated as fit surface concentration.

2.0 Ne and Ar solubility calculations for beryl and cordierite

Supplementary Figure 2 displays Ne/He and Ar/He measurement in beryl and cordierite as a function of depth. Neon solubility in beryl and cordierite is calculated as the product of the measured Ne/He ratio and the measured solubility of He. We use this approach because many of the ablation pits on beryl and cordierite where Ne was present are extremely shallow. Consequently, the volume of these shallow pits is highly uncertain and likely biased to lower values, leading to systematically higher concentrations. This approach is valid for Ne because there is no correlation between Ne/He and pit depth for either beryl or cordierite (Supplementary Figure 2). Argon concentrations, however, must be determined using an approach similar to that taken for He in mica because Ar/He

measurements are not constant with depth (Supplementary Figure 2). We fit these data using a diffusion model, and Ar solubility is calculated as the product of the modeled surface Ar/He ratio and the measured He solubility. Error bars for Ne/He and Ar/He ratios in Supplementary Figure 2 are 1 σ and only include the propagated the analytical uncertainties. Volume uncertainties are not factored into elemental ratios.

3.0 SEM images of antigorite

Supplementary Figure 3 displays two series of SEM BSE images from the antigorite material. The antigorite material was prepared following the same techniques used to prepare the experimental starting materials. The first series (left column) shows an area centered in the region of the sample that has a higher concentration of the "clouding" material (see lower-left image for location of series), and images are ordered from lowest magnification at the top to highest magnification at the bottom. Micron scale pitting is observed throughout the sample and appears concentrated in certain regions. The second series shows an area centered in the region on the sample that has a lower concentration of "clouding" material. Pitting is still observed, although pits appear more evenly distributed. Several grains of micron-scale magnetite were identified throughout the sample as well, and their composition was confirmed by EDS analysis to be nearly pure iron oxide (not shown). The mode of micron-scale magnetite <<1 %, but greater amounts of magnetite may form during the experiments due to hydrogen loss.

Chapter 3, Supplementary Figure 1: He diffusion in mica

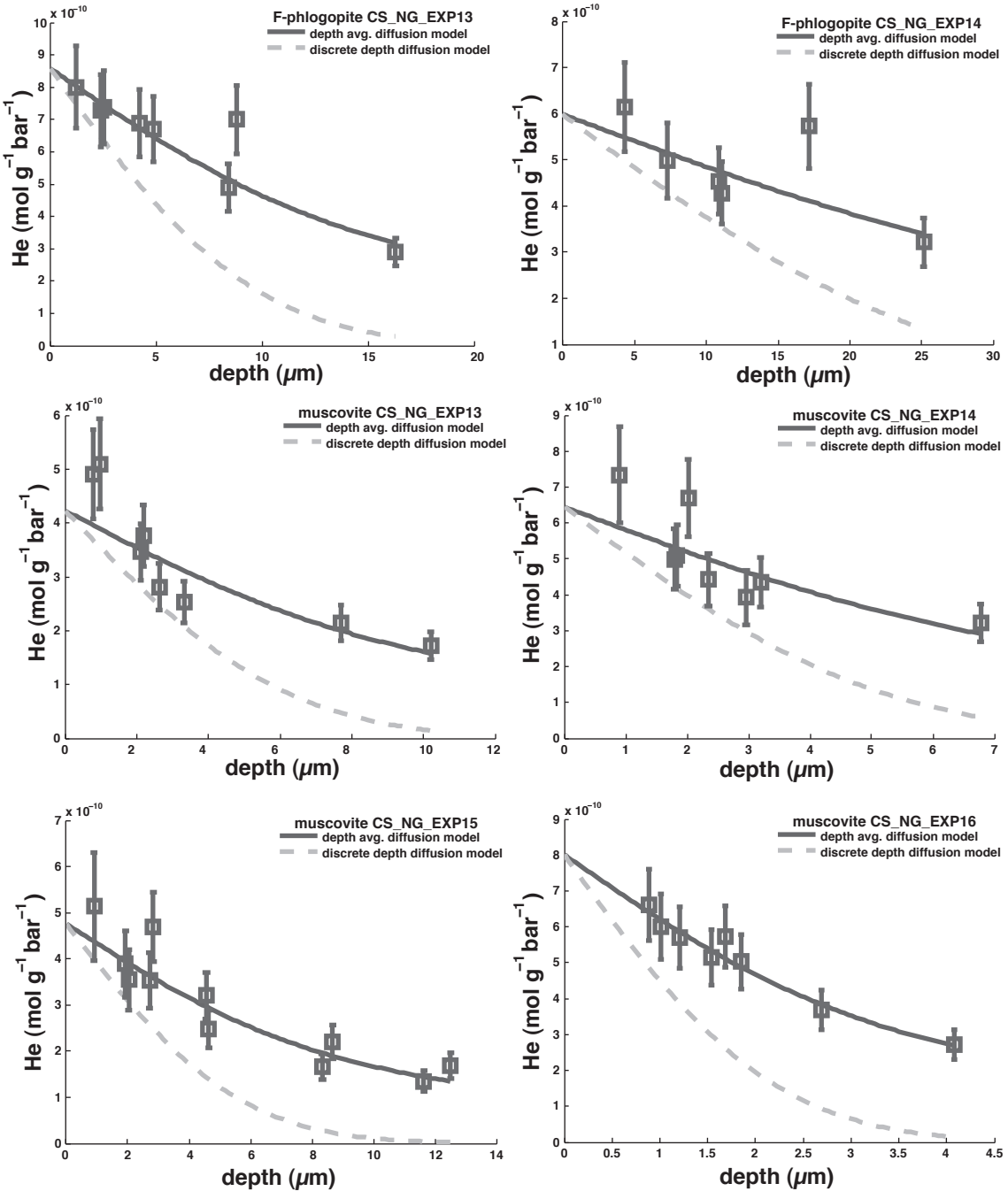

Chapter 3, Supplementary Figure 2: Ne and Ar in beryl and cordierite

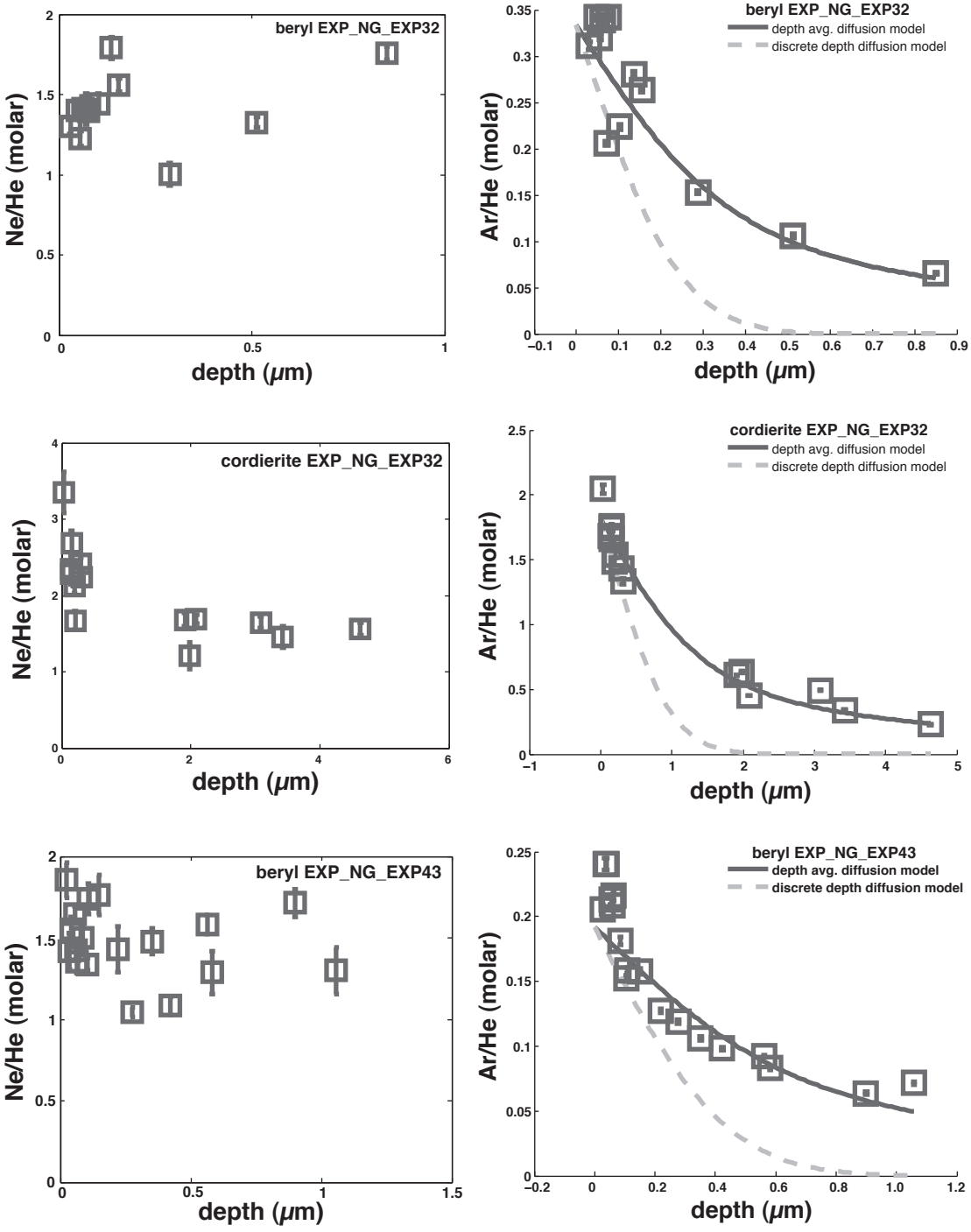

Chapter 3, Supplementary Figure 3
SEM images of antigorite

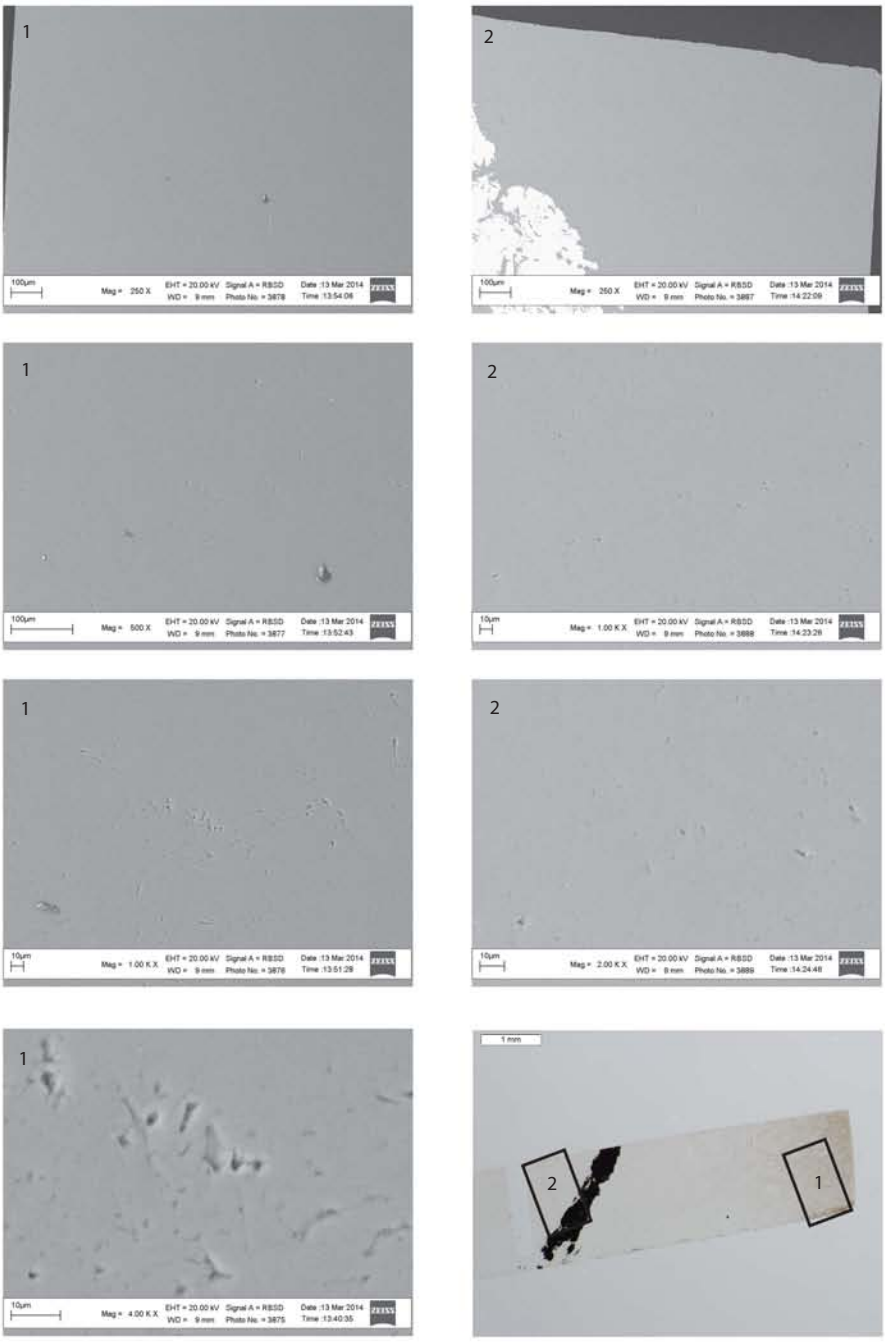

Supplementary Table 1: Noble gas analyses

Depth	Volume (um^3)	He (mol)	He uncert. (mol)	Ne (mol)	Ne uncert. (mol)	Ar (mol)	Ar uncert. (mol)	He (mol/g)	He uncert. (mol/g)	Ne (mol/g)	Ne uncert. (mol/g)	Ar (mol/g)	Ar uncert. (mol/g)	kbar	temp. (°C)	duration (hr.)	P_{He} (kbar)	P_{Ne}	P_{Ar}	Note
	beryl																			
	EHPV_NG_EXP13																			
9.34E-01	2.22E+03	8.86E-13	1.33E-14	4.00E-16	7.97E-16	-7.23E-18	7.88E-16	1.45E-04	2.19E-05	6.56E-08	1.31E-07	-1.18E-09	1.29E-07	1.48	750	8	1.48	0.00	0.00	
1.11E+00	1.40E+03	4.42E-13	7.20E-15	3.12E-15	9.31E-16	-6.36E-16	7.92E-16	1.15E-04	1.74E-05	8.13E-07	2.71E-07	-1.66E-07	2.08E-07	1.48	750	8	1.48	0.00	0.00	
3.50E+00	4.40E+03	1.30E-12	1.09E-14	1.34E-15	8.19E-16	5.66E-17	7.89E-16	1.07E-04	1.61E-05	1.10E-07	6.98E-08	4.68E-09	6.53E-08	1.48	750	8	1.48	0.00	0.00	
3.78E+00	4.76E+03	1.36E-12	7.26E-15	9.10E-16	8.50E-16	2.14E-16	8.03E-16	1.04E-04	1.56E-05	6.96E-08	6.58E-08	1.63E-08	6.15E-08	1.48	750	8	1.48	0.00	0.00	
4.65E+00	5.84E+03	1.64E-12	7.33E-15	2.36E-15	7.97E-16	5.65E-16	7.91E-16	1.02E-04	1.53E-05	1.47E-07	5.43E-08	3.52E-08	4.95E-08	1.48	750	8	1.48	0.00	0.00	
3.97E+00	4.99E+03	1.53E-12	1.70E-14	2.44E-15	9.31E-16	5.08E-16	7.89E-16	1.11E-04	1.67E-05	1.78E-07	7.29E-08	3.70E-08	5.78E-08	1.48	750	8	1.48	0.00	0.00	
1.26E+00	1.59E+03	5.83E-13	7.33E-15	-1.10E-16	8.19E-16	-4.52E-17	7.88E-16	1.33E-04	2.01E-05	-2.52E-08	1.88E-07	-1.03E-08	1.81E-07	1.48	750	8	1.48	0.00	0.00	
1.18E+00	1.49E+03	5.24E-13	7.30E-15	5.70E-16	8.50E-16	-4.65E-16	7.95E-16	1.28E-04	1.93E-05	1.39E-07	2.09E-07	-1.14E-07	1.95E-07	1.48	750	8	1.48	0.00	0.00	
1.21E+00	1.52E+03	5.80E-13	7.50E-15	4.00E-16	8.19E-16	6.53E-16	7.88E-16	1.39E-04	2.09E-05	9.58E-08	1.97E-07	1.56E-07	1.90E-07	1.48	750	8	1.48	0.00	0.00	
1.08E+00	4.15E+03	1.35E-12	9.53E-15	1.42E-15	8.50E-16	-3.32E-16	7.89E-16	1.19E-04	1.78E-05	1.24E-07	7.67E-08	-2.91E-08	6.93E-08	1.48	750	8	1.48	0.00	0.00	
1.13E+00	1.42E+03	2.80E-13	8.02E-15	-1.95E-16	8.50E-16	-4.62E-16	7.96E-16	7.17E-05	1.09E-05	-4.99E-08	2.18E-07	-1.18E-07	2.05E-07	1.48	750	8	1.48	0.00	0.00	
1.23E+00	9.62E+03	3.48E-12	4.36E-14	8.25E-16	8.50E-16	1.61E-16	7.91E-16	1.32E-04	1.98E-05	3.12E-08	3.24E-08	6.10E-09	2.99E-08	1.48	750	8	1.48	0.00	0.00	
2.44E+00	3.07E+03	7.16E-13	7.60E-15	2.19E-15	1.15E-15	3.50E-16	7.87E-16	8.48E-05	1.27E-05	2.59E-07	1.42E-07	4.14E-08	9.34E-08	1.48	750	8	1.48	0.00	0.00	
2.27E+00	2.85E+03	8.84E-13	1.89E-14	-1.05E-15	7.83E-16	3.37E-17	7.97E-16	1.13E-04	1.71E-05	-1.33E-07	1.02E-07	4.30E-09	1.02E-07	1.48	750	8	1.48	0.00	0.00	
3.57E+00	4.48E+03	1.31E-12	8.34E-15	1.59E-15	7.97E-16	-6.62E-18	7.89E-16	1.06E-04	1.59E-05	1.29E-07	6.74E-08	-5.37E-10	6.40E-08	1.48	750	8	1.48	0.00	0.00	
3.52E+00	4.42E+03	1.33E-12	1.17E-14	-1.30E-15	9.31E-16	1.35E-16	7.90E-16	1.10E-04	1.65E-05	-1.07E-07	7.83E-08	1.12E-08	6.50E-08	1.48	750	8	1.48	0.00	0.00	
6.66E-01	8.37E+02	3.40E-13	6.81E-15	1.25E-15	8.19E-16	8.43E-17	7.89E-16	1.48E-04	2.24E-05	5.43E-07	3.65E-07	3.66E-08	3.43E-07	1.48	750	8	1.48	0.00	0.00	
7.04E-01	8.85E+02	3.36E-13	7.11E-15	-2.41E-15	9.80E-16	-8.31E-17	7.93E-16	1.38E-04	2.09E-05	-9.89E-07	4.29E-07	-3.42E-08	3.26E-07	1.48	750	8	1.48	0.00	0.00	
1.22E+00	4.68E+03	1.47E-12	5.19E-15	-2.49E-16	1.52E-15	-3.38E-16	2.15E-16	1.14E-04	1.71E-05	-1.93E-08	1.18E-07	-2.63E-08	1.72E-08	1.48	750	8	1.48	0.00	0.00	
9.39E-01	3.61E+03	1.17E-12	5.97E-15	-2.97E-15	1.53E-15	2.08E-16	2.12E-16	1.18E-04	1.77E-05	-2.99E-07	1.61E-07	2.09E-08	2.16E-08	1.48	750	8	1.48	0.00	0.00	
6.98E-01	2.69E+03	9.53E-13	8.58E-15	1.03E-15	1.52E-15	2.34E-16	2.42E-16	1.29E-04	1.94E-05	1.39E-07	2.06E-07	3.17E-08	3.32E-08	1.48	750	8	1.48	0.00	0.00	
3.62E-01	1.39E+03	7.06E-13	4.05E-15	6.87E-16	1.50E-15	5.11E-16	2.16E-16	1.84E-04	2.77E-05	1.79E-07	3.91E-07	1.33E-07	5.97E-08	1.48	750	8	1.48	0.00	0.00	
1.55E-01	5.98E+02	3.94E-13	4.60E-15	-1.95E-15	1.53E-15	3.31E-16	2.47E-16	2.40E-04	3.60E-05	-1.19E-06	9.49E-07	2.02E-07	1.53E-07	1.48	750	8	1.48	0.00	0.00	shallow
2.45E+00	9.42E+03	2.50E-12	1.26E-14	2.05E-15	1.58E-15	2.63E-16	2.22E-16	9.65E-05	1.45E-05	7.90E-08	6.20E-08	1.02E-08	8.71E-09	1.48	750	8	1.48	0.00	0.00	
	EHPV_NG_EXP15																			
4.00E+00	9.52E+03	3.21E-12	2.48E-14	-3.36E-16	1.54E-15	4.78E-16	1.84E-16	1.22E-04	1.84E-05	-1.29E-08	5.89E-08	1.83E-08	7.56E-09	1.77	800	24	1.77	0.00	0.00	
3.43E+00	8.15E+03	2.81E-12	2.49E-14	-1.66E-16	1.55E-15	6.50E-16	1.81E-16	1.25E-04	1.88E-05	-7.42E-09	6.90E-08	2.90E-08	9.15E-09	1.77	800	24	1.77	0.00	0.00	
4.08E+00	9.70E+03	3.35E-12	1.91E-14	3.83E-15	1.60E-15	5.22E-16	1.84E-16	1.26E-04	1.89E-05	1.44E-07	6.36E-08	1.96E-08	7.50E-09	1.77	800	24	1.77	0.00	0.00	
4.18E+00	9.93E+03	3.20E-12	2.93E-14	1.79E-15	1.56E-15	5.01E-16	1.80E-16	1.17E-04	1.76E-05	6.55E-08	5.79E-08	1.84E-08	7.14E-09	1.77	800	24	1.77	0.00	0.00	
8.21E+00	1.95E+04	6.15E-12	3.42E-14	6.84E-16	1.55E-15	8.70E-16	1.80E-16	1.15E-04	1.72E-05	1.27E-08	2.89E-08	1.62E-08	4.14E-09	1.77	800	24	1.77	0.00	0.00	
8.02E+00	1.91E+04	5.71E-12	2.37E-14	1.28E-15	1.56E-15	6.88E-16	1.79E-16	1.09E-04	1.64E-05	2.44E-08	3.00E-08	1.31E-08	3.94E-09	1.77	800	24	1.77	0.00	0.00	
2.20E+00	5.23E+03	1.68E-12	1.89E-14	2.81E-15	1.62E-15	5.41E-16	1.91E-16	1.17E-04	1.76E-05	1.95E-07	1.16E-07	3.76E-08	1.44E-08	1.77	800	24	1.77	0.00	0.00	
1.51E+00	3.59E+03	1.71E-12	1.83E-14	-9.32E-16	1.56E-15	6.95E-16	1.82E-16	1.73E-04	2.60E-05	-9.44E-08	1.59E-07	7.04E-08	2.13E-08	1.77	800	24	1.77	0.00	0.00	
	EHPV_NG_EXP16																			
3.65E-01	2.87E+03	1.12E-12	2.10E-14	1.48E-15	8.50E-16	-1.13E-16	1.50E-16	1.42E-04	2.14E-05	1.87E-07	1.11E-07	-1.43E-08	1.92E-08	1.55	700	15.5	1.55	0.00	0.00	
7.77E-01	6.10E+03	1.81E-12	2.50E-14	9.68E-16	8.50E-16	-1.07E-16	1.47E-16	1.08E-04	1.63E-05	5.77E-08	5.14E-08	-6.36E-09	8.84E-09	1.55	700	15.5	1.55	0.00	0.00	
1.70E+00	1.33E+04	3.29E-12	2.36E-14	1.31E-15	9.00E-16	2.24E-16	1.57E-16	8.96E-05	1.35E-05	3.57E-08	2.51E-08	6.10E-09	4.36E-09	1.55	700	15.5	1.55	0.00	0.00	
1.68E+00	1.32E+04	3.54E-12	4.03E-14	1.73E-15	9.00E-16	3.36E-16	1.51E-16	9.72E-05	1.46E-05	4.77E-08	2.58E-08	9.24E-09	4.37E-09	1.55	700	15.5	1.55	0.00	0.00	
2.37E+00	1.86E+04	4.88E-12	2.55E-14	3.86E-15	8.50E-16	1.00E-16	1.83E-16	9.55E-05	1.43E-05	7.55E-08	2.01E-08	1.96E-09	3.59E-09	1.55	700	15.5	1.55	0.00	0.00	
2.58E+00	2.03E+04	5.12E-12	3.50E-14	1.31E-15	9.35E-16	-5.13E-17	1.49E-16	9.18E-05	1.38E-05	2.35E-08	1.71E-08	-9.21E-10	2.67E-09	1.55	700	15.5	1.55	0.00	0.00	
8.55E-01	6.71E+03	2.07E-12	2.26E-14	6.28E-16	8.71E-16	2.29E-16	1.41E-16	1.12E-04	1.69E-05	3.40E-08	4.75E-08	1.24E-08	7.86E-09	1.55	700	15.5	1.55	0.00	0.00	
9.30E-01	7.30E+03	2.18E-12	2.73E-14	-1.67E-15	9.35E-16	-1.76E-17	1.45E-16	1.08E-04	1.63E-05	-8.30E-08	4.82E-08	-8.78E-10	7.21E-09	1.55	700	15.5	1.55	0.00	0.00	
	EHPV_NG_EXP17																			
6.63E-01	5.21E+03	1.11E-12	2.18E-14	2.41E-15	9.35E-16	3.42E-15	1.70E-16	7.74E-05	1.17E-05	1.68E-07	7.00E-08	2.39E-07	3.77E-08	1.01	700	21	1.01	0.00	0.00	
7.14E-01	5.61E+03	1.32E-12	2.38E-14	2.67E-15	8.50E-16	3.33E-15	1.49E-16	8.55E-05	1.29E-05	1.73E-07	6.09E-08	2.16E-07	3.38E-08	1.01	700	21	1.01	0.00	0.00	

1.31E+00	1.03E+04	1.94E-12	2.66E-14	1.31E-15	9.35E-16	3.39E-15	1.44E-16	6.86E-05	1.03E-05	4.62E-08	3.38E-08	1.20E-07	1.87E-08	1.01	700	21	1.01	0.00	0.00	
1.33E+00	1.04E+04	1.89E-12	2.88E-14	4.88E-15	1.02E-15	3.56E-15	1.43E-16	6.58E-05	9.93E-06	1.70E-07	4.39E-08	1.24E-07	1.93E-08	1.01	700	21	1.01	0.00	0.00	
2.36E+00	1.85E+04	3.51E-12	2.83E-14	4.71E-15	9.00E-16	3.53E-15	1.86E-16	6.89E-05	1.04E-05	9.25E-08	2.25E-08	6.93E-08	1.10E-08	1.01	700	21	1.01	0.00	0.00	
2.40E+00	1.89E+04	3.46E-12	2.17E-14	6.66E-15	1.02E-15	3.89E-15	1.60E-16	6.67E-05	1.00E-05	1.28E-07	2.76E-08	7.50E-08	1.17E-08	1.01	700	21	1.01	0.00	0.00	
1.52E+00	1.19E+04	2.06E-12	2.58E-14	7.98E-16	9.00E-16	4.23E-15	1.54E-16	6.26E-05	9.43E-06	2.43E-08	2.76E-08	1.29E-07	1.99E-08	1.01	700	21	1.01	0.00	0.00	
1.43E+00	1.12E+04	1.99E-12	2.36E-14	7.13E-16	1.02E-15	3.27E-15	1.84E-16	6.43E-05	9.68E-06	2.31E-08	3.33E-08	1.06E-07	1.70E-08	1.01	700	21	1.01	0.00	0.00	
EHPV_NG_EXP18																				
1.78E+00	1.39E+04	1.37E-12	2.00E-14	7.69E-16	1.55E-15	5.27E-16	1.91E-16	3.56E-05	5.37E-06	2.00E-08	4.05E-08	1.37E-08	5.40E-09	0.50	700	16	0.50	0.00	0.00	
2.07E+00	1.63E+04	1.27E-12	1.97E-14	-2.72E-15	1.65E-15	2.50E-16	1.84E-16	2.84E-05	4.28E-06	-6.08E-08	3.80E-08	5.58E-09	4.21E-09	0.50	700	16	0.50	0.00	0.00	
3.79E+00	2.97E+04	2.60E-12	1.93E-14	2.55E-15	1.62E-15	2.40E-16	1.81E-16	3.18E-05	4.77E-06	3.12E-08	2.04E-08	2.94E-09	2.26E-09	0.50	700	16	0.50	0.00	0.00	
3.50E+00	2.75E+04	2.76E-12	1.78E-14	1.36E-15	1.72E-15	2.03E-16	1.87E-16	3.65E-05	5.48E-06	1.80E-08	2.29E-08	2.69E-09	2.51E-09	0.50	700	16	0.50	0.00	0.00	
4.56E+00	3.58E+04	1.21E-12	1.83E-14	1.02E-15	1.55E-15	2.01E-17	1.88E-16	1.23E-05	1.85E-06	1.04E-08	1.58E-08	2.04E-10	1.91E-09	0.50	700	16	0.50	0.00	0.00	
4.18E+00	3.28E+04	1.35E-12	2.18E-14	2.04E-15	1.62E-15	2.07E-16	1.84E-16	1.49E-05	2.25E-06	2.27E-08	1.83E-08	2.30E-09	2.07E-09	0.50	700	16	0.50	0.00	0.00	
1.99E+00	1.56E+04	2.20E-12	1.89E-14	-8.13E-17	1.89E-15	4.40E-16	1.79E-16	5.11E-05	7.67E-06	-1.89E-09	4.40E-08	1.02E-08	4.43E-09	0.50	700	16	0.50	0.00	0.00	
1.90E+00	1.50E+04	2.34E-12	2.14E-14	-1.10E-15	1.62E-15	2.64E-16	1.81E-16	5.69E-05	8.55E-06	-2.68E-08	3.96E-08	6.42E-09	4.50E-09	0.50	700	16	0.50	0.00	0.00	
EHPV_NG_EXP24																				
1.44E+00	1.13E+04	3.26E-12	4.49E-14	9.68E-16	9.00E-16	2.99E-16	1.51E-16	1.05E-04	1.58E-05	3.12E-08	2.93E-08	9.63E-09	5.07E-09	1.51	650	27	1.51	0.00	0.00	
1.51E+00	1.18E+04	3.19E-12	2.68E-14	2.50E-15	9.00E-16	4.14E-17	1.44E-16	9.80E-05	1.47E-05	7.67E-08	2.99E-08	1.27E-09	4.42E-09	1.51	650	27	1.51	0.00	0.00	
8.80E-01	6.91E+03	2.08E-12	2.89E-14	-3.07E-16	8.50E-16	1.42E-16	1.59E-16	1.09E-04	1.65E-05	-1.62E-08	4.48E-08	7.47E-09	8.43E-09	1.51	650	27	1.51	0.00	0.00	
8.07E-01	6.34E+03	1.87E-12	2.94E-14	7.13E-16	8.71E-16	-1.05E-16	1.43E-16	1.08E-04	1.62E-05	4.09E-08	5.03E-08	-6.02E-09	8.22E-09	1.51	650	27	1.51	0.00	0.00	
1.25E+00	9.78E+03	2.78E-12	3.32E-14	4.58E-16	9.77E-16	1.56E-16	1.45E-16	1.03E-04	1.56E-05	1.70E-08	3.64E-08	5.79E-09	5.47E-09	1.51	650	27	1.51	0.00	0.00	
1.30E+00	1.02E+04	2.95E-12	2.43E-14	2.67E-15	9.00E-16	1.91E-17	1.54E-16	1.05E-04	1.58E-05	9.54E-08	3.52E-08	6.83E-10	5.50E-09	1.51	650	27	1.51	0.00	0.00	
2.27E+00	1.79E+04	4.59E-12	5.99E-14	1.48E-15	8.37E-16	1.10E-16	1.69E-16	9.36E-05	1.41E-05	3.01E-08	1.76E-08	2.24E-09	3.46E-09	1.51	650	27	1.51	0.00	0.00	
2.26E+00	1.78E+04	4.63E-12	4.13E-14	8.83E-16	8.71E-16	1.92E-16	1.42E-16	9.46E-05	1.42E-05	1.81E-08	1.80E-08	3.93E-09	2.96E-09	1.51	650	27	1.51	0.00	0.00	
EHPV_NG_EXP32																				
6.15E-02	1.09E+03	3.55E-13	4.28E-15	5.02E-13	2.62E-14	1.20E-13	1.76E-15	1.19E-04	1.79E-05	1.68E-04	2.66E-05	4.02E-05	6.06E-06	1.55	750	40	0.52	0.52	0.52	shallow
2.98E-02	9.35E+02	5.16E-13	4.31E-15	6.71E-13	2.32E-14	1.61E-13	1.71E-15	2.01E-04	3.02E-05	2.61E-04	4.02E-05	6.25E-05	9.41E-06	1.55	750	40	0.52	0.52	0.52	shallow
1.03E-01	3.23E+03	7.65E-13	4.40E-15	1.10E-12	4.61E-14	1.71E-13	1.76E-15	8.63E-05	1.29E-05	1.24E-04	1.94E-05	1.93E-05	2.90E-06	1.55	750	40	0.52	0.52	0.52	shallow
7.13E-02	4.24E+03	1.14E-12	4.89E-15	1.61E-12	1.09E-13	2.35E-13	1.78E-15	9.80E-05	1.47E-05	1.38E-04	2.27E-05	2.02E-05	3.03E-06	1.55	750	40	0.52	0.52	0.52	shallow
4.85E-02	2.88E+03	1.19E-12	7.06E-15	1.67E-12	2.66E-14	4.06E-13	1.85E-15	1.50E-04	2.25E-05	2.10E-04	3.17E-05	5.12E-05	7.69E-06	1.55	750	40	0.52	0.52	0.52	shallow
5.53E-02	3.29E+03	8.92E-13	4.90E-15	1.09E-12	4.07E-14	2.85E-13	1.76E-15	9.87E-05	1.48E-05	1.21E-04	1.87E-05	3.16E-05	4.74E-06	1.55	750	40	0.52	0.52	0.52	shallow
7.55E-02	2.37E+03	7.47E-13	4.36E-15	1.04E-12	3.21E-14	2.56E-13	1.80E-15	1.15E-04	1.72E-05	1.60E-04	2.45E-05	3.92E-05	5.89E-06	1.55	750	40	0.52	0.52	0.52	shallow
1.55E-01	4.87E+03	1.01E-12	5.05E-15	1.57E-12	4.05E-14	2.66E-13	2.01E-15	7.55E-05	1.13E-05	1.18E-04	1.79E-05	1.99E-05	2.98E-06	1.55	750	40	0.52	0.52	0.52	shallow
1.36E-01	4.26E+03	9.72E-13	6.03E-15	1.74E-12	6.50E-14	2.73E-13	1.91E-15	8.29E-05	1.25E-05	1.49E-04	2.30E-05	2.33E-05	3.49E-06	1.55	750	40	0.52	0.52	0.52	shallow
2.88E-01	9.03E+03	1.31E-12	6.65E-15	1.31E-12	9.34E-14	2.00E-13	1.73E-15	5.27E-05	7.92E-06	5.29E-05	8.78E-06	8.06E-06	1.21E-06	1.55	750	40	0.52	0.52	0.52	shallow
5.13E-01	9.06E+03	9.43E-13	5.13E-15	1.25E-12	2.82E-14	1.00E-13	1.72E-15	3.79E-05	5.68E-06	5.02E-05	7.62E-06	4.01E-06	6.06E-07	1.55	750	40	0.52	0.52	0.52	
8.50E-01	1.50E+04	1.35E-12	4.79E-15	2.38E-12	5.35E-14	8.85E-14	1.71E-15	3.27E-05	4.91E-06	5.76E-05	8.74E-06	2.14E-06	3.24E-07	1.55	750	40	0.52	0.52	0.52	
EHPV_NG_EXP43																				
6.35E-02	3.77E+03	7.82E-13	1.03E-14	1.06E-12	5.37E-14	1.69E-13	2.15E-15	8.13E-05	1.22E-05	1.10E-04	1.74E-05	1.76E-05	2.65E-06	1.27	800	41.5	0.42	0.42	0.42	shallow
1.49E-01	8.88E+03	1.27E-12	1.09E-14	2.25E-12	1.52E-13	2.01E-13	2.29E-15	5.63E-05	8.46E-06	9.93E-05	1.63E-05	8.86E-06	1.33E-06	1.27	800	41.5	0.42	0.42	0.42	shallow
8.47E-02	5.03E+03	9.57E-13	1.21E-14	1.43E-12	5.99E-14	1.73E-13	2.15E-15	7.46E-05	1.12E-05	1.12E-04	1.74E-05	1.35E-05	2.04E-06	1.27	800	41.5	0.42	0.42	0.42	shallow
2.77E-01	1.64E+04	1.87E-12	1.03E-14	1.95E-12	5.88E-14	2.22E-13	2.15E-15	4.45E-05	6.67E-06	4.64E-05	7.10E-06	5.30E-06	7.96E-07	1.27	800	41.5	0.42	0.42	0.42	shallow
5.62E-01	3.34E+04	2.73E-12	1.23E-14	4.33E-12	1.60E-13	2.52E-13	2.15E-15	3.21E-05	4.81E-06	5.08E-05	7.84E-06	2.96E-06	4.44E-07	1.27	800	41.5	0.42	0.42	0.42	
4.23E-01	2.51E+04	2.29E-12	2.19E-14	2.48E-12	1.24E-13	2.25E-13	2.24E-15	3.58E-05	5.38E-06	3.87E-05	6.12E-06	3.51E-06	5.27E-07	1.27	800	41.5	0.42	0.42	0.42	
3.51E-01	2.09E+04	2.04E-12	1.19E-14	3.02E-12	1.60E-13	2.17E-13	2.15E-15	3.84E-05	5.76E-06	5.68E-05	9.03E-06	4.07E-06	6.12E-07	1.27	800	41.5	0.42	0.42	0.42	
2.20E-01	1.31E+04	1.71E-12	1.02E-14	2.45E-12	2.39E-13	2.17E-13	2.21E-15	5.14E-05	7.72E-06	7.37E-05	1.32E-05	6.53E-06	9.82E-07	1.27	800	41.5	0.42	0.42	0.42	shallow
1.05E-01	6.27E+03	1.28E-12	1.16E-14	1.72E-12	4.37E-14	1.96E-13	2.16E-15	8.04E-05	1.21E-05	1.08E-04	1.64E-05	1.23E-05	1.85E-06	1.27	800	41.5	0.42	0.42	0.42	shallow
1.07E-01	6.37E+03	1.32E-12	1.03E-14	2.30E-12	1.23E-13	2.10E-13	2.23E-15	8.14E-05	1.22E-05	1.42E-04	2.25E-05	1.29E-05	1.94E-06	1.27	800	41.5	0.42	0.42	0.42	shallow
5.99E-02	3.56E+03	8.43E-13	1.23E-14	1.20E-12	4.46E-14	1.76E-13	2.40E-15	9.29E-05	1.40E-05	1.32E-04	2.04E-05	1.94E-05	2.92E-06	1.27	800	41.5	0.42	0.42	0.42	shallow

2.54E-02	1.51E+03	8.75E-13	1.15E-14	1.62E-12	9.14E-14	1.80E-13	2.25E-15	2.27E-04	3.42E-05	4.22E-04	6.75E-05	4.67E-05	7.03E-06	1.27	800	41.5	0.42	0.42	0.42	shallow
5.48E-02	3.25E+03	8.74E-13	1.08E-14	1.44E-12	4.08E-14	1.86E-13	2.46E-15	1.05E-04	1.59E-05	1.73E-04	2.64E-05	2.25E-05	3.38E-06	1.27	800	41.5	0.42	0.42	0.42	shallow
3.51E-02	2.09E+03	7.22E-13	1.07E-14	1.02E-12	7.93E-14	1.74E-13	2.23E-15	1.36E-04	2.04E-05	1.92E-04	3.25E-05	3.26E-05	4.91E-06	1.27	800	41.5	0.42	0.42	0.42	shallow
4.04E-02	2.40E+03	7.29E-13	1.02E-14	1.13E-12	5.73E-14	1.75E-13	2.37E-15	1.19E-04	1.80E-05	1.85E-04	2.93E-05	2.87E-05	4.32E-06	1.27	800	41.5	0.42	0.42	0.42	shallow
5.81E-01	1.83E+04	1.52E-12	1.14E-14	1.96E-12	2.00E-13	1.27E-13	2.17E-15	3.28E-05	4.92E-06	4.22E-05	7.65E-06	2.72E-06	4.10E-07	1.27	800	41.5	0.42	0.42	0.42	
1.06E+00	3.32E+04	2.53E-12	1.02E-14	3.28E-12	3.58E-13	1.81E-13	2.38E-15	2.98E-05	4.47E-06	3.87E-05	7.18E-06	2.13E-06	3.21E-07	1.27	800	41.5	0.42	0.42	0.42	
9.00E-01	2.83E+04	1.89E-12	1.56E-14	3.24E-12	1.60E-13	1.20E-13	2.30E-15	2.62E-05	3.94E-06	4.49E-05	7.10E-06	1.67E-06	2.53E-07	1.27	800	41.5	0.42	0.42	0.42	
	cordierite																			
	EHPV_NG_EXP13																			
2.76E-01	2.17E+03	2.71E-12	1.80E-13	8.48E-15	1.09E-15	1.78E-15	7.94E-16	4.91E-04	8.05E-05	1.53E-06	3.03E-07	3.22E-07	1.52E-07	1.48	750	8	1.48	0.00	0.00	shallow
1.42E+00	3.38E+03	3.26E-12	1.94E-14	6.27E-15	1.57E-15	1.34E-15	7.94E-16	3.78E-04	5.67E-05	7.26E-07	2.12E-07	1.55E-07	9.49E-08	1.48	750	8	1.48	0.00	0.00	
1.41E+00	3.36E+03	3.28E-12	1.37E-14	1.85E-15	8.50E-16	1.33E-15	7.88E-16	3.83E-04	5.75E-05	2.16E-07	1.04E-07	1.56E-07	9.50E-08	1.48	750	8	1.48	0.00	0.00	
1.30E+00	3.09E+03	2.95E-12	1.35E-14	3.12E-15	8.87E-16	1.51E-15	7.90E-16	3.74E-04	5.61E-05	3.96E-07	1.27E-07	1.92E-07	1.04E-07	1.48	750	8	1.48	0.00	0.00	
1.28E+00	3.05E+03	2.72E-12	1.96E-14	4.91E-15	8.87E-16	1.34E-15	8.08E-16	3.50E-04	5.25E-05	6.31E-07	1.48E-07	1.73E-07	1.07E-07	1.48	750	8	1.48	0.00	0.00	
1.34E+00	3.19E+03	2.84E-12	1.38E-14	7.03E-15	9.80E-16	1.15E-15	7.87E-16	3.50E-04	5.25E-05	8.65E-07	1.77E-07	1.41E-07	9.91E-08	1.48	750	8	1.48	0.00	0.00	
1.33E+00	3.16E+03	3.09E-12	1.36E-14	2.78E-15	9.31E-16	1.78E-15	7.90E-16	3.83E-04	5.74E-05	3.45E-07	1.26E-07	2.20E-07	1.03E-07	1.48	750	8	1.48	0.00	0.00	
1.39E+00	3.30E+03	3.45E-12	1.01E-14	8.82E-15	8.50E-16	1.53E-15	7.90E-16	4.09E-04	6.14E-05	1.05E-06	1.87E-07	1.82E-07	9.77E-08	1.48	750	8	1.48	0.00	0.00	
1.40E+00	3.33E+03	3.20E-12	1.80E-14	2.87E-15	1.22E-15	1.35E-15	7.98E-16	3.77E-04	5.66E-05	3.37E-07	1.52E-07	1.59E-07	9.69E-08	1.48	750	8	1.48	0.00	0.00	
7.07E-01	2.72E+03	2.45E-12	1.94E-14	6.35E-15	8.50E-16	1.41E-15	7.88E-16	3.54E-04	5.31E-05	9.16E-07	1.84E-07	2.03E-07	1.18E-07	1.48	750	8	1.48	0.00	0.00	
1.33E+00	5.11E+03	5.15E-12	1.85E-14	9.16E-15	9.80E-16	2.27E-15	7.88E-16	3.95E-04	5.93E-05	7.03E-07	1.30E-07	1.74E-07	6.59E-08	1.48	750	8	1.48	0.00	0.00	
2.17E+00	1.54E+03	2.02E-12	7.06E-15	2.27E-15	8.19E-16	1.11E-15	7.89E-16	5.15E-04	7.72E-05	5.80E-07	2.27E-07	2.84E-07	2.06E-07	1.48	750	8	1.48	0.00	0.00	
1.33E+00	5.14E+03	5.71E-12	4.08E-14	9.16E-15	9.80E-16	2.44E-15	7.89E-16	4.36E-04	6.55E-05	6.99E-07	1.29E-07	1.86E-07	6.64E-08	1.48	750	8	1.48	0.00	0.00	
2.33E+00	1.65E+03	2.21E-12	6.84E-15	1.42E-15	9.80E-16	-1.32E-16	7.88E-16	5.27E-04	7.91E-05	3.38E-07	2.39E-07	-3.16E-08	1.88E-07	1.48	750	8	1.48	0.00	0.00	
6.35E+00	7.98E+03	8.04E-12	1.46E-14	1.32E-14	1.09E-15	1.65E-15	7.90E-16	3.95E-04	5.93E-05	6.46E-07	1.11E-07	8.09E-08	4.07E-08	1.48	750	8	1.48	0.00	0.00	
3.67E+00	2.59E+03	3.63E-12	3.25E-14	5.96E-15	1.58E-15	6.23E-16	2.09E-16	5.49E-04	8.24E-05	9.01E-07	2.74E-07	9.43E-08	3.47E-08	1.48	750	8	1.48	0.00	0.00	not used
2.92E+00	2.06E+03	2.97E-12	9.74E-15	2.98E-15	1.58E-15	1.09E-15	2.42E-16	5.64E-04	8.46E-05	5.67E-07	3.12E-07	2.08E-07	5.56E-08	1.48	750	8	1.48	0.00	0.00	not used
2.16E+00	1.52E+03	2.24E-12	4.13E-15	1.54E-15	1.50E-15	6.58E-16	2.11E-16	5.76E-04	8.65E-05	3.96E-07	3.91E-07	1.69E-07	5.99E-08	1.48	750	8	1.48	0.00	0.00	not used
1.33E+00	9.39E+02	1.33E-12	9.28E-15	1.45E-15	1.52E-15	3.37E-16	2.16E-16	5.57E-04	8.36E-05	6.06E-07	6.39E-07	1.41E-07	9.28E-08	1.48	750	8	1.48	0.00	0.00	not used
4.97E-01	3.51E+02	4.92E-13	5.60E-15	-1.86E-15	1.61E-15	2.95E-16	2.32E-16	5.49E-04	8.26E-05	-2.08E-06	1.82E-06	3.30E-07	2.63E-07	1.48	750	8	1.48	0.00	0.00	not used
	EHPV_NG_EXP15																			
9.86E-01	7.74E+03	9.31E-12	1.79E-14	-9.32E-16	1.60E-15	1.83E-14	2.50E-16	4.72E-04	7.08E-05	-4.72E-08	8.11E-08	9.29E-07	1.40E-07	1.77	800	24	1.77	0.00	0.00	
2.41E+00	5.73E+03	6.86E-12	2.60E-14	2.59E-16	1.55E-15	1.81E-14	2.03E-16	4.70E-04	7.05E-05	1.77E-08	1.06E-07	1.24E-06	1.87E-07	1.77	800	24	1.77	0.00	0.00	
1.67E+00	3.96E+03	4.49E-12	1.92E-14	-1.66E-16	1.60E-15	1.74E-14	1.97E-16	4.44E-04	6.67E-05	-1.65E-08	1.58E-07	1.72E-06	2.59E-07	1.77	800	24	1.77	0.00	0.00	
7.78E-01	1.85E+03	2.01E-12	2.02E-14	1.28E-15	1.54E-15	1.27E-14	1.93E-16	4.27E-04	6.41E-05	2.71E-07	3.29E-07	2.68E-06	4.05E-07	1.77	800	24	1.77	0.00	0.00	
2.70E+00	6.41E+03	7.86E-12	5.77E-14	-9.32E-16	1.72E-15	1.96E-14	2.61E-16	4.80E-04	7.21E-05	-5.70E-08	1.05E-07	1.20E-06	1.80E-07	1.77	800	24	1.77	0.00	0.00	
1.94E+00	4.62E+03	5.21E-12	1.93E-14	-8.47E-16	1.55E-15	1.67E-14	1.91E-16	4.42E-04	6.64E-05	-7.19E-08	1.32E-07	1.41E-06	2.13E-07	1.77	800	24	1.77	0.00	0.00	
1.48E+00	3.51E+03	4.01E-12	2.76E-14	7.69E-16	1.65E-15	1.46E-14	1.81E-16	4.49E-04	6.74E-05	8.60E-08	1.85E-07	1.64E-06	2.47E-07	1.77	800	24	1.77	0.00	0.00	
1.13E+00	2.68E+03	2.90E-12	1.92E-14	-2.21E-15	1.55E-15	1.32E-14	1.79E-16	4.23E-04	6.36E-05	-3.23E-07	2.31E-07	1.93E-06	2.91E-07	1.77	800	24	1.77	0.00	0.00	
	EHPV_NG_EXP16																			
3.80E-01	1.46E+03	1.83E-12	2.28E-14	-3.07E-16	8.71E-16	4.74E-16	1.46E-16	4.90E-04	7.38E-05	-8.24E-08	2.34E-07	1.27E-07	4.37E-08	1.55	700	15.5	1.55	0.00	0.00	
3.84E-01	1.48E+03	1.66E-12	2.17E-14	-1.84E-15	9.00E-16	3.12E-16	1.57E-16	4.42E-04	6.65E-05	-4.88E-07	2.50E-07	8.29E-08	4.35E-08	1.55	700	15.5	1.55	0.00	0.00	
4.43E-01	1.70E+03	2.06E-12	2.25E-14	-9.87E-16	8.71E-16	5.30E-16	1.49E-16	4.75E-04	7.15E-05	-2.27E-07	2.04E-07	1.22E-07	3.89E-08	1.55	700	15.5	1.55	0.00	0.00	
2.25E+00	8.68E+03	8.44E-12	5.10E-14	-5.20E-17	8.71E-16	2.41E-15	1.43E-16	3.82E-04	5.73E-05	-2.35E-09	3.94E-08	1.09E-07	1.76E-08	1.55	700	15.5	1.55	0.00	0.00	
1.52E+00	5.84E+03	5.56E-12	5.01E-14	-1.07E-15	9.77E-16	1.22E-15	1.47E-16	3.74E-04	5.61E-05	-7.21E-08	6.65E-08	8.19E-08	1.58E-08	1.55	700	15.5	1.55	0.00	0.00	
1.44E+00	5.54E+03	5.70E-12	3.61E-14	1.56E-15	8.50E-16	1.54E-15	1.44E-16	4.03E-04	6.06E-05	1.11E-07	6.24E-08	1.09E-07	1.92E-08	1.55	700	15.5	1.55	0.00	0.00	
5.48E-01	2.11E+03	2.39E-12	2.26E-14	3.31E-17	8.71E-16	7.06E-16	1.48E-16	4.45E-04	6.69E-05	6.15E-09	1.62E-07	1.31E-07	3.38E-08	1.55	700	15.5	1.55	0.00	0.00	
7.73E-01	2.97E+03	3.31E-12	2.32E-14	-2.01E-15	1.08E-15	2.59E-16	1.50E-16	4.36E-04	6.55E-05	-2.65E-07	1.47E-07	3.42E-08	2.04E-08	1.55	700	15.5	1.55	0.00	0.00	
9.23E-01	3.55E+03	4.02E-12	3.94E-14	1.39E-15	9.00E-16	1.05E-15	1.41E-16	4.44E-04	6.67E-05	1.54E-07	1.02E-07	1.16E-07	2.34E-08	1.55	700	15.5	1.55	0.00	0.00	
9.78E-01	3.77E+03	4.09E-12	4.02E-14	1.73E-15	9.00E-16	8.65E-16	1.41E-16	4.26E-04	6.41E-05	1.81E-07	9.76E-08	9.01E-08	2.00E-08	1.55	700	15.5	1.55	0.00	0.00	

EHPV_NG_EXP17																			
5.69E-01	2.19E+03	1.49E-12	2.30E-14	1.65E-15	1.08E-15	5.80E-14	1.67E-16	2.66E-04	4.02E-05	2.95E-07	1.98E-07	1.04E-05	1.56E-06	1.01	700	21	1.01	0.00	0.00	
7.14E-01	2.75E+03	1.72E-12	2.65E-14	2.03E-16	8.71E-16	5.72E-14	1.43E-16	2.45E-04	3.70E-05	2.90E-08	1.24E-07	8.17E-06	1.23E-06	1.01	700	21	1.01	0.00	0.00	
1.50E+00	5.77E+03	3.27E-12	4.48E-14	-5.20E-17	1.19E-15	6.33E-14	4.13E-16	2.22E-04	3.34E-05	-3.53E-09	8.09E-08	4.30E-06	6.46E-07	1.01	700	21	1.01	0.00	0.00	
1.75E+00	6.72E+03	4.02E-12	3.58E-14	3.01E-15	1.74E-15	6.66E-14	2.12E-16	2.35E-04	3.52E-05	1.76E-07	1.05E-07	3.89E-06	5.83E-07	1.01	700	21	1.01	0.00	0.00	
1.86E+00	7.16E+03	4.20E-12	5.31E-14	6.15E-15	1.60E-15	6.95E-14	2.75E-16	2.30E-04	3.46E-05	3.37E-07	1.01E-07	3.81E-06	5.71E-07	1.01	700	21	1.01	0.00	0.00	
2.58E+00	9.93E+03	6.12E-12	2.81E-14	5.90E-15	1.13E-15	7.49E-14	1.41E-16	2.42E-04	3.63E-05	2.33E-07	5.67E-08	2.96E-06	4.43E-07	1.01	700	21	1.01	0.00	0.00	
2.29E+00	8.80E+03	5.29E-12	2.24E-14	4.28E-15	1.25E-15	7.22E-14	3.83E-16	2.36E-04	3.54E-05	1.91E-07	6.27E-08	3.22E-06	4.83E-07	1.01	700	21	1.01	0.00	0.00	
1.28E+00	4.94E+03	3.06E-12	2.16E-14	3.86E-15	1.02E-15	7.24E-14	1.75E-16	2.43E-04	3.64E-05	3.06E-07	9.33E-08	5.75E-06	8.62E-07	1.01	700	21	1.01	0.00	0.00	
1.25E+00	4.80E+03	3.02E-12	2.85E-14	2.33E-15	1.08E-15	6.94E-14	1.76E-16	2.47E-04	3.71E-05	1.90E-07	9.24E-08	5.67E-06	8.51E-07	1.01	700	21	1.01	0.00	0.00	
EHPV_NG_EXP18																			
2.11E+00	5.02E+03	1.64E-12	1.88E-14	7.69E-16	1.55E-15	1.61E-15	1.83E-16	1.28E-04	1.93E-05	6.01E-08	1.21E-07	1.26E-07	2.37E-08	0.50	700	16	0.50	0.00	0.00	
3.76E+00	8.93E+03	2.67E-12	3.41E-14	2.04E-15	1.60E-15	2.51E-15	2.30E-16	1.17E-04	1.76E-05	8.98E-08	7.14E-08	1.10E-07	1.94E-08	0.50	700	16	0.50	0.00	0.00	
2.83E+00	6.72E+03	2.09E-12	4.42E-14	-8.47E-16	1.60E-15	2.08E-15	2.02E-16	1.22E-04	1.85E-05	-4.94E-08	9.34E-08	1.21E-07	2.17E-08	0.50	700	16	0.50	0.00	0.00	
2.93E+00	6.96E+03	2.08E-12	2.44E-14	4.29E-16	1.55E-15	1.82E-15	1.96E-16	1.17E-04	1.77E-05	2.42E-08	8.73E-08	1.02E-07	1.89E-08	0.50	700	16	0.50	0.00	0.00	
7.01E-01	1.67E+03	6.08E-13	2.06E-14	1.28E-15	1.56E-15	8.62E-16	1.93E-16	1.43E-04	2.20E-05	3.01E-07	3.70E-07	2.03E-07	5.47E-08	0.50	700	16	0.50	0.00	0.00	
8.97E-01	2.13E+03	8.31E-13	1.82E-14	-8.47E-16	1.65E-15	6.50E-16	1.89E-16	1.53E-04	2.32E-05	-1.56E-07	3.04E-07	1.20E-07	3.91E-08	0.50	700	16	0.50	0.00	0.00	
3.92E+00	9.30E+03	2.97E-12	6.43E-14	-1.66E-16	1.80E-15	2.05E-15	2.25E-16	1.25E-04	1.90E-05	-7.01E-09	7.59E-08	8.63E-08	1.60E-08	0.50	700	16	0.50	0.00	0.00	
4.10E+00	9.74E+03	2.98E-12	2.55E-14	-1.66E-16	1.58E-15	2.54E-15	3.07E-16	1.20E-04	1.80E-05	-6.69E-09	6.34E-08	1.02E-07	1.97E-08	0.50	700	16	0.50	0.00	0.00	
EHPV_NG_EXP24																			
1.11E+00	4.27E+03	4.21E-12	2.54E-14	-2.22E-16	9.00E-16	1.02E-15	1.44E-16	3.87E-04	5.81E-05	-2.04E-08	8.28E-08	9.33E-08	1.92E-08	1.51	650	27	1.51	0.00	0.00	
1.26E+00	4.84E+03	4.72E-12	3.49E-14	-1.50E-15	9.77E-16	1.34E-15	1.47E-16	3.82E-04	5.74E-05	-1.21E-07	8.12E-08	1.09E-07	2.02E-08	1.51	650	27	1.51	0.00	0.00	
5.32E-01	2.05E+03	2.42E-12	2.17E-14	3.31E-17	8.37E-16	3.21E-16	1.42E-16	4.63E-04	6.95E-05	6.33E-09	1.60E-07	6.15E-08	2.86E-08	1.51	650	27	1.51	0.00	0.00	
6.32E-01	2.43E+03	2.52E-12	4.92E-14	2.67E-15	1.19E-15	6.38E-16	1.54E-16	4.07E-04	6.15E-05	4.30E-07	2.02E-07	1.03E-07	2.92E-08	1.51	650	27	1.51	0.00	0.00	
1.69E+00	6.50E+03	6.51E-12	6.64E-14	1.82E-15	8.50E-16	1.68E-15	1.62E-16	3.93E-04	5.91E-05	1.10E-07	5.39E-08	1.01E-07	1.81E-08	1.51	650	27	1.51	0.00	0.00	
1.43E+00	5.50E+03	5.63E-12	3.72E-14	-8.17E-16	1.02E-15	1.40E-15	1.51E-16	4.02E-04	6.03E-05	-5.83E-08	7.36E-08	9.96E-08	1.84E-08	1.51	650	27	1.51	0.00	0.00	
8.84E-01	3.40E+03	3.67E-12	3.06E-14	-1.33E-15	9.00E-16	9.38E-16	1.52E-16	4.23E-04	6.36E-05	-1.53E-07	1.06E-07	1.08E-07	2.39E-08	1.51	650	27	1.51	0.00	0.00	
8.20E-01	3.15E+03	3.35E-12	4.21E-14	2.58E-15	9.00E-16	7.31E-16	1.54E-16	4.16E-04	6.27E-05	3.21E-07	1.22E-07	9.08E-08	2.34E-08	1.51	650	27	1.51	0.00	0.00	
EHPV_NG_EXP32																			
2.08E+00	4.95E+03	1.34E-12	4.67E-15	2.27E-12	8.04E-14	6.06E-13	2.13E-15	1.06E-04	1.59E-05	1.80E-04	2.77E-05	4.80E-05	7.20E-06	1.55	750	40	0.52	0.52	0.52	
3.09E+00	3.88E+03	8.99E-13	7.75E-15	1.48E-12	6.53E-14	4.44E-13	1.71E-15	9.09E-05	1.37E-05	1.50E-04	2.34E-05	4.49E-05	6.73E-06	1.55	750	40	0.52	0.52	0.52	
1.98E+00	2.49E+03	6.92E-13	4.77E-15	8.36E-13	1.19E-13	4.40E-13	1.97E-15	1.09E-04	1.63E-05	1.32E-04	2.72E-05	6.92E-05	1.04E-05	1.55	750	40	0.52	0.52	0.52	
1.91E+00	2.40E+03	6.70E-13	5.18E-15	1.13E-12	6.07E-14	4.08E-13	1.72E-15	1.09E-04	1.64E-05	1.84E-04	2.94E-05	6.67E-05	1.00E-05	1.55	750	40	0.52	0.52	0.52	
3.43E+00	2.42E+03	7.19E-13	4.41E-15	1.05E-12	1.01E-13	2.44E-13	1.73E-15	1.16E-04	1.75E-05	1.69E-04	3.02E-05	3.95E-05	5.93E-06	1.55	750	40	0.52	0.52	0.52	
4.63E+00	3.27E+03	9.34E-13	9.08E-15	1.46E-12	7.42E-14	2.13E-13	1.86E-15	1.12E-04	1.68E-05	1.75E-04	2.77E-05	2.55E-05	3.84E-06	1.55	750	40	0.52	0.52	0.52	
1.49E-01	5.74E+02	1.97E-13	4.40E-15	4.61E-13	3.55E-14	3.27E-13	2.16E-15	1.34E-04	2.04E-05	3.15E-04	5.31E-05	2.23E-04	3.35E-05	1.55	750	40	0.52	0.52	0.52	shallow
3.17E-01	1.22E+03	3.89E-13	4.84E-15	8.73E-13	3.88E-14	5.19E-13	6.80E-15	1.25E-04	1.88E-05	2.81E-04	4.39E-05	1.67E-04	2.51E-05	1.55	750	40	0.52	0.52	0.52	shallow
1.47E-01	1.16E+03	3.86E-13	4.98E-15	8.83E-13	5.25E-14	6.52E-13	2.29E-15	1.31E-04	1.97E-05	2.99E-04	4.83E-05	2.21E-04	3.31E-05	1.55	750	40	0.52	0.52	0.52	shallow
3.25E-02	5.75E+02	2.63E-13	4.57E-15	8.83E-13	6.93E-14	5.39E-13	2.09E-15	1.80E-04	2.71E-05	6.03E-04	1.02E-04	3.68E-04	5.52E-05	1.55	750	40	0.52	0.52	0.52	shallow
2.00E-01	7.70E+02	2.47E-13	4.83E-15	5.24E-13	2.08E-14	3.67E-13	1.85E-15	1.26E-04	1.90E-05	2.67E-04	4.14E-05	1.87E-04	2.81E-05	1.55	750	40	0.52	0.52	0.52	shallow
1.56E-01	1.22E+03	3.66E-13	4.31E-15	9.83E-13	5.87E-14	6.43E-13	1.89E-15	1.17E-04	1.77E-05	3.15E-04	5.08E-05	2.06E-04	3.09E-05	1.55	750	40	0.52	0.52	0.52	shallow
2.96E-01	1.14E+03	3.18E-13	4.35E-15	7.67E-13	2.51E-14	4.56E-13	1.78E-15	1.09E-04	1.65E-05	2.64E-04	4.05E-05	1.57E-04	2.36E-05	1.55	750	40	0.52	0.52	0.52	shallow
1.57E-01	1.23E+03	3.62E-13	4.41E-15	8.28E-13	5.25E-14	6.29E-13	2.05E-15	1.15E-04	1.73E-05	2.64E-04	4.29E-05	2.00E-04	3.01E-05	1.55	750	40	0.52	0.52	0.52	shallow
2.09E-01	8.05E+02	2.46E-13	4.45E-15	4.10E-13	2.84E-14	3.79E-13	1.78E-15	1.20E-04	1.81E-05	2.00E-04	3.30E-05	1.85E-04	2.77E-05	1.55	750	40	0.52	0.52	0.52	shallow
tourmaline																			
EHPV_NG_EXP13																			
3.36E+00	4.23E+03	8.04E-15	6.62E-15	1.34E-15	8.50E-16	-3.78E-16	7.89E-16	6.34E-07	5.31E-07	1.05E-07	6.89E-08	-2.98E-08	6.24E-08	1.48	750	8	1.48	0.00	0.00	
5.34E+00	4.19E+04	5.29E-14	6.74E-15	-1.10E-16	1.03E-15	-3.94E-16	7.96E-16	4.20E-07	8.27E-08	-8.75E-10	8.22E-09	-3.13E-09	6.35E-09	1.48	750	8	1.48	0.00	0.00	
4.21E+00	1.32E+05	1.47E-13	7.00E-15	1.17E-15	8.19E-16	1.49E-16	7.89E-16	3.71E-07	5.84E-08	2.93E-09	2.11E-09	3.76E-10	1.99E-09	1.48	750	8	1.48	0.00	0.00	

8.34E+00	2.62E+05	2.05E-13	7.65E-15	-1.22E-15	8.50E-16	-1.19E-16	7.87E-16	2.61E-07	4.04E-08	-1.55E-09	1.11E-09	-1.51E-10	1.00E-09	1.48	750	8	1.48	0.00	0.00	
5.30E+00	3.15E+05	3.15E-13	3.01E-15	5.17E-16	1.52E-15	1.39E-16	2.10E-16	3.34E-07	5.02E-08	5.47E-10	1.61E-09	1.47E-10	2.23E-10	1.48	750	8	1.48	0.00	0.00	
2.61E+00	1.55E+05	1.80E-13	4.56E-15	7.72E-16	1.58E-15	1.25E-16	2.08E-16	3.86E-07	5.88E-08	1.66E-09	3.40E-09	2.69E-10	4.50E-10	1.48	750	8	1.48	0.00	0.00	
1.80E+00	1.07E+05	1.33E-13	2.69E-15	9.42E-16	1.50E-15	4.53E-16	2.37E-16	4.16E-07	6.29E-08	2.94E-09	4.72E-09	1.42E-09	7.71E-10	1.48	750	8	1.48	0.00	0.00	
1.27E+00	7.54E+04	9.75E-14	2.91E-15	1.03E-15	1.52E-15	-8.77E-17	2.18E-16	4.31E-07	6.59E-08	4.54E-09	6.73E-09	-3.87E-10	9.66E-10	1.48	750	8	1.48	0.00	0.00	
7.25E-01	4.30E+04	5.36E-14	2.57E-15	-4.19E-16	1.50E-15	-2.47E-16	2.23E-16	4.15E-07	6.54E-08	-3.24E-09	1.17E-08	-1.92E-09	1.75E-09	1.48	750	8	1.48	0.00	0.00	
2.06E-01	1.23E+04	2.58E-14	2.45E-15	-1.44E-15	1.50E-15	-1.26E-16	2.21E-16	7.03E-07	1.25E-07	-3.91E-08	4.13E-08	-3.42E-09	6.03E-09	1.48	750	8	1.48	0.00	0.00	shallow
	EHPV_NG_EXP16																			
2.39E+00	3.00E+05	1.61E-13	1.53E-14	2.22E-16	1.15E-15	1.16E-17	1.14E-16	1.79E-07	3.18E-08	2.47E-10	1.28E-09	1.29E-11	1.27E-10	1.55	700	15.5	1.55	0.00	0.00	
5.31E+00	6.68E+05	2.70E-13	1.50E-14	-1.22E-15	1.11E-15	2.42E-16	1.11E-16	1.35E-07	2.15E-08	-6.11E-10	5.62E-10	1.21E-10	5.84E-11	1.55	700	15.5	1.55	0.00	0.00	
1.29E+00	1.62E+05	2.51E-13	1.51E-14	-5.43E-16	1.13E-15	2.50E-16	1.06E-16	5.17E-07	8.35E-08	-1.12E-09	2.33E-09	5.15E-10	2.32E-10	1.55	700	15.5	1.55	0.00	0.00	
1.77E+00	5.94E+05	3.85E-13	1.54E-14	-2.03E-16	1.13E-15	2.16E-16	1.10E-16	2.16E-07	3.35E-08	-1.14E-10	6.33E-10	1.21E-10	6.45E-11	1.55	700	15.5	1.55	0.00	0.00	
2.45E+00	2.88E+05	1.16E-13	1.44E-14	6.47E-16	1.11E-15	2.87E-16	1.10E-16	1.34E-07	2.61E-08	7.48E-10	1.29E-09	3.31E-10	1.37E-10	1.55	700	15.5	1.55	0.00	0.00	
	EHPV_NG_EXP17																			
1.53E+00	1.92E+05	2.02E-13	1.53E-14	3.92E-16	1.21E-15	2.49E-15	1.17E-16	3.50E-07	5.89E-08	6.81E-10	2.10E-09	4.33E-09	6.80E-10	1.01	700	21	1.01	0.00	0.00	
1.04E+00	1.31E+05	6.21E-14	1.47E-14	3.03E-15	1.25E-15	1.57E-15	1.30E-16	1.59E-07	4.44E-08	7.73E-09	3.39E-09	4.01E-09	6.87E-10	1.01	700	21	1.01	0.00	0.00	
1.67E+00	2.10E+05	1.29E-13	1.44E-14	2.52E-15	1.15E-15	1.25E-15	1.10E-16	2.05E-07	3.84E-08	4.00E-09	1.92E-09	1.98E-09	3.44E-10	1.01	700	21	1.01	0.00	0.00	
2.65E+00	3.33E+05	1.37E-13	1.45E-14	1.24E-15	1.13E-15	1.85E-15	1.13E-16	1.37E-07	2.52E-08	1.24E-09	1.14E-09	1.85E-09	2.99E-10	1.01	700	21	1.01	0.00	0.00	
1.53E+00	1.92E+05	7.22E-14	1.48E-14	8.18E-16	1.18E-15	4.16E-16	1.12E-16	1.25E-07	3.18E-08	1.42E-09	2.06E-09	7.21E-10	2.23E-10	1.01	700	21	1.01	0.00	0.00	
	EHPV_NG_EXP18																			
1.99E+00	2.50E+05	1.09E-13	1.61E-14	-9.68E-16	1.13E-15	2.36E-16	1.16E-16	1.45E-07	3.06E-08	-1.29E-09	1.52E-09	3.14E-10	1.62E-10	0.50	700	16	0.50	0.00	0.00	
4.17E+00	5.23E+05	1.25E-13	1.46E-14	1.92E-15	1.15E-15	2.33E-16	1.13E-16	7.96E-08	1.51E-08	1.22E-09	7.55E-10	1.48E-10	7.55E-11	0.50	700	16	0.50	0.00	0.00	
8.88E+00	1.12E+06	1.03E-13	1.56E-14	3.62E-15	1.10E-15	2.54E-16	1.14E-16	3.07E-08	6.56E-09	1.08E-09	3.67E-10	7.59E-11	3.58E-11	0.50	700	16	0.50	0.00	0.00	
9.50E+00	1.19E+06	2.00E-13	1.72E-14	4.98E-15	1.50E-15	1.62E-16	1.05E-16	5.58E-08	9.65E-09	1.39E-09	4.68E-10	4.51E-11	3.01E-11	0.50	700	16	0.50	0.00	0.00	
	EHPV_NG_EXP24																			
3.34E+00	1.99E+05	5.50E-14	1.48E-14	1.41E-15	1.10E-15	1.15E-16	1.21E-16	9.23E-08	2.85E-08	2.37E-09	1.88E-09	1.92E-10	2.06E-10	1.51	650	27	1.51	0.00	0.00	
6.36E+00	3.78E+05	1.00E-13	1.50E-14	9.03E-16	1.15E-15	4.59E-17	1.10E-16	8.84E-08	1.87E-08	7.97E-10	1.02E-09	4.05E-11	9.71E-11	1.51	650	27	1.51	0.00	0.00	
4.94E+00	6.20E+05	2.14E-13	1.46E-14	1.84E-15	1.18E-15	9.17E-18	1.09E-16	1.15E-07	1.90E-08	9.88E-10	6.50E-10	4.93E-12	5.83E-11	1.51	650	27	1.51	0.00	0.00	
9.71E+00	1.22E+06	2.40E-13	1.45E-14	2.60E-15	1.29E-15	2.83E-16	1.06E-16	6.55E-08	1.06E-08	7.11E-10	3.69E-10	7.74E-11	3.11E-11	1.51	650	27	1.51	0.00	0.00	
2.54E+00	3.19E+05	1.51E-13	1.63E-14	6.47E-16	1.11E-15	1.11E-16	1.22E-16	1.58E-07	2.91E-08	6.76E-10	1.17E-09	1.16E-10	1.29E-10	1.51	650	27	1.51	0.00	0.00	
1.45E+00	1.82E+05	1.16E-13	1.44E-14	-1.05E-15	1.21E-15	1.29E-16	1.09E-16	2.12E-07	4.14E-08	-1.93E-09	2.24E-09	2.37E-10	2.02E-10	1.51	650	27	1.51	0.00	0.00	
1.49E+00	1.87E+05	1.18E-13	1.49E-14	-1.90E-15	1.11E-15	-3.00E-17	1.05E-16	2.11E-07	4.13E-08	-3.39E-09	2.04E-09	-5.34E-11	1.87E-10	1.51	650	27	1.51	0.00	0.00	
2.15E+00	2.70E+05	1.21E-13	1.47E-14	-1.05E-15	1.11E-15	2.45E-16	1.08E-16	1.50E-07	2.89E-08	-1.30E-09	1.39E-09	3.02E-10	1.41E-10	1.51	650	27	1.51	0.00	0.00	
8.03E-01	1.01E+05	3.40E-13	1.47E-14	3.07E-16	1.44E-15	2.06E-16	1.06E-16	1.12E-06	1.76E-07	1.02E-09	4.77E-09	6.81E-10	3.65E-10	1.51	650	27	1.51	0.00	0.00	not used
8.19E-01	1.03E+05	3.00E-13	1.43E-14	-2.88E-16	1.11E-15	-1.87E-16	1.20E-16	9.73E-07	1.53E-07	-9.33E-10	3.60E-09	-6.06E-10	3.99E-10	1.51	650	27	1.51	0.00	0.00	not used
6.63E-01	8.34E+04	9.37E-14	1.43E-14	4.77E-16	1.13E-15	-1.96E-16	1.11E-16	3.74E-07	8.02E-08	1.91E-09	4.52E-09	-7.84E-10	4.57E-10	1.51	650	27	1.51	0.00	0.00	
9.03E-01	1.13E+05	3.64E-13	1.49E-14	-2.03E-16	1.10E-15	6.10E-17	1.06E-16	1.07E-06	1.66E-07	-5.96E-10	3.24E-09	1.79E-10	3.12E-10	1.51	650	27	1.51	0.00	0.00	not used
4.59E-01	5.76E+04	2.08E-13	1.47E-14	4.73E-15	1.21E-15	2.72E-17	1.05E-16	1.20E-06	1.99E-07	2.73E-08	8.12E-09	1.58E-10	6.08E-10	1.51	650	27	1.51	0.00	0.00	not used
9.51E-01	1.20E+05	6.20E-14	1.46E-14	-1.56E-15	1.18E-15	-1.36E-16	1.19E-16	1.73E-07	4.82E-08	-4.36E-09	3.35E-09	-3.79E-10	3.36E-10	1.51	650	27	1.51	0.00	0.00	
1.28E+00	1.61E+05	1.30E-13	1.59E-14	2.26E-15	1.15E-15	1.44E-16	1.10E-16	2.69E-07	5.20E-08	4.68E-09	2.48E-09	2.98E-10	2.31E-10	1.51	650	27	1.51	0.00	0.00	
	antigorite																			
	CS_NG_EXP17																			
5.61E+00	9.92E+04	6.82E-13	8.22E-15	-5.11E-14	3.63E-14	4.82E-15	9.78E-15	2.50E-06	3.76E-07	-1.87E-07	1.36E-07	1.77E-08	3.60E-08	1.57	375	46	1.42	0.00	0.00	
1.57E+01	2.77E+05	1.82E-12	8.29E-15	6.25E-15	3.59E-14	-2.73E-15	9.63E-15	2.39E-06	3.58E-07	8.21E-09	4.72E-08	-3.58E-09	1.27E-08	1.57	375	46	1.42	0.00	0.00	
1.08E+01	1.91E+05	1.29E-12	7.00E-15	2.90E-14	3.66E-14	1.46E-14	9.64E-15	2.46E-06	3.69E-07	5.52E-08	7.01E-08	2.78E-08	1.88E-08	1.57	375	46	1.42	0.00	0.00	
8.82E+00	1.56E+05	1.03E-12	9.37E-15	6.87E-14	3.59E-14	5.68E-15	9.61E-15	2.41E-06	3.62E-07	1.60E-07	8.71E-08	1.32E-08	2.25E-08	1.57	375	46	1.42	0.00	0.00	
	CS_NG_EXP18																			
1.62E+01	5.10E+05	8.32E-15	4.06E-14	-1.22E-13	1.37E-13	5.07E-13	3.23E-14	5.93E-09	2.89E-08	-8.68E-08	9.84E-08	3.62E-07	5.89E-08	1.57	350	48	0.00	0.00	1.42	
1.62E+01	5.10E+05	4.90E-14	4.09E-14	-1.80E-13	1.35E-13	5.28E-13	2.48E-14	3.49E-08	2.97E-08	-1.29E-07	9.78E-08	3.76E-07	5.91E-08	1.57	350	48	0.00	0.00	1.42	

2.22E+01	6.99E+05	1.15E-13	4.03E-14	2.81E-13	1.35E-13	1.03E-12	3.12E-14	5.97E-08	2.28E-08	1.46E-07	7.38E-08	5.38E-07	8.24E-08	1.57	350	48	0.00	0.00	1.42
2.22E+01	6.99E+05	1.10E-13	4.02E-14	6.75E-15	1.48E-13	5.98E-13	4.95E-14	5.72E-08	2.26E-08	3.51E-09	7.72E-08	3.12E-07	5.34E-08	1.57	350	48	0.00	0.00	1.42
1.18E+01	3.71E+05	6.80E-14	4.14E-14	6.24E-14	1.37E-13	4.96E-13	2.66E-14	6.66E-08	4.18E-08	6.11E-08	1.35E-07	4.86E-07	7.75E-08	1.57	350	48	0.00	0.00	1.42
6.54E+00	2.05E+05	4.10E-14	4.58E-14	-5.58E-14	1.34E-13	1.87E-13	2.92E-14	7.26E-08	8.17E-08	-9.87E-08	2.38E-07	3.31E-07	7.16E-08	1.57	350	48	0.00	0.00	1.42
1.46E+01	4.57E+05	1.13E-14	4.04E-14	7.20E-14	1.44E-13	6.43E-13	2.83E-14	9.00E-09	3.22E-08	5.73E-08	1.15E-07	5.11E-07	7.99E-08	1.57	350	48	0.00	0.00	1.42
9.68E+00	3.04E+05	3.02E-14	4.00E-14	-4.60E-14	1.39E-13	3.80E-13	2.65E-14	3.61E-08	4.82E-08	-5.50E-08	1.66E-07	4.54E-07	7.51E-08	1.57	350	48	0.00	0.00	1.42
2.57E+01	8.07E+05	1.07E-13	4.00E-14	2.75E-13	1.44E-13	8.97E-13	2.75E-14	4.80E-08	1.94E-08	1.24E-07	6.76E-08	4.04E-07	6.19E-08	1.57	350	48	0.00	0.00	1.42
	CS_NG_EXP20																		
7.99E+00	1.41E+05	8.51E-13	6.98E-15	-1.01E-14	3.61E-14	2.55E-14	9.64E-15	2.19E-06	3.29E-07	-2.61E-08	9.31E-08	6.56E-08	2.67E-08	1.53	350	45.5	1.53	0.00	0.00
1.46E+01	2.58E+05	1.67E-12	7.14E-15	-7.06E-15	3.63E-14	4.83E-14	1.01E-14	2.34E-06	3.52E-07	-9.93E-09	5.10E-08	6.80E-08	1.75E-08	1.53	350	45.5	1.53	0.00	0.00
1.00E+01	1.77E+05	1.12E-12	6.52E-15	-4.52E-14	3.56E-14	1.54E-14	9.63E-15	2.31E-06	3.46E-07	-9.28E-08	7.44E-08	3.16E-08	2.03E-08	1.53	350	45.5	1.53	0.00	0.00
5.43E+00	9.59E+04	5.97E-13	6.96E-15	1.20E-13	4.10E-14	1.77E-16	9.75E-15	2.26E-06	3.41E-07	4.55E-07	1.70E-07	6.70E-10	3.70E-08	1.53	350	45.5	1.53	0.00	0.00
	CS_NG_EXP21																		
3.49E+00	2.08E+05	2.53E-13	5.29E-15	-7.41E-14	1.85E-14	1.60E-13	9.88E-14	4.43E-07	6.71E-08	-1.30E-07	3.78E-08	2.81E-07	1.78E-07	0.97	350	48	0.32	0.32	0.32
3.36E+00	1.99E+05	2.44E-13	3.54E-15	6.44E-14	2.12E-14	2.48E-13	1.21E-13	4.46E-07	6.71E-08	1.18E-07	4.24E-08	4.52E-07	2.30E-07	0.97	350	48	0.32	0.32	0.32
8.42E+00	2.64E+05	3.41E-13	3.55E-15	3.62E-14	2.40E-14	3.68E-13	8.97E-14	4.69E-07	7.05E-08	4.98E-08	3.39E-08	5.06E-07	1.45E-07	0.97	350	48	0.32	0.32	0.32
8.27E+00	2.60E+05	3.35E-13	5.43E-15	5.68E-14	1.81E-14	5.01E-13	9.92E-14	4.70E-07	7.09E-08	7.95E-08	2.81E-08	7.01E-07	1.74E-07	0.97	350	48	0.32	0.32	0.32
1.12E+01	1.98E+05	2.42E-13	4.89E-15	1.19E-14	1.83E-14	4.81E-13	8.89E-14	4.46E-07	6.75E-08	2.19E-08	3.38E-08	8.84E-07	2.11E-07	0.97	350	48	0.32	0.32	0.32
1.13E+01	1.99E+05	2.50E-13	4.30E-15	5.81E-14	2.58E-14	4.58E-13	9.71E-14	4.57E-07	6.90E-08	1.06E-07	4.98E-08	8.36E-07	2.17E-07	0.97	350	48	0.32	0.32	0.32
2.82E+01	2.21E+05	2.83E-13	6.32E-15	-9.21E-15	1.93E-14	3.57E-13	8.88E-14	4.65E-07	7.05E-08	-1.51E-08	3.18E-08	5.86E-07	1.70E-07	0.97	350	48	0.32	0.32	0.32
2.75E+01	2.16E+05	2.76E-13	4.48E-15	2.04E-14	1.81E-14	4.71E-13	9.01E-14	4.65E-07	7.02E-08	3.44E-08	3.09E-08	7.93E-07	1.93E-07	0.97	350	48	0.32	0.32	0.32
	CS_NG_EXP22																		
8.25E+00	4.90E+05	1.72E-14	1.50E-15	-3.39E-15	2.11E-15	1.57E-12	3.51E-14	1.27E-08	2.21E-09	-2.52E-09	1.61E-09	1.16E-06	1.77E-07	1.73	350	48	0.00	0.00	1.73
3.04E+00	1.80E+05	5.37E-15	1.30E-15	6.35E-16	2.03E-15	5.15E-13	2.32E-14	1.08E-08	3.08E-09	1.28E-09	4.09E-09	1.04E-06	1.63E-07	1.73	350	48	0.00	0.00	1.73
2.98E+00	1.77E+05	8.77E-15	1.35E-15	4.23E-15	2.06E-15	6.49E-13	1.94E-14	1.80E-08	3.88E-09	8.69E-09	4.43E-09	1.33E-06	2.04E-07	1.73	350	48	0.00	0.00	1.73
1.48E+00	8.78E+04	1.78E-15	1.31E-15	9.23E-16	2.03E-15	4.53E-13	2.35E-14	7.38E-09	5.53E-09	3.82E-09	8.41E-09	1.88E-06	2.98E-07	1.73	350	48	0.00	0.00	1.73
6.13E+00	3.64E+05	1.58E-14	1.31E-15	6.35E-16	2.22E-15	1.66E-12	3.10E-14	1.58E-08	2.71E-09	6.34E-10	2.22E-09	1.66E-06	2.51E-07	1.73	350	48	0.00	0.00	1.73
4.65E+00	2.76E+05	8.63E-15	1.46E-15	3.80E-15	2.16E-15	8.99E-13	3.79E-14	1.13E-08	2.57E-09	5.00E-09	2.94E-09	1.18E-06	1.84E-07	1.73	350	48	0.00	0.00	1.73
2.36E+01	7.40E+05	2.80E-14	1.44E-15	5.67E-15	2.11E-15	1.99E-12	3.16E-14	1.37E-08	2.18E-09	2.78E-09	1.12E-09	9.76E-07	1.47E-07	1.73	350	48	0.00	0.00	1.73
2.45E+01	4.32E+05	1.38E-14	1.46E-15	-2.67E-15	2.53E-15	1.19E-12	2.63E-14	1.16E-08	2.13E-09	-2.25E-09	2.16E-09	1.00E-06	1.52E-07	1.73	350	48	0.00	0.00	1.73
1.54E+01	2.72E+05	9.65E-15	1.29E-15	-2.24E-15	2.22E-15	8.95E-13	2.22E-14	1.29E-08	2.59E-09	-3.00E-09	3.01E-09	1.20E-06	1.82E-07	1.73	350	48	0.00	0.00	1.73
1.21E+01	2.13E+05	7.74E-15	1.33E-15	-9.47E-16	2.11E-15	6.10E-13	2.46E-14	1.32E-08	3.01E-09	-1.62E-09	3.60E-09	1.04E-06	1.62E-07	1.73	350	48	0.00	0.00	1.73
	CS_NG_EXP23																		
7.02E+00	5.51E+04	3.46E-13	5.72E-15	2.07E-13	3.35E-14	1.04E-13	2.47E-14	2.28E-06	3.44E-07	1.36E-06	3.01E-07	6.88E-07	1.93E-07	1.68	350	92	1.68	0.00	0.00
5.90E+00	1.04E+05	6.69E-13	6.91E-15	4.02E-14	2.70E-14	6.81E-14	2.14E-14	2.33E-06	3.51E-07	1.40E-07	9.67E-08	2.38E-07	8.26E-08	1.68	350	92	1.68	0.00	0.00
8.55E+00	1.51E+05	9.79E-13	5.97E-15	-6.63E-15	2.71E-14	7.91E-14	1.92E-14	2.36E-06	3.54E-07	-1.60E-08	6.52E-08	1.90E-07	5.44E-08	1.68	350	92	1.68	0.00	0.00
2.99E+00	5.28E+04	3.29E-13	6.16E-15	-4.83E-14	2.70E-14	-1.83E-14	1.91E-14	2.27E-06	3.43E-07	-3.33E-07	1.93E-07	-1.26E-07	1.33E-07	1.68	350	92	1.68	0.00	0.00
6.96E+00	1.23E+05	7.84E-13	5.55E-15	-6.12E-15	2.77E-14	5.49E-14	2.02E-14	2.32E-06	3.48E-07	-1.81E-08	8.18E-08	1.62E-07	6.44E-08	1.68	350	92	1.68	0.00	0.00
1.33E+01	2.36E+05	1.48E-12	6.97E-15	9.47E-14	2.66E-14	-1.14E-14	1.89E-14	2.28E-06	3.43E-07	1.46E-07	4.65E-08	-1.76E-08	2.92E-08	1.68	350	92	1.68	0.00	0.00
	CS_NG_EXP24																		
1.32E+01	4.14E+05	7.24E-13	6.71E-15	5.87E-14	2.12E-14	1.05E-12	1.11E-13	6.36E-07	9.55E-08	5.15E-08	2.01E-08	9.22E-07	1.69E-07	1.30	350	65	0.43	0.43	0.43
7.26E+00	2.28E+05	4.07E-13	3.84E-15	8.07E-14	1.98E-14	1.81E-13	8.88E-14	6.48E-07	9.74E-08	1.29E-07	3.69E-08	2.88E-07	1.48E-07	1.30	350	65	0.43	0.43	0.43
1.35E+01	2.38E+05	4.23E-13	3.54E-15	2.23E-14	2.27E-14	7.99E-13	1.20E-13	6.46E-07	9.71E-08	3.41E-08	3.50E-08	1.22E-06	2.59E-07	1.30	350	65	0.43	0.43	0.43
1.05E+01	1.86E+05	3.30E-13	7.52E-15	5.48E-14	1.82E-14	3.43E-13	1.06E-13	6.46E-07	9.81E-08	1.07E-07	3.91E-08	6.72E-07	2.30E-07	1.30	350	65	0.43	0.43	0.43
2.34E+01	1.83E+05	3.76E-13	5.92E-15	4.97E-14	1.94E-14	4.54E-13	1.29E-13	7.46E-07	1.13E-07	9.86E-08	4.13E-08	9.00E-07	2.89E-07	1.30	350	65	0.43	0.43	0.43
2.38E+01	1.87E+05	3.79E-13	8.06E-15	1.02E-14	2.44E-14	3.38E-13	1.03E-13	7.37E-07	1.12E-07	1.98E-08	4.76E-08	6.58E-07	2.24E-07	1.30	350	65	0.43	0.43	0.43
1.01E+01	1.79E+05	3.15E-13	3.54E-15	-1.60E-14	1.96E-14	5.07E-13	8.91E-14	6.41E-07	9.65E-08	-3.25E-08	4.03E-08	1.03E-06	2.39E-07	1.30	350	65	0.43	0.43	0.43
6.04E+00	1.90E+05	3.31E-13	4.49E-15	8.18E-14	2.76E-14	2.48E-13	9.52E-14	6.34E-07	9.55E-08	1.57E-07	5.79E-08	4.75E-07	1.96E-07	1.30	350	65	0.43	0.43	0.43
2.71E+00	1.61E+05	3.22E-13	5.33E-15	1.65E-14	1.89E-14	2.98E-13	1.02E-13	7.28E-07	1.10E-07	3.73E-08	4.30E-08	6.73E-07	2.51E-07	1.30	350	65	0.43	0.43	0.43

	CS_NG_EXP25																			
1.42E+01	4.47E+05	3.03E-13	4.24E-14	1.25E-13	1.32E-13	7.86E-13	2.76E-14	2.46E-07	5.06E-08	9.10E-08	1.13E-07	6.40E-07	9.85E-08	0.50	350	48	0.17	0.17	0.17	
8.64E+00	5.13E+05	3.12E-13	4.18E-14	-2.51E-13	1.46E-13	5.45E-13	2.48E-14	2.21E-07	4.45E-08	-1.88E-07	1.11E-07	3.86E-07	6.05E-08	0.50	350	48	0.17	0.17	0.17	
1.29E+01	7.69E+05	4.70E-13	4.18E-14	7.45E-14	1.32E-13	1.02E-12	3.40E-14	2.22E-07	3.88E-08	2.88E-08	6.54E-08	4.84E-07	7.44E-08	0.50	350	48	0.17	0.17	0.17	
1.65E+01	9.79E+05	6.08E-13	4.01E-14	2.02E-13	1.53E-13	1.31E-12	3.22E-14	2.26E-07	3.70E-08	6.99E-08	5.98E-08	4.87E-07	7.40E-08	0.50	350	48	0.17	0.17	0.17	
3.31E+01	1.04E+06	6.18E-13	4.00E-14	3.71E-13	1.30E-13	2.06E-12	4.01E-14	2.16E-07	3.53E-08	1.25E-07	5.13E-08	7.20E-07	1.09E-07	0.50	350	48	0.17	0.17	0.17	
2.52E+01	7.91E+05	4.92E-13	4.35E-14	3.16E-13	1.33E-13	1.32E-12	3.14E-14	2.26E-07	3.94E-08	1.39E-07	6.74E-08	6.08E-07	9.24E-08	0.50	350	48	0.17	0.17	0.17	
2.90E+01	5.13E+05	3.40E-13	4.14E-14	5.38E-14	1.29E-13	5.80E-13	3.04E-14	2.41E-07	4.65E-08	2.86E-08	9.61E-08	4.11E-07	6.53E-08	0.50	350	48	0.17	0.17	0.17	
1.97E+01	3.48E+05	1.56E-13	4.02E-14	8.63E-14	1.28E-13	6.39E-13	3.18E-14	1.63E-07	4.85E-08	7.59E-08	1.41E-07	6.67E-07	1.05E-07	0.50	350	48	0.17	0.17	0.17	
	CS_NG_EXP29																			
3.53E+00	1.11E+05	2.38E-13	8.21E-15	-2.21E-16	5.57E-16	1.09E-15	1.88E-15	7.80E-07	1.20E-07	-7.23E-10	1.83E-09	3.56E-09	6.19E-09	0.68	350	29.5	0.68	0.00	0.00	
3.70E+00	1.16E+05	2.42E-13	4.73E-15	-7.67E-16	5.64E-16	1.59E-16	1.88E-15	7.58E-07	1.15E-07	-2.40E-09	1.80E-09	4.99E-10	5.90E-09	0.68	350	29.5	0.68	0.00	0.00	
1.36E+01	2.40E+05	4.72E-13	4.97E-15	1.35E-15	5.40E-16	1.05E-15	1.88E-15	7.15E-07	1.08E-07	2.05E-09	8.74E-10	1.59E-09	2.87E-09	0.68	350	29.5	0.68	0.00	0.00	
1.53E+01	4.80E+05	1.00E-12	4.26E-15	4.56E-16	5.72E-16	9.58E-16	1.88E-15	7.57E-07	1.14E-07	3.46E-10	4.36E-10	7.26E-10	1.43E-09	0.68	350	29.5	0.68	0.00	0.00	
6.41E+00	3.81E+05	7.98E-13	8.08E-15	-2.43E-17	5.40E-16	1.10E-15	1.89E-15	7.61E-07	1.14E-07	-2.32E-11	5.15E-10	1.05E-09	1.81E-09	0.68	350	29.5	0.68	0.00	0.00	
2.52E+01	4.45E+05	9.15E-13	4.79E-15	9.15E-16	5.72E-16	1.98E-15	1.89E-15	7.49E-07	1.12E-07	7.49E-10	4.81E-10	1.62E-09	1.56E-09	0.68	350	29.5	0.68	0.00	0.00	
	CS_NG_EXP30																			
2.06E+00	6.49E+04	2.61E-13	5.30E-15	1.31E-15	5.64E-16	2.98E-15	1.88E-15	1.47E-06	2.22E-07	7.33E-09	3.35E-09	1.67E-08	1.09E-08	1.11	350	37	1.11	0.00	0.00	
2.05E+00	6.45E+04	2.67E-13	4.30E-15	2.60E-16	5.40E-16	2.40E-15	1.89E-15	1.51E-06	2.27E-07	1.46E-09	3.05E-09	1.35E-08	1.08E-08	1.11	350	37	1.11	0.00	0.00	
7.09E+00	2.23E+05	9.00E-13	5.79E-15	4.34E-16	5.64E-16	3.33E-15	1.89E-15	1.47E-06	2.21E-07	7.10E-10	9.27E-10	5.44E-09	3.19E-09	1.11	350	37	1.11	0.00	0.00	
8.26E+00	1.46E+05	5.85E-13	6.18E-15	-8.98E-17	5.57E-16	1.97E-15	1.90E-15	1.46E-06	2.19E-07	-2.24E-10	1.39E-09	4.92E-09	4.79E-09	1.11	350	37	1.11	0.00	0.00	
9.54E-01	5.67E+04	2.40E-13	4.38E-15	-6.80E-17	5.57E-16	2.62E-15	1.88E-15	1.54E-06	2.33E-07	-4.36E-10	3.57E-09	1.68E-08	1.23E-08	1.11	350	37	1.11	0.00	0.00	
3.71E+00	2.21E+05	9.08E-13	1.14E-14	8.50E-17	5.57E-16	3.30E-15	1.89E-15	1.50E-06	2.25E-07	1.40E-10	9.18E-10	5.44E-09	3.22E-09	1.11	350	37	1.11	0.00	0.00	
1.25E+01	2.21E+05	1.24E-12	1.21E-14	9.81E-16	6.46E-16	3.43E-15	1.89E-15	2.05E-06	3.08E-07	1.62E-09	1.09E-09	5.65E-09	3.23E-09	1.11	350	37	1.11	0.00	0.00	magnetite
	EHPV_NG_EXP53																			
7.59E+00	4.51E+05	1.09E-13	4.48E-15	-7.77E-15	1.86E-14	-2.26E-14	9.00E-14	8.83E-08	1.37E-08	-6.27E-09	1.50E-08	-1.82E-08	7.26E-08	1.57	450	48	0.00	0.00	1.42	
2.68E+01	1.59E+06	3.46E-13	4.52E-15	-2.16E-15	1.88E-14	-9.96E-15	9.29E-14	7.88E-08	1.19E-08	-4.94E-10	4.28E-09	-2.27E-09	2.12E-08	1.57	450	48	0.00	0.00	1.42	
2.61E+01	1.55E+06	3.47E-13	5.45E-15	5.46E-15	1.81E-14	1.46E-14	9.04E-14	8.14E-08	1.23E-08	1.28E-09	4.26E-09	3.43E-09	2.12E-08	1.57	450	48	0.00	0.00	1.42	
2.60E+01	3.27E+06	7.35E-13	3.77E-15	-3.47E-14	1.81E-14	-5.99E-14	8.93E-14	8.16E-08	1.23E-08	-3.85E-09	2.09E-09	-6.65E-09	9.97E-09	1.57	450	48	0.00	0.00	1.42	
	F-phlogopite																			
	CS_NG_EXP2																			
2.26E+01	3.99E+05	3.95E-13	4.58E-15	-7.82E-15	1.02E-14	2.45E-16	1.01E-15	3.60E-07	5.42E-08	-7.13E-09	9.34E-09	2.24E-10	9.25E-10	1.38	450	43	0.46	0.46	0.46	
2.00E+01	1.57E+05	1.36E-13	3.95E-15	2.83E-14	1.03E-14	-4.30E-16	1.03E-15	3.14E-07	4.79E-08	6.55E-08	2.58E-08	-9.94E-10	2.39E-09	1.38	450	43	0.46	0.46	0.46	
1.17E+01	9.19E+04	9.81E-14	3.87E-15	2.03E-14	1.03E-14	2.50E-15	1.01E-15	3.88E-07	6.02E-08	8.04E-08	4.25E-08	9.91E-09	4.26E-09	1.38	450	43	0.46	0.46	0.46	
1.22E+01	9.58E+04	1.07E-13	3.77E-15	2.31E-14	1.04E-14	-4.42E-16	1.01E-15	4.07E-07	6.27E-08	8.78E-08	4.15E-08	-1.68E-09	3.86E-09	1.38	450	43	0.46	0.46	0.46	
	CS_NG_EXP11																			
1.55E+01	9.18E+05	7.01E-12	2.69E-14	7.37E-14	1.03E-14	9.07E-16	1.00E-15	2.78E-06	4.17E-07	2.92E-08	6.00E-09	3.59E-10	4.01E-10	1.27	700	44.5	0.42	0.42	0.42	not used
9.42E+00	2.96E+05	2.76E-13	3.69E-15	1.79E-14	1.07E-14	5.91E-16	1.03E-15	3.39E-07	5.11E-08	2.20E-08	1.35E-08	7.25E-10	1.27E-09	1.27	700	44.5	0.42	0.42	0.42	
1.81E+01	5.68E+05	5.55E-13	3.66E-15	1.07E-14	1.15E-14	3.71E-17	1.01E-15	3.56E-07	5.34E-08	6.86E-09	7.43E-09	2.38E-11	6.44E-10	1.27	700	44.5	0.42	0.42	0.42	
2.43E+01	7.63E+05	7.45E-13	3.80E-15	6.97E-15	9.94E-15	-4.48E-16	1.04E-15	3.55E-07	5.33E-08	3.32E-09	4.77E-09	-2.14E-10	4.99E-10	1.27	700	44.5	0.42	0.42	0.42	
7.00E+00	4.16E+05	4.25E-13	4.80E-15	3.42E-14	1.11E-14	3.39E-16	1.00E-15	3.72E-07	5.59E-08	2.99E-08	1.07E-08	2.96E-10	8.77E-10	1.27	700	44.5	0.42	0.42	0.42	
2.51E+00	1.49E+05	1.64E-13	4.68E-15	3.75E-14	1.20E-14	8.78E-16	1.00E-15	4.00E-07	6.10E-08	9.14E-08	3.23E-08	2.14E-09	2.47E-09	1.27	700	44.5	0.42	0.42	0.42	
1.85E+00	1.10E+05	1.04E-13	3.79E-15	2.08E-14	1.13E-14	7.87E-17	1.00E-15	3.44E-07	5.31E-08	6.88E-08	3.87E-08	2.60E-10	3.31E-09	1.27	700	44.5	0.42	0.42	0.42	
2.70E+01	8.49E+05	9.35E-13	3.94E-15	5.37E-14	1.18E-14	8.56E-15	1.01E-15	4.01E-07	6.01E-08	2.30E-08	6.12E-09	3.67E-09	6.99E-10	1.27	700	44.5	0.42	0.42	0.42	
	CS_NG_EXP13																			
2.54E+00	7.98E+04	4.04E-14	1.36E-15	1.38E-15	2.52E-14	7.26E-15	4.71E-15	1.84E-07	2.83E-08	6.28E-09	1.15E-07	3.31E-08	2.20E-08	0.24	500	24	0.24	0.00	0.00	
4.89E+00	1.54E+05	7.07E-14	1.26E-15	-2.14E-14	2.45E-14	1.40E-14	4.98E-15	1.67E-07	2.53E-08	-5.06E-08	5.84E-08	3.31E-08	1.28E-08	0.24	500	24	0.24	0.00	0.00	
8.82E+00	2.77E+05	1.33E-13	1.41E-15	1.47E-14	2.52E-14	4.87E-15	4.70E-15	1.75E-07	2.62E-08	1.93E-08	3.33E-08	6.40E-09	6.25E-09	0.24	500	24	0.24	0.00	0.00	
1.63E+01	5.12E+05	1.02E-13	1.41E-15	-1.12E-14	2.47E-14	-9.99E-16	4.63E-15	7.24E-08	1.09E-08	-7.92E-09	1.76E-08	-7.10E-10	3.29E-09	0.24	500	24	0.24	0.00	0.00	

4.22E+00	1.33E+05	6.27E-14	1.20E-15	-1.86E-14	2.70E-14	-4.48E-15	5.09E-15	1.72E-07	2.60E-08	-5.09E-08	7.45E-08	-1.23E-08	1.41E-08	0.24	500	24	0.24	0.00	0.00
8.42E+00	2.65E+05	8.88E-14	1.54E-15	-1.56E-16	2.48E-14	6.55E-15	4.74E-15	1.22E-07	1.84E-08	-2.15E-10	3.41E-08	9.01E-09	6.66E-09	0.24	500	24	0.24	0.00	0.00
2.41E+00	7.56E+04	3.77E-14	1.20E-15	-2.24E-14	2.56E-14	2.96E-15	4.48E-15	1.82E-07	2.78E-08	-1.08E-07	1.24E-07	1.42E-08	2.17E-08	0.24	500	24	0.24	0.00	0.00
1.23E+00	3.87E+04	2.12E-14	1.17E-15	4.33E-14	2.62E-14	-1.02E-15	4.54E-15	2.00E-07	3.19E-08	4.07E-07	2.54E-07	-9.59E-09	4.27E-08	0.24	500	24	0.24	0.00	0.00
	CS_NG_EXP14																		
4.40E+00	1.38E+05	2.38E-14	1.21E-15	3.42E-15	2.52E-14	9.69E-15	4.72E-15	6.25E-08	9.90E-09	9.01E-09	6.62E-08	2.55E-08	1.30E-08	0.10	500	24	0.10	0.00	0.00
7.33E+00	1.30E+05	1.81E-14	1.17E-15	-4.49E-14	2.58E-14	-3.93E-15	4.77E-15	5.08E-08	8.30E-09	-1.26E-07	7.49E-08	-1.10E-08	1.35E-08	0.10	500	24	0.10	0.00	0.00
1.11E+01	1.97E+05	2.36E-14	1.16E-15	3.10E-14	2.59E-14	-1.18E-15	4.50E-15	4.36E-08	6.88E-09	5.73E-08	4.86E-08	-2.18E-09	8.32E-09	0.10	500	24	0.10	0.00	0.00
1.10E+01	1.94E+05	2.46E-14	1.14E-15	-3.44E-14	2.44E-14	7.28E-15	4.56E-15	4.62E-08	7.26E-09	-6.47E-08	4.69E-08	1.37E-08	8.82E-09	0.10	500	24	0.10	0.00	0.00
1.73E+01	1.36E+05	2.17E-14	1.17E-15	-4.12E-16	3.14E-14	4.04E-15	4.52E-15	5.83E-08	9.29E-09	-1.11E-09	8.41E-08	1.08E-08	1.22E-08	0.10	500	24	0.10	0.00	0.00
2.52E+01	1.98E+05	1.78E-14	1.17E-15	5.89E-14	2.43E-14	2.90E-15	4.64E-15	3.28E-08	5.36E-09	1.08E-07	4.75E-08	5.32E-09	8.55E-09	0.10	500	24	0.10	0.00	0.00
	CS_NG_EXP15																		
1.46E+01	1.15E+05	1.11E-14	1.15E-15	9.82E-15	2.47E-14	-5.61E-15	4.47E-15	3.50E-08	6.38E-09	3.11E-08	7.85E-08	-1.78E-08	1.44E-08	0.06	500	24	0.06	0.00	0.00
2.68E+01	2.11E+05	1.71E-14	1.20E-15	2.91E-15	2.45E-14	3.24E-15	4.57E-15	2.95E-08	4.88E-09	5.02E-09	4.22E-08	5.59E-09	7.93E-09	0.06	500	24	0.06	0.00	0.00
8.73E+00	2.74E+05	2.12E-14	1.16E-15	-1.68E-14	2.46E-14	1.26E-14	4.76E-15	2.81E-08	4.48E-09	-2.23E-08	3.29E-08	1.67E-08	6.80E-09	0.06	500	24	0.06	0.00	0.00
1.53E+01	2.70E+05	1.80E-14	1.16E-15	6.23E-14	2.46E-14	3.08E-16	4.54E-15	2.43E-08	3.96E-09	8.38E-08	3.53E-08	4.14E-10	6.11E-09	0.06	500	24	0.06	0.00	0.00
1.22E+01	2.16E+05	1.06E-14	1.29E-15	4.97E-14	2.44E-14	1.24E-14	5.03E-15	1.79E-08	3.45E-09	8.38E-08	4.31E-08	2.09E-08	9.04E-09	0.06	500	24	0.06	0.00	0.00
7.49E+00	1.32E+05	2.67E-15	1.20E-15	2.57E-14	2.46E-14	-6.05E-16	4.52E-15	7.34E-09	3.48E-09	7.05E-08	6.85E-08	-1.66E-09	1.24E-08	0.06	500	24	0.06	0.00	0.00
	muscovite																		
	CS_NG_EXP2																		
7.32E+00	2.30E+05	2.09E-13	4.02E-15	2.38E-15	1.01E-14	7.56E-15	1.01E-15	3.24E-07	4.89E-08	3.69E-09	1.57E-08	1.17E-08	2.36E-09	1.38	450	43	0.46	0.46	0.46
1.41E+01	4.42E+05	3.68E-13	3.75E-15	1.20E-14	1.01E-14	9.75E-15	1.00E-15	2.97E-07	4.47E-08	9.68E-09	8.25E-09	7.88E-09	1.43E-09	1.38	450	43	0.46	0.46	0.46
4.95E+00	2.94E+05	2.62E-13	3.64E-15	2.14E-14	1.06E-14	5.09E-15	1.03E-15	3.18E-07	4.79E-08	2.60E-08	1.34E-08	6.18E-09	1.55E-09	1.38	450	43	0.46	0.46	0.46
6.47E+00	3.85E+05	3.79E-13	3.83E-15	-3.66E-15	9.94E-15	8.35E-15	1.02E-15	3.52E-07	5.29E-08	-3.40E-09	9.25E-09	7.75E-09	1.50E-09	1.38	450	43	0.46	0.46	0.46
1.33E+01	7.91E+05	5.61E-13	3.79E-15	1.53E-14	1.00E-14	1.66E-14	1.01E-15	2.54E-07	3.81E-08	6.91E-09	4.64E-09	7.51E-09	1.21E-09	1.38	450	43	0.46	0.46	0.46
1.66E+01	9.86E+05	7.66E-13	4.92E-15	-4.59E-15	1.04E-14	3.65E-14	1.01E-15	2.77E-07	4.16E-08	-1.66E-09	3.77E-09	1.32E-08	2.02E-09	1.38	450	43	0.46	0.46	0.46
1.50E+01	8.91E+05	5.86E-13	4.16E-15	3.00E-14	1.09E-14	2.92E-14	1.00E-15	2.35E-07	3.53E-08	1.20E-08	4.73E-09	1.17E-08	1.80E-09	1.38	450	43	0.46	0.46	0.46
1.59E+01	9.47E+05	6.30E-13	3.71E-15	1.03E-14	1.02E-14	2.14E-14	1.00E-15	2.37E-07	3.56E-08	3.88E-09	3.89E-09	8.09E-09	1.27E-09	1.38	450	43	0.46	0.46	0.46
8.94E+00	1.12E+06	7.29E-13	5.09E-15	2.65E-14	1.05E-14	2.71E-14	1.03E-15	2.32E-07	3.48E-08	8.44E-09	3.59E-09	8.62E-09	1.33E-09	1.38	450	43	0.46	0.46	0.46
8.42E+00	1.06E+06	7.60E-13	4.34E-15	1.08E-14	1.15E-14	2.33E-14	1.01E-15	2.57E-07	3.85E-08	3.64E-09	3.93E-09	7.87E-09	1.23E-09	1.38	450	43	0.46	0.46	0.46
4.63E+00	5.82E+05	5.11E-13	4.75E-15	1.19E-14	1.01E-14	1.21E-14	1.03E-15	3.13E-07	4.71E-08	7.30E-09	6.30E-09	7.41E-09	1.28E-09	1.38	450	43	0.46	0.46	0.46
	CS_NG_EXP7																		
1.23E+01	7.30E+05	7.32E-13	4.15E-15	2.30E-14	1.04E-14	2.89E-14	1.01E-15	3.58E-07	5.38E-08	1.13E-08	5.38E-09	1.41E-08	2.18E-09	1.36	600	68	0.45	0.45	0.45
4.78E+00	2.84E+05	3.01E-13	3.70E-15	4.42E-15	1.07E-14	6.67E-15	1.01E-15	3.78E-07	5.70E-08	5.56E-09	1.35E-08	8.40E-09	1.79E-09	1.36	600	68	0.45	0.45	0.45
8.24E+00	4.90E+05	5.14E-13	4.18E-15	1.18E-14	1.02E-14	3.36E-14	1.02E-15	3.75E-07	5.63E-08	8.62E-09	7.57E-09	2.45E-08	3.75E-09	1.36	600	68	0.45	0.45	0.45
1.19E+01	7.08E+05	7.05E-13	4.35E-15	1.79E-14	1.09E-14	2.75E-14	1.00E-15	3.56E-07	5.34E-08	9.06E-09	5.68E-09	1.39E-08	2.15E-09	1.36	600	68	0.45	0.45	0.45
8.06E+00	4.79E+05	4.94E-13	4.79E-15	3.27E-14	1.06E-14	8.79E-14	1.07E-15	3.69E-07	5.54E-08	2.44E-08	8.74E-09	6.55E-08	9.86E-09	1.36	600	68	0.45	0.45	0.45
7.85E+00	4.67E+05	4.90E-13	3.71E-15	2.45E-14	9.96E-15	1.47E-14	1.00E-15	3.75E-07	5.64E-08	1.87E-08	8.12E-09	1.12E-08	1.85E-09	1.36	600	68	0.45	0.45	0.45
4.25E+00	2.52E+05	2.79E-13	3.76E-15	8.84E-15	1.02E-14	6.90E-15	1.01E-15	3.94E-07	5.94E-08	1.25E-08	1.45E-08	9.75E-09	2.04E-09	1.36	600	68	0.45	0.45	0.45
	CS_NG_EXP13																		
2.12E+00	1.26E+05	2.99E-14	7.18E-16	-1.83E-14	2.22E-14	-3.67E-15	2.23E-14	8.48E-08	1.29E-08	-5.21E-08	6.36E-08	-1.04E-08	6.34E-08	0.24	500	24	0.24	0.00	0.00
2.19E+00	1.30E+05	3.36E-14	8.89E-16	-7.60E-15	2.16E-14	-3.04E-14	1.80E-14	9.22E-08	1.40E-08	-2.09E-08	5.93E-08	-8.36E-08	5.11E-08	0.24	500	24	0.24	0.00	0.00
7.70E+00	1.36E+05	2.00E-14	6.85E-16	-1.35E-14	2.19E-14	1.23E-14	1.71E-14	5.25E-08	8.08E-09	-3.54E-08	5.77E-08	3.22E-08	4.52E-08	0.24	500	24	0.24	0.00	0.00
1.02E+01	6.07E+05	7.17E-14	1.27E-15	6.75E-15	2.52E-14	-2.16E-14	1.30E-14	4.22E-08	6.37E-09	3.97E-09	1.49E-08	-1.27E-08	7.90E-09	0.24	500	24	0.24	0.00	0.00
3.32E+00	1.97E+05	3.43E-14	1.32E-15	3.44E-14	2.52E-14	3.98E-15	5.64E-15	6.20E-08	9.61E-09	6.22E-08	4.65E-08	7.21E-09	1.03E-08	0.24	500	24	0.24	0.00	0.00
2.63E+00	1.56E+05	3.02E-14	1.22E-15	-3.72E-14	2.49E-14	1.87E-14	4.99E-15	6.90E-08	1.07E-08	-8.50E-08	5.82E-08	4.27E-08	1.31E-08	0.24	500	24	0.24	0.00	0.00
9.77E-01	5.80E+04	2.03E-14	1.37E-15	8.80E-15	2.58E-14	1.46E-15	4.55E-15	1.25E-07	2.05E-08	5.42E-08	1.59E-07	9.00E-09	2.81E-08	0.24	500	24	0.24	0.00	0.00
7.89E-01	4.69E+04	1.58E-14	1.23E-15	-9.62E-15	2.46E-14	1.39E-14	4.88E-15	1.20E-07	2.03E-08	-7.33E-08	1.87E-07	1.06E-07	4.04E-08	0.24	500	24	0.24	0.00	0.00
	CS_NG_EXP14																		

2.02E+00	1.20E+05	2.25E-14	1.26E-15	-3.99E-15	2.58E-14	8.25E-15	4.98E-15	6.70E-08	1.07E-08	-1.19E-08	7.69E-08	2.46E-08	1.53E-08	0.10	500	24	0.10	0.00	0.00	
6.78E+00	2.13E+05	1.92E-14	1.37E-15	-1.50E-14	2.45E-14	8.06E-15	4.68E-15	3.21E-08	5.34E-09	-2.51E-08	4.13E-08	1.35E-08	8.10E-09	0.10	500	24	0.10	0.00	0.00	
2.96E+00	9.30E+04	1.02E-14	1.24E-15	-3.75E-14	2.54E-14	2.36E-14	5.07E-15	3.93E-08	7.57E-09	-1.44E-07	9.99E-08	9.07E-08	2.38E-08	0.10	500	24	0.10	0.00	0.00	
2.35E+00	1.39E+05	1.73E-14	1.17E-15	-5.59E-14	2.62E-14	3.28E-15	4.65E-15	4.42E-08	7.29E-09	-1.43E-07	7.04E-08	8.39E-09	1.20E-08	0.10	500	24	0.10	0.00	0.00	
3.20E+00	1.90E+05	2.31E-14	1.15E-15	3.77E-14	2.48E-14	8.32E-15	4.79E-15	4.34E-08	6.86E-09	7.09E-08	4.78E-08	1.56E-08	9.31E-09	0.10	500	24	0.10	0.00	0.00	
8.99E-01	5.34E+04	1.10E-14	1.14E-15	-9.62E-15	2.50E-14	3.66E-15	5.04E-15	7.34E-08	1.34E-08	-6.44E-08	1.67E-07	2.45E-08	3.40E-08	0.10	500	24	0.10	0.00	0.00	
1.84E+00	1.09E+05	1.56E-14	1.15E-15	-1.27E-14	3.00E-14	-1.26E-14	5.08E-15	5.09E-08	8.51E-09	-4.15E-08	9.82E-08	-4.12E-08	1.77E-08	0.10	500	24	0.10	0.00	0.00	
1.80E+00	1.07E+05	1.49E-14	1.16E-15	2.75E-14	2.47E-14	5.39E-15	4.94E-15	4.99E-08	8.43E-09	9.18E-08	8.38E-08	1.80E-08	1.67E-08	0.10	500	24	0.10	0.00	0.00	
	CS_NG_EXP15																			
8.68E+00	2.73E+05	9.23E-15	7.11E-16	2.63E-15	2.23E-14	-1.72E-14	1.63E-14	1.21E-08	2.04E-09	3.45E-09	2.92E-08	-2.25E-08	2.17E-08	0.06	500	24	0.06	0.00	0.00	
1.25E+01	3.93E+05	1.02E-14	6.67E-16	-2.09E-14	2.24E-14	-2.54E-14	2.09E-14	9.27E-09	1.52E-09	-1.90E-08	2.06E-08	-2.31E-08	1.93E-08	0.06	500	24	0.06	0.00	0.00	
1.16E+01	6.91E+05	1.44E-14	7.87E-16	6.58E-14	2.28E-14	1.87E-14	2.62E-14	7.44E-09	1.19E-09	3.40E-08	1.28E-08	9.66E-09	1.36E-08	0.06	500	24	0.06	0.00	0.00	
8.34E+00	4.95E+05	1.27E-14	8.68E-16	-4.21E-14	2.45E-14	1.64E-15	2.92E-14	9.14E-09	1.51E-09	-3.04E-08	1.82E-08	1.18E-09	2.10E-08	0.06	500	24	0.06	0.00	0.00	
4.57E+00	2.71E+05	1.34E-14	6.89E-16	-1.48E-14	2.50E-14	-6.85E-14	3.84E-14	1.76E-08	2.79E-09	-1.94E-08	3.30E-08	-9.01E-08	5.23E-08	0.06	500	24	0.06	0.00	0.00	
4.64E+00	2.76E+05	1.05E-14	7.29E-16	1.67E-14	2.19E-14	3.34E-14	2.62E-14	1.36E-08	2.25E-09	2.16E-08	2.86E-08	4.33E-08	3.46E-08	0.06	500	24	0.06	0.00	0.00	
2.83E+00	1.68E+05	1.21E-14	6.99E-16	1.62E-14	2.21E-14	5.71E-14	1.78E-14	2.58E-08	4.14E-09	3.44E-08	4.73E-08	1.21E-07	4.20E-08	0.06	500	24	0.06	0.00	0.00	
9.07E-01	5.39E+04	4.26E-15	7.30E-16	1.44E-14	2.17E-14	-1.98E-14	1.62E-14	2.83E-08	6.43E-09	9.55E-08	1.45E-07	-1.31E-07	1.09E-07	0.06	500	24	0.06	0.00	0.00	
2.04E+00	1.21E+05	6.64E-15	7.30E-16	2.08E-14	2.21E-14	2.13E-14	1.67E-14	1.95E-08	3.63E-09	6.11E-08	6.57E-08	6.26E-08	4.99E-08	0.06	500	24	0.06	0.00	0.00	
1.92E+00	1.14E+05	6.84E-15	7.47E-16	3.91E-15	2.18E-14	-1.87E-14	1.68E-14	2.14E-08	3.97E-09	1.22E-08	6.82E-08	-5.84E-08	5.33E-08	0.06	500	24	0.06	0.00	0.00	
2.71E+00	1.61E+05	8.77E-15	6.73E-16	2.13E-14	2.17E-14	5.02E-14	1.58E-14	1.94E-08	3.27E-09	4.72E-08	4.86E-08	1.11E-07	3.88E-08	0.06	500	24	0.06	0.00	0.00	
	CS_NG_EXP16																			
1.69E+00	1.00E+05	1.29E-13	1.19E-15	7.26E-15	2.49E-14	1.03E-16	4.62E-15	4.58E-07	6.89E-08	2.59E-08	8.86E-08	3.67E-10	1.64E-08	0.80	500	24	0.80	0.00	0.00	
8.84E-01	5.25E+04	7.78E-14	1.29E-15	1.38E-15	2.92E-14	1.74E-15	5.23E-15	5.29E-07	7.99E-08	9.38E-09	1.99E-07	1.18E-08	3.56E-08	0.80	500	24	0.80	0.00	0.00	
1.99E+00	1.18E+05	3.35E-13	1.34E-15	-2.50E-14	2.61E-14	-2.13E-14	4.75E-15	1.01E-06	1.52E-07	-7.56E-08	7.98E-08	-6.45E-08	1.73E-08	0.80	500	24	0.80	0.00	0.00	not used
1.21E+00	7.17E+04	9.15E-14	1.31E-15	8.54E-15	2.47E-14	1.08E-14	4.54E-15	4.56E-07	6.86E-08	4.25E-08	1.23E-07	5.39E-08	2.40E-08	0.80	500	24	0.80	0.00	0.00	
2.69E+00	8.46E+04	6.99E-14	1.19E-15	-7.83E-15	2.52E-14	5.92E-15	4.61E-15	2.95E-07	4.46E-08	-3.31E-08	1.06E-07	2.50E-08	1.98E-08	0.80	500	24	0.80	0.00	0.00	
4.08E+00	1.28E+05	7.78E-14	1.61E-15	-6.04E-15	2.49E-14	3.99E-15	4.66E-15	2.17E-07	3.28E-08	-1.68E-08	6.93E-08	1.11E-08	1.31E-08	0.80	500	24	0.80	0.00	0.00	
1.01E+00	6.03E+04	8.11E-14	1.37E-15	2.66E-15	2.46E-14	-8.05E-15	5.75E-15	4.81E-07	7.26E-08	1.57E-08	1.46E-07	-4.77E-08	3.48E-08	0.80	500	24	0.80	0.00	0.00	
1.54E+00	9.14E+04	1.05E-13	1.14E-15	1.34E-14	2.64E-14	1.52E-16	4.96E-15	4.11E-07	6.18E-08	5.24E-08	1.03E-07	5.93E-10	1.94E-08	0.80	500	24	0.80	0.00	0.00	
1.85E+00	1.10E+05	1.24E-13	1.27E-15	3.44E-14	2.49E-14	8.53E-15	4.57E-15	4.02E-07	6.05E-08	1.12E-07	8.28E-08	2.78E-08	1.55E-08	0.80	500	24	0.80	0.00	0.00	

Supplementary Table 2: Diffusion Coefficients					
Experiment	Phase	D ($m^2 s^{-1}$)	D uncert. +	D uncert. +	temp. (˚C)
helium					
CS_NG_EXP13	muscovite	1.35E-16	2.08E-16	7.94E-17	500
CS_NG_EXP13	F-phlogopite	3.35E-16	1.99E-16	1.43E-16	500
CS_NG_EXP14	muscovite	9.33E-17	2.84E-16	6.42E-17	500
CS_NG_EXP14	F-phlogopite	2.48E-15	1.90E-14	1.72E-15	500
CS_NG_EXP15	muscovite	1.12E-16	2.65E-16	8.32E-17	500
CS_NG_EXP16	muscovite	1.71E-17	5.53E-18	4.17E-18	500
argon					
EHPV_NG_EXP32	beryl	1.23E-19	1.65E-19	5.99E-20	750
EHPV_NG_EXP32	cordierite	1.86E-18	6.50E-19	6.03E-19	750
EHPV_NG_EXP43	beryl	3.89E-19	2.87E-19	1.26E-19	800

CHAPTER 4: Visible-Infrared spectral properties of iron-bearing aluminate spinel under lunar-like redox conditions

Colin R.M. Jackson[1], Leah C. Cheek[2], Kelsey B. Williams[1], Kerri Donaldson Hanna[3], Carle M. Pieters[1], Stephen W. Parman[1], Reid F. Cooper[1], Darby Dyar[4], Melissa Nelms[4], Mark R. Salvatore[5]

1 Geological Sciences, Brown University, Providence, RI 02912
2 Department of Astronomy, University of Maryland, College Park, MD 20842
3 Department of Physics, Oxford University, Oxford, UK
4 Department of Astronomy, Mount Holyoke College, South Hadley, MA, 01075
5 School of Earth and Space Exploration, Arizona State University, Tempe, AZ, 85287

Submitted to American Mineralogist, Lunar Highland Special Issue:
October 10, 2013

Revised:
March 6, 2014

Currently under review

Title: Visible-Infrared Spectral Properties of Iron-bearing Aluminate Spinel Under Lunar-like Redox Conditions

Authors: Colin R.M. Jackson, Leah C. Cheek, Kelsey B. Williams, Kerri Donaldson Hanna, Carle M. Pieters, Stephen W. Parman, Reid F. Cooper, Darby Dyar, Melissa Nelms, Mark R. Salvatore

Abstract: Remote sensing observations have identified aluminate spinel, in the absence of measureable olivine and pyroxene, as a globally distributed component of the lunar crust. Earlier remote sensing observations and returned samples did not indicate the presence of this component, leaving its geologic significance unclear. Here, we report visible to mid-infrared (V-IR) reflectance (300-25000 nm) and Mössbauer spectra of aluminate spinels, synthesized at lunar-like oxygen fugacity (fO_2), that vary systematically in Fe abundance. Reflectance spectra of particulate (<45 μm), nominally stoichiometric aluminate spinels display systematic behavior, with bands at 700, 1000, 2000, and 2800 nm increasing in strength with increasing bulk Fe content. The especially strong bands at 2000 and 2800 are discernible for all spinel compositions and saturate at <15 Fe# (Fe/(Mg+Fe)×100, molar). Absorption bands at 700 and 1000 nm, collectively referred to as the 1000 nm bands, are weaker and become observable at >6 Fe#. Although the 2000 and 2800 nm bands are assigned to Fe_{IV}^{+2} electronic transitions, spectra of aluminate spinels with excess Al_2O_3 demonstrate that the strengths of the 1000 nm bands are related to the abundance of Fe_{VI}^{+2}. The abundance of Fe_{VI}^{+2} depends on bulk Fe content as well as factors that control the degree of structural order-disorder, such as

cooling rate. Consequently the strength of the 1000 nm bands are useful for constraining the Fe content and cooling rate of remotely sensed spinel. Controlling for cooling rate, particle size, and fO_2, we conclude that spinels with >12 Fe# (<88 Mg#) have observable 1000 nm bands under ambient lunar conditions and that only very Mg-rich spinels lack 1000 nm bands in their spectra. This links remote observations of spinel anorthosite to Mg-Suite magmatism. The combined effects of Fe oxidation state, abundance of co-existing plagioclase, and space weathering have not been explored here, and may add additional constraints. The relative strengths of the distinctive 1000 and 2000 nm bands of the spinels associated with pyroclastic deposits at Sinus Aestuum suggest fast cooling rates, possibly in the absence of an extensive vapor cloud.

1.0 Introduction

Recent observations by the Moon Mineralogy Mapper (M^3) and SELENE Spectral Profiler have identified aluminate spinel (i.e. $(Mg,Fe)Al_2O_4$-rich spinel) in exposures distributed globally across the lunar surface (Pieters et al., 2011; Dhingra et al., 2011; Dhingra and Pieters, 2011; Bhattacharya et al., 2012; Kaur et al., 2012; Lal et al., 2012; Yamamoto et al., 2013; Pieters et al., 2014). These identifications are based on the occurrence of strong absorption bands near 2000 and 2800 nm in reflectance spectra that are diagnostic of ferrous iron situated in tetrahedral coordination (i.e. Fe_{IV}^{+2}) within a spinel lattice (e.g. Cloutis et al., 2004). In many of these identifications aluminate spinel is the only observable mineral using visible to near-infrared (V-NIR) remote sensing techniques, suggesting low proportions of the mafic silicates. Analogous materials with

aluminate spinel as the dominant Fe-bearing phase have not been found in lunar samples from the Apollo and Luna missions, nor in lunar meteorites, leaving the petrogenesis and geologic significance of these new observations unclear.

Distinguishing between various new formation hypotheses (discussed below) for these spinel-bearing materials is challenging without information about the composition of the observed spinels. In particular, estimates of spinel Fe# (Fe/(Mg+Fe)×100, molar, 100-Mg#) are useful for constraining the composition of parental liquids involved in their formation. Importantly, laboratory analyses of spinel V-NIR spectra have shown that while strong absorptions at wavelengths >2000 nm are common for nearly all spinel compositions (and are therefore useful for spinel identification), additional absorptions at <1000 nm may also be apparent only for spinel with more than a few weight percent Fe (Cloutis et al., 2004). Thus, observations of V-NIR characteristics near 1000 nm in spinel spectra may provide significant leverage for estimating spinel Fe#. However, the specific causes of the <1000 nm absorptions and the nature of their dependence on Fe# have remained difficult to define and are the focus of the current work.

Here, we present a coordinated analysis of <1000 nm absorption strengths and Fe# using spinel samples that are synthesized at lunar-like conditions. This work builds upon the study by Cloutis et al. (2004) that characterized spectra of natural terrestrial spinels and aims to better resolve the observed relationship between spinel spectral characteristics and mineral composition. Specifically, we 1) analyze the change in absorption strengths for spinels of various bulk Fe contents produced under identical conditions, and 2) characterize these results in terms of other factors (Al_2O_3 activity, cooling rate) that control the partitioning of Fe between the octahedral and tetrahedral

crystallographic sites. This dataset, in combination with theoretical considerations, serves as a basis to constrain the Fe content and cooling rate of spinels recently identified in remotely sensed data. This information provides additional context for petrogenetic hypotheses regarding spinel deposits and additional insight into the magmatic history of the Moon.

1.1 Origin of spinel V-NIR absorptions

The dominant features in spectra of normal spinels are the strong 2000 and 2800 nm absorptions owing to Fe_{IV}^{+2} (e.g. Cloutis et al., 2004). However, crystal field theory also predicts that Fe_{VI}^{+2} should generate absorption bands near 1000 nm associated with a $^5T_2$-^5E electron transition (e.g. Mao and Bell, 1975; Dickson and Smith, 1976). Similarly, crystal field theory predicts Fe_{IV}^{+2} is responsible for a series of bands near 700 nm (Gaffney, 1973; Mao and Bell, 1975). A study of absorption properties of synthetic aluminate spinel, however, produced linear correlations between the product of octahedral divalent and trivalent Fe concentration ($[Fe_{VI}^{+2}]\times[Fe_{VI}^{+3}]$) and the net linear extinction coefficients at ~700 and ~1000 nm (Halenius et al., 2002). These observations, in combination with the general spectral shape and band positions, were used to argue that the bands at ~700 and 1000 nm are caused by exchanged-coupled pair transitions and intervalence charge transfers, respectively. More recently, it has been argued that bands at ~700 and 1000 nm are caused by spin-forbidden transitions of Fe_{VI}^{+3} based on observed pressure and temperature systematics of spinel spectra (Taran et al., 2005). Importantly, the strength of bands near 1000 nm in the latter two mechanisms

depends on the abundance of Fe^{+3}, which is relatively scarce given the reduced nature of lunar rocks (e.g. Sato et al., 1973; Delano, 1990; Fogel and Rutherford, 1995; Karner et al., 2006). Thus, lunar spinels may require relatively large concentrations of total Fe in order to generate prominent bands near 1000 nm. Moreover, $[Fe_{VI}^{+2}]$ is related the degree of ordering in spinel (e.g. Harrison et al., 1998), which is uncertain for remotely sensed samples. Thus, a primary objective of this study is to determine the V-IR (300-25000 nm) spectral properties of synthetic spinel under the environmental conditions (e.g. fO_2 and cooling rate) applicable to the Moon.

1.2 Remote identifications of spinel on the Moon

Aluminate spinel identifications on the Moon can be divided into two general categories, here termed Group 1 and Group 2, based on observed geologic context and V-NIR characteristics. Group 1 identifications are associated with basin walls or large craters (see summary in Pieters et al., 2014). These structural units are thought to represent materials uplifted from significant depth (Cintala and Grieve, 1998), suggesting an origin related to the deep crust. Characteristic spectra of Group 1 lithologies display a strong absorption centered at 2000 nm but little to no associated structure at shorter wavelengths in the V-NIR spectral range (500-1000 nm). Olivine and pyroxene have characteristic absorption bands near 1000 nm (Burns, 1970; Adams, 1974), suggesting mafic silicates are absent or are only a minor component of these aluminate spinel-bearing units. Spinel can also absorb radiation near 1000 nm, but such spectral features are associated with relatively high Fe/Mg and/or Cr/Al ratios (Cloutis et al., 2004). Thus,

the lack of absorption features near 1000 nm suggests the spinel-bearing rock observed in Group 1 is a Mg-rich, Fe-poor aluminate spinel anorthosite. The presence of plagioclase is supported by the relatively high albedo the regions associated with Group 1 and the observation that their surrounding host material is highly anorthositic (Pieters et al., 2014).

Group 2 identifications are associated with dark mantle deposits (DMDs) at Sinus Aestuum (Sunshine et al., 2010, Yamamoto et al., 2013). It is hypothesized that these spinels were transported to the lunar surface through pyroclastic eruptions and are not associated with impact structures. Characteristic V-NIR spectra of Group 2 are distinctive from Group 1. Specifically, the continuum-corrected spectra of spinels associated with the DMDs of Sinus Aestuum have a doublet absorption band, with minima near 700 and 1000 nm, in addition to a prominent band centered near 2000 nm. The doublet band at shorter wavelengths is associated with aluminate spinels that are relatively rich in Fe (e.g. Cloutis et al., 2004), suggesting that the DMD spinels of Sinus Aestuum are distinctly richer in Fe compared to the spinels associated with Group 1 (Yamamoto et al., 2013).

Following the identification of aluminate spinel associated with basin walls and large craters (Group 1), several hypotheses for the formation of spinel anorthosite have been advanced. These include fractional crystallization-assimilation of anorthositic country rock by picritic liquids (Gross and Treiman, 2011), reaction between Mg-Suite parental liquids and anorthositic crust (Prissel et al., 2014), and fractional crystallization of a plagioclase-rich impact melt (Vaughan et al., 2013). Group 1 spinel deposits have also been proposed to be possibly exogenic, derived from relatively slow colliding

impactors (Yue et al., 2013). The aluminate spinels associated with DMDs (Group 2) have been proposed to be derived from fire-fountain eruptions of relatively Fe-rich picritic liquids with high normative plagioclase as a result of melt-wallrock interactions in the lunar crust (Yamamoto et al., 2013). Evaluating formation hypotheses requires a systematic understanding of the major controls on spinel absorption characteristics in order to place compositional constraints on these spinel-bearing materials. Toward this goal, the current work focuses on a detailed characterization of 1000 nm absorption band strengths as a function of both Fe# as well as partitioning of Fe among different crystallographic sites.

2.0 Methods

2.1 Mineral synthesis

Three series of spinels were synthesized: (1) FeSp6, which investigates the effect of varying Fe#, (2) FeSp8, which incorporates excess alumina, and (3) FeSp10, which tests the effect of cooling rate on spectral properties. The Fe# series (FeSp6) is the primary focus of this work, whereas the cooling rate experiment (FeSp10) consists of one sample and is intended to demonstrate the effects of partitioning between different crystallographic sites. The series investigating the effects of excess alumina (FeSp8) also characterizes the effects of partitioning, but, more importantly, is used to demonstrate that the <1000 nm bands in spinel are related to [Fe^{+2}_{VI}].

For the FeSp6 series, reagent grade oxides (MgO, Fe_2O_3, and Al_2O_3) were mixed in stoichiometric proportions to form aluminate spinel. Ten different starting compositions were produced that vary systematically in Fe# from ~0 to 32. Oxides were homogenized using an agate mortar and pestle under ethanol. The dry powders were mixed with polyvinyl alcohol to provide additional binding strength and then pressed into 1 cm diameter compacts (~1 cm height). Compacts were then placed on a bed of zirconia beads (~1 mm in diameter) contained by an alumina boat and loaded into a horizontal gas-mixing furnace. Sintering durations were 72 hours and temperatures were 1450°C. Oxygen fugacity was fixed by streaming a CO-CO_2 mixture through the furnace. The necessary CO/CO_2 ratio for a given fO_2 was determined using yittra-doped zirconia fO_2 sensor, but fO_2 was not actively monitored for the duration of sintering. After sintering, the temperature was ramped down to room temperature over approximately 6 hours, for an integrated cooling rate of ~$5x10^{-2}$ °C s^{-1}.

The FeSp8 series was produced following the same procedure as above, using surplus powder from select FeSp6 starting compositions with additional Al_2O_3 (2.5-7.5 wt. %) added to document the effect of point defect chemistry on V-NIR spectra (see V-NIR $a Al_2O_3$ section). The stoichiometry calculated for the FeSp8 spinels supports presence of excess Al_2O_3 in FeSp8 spinels (Appendix Table 1). The FeSp10 series is comprised of a single experiment that was conducted using a vertical gas-mixing furnace configured for rapid quenching of samples. In this furnace, a compact is suspended in the hotspot by platinum (Pt) hooks and a Pt basket. The sample is drop quenched in water by passing a current through and melting a thin Pt wire that connects the basket and hooks. The starting oxides for the FeSp10 compact were taken from surplus FeSp6_11 powders.

Duration and fO_2 were the same as for the FeSp6 and FeSp8 experiments, but temperature was 1400 °C. Fragments of the sintered compacts were mounted for major element analysis by electron microprobe, and the remainder was crushed and dry sieved into particle size separates for V-IR, Mössbauer, and Flux Fusion analysis. Particle size separate were <45 μm, 45-75 μm, 75-125 μm.

2.2 Electron microprobe analysis

Major element compositions of the sintered spinels were determined using an electron microprobe (Cameca SX-100, Brown University). Analyses were completed using wavelength dispersive spectrometry, and the PAP correction was applied. The analytical parameters were 15 kV, 20 nA, and a focused beam. Counting times on all elements were 45 seconds, excepting Fe (90 seconds). Internal standards of a stoichiometric spinel *sensu stricto* (*ss*, $MgAl_2O_4$) and Fe-bearing spinel were analyzed between samples to correct for any drift over the course of the analytical sessions. Spot locations were distributed throughout each sample to document any compositional heterogeneity.

2.3 Flux Fusion analysis

Inductively coupled plasma-atomic emission spectroscopy (ICP-AES) was utilized to measure the bulk chemistry of the FeSp6 series spinels in a fashion similar to that described in Murray et al. (2000). Forty milligram sample aliquots were sieved to

particle sizes < 125 μm and combined with a flux composed of 160 mg $LiBO_2$. The mixture was then fused for 15 minutes at 1050 ºC; because of the high melting temperature of spinel and the absence of volatile components, the fusion duration was extended from the traditional 10 minutes (as discussed in Murray et al., 2000) to 15 minutes. Following fusion, the melts were quenched in 20 mL of 10% HNO_3 and agitated for one hour. Over the hour duration the quench bead dissolved into the HNO_3 solution. The solutions were then filtered through 0.45 μm filters and diluted in additional 10% HNO_3 for analysis. A JY2000 Ultrace ICP Atomic Emission Spectrometer was used to perform elemental analyses on the diluted samples and analyzed for Al, Ca, Cr, Fe, Mg, Ni, Si, and Ti using a Gaussian peak search technique. Intensity measurements were calibrated and converted to geologically relevant units using a series of blanks and geochemical standards that were processed simultaneously and in the same fashion as the samples. All samples, standards, and blanks were run in duplicate, at minimum, to increase the robustness of the measurements and to ensure the reproducibility of the results.

Six replicates of FeSp6_10 were measured to provide an estimate of the precision of our flux fusion analysis. The average Fe# for FeSp6_10 was 25.06 ± 0.28 % (95% confidence). Average yield on all flux fusion analyses was 97.63 ± 8.78 % (95% confidence), neglecting a single outlier (outlier yield = 69.0 %), indicating complete or nearly complete dissolution of the spinel into the flux. The outlier Fe# (10.25 Fe#) is similar to the duplicate Fe# (10.26 Fe#) run on the same sample.

2.4 Reflectance spectroscopy

In preparation for the reflectance measurements, samples were dry sieved to a uniform particle size of <45 μm and loaded into 9-mm diameter Teflon-coated sample dishes. Reflectance spectra were acquired in RELAB at Brown University using both the Bidirectional Reflectance spectrometer (BDR) (300 – 2600 nm), which measures V-NIR wavelengths and the Thermo Nicolet Nexus 870 Fourier-Transform infrared spectrometer (FTIR) (800-25000 nm), which measures out to mid-infrared wavelengths. All BDR spectra were acquired with an incidence angle of 30° and a 0° emergence angle (Pieters and Hiroi, 2004). Following conventional RELAB procedures, the BDR and FTIR data were spliced near 1000 nm by adjusting the reflectance scale of the FTIR data to the BDR data using a multiplicative factor. The connecting wavelength was chosen so that the two spectra connect smoothly with similar inclinations. Larger particle size fractions (45-75 and 75-125 μm) were also measured for select samples. All reflectance spectra will be available through the RELAB archive.

The strengths of the V-NIR bands are expected to increase with increasing Fe abundance in the spinel, as described above. To measure this effect for the bands at 1000, 2000, and 2800 nm, the spectra for all samples were first scaled so that the reflectance maximum between 1000-2000 nm (determined by a polynomial fit) equaled one. This procedure effectively minimizes albedo variations among samples in order to facilitate comparison of band strengths, making a further continuum removal unnecessary. A second-degree polynomial was then fit, in a least squares sense, between 825-1100 nm, 1700-2200 nm, and 2700-3000 nm, and minimum reflectance value for each polynomial was identified. The minimum reflectance value for each polynomial is expected to

negatively correlate with the concentration of the cation species responsible for the band. The natural log of the reflectance minimum ($\ln(\text{reflectance}_{min})$) for each band was then calculated. We term the slope of proportionality between the natural log of the reflectance minimum and the concentration of the cation species responsible for the band a "reflectance coefficient."

Across the mid-infrared (mid-IR) spectral range (1250 – 400 cm^{-1} or 8000 – 25000 nm), radiation is commonly measured and reported in terms of emissivity, which can be approximated from our data by subtracting the measured reflectance values from one (Hapke, 1993). For the following discussions we report the mid-IR spectra in this way to facilitate comparison with previous laboratory studies. The primary spectral features in the mid-IR are 1) the Christiansen feature (CF), an emissivity maximum between ~900 – 1000 cm^{-1} (with a secondary CF between ~550 – 650 cm^{-1}) that is often diagnostic of mineralogy and average composition (Conel, 1969), and 2) the restsrahlen bands (RB), which occur between ~650 – 850 cm^{-1} and ~400 – 650 cm^{-1} and represent molecular vibrations related to stretching and bending motions. To determine the frequency (cm^{-1}) of these spectral features, a second degree polynomial was fit to each spectral feature in each spectrum following the approach used to calculate band positions in the V-NIR spectral region. For the CF, a polynomial was fit to a portion of the ~900 – 1000 cm^{-1} spectral range of each spectrum and the frequency of the maximum emissivity value in the polynomial fit was used to represent the CF position. The same method was used to find the position of the secondary CF in the ~550 – 650 cm^{-1} spectral range. Diagnostic absorptions in the RB are also fit to determine frequencies at which the emissivity minimum values are identified. The spectral range was varied in order to best

fit the emissivity and shape of each spectral feature for each sample spectrum. Due to the non-unique nature of identifying the spectral features using this methodology, the positions of spectral features can vary by ± 3 cm^{-1} as the spectral range and polynomial order are changed (Donaldson Hanna et al., 2012). In wavelength space, a ± 3 cm^{-1} error at ~7500 – 8000 nm equates to an error of ± 20 nm.

2.5 Mössbauer analysis

To determine the coordination state of Fe in each synthetic spinel sample, Mössbauer data were collected for all samples from the FeSp6 and FeSp8 series, with the exception of the nominally Fe-free FeSp6_1. Approximately 10-30 mg of each sample was mixed with sugar under acetone before mounting in a sample holder confined by Kapton® polyimide film tape. Mössbauer spectra were acquired at 22 ˚C using a WEB Research Co. model WT302 spectrometer (Mount Holyoke College) with a 100-60 mCi 57Co in Rh source. Results were calibrated against a 25 μm α-Fe foil. Spectra were collected in 2048 channels and corrected for nonlinearity via interpolation to a linear velocity scale, which is defined by the spectrum of the 25 μm Fe foil used for calibration. The WMOSS algorithm fits a straight line to the points defined by the published values of the Fe metal peak positions (as y values) and the observed positions in channels (x values). Data were then folded before fitting, using the WMOSS Auto-fold procedure that folds the spectrum about the channel value that produces the minimum least squares sum difference between the first half of the spectrum and the reflected second half of the spectrum.

For each sample, the fraction of the baseline due to the Compton scattering of 122 keV gammas by electrons inside the detector was determined by measuring the count rate with and without a 14.4-keV stop filter (~2 mm of Al foil) in the gamma beam. Compton-corrected absorption was calculated for each individual spectrum using the formulation A/(1 - b), where b is the Compton fraction and A is the uncorrected absorption. This correction does not change the results of the fits per se but does allow accurate determination of % absorption in the spectra. It is necessary because the range of energy deposited in the detector by Compton events extends from 0 keV to 40 keV, overlapping both the 14 keV and 2 keV energies deposited by the 14.4 keV gammas. Run times were 6-24 hours per spectrum, and baseline counts ranged from ~2.2 to 14.0 million after the Compton correction.

Spectra were fit with two or three Lorentzian doublets using the MEX_FielDD program acquired from the University of Ghent courtesy of E. DeGrave. Center shifts (CS, or δ), and quadrupole splittings (QS, or Δ) of the doublets were allowed to vary, and widths (full width at half maximum) of all four peaks were coupled to vary in pairs. Errors on center shift and quadrupole splitting of well-resolved peaks are usually $\pm$0.02 mm/s in natural samples (e.g., Skogby et al. 1992), though these can be reduced by use of consistent sample preparation, run conditions, and fitting procedures to $\pm$ 0.005 mm/s. Reproducibility (precision) of peak areas based on repeated fits using different constraints (δ, Δ, width, and areas constrained in all possible combinations of individual peaks and pairs) and fitting models (Lorentzian, Gaussian, quadrupole splitting distributions) are $\pm$ 0.3% absolute for these well-resolved spectra; accuracy has been determined in previous analogous studies of amphiboles to be $\pm$ 3-5% (Dyar, 1989).

3.0 Results

3.1 Sample descriptions and major element compositions

A backscattered image of a typical run product is shown in Figure 1. The samples contain both large scale porosity (~100 μm diameter) and small scale porosity (~1 μm diameter), as is typical for sintered products. Major element compositions of the synthesized spinels as determined by electron microprobe are provided in Appendix Table 1. The overwhelmingly dominant phase present is (Fe,Mg) aluminate spinel. Minor amounts of ferro-periclase were observed in some run products (noted in Appendix Table 1). Spot analysis showed some within-sample variability in the spinel Fe#, but this variability is minor compared to the full range of compositions synthesized (Appendix Table 1). Some electron microprobe analyses have low totals, presumably because the activated volume of spinel included a small porous component.

Flux fusion is a bulk analytical technique that averages out compositional heterogeneities and provides an effective composition for comparison with spectral signatures, which also represent bulk measurements. For this reason we choose to use the flux fusion determinations of Fe#, which are provided in Appendix Table 1, for inter-sample comparisons within the FeSp6 series. Absolute values of oxide abundances determined by flux fusion are not reported because the yields are deemed less reliable compared to electron microprobe analysis. For higher Fe samples, flux fusion and electron microprobe measurements agree in Fe# to within 20% and usually to within 10%

(Appendix Table 1). For the lowest Fe samples (<3 Fe#), the disagreement between the two techniques can be larger on a percent basis due to increased uncertainties at such low concentrations of the species of interest.

3.2 Mössbauer - Distribution of ferric iron

Halenius et al. (2002) demonstrated a linear dependence between the strength of 700 and 1000 nm bands and $[Fe_{VI}^{+2}]\times[Fe_{VI}^{+3}]$ in spinel, suggesting Fe_{VI}^{+3} also contributes to the strength of short wavelength bands in the V-NIR spectral range. A comparison of Group B and C V-NIR spectra from Cloutis et al. (2004) also provides evidence that Fe_{VI}^{+3} contributes to the strength of the 700 and 1000 nm bands. The abundance of Fe_{VI}^{+3} in spinel is positively related to the fO_2 of the system, suggesting the 1000 nm bands could be relatively weak in lunar spinels for a given bulk Fe content because the Moon is a reducing environment compared to Earth's uppermost mantle and crust (e.g. Delano, 1990; Fogel and Rutherford, 1995; Karner et al., 2006; Sato et al., 1973).

The spinels presented here were synthesized under low fO_2 that is directly applicable to the Moon (IW-1). The abundance of Fe_{VI}^{+3} was measured by Mössbauer spectroscopy for samples from the Fe# series (FeSp6) and the excess alumina series (FeSp8) (Appendix Table 2), allowing for an independent check that reducing experimental conditions were achieved. Measured Fe_{VI}^{+3}/Fe^{tot} are very low for all samples measured (Appendix Table 2). Neglecting FeSp6_2, Fe_{VI}^{+3}/Fe^{tot} varies between 0.1 and 0.03 for the FeSp6 series. FeSp6_2 is the lowest Fe# sample measured by Mössbauer, and therefore, the most difficult to precisely measure. This range of

Fe_{VI}^{+3}/Fe^{tot} is similar to that determined for spinels synthesized via flux crystallization between IW+1.6 and IW-0.3 (Fe_{VI}^{+3}/Fe^{tot} = 0.03-0.14, Halenius et al., 2002). Thus, the reduced nature of the spinels synthesized in the FeSp6 series provide a more direct analog to remotely sensed lunar spinels.

The Fe^{+3} contents of spinels from the FeSp8 series are less well constrained. For example, FeSp8_1 Fe_{VI}^{+3}/Fe^{tot} is 0.17, whereas, for FeSp8_2 Fe_{VI}^{+3}/Fe^{tot} is 0.03. FeSp8_3 and FeSp8_4 could not be successfully fit with the same routine applied to the remainder of the samples, leaving their Fe_{VI}^{+3}/Fe^{tot} uncertain (Appendix Table 2). Mössbauer spectra are given in Appendix Table 3.

3.3 V-NIR spectra

Effect of iron. Increasing Fe content in (Fe,Mg) aluminate spinel increases the abundance of all Fe cation species (Fe_{IV}^{+2}, Fe_{VI}^{+2}, Fe_{VI}^{+3}). Thus, it is expected that spinel becomes a uniformly stronger absorber across the V-NIR with increasing Fe content. The individual V-NIR spectra of the FeSp6 series, in which samples increase systematically in Fe#, are shown in Figure 2.

Several notable features are present in the V-NIR spectra. First, the long wavelength bands (>2000 nm) are present even at extremely low Fe content. FeSp6_1 and FeSp6 _2 both have <1 Fe# and yet possess prominent bands centered near 2000 and 2800 nm. The strength of these bands has been noted previously, and they are associated with crystal field electronic transitions of Fe_{IV}^{+2} (e.g. Slack, 1964; Gaffney, 1973; Mao and Bell, 1975; Halenius et al., 2002; Skogby et al. 2003). These longer wavelength

bands begin to saturate at relatively moderate Fe content (>5 Fe#). This phenomenon can be observed by plotting the ln(reflectance$_{min}$) parameter, which is inversely related to band strength, of the 2000 and 2800 nm bands against Fe# (Figure 3). For >15 Fe#, ln(reflectance$_{min}$) at 2000 and 2800 nm reaches a minimum value and does not change with increasing Fe content.

Second, spinels with <6 Fe# do not display prominent shorter wavelength bands (<1000 nm), and therefore share spectral properties similar with Group 1 spinel identified in basin walls and large craters on the Moon (e.g. Pieters et al., 2014). However, other variables that may affect <1000 nm band strengths, such as cooling rate and sample texture, must be considered before spinel compositions can be reasonably estimated based on spectral properties. These additional considerations are discussed in more detail in following sections.

Third, spinels with >6 Fe# display two well-defined bands centered near 700 and 1000 nm and are more spectrally similar to the Group 2 spinels associated with pyroclastic deposits discussed by Yamamoto et al. (2013). Collectively, these bands are referred to as the "1000 nm bands" here. The strength of these bands progressively increase with increasing Fe# (Figure 2), and do not saturate, as did the longer wavelength bands, even for the most Fe-rich composition explored (Figure 3).

Across the range of Fe contents explored, ln(reflectance$_{min}$) for the band at 1000 nm is linearly correlated with $[Fe_{VI}^{+2}]_{apfu}$ (apfu = atoms per functional unit, Figure 3a), with a reflectance coefficient of 9.04±1.50 $[Fe_{VI}^{+2}]^{-1}_{apfu}$ (95% confidence, R^2=0.90). Note that ln(reflectance$_{min}$) can only be calculated for spectra that have an observable absorption band near 1000 nm – for those samples without 1000 nm bands (FeSp6_1 –

FeSp6_4), the minimum reflectance value is calculated by simply averaging the reflectance between 825 and 1100 nm. At 2000 nm, samples with >0.05 $[Fe_{IV}^{+2}]_{apfu}$ show signs of saturation (Figures 2 and 3b). However, at low Fe# there is a linear relationship between ln(reflectance$_{min}$) and $[Fe_{IV}^{+2}]_{apfu}$. Using samples FeSp6_1-4, the reflectance coefficient for the 2000 nm band is 35.50 ± 6.81 $[Fe_{IV}^{+2}]^{-1}_{apfu}$ (95% confidence, R^2=0.95). Similar to the 2000 nm band, samples with >0.05 $[Fe_{IV}^{+2}]_{apfu}$ show signs of saturation at 2800 nm (Figures 2 and 3c) . Although there a general negative relationship between ln(reflectance$_{min}$) and $[Fe_{IV}^{+2}]_{apfu}$ for the lowest Fe# samples at 2800 nm, we choose to not report a reflectance coefficient as unsatisfactory fits are achieved for a regression forced through the origin. This may reflect a small contribution of OH to longer wavelength region of the V-NIR. Concentrations of Fe species are calculated for Q = 0.82 (Q = $^{VI}X_B$ - $^{IV}X_B$ for AB_2O_4 spinel, where the A and B cations are not restricted to their ordered site), as supported by the Mössbauer spectra and cooling rate-ordering model (discussed below), and assume all Fe is Fe^{+2}.

Effect of particle size. In addition to Fe abundance, band strength in the V-NIR is also dependent on the mean free path length of light travelling through a mineral lattice. Consequently, coarser particles are expected to be uniformly better absorbers, keeping all other variables constant. To demonstrate the magnitude of this effect in the synthetic spinels produced for this study, spectra of additional particle size separates were acquired for select samples from the FeSp6 series. A comparison of the different particle size separates (<45 μm, 45-75 μm, 75-125 μm) is shown in Figure 4. From Figure 4, it is apparent that both the 1000 nm and the >2000 nm bands increase in strength with increasing particle size, as expected. The increase in band strength is more pronounced at

the longer wavelengths than for the 1000 nm bands. In general, the effect of varying particle size on band strength of these synthetic samples is small compared to the effect of increasing Fe#. It has been shown that <45 μm particle size fraction dominates the optical properties of the lunar soils at V-NIR wavelengths (Pieters et al., 1993; Fischer 1995). Consequently, the <45 μm particle size separates of the spinels synthesized here provide the most direct analogy to lunar spinels and are the focus of the work presented here.

3.4 Mid-IR spectra

Full resolution laboratory emissivity (calculated as 1 – reflectace, Kirchoff's Law) spectra for the FeSp6 series are plotted across the mid-IR spectral range (1250 – 400 cm^{-1} or 8000 – 25000 nm) in Figure 5. Diagnostic spectral features include the primary Christiansen feature (CF) observed near ~980 cm^{-1} (~10200 nm) and the secondary CF observed near ~620 cm^{-1} (~16100 nm). Mid-IR laboratory spectra show a systematic shift of the primary and secondary CF positions to lower wavenumbers (longer wavelengths) as the Fe# increases. While the 18.9 Fe# sample (FeSp6_9) falls off the trend, it is clear in Figure 6, the primary and secondary CF position is related to Fe# for the other FeSp6 series compositions. FeSp6_9 is not used for regression purposes. Thus, the primary and secondary CF positions can be used to distinguish between compositions of aluminate spinel. The equations fit to the CF positions (wavenumber, cm^{-1}) are as follows:

$$CF1_{pos.} = -0.460 \pm 0.035 \cdot Fe\# + 982.972 \pm 0.526, R^2 = 0.99$$

$$CF2_{pos.} = -0.705 \pm 0.175 \cdot Fe\#^{0.5} + 625.667 \pm 0.559, R^2 = 0.93$$

A similar linear trend is observed between the primary and secondary CF positions and Fe# in emissivity spectra of the olivine solid solution series (Hamilton, 2010). Diagnostic absorptions in the reststrahlen band (RB) regions were identified near ~865, 755, 706, and 530 cm^{-1} (~11600, 13200, 14200, and 18900 nm). As seen in Figure 6, the RB bands near ~865 and 530 cm^{-1} also have linear relationships with Fe# as the diagnostic band positions shift to lower wavenumbers (longer wavelengths). The equations fit to the RB positions (wavenumber, cm^{-1}) are as follows:

$$RB1_{pos.} = -0.280 \pm 0.083 \cdot Fe\# + 866.643 \pm 1.236, R^2 = 0.90$$

$$RB4_{pos.} = -0.208 \pm 0.065 \cdot Fe\# + 532.828 \pm 0.960, R^2 = 0.89$$

Thus, diagnostic absorption bands in the RB regions can also be used to distinguish between aluminate spinel compositions. Similar trends are observed between RB absorption band positions and Fe# in spinels (Cloutis et al., 2004) and olivines (Hamilton, 2010). Uncertainties in regression equations are 95% confidence intervals.

4.0 Discussion

4.1 Distribution of Fe species in spinel

Experimental and theoretical arguments suggest the strength of 1000 nm bands in spinel are potentially sensitive to Fe_{VI}^{+2} and Fe_{VI}^{+3} content (e.g. Dickson and Smith, 1976; Halenius et al., 2002; Mao and Bell, 1975; Taran et al., 2005). Both Fe_{VI}^{+2} and Fe_{VI}^{+3} will increase with Fe#, but other variables, such as fO_2, cooling rate, and

$a\mathrm{Al_2O_3}/(a\mathrm{MgO}+a\mathrm{FeO})$ (where a denotes the activity of an oxide) can affect the distribution of Fe species within the spinel lattice. As such, these variables should affect the relative concentrations of different Fe species for a given bulk Fe content, and consequently, their importance must be evaluated when linking spectral characteristics to mineral composition. The following discussion is focused on determining the root causes of 1000 nm bands in aluminate spinel and the relative strength of the 1000 and 2000 nm bands. This information is then applied to providing further geologic context to Group 1 and 2 spinel identifications on the lunar surface.

4.2 Effect of $a\mathrm{Al_2O_3}$ on V-NIR spectra

Aluminate spinel can accommodate significant non-stoichiometry. This non-stoichiometry affects the point defect population, and potentially, the distribution of Fe ions in the spinel lattice. Thus, $a\mathrm{Al_2O_3}$ may be expected to affect the V-NIR spectral properties of aluminate spinel, which are dependent on the particular coordination environments of the absorbing species. We stress that the potential effect of Al-rich non-stoichiometry is large and increases rapidly with temperature. For example, at 1 GPa pure Mg-aluminate spinel is capable of hosting ~2.04 Al per 4 O at 1400 °C and ~2.14 Al per 4 O at 1600 °C (Watson and Price, 2002). There is some uncertainty regarding how excess $\mathrm{Al_2O_3}$ can be accommodated into the spinel structure, but three potential mechanisms (defect disorders) are argued as reasonable (Murphy et al., 2010); the extrinsic reactions are:

$$3Al_2O_3 + 2Mg_{IV}^{x} = 2Al_{IV} + O_i + 2MgAl_2O_4 \text{ , (1)}$$

$$4Al_2O_3 + 3Mg_{IV}^{x} = 2Al_{IV} + V_{IV} + 3MgAl_2O_4 \text{, and (2)}$$

$$4Al_2O_3 + 3Mg_{IV}^{x} + Al_{VI}^{x} = 3Al_{IV} + V_{VI} + 3MgAl_2O_4 \text{. (3)}$$

Reactions (1)–(3) are written in Kröger-Vink notation (e.g. Schmalzried, 1981, pp 39): subscripts refer to lattice sites and superscripts refer to charge on that site relative to whatever species occupies the site in the perfect crystal. A subscript of "*i*" indicates a interstitial site, i.e., an interstice not occupied in the perfect crystal. For superscripts, a prime is a single negative charge, a dot is a single positive charge, and an "×" indicates neutrality. Thus, Al_{IV} is an "antisite" defect, i.e., an Al^{+3} occupying a tetrahedral site that, in the perfect, non-disordered spinel crystal holds an Mg^{+2}; O_i is an interstitial O^{-2}; V_{VI} is a vacant octahedral site, one that normally would have contained an Al^{+3} (i.e., Al_{IV}^{X}) in the perfect crystal. (An important aspect of point-defect reactions such as these is that matter, charge, and lattice sites must all be conserved, which is the case for each of these reactions.) Note that all these reactions create the Al antisite defect when excess Al_2O_3 is incorporated into the spinel structure. Consequently, in spinel where $a$$Al_2O_3$/($a$FeO+$a$MgO) is high (i.e. spinel with excess Al_2O_3), reactions (1, 2, and 3) are driven toward products and Al_{IV} is produced.

Under typical geologic conditions, Mg and Fe^{+2} favor the tetrahedral site (generically the A site, in AB_2O_4) in aluminate spinel, and it is Fe_{IV}^{+2} that causes the prominent 2000 nm absorption that is common to all remotely sensed lunar spinels. Bands near 1000 nm in spinel are associated, in part, with Fe^{+2} partitioning onto the

octahedral site that is normally occupied by Al^{+3} or Cr^{+3} as denoted in the following disorder reaction (Navrotsky and Kleppa, 1967):

$$Fe_{IV}^{X} + Al_{VI}^{X} = Fe'_{VI} + Al_{IV} \quad (4)$$

Following reaction (4), there are two ways to generate Fe_{VI}^{+2}, where Fe_{VI}^{+2} is equivalent to Fe'_{VI} and $Fe_{IV}^{+2}$is equivalent to Fe_{IV}^{x}. First, increasing bulk Fe^{+2} content in spinel creates Fe_{VI}^{+2} and Fe_{IV}^{+2}in order to maintain equilibrium in reaction (4). Second, increasing the degree of disorder (reaction (4) driven to the right) generates Fe_{VI}^{+2}at the expense of Fe_{IV}^{+2}, causing $Fe_{IV}^{+2}/Fe_{VI}^{+2}$ to decrease.

In order to maintain the equilibrium described by reaction (4), the generation of Al_{IV} through reactions (1, 2, and 3) reduces $[Fe_{VI}^{+2}]$ for a given total Fe content, increasing $Fe_{IV}^{+2}/Fe_{VI}^{+2}$. In turn, lowering $[Fe_{VI}^{+2}]$ should result in weaker 1000 nm bands, assuming Fe_{VI}^{+2} contributes to these features. In fact, this is what is observed in our experimental dataset.

Figure 7 compares the V-NIR spectra of aluminate spinels that are nominally stoichiometric and aluminate spinels that contain excess Al_2O_3 (non-stoichiometric, Al-rich) but have the same Fe#. The samples with excess Al_2O_3 (dashed and dotted lines, FeSp8 series, Figure 7) have significantly weakened 700 and 1000 nm bands, whereas their 2000 and 2800 nm bands are strengthened compared to the nominally stoichiometric spinel (FeSp6 series, solid lines). These observations provide experimental support for the coupling of reactions (1, 2 and 3) with reaction (4) and strongly implies that $[Fe_{VI}^{+2}]$ is

a major control on the strength 1000 nm bands in aluminate spinel. Moreover, these observations confirm [Fe_{IV}^{+2}] as the major control on 2000 and 2800 nm band strength.

It is important to stress that lunar spinels are close to stoichiometric, even in systems that have a high normative abundance of plagioclase. This is because 1) $a$$Al_2O_3$/($a$FeO+$a$MgO) of melts with high normative plagioclase and saturated in spinel is still close to one (calculated using MELTS software, Ghiorso and Sack, 1995). Only values of $a$$Al_2O_3$/($a$FeO+$a$MgO) >>1 generate spinel with significant excess Al_2O_3, and 2) the maximum degree of non-stoichiometry for spinel below 1000°C is very small (Watson and Price, 2002). Lunar spinels excavated from mid to lower crustal depths likely had significant time to reequilibrate at temperatures where only minor amounts of excess Al_2O_3 could be accommodated. Indeed, the composition of Mg-rich aluminate spinels found in lunar troctolities are very nearly stoichiometric (e.g. Prinz et al. 1974, Ridley et al., 1973). Thus, the synthesis runs that are nominally stoichiometric are most applicable to lunar conditions (FeSp6 series). The FeSp8 series demonstrates the coupling of reactions (1, 2, and 3) with reaction (4) and highlights the importance of [Fe_{VI}^{+2}] in generating the 1000 nm bands in spinel.

4.3 Effect of cooling rate on V-NIR spectra

The ratio of Fe_{IV}^{+2} to Fe_{VI}^{+2} in aluminate spinel can be quantified using the ordering parameter, Q ($Q = {}^{VI}X_B - {}^{IV}X_B$ for AB_2O_4 spinel, where the A and B cations are not restricted to their ordered site). The equilibrium for reaction (4) is highly temperature sensitive, where increasing temperature favors higher entropy states, and consequently

lower Q values and lower Fe_{IV}^{+2}/ Fe_{VI}^{+2} (reaction (4) driven to the right). Similarly, at absolute zero, Q goes to unity and no Fe_{VI}^{+2} is present in stoichiometric (Mg,Fe) aluminate spinel.

Disordering in reaction (4) is a thermally activated process, hindering the approach to an equilibrium distribution at low temperatures and fast cooling rates (Dodson, 1973). Experimental evidence supports rapid attainment of equilibrium ordering at moderate (>500°C) temperatures for most geologic cooling rates, but at lower temperatures ordering kinetics become sluggish and higher degrees of disorder become locked in upon cooling. Given that $Fe_{IV}^{+2}/Fe_{VI}^{+2}$ strongly controls the relative strengths of the 1000 and 2000 nm bands (Figure 7), it is expected that the relative strength of the 1000 and 2000 nm bands is sensitive to the cooling rate of a particular spinel.

To quantify the sensitivity of Fe^{+2}-Al ordering to cooling rate we solved the rate law equation for different cooling rates (Salje, 1988):

$$\frac{dQ}{dt} = \frac{\gamma \exp(-\frac{\Delta H}{RT})}{2RT} \frac{\delta \Delta G}{\delta Q} \quad (5)$$

and

$$\Delta G = -Q + \frac{1}{2}a'(T - T_c)Q^2 + \frac{1}{6}c'Q^6 \text{ , } (6)$$

where a' and c' are fitting parameters for a Taylor expansion of the Gibbs free energy potential, T_c is a critical temperature, γ is the frequency factor, and ΔH is the activation energy. We use the ΔH, γ, T_c, and c' fit for a stoichiometric hercynite (Harrison et al., 1998) and adopt an $a' = 0.002$ while ranging cooling rate from (10^3 to 10^{-13} °C s^{-1} or $3x10^{15}$ to 3 °C Ma^{-1}). Examples of solutions for a range of cooling rates are plotted in

Figure 8a. At low temperature, Q deviates from the equilibrium Fe_{IV}^{+2}-Fe_{VI}^{+2} distribution (O'Neill and Navrotsky, 1983, dashed line, Figure 8) and closes (stagnates) at a value that is inversely proportional to cooling rate. The value of Q at closure is plotted as a function of cooling rate in Figure 8b.

Values of Q can be calculated for the synthetic spinels produced here from the distribution of Fe coordination states as determined by Mössbauer spectroscopy. This calculation requires the assumption that Fe^{+2} and Mg are equally disordered for a given sample. Studies comparing Q for spinel *ss* and hercynite have demonstrated that both minerals share similar Q-temperature relationships (e.g. Redfern et al. 1998), supporting this assumption. Given a cooling rate of 10^{-2} °C s^{-1} for the laboratory spinels, the cooling model predicts a Q value of 0.82. Calculations of Q from Mössbauer spectra range between 0.65 and 0.93, with an average of 0.80±0.17 (95% confidence) for the FeSp6 series. This is in good agreement with the modeled value and provides confidence in applying the cooling model to natural scenarios (see below). Mössbauer spectra were not used to quantify cation ordering in the FeSp8 series because the fitting routine did not converge for all samples in this series.

A single drop-quench cooling experiment was conducted to directly explore the effect of cooling rate on aluminate spinel V-NIR spectra (FeSp10 series). The drop-quench spinel had a 31% lower ln($reflectance_{min}$) value at 1000 nm (greater band strength) compared to the more slowly cooled equivalent (FeSp6_11, calculated using scaled spectra). For cooling rates of 100 and 1000 °C s^{-1}, the cooling rate-ordering model (Figure 8) predicts ln($reflectance_{min}$) at 1000 nm to decrease by 55 and 75%, respectively, assuming ln($reflectance_{min}$) at 1000 nm is inversely proportional [Fe_{VI}^{+2}] and that Q = 0.82

for all samples of the FeSp6 series. Thus, the drop-quench experiment supports cooling rate and Fe_{VI}^{+2} being important controls of V-NIR spinel spectra, albeit with some discrepancy between the experimental observation and model prediction.

4.4 Spinel anorthosite and DMD spinel (Groups 1 & 2) – Relation to cooling rate

Given the sensitivity of aluminate spinel spectra to cooling rate, potential cooling scenarios must be evaluated for Group 1 and 2 spinels. The paleo-temperature field of the lunar mantle is not well known, but recent modeling of lunar thermal history suggests a radially averaged temperature of ~500 °C at 3.9 Ga for the lower crust (Zhang et al., 2013, preferred model: H50E100MR2500). This temperature is greater than the Fe^{+2}-Al ordering closure temperature associated with slowly cooled rocks (closure temperature <400 °C for cooling rates $<10^{-13}$ °C s^{-1}, McCallum and O'Brien, 1996). Moreover, the generation of spinel anorthosite implies additional magmatic heat input into the crust local to the spinel anorthosite lithologies, raising the temperature above the radial average. Thus, if spinel anorthosite (Group 1) was excavated from the mid to lower lunar crust, as implied by its association with basin walls and large craters, this suggests that the spinels were in a relatively disordered state before excavation. Similarly, DMD spinels associated with pyroclastic eruptions (Group 2) are expected to rapidly cool from magmatic to ambient temperatures. Consequently, the Fe^{+2}-Al closure for both Group 1 and 2 is likely set by the relatively rapid cooling at or near the lunar surface, and as such, near-surface cooling rates need to be evaluated.

Saal et al. (2008) argued for cooling rates of 2-3 °C s^{-1} for lunar pyroclasitc glass beads on the basis of measured volatile loss profiles. This rate is supported by textural comparisons betweeen experimental and natural lunar pyroclastic glass beads (Arndt et al., 1987) and has been interpreted to require an insulating vapor cloud. We use this rate as a lower limit for the Group 2 spinels. However, the high temperature cooling rates of pyroclastic deposits are expected to be faster if cooled under vacuum (~1000 °C s^{-1} at ~1000 °C, Arndt et al., 1979). We take 1000 °C s^{-1} as an upper limit for Group 2 cooling rates.

Cooling rates for spinels found in basin walls and large craters (Group 1) are more difficult to estimate, but limits can be evaluated. Erosion of outcropping rock on the Moon is slow, with estimates for the combined effects of mass wasting and spallation totaling to 1 cm Ma^{-1} or ~45 m over lunar history (Arvidson et al., 1975), suggesting the spinel-bearing materials observed on the Moon are sourced from the upper 10s of meters of the material exposed during impact related excavation. Studies of mare basalts infer cooling rates on the order of 10^{-4} °C s^{-1} near 500°C for flows that are on the order of meters in thickness (Takeda et al., 1975). This rate would apply to exposed material where typical amounts of erosion have occurred. If erosion rates were extraordinarily high, the spinel anorthosite material exposed today could have been sourced from deeper, better-insulated rocks. Cooling rates for lunar rocks inferred to be sourced from ~200 m deep are 10^{-9} °C s^{-1} (McCallum and O'Brien, 1996), which is a reasonable lower limit on the cooling rate for the spinels exposed on surface of the Moon via excavation from mid to lower lunar crust.

The effect of these cooling rates on spinel order-disorder can be evaluated using the calculations presented in Figure 8b. Compared to the laboratory cooling rate near 500°C (~10^{-2} °C s^{-1}), a cooling rate of 10^{-9} °C s^{-1} results in an increase of 0.08 for Q, or a 44% decrease in $[Fe_{VI}^{+2}]$. For the alternative scenario involving shallower sourced material for the spinel anorthosite, a cooling rate of 10^{-4} °C s^{-1} results in an increase of 0.03 for Q, or a 17% decrease in $[Fe_{VI}^{+2}]$. The DMD spinels (Group 2) likely cooled more rapidly than the laboratory spinels, and correspondingly, the 1000 nm bands should be relatively strong. For the slow cooling pyroclastic scenario (Saal et al, 2008), a cooling rate of 1 °C s^{-1} results in a decrease of 0.04 for Q, or a 22% increase in $[Fe_{VI}^{+2}]$. For pyroclastic material cooling into vacuum, a cooling rate 1000 °C s^{-1} results in a decrease of 0.1 for Q, or a 75% increase in $[Fe_{VI}^{+2}]$.

5.0 Implications

5.1 Mid-IR

Analysis of the lunar spinel locations identified by V-NIR techniques (e.g., Pieters et al., 2014) across the mid-IR spectral range is limited by the spectral resolution and spectral coverage of current sensors. Our results indicate that the mid-IR spectral range can be used to distinguish aluminate spinel compositions from: (1) one another based on the position of diagnostic spectral features such as the CF and RB and (2) other silicate minerals found on the lunar surface such as plagioclase, pyroxene, and olivine. As seen in Figure 6, diagnostic spectral features of aluminate spinel systematically shift to lower

wavenumbers (longer wavelengths) as the Fe# increases. In addition, the CF and RB positions of aluminate spinel occur at lower wavenumbers (longer wavelengths) that are distinct from the CF and RB positions of other silicate minerals like plagioclase, pyroxene, and olivine. Detailed coordinated analyses of remote observations of lunar spinel locations identified by V-NIR (e.g., Pieters et al., 2014) using additional hyperspectral mid-IR data sets, along with the laboratory mid-IR spectra of aluminate spinels presented here, may be able to constrain the abundances of spinel and plagioclase in spinel-rich areas

5.2 Spinel anorthosite (Group 1)

The Group 1 spinels associated with spinel anorthosite lack observable 1000 nm bands (e.g. Pieters et al., 2014). The results of the current work have demonstrated the effects of particle size, cooling rate, and Fe content on 1000 nm band strengths for spinels at lunar-relevant fO_2. Making assumptions for particle size and cooling rate of the Group 1 spinels, we can estimate the composition of the spinels that are most consistent with the remotely observed spectral characteristics. First, we have assumed that the particle sizes of the synthetic spinel studies here (<45 um) is an appropriate analog for the textures of lunar spinels (Pieters et al., 1993; Fischer 1995). As discussed in the cooling rate section, the cooling rate for Group 1 spinels is uncertain, but different scenarios can be evaluated. Essentially, slower cooling rates are associated with deeper burial and weaker 1000 nm bands for a given Fe content. Compared to the laboratory cooling rates (~10^{-2} °C s^{-1}), the slowest cooling scenario results in ~50% less Fe_{VI}^{+2}. The lowest Fe# spinel that has

prominent 1000 nm bands is FeSp6_6 (Fe# = 6.2, Fe_{VI}^{+3}/Fe^{tot}= 0.06). Accounting for cooling rate, this implies that spectra of lunar spinels with >12 Fe# (<88 Mg#) would have observable 1000 nm bands. Generation of spinel with <12 Fe# suggests Group 1 formation occurred within a relatively Fe-poor system, such as those associated with Mg-Suite magmatism (Prissel et al. 2014).

It is also possible to form aluminate spinel in more Fe-rich systems, possibly associated with mare basalt liquids or picritic liquids (Gross and Treiman, 2011), but experiments have shown that lowest Fe# picritic glass composition would produce spinel with 20 Fe# when reacted with anorthite (A15C, Prissel et al., 2014). A cooling rate of 10^{-19} °C s^{-1}, which corresponds to Q at closure equal to 0.946, is sufficient to raise the threshold for observable 1000 nm bands to 20 Fe#. This cooling rate is much slower than rates calculated for lunar highlands samples inferred to be very deeply buried (6×10^{-13} °C s^{-1}, 21 km depth, McCallum and O'Brien, 1996) and would result in negligible cooling over the course of lunar history. This calculation assumes a Q value of 0.82 for the FeSp6 series, as supported by the cooling rate of these samples and the Mössbauer spectra. Thus, the petrogenesis of Group 1 spinels most plausibly involved Mg-Suite magmas, implying a global distribution of Mg-suite magmatism. This association is supported by the link between Group 1 and deep crustal lithologies (Pieters et al., 2014) and the low Cr# of Group 1 spinels (e.g. Cloutis et al., 2004), as the Mg-Suite is also associated with deep crustal lithologies and is relatively Cr-poor rock suite (e.g. Elardo et al., 2011). However, it is important to stress that further reduction of Fe, space weathering, and mixing with plagioclase could all act to weaken the 1000 nm bands independently of Fe# of the spinel (e.g. Cheek and Pieters, 2014; Isaacson et al., 2014).

Moreover, chromite spinels are more ordered for a given cooling rate due to the strong ordering of Cr^{+3} onto the octahedral site (e.g. Navrotsky and Kleppa, 1967), and consequently, a small (undetectable) amount of Cr may also cause an underestimate of Fe# based on the above analysis.

5.3 DMD spinel at Sinus Aestuum (Group 2)

The spinels observed in the DMD of Sinus Aestuum are unique for the Moon and display both short and long wavelength bands across the V-NIR (Yamamoto et al, 2013). The relative strength of the short and long wavelength bands in aluminate spinel is an expression of $Fe_{VI}^{+2}/Fe_{IV}^{+2}$, and thus, cooling rate. To quantify the relative strength of the 1000 and 2000 nm bands of the FeSp6 series spinels, we calculated the product of the reflectance coefficient for the 1000 and 2000 nm bands (Figure 3) and abundance of $Fe_{VI}^{+2}$and Fe_{IV}^{+2}, respectively. The ratio of these two products defines the relative strengths of the 1000 and 2000 nm bands independently of Fe#. This ratio is 0.0357 ± 0.0090 (95% confidence) for the FeSp6 series. The ratio of ln(reflectance$_{min}$) values for 1000 and 2000 nm bands has also been calculated for continuum-corrected spectra reported by Yamomato et al. (2013), yielding values of 0.108, 0.114, 0.115, and 0.103 for four of their reported spectra (A7, B14, C2, and F4). The average of this population is 0.109 ± 0.0109 (95% confidence). The higher band minimum ratio (stronger 1000 nm relative to 2000 nm bands) measured at Sinus Aestuum compared to the synthetic spinels are consistent with a relatively fast cooling rate of Group 2 spinels compared to the spinels synthesized for this study.

Fast cooling rates for Sinus Aestuum spinels are consistent with a pyroclastic origin (cooling in the presence or absence of a vapor cloud). Arndt et al. (1987) calculate cooling rates of 1080 and 86 °C s^{-1} across 1050 °C under vacuum for orange glass bead sizes of 0.16 mm and 2.0 mm, respectively. The presence a vapor cloud is expected to slow cooling rates. The cooling rate-ordering model (Figure 8) predicts a cooling rate of 1000 °C s^{-1} results in a 102% increase in the 1000 nm and 2000 nm ln($reflectance_{min}$) ratio band compared to cooling at 10^{-2} °C s^{-1}. The difference between the 1000 nm-2000 nm ln($reflectance_{min}$) ratio associated with Sinus Aestuum and the FeSp6 series is large, a 207 ± 56 % increase. Thus, the large offset between Sinus Aestuum and FeSp6 1000 nm-2000 nm ln($reflectance_{min}$) ratios is more consistent with cooling in the absence of a vapor cloud and small grain size, but may also may partly reflect relatively small pyroclastic bead size, high [Fe_{VI}^{+3}], systematic errors introduced during continuum or thermal corrections of the Sinus Aestuum spectra.

Further, it is important to note that the V-NIR spectra of the Group 2 spinels do not necessarily require a higher Fe# compared to the Group 1 spinels, as faster cooling, and potentially higher [Fe_{VI}^{+3}], should act to preferentially strengthen 1000 nm bands. However, the age inferred from superposition relations and the density of craters at Sinus Aestuum (Yamamoto et al., 2013) argues against a relationship to early Mg-suite magmatism and supports a relationship to later, more Fe-rich magmas.

References:

Adams, J.B. (1974) Visible and near-infrared diffuse reflectance spectra of pyroxenes as applied to remote sensing of solid objects in the solar system. Journal of Geophysical Research, 79, 4829-4836.

Arndt, J., Flad, K., and Feth, M. (1979) Radiative cooling experiments on lunar glass analogues. Lunar and Planetary Science Conference Proceedings, 10, p. 355-373.

Arndt, J., and Von Engelhardt, W. (1987) Formation of Apollo 17 orange and black glass beads. Journal of Geophysical Research, 92, E372-E376.

Arvidson, R., Drozd, R.J., Hohenberg, C.M., Morgan, C.J., and Poupeau, G. (1975) Horizontal transport of regolith, modification of features, and erosion rates on the lunar surface. Moon, 13, 67-79.

Bhattacharya, S., Chauhan, P., and Ajai. (2012) Discovery of orthopyroxene-olivine-spinel assemblage from the lunar nearside using Chandrayaan-1 Moon Mineralogy Mapper data. Current Science, 103, 21-23.

Burns, R.G. (1970) Crystal field spectra and evidence of cation ordering in olivine minerals. American Mineralogist, 55, 1608-1632.

Cheek, L.C., Pieters, C.M., Reflectance spectroscopy of plagioclase and mafic mineral mixtures: Implications for characterizing lunar anorthosites remotely, Submitted to American Mineralogist, lunar highlands special issue

Cintala, M.J., and Grieve, R.A.F. (1998) Scaling impact melting and crater dimensions: Implications for the lunar cratering record. Meteoritics & Planetary Science, 33, 889-912.

Cloutis, E.A., Sunshine, J.M., and Morris, R.V. (2004) Spectral reflectance-compositional properties of spinels and chromites: Implications for planetary remote sensing and geothermometry. Meteoritics & Planetary Science, 39, 545-565

Conel, J. E. (1969) Infrared emissivities of silicates: Experimental results and a cloudy atmospheric model of spectral emission from condensed particulate mediums. Journal of Geophysical Research, 74, 1614-1634.

Delano, J. (1990) Experimental constraints on the oxidation state of the lunar mantle. Lunar and Planetary Institute Science Conference Abstracts, 21, p. 278.

Dhingra, D., and Pieters, C. (2011) Mg-Spinel Rich Lithology at Crater Copernicus. LEAG Conference (2011).

Dhingra, D., Pieters, C.M., Boardman, J.W., Head, J.W., Isaacson, P.J., and Taylor, L.A. (2011) Compositional diversity at Theophilus Crater: Understanding the geological context of Mg-spinel bearing central peaks. Geophysical Research Letters, 38, L11209.

Dickson, B., and Smith, G. (1976) Low Temperature Optical Absorption and Mossbauer Spectra of Staurolite and Spinel. Canadian Mineralogist, 14, 206-215.

Dodson, M.H. (1973) Closure temperature in cooling geochronological and petrological systems. Contributions to Mineralogy and Petrology, 40, 259-274.

Donaldson Hanna, K. L., I. R. Thomas, N. E. Bowles, B. T. Greenhagen, C. M. Pieters, J. F. Mustard, C. R. M. Jackson, and M. B. Wyatt (2012) Laboratory emissivity measurements of the plagioclase solid solution series under varying environmental conditions, JGR, 117, E11,

Dyar, M.D., McGuire, A.V., and Ziegler, R.D. (1989) Redox equilibria and crystal chemistry of coexisting minerals from spinel lherzolite mantle xenoliths. American Mineralogist, 74, 969-980.

Elardo, S.M., Draper, D.S., and Shearer Jr, C.K. (2011) Lunar Magma Ocean crystallization revisited: Bulk composition, early cumulate mineralogy, and the source regions of the highlands Mg-suite. Geochimica et Cosmochimica Acta, 75, 3024-3045.

Fischer, E. M. (1995) Quantitative compositional analysis of the lunar surface from reflectance spectroscopy: Iron, aluminum, and a model for removing the optical effects of space weathering. Ph.D. dissertation, Brown University, Providence, RI.

Fogel, R.A., and Rutherford, M.J. (1995) Magmatic volatiles in primitive lunar glasses: I. FTIR and EPMA analyses of Apollo 15 green and yellow glasses and revision of the volatile-assisted fire-fountain theory. Geochimica et Cosmochimica Acta, 59, 201-215.

Gaffney, E.S. (1973) Spectra of tetrahedral Fe^{+2} $MgAl_2O_4$. Physical Review B, 8. 3484-3486.

Ghiorso, M.S., and Sack, R.O. (1995) Chemical mass transfer in magmatic processes IV. A revised and internally consistent thermodynamic model for the interpolation of extrapolation of liquid-solid equilibria in magmatic systems at elevated temperatures and pressures. Contributions to Mineralogy and Petrology, 119, 197-212.

Gross, J., and Treiman, A.H. (2011) Unique spinel-rich lithology in lunar meteorite ALHA 81005: Origin and possible connection to M-3 observations of the farside highlands. Journal of Geophysical Research-Planets, 116, E10009.

Hamilton, V. E. (2010) Thermal infrared (vibrational) spectroscopy of Mg-Fe olivines: A review and applications to determining the composition of planetary surfaces. Chemie der Erde, 70, 7-33

Hapke, B. (1993) Theory of Reflectance and Emittance Spectroscopy, Cambridge University Press, New York.

Harrison, R.J., Redfern, S.A.T., and O'Neill, H.S.C. (1998) The temperature dependence of the cation distribution in synthetic hercynite ($FeAl_2O_4$) from in-situ neutron structure refinements. American Mineralogist, 83, 9-10.

Halenius, U., Skogby, H., and Andreozzi, G.B. (2002) Influence of cation distribution on the optical absorption spectra of Fe3+-bearing spinel s.s.-hercynite crystals: evidence for electron transitions in Fe-VI(2+)-Fe-VI(3+) clusters. Physics and Chemistry of Minerals, 29, 39-330.

Isaacson, P.J., Gillis-Davis, J.J., Jackson, C., Prissel, T.C., Parman, S., Donaldson Hanna, K., and Cheek, L. (2014), Experimental weathering of synthetic spinels, LPSC 45, #1612.

Karner, J.M., Sutton, S.R., Papike, J.J., Shearer, C.K., Jones, J.H., and Newville, M. (2006) Application of a new vanadium valence oxybarometer to basaltic glasses from the Earth, Moon, and Mars. American Mineralogist, 91, 270-277.

Kaur, P., Chauhan, P., Bhattacharya, S., Ajai, and Kumar, A.S.K. (2012) Compositional Diversity at Tycho Crater: Mg-Spinel Exposures Detected from Moon Mineralogy Mapper (M3) Data, p. Abstract# 1434, Lunar Planetary Science Conference.

Lal, D., Chauhan, P., Shah, R.D., Bhattacharya, S., Ajai, and Kumar, A.S.K. (2012) Detection of Mg spinel lithologies on central peak of crater Theophilus using Moon Mineralogy Mapper (M3) data from Chandrayaan-1. Journal of Earth System Science, 121, 847-853.

Mao, H.K., and Bell, P.M. (1975) Crystal-field effects in spinel: oxidation states of iron and chromium. Geochimica Et Cosmochimica Acta, 39, 865-866, IN1-IN2, 867-874.

McCallum, I.S., and O'Brien, H.E. (1996) Stratigraphy of the lunar highland crust: Depths of burial of lunar samples from cooling-rate studies. American Mineralogist, 81, 1166-1175.

Murphy, S.T., Gilbert, C.A., Smith, R., Mitchell, T.E., Grimes, R.W. (2010) Non-stoichiometry in $MgAl_2O_4$ spinel. Philosophical Magazine, 90:10, 1297-1305.

Murray R. W., Miller D. J. and Kryc K. A. (2000), Analysis of major and trace elements in rocks, sediments, and interstitial waters by Inductively Coupled Plasma-Atomic Emission Spectroscopy (ICP-AES). Texas A&M University, ODP Technical Note 29, 21 pp.

Navrotsky, A. , and Kleppa, O.J. (1967) Thermodynamics of cation distributions in simple spinels. Journal of Inorganic & Nuclear Chemistry, 29, 2701-2714.

O'Neill, H.S.C., and Navrotsky, A. (1983) Simple spinels; crystallographic parameters, cation radii, lattice energies, and cation distribution. American Mineralogist, 68, 181-194.

Pieters, C. M., E. M. Fischer, O. Rode, and A. Basu (1993) Optical effects of space weathering: The role of the finest fraction. Joournal of Geophysical Research, 98, 20,817-20,824.

Pieters, C.M., and T. Hiroi (2004) RELAB (Refectance Experiment Laboratory): A NASA Multiuser Spectroscopy Facility, *Lunar and Planetary Science Conference XXXV*, #1720.

Pieters, C.M., Besse, S., Boardman, J., Buratti, B., Cheek, L., Clark, R.N., Combe, J.P., Dhingra, D., Goswami, J.N., Green, R.O., Head, J.W., Isaacson, P., Klima, R., Kramer, G., Lundeen, S., Malaret, E., McCord, T., Mustard, J., Nettles, J., Petro, N., Runyon, C., Staid, M., Sunshine, J., Taylor, L.A., Thaisen, K., Tompkins, S., and Whitten, J. (2011) Mg-spinel lithology: A new rock type on the lunar farside. Journal of Geophysical Research-Planets, 116, E00G08

Pieters, C.M., Donaldson-Hanna, Kerri, Cheek, L, Dhingra, D, Prissel, T, Jackson, C, Moriarty, D, Parman, S, Taylor, L.A. The Distribution and Origin of Mg-Spinel on the Moon. Submitted to American Mineralogist, lunar highlands special issue

Prinz, M., Dowty, E., Keil, K., and Bunch, T.E. (1973) Spinel troctolite and anorthosite in Apollo 16 samples. Science, 179, 74-76.

Prissel, T.C., Parman, S.W., Jackson, C.R.M., Rutherford, M.J., Hess, P.C, Head, J.W., Cheek, L., Dhingra, D., Pieters, C.M.,Pink Moon: Lunar Melt-Rock Interactions

& the Petrogenesis of Pink Spinel Anorthosites, Submitted to Earth and Planetary Sciences Letters

Redfern, S.A.T., Harrison, R.J., O'Neill, H.S.C., and Wood, D.R.R. (1999) Thermodynamics and kinetics of cation ordering in $MgAl_2O_4$ spinel up to 1600 ˚C from in situ neutron diffraction. American Mineralogist, 84, 299-310.

Ridley, W.I., Hubbard, N.J., Rhodes, J.M., Weismann, H., and Bansal, B. (1973) The Petrology of Lunar Breccia 15445 and Petrogenetic Implications. The Journal of Geology, 81, 621-631.

Saal, A.E., Hauri, E.H., Cascio, M.L., Van Orman, J.A., Rutherford, M.C., and Cooper, R.F. (2008) Volatile content of lunar volcanic glasses and the presence of water in the Moon's interior. Nature, 454, 192-195.

Sato, M., Hickling, N., and McLane, J.E. (1973) Oxygen fugacity values of Apollo 12, 14, and 15 lunar samples and reduced state of lunar magmas. Lunar and Planetary Science Conference Proceedings, 4, p. 1061.

Salisbury, J. W. and Walter, L. S. (1989) Thermal infrared (2.5 – 13.5 microns) spectroscopic remote sensing of igneous rock types on particulate planetary surfaces. Journal of Geophysical Research, 94, 9192-9202.

Salje, E. (1988) Kinetic rate laws as derived from order parameter theory I: Theoretical concepts. Physics and Chemistry of Minerals, 15, 336-348.

Schmalzried, H., *Solid State Reactions*, (2^{nd} edition), 254 pp., Verlag Chemie, Weinheim, FRG, 1981.

Skogby, H., Annersten, H., Domeneghetti, M.C., Molin, G., and Tazzoli, V. (1992) Iron distribution in orthopyroxene: A comparison of Mössbauer spectroscopy and X-ray refinement results. European journal of mineralogy, 4(3), 441-452.

Skogby, H., and Halenius, U. (2003) An FTIR study of tetrahedrally coordinated ferrous iron in the spinel-hercynite solid solution. American Mineralogist, 88(4).

Sunshine, J.M., Pieters, C.M., and Pratt, S.F. (1990) Deconvolution of mineral absorption bands: An improved approach. Journal of Geophysical Research: Solid Earth (1978–2012), 95(B5), 6955-6966.

Sunshine, J., Besse, S., Petro, N., Pieters, C., Head, J., Taylor, L., Klima, R., Isaacson, P., Boardman, J., and Clark, R. (2010) Hidden in plain sight: Spinel-rich deposits on the nearside of the Moon as revealed by Moon Mineralogy Mapper (M3). Lunar and Planetary Institute Science Conference Abstracts, 41, p. 1508.

Takeda, H., Miyamoto, M., Ishii, T., and Lofgren, G.E. (1975) Relative cooling rates of mare basalts at the Apollo 12 and 15 sites as estimated from pyroxene exsolution data, p. 987-996. Lunar Science Conference VI.

Taran, M.N., Koch-Muller, M., and Langer, K. (2005) Electronic absorption spectroscopy of natural (Fe2+, Fe3+)-bearing spinels of spinel s.s.-hercynite and gahnite-hercynite solid solutions at different temperatures and high-pressures. Physics and Chemistry of Minerals, 32, 175-188.

Vaughan, W.M., Head, J.W., Wilson, L., and Hess, P.C. (2013) Geology and petrology of enormous volumes of impact melt on the Moon: A case study of the Orientale basin impact melt sea. Icarus, 223(2), 749-765.

Watson, E.B., and Price, J.D. (2002) Kinetics of the reaction $MgO+Al_2O_3$ -> $MgAl_2O_4$ and Al-Mg interdiffusion in spinel at 1200 to 2000 ˚C and 1.0 to 4.0 GPa. Geochimica Et Cosmochimica Acta, 66, 2123-2138.

Yamamoto, S., Nakamura, R., Matsunaga, T., Ogawa, Y., Ishihara, Y., Morota, T., Hirata, N., Ohtake, M., Hiroi, T., and Yokota, Y. (2013) A new type of pyroclastic deposit on the Moon containing Fe-spinel and chromite. Geophysical Research Letters, 40, 4549-4554.

Yue, Z., Johnson, B., Minton, D., Melosh, H., Di, K., Hu, W., and Liu, Y. (2013) Projectile remnants in central peaks of lunar impact craters. Nature Geoscience, 6(6), 435-437.

Zhang, N., Parmentier, E., and Liang, Y. (2013) Effects of lunar cumulate mantle overturn and megaregolith on the expansion and contraction history of the Moon. Geophysical Research Letters, 40, 5019-5023.

Figure Captions:

Figure 1, Backscattered electron image of typical run products: Image a) FeSp6_7 (10.2 Fe#), and image b) FeSp6_6 (6.2 Fe#). No obvious gradients in contrast are present in either image, indicating a homogenous distribution of Mg and Fe. Large (~100 μm diameter) and small scale (~1 μm diameter) porosity is present in all samples. The small scale porosity is more easily observed in the FeSp6_6 sample (b). Small modes of ferro-periclase were observed during inspection of some samples using back-scatter electron imaging (a).

Figure 2, V-NIR spectra from the FeSp6 series (<45 μm) a) scaled and b) unscaled. The lowest Fe# samples only display bands at 2000 and 2800 nm. The lowest Fe# with observable 700 and 1000 nm bands is FeSp6_7 (6.2 Fe#). Above 6.2 Fe# all spinels display four prominent band centers at 700, 1000, 2000, and 2800 nm are present. The 1000 nm band is uniformly stronger than the 700 nm band.

Figure 3, Correlations between ln(reflectance$_{min}$) and various Fe species for the a) 1000, b) 2000, and c) 2800 nm bands. a) ln(reflectance$_{min}$) for the 1000 nm band correlates linearly with $[Fe_{VI}^{+2}]_{apfu}$, or equivalently, Fe#. b) At low Fe contents (FeSp6_1-4) there is a linear relationship between ln(reflectance$_{min}$) for the 2000 nm band $[Fe_{IV}^{+2}]_{apfu}$. c) Similar to the 2000 nm band, high Fe samples with show signs of saturation at 2800 nm. There is a negative relationship between ln(reflectance$_{min}$) and $[Fe_{IV}^{+2}]_{apfu}$ for the lowest Fe# samples at 2800 nm, but the regression does not pass through the origin. This may

reflect a small contribution of OH to longer wavelength region of the V-NIR. Concentrations of Fe species are calculated for Q = 0.82, as supported by the Mössbauer spectra and cooling rate-ordering model (see section V-NIR- Mössbauer - Cooling Rate), and assume all Fe is Fe^{+2}.

Figure 4, Scaled reflectance spectra for FeSp6 series illustrating the effect of particle size on FeSp6 V-NIR spectra: The solid lines are the <45 μm particle size spectra (scaled), and the dashed and dotted lines are the 45-75 and 75-125 μm particle size spectra, respectively. In all cases, increasing particle size results in stronger bands at 700, 1000, 2000, and 2800 nm, in line with the correlation between mean free path length and particle size.

Figure 5, Mid-IR spectra from the FeSp6 series (<45 μm). Spectra are offset for clarity and vertical lines highlight the positions of identified features. The primary Christiansen feature is near ~980 cm^{-1} (~10200 nm) and the secondary CF is near ~620 cm^{-1} (~16100 nm). Reststrahlen band regions are located near ~865, 755, 706, and 530 cm^{-1} (~11600, 13200, 14200, and 18900 nm). The mid-IR spectrum for FeSp6_9 (18.9 Fe#) is anomalous compared to the other mid-IR spectra of the FeSp6 series and is not used for further comparisons.

Figure 6, Mid-IR spectral systematics from the FeSp6 series (<45 μm). The positions of both Christiansen features (CF) are negatively related to Fe#. a) The primary CF position is linearly related to Fe#, and b) the secondary CF position is linearly related to $Fe\#^{0.5}$.

Four Reststrahlen bands (RB) are identified (Absorptions 1-4, c-f). The positions of Absorption 1 and Absorption 4 show clear, negative relationships to Fe#. The position of Absorption 2 is only weakly correlated with Fe#, and consequently, no regression is reported for this band. The position of Absorption 3 appears independent of Fe#.

Figure 7, Effect of excess Al_2O_3 on V-NIR spectra: Samples for the FeSp8 series were prepared by mixing 7.5 wt% additional Al_2O_3 into the same oxide powders mixed for the FeSp6 series (dashed lines). This ensures an excess of Al_2O_3 was present in the FeSp8 series spinels over their baseline (FeSp6). Compared to the equivalent samples from the FeSp6 series (solid lines), the samples with excess Al_2O_3 have severely weakened 700 and 1000 bands (dashed and dotted lines). Moreover, the 2000 and 2800 nm bands are relatively strengthened. This result is consistent with the coupling of reactions (1 and 2) with reaction (3), limiting the degree of disordering of Fe in aluminate spinel. Less Al_2O_3 (2.5 wt %) was added to the dotted line sample (panel c, FeSp8_4), and this spectrum is intermediate to the FeSp6 baseline and the sample with more Al_2O_3 added. Note the presence of a new band located at 550 nm in the samples with excess Al_2O_3.

Figure 8, Cooling Model: a) Examples of solutions for selected linear cooling rate scenarios and b) Q at closure for various cooling rate scenarios. a) At temperatures >700 °C, Q follows an equilibrium distribution for the selected range of cooling rates explored. At lower temperatures, Q departs from the equilibrium value and eventually stops evolving after a given amount of cooling. More rapid cooling results in lower Q (greater amounts of disorder) at closure. c) Values of Q at closure have been tabulated for

a wide range of cooling rates applicable to Group 1 and Group 2 spinel exposures. The relationship between Q and cooling rate is not linear. Rather, Q asymptotically approaches 1 with progressively slower cooling rates.

Chapter 4. Figure 1

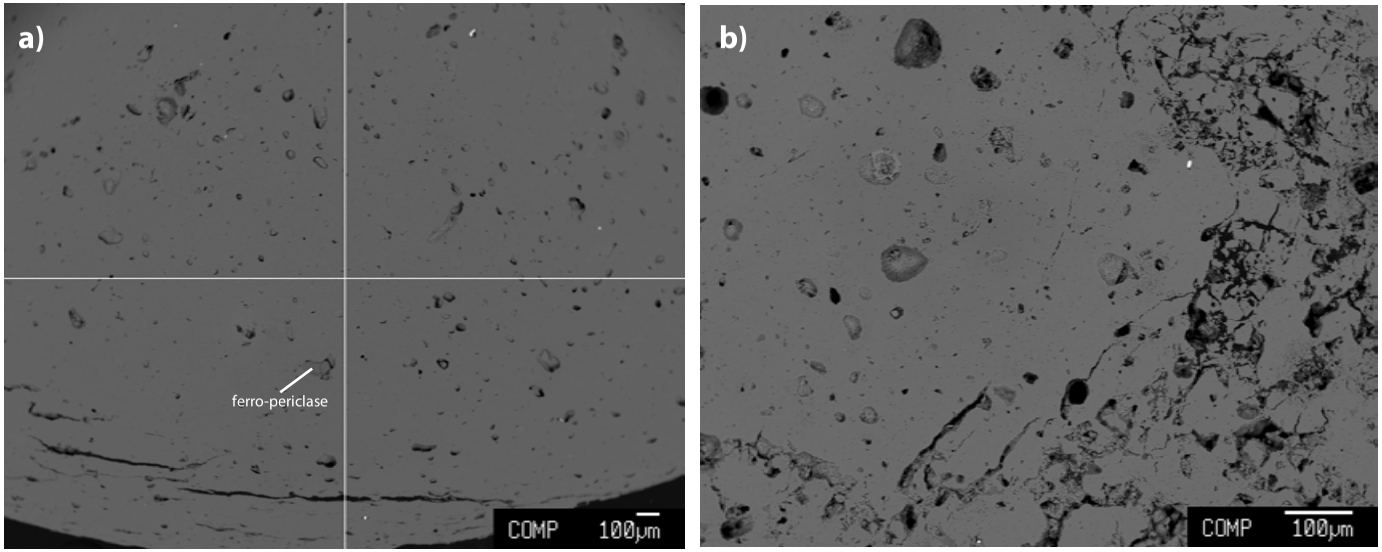

Chapter 4, Figure 2

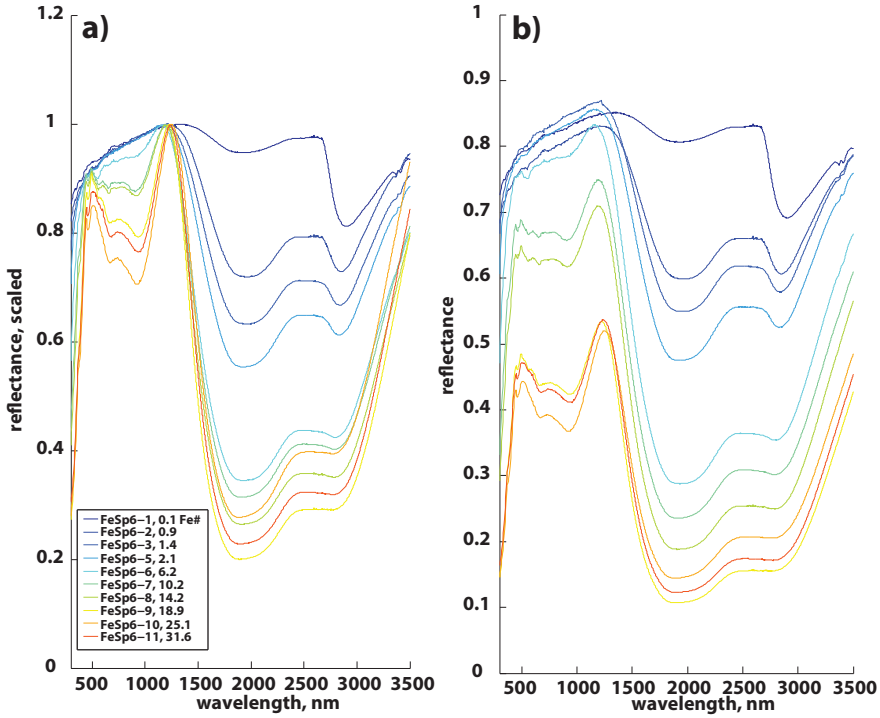

Chapter 4, Figure 3

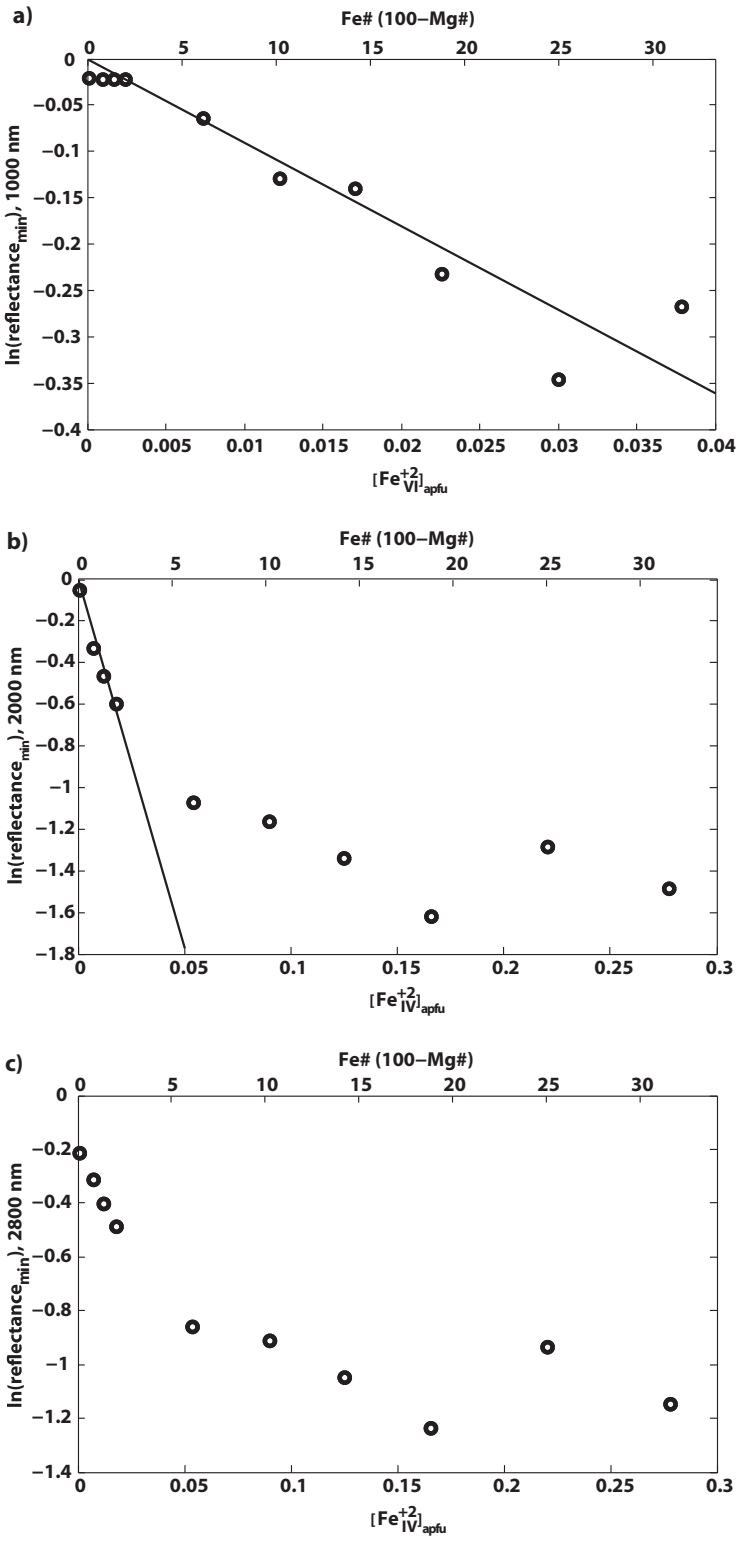

Chapter 4, Figure 4

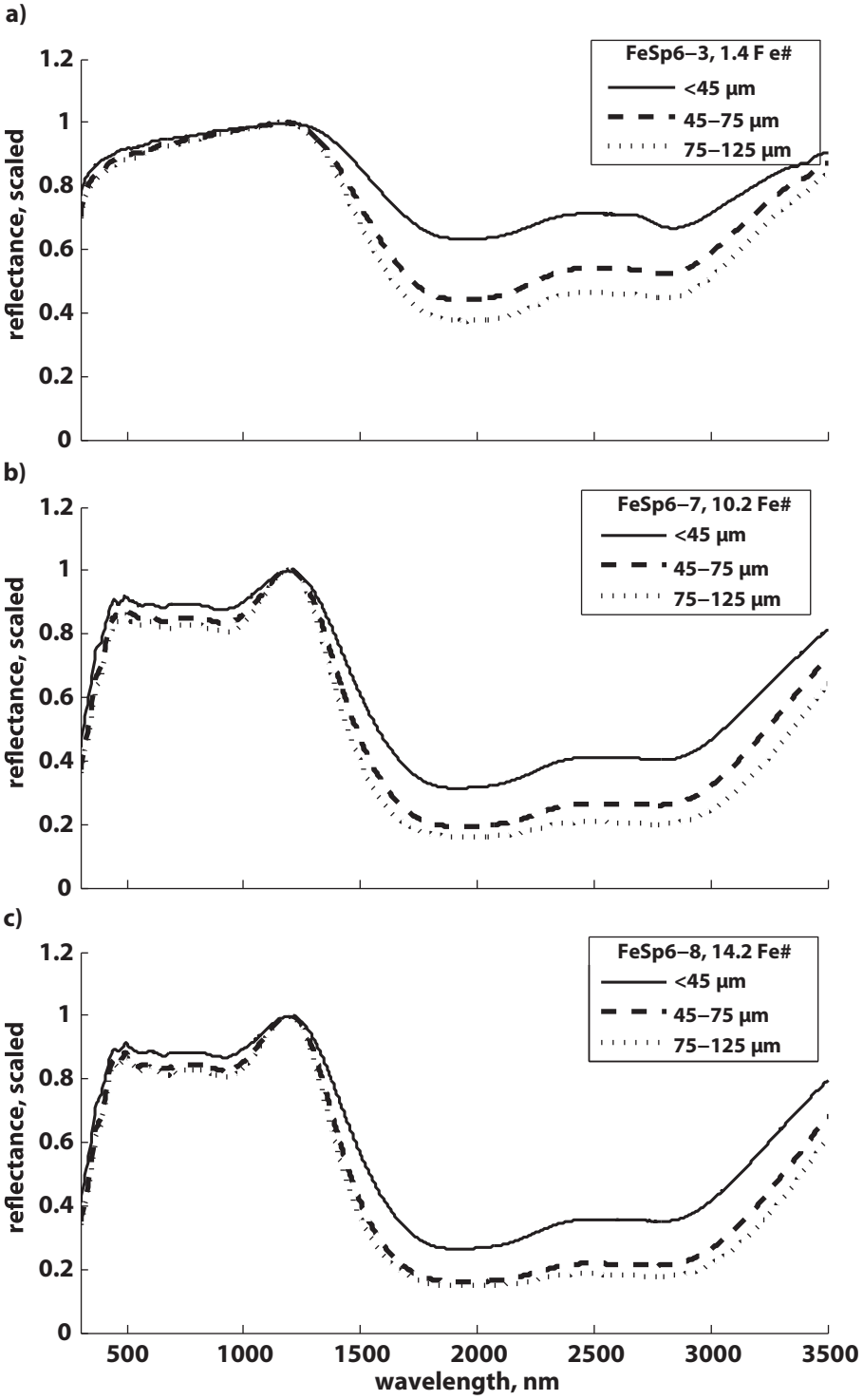

Chapter 4, figure 5

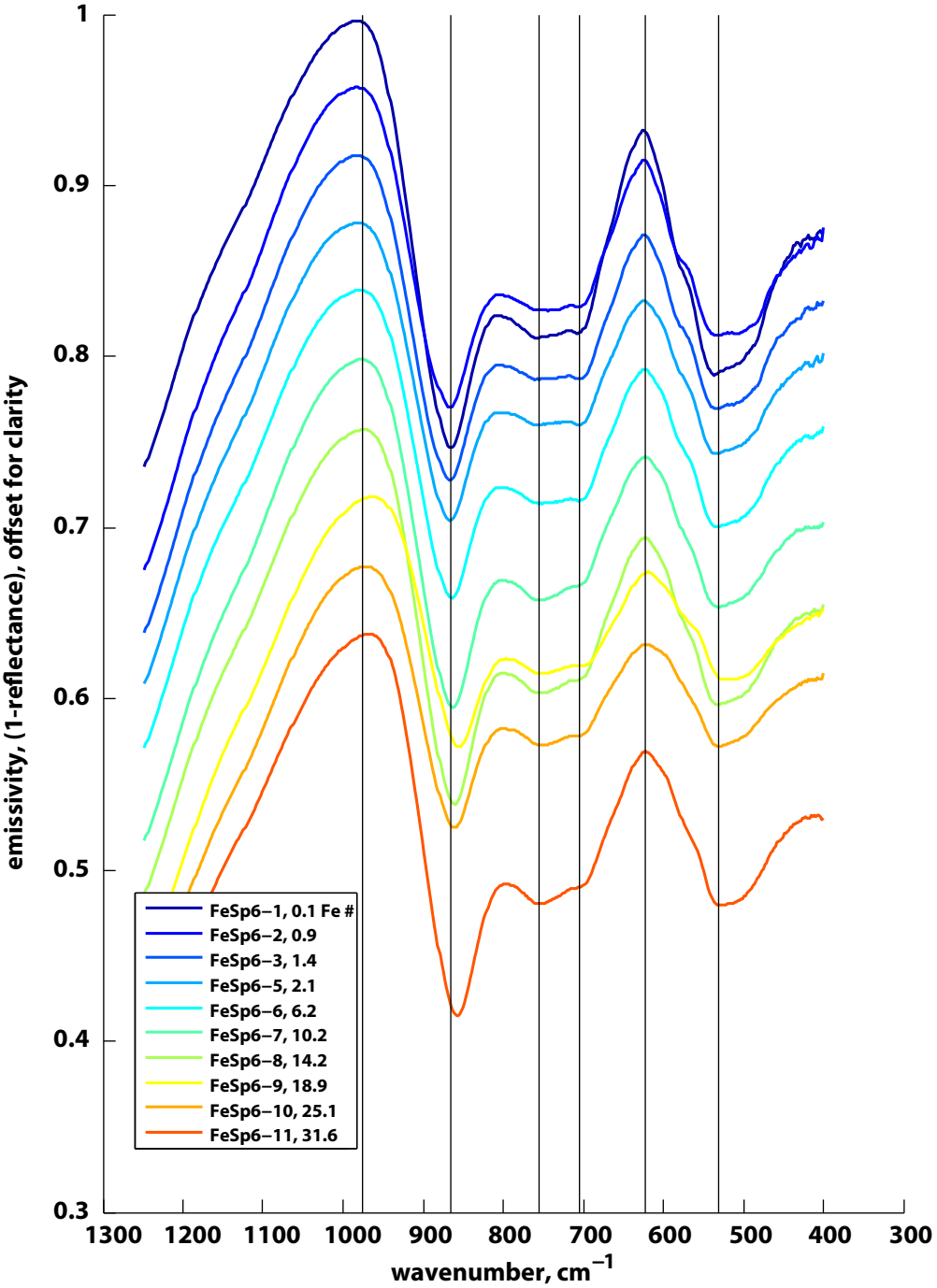

Chapter 4, Figure 6

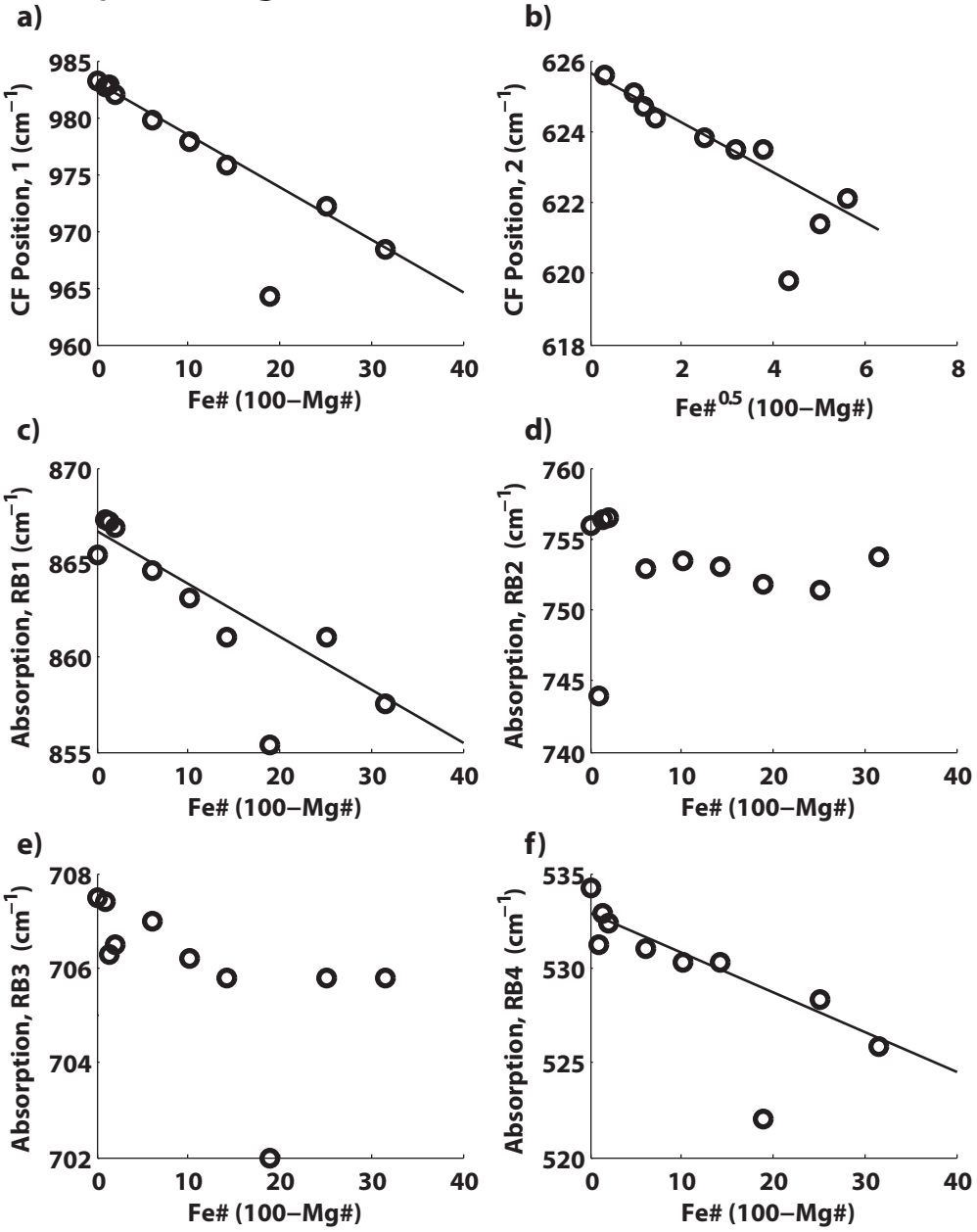

Chapter 4, Figure 7

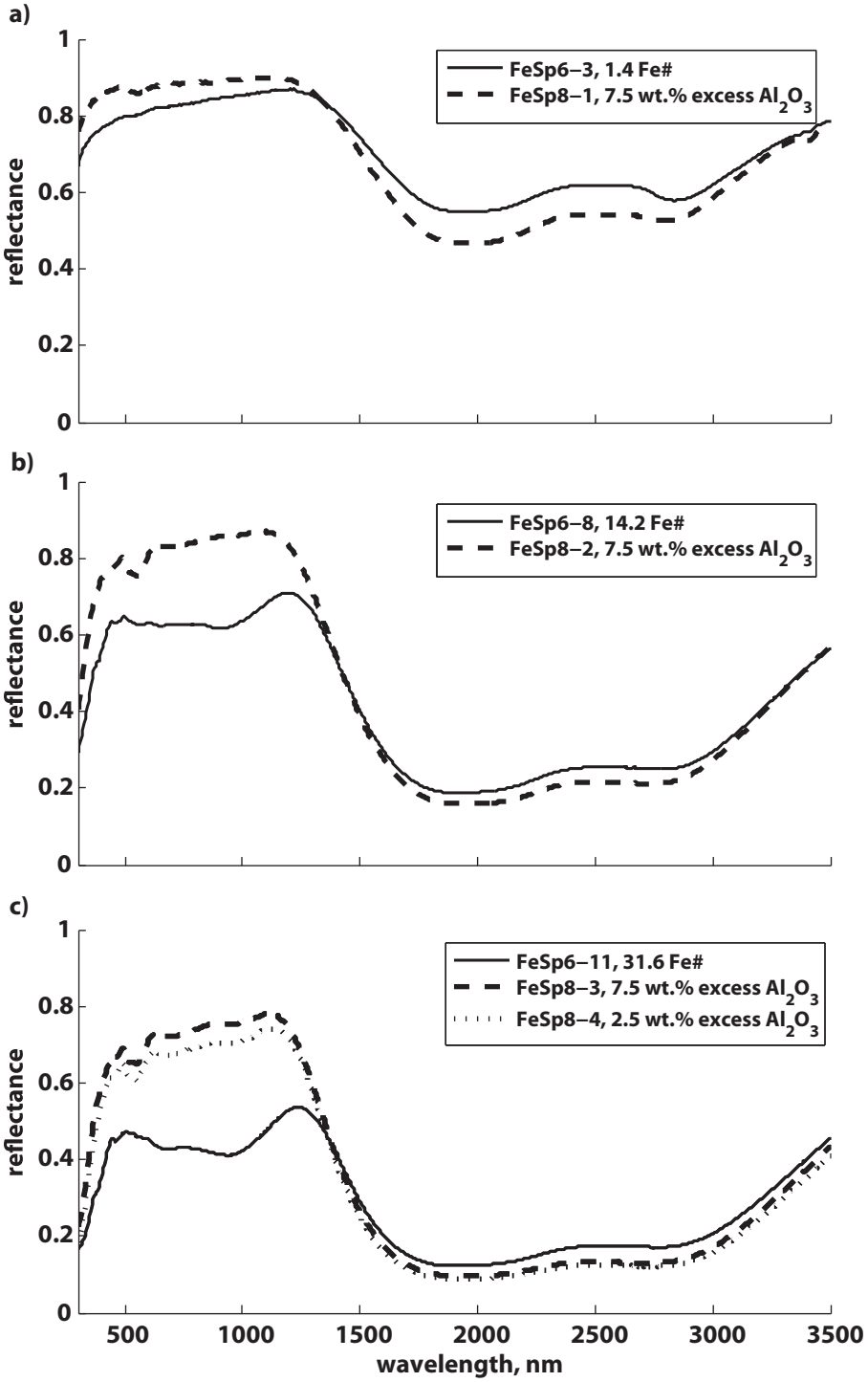

Chapter 4. Figure 8

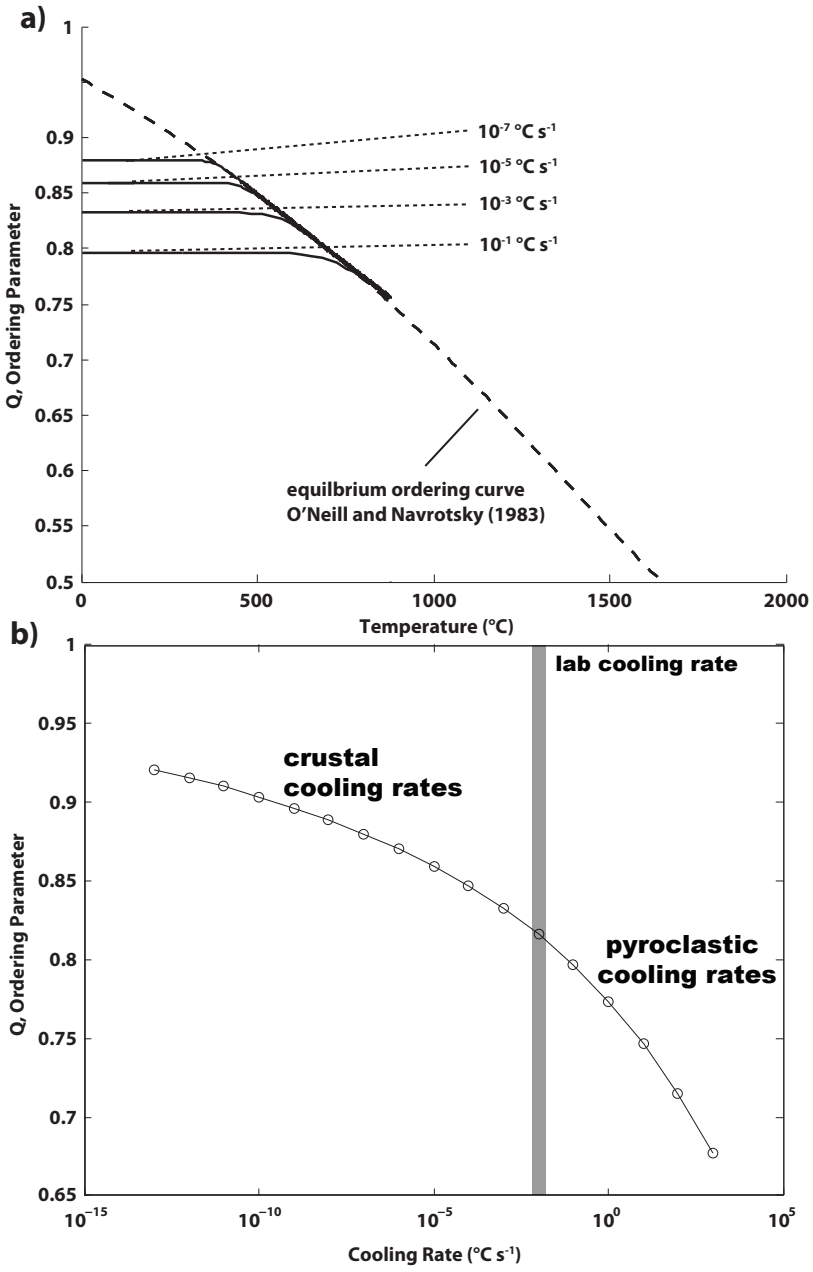

Supplementary Information for "Visible-Infrared Spectral Properties of Iron-bearing Aluminate Spinel Under Lunar-like Redox Conditions"

1.0 List of Supplementary Tables

Supplementary Table 1: Major element analyses of synthetic spinel. Individual spot electron microprobe analyses and stoichiometry calculations are presented. Flux fusion determinations of Fe# and Mg# are also presented for whole samples, i.e. one value per sample. Mössbauer spectroscopy determinations of ferric iron abundance ratios are also presented. The associated fitting parameters and spectra are presented in Tables 2 and 3, respectively.

Supplementary Table 2: Fitting parameters for Mössbauer spectra. Note that the Mössbauer spectra for FeSp8_3 and FeSp8_4 series samples did not converge using the fitting routine applied to the remainder of samples.

Supplementary Table 3: Mössbauer spectra of FeSp6 and FeSp8 series samples. Note that the velocity scales are different between FeSp6 and FeSp8 series.

Supplementary Table 1: major element compositions of synthetic spinel

Run	Sample	SiO2	Cr2O3	Al2O3	TiO2	FeO	MnO	MgO	NiO	Total (wt. %)	Fe+3/Fetot	Si	Cr	Al	Ti	Fe+3	Fe+2	Mn	Mg	Ni	Total (cations/4 O)	Mg# (EMP)	Mg# (EMP+MB)	Mg# (FF)	Fe# (FF)	acc. phases	Note
FeSp6	1	0.12	0.02	71.79	0.01	0.06	0.03	28.43	0.00	100.44	NA	0.00	0.00	1.99	0.00	0.00	0.00	0.00	1.00	0.00	3.00	99.87	N/A	99.89	0.11	FP	
FeSp6	1	0.27	0.00	71.62	0.02	0.07	0.02	28.17	0.21	100.38	NA	0.01	0.00	1.99	0.00	0.00	0.00	0.00	0.99	0.00	3.00	99.86	N/A	99.89	0.11	FP	
FeSp6	1	0.24	0.02	71.36	0.04	0.07	0.00	28.19	0.00	99.92	NA	0.01	0.00	1.99	0.00	0.00	0.00	0.00	1.00	0.00	3.00	99.86	N/A	99.89	0.11	FP	
FeSp6	1	0.10	0.02	71.68	0.00	0.13	0.00	28.15	0.01	100.09	NA	0.00	0.00	2.00	0.00	0.00	0.00	0.00	0.99	0.00	3.00	99.75	N/A	99.89	0.11	FP	
FeSp6	**1 Avg**	**0.18**	**0.01**	**71.61**	**0.02**	**0.08**	**0.01**	**28.24**	**0.05**	**100.21**	**NA**	**0.00**	**0.00**	**1.99**	**0.00**	**0.00**	**0.00**	**0.00**	**0.99**	**0.00**	**3.00**	**99.84**	N/A	**99.89**	**0.11**	**FP**	
FeSp6	1 2sd	0.17	0.02	0.35	0.03	0.06	0.03	0.26	0.21																		
FeSp6	2	0.09	0.00	72.04	0.00	0.29	0.00	27.91	0.00	100.33	0.19	0.00	0.00	2.00	0.00	0.00	0.00	0.00	0.98	0.00	2.99	99.43	99.54	99.15	0.85	FP	
FeSp6	2	0.08	0.00	71.56	0.00	0.33	0.00	28.22	0.01	100.20	0.19	0.00	0.00	2.00	0.00	0.00	0.01	0.00	1.00	0.00	3.00	99.35	99.47	99.15	0.85	FP	
FeSp6	2	0.10	0.00	72.09	0.00	0.36	0.00	28.06	0.00	100.61	0.19	0.00	0.00	2.00	0.00	0.00	0.01	0.00	0.99	0.00	3.00	99.29	99.42	99.15	0.85	FP	
FeSp6	2	0.06	0.00	71.34	0.03	0.38	0.00	28.34	0.00	100.15	0.19	0.00	0.00	1.99	0.00	0.00	0.01	0.00	1.00	0.00	3.00	99.25	99.39	99.15	0.85	FP	
FeSp6	2	0.55	0.01	71.70	0.00	0.37	0.00	28.03	0.00	100.66	0.19	0.01	0.00	1.99	0.00	0.00	0.01	0.00	0.98	0.00	2.99	99.26	99.40	99.15	0.85	FP	
FeSp6	**2 Avg**	**0.18**	**0.00**	**71.75**	**0.01**	**0.35**	**0.00**	**28.11**	**0.00**	**100.39**	**0.19**	**0.00**	**0.00**	**2.00**	**0.00**	**0.00**	**0.01**	**0.00**	**0.99**	**0.00**	**3.00**	**99.32**	**99.45**	**99.15**	**0.85**	**FP**	
FeSp6	2 2sd	0.42	0.01	0.64	0.02	0.08	0.00	0.34	0.01																		
FeSp6	3	0.07	0.00	70.68	0.00	1.55	0.00	27.06	0.02	99.38	0.10	0.00	0.00	2.00	0.00	0.00	0.03	0.00	0.97	0.00	3.00	96.89	97.19	98.59	1.41	FP	
FeSp6	3	0.05	0.00	71.27	0.00	1.50	0.01	27.49	0.00	100.32	0.10	0.00	0.00	2.00	0.00	0.00	0.03	0.00	0.97	0.00	3.00	97.03	97.32	98.59	1.41	FP	
FeSp6	3	0.03	0.01	71.64	0.00	0.88	0.00	27.74	0.01	100.30	0.10	0.00	0.00	2.00	0.00	0.00	0.02	0.00	0.98	0.00	3.00	98.26	98.43	98.59	1.41	FP	
FeSp6	3	0.10	0.02	71.57	0.00	0.74	0.00	28.00	0.00	100.43	0.10	0.00	0.00	1.99	0.00	0.00	0.01	0.00	0.99	0.00	3.00	98.54	98.69	98.59	1.41	FP	
FeSp6	3	0.06	0.01	71.37	0.00	0.97	0.00	27.81	0.00	100.22	0.10	0.00	0.00	2.00	0.00	0.00	0.02	0.00	0.98	0.00	3.00	98.08	98.27	98.59	1.41	FP	
FeSp6	3	0.10	0.00	70.53	0.00	0.95	0.00	27.33	0.00	98.92	0.10	0.00	0.00	2.00	0.00	0.00	0.02	0.00	0.98	0.00	3.00	98.08	98.27	98.59	1.41	FP	
FeSp6	3	0.09	0.00	71.65	0.02	0.83	0.00	27.63	0.00	100.22	0.10	0.00	0.00	2.00	0.00	0.00	0.01	0.00	0.98	0.00	3.00	98.34	98.51	98.59	1.41	FP	
FeSp6	3	0.09	0.00	71.56	0.02	0.78	0.00	27.87	0.00	100.32	0.10	0.00	0.00	2.00	0.00	0.00	0.01	0.00	0.98	0.00	3.00	98.45	98.60	98.59	1.41	FP	
FeSp6	3	0.08	0.01	71.59	0.00	0.55	0.01	27.97	0.00	100.22	0.10	0.00	0.00	2.00	0.00	0.00	0.01	0.00	0.99	0.00	3.00	98.90	99.01	98.59	1.41	FP	
FeSp6	3	0.07	0.00	71.43	0.01	0.72	0.03	27.90	0.00	100.16	0.10	0.00	0.00	2.00	0.00	0.00	0.01	0.00	0.99	0.00	3.00	98.58	98.72	98.59	1.41	FP	
FeSp6	**3 Avg**	**0.08**	**0.00**	**71.53**	**0.01**	**0.95**	**0.01**	**27.68**	**0.00**	**100.05**	**0.10**	**0.00**	**0.00**	**2.00**	**0.00**	**0.00**	**0.02**	**0.00**	**0.98**	**0.00**	**3.00**	**98.12**	**98.30**	**98.59**	**1.41**	**FP**	
FeSp6	3 2sd	0.05	0.01	0.80	0.01	0.66	0.02	0.61	0.01																		
FeSp6	4	0.16	0.00	71.49	0.00	1.44	0.01	27.26	0.00	100.37	0.10	0.00	0.00	2.00	0.00	0.00	0.03	0.00	0.96	0.00	3.00	97.12	97.40	97.95	2.05	FP	
FeSp6	4	0.07	0.03	72.23	0.00	1.16	0.02	27.86	0.00	101.37	0.10	0.00	0.00	2.00	0.00	0.00	0.02	0.00	0.97	0.00	3.00	97.72	97.94	97.95	2.05	FP	
FeSp6	4	0.04	0.00	71.64	0.00	1.31	0.00	27.71	0.00	100.70	0.10	0.00	0.00	2.00	0.00	0.00	0.02	0.00	0.98	0.00	3.00	97.42	97.67	97.95	2.05	FP	
FeSp6	4	0.08	0.02	71.59	0.00	0.98	0.00	27.79	0.00	100.46	0.10	0.00	0.00	2.00	0.00	0.00	0.02	0.00	0.98	0.00	3.00	98.05	98.24	97.95	2.05	FP	
FeSp6	4	0.05	0.00	71.44	0.00	1.24	0.01	27.80	0.00	100.54	0.10	0.00	0.00	1.99	0.00	0.00	0.02	0.00	0.98	0.00	3.00	97.57	97.80	97.95	2.05	FP	
FeSp6	**4 Avg**	**0.08**	**0.01**	**71.68**	**0.00**	**1.23**	**0.01**	**27.68**	**0.00**	**100.69**	**0.10**	**0.00**	**0.00**	**2.00**	**0.00**	**0.00**	**0.02**	**0.00**	**0.98**	**0.00**	**3.00**	**97.58**	**97.81**	**97.95**	**2.05**	**FP**	
FeSp6	4 2sd	0.10	0.03	0.64	0.00	0.34	0.02	0.49	0.00																		
FeSp6	5	0.56	0.00	72.51	0.00	2.80	0.00	26.06	0.03	101.96	0.05	0.01	0.00	2.00	0.00	0.00	0.05	0.00	0.91	0.00	2.98	94.32	94.58	93.85	6.15	FP	
FeSp6	5	2.59	0.00	68.51	0.00	3.16	0.01	25.62	0.02	99.90	0.05	0.06	0.00	1.93	0.00	0.00	0.06	0.00	0.91	0.00	2.97	93.53	93.83	93.85	6.15	FP	
FeSp6	5	0.14	0.00	70.62	0.00	2.76	0.00	26.67	0.00	100.19	0.05	0.00	0.00	1.99	0.00	0.00	0.05	0.00	0.95	0.00	3.00	94.51	94.77	93.85	6.15	FP	
FeSp6	5	0.09	0.00	70.70	0.00	3.41	0.01	26.42	0.03	100.67	0.05	0.00	0.00	1.99	0.00	0.00	0.06	0.00	0.94	0.00	3.00	93.25	93.56	93.85	6.15	FP	
FeSp6	5	0.14	0.00	69.77	0.01	3.08	0.00	26.20	0.02	99.22	0.05	0.00	0.00	1.99	0.00	0.00	0.06	0.00	0.94	0.00	3.00	93.81	94.10	93.85	6.15	FP	
FeSp6	**5 Avg**	**0.23**	**0.00**	**70.90**	**0.00**	**3.01**	**0.00**	**26.34**	**0.02**	**100.39**	**0.05**	**0.01**	**0.00**	**1.99**	**0.00**	**0.00**	**0.06**	**0.00**	**0.94**	**0.00**	**3.00**	**93.97**	**94.25**	**93.85**	**6.15**	**FP**	
FeSp6	5 2sd	0.44	0.00	2.31	0.01	0.60	0.01	0.53	0.03																		
FeSp6	7	0.01	0.00	69.98	0.00	4.90	0.00	25.46	0.01	100.37	0.06	0.00	0.00	1.99	0.00	0.01	0.09	0.00	0.91	0.00	3.00	90.26	90.79	89.76	10.24	FP	
FeSp6	7	0.09	0.00	69.96	0.01	5.81	0.00	24.95	0.01	100.83	0.06	0.00	0.00	1.99	0.00	0.01	0.11	0.00	0.90	0.00	3.00	88.45	89.06	89.76	10.24	FP	
FeSp6	7	0.01	0.00	70.35	0.01	5.63	0.00	24.92	0.00	100.93	0.06	0.00	0.00	1.99	0.00	0.01	0.11	0.00	0.89	0.00	3.00	88.75	89.35	89.76	10.24	FP	
FeSp6	7	0.01	0.01	70.35	0.02	5.74	0.00	25.00	0.01	101.13	0.06	0.00	0.00	1.99	0.00	0.01	0.11	0.00	0.89	0.00	3.00	88.59	89.20	89.76	10.24	FP	
FeSp6	7	0.04	0.01	70.38	0.01	4.97	0.00	25.57	0.00	100.98	0.06	0.00	0.00	1.99	0.00	0.01	0.09	0.00	0.91	0.00	3.00	90.17	90.70	89.76	10.24	FP	
FeSp6	**7 Avg**	**0.03**	**0.00**	**70.20**	**0.01**	**5.41**	**0.00**	**25.18**	**0.01**	**100.85**	**0.06**	**0.00**	**0.00**	**1.99**	**0.00**	**0.01**	**0.10**	**0.00**	**0.90**	**0.00**	**3.00**	**89.24**	**89.82**	**89.76**	**10.24**	**FP**	
FeSp6	7 2sd	0.07	0.01	0.43	0.01	0.88	0.00	0.62	0.01																		
FeSp6	8	0.06	0.00	70.20	0.00	5.89	0.00	24.63	0.05	100.84	0.04	0.00	0.00	1.99	0.00	0.00	0.11	0.00	0.88	0.00	3.00	88.17	88.59	85.77	14.23	NONE	
FeSp6	8	0.09	0.02	70.17	0.00	5.75	0.02	24.88	0.02	100.95	0.04	0.00	0.00	1.99	0.00	0.00	0.11	0.00	0.89	0.00	3.00	88.52	88.93	85.77	14.23	NONE	
FeSp6	8	0.06	0.02	70.64	0.00	5.19	0.00	25.06	0.04	101.01	0.04	0.00	0.00	1.99	0.00	0.00	0.10	0.00	0.90	0.00	3.00	89.59	89.97	85.77	14.23	NONE	
FeSp6	8	0.07	0.03	69.91	0.00	7.14	0.00	23.88	0.06	101.09	0.04	0.00	0.00	1.99	0.00	0.01	0.14	0.00	0.86	0.00	3.00	85.64	86.13	85.77	14.23	NONE	
FeSp6	8	0.11	0.01	70.36	0.02	6.56	0.00	24.41	0.02	101.49	0.04	0.00	0.00	1.99	0.00	0.01	0.13	0.00	0.87	0.00	3.00	86.90	87.36	85.77	14.23	NONE	
FeSp6	**8 Avg**	**0.08**	**0.02**	**70.26**	**0.00**	**6.11**	**0.00**	**24.57**	**0.04**	**101.08**	**0.04**	**0.00**	**0.00**	**1.99**	**0.00**	**0.00**	**0.12**	**0.00**	**0.88**	**0.00**	**3.00**	**87.77**	**88.20**	**85.77**	**14.23**	**NONE**	
FeSp6	8 2sd	0.04	0.02	0.54	0.02	1.51	0.02	0.92	0.03																		
FeSp6	9	0.07	0.00	69.10	0.02	8.89	0.01	22.89	0.03	101.01	0.03	0.00	0.00	1.99	0.00	0.01	0.18	0.00	0.83	0.00	3.00	82.11	82.55	81.14	18.86	NONE	
FeSp6	9	0.07	0.02	69.70	0.02	8.38	0.03	23.26	0.03	101.51	0.03	0.00	0.00	1.99	0.00	0.01	0.16	0.00	0.84	0.00	3.00	83.19	83.61	81.14	18.86	NONE	
FeSp6	9	0.05	0.01	69.66	0.01	7.75	0.01	23.78	0.03	101.30	0.03	0.00	0.00	1.99	0.00	0.00	0.15	0.00	0.86	0.00	3.00	84.54	84.94	81.14	18.86	NONE	
FeSp6	9	0.13	0.00	69.77	0.01	5.96	0.00	25.04	0.02	100.93	0.03	0.00	0.00	1.98	0.00	0.00	0.12	0.00	0.90	0.00	3.00	88.22	88.53	81.14	18.86	NONE	
FeSp6	9	0.07	0.03	69.10	0.02	8.41	0.04	23.30	0.02	100.99	0.03	0.00	0.00	1.98	0.00	0.01	0.17	0.00	0.85	0.00	3.00	83.16	83.58	81.14	18.86	NONE	
FeSp6	**9 Avg**	**0.08**	**0.01**	**69.47**	**0.02**	**7.88**	**0.02**	**23.65**	**0.02**	**101.15**	**0.03**	**0.00**	**0.00**	**1.99**	**0.00**	**0.00**	**0.15**	**0.00**	**0.86**	**0.00**	**3.00**	**84.26**	**84.66**	**81.14**	**18.86**	**NONE**	
FeSp6	9 2sd	0.06	0.03	0.67	0.01	2.29	0.03	1.67	0.01																		
FeSp6	10	0.05	0.00	69.67	0.00	8.66	0.04	23.12	0.03	101.57	0.08	0.00	0.00	1.99	0.00	0.01	0.16	0.00	0.83	0.00	3.00	82.64	83.80	74.94	25.06	NONE	
FeSp6	10	0.04	0.00	68.51	0.00	11.36	0.00	21.29	0.03	101.22	0.08	0.00	0.00	1.98	0.00	0.02	0.21	0.00	0.78	0.00	3.00	76.96	78.41	74.94	25.06	NONE	
FeSp6	10	0.40	0.00	68.36	0.01	11.97	0.00	20.62	0.05	101.42	0.08	0.01	0.00	1.98	0.00	0.02	0.23	0.00	0.76	0.00	2.99	75.43	76.95	74.94	25.06	NONE	
FeSp6	10	0.13	0.01	68.50	0.00	11.71	0.00	21.21	0.04	101.60	0.08	0.00	0.00	1.98	0.00	0.02	0.22	0.00	0.77	0.00	3.00	76.35	77.82	74.94	25.06	NONE	
FeSp6	10	0.03	0.02	68.01	0.01	13.13	0.02	20.18	0.06	101.46	0.08	0.00	0.00	1.98	0.00	0.02	0.25	0.00	0.74	0.00	3.00	73.26	74.86	74.94	25.06	NONE	
FeSp6	**10 Avg**	**0.13**	**0.01**	**68.61**	**0.01**	**11.37**	**0.01**	**21.28**	**0.04**	**101.45**	**0.08**	**0.00**	**0.00**	**1.98**	**0.00**	**0.02**	**0.21**	**0.00**	**0.78**	**0.00**	**3.00**	**76.95**	**78.39**	**74.94**	**25.06**	**NONE**	
FeSp6	10 2sd	0.32	0.02	1.25	0.01	3.30	0.04	2.24	0.03																		
FeSp6	11	0.07	0.00	68.18	0.01	15.48	0.00	18.37	0.06	102.17	0.04	0.00	0.00	1.99	0.00	0.01	0.31	0.00	0.68	0.00	3.00	67.90	68.78	68.41	31.59	NONE	
FeSp6	11	0.03	0.00	67.63	0.00	15.86	0.01	18.21	0.06	101.81	0.04	0.00	0.00	1.99	0.00	0.01	0.32	0.00	0.68	0.00	3.00	67.18	68.07	68.41	31.59	NONE	
FeSp6	11	0.04	0.00	67.83	0.03	15.06	0.00	18.56	0.05	101.56	0.04	0.00	0.00	1.99	0.00	0.01	0.30	0.00	0.69	0.00	3.00	68.72	69.59	68.41	31.59	NONE	
FeSp6	11	0.03	0.00	67.99	0.03	15.03	0.02	18.68	0.07	101.75	0.04	0.00	0.00	1.99	0.00	0.01	0.30	0.00	0.69	0.00	3.00	68.90	69.77	68.41	31.59	NONE	
FeSp6	11	0.06	0.00	68.20	0.02	14.97	0.03	18.73	0.06	102.07	0.04	0.00	0.00	1.99	0.00	0.01	0.30	0.00	0.69	0.00	3.00	69.04	69.91	68.41	31.59	NONE	
FeSp6	**11 Avg**	**0.05**	**0.00**	**67.95**	**0.02**	**15.28**	**0.01**	**18.51**	**0.06**	**101.87**	**0.04**	**0.00**	**0.00**	**1.99**	**0.00**	**0.01**	**0.30**	**0.00**	**0.69**	**0.00**	**3.00**	**68.35**	**69.22**	**68.41**	**31.59**	**NONE**	
FeSp6	11 2sd	0.03	0.00	0.45	0.03	0.76	0.02	0.44	0.02																		
FeSp8	1	0.06	-0.04	69.29	-0.01	1.26	0.02	24.97	0.02	95.61	0.02	0.00	0.00	2.03	0.00	0.00	0.03	0.00	0.93	0.00	2.98	97.26	97.30	NA	NA	NONE	same as FeSp6_3
FeSp8	1	0.04	0.01	70.94	0.01	1.28	-0.01	26.19	0.02	98.52	0.02	0.00	0.00	2.02	0.00	0.00	0.03	0.00	0.94	0.00	2.99	97.34	97.38	NA	NA	NONE	same as FeSp6_3
FeSp8	1	0.07	0.02	70.97	0.00	1.21	0.03	25.95	0.01	98.25	0.02	0.00	0.00	2.02	0.00	0.00	0.02	0.00	0.94	0.00	2.99	97.44	97.49	NA	NA	NONE	same as FeSp6_3
FeSp8	1	0.01	0.02	71.28	0.00	1.17	-0.27	26.73	-0.58	97.36	0.02	0.00	0.00	2.02	0.00	0.00	0.02	-0.01	0.96	-0.01	2.99	97.59	97.63	NA	NA	NONE	same as FeSp6_3
FeSp8	1	0.06	0.01	72.30	0.00	1.20	0.48	26.61	-0.09	100.08	0.02	0.00	0.00	2.02	0.00	0.00	0.02	0.01	0.94	0.00	2.99	97.54	97.58	NA	NA	NONE	same as FeSp6_3
FeSp8	1	0.02	-0.04	71.26	0.00	1.12	-0.07	26.28	0.70	99.33	0.02	0.00	0.00	2.02	0.00	0.00	0.02	0.00	0.94	0.01	2.99	97.67	97.71	NA	NA	NONE	same as FeSp6_3
FeSp8	1	0.05	0.00	71.31	0.00	1.24	-0.26	26.23	-0.33	98.36	0.02	0.00	0.00	2.03	0.00	0.00	0.02	-0.01	0.94	-0.01	2.98	97.42	97.47	NA	NA	NONE	same as FeSp6_3
FeSp8	1	0.03	-0.02	72.04	0.01	1.26	-0.04	26.50	0.09	99.91	0.02	0.00	0.00	2.02	0.00	0.00	0.02	0.00	0.94	0.00	2.99	97.40	97.44	NA	NA	NONE	same as FeSp6_3
FeSp8	1	0.02	-0.02	71.82	0.00	1.16	0.00	26.23	-0.01	99.26	0.02	0.00	0.00	2.03	0.00	0.00	0.02	0.00	0.94	0.00	2.99	97.58	97.62	NA	NA	NONE	same as FeSp6_3
FeSp8	**1 Avg**	**0.04**	**0.00**	**71.52**	**0.00**	**1.21**	**0.02**	**26.28**	**0.06**	**99.10**	**0.02**	**0.00**	**0.00**	**2.02**	**0.00**	**0.00**	**0.02**	**0.00**	**0.94**	**0.00**	**2.99**	**97.49**	**97.53**	**NA**	**NA**	**NONE**	**same as FeSp6_3**
FeSp8	1 2sd	0.04	0.04	1.07	0.01	0.11	0.45	0.43	0.63																		
FeSp8	2	0.03	0.01	71.62	0.01	6.75	0.01	22.17	0.04	100.71	0.03	0.00	0.00	2.04	0.00	0.00	0.13	0.00	0.80	0.00	2.98	85.42	85.80	NA	NA	NONE	same as FeSp6_8
FeSp8	2	0.02	0.00	70.47	-0.01	6.76	-0.01	21.83	0.02	99.17	0.03	0.00	0.00	2.04	0.00	0.00	0.13	0.00	0.80	0.00	2.98	85.21	85.59	NA	NA	NONE	same as FeSp6_8
FeSp8	2	0.03	-0.04	70.90	0.00	6.51	0.03	22.15	0.03	99.64	0.03	0.00	0.00	2.04	0.00	0.00	0.13	0.00	0.81	0.00	2.98	85.84	86.21	NA	NA	NONE	same as FeSp6_8
FeSp8	2	0.04	0.02	71.17	0.00	6.74	-0.02	22.40	0.04	100.46	0.03	0.00	0.00	2.03	0.00	0.00	0.13	0.00	0.81	0.00	2.98	85.56	85.93	NA	NA	NONE	same as FeSp6_8
FeSp8	2	0.03	0.00	71.30	0.00	6.71	0.01	22.45	0.06	100.67	0.03	0.00	0.00	2.03	0.00	0.00	0.13	0.00	0.81	0.00	2.98	85.63	86.00	NA	NA	NONE	same as FeSp6_8
FeSp8	2	0.04	0.00	71.36	0.00	6.64	-0.03	22.03	0.01	100.10	0.03	0.00	0.00	2.04	0.00	0.00	0.13	0.00	0.80	0.00	2.98	85.53	85.90	NA	NA	NONE	same as FeSp6_8
FeSp8	2	0.01	0.01	71.36	0.01	6.72	-0.02	22.00	0.02	100.17	0.03	0.00	0.00	2.04	0.00	0.00	0.13	0.00	0.80	0.00	2.98	85.37	85.74	NA	NA	NONE	same as FeSp6_8
FeSp8	2	0.02	-0.01	71.41	0.01	7.11	0.01	21.89	0.01	100.54	0.03	0.00	0.00	2.04	0.00	0.00	0.14	0.00	0.79	0.00	2.98	84.99	84.99	NA	NA	NONE	same as FeSp6_8
FeSp8	2	0.03	-0.03	72.07	0.00	6.82	0.02	22.17	-0.04	101.15	0.03	0.00	0.00	2.04	0.00	0.00	0.13	0.00	0.80	0.00	2.98	85.28	85.66	NA	NA	NONE	same as FeSp6_8
FeSp8	2	0.03	-0.01	71.26	0.00	7.05	-0.01	21.92	0.03	100.28	0.03	0.00	0.00	2.04	0.00	0.00	0.14	0.00	0.79	0.00	2.98	84.71	85.10	NA	NA	NONE	same as FeSp6_8
FeSp8	**2 Avg**	**0.03**	**0.00**	**71.29**	**0.00**	**6.78**	**0.00**	**22.10**	**0.02**	**100.29**	**0.03**	**0.00**	**0.00**	**2.04**	**0.00**	**0.00**	**0.13**	**0.00**	**0.80**	**0.00**	**2.98**	**85.32**	**85.69**	**NA**	**NA**	**NONE**	**same as FeSp6_8**
FeSp8	2 2sd	0.02	0.04	0.84	0.02	0.36	0.04	0.42	0.05																		
FeSp8	3	0.02	0.02	68.92	0.00	14.54	-0.03	17.28	0.03	100.80	NA	0.00	0.00	2.03	0.00	0.00	0.30	0.00	0.64	0.00	2.98	67.94	67.94	NA	NA	NONE	same as FeSp6_11
FeSp8	3	0.07	-0.04	68.14	0.00	13.96	0.02	16.85	-0.01	99.11	NA	0.00	0.00	2.04	0.00	0.00	0.30	0.00	0.64	0.00	2.98	68.28	68.28	NA	NA	NONE	same as FeSp6_11
FeSp8	3	0.04	0.04	68.75	0.00	14.25	-0.01	17.18	0.04	100.30	NA	0.00	0.00	2.04	0.00	0.00	0.30	0.00	0.64	0.00	2.98	68.25	68.25	NA	NA	NONE	same as FeSp6_11
FeSp8	3	0.03	-0.02	68.76	-0.01	14.72	-0.07	17.27	0.02	100.75	NA	0.00	0.00	2.03	0.00	0.00	0.31	0.00	0.65	0.00	2.98	67.66	67.66	NA	NA	NONE	same as FeSp6_11
FeSp8	3	0.00	-0.02	68.69	-0.01	14.45	-0.01	17.46	0.05	100.56	NA	0.00	0.00	2.03	0.00	0.00	0.30	0.00	0.65	0.00	2.98	68.28	68.28	NA	NA	NONE	same as FeSp6_11
FeSp8	3	0.05	0.00	68.56	0.00	14.15	-0.01

FeSp10	1	0.03	-0.07	66.85	0.01	16.08	-0.01	19.66	-0.01	102.63	NA	0.00	0.00	1.96	0.00	0.00	0.33	0.00	0.73	0.00	3.02	68.55	N/A	NA	NA	NONE	same as FeSp6_11
FeSp10	1	0.02	0.03	64.76	0.01	18.65	-0.01	17.47	-0.03	100.93	NA	0.00	0.00	1.95	0.00	0.00	0.40	0.00	0.67	0.00	3.02	62.54	N/A	NA	NA	NONE	same as FeSp6_11
FeSp10	1	0.02	0.13	66.36	0.01	15.88	-0.03	19.54	0.01	101.96	NA	0.00	0.00	1.96	0.00	0.00	0.33	0.00	0.73	0.00	3.02	68.69	N/A	NA	NA	NONE	same as FeSp6_11
FeSp10	1	0.03	-0.05	65.94	0.01	15.21	-0.01	19.67	0.07	100.94	NA	0.00	0.00	1.96	0.00	0.00	0.32	0.00	0.74	0.00	3.02	69.74	N/A	NA	NA	NONE	same as FeSp6_11
FeSp10	1	0.02	-0.05	65.43	0.00	17.75	-0.01	18.18	0.01	101.39	NA	0.00	0.00	1.96	0.00	0.00	0.38	0.00	0.69	0.00	3.02	64.61	N/A	NA	NA	NONE	same as FeSp6_11
FeSp10	1	0.02	-0.05	66.32	0.00	17.84	0.00	18.48	-0.04	102.67	NA	0.00	0.00	1.96	0.00	0.00	0.37	0.00	0.69	0.00	3.02	64.87	N/A	NA	NA	NONE	same as FeSp6_11
FeSp10	1	0.02	0.10	64.95	0.01	18.32	0.00	17.56	-0.03	100.95	NA	0.00	0.00	1.96	0.00	0.00	0.39	0.00	0.67	0.00	3.02	63.09	N/A	NA	NA	NONE	same as FeSp6_11
FeSp10	1	0.03	0.03	67.29	0.01	15.46	-0.02	19.70	0.04	102.56	NA	0.00	0.00	1.97	0.00	0.00	0.32	0.00	0.73	0.00	3.02	69.44	N/A	NA	NA	NONE	same as FeSp6_11
FeSp10	**1 Avg**	**0.03**	**0.00**	**66.07**	**0.01**	**16.76**	**-0.01**	**18.75**	**0.00**	**101.67**	**NA**	**0.00**	**0.00**	**1.96**	**0.00**	**0.00**	**0.35**	**0.00**	**0.70**	**0.00**	**3.02**	**66.60**	N/A	**NA**	**NA**	**NONE**	**same as FeSp6_11**
FeSp10	1 2sd	0.05	0.13	1.57	0.01	2.29	0.02	1.78	0.07																		

Notes:

NA	not analyzed
FP	ferro-periclase
Fe+3/Fetot	calculated by mossbauer, if NA assumed to be 0
Mg# (EMP)	calculated from EMP assuming all Fe as Fe+2
Mg# (EMP+MB)	calculated from EMP using Fe+3/Fetot from mossbauer, when available
Mg # (FF)	calculated from flux fusion data assuming all Fe as Fe+2
Fe# (FF)	100-Mg #
stoichiometry	calculated on a 4 oxygen basis

Supplementary Table 2: mossbauer spectral fits

sample		FeSp6_1	FeSp6_2	FeSp6_3	FeSp6_4	FeSp6_5	FeSp6_7	FeSp6_8	FeSp6_9	FeSp6_10	FeSp6_11	FeSp8-1	FeSp8-2	FeSp8-3	FeSp8-4
velocity scale (mm/s)		+/- 4	+/- 4	+/- 4	+/- 4	+/- 4	+/- 4	+/- 4	+/- 4	+/- 4	+/- 4	+/- 4	+/- 4	+/- 4	+/- 4
spectrum temp (K)		295	295	295	295	295	295	295	295	295	295	295	295	295	295
filename		low iron, not fit	12101501eh	12102401ch	12100501bg	12080301ff	12072601ac	12072701cd	12080701ej	12080801bc	12080901bd	13070301a	13070303n	13070401ad	13070402r
ferric 4-coord	**IS**		0.21	0.21	0.19	0.22	0.18	0.20	0.18	0.21	0.18	0.21	0.21		
	QS		0.60	0.68	0.74	0.77	0.77	0.77	0.91	0.77	0.78	0.66	0.77		
	Width		0.40*	0.30*	0.30*	0.23*	0.23	0.23*	0.23*	0.30	0.24	0.400*	0.230*		
	Area		19	10	10	5	6	4	3	8	4	17	3		
ED ferric/ferrous	**IS**													0.73	0.75
	QS													1.64	1.63
	Width													0.35*	0.35*
	Area													26	27
ferrous 4-coord	**IS**		0.89	0.89	0.91	0.91	0.91	0.92	0.92	0.91	0.92	0.89	0.92	0.92	0.92
	QS		1.13	1.13	1.13	1.06	1.07	1.07	0.98	1.07	1.07	1.13	1.06	0.65	0.65
	Width		0.59	0.60	0.56	0.53	0.53	0.52	0.48	0.51	0.53	0.55	0.52	0.31	0.34
	Area		65	74	58	61	58	57	55	49	56	62	65	29	34
ferrous 4-coord	**IS**		0.82	0.86	0.87	0.85	0.84	0.84	0.81	0.84	0.84	0.79	0.85	0.95	0.95
	QS		1.93	1.80	1.80	1.68	1.65	1.66	1.65	1.95	1.65	1.91	1.67	1.54	1.53
	Width		0.30*	0.30*	0.40*	0.30*	0.27	0.30*	0.23	0.30*	0.27	0.30*	0.30*	0.30*	0.30
	Area		12	12	22	21	20	23	19	26	24	12	20	26	21
ferrous 6-coord	**IS**		1.03	1.02	1.07	1.04	1.05	1.07	1.05	1.08	1.08	1.01	1.05	1.16	1.14
	QS		1.82	1.81	1.85	1.70	1.73	1.79	1.75	1.76	1.82	1.84	1.79	1.67	1.55
	Width		0.30*	0.30*	0.30*	0.30*	0.30*	0.30*	0.30*	0.30*	0.30*	0.30*	0.30*	0.33	0.30*
	Area		5	4	9	13	17	15	23	17	15	8	12	19	18
	χ^2		467.24	630.19	491.50	477.59	411.62	444.22	1922.33	543.24	688.85	478.78	1394.57	2455.61	1690.76
	χ^2_{norm}		0.9127	1.2308	0.9602	0.9319	0.804	0.8671	3.7332	1.0603	1.3419	0.9352	2.7113	4.7635	3.2829
	total		99.99	100.00	100.00	100.00	100.01	100.00	100.00	100.00	100.00	99.99	100.00	100.00	100.01
	Q		0.92	0.93	0.85	0.80	0.73	0.77	0.65	0.73	0.76	0.85	0.81	0.61	0.64

Notes:
* = parameter fixed
Q = ordering parameter

Supplementary Table 3: Mossbauer Spectra

velocity (mm/s)	FeSp6_2	FeSp6_3	FeSp6_4	FeSp6_5	FeSp6_7	FeSp6_8	FeSp6_9	FeSp6_10	FeSp6_11	velocity (mm/s)	FeSp8_1	FeSp8_2	FeSp8_3	FeSp8_4
-4.233	99.985	99.971	99.977	100.035	99.962	99.874	99.938	99.998	99.958	-4.2492	99.976	99.91	99.912	99.928
-4.216	99.995	99.965	99.959	100.061	99.937	99.869	99.935	99.987	99.938	-4.2321	99.978	99.904	99.926	99.927
-4.199	99.989	99.98	99.964	99.954	99.95	99.931	99.924	99.985	99.974	-4.2151	99.995	99.947	99.956	99.982
-4.182	99.975	99.985	99.982	99.931	99.951	100.012	99.949	99.965	99.928	-4.198	100.018	99.944	99.944	99.944
-4.1651	99.968	99.987	99.985	99.968	99.958	99.985	99.953	99.964	99.958	-4.181	100	99.893	99.926	99.966
-4.1481	99.973	99.99	99.996	100.002	99.964	100.015	99.94	99.899	100.021	-4.1639	99.991	99.925	99.923	99.886
-4.1311	99.973	99.97	100.001	99.967	99.967	100.044	99.937	99.937	99.966	-4.1469	99.984	99.894	99.951	99.915
-4.1141	99.955	99.965	100	99.966	99.966	99.968	99.902	99.999	99.947	-4.1298	99.991	99.919	99.93	99.875
-4.0972	99.964	99.976	99.982	99.975	100.001	99.987	99.897	99.998	99.93	-4.1127	99.973	99.935	99.962	99.883
-4.0802	99.98	99.978	99.965	99.966	99.957	99.943	99.937	99.991	99.908	-4.0957	99.929	99.952	100.006	99.886
-4.0632	99.987	99.964	99.958	99.992	100.001	99.975	99.936	99.997	99.869	-4.0786	99.959	99.924	99.939	99.932
-4.0462	99.982	99.988	99.947	99.995	99.978	99.937	99.939	99.986	99.95	-4.0616	99.961	99.939	99.94	99.936
-4.0293	99.97	99.977	99.923	99.964	99.915	99.959	99.941	99.983	100.017	-4.0445	99.946	99.925	99.95	99.919
-4.0123	99.983	99.958	99.95	99.965	99.939	99.961	99.941	99.952	99.966	-4.0275	99.988	99.901	99.937	99.925
-3.9953	100.005	99.974	99.971	100.007	99.931	99.986	99.936	99.948	99.956	-4.0104	99.979	99.934	99.913	99.914
-3.9783	99.999	99.966	100.013	99.975	99.996	100.037	99.931	99.992	99.94	-3.9934	99.974	99.953	99.903	99.933
-3.9614	99.981	99.945	99.986	99.944	99.939	99.979	99.973	99.983	99.935	-3.9763	99.965	99.947	99.935	99.957
-3.9444	99.978	99.961	99.961	99.967	99.937	99.945	99.946	99.954	99.915	-3.9593	99.976	99.949	99.95	99.934
-3.9274	99.978	99.987	99.98	99.985	99.938	99.933	99.915	99.938	99.934	-3.9422	99.989	99.914	99.965	99.889
-3.9104	99.979	99.984	99.966	99.967	99.904	99.933	99.917	99.951	99.985	-3.9252	100.001	99.909	99.952	99.908
-3.8935	99.976	99.972	99.948	99.924	99.965	99.946	99.937	99.955	99.994	-3.9081	99.983	99.915	99.937	99.952
-3.8765	99.979	100.004	99.942	99.947	99.98	99.923	99.965	99.895	99.953	-3.891	99.977	99.943	99.963	99.904
-3.8595	100.014	100.016	99.946	99.957	99.937	99.959	99.999	99.896	99.971	-3.874	100.005	99.948	99.933	99.881
-3.8425	100.011	100.004	99.974	100	99.943	99.985	99.978	99.946	99.908	-3.8569	100	99.957	99.924	99.962
-3.8256	100.002	99.977	99.98	100.015	99.929	99.97	99.942	99.956	99.866	-3.8399	99.971	99.986	99.935	100.03
-3.8086	99.987	99.983	100.013	99.974	99.943	100.011	99.93	99.968	99.939	-3.8228	99.983	99.98	99.916	99.959
-3.7916	99.958	99.977	100.013	99.958	99.962	100.014	99.928	99.969	100.015	-3.8058	99.971	99.92	99.912	99.906
-3.7746	99.957	99.979	99.999	99.963	99.98	99.955	99.927	99.953	99.986	-3.7887	99.957	99.939	99.962	99.884
-3.7577	100.006	99.966	100.007	99.968	99.995	99.917	99.941	99.955	99.929	-3.7717	99.966	99.974	99.964	99.89
-3.7407	99.997	99.952	100.018	99.97	99.93	99.928	99.967	99.924	99.985	-3.7546	99.99	99.913	99.96	99.912
-3.7237	99.973	99.975	99.996	99.963	99.93	99.931	99.963	99.923	99.973	-3.7376	99.973	99.857	99.94	99.913
-3.7067	99.977	99.984	99.973	99.948	99.969	99.954	99.963	99.928	99.994	-3.7205	99.972	99.914	99.911	99.939
-3.6898	99.995	99.99	99.973	100	99.966	99.978	99.954	99.948	99.996	-3.7035	99.986	100.025	99.927	99.954
-3.6728	100.012	99.987	99.979	99.977	99.974	99.952	99.962	99.929	99.964	-3.6864	99.994	99.978	99.919	99.952
-3.6558	100.007	99.977	99.983	99.986	99.979	99.988	99.931	99.979	99.919	-3.6693	99.984	99.897	99.939	99.95
-3.6388	99.988	99.988	99.978	99.994	99.99	99.938	99.918	99.961	99.923	-3.6523	99.988	99.926	99.946	99.932
-3.6219	99.998	99.989	99.991	99.998	99.987	99.975	99.921	99.987	99.948	-3.6352	99.976	99.948	99.937	99.879
-3.6049	99.994	99.988	100.005	99.93	99.962	99.971	99.935	99.947	99.963	-3.6182	99.948	99.966	99.933	99.881
-3.5879	99.99	99.992	99.995	99.964	99.97	99.954	99.947	99.957	99.998	-3.6011	99.96	99.995	99.935	99.86
-3.5709	99.999	99.978	99.976	100.005	99.956	99.936	99.948	99.949	99.994	-3.5841	99.97	99.98	99.941	99.876
-3.554	99.999	99.995	99.964	99.966	99.96	99.956	99.945	99.946	99.97	-3.567	99.989	99.939	99.909	99.924
-3.537	99.98	100.002	99.976	99.949	99.926	99.954	99.931	99.966	99.979	-3.55	100.008	99.916	99.901	99.96
-3.52	99.961	99.963	99.985	99.977	99.913	99.956	99.934	99.966	99.957	-3.5329	99.994	99.924	99.914	99.957
-3.503	99.974	99.968	99.999	99.964	99.949	99.958	99.935	99.971	99.927	-3.5159	99.97	99.934	99.935	99.924
-3.4861	99.987	99.977	100.003	99.923	99.973	99.951	99.955	99.98	99.891	-3.4988	99.998	99.897	99.975	99.926
-3.4691	99.987	99.989	99.986	99.906	99.973	100.009	99.962	99.948	99.932	-3.4817	99.997	99.921	99.989	99.943
-3.4521	99.988	100.009	99.965	99.884	99.975	100.002	99.954	99.931	99.954	-3.4647	99.987	99.966	99.995	99.96
-3.4351	99.998	99.981	99.949	99.903	100	99.925	99.957	99.936	99.899	-3.4476	100.006	99.931	100	99.923
-3.4182	99.997	99.971	99.95	99.927	99.939	99.943	99.959	99.989	99.912	-3.4306	100.015	99.91	99.975	99.914
-3.4012	99.977	99.984	99.958	99.959	99.863	99.952	99.949	99.964	100.007	-3.4135	99.996	99.901	99.968	99.896
-3.3842	99.973	99.982	99.975	99.983	99.935	99.924	99.913	99.955	99.955	-3.3965	100.004	99.913	99.99	99.956
-3.3672	99.991	99.983	99.98	99.999	99.965	99.986	99.91	99.948	99.922	-3.3794	100.003	99.956	99.958	99.958
-3.3503	99.995	99.988	99.997	99.96	99.957	100.02	99.917	99.963	99.943	-3.3624	99.995	100.016	99.923	99.962
-3.3333	99.984	99.986	99.999	99.972	100.003	99.998	99.899	99.966	99.944	-3.3453	99.971	99.969	99.923	99.936
-3.3163	99.972	99.983	99.945	100.012	99.985	100.004	99.911	99.901	99.923	-3.3283	99.997	99.935	99.937	99.966
-3.2993	99.968	100.004	99.976	99.973	100.021	100.051	99.935	99.877	99.902	-3.3112	99.976	99.854	99.93	99.889
-3.2824	99.98	99.999	99.995	99.998	99.971	100.029	99.943	99.966	99.901	-3.2942	99.976	99.868	99.9	99.897
-3.2654	99.992	99.984	99.979	99.967	99.95	100.027	99.971	99.932	99.959	-3.2771	99.975	99.936	99.931	99.905
-3.2484	99.986	100	99.975	99.913	99.988	99.949	99.947	99.95	99.935	-3.26	100.026	99.963	99.872	99.92
-3.2314	99.984	99.996	99.961	99.946	99.911	99.915	99.947	99.987	99.937	-3.243	99.961	99.985	99.893	99.972
-3.2145	99.977	99.982	99.981	99.959	99.912	99.94	99.956	99.977	99.888	-3.2259	99.975	99.971	99.921	99.978
-3.1975	99.981	99.995	99.983	99.942	99.951	100.051	99.953	99.979	99.942	-3.2089	99.98	99.941	99.944	99.974
-3.1805	99.98	99.989	99.993	99.964	99.981	100.034	99.929	99.962	99.889	-3.1918	99.947	99.896	99.936	99.909
-3.1635	99.986	99.969	99.981	99.938	99.99	99.991	99.938	99.939	99.938	-3.1748	99.981	99.954	99.967	99.978
-3.1466	99.984	99.977	99.975	99.988	99.946	99.978	99.934	99.927	99.992	-3.1577	99.981	99.982	99.96	99.947
-3.1296	99.994	99.983	99.991	99.969	99.923	99.998	99.959	99.973	99.965	-3.1407	99.977	100.016	99.971	99.884
-3.1126	99.981	99.986	99.998	99.957	99.934	99.979	99.953	99.991	99.946	-3.1236	99.97	100.005	99.948	99.895
-3.0956	99.977	99.97	99.986	99.984	99.956	100	99.943	99.964	99.904	-3.1066	100.002	99.988	99.92	99.902
-3.0787	99.994	99.98	99.972	99.947	99.967	99.938	99.937	100.017	99.95	-3.0895	100.007	99.972	99.948	99.891
-3.0617	99.997	99.967	99.96	99.936	99.942	99.977	99.926	99.961	99.955	-3.0724	100.003	99.964	99.936	99.889
-3.0447	99.978	99.975	99.967	99.924	99.993	100.002	99.917	99.977	99.954	-3.0554	99.987	99.934	99.942	99.907
-3.0277	99.992	99.999	99.991	99.912	99.946	99.999	99.951	99.939	99.941	-3.0383	99.988	99.923	99.968	99.923
-3.0108	99.996	100.001	99.999	99.975	99.921	99.936	99.944	99.962	99.974	-3.0213	99.995	99.964	99.964	99.954
-2.9938	99.987	99.985	99.994	100.016	99.938	99.971	99.947	99.958	99.981	-3.0042	99.988	99.986	99.954	99.919
-2.9768	99.983	99.967	99.987	99.945	99.956	100.002	99.94	99.913	99.973	-2.9872	99.993	99.961	99.928	99.912
-2.9598	99.994	99.988	99.984	99.909	99.947	99.975	99.922	99.918	99.977	-2.9701	100.031	99.955	99.951	99.923
-2.9429	99.986	99.966	99.955	99.968	99.996	99.914	99.924	99.98	99.974	-2.9531	100.03	100	99.933	99.985
-2.9259	99.999	99.978	99.974	100.025	99.966	99.969	99.967	100.03	99.978	-2.936	99.985	99.907	99.935	99.927
-2.9089	99.994	99.982	99.965	99.964	99.97	99.993	99.968	99.973	99.954	-2.919	99.985	99.887	99.933	99.899
-2.8919	99.982	99.976	99.964	99.922	99.994	99.988	99.939	99.952	99.935	-2.9019	100.005	99.94	99.93	99.911
-2.875	99.991	99.989	99.974	99.934	99.935	99.975	99.954	99.996	99.966	-2.8849	99.951	99.94	99.947	99.907
-2.858	100.01	99.984	99.976	99.977	99.952	99.909	99.923	100.019	99.974	-2.8678	99.961	99.9	99.923	99.913
-2.841	100	99.984	99.97	99.984	100.015	99.949	99.919	100.029	99.958	-2.8507	99.959	99.906	99.917	99.933
-2.824	100	100.003	99.97	99.925	99.961	99.965	99.919	99.954	99.935	-2.8337	99.948	99.943	99.932	99.933
-2.8071	99.986	99.984	99.983	99.945	99.969	99.973	99.923	99.937	99.912	-2.8166	99.957	99.951	99.919	99.937
-2.7901	99.98	99.975	99.998	99.966	99.999	99.975	99.924	99.972	99.918	-2.7996	99.972	99.953	99.912	99.976
-2.7731	99.989	99.96	99.979	99.929	100.015	99.938	99.923	99.933	99.947	-2.7825	99.969	99.934	99.941	99.942
-2.7561	99.999	99.969	99.958	99.962	100.042	99.895	99.9	99.946	99.946	-2.7655	99.982	99.92	99.971	99.87
-2.7392	100.014	99.978	99.951	99.963	99.999	99.945	99.91	99.953	99.938	-2.7484	99.968	99.952	99.948	99.889
-2.7222	99.992	99.986	99.968	99.985	99.95	99.995	99.943	99.934	99.906	-2.7314	99.944	99.908	99.951	99.878
-2.7052	99.983	99.98	99.964	100.001	99.978	100.005	99.965	99.962	99.924	-2.7143	99.946	99.915	99.943	99.905
-2.6882	100	99.984	99.975	100.002	99.977	100.001	99.95	99.991	99.939	-2.6973	99.978	99.912	99.943	99.919
-2.6713	100.002	99.973	99.986	99.981	99.948	99.973	99.937	99.984	99.916	-2.6802	99.985	99.901	99.94	99.891
-2.6543	100.001	99.988	100.002	99.953	99.943	99.931	99.928	99.956	99.904	-2.6632	99.976	99.891	99.91	99.906
-2.6373	100.002	99.978	99.992	99.951	99.979	99.911	99.942	99.99	99.93	-2.6461	99.978	99.931	99.877	99.883
-2.6203	99.999	99.98	99.995	99.951	100.014	99.947	99.952	99.978	99.959	-2.629	99.971	99.967	99.903	99.883
-2.6034	99.988	99.988	100.005	99.945	99.986	99.946	99.935	99.974	99.97	-2.612	99.97	100.019	99.944	99.916
-2.5864	99.982	99.977	100.004	99.949	100.008	99.942	99.925	99.998	99.978	-2.5949	99.988	100.019	99.894	99.885
-2.5694	99.97	99.971	99.989	99.9	99.98	99.959	99.964	99.991	99.908	-2.5779	99.959	99.966	99.878	99.894
-2.5524	99.969	99.98	99.983	99.947	99.972	99.942	99.949	99.931	99.916	-2.5608	99.96	100.01	99.931	99.96
-2.5355	99.987	99.97	99.961	99.986	99.981	99.93	99.928	99.948	99.915	-2.5438	100.014	100.004	99.903	99.93
-2.5185	99.994	99.977	99.95	99.967	99.968	99.959	99.961	100	99.915	-2.5267	100.013	99.937	99.918	99.827
-2.5015	99.995	99.999	99.982	99.885	99.987	99.991	99.966	100.006	99.923	-2.5097	99.996	99.964	99.955	99.846
-2.4846	99.99	99.995	100.005	99.933	100.021	100.029	99.952	100.023	99.954	-2.4926	100.021	99.949	99.91	99.872
-2.4676	99.988	100.01	99.984	99.924	100.042	99.972	99.947	99.945	100.019	-2.4756	100.006	99.951	99.915	99.916
-2.4506	99.986	99.998	100.007	99.987	99.986	99.961	99.943	99.914	100.073	-2.4585	99.959	99.971	99.973	99.958

-2.4336	99.979	99.951	99.979	100.034	99.967	99.939	99.972	99.948	99.993	-2.4414	99.975	99.986	99.974	99.917
-2.4167	99.979	99.957	99.985	100.01	99.942	99.955	99.939	99.979	99.94	-2.4244	99.99	99.988	99.95	99.937
-2.3997	99.997	99.989	99.972	99.953	99.974	99.958	99.937	99.983	99.945	-2.4073	100.018	99.93	99.929	99.933
-2.3827	100.011	99.993	100.028	99.963	100.069	99.959	99.931	99.974	99.958	-2.3903	99.992	99.944	99.939	99.88
-2.3657	99.998	99.986	99.985	99.924	100.049	99.901	99.938	99.954	99.926	-2.3732	99.96	99.979	99.912	99.849
-2.3488	99.997	99.971	99.977	99.92	99.979	99.981	99.936	99.959	99.914	-2.3562	99.975	99.947	99.924	99.908
-2.3318	99.997	99.974	100.022	99.95	99.953	100.032	99.934	99.94	99.915	-2.3391	99.98	99.901	99.956	99.984
-2.3148	99.964	99.97	100.012	99.962	99.951	99.993	99.928	99.905	99.923	-2.3221	99.963	99.926	99.904	99.967
-2.2978	99.974	99.967	99.985	99.914	99.977	99.912	99.933	99.899	99.913	-2.305	99.945	99.942	99.89	99.965
-2.2809	99.988	99.964	99.978	99.971	99.97	99.941	99.954	99.957	99.946	-2.288	99.949	99.958	99.929	99.964
-2.2639	99.989	99.981	99.972	100.002	99.966	99.951	99.937	99.947	99.951	-2.2709	99.978	99.932	99.941	99.949
-2.2469	99.984	99.979	99.997	99.966	100.003	99.958	99.922	99.932	99.923	-2.2539	100.001	99.909	99.918	99.911
-2.2299	99.997	99.979	99.996	99.942	100	99.976	99.936	99.933	99.93	-2.2368	99.997	99.898	99.937	99.863
-2.213	99.984	99.988	99.993	99.959	99.96	99.991	99.918	99.933	99.925	-2.2197	99.973	99.908	99.935	99.893
-2.196	99.99	99.989	99.985	99.933	99.926	99.915	99.907	99.962	99.951	-2.2027	99.983	99.914	99.935	99.895
-2.179	99.995	99.985	99.978	99.923	99.962	99.893	99.913	99.964	99.95	-2.1856	99.997	99.917	99.973	99.935
-2.162	99.988	99.96	99.972	99.97	99.941	99.962	99.935	99.94	99.901	-2.1686	99.976	99.951	99.972	99.927
-2.1451	99.989	99.944	99.973	100.041	99.934	100.008	99.939	99.935	99.941	-2.1515	99.963	99.897	99.957	99.909
-2.1281	99.993	99.956	99.989	100.007	99.969	99.936	99.948	99.96	99.918	-2.1345	99.981	99.891	99.927	99.916
-2.1111	99.988	99.979	99.987	99.989	99.989	99.902	99.962	99.963	99.869	-2.1174	100.031	99.885	99.935	99.898
-2.0941	99.995	99.979	99.988	99.972	99.93	99.938	99.976	99.951	99.907	-2.1004	100.003	99.896	99.923	99.891
-2.0772	99.996	99.972	100.007	99.958	99.949	99.982	99.95	99.999	99.973	-2.0833	99.998	99.937	99.928	99.9
-2.0602	99.995	99.985	99.998	99.962	99.955	99.959	99.922	99.921	99.952	-2.0663	99.959	99.928	99.899	99.949
-2.0432	99.997	99.985	99.973	99.948	99.992	99.945	99.932	99.92	99.894	-2.0492	99.992	99.969	99.91	99.878
-2.0262	99.995	99.984	99.975	99.927	99.977	99.967	99.9	99.963	99.961	-2.0321	99.979	99.942	99.946	99.905
-2.0093	100.001	99.978	99.992	99.986	99.993	99.975	99.895	99.976	99.953	-2.0151	99.958	99.942	99.964	99.931
-1.9923	99.986	99.979	100.007	99.984	99.977	99.978	99.899	99.996	99.929	-1.998	100.009	99.948	99.923	99.932
-1.9753	99.992	99.973	99.972	99.979	99.982	99.992	99.927	99.962	99.944	-1.981	99.994	99.976	99.906	99.922
-1.9583	99.982	99.961	99.995	100.011	99.966	99.995	99.921	99.971	99.905	-1.9639	99.983	99.956	99.894	99.934
-1.9414	99.994	99.974	100.011	99.994	99.907	99.964	99.934	99.963	99.877	-1.9469	99.962	99.94	99.905	99.942
-1.9244	99.974	99.981	99.982	99.998	99.928	99.956	99.944	99.965	99.932	-1.9298	99.957	99.936	99.892	99.922
-1.9074	99.983	99.988	99.999	100.004	99.93	99.959	99.937	99.996	99.986	-1.9128	99.961	99.915	99.869	99.933
-1.8904	99.986	99.99	99.987	99.935	99.909	99.973	99.928	100.005	99.966	-1.8957	99.971	99.929	99.877	99.927
-1.8735	99.981	99.975	99.986	99.92	99.939	99.972	99.939	100.03	99.942	-1.8787	99.993	99.942	99.919	99.897
-1.8565	99.978	99.976	99.991	99.961	99.965	99.966	99.926	99.997	99.961	-1.8616	99.986	99.919	99.877	99.929
-1.8395	99.984	99.985	99.987	99.97	99.946	99.97	99.892	99.953	99.943	-1.8446	99.987	99.903	99.886	99.909
-1.8225	99.991	99.981	99.977	99.963	99.932	99.993	99.875	99.903	99.898	-1.8275	99.968	99.893	99.916	99.883
-1.8056	99.989	99.978	99.972	99.97	99.943	99.993	99.884	99.898	99.898	-1.8104	99.961	99.923	99.942	99.911
-1.7886	99.985	99.965	99.97	99.98	99.952	99.968	99.89	99.922	99.917	-1.7934	99.982	99.967	99.953	99.903
-1.7716	99.984	99.962	99.982	99.988	99.958	99.959	99.915	99.87	99.935	-1.7763	99.986	99.943	99.948	99.893
-1.7546	99.983	99.979	99.959	99.972	99.981	99.985	99.912	99.903	99.947	-1.7593	100.002	99.968	99.906	99.903
-1.7377	99.988	99.992	99.96	99.953	99.965	99.98	99.921	99.965	99.913	-1.7422	100.003	99.942	99.914	99.966
-1.7207	99.974	99.991	99.98	99.96	99.944	99.997	99.929	99.921	99.904	-1.7252	100.008	99.879	99.914	99.868
-1.7037	99.983	99.996	100.01	99.995	99.944	99.996	99.899	99.92	99.907	-1.7081	100.021	99.95	99.909	99.837
-1.6867	99.977	99.986	99.995	99.961	99.963	99.968	99.915	99.924	99.903	-1.6911	99.974	99.946	99.927	99.877
-1.6698	99.989	99.969	99.974	99.941	99.935	99.886	99.904	99.958	99.949	-1.674	99.995	99.956	99.876	99.839
-1.6528	100.007	99.975	99.963	99.974	99.953	99.937	99.897	99.956	99.938	-1.657	99.976	99.972	99.928	99.9
-1.6358	99.989	99.973	99.989	99.933	99.964	99.973	99.887	99.978	99.965	-1.6399	99.998	99.919	99.92	99.923
-1.6188	99.999	99.984	100.003	99.869	99.944	99.932	99.925	100	99.972	-1.6229	100.006	99.939	99.888	99.89
-1.6019	99.96	99.996	99.991	99.895	99.956	99.885	99.928	99.958	99.92	-1.6058	99.98	99.878	99.897	99.914
-1.5849	99.983	99.993	99.969	99.946	99.933	99.942	99.891	99.968	99.902	-1.5887	99.953	99.925	99.9	99.931
-1.5679	99.992	99.986	99.951	99.946	100.008	99.97	99.899	99.941	99.905	-1.5717	99.975	99.96	99.874	99.885
-1.5509	100.003	99.975	99.973	99.978	100.033	99.965	99.918	99.936	99.991	-1.5546	100.001	99.924	99.869	99.874
-1.534	99.99	99.992	99.98	99.975	100.032	99.87	99.926	99.971	99.95	-1.5376	100.023	99.91	99.927	99.889
-1.517	99.981	100	99.968	99.925	99.941	99.891	99.924	99.981	99.947	-1.5205	100.003	99.929	99.897	99.862
-1.5	99.978	99.981	99.969	99.914	99.953	99.958	99.896	100.009	99.911	-1.5035	99.961	99.975	99.91	99.879
-1.483	99.988	99.979	99.999	99.926	99.968	99.991	99.859	99.977	99.952	-1.4864	99.988	99.95	99.894	99.925
-1.4661	99.989	99.99	100.006	99.91	99.941	99.974	99.877	99.922	99.934	-1.4694	99.974	99.953	99.912	99.88
-1.4491	99.994	99.983	99.987	99.927	99.97	99.957	99.897	99.962	99.906	-1.4523	99.978	99.972	99.924	99.837
-1.4321	99.994	99.969	99.97	99.961	99.977	99.969	99.905	99.91	99.886	-1.4353	99.968	99.958	99.922	99.871
-1.4151	99.999	99.978	99.987	99.951	99.927	99.914	99.908	99.925	99.913	-1.4182	99.964	99.937	99.893	99.888
-1.3982	99.987	99.984	99.965	99.917	99.946	99.948	99.897	99.917	99.965	-1.4011	99.984	99.92	99.873	99.875
-1.3812	99.977	99.994	99.966	99.918	99.954	99.921	99.884	99.915	99.932	-1.3841	99.982	99.909	99.864	99.885
-1.3642	99.987	100.004	99.99	99.918	99.97	99.892	99.902	99.913	99.909	-1.367	99.997	99.906	99.862	99.896
-1.3472	99.994	99.99	99.982	100	99.923	99.896	99.892	99.948	99.981	-1.35	99.997	99.845	99.859	99.881
-1.3303	99.995	99.974	99.987	99.948	99.914	99.963	99.875	99.907	99.9	-1.3329	99.982	99.88	99.852	99.845
-1.3133	99.98	99.97	99.98	99.92	99.908	99.903	99.88	99.92	99.891	-1.3159	100.029	99.973	99.859	99.803
-1.2963	99.968	100.001	99.964	99.962	99.927	99.921	99.867	99.891	99.882	-1.2988	100.01	99.976	99.853	99.878
-1.2793	99.962	100.008	99.953	99.96	99.939	99.955	99.885	99.909	99.858	-1.2818	99.997	99.928	99.872	99.876
-1.2624	99.977	100.002	99.991	99.979	99.914	99.98	99.918	99.963	99.897	-1.2647	100.016	99.898	99.85	99.915
-1.2454	99.999	99.985	99.973	100.014	99.921	99.935	99.888	99.913	99.871	-1.2477	100.013	99.924	99.84	99.889
-1.2284	100.002	99.975	99.984	99.982	99.903	99.907	99.857	99.928	99.885	-1.2306	99.987	99.93	99.88	99.824
-1.2114	99.996	99.98	99.981	99.91	99.922	99.939	99.881	99.963	99.914	-1.2136	99.989	99.904	99.901	99.844
-1.1945	99.993	99.985	99.976	99.904	99.942	99.958	99.899	99.963	99.852	-1.1965	99.982	99.946	99.891	99.904
-1.1775	100.027	99.983	99.972	99.937	99.93	99.957	99.904	99.97	99.894	-1.1794	100.001	99.989	99.888	99.916
-1.1605	100.011	99.998	99.985	99.956	99.912	99.953	99.87	99.951	99.929	-1.1624	100.003	99.94	99.862	99.853
-1.1435	99.999	99.982	99.978	99.984	99.938	99.937	99.838	99.932	99.868	-1.1453	100.021	99.913	99.882	99.838
-1.1266	99.987	100.003	99.951	99.962	99.958	99.885	99.837	99.939	99.872	-1.1283	100.027	99.903	99.887	99.808
-1.1096	99.991	99.995	99.968	99.911	99.912	99.902	99.845	99.996	99.915	-1.1112	99.999	99.865	99.901	99.814
-1.0926	99.989	99.963	99.975	99.922	99.871	99.948	99.87	99.972	99.875	-1.0942	99.987	99.878	99.88	99.865
-1.0756	99.992	99.989	99.977	99.95	99.929	99.943	99.869	99.937	99.854	-1.0771	99.989	99.907	99.884	99.853
-1.0587	99.985	99.985	99.965	99.939	99.969	99.924	99.865	99.914	99.869	-1.0601	99.97	99.92	99.878	99.828
-1.0417	99.98	99.973	99.941	99.969	99.932	99.948	99.863	99.914	99.857	-1.043	99.946	99.952	99.852	99.812
-1.0247	99.992	99.965	99.944	99.996	99.909	99.966	99.85	99.904	99.817	-1.026	99.96	99.949	99.857	99.801
-1.0077	99.989	99.972	99.958	99.968	99.907	99.926	99.87	99.878	99.844	-1.0089	99.999	99.867	99.846	99.779
-0.9908	99.981	99.955	99.961	99.95	99.925	99.913	99.867	99.893	99.865	-0.9918	100.018	99.845	99.852	99.755
-0.9738	99.962	99.956	99.983	99.935	99.941	99.932	99.846	99.913	99.849	-0.9748	99.988	99.85	99.812	99.759
-0.9568	99.961	99.959	99.99	99.925	99.938	99.899	99.839	99.9	99.847	-0.9577	100.009	99.886	99.773	99.816
-0.9398	99.974	99.948	99.985	99.935	99.931	99.926	99.837	99.88	99.882	-0.9407	99.994	99.851	99.772	99.766
-0.9229	99.98	99.968	99.993	99.938	99.897	99.921	99.832	99.903	99.873	-0.9236	99.983	99.884	99.789	99.797
-0.9059	99.974	99.992	99.988	99.926	99.881	99.89	99.823	99.862	99.858	-0.9066	100.008	99.916	99.814	99.839
-0.8889	99.973	99.98	99.995	99.892	99.944	99.893	99.812	99.863	99.878	-0.8895	100	99.875	99.809	99.806
-0.8719	99.968	99.972	99.985	99.917	99.976	99.87	99.821	99.866	99.807	-0.8725	100.025	99.85	99.811	99.784
-0.855	99.972	99.973	99.979	99.902	99.925	99.875	99.809	99.888	99.827	-0.8554	100	99.839	99.805	99.741
-0.838	99.965	99.973	99.984	99.912	99.911	99.861	99.789	99.94	99.835	-0.8384	99.97	99.865	99.791	99.724
-0.821	99.964	99.977	99.965	99.895	99.89	99.857	99.802	99.855	99.81	-0.8213	99.99	99.822	99.813	99.753
-0.804	99.972	99.982	99.975	99.842	99.885	99.841	99.802	99.898	99.855	-0.8043	100.021	99.897	99.79	99.732
-0.7871	99.978	99.971	99.979	99.879	99.893	99.905	99.799	99.867	99.809	-0.7872	99.98	99.876	99.794	99.739
-0.7701	99.983	99.97	99.977	99.885	99.87	99.851	99.779	99.875	99.809	-0.7701	99.974	99.83	99.804	99.714
-0.7531	99.983	99.966	99.958	99.911	99.863	99.798	99.75	99.835	99.755	-0.7531	99.934	99.8	99.763	99.716
-0.7361	99.984	99.967	99.982	99.869	99.923	99.817	99.74	99.792	99.792	-0.736	99.977	99.785	99.715	99.715
-0.7192	99.978	99.96	99.983	99.9	99.965	99.829	99.76	99.848	99.789	-0.719	99.979	99.821	99.703	99.715
-0.7022	99.96	99.945	99.977	99.897	99.879	99.849	99.724	99.86	99.754	-0.7019	99.965	99.81	99.744	99.679
-0.6852	99.955	99.952	99.963	99.919	99.825	99.906	99.72	99.888	99.683	-0.6849	99.963	99.787	99.719	99.655
-0.6682	99.977	99.964	99.955	99.874	99.839	99.863	99.688	99.831	99.778	-0.6678	99.957	99.79	99.703	99.663
-0.6513	99.96	99.962	99.976	99.812	99.84	99.815	99.652	99.852	99.811	-0.6508	100.019	99.768	99.715	99.634
-0.6343	99.966	99.95	99.986	99.808	99.85	99.833	99.674	99.863	99.793	-0.6337	99.99	99.762	99.703	99.6
-0.6173	99.967	99.955	99.956	99.847	99.848	99.831	99.672	99.799	99.735	-0.6167	99.966	99.752	99.649	99.602

-0.6003	99.953	99.958	99.937	99.837	99.844	99.812	99.648	99.844	99.724	-0.5996	99.981	99.797	99.602	99.595
-0.5834	99.951	99.94	99.937	99.792	99.832	99.828	99.616	99.826	99.73	-0.5826	99.966	99.763	99.593	99.648
-0.5664	99.941	99.926	99.926	99.773	99.795	99.807	99.599	99.737	99.659	-0.5655	99.958	99.705	99.591	99.613
-0.5494	99.948	99.932	99.934	99.787	99.788	99.777	99.593	99.743	99.636	-0.5484	99.972	99.788	99.556	99.529
-0.5324	99.961	99.936	99.933	99.825	99.745	99.754	99.557	99.758	99.578	-0.5314	99.932	99.789	99.515	99.495
-0.5155	99.966	99.94	99.921	99.769	99.774	99.724	99.518	99.753	99.564	-0.5143	99.938	99.721	99.502	99.474
-0.4985	99.965	99.942	99.926	99.709	99.75	99.702	99.504	99.707	99.563	-0.4973	99.971	99.664	99.49	99.462
-0.4815	99.954	99.931	99.892	99.739	99.723	99.692	99.459	99.62	99.519	-0.4802	99.962	99.638	99.431	99.394
-0.4645	99.95	99.914	99.887	99.768	99.73	99.71	99.416	99.6	99.51	-0.4632	99.954	99.622	99.352	99.348
-0.4476	99.932	99.896	99.902	99.714	99.732	99.735	99.357	99.582	99.454	-0.4461	99.966	99.551	99.291	99.282
-0.4306	99.935	99.892	99.881	99.693	99.726	99.649	99.33	99.57	99.385	-0.4291	99.957	99.521	99.249	99.258
-0.4136	99.928	99.917	99.86	99.659	99.701	99.6	99.238	99.506	99.304	-0.412	99.926	99.521	99.188	99.18
-0.3966	99.914	99.912	99.826	99.606	99.597	99.6	99.142	99.453	99.255	-0.395	99.91	99.501	99.116	99.085
-0.3797	99.919	99.914	99.825	99.603	99.529	99.584	99.051	99.425	99.242	-0.3779	99.91	99.472	99.029	99.05
-0.3627	99.915	99.879	99.838	99.55	99.502	99.535	98.982	99.409	99.167	-0.3608	99.88	99.443	98.93	98.921
-0.3457	99.898	99.865	99.831	99.495	99.512	99.466	98.913	99.347	99.059	-0.3438	99.864	99.373	98.834	98.8
-0.3288	99.902	99.841	99.798	99.489	99.493	99.448	98.827	99.227	98.939	-0.3267	99.888	99.299	98.731	98.726
-0.3118	99.889	99.854	99.757	99.419	99.412	99.398	98.701	99.181	98.877	-0.3097	99.888	99.254	98.61	98.592
-0.2948	99.849	99.848	99.751	99.34	99.326	99.305	98.574	99.13	98.831	-0.2926	99.86	99.185	98.492	98.45
-0.2778	99.854	99.808	99.726	99.291	99.25	99.234	98.483	99.036	98.704	-0.2756	99.811	99.132	98.351	98.306
-0.2609	99.842	99.779	99.685	99.268	99.201	99.16	98.371	98.954	98.546	-0.2585	99.799	99.037	98.166	98.094
-0.2439	99.829	99.763	99.65	99.247	99.171	99.106	98.224	98.872	98.456	-0.2415	99.787	98.949	98.02	97.932
-0.2269	99.832	99.74	99.641	99.158	99.112	98.99	98.083	98.829	98.398	-0.2244	99.785	98.943	97.918	97.85
-0.2099	99.796	99.72	99.632	99.08	99.053	98.915	97.956	98.773	98.32	-0.2074	99.761	98.841	97.79	97.64
-0.193	99.792	99.672	99.613	99.039	99.019	98.911	97.85	98.651	98.206	-0.1903	99.733	98.706	97.664	97.469
-0.176	99.773	99.689	99.582	99.057	98.989	98.835	97.7	98.561	98.092	-0.1733	99.732	98.572	97.502	97.322
-0.159	99.765	99.675	99.58	98.973	98.909	98.749	97.561	98.529	98.025	-0.1562	99.741	98.512	97.357	97.202
-0.142	99.761	99.656	99.576	98.857	98.894	98.699	97.441	98.5	97.912	-0.1391	99.721	98.515	97.235	96.974
-0.1251	99.758	99.643	99.557	98.826	98.854	98.692	97.332	98.402	97.806	-0.1221	99.699	98.44	97.118	96.781
-0.1081	99.756	99.619	99.565	98.796	98.791	98.646	97.24	98.341	97.718	-0.105	99.727	98.256	97.017	96.634
-0.0911	99.762	99.62	99.564	98.759	98.734	98.597	97.112	98.327	97.644	-0.088	99.733	98.252	96.91	96.521
-0.0741	99.765	99.59	99.537	98.679	98.74	98.583	97.032	98.293	97.596	-0.0709	99.77	98.191	96.78	96.392
-0.0572	99.758	99.572	99.501	98.71	98.667	98.551	96.957	98.246	97.6	-0.0539	99.762	98.126	96.638	96.208
-0.0402	99.764	99.578	99.491	98.698	98.665	98.504	96.862	98.201	97.545	-0.0368	99.749	98.063	96.57	96.085
-0.0232	99.773	99.574	99.499	98.612	98.584	98.445	96.81	98.137	97.51	-0.0198	99.775	97.997	96.46	96.061
-0.0062	99.769	99.581	99.513	98.597	98.557	98.468	96.756	98.128	97.431	-0.0027	99.736	97.879	96.391	95.899
0.0107	99.756	99.575	99.512	98.61	98.527	98.437	96.72	98.136	97.372	0.0143	99.754	97.917	96.303	95.767
0.0277	99.762	99.55	99.484	98.561	98.519	98.384	96.642	98.13	97.293	0.0314	99.73	97.84	96.242	95.717
0.0447	99.766	99.558	99.481	98.5	98.52	98.318	96.576	98.105	97.307	0.0485	99.712	97.722	96.147	95.618
0.0617	99.76	99.568	99.484	98.465	98.476	98.34	96.532	98.129	97.302	0.0655	99.693	97.695	96.088	95.517
0.0786	99.753	99.566	99.47	98.48	98.418	98.361	96.493	98.107	97.236	0.0826	99.696	97.68	96.047	95.459
0.0956	99.754	99.561	99.462	98.446	98.431	98.312	96.462	98.077	97.208	0.0996	99.698	97.679	95.969	95.346
0.1126	99.748	99.544	99.47	98.397	98.417	98.316	96.428	98.079	97.199	0.1167	99.707	97.617	95.91	95.305
0.1296	99.741	99.53	99.46	98.392	98.433	98.298	96.355	98.114	97.123	0.1337	99.712	97.554	95.883	95.25
0.1465	99.735	99.536	99.427	98.371	98.456	98.242	96.358	98.147	97.12	0.1508	99.691	97.498	95.844	95.251
0.1635	99.733	99.536	99.409	98.339	98.449	98.248	96.372	98.135	97.178	0.1678	99.709	97.531	95.789	95.168
0.1805	99.734	99.519	99.422	98.337	98.479	98.222	96.348	98.152	97.198	0.1849	99.725	97.53	95.756	95.095
0.1975	99.737	99.514	99.448	98.339	98.435	98.192	96.295	98.122	97.151	0.2019	99.713	97.498	95.731	95.053
0.2144	99.733	99.519	99.439	98.351	98.41	98.201	96.297	98.075	97.147	0.219	99.674	97.407	95.701	94.961
0.2314	99.726	99.516	99.434	98.374	98.385	98.216	96.296	98.095	97.155	0.236	99.656	97.438	95.692	94.931
0.2484	99.731	99.513	99.448	98.353	98.358	98.224	96.31	98.095	97.152	0.2531	99.691	97.456	95.682	94.96
0.2654	99.724	99.515	99.465	98.298	98.358	98.211	96.323	98.065	97.169	0.2702	99.737	97.405	95.707	94.973
0.2823	99.707	99.51	99.432	98.336	98.381	98.228	96.341	98.061	97.216	0.2872	99.71	97.402	95.653	94.92
0.2993	99.721	99.497	99.414	98.354	98.422	98.225	96.34	98.096	97.212	0.3043	99.689	97.479	95.685	94.873
0.3163	99.716	99.485	99.44	98.316	98.413	98.238	96.349	98.153	97.191	0.3213	99.715	97.478	95.694	94.87
0.3333	99.708	99.483	99.43	98.314	98.381	98.226	96.384	98.124	97.13	0.3384	99.674	97.4	95.703	94.879
0.3502	99.715	99.489	99.415	98.316	98.387	98.267	96.416	98.161	97.148	0.3554	99.622	97.443	95.711	94.897
0.3672	99.707	99.489	99.437	98.4	98.417	98.218	96.452	98.14	97.239	0.3725	99.658	97.423	95.705	94.915
0.3842	99.694	99.481	99.433	98.445	98.434	98.199	96.481	98.175	97.291	0.3895	99.701	97.452	95.755	94.986
0.4012	99.684	99.492	99.443	98.421	98.459	98.203	96.535	98.25	97.308	0.4066	99.713	97.419	95.78	95.007
0.4181	99.69	99.513	99.425	98.423	98.468	98.28	96.592	98.284	97.277	0.4236	99.703	97.458	95.837	95.029
0.4351	99.683	99.519	99.453	98.423	98.471	98.29	96.644	98.334	97.372	0.4407	99.655	97.548	95.916	95.106
0.4521	99.702	99.501	99.465	98.46	98.537	98.31	96.72	98.37	97.437	0.4577	99.656	97.594	95.997	95.13
0.4691	99.717	99.522	99.455	98.442	98.639	98.437	96.765	98.403	97.483	0.4748	99.665	97.618	96.069	95.174
0.486	99.708	99.523	99.483	98.501	98.596	98.49	96.8	98.417	97.546	0.4919	99.681	97.701	96.193	95.32
0.503	99.724	99.546	99.517	98.514	98.634	98.536	96.905	98.45	97.666	0.5089	99.705	97.757	96.301	95.479
0.52	99.756	99.566	99.527	98.613	98.638	98.506	97.02	98.42	97.747	0.526	99.736	97.783	96.385	95.6
0.537	99.761	99.564	99.532	98.62	98.743	98.584	97.097	98.468	97.815	0.543	99.734	97.824	96.5	95.679
0.5539	99.774	99.562	99.542	98.685	98.746	98.615	97.21	98.57	97.881	0.5601	99.746	97.878	96.624	95.789
0.5709	99.771	99.597	99.563	98.805	98.818	98.718	97.343	98.63	97.947	0.5771	99.737	97.951	96.752	95.954
0.5879	99.791	99.602	99.567	98.791	98.831	98.721	97.435	98.721	97.991	0.5942	99.76	98.06	96.856	96.075
0.6049	99.806	99.618	99.596	98.723	98.875	98.746	97.526	98.812	98.056	0.6112	99.784	98.185	97.014	96.235
0.6218	99.797	99.643	99.628	98.833	98.956	98.826	97.653	98.803	98.101	0.6283	99.783	98.185	97.086	96.384
0.6388	99.793	99.662	99.639	98.892	98.995	98.881	97.736	98.882	98.2	0.6453	99.818	98.24	97.225	96.507
0.6558	99.807	99.681	99.647	98.921	99.067	98.922	97.826	98.949	98.35	0.6624	99.791	98.421	97.423	96.699
0.6728	99.819	99.694	99.641	98.967	99.099	99.029	97.919	98.868	98.385	0.6795	99.805	98.509	97.562	96.837
0.6897	99.815	99.692	99.651	99.055	99.138	99.059	98.012	98.856	98.473	0.6965	99.771	98.55	97.675	97.012
0.7067	99.839	99.706	99.691	99.119	99.193	99.103	98.131	98.961	98.566	0.7136	99.811	98.604	97.778	97.217
0.7237	99.846	99.75	99.706	99.139	99.196	99.155	98.234	99.035	98.647	0.7306	99.816	98.759	97.93	97.392
0.7407	99.837	99.747	99.726	99.183	99.207	99.186	98.338	99.102	98.705	0.7477	99.824	98.852	98.103	97.52
0.7576	99.852	99.761	99.727	99.192	99.303	99.216	98.389	99.173	98.766	0.7647	99.872	98.938	98.237	97.695
0.7746	99.866	99.781	99.744	99.259	99.386	99.25	98.509	99.205	98.818	0.7818	99.886	98.913	98.363	97.815
0.7916	99.859	99.797	99.777	99.308	99.394	99.279	98.592	99.237	98.86	0.7988	99.879	98.991	98.448	97.926
0.8086	99.865	99.785	99.8	99.347	99.375	99.305	98.653	99.283	98.936	0.8159	99.889	99.106	98.505	98.075
0.8255	99.874	99.791	99.811	99.384	99.397	99.345	98.736	99.296	99.018	0.8329	99.88	99.157	98.601	98.2
0.8425	99.874	99.796	99.811	99.424	99.41	99.397	98.8	99.355	99.025	0.85	99.877	99.159	98.692	98.299
0.8595	99.878	99.805	99.791	99.461	99.476	99.42	98.826	99.414	99.047	0.867	99.871	99.228	98.777	98.358
0.8765	99.878	99.806	99.792	99.464	99.535	99.446	98.864	99.397	99.085	0.8841	99.936	99.29	98.837	98.374
0.8934	99.894	99.83	99.808	99.446	99.526	99.454	98.904	99.382	99.119	0.9012	99.925	99.216	98.847	98.4
0.9104	99.913	99.827	99.806	99.45	99.489	99.485	98.932	99.351	99.146	0.9182	99.915	99.223	98.841	98.465
0.9274	99.918	99.805	99.813	99.506	99.504	99.48	98.959	99.387	99.143	0.9353	99.885	99.302	98.839	98.423
0.9444	99.918	99.818	99.828	99.535	99.464	99.475	98.939	99.485	99.137	0.9523	99.875	99.253	98.85	98.388
0.9613	99.905	99.793	99.833	99.507	99.431	99.4	98.921	99.526	99.149	0.9694	99.883	99.215	98.804	98.33
0.9783	99.876	99.794	99.823	99.456	99.476	99.406	98.908	99.486	99.15	0.9864	99.888	99.163	98.758	98.302
0.9953	99.886	99.782	99.78	99.436	99.527	99.445	98.881	99.519	99.095	1.0035	99.871	99.132	98.683	98.239
1.0123	99.9	99.811	99.774	99.36	99.462	99.426	98.786	99.404	99.104	1.0205	99.866	99.101	98.585	98.121
1.0292	99.893	99.777	99.766	99.364	99.525	99.378	98.732	99.401	99.101	1.0376	99.859	99.081	98.519	97.995
1.0462	99.895	99.769	99.783	99.385	99.467	99.293	98.708	99.401	99.038	1.0546	99.854	99.039	98.436	97.85
1.0632	99.885	99.776	99.802	99.377	99.403	99.341	98.628	99.338	98.958	1.0717	99.875	98.929	98.338	97.748
1.0802	99.873	99.743	99.801	99.306	99.407	99.336	98.548	99.336	98.947	1.0888	99.894	98.847	98.203	97.592
1.0971	99.87	99.743	99.787	99.254	99.335	99.295	98.463	99.311	98.887	1.1058	99.886	98.762	98.092	97.441
1.1141	99.871	99.734	99.765	99.206	99.3	99.259	98.383	99.283	98.809	1.1229	99.829	98.697	97.997	97.277
1.1311	99.869	99.716	99.75	99.148	99.306	99.224	98.286	99.162	98.751	1.1399	99.822	98.694	97.831	97.148
1.1481	99.85	99.684	99.741	99.07	99.29	99.159	98.216	99.129	98.62	1.157	99.83	98.586	97.698	96.985
1.165	99.835	99.665	99.723	99.059	99.208	99.091	98.106	99.08	98.5	1.174	99.822	98.458	97.598	96.874
1.182	99.832	99.659	99.697	99.061	99.134	99.039	97.993	99.066	98.47	1.1911	99.789	98.411	97.471	96.683
1.199	99.836	99.663	99.679	98.997	99.118	98.975	97.889	99.056	98.378	1.2081	99.815	98.384	97.304	96.503
1.216	99.832	99.652	99.661	98.963	99.089	98.874	97.779	98.974	98.343	1.2252	99.807	98.32	97.183	96.442

1.2329	99.821	99.63	99.646	98.916	99.025	98.848	97.675	98.918	98.251	1.2422	99.802	98.135	97.08	96.294
1.2499	99.811	99.62	99.654	98.885	98.975	98.804	97.58	98.884	98.166	1.2593	99.796	98.125	96.996	96.095
1.2669	99.802	99.629	99.633	98.799	98.918	98.744	97.506	98.846	98.065	1.2763	99.769	98.026	96.828	96.02
1.2839	99.793	99.615	99.624	98.771	98.906	98.742	97.391	98.803	98.067	1.2934	99.762	97.916	96.713	95.896
1.3008	99.805	99.59	99.597	98.708	98.832	98.691	97.331	98.764	98.036	1.3105	99.791	97.836	96.652	95.754
1.3178	99.793	99.599	99.611	98.646	98.778	98.688	97.225	98.664	97.89	1.3275	99.772	97.794	96.533	95.681
1.3348	99.774	99.587	99.607	98.649	98.796	98.616	97.102	98.628	97.838	1.3446	99.774	97.759	96.379	95.604
1.3518	99.802	99.57	99.568	98.658	98.755	98.568	97.037	98.602	97.82	1.3616	99.759	97.733	96.305	95.484
1.3687	99.801	99.589	99.564	98.649	98.718	98.528	96.988	98.521	97.693	1.3787	99.771	97.663	96.239	95.367
1.3857	99.79	99.586	99.567	98.582	98.646	98.49	96.907	98.534	97.564	1.3957	99.749	97.633	96.157	95.348
1.4027	99.775	99.572	99.552	98.501	98.598	98.506	96.875	98.503	97.607	1.4128	99.734	97.641	96.114	95.338
1.4197	99.758	99.55	99.527	98.5	98.602	98.444	96.785	98.435	97.492	1.4298	99.726	97.572	96.059	95.299
1.4366	99.785	99.565	99.523	98.474	98.616	98.414	96.718	98.444	97.509	1.4469	99.724	97.497	95.939	95.22
1.4536	99.783	99.546	99.512	98.477	98.616	98.347	96.671	98.442	97.536	1.4639	99.734	97.49	95.879	95.127
1.4706	99.774	99.57	99.513	98.503	98.561	98.321	96.615	98.38	97.462	1.481	99.738	97.498	95.854	95.087
1.4876	99.76	99.534	99.515	98.475	98.555	98.339	96.558	98.352	97.393	1.498	99.728	97.494	95.825	95.02
1.5045	99.757	99.539	99.53	98.433	98.526	98.288	96.506	98.306	97.355	1.5151	99.724	97.46	95.799	94.993
1.5215	99.784	99.562	99.52	98.378	98.472	98.27	96.46	98.257	97.339	1.5322	99.737	97.446	95.769	94.988
1.5385	99.785	99.557	99.494	98.352	98.473	98.299	96.417	98.246	97.296	1.5492	99.731	97.468	95.744	94.937
1.5555	99.78	99.559	99.481	98.383	98.523	98.313	96.387	98.212	97.205	1.5663	99.707	97.458	95.715	94.888
1.5724	99.78	99.564	99.462	98.394	98.509	98.288	96.39	98.211	97.169	1.5833	99.701	97.412	95.702	94.909
1.5894	99.774	99.557	99.478	98.374	98.434	98.228	96.379	98.22	97.182	1.6004	99.731	97.418	95.705	94.94
1.6064	99.771	99.593	99.494	98.378	98.438	98.245	96.339	98.233	97.197	1.6174	99.744	97.442	95.709	94.948
1.6234	99.775	99.571	99.496	98.391	98.495	98.266	96.318	98.244	97.18	1.6345	99.765	97.492	95.729	94.973
1.6403	99.791	99.57	99.504	98.366	98.508	98.258	96.298	98.229	97.183	1.6515	99.774	97.501	95.742	95.014
1.6573	99.797	99.592	99.501	98.388	98.492	98.241	96.302	98.186	97.211	1.6686	99.777	97.545	95.749	95.036
1.6743	99.791	99.607	99.491	98.418	98.482	98.279	96.309	98.189	97.196	1.6856	99.795	97.607	95.769	95.111
1.6913	99.787	99.594	99.522	98.42	98.478	98.323	96.347	98.181	97.217	1.7027	99.767	97.569	95.813	95.183
1.7082	99.799	99.607	99.513	98.457	98.576	98.337	96.369	98.272	97.247	1.7198	99.752	97.604	95.886	95.219
1.7252	99.798	99.619	99.517	98.491	98.562	98.372	96.448	98.301	97.305	1.7368	99.74	97.615	95.944	95.233
1.7422	99.804	99.622	99.495	98.52	98.568	98.356	96.465	98.287	97.34	1.7539	99.761	97.719	96.004	95.373
1.7591	99.8	99.612	99.511	98.572	98.633	98.383	96.523	98.281	97.367	1.7709	99.777	97.767	96.075	95.476
1.7761	99.805	99.629	99.531	98.641	98.634	98.416	96.563	98.355	97.381	1.788	99.786	97.763	96.118	95.613
1.7931	99.817	99.657	99.543	98.622	98.623	98.445	96.638	98.363	97.433	1.805	99.79	97.847	96.201	95.756
1.8101	99.808	99.681	99.573	98.639	98.669	98.456	96.7	98.399	97.487	1.8221	99.818	97.952	96.312	95.836
1.827	99.831	99.677	99.575	98.617	98.732	98.488	96.791	98.354	97.563	1.8391	99.816	98.062	96.393	95.964
1.844	99.84	99.693	99.574	98.685	98.749	98.523	96.865	98.434	97.626	1.8562	99.814	98.083	96.481	96.063
1.861	99.834	99.708	99.589	98.728	98.763	98.6	96.961	98.459	97.684	1.8732	99.817	98.162	96.597	96.166
1.878	99.846	99.704	99.61	98.82	98.777	98.678	97.088	98.466	97.788	1.8903	99.831	98.23	96.709	96.327
1.8949	99.859	99.729	99.629	98.862	98.799	98.652	97.138	98.508	97.843	1.9073	99.839	98.289	96.817	96.492
1.9119	99.856	99.753	99.619	98.914	98.872	98.706	97.236	98.529	97.851	1.9244	99.836	98.285	96.947	96.62
1.9289	99.863	99.769	99.643	98.947	98.903	98.788	97.351	98.609	97.923	1.9415	99.827	98.352	97.06	96.762
1.9459	99.852	99.778	99.66	99.008	98.978	98.875	97.443	98.738	98.03	1.9585	99.819	98.445	97.173	96.901
1.9628	99.861	99.78	99.685	99.076	99.059	98.893	97.547	98.789	98.077	1.9756	99.869	98.506	97.306	97.058
1.9798	99.889	99.77	99.683	99.11	99.106	98.933	97.668	98.748	98.206	1.9926	99.881	98.588	97.407	97.232
1.9968	99.914	99.822	99.712	99.166	99.132	99.027	97.782	98.776	98.285	2.0097	99.879	98.654	97.54	97.373
2.0138	99.908	99.819	99.714	99.225	99.216	99.025	97.891	98.911	98.319	2.0267	99.872	98.72	97.678	97.565
2.0307	99.905	99.829	99.707	99.271	99.255	99.047	97.998	98.952	98.385	2.0438	99.896	98.852	97.804	97.715
2.0477	99.908	99.847	99.716	99.296	99.252	99.135	98.122	98.952	98.484	2.0608	99.903	98.991	97.932	97.799
2.0647	99.909	99.836	99.743	99.315	99.243	99.195	98.232	99.029	98.596	2.0779	99.907	99.013	98.066	97.925
2.0817	99.914	99.862	99.771	99.334	99.318	99.27	98.34	99.062	98.689	2.0949	99.928	99.073	98.179	98.103
2.0986	99.929	99.845	99.77	99.382	99.386	99.296	98.43	99.124	98.759	2.112	99.949	99.114	98.289	98.303
2.1156	99.919	99.869	99.769	99.423	99.418	99.345	98.553	99.186	98.795	2.1291	99.926	99.186	98.433	98.435
2.1326	99.941	99.881	99.793	99.488	99.403	99.412	98.677	99.251	98.878	2.1461	99.922	99.256	98.566	98.479
2.1496	99.956	99.884	99.841	99.51	99.446	99.445	98.775	99.349	98.989	2.1632	99.921	99.317	98.624	98.62
2.1665	99.95	99.905	99.843	99.558	99.496	99.448	98.855	99.445	99.096	2.1802	99.976	99.356	98.76	98.715
2.1835	99.945	99.908	99.821	99.578	99.557	99.489	98.952	99.503	99.149	2.1973	99.953	99.433	98.889	98.79
2.2005	99.96	99.91	99.824	99.557	99.584	99.508	99.049	99.46	99.201	2.2143	99.985	99.488	98.954	98.905
2.2175	99.962	99.906	99.851	99.615	99.625	99.565	99.096	99.471	99.21	2.2314	99.954	99.556	99.015	99.022
2.2344	99.958	99.913	99.874	99.686	99.668	99.617	99.163	99.488	99.232	2.2484	99.93	99.544	99.105	99.094
2.2514	99.953	99.942	99.888	99.681	99.686	99.654	99.211	99.533	99.326	2.2655	99.97	99.561	99.216	99.181
2.2684	99.96	99.97	99.886	99.729	99.69	99.684	99.237	99.584	99.427	2.2825	99.944	99.602	99.26	99.177
2.2854	99.964	99.959	99.891	99.753	99.739	99.644	99.321	99.617	99.472	2.2996	99.952	99.654	99.309	99.217
2.3023	99.962	99.932	99.911	99.774	99.75	99.724	99.354	99.634	99.548	2.3166	99.967	99.69	99.373	99.319
2.3193	99.958	99.946	99.925	99.773	99.81	99.739	99.382	99.666	99.584	2.3337	99.96	99.739	99.417	99.359
2.3363	99.958	99.968	99.922	99.804	99.741	99.785	99.461	99.662	99.595	2.3508	99.962	99.724	99.462	99.415
2.3533	99.963	99.957	99.922	99.827	99.77	99.778	99.544	99.726	99.589	2.3678	99.954	99.76	99.474	99.472
2.3702	99.973	99.972	99.955	99.825	99.763	99.777	99.547	99.783	99.647	2.3849	99.953	99.717	99.504	99.523
2.3872	99.985	99.991	99.951	99.809	99.815	99.795	99.555	99.75	99.655	2.4019	99.991	99.696	99.545	99.543
2.4042	99.978	99.952	99.936	99.893	99.799	99.75	99.624	99.799	99.626	2.419	99.984	99.784	99.609	99.542
2.4212	99.968	99.953	99.923	99.865	99.834	99.793	99.626	99.837	99.71	2.436	99.978	99.78	99.641	99.609
2.4381	100.005	99.941	99.926	99.835	99.884	99.805	99.645	99.842	99.73	2.4531	99.967	99.84	99.655	99.675
2.4551	99.998	99.959	99.932	99.868	99.874	99.843	99.643	99.846	99.696	2.4701	99.936	99.789	99.664	99.631
2.4721	99.97	99.969	99.918	99.906	99.845	99.873	99.643	99.861	99.739	2.4872	99.917	99.766	99.667	99.597
2.4891	99.982	99.954	99.92	99.854	99.869	99.895	99.669	99.833	99.781	2.5042	99.925	99.784	99.674	99.631
2.506	99.982	99.964	99.945	99.904	99.855	99.878	99.66	99.76	99.763	2.5213	99.949	99.757	99.712	99.694
2.523	99.992	99.964	99.964	99.943	99.845	99.884	99.673	99.838	99.746	2.5383	99.995	99.822	99.731	99.718
2.54	99.984	99.982	99.964	99.861	99.891	99.859	99.731	99.913	99.769	2.5554	99.997	99.85	99.754	99.65
2.557	99.99	99.988	99.968	99.864	99.879	99.883	99.763	99.952	99.676	2.5725	100.001	99.821	99.786	99.615
2.5739	99.996	99.996	99.94	99.837	99.88	99.861	99.751	99.88	99.757	2.5895	99.986	99.776	99.784	99.7
2.5909	99.99	99.988	99.936	99.813	99.898	99.847	99.758	99.831	99.792	2.6066	100.035	99.833	99.777	99.727
2.6079	100.001	99.985	99.976	99.908	99.887	99.861	99.774	99.817	99.819	2.6236	100.019	99.798	99.745	99.765
2.6249	99.997	99.982	99.983	99.947	99.856	99.89	99.778	99.817	99.846	2.6407	99.968	99.851	99.811	99.757
2.6418	99.992	99.97	99.979	99.941	99.875	99.887	99.805	99.912	99.799	2.6577	99.964	99.814	99.836	99.73
2.6588	99.991	99.979	99.958	99.953	99.915	99.909	99.81	99.937	99.775	2.6748	99.982	99.853	99.814	99.759
2.6758	99.987	99.993	99.955	99.917	99.92	99.907	99.78	99.889	99.778	2.6918	99.976	99.859	99.792	99.751
2.6928	99.988	99.991	99.977	99.904	99.916	99.9	99.798	99.899	99.826	2.7089	99.997	99.885	99.786	99.765
2.7097	99.989	99.988	99.98	99.912	99.924	99.945	99.834	99.923	99.883	2.7259	99.989	99.882	99.798	99.761
2.7267	99.982	99.996	99.97	99.913	99.945	99.955	99.822	99.951	99.905	2.743	99.994	99.892	99.807	99.79
2.7437	99.984	99.989	99.999	99.942	99.941	99.91	99.807	99.947	99.912	2.7601	99.984	99.9	99.801	99.791
2.7607	99.97	99.976	100.024	99.942	99.947	99.881	99.836	99.915	99.908	2.7771	99.968	99.891	99.788	99.754
2.7776	99.966	99.978	100.011	99.941	99.928	99.872	99.86	99.938	99.892	2.7942	99.981	99.911	99.805	99.802
2.7946	100.002	99.962	99.962	99.922	99.921	99.867	99.858	99.948	99.876	2.8112	99.989	99.938	99.844	99.845
2.8116	99.992	99.964	99.96	99.914	99.973	99.886	99.856	99.915	99.892	2.8283	99.992	99.864	99.842	99.819
2.8286	100.002	99.961	99.954	99.969	99.96	99.942	99.865	99.865	99.898	2.8453	99.988	99.865	99.856	99.817
2.8455	99.995	99.995	99.969	99.967	99.939	99.994	99.852	99.912	99.904	2.8624	99.988	99.911	99.874	99.878
2.8625	99.987	99.982	99.947	99.949	99.929	99.968	99.841	99.966	99.849	2.8794	99.968	99.896	99.874	99.899
2.8795	99.996	99.979	99.962	99.875	99.913	99.994	99.845	100.001	99.864	2.8965	99.955	99.901	99.891	99.848
2.8965	100.006	99.966	99.972	99.891	99.888	99.911	99.851	99.976	99.879	2.9135	99.975	99.953	99.871	99.878
2.9134	99.997	99.974	99.972	99.928	99.93	99.923	99.866	99.94	99.92	2.9306	99.994	99.905	99.908	99.88
2.9304	100.005	99.984	99.979	99.881	99.911	99.904	99.869	99.923	99.888	2.9476	99.98	99.867	99.891	99.894
2.9474	100.027	99.965	99.965	99.959	99.923	99.9	99.848	99.958	99.871	2.9647	100.001	99.862	99.878	99.905
2.9644	100.01	99.961	99.984	99.895	99.968	99.883	99.873	99.956	99.87	2.9818	100.037	99.862	99.892	99.849
2.9813	99.998	99.99	99.967	99.925	99.946	99.935	99.849	99.88	99.878	2.9988	100.019	99.891	99.866	99.803
2.9983	100.007	99.981	99.979	99.928	99.985	99.916	99.841	99.91	99.895	3.0159	99.991	99.894	99.835	99.886
3.0153	100.009	99.979	99.967	99.924	100.003	99.915	99.856	99.906	99.871	3.0329	100.008	99.917	99.82	99.81
3.0323	100.012	100.007	99.987	99.917	99.984	99.943	99.854	99.941	99.916	3.05	100.044	99.948	99.922	99.893
3.0492	100.011	100.009	99.997	99.962	99.965	99.909	99.888	99.94	99.91	3.067	100.01	99.971	99.943	99.881

3.0662	100.018	100.012	100.005	99.938	99.921	99.898	99.899	99.938	99.873	3.0841	100.035	99.959	99.893	99.883
3.0832	99.997	100.007	99.996	99.913	99.962	99.944	99.849	99.931	99.857	3.1011	100.044	99.983	99.884	99.846
3.1002	99.989	99.979	99.959	99.98	99.989	99.944	99.87	99.961	99.909	3.1182	100.053	99.956	99.892	99.846
3.1171	99.993	99.971	99.954	99.99	99.982	99.955	99.889	99.957	99.949	3.1352	100.034	99.951	99.887	99.953
3.1341	99.988	99.99	99.977	99.976	99.981	99.967	99.887	99.911	99.935	3.1523	99.978	99.929	99.883	99.89
3.1511	100.011	99.996	99.988	99.924	99.979	99.962	99.928	99.889	99.945	3.1694	100.003	99.933	99.896	99.845
3.1681	99.976	100.003	100	99.909	99.985	99.962	99.929	99.913	99.936	3.1864	100.02	99.961	99.879	99.925
3.185	99.973	99.979	99.993	99.959	100.013	99.973	99.886	99.95	99.935	3.2035	100.027	99.938	99.868	99.923
3.202	99.997	99.992	100.003	99.968	99.974	99.943	99.871	100.006	99.941	3.2205	100.011	99.939	99.886	99.936
3.219	99.999	99.991	99.997	99.958	99.948	99.898	99.872	99.959	99.957	3.2376	99.999	99.921	99.9	99.935
3.236	100.013	99.975	99.995	99.969	99.971	99.934	99.887	99.93	99.967	3.2546	99.976	99.888	99.896	99.912
3.2529	100.003	99.985	100.004	99.979	99.987	99.94	99.907	99.964	99.964	3.2717	99.957	99.904	99.91	99.885
3.2699	100.004	99.986	99.994	100.021	99.964	99.892	99.896	99.975	99.912	3.2887	99.981	99.902	99.925	99.866
3.2869	99.997	100.015	99.972	99.999	99.946	99.91	99.885	99.974	99.903	3.3058	100.019	99.961	99.933	99.872
3.3039	99.992	99.994	99.968	99.968	99.914	99.963	99.907	99.98	99.894	3.3228	100.013	99.969	99.905	99.88
3.3208	99.981	99.98	99.968	99.903	99.896	99.956	99.901	99.976	99.897	3.3399	100.016	99.87	99.885	99.942
3.3378	99.988	100.003	99.976	99.961	99.967	99.957	99.903	99.972	99.955	3.3569	100.014	99.895	99.934	99.943
3.3548	100.009	99.996	99.979	99.964	99.99	99.964	99.924	99.954	99.963	3.374	100.044	99.926	99.942	99.906
3.3718	100.005	99.977	99.99	99.988	99.942	99.969	99.925	99.947	99.91	3.3911	100.032	99.914	99.921	99.883
3.3887	100.006	99.986	99.995	99.954	99.95	99.952	99.939	99.962	99.918	3.4081	99.997	99.977	99.939	99.908
3.4057	99.996	99.972	99.985	99.921	99.949	99.915	99.943	99.978	99.91	3.4252	99.993	99.986	99.922	99.881
3.4227	100.025	99.988	99.968	99.983	99.97	99.908	99.952	99.98	99.954	3.4422	99.991	99.961	99.9	99.948
3.4397	100.026	99.987	99.969	100	100.022	99.934	99.91	99.971	99.825	3.4593	99.968	99.941	99.904	99.905
3.4566	100	99.998	99.977	99.964	99.997	99.931	99.921	99.94	99.852	3.4763	99.979	99.956	99.86	99.86
3.4736	100.021	100.016	99.992	99.891	100.011	99.971	99.927	99.988	99.919	3.4934	100.014	99.921	99.902	99.885
3.4906	100.015	99.998	100.008	99.925	100.062	99.983	99.935	99.96	99.91	3.5104	100.021	99.909	99.921	99.934
3.5076	100.004	100.002	100	99.911	100.006	99.987	99.935	99.969	99.901	3.5275	100.001	99.939	99.929	99.925
3.5245	99.981	100.004	99.997	99.927	100.016	99.961	99.949	100.006	99.929	3.5445	99.977	99.905	99.923	99.916
3.5415	99.989	100.014	99.999	99.924	100.013	99.989	99.919	100	99.92	3.5616	100.006	99.93	99.884	99.968
3.5585	100.006	100.003	99.994	99.953	99.988	99.965	99.942	99.959	99.9	3.5786	100.033	99.92	99.905	99.976
3.5755	100.018	99.997	99.995	100.011	99.945	99.949	99.933	99.983	99.892	3.5957	100.007	99.936	99.907	99.947
3.5924	99.993	100	100	100.012	99.963	99.94	99.909	100.004	99.969	3.6128	100.026	99.959	99.94	99.916
3.6094	99.992	99.984	100.009	99.964	99.954	99.96	99.898	99.984	99.997	3.6298	100.012	99.929	99.914	99.904
3.6264	100.011	99.989	100.013	99.945	99.95	100.007	99.936	99.969	99.964	3.6469	99.999	99.977	99.937	99.919
3.6434	100.006	100.013	100.01	99.983	99.973	99.96	99.956	99.947	99.936	3.6639	99.997	99.996	99.942	99.879
3.6603	100.004	99.992	99.991	99.996	99.993	99.948	99.929	99.973	99.928	3.681	99.992	99.912	99.934	99.93
3.6773	100.008	99.99	99.99	99.959	99.974	99.916	99.925	100.009	99.95	3.698	100.003	99.928	99.966	99.92
3.6943	99.996	99.998	99.99	99.937	99.966	99.937	99.935	99.965	99.962	3.7151	100.006	99.963	99.946	99.893
3.7113	100.003	99.995	99.977	99.968	99.948	99.946	99.976	100	99.918	3.7321	100.038	99.951	99.952	99.89
3.7282	100.01	100.005	99.963	99.994	99.946	99.943	99.964	99.951	99.948	3.7492	100.048	99.965	99.969	99.882
3.7452	100.01	100.003	100.007	99.942	99.953	100.009	99.951	99.95	99.974	3.7662	99.995	99.992	99.951	99.943
3.7622	100.008	100	99.987	100.041	99.969	100.015	99.926	99.918	99.987	3.7833	100.002	100.012	99.931	99.95
3.7792	100.02	99.991	100.012	100.059	99.974	99.994	99.952	99.906	99.92	3.8004	100.003	100.01	99.927	99.932
3.7961	100.018	99.997	99.996	100.004	99.941	99.976	99.963	99.933	99.953	3.8174	99.995	99.981	99.917	99.871
3.8131	99.991	99.999	100.009	99.999	99.946	100.009	99.948	99.967	99.984	3.8345	100	99.946	99.881	99.931
3.8301	100.002	99.995	99.983	99.999	99.984	99.984	99.951	99.941	99.98	3.8515	100.018	99.975	99.883	99.929
3.847	100.016	99.979	99.975	99.979	99.987	99.964	99.973	99.943	99.991	3.8686	100.025	99.971	99.86	99.919
3.864	100.013	99.989	99.99	99.927	99.947	99.935	99.982	99.966	99.965	3.8856	100.004	99.941	99.895	99.892
3.881	99.991	99.993	100.001	99.915	99.961	99.978	99.962	99.963	99.967	3.9027	100.002	99.97	99.942	99.872
3.898	99.989	99.985	100.008	99.894	100.011	100.004	99.943	99.969	99.944	3.9197	100.009	99.964	99.948	99.909
3.9149	99.998	99.967	100.032	99.932	100.005	100.01	99.939	99.944	99.922	3.9368	100.016	99.964	99.93	99.949
3.9319	99.984	99.977	99.99	99.969	99.994	100.012	99.901	99.96	99.912	3.9538	100	99.923	99.909	99.954
3.9489	100.002	99.983	99.972	99.965	99.984	99.993	99.904	100.007	99.918	3.9709	99.993	99.933	99.909	99.935
3.9659	99.999	99.993	99.978	99.972	99.976	99.983	99.948	100.017	99.984	3.9879	100.005	99.954	99.931	99.914
3.9828	99.995	100.017	99.988	99.962	99.993	99.984	99.946	100.005	99.995	4.005	99.995	99.955	99.937	99.906
3.9998	99.984	100.015	99.987	99.921	99.98	99.951	99.94	99.966	100.01	4.0221	100.016	99.922	99.94	99.953
4.0168	100.005	100.012	99.981	99.964	99.986	99.952	99.935	99.985	99.963	4.0391	100.054	99.954	99.917	99.955
4.0338	99.99	99.991	99.992	99.943	99.989	99.995	99.919	99.957	99.875	4.0562	100.008	100.02	99.923	99.928
4.0507	100.005	99.98	100.005	99.973	99.988	100.015	99.963	99.955	99.965	4.0732	100.035	100.028	99.943	99.905
4.0677	100.012	99.99	100.016	99.979	99.996	99.988	99.96	99.947	99.956	4.0903	100.066	99.961	99.939	99.926
4.0847	100.008	99.983	100.018	99.943	100.003	99.965	99.94	100.004	99.899	4.1073	100.052	99.998	99.938	99.899
4.1017	100.006	99.981	100.001	99.963	99.955	100.016	99.945	100.03	99.946	4.1244	100.002	100.008	99.939	99.88
4.1186	99.994	99.998	99.981	99.965	99.96	99.959	99.953	99.982	99.966	4.1414	99.981	99.982	99.93	99.907
4.1356	99.998	100.017	99.986	99.946	99.961	99.897	99.954	99.949	99.942	4.1585	100.018	99.93	99.919	99.974
4.1526	100.009	100.023	99.986	99.942	100.017	99.889	99.944	99.958	100.013	4.1755	100.009	99.935	99.975	99.975
4.1696	100.016	100.01	99.977	99.946	100.06	99.984	99.932	100.007	100.049	4.1926	100.014	99.948	99.934	99.909
4.1865	100.009	100.002	100.008	99.98	100.054	99.951	99.916	100.064	100.018	4.2097	100.019	99.927	99.924	99.947
4.2035	99.99	100.012	100.028	99.992	99.976	99.953	99.93	100.005	99.967	4.2267	100.006	99.922	99.939	99.95
4.2205	99.992	100.01	99.987	99.969	100.02	100.004	99.964	99.953	99.976	4.2438	99.989	99.912	99.926	99.916
4.2375	100.002	100.004	99.987	99.986	100.025	100.004	100	99.954	99.898	4.2608	100.041	99.97	99.941	99.877
4.2544	100.026	99.999	99.952	99.975	99.971	100.004	99.954	99.963	99.944	4.2779	100.049	99.955	99.954	99.955
4.2714	100.02	100.004	100.009	99.985	100.005	99.98	99.938	99.963	99.958	4.2949	99.997	99.99	99.965	99.899
4.2884	100.012	99.979	100.03	99.997	100.008	100.006	99.96	99.959	99.947	4.312	99.968	99.961	99.928	99.964
4.3054	100.009	99.983	100.038	99.998	99.988	99.993	99.955	99.956	99.952	4.329	99.96	99.944	99.905	99.928
4.3223	100.024	99.973	100.031	100.002	99.991	99.948	99.955	99.947	99.935	4.3461	99.968	99.957	99.957	99.916
4.3393	100.012	99.97	100.005	99.971	99.959	99.925	99.959	99.916	99.901	4.3631	99.966	99.958	99.945	99.982
4.3563	100.012	100.007	99.991	99.945	100.004	99.959	99.964	99.903	99.943	4.3802	99.977	99.952	99.95	99.935
4.3733	100.013	100.009	99.996	99.936	100.064	99.963	99.974	99.942	99.948	4.3972	99.999	99.913	99.984	99.907
4.3902	100.005	99.99	99.975	100.015	100.035	100.016	99.969	99.978	99.94	4.4143	100.043	99.959	100.009	99.939
4.4072	100.019	100.01	99.968	100.051	100.011	100.035	99.954	99.992	99.961	4.4314	100.025	99.967	99.99	99.948
4.4242	100.015	100.012	99.975	100.003	100.001	100.038	99.937	99.995	99.942	4.4484	99.991	99.968	100.006	99.935
4.4412	100.014	99.99	99.978	99.995	100.005	100.05	99.938	99.942	99.967	4.4655	99.98	99.946	99.988	99.899

Appendix 1: unpublished noble gas analyses

Appendix 1: unpublished noble gas data

pit type	Depth	Volume (μm^3)	He (mol)	He uncert. (mol)	Ne (mol)	Ne uncert. (mol)	Ar (mol)	Ar uncert. (mol)	He (mol/g)	He uncert. (mol/g)	Ne (mol/g)	Ne uncert. (mol/g)	Ar (mol/g)	Ar uncert. (mol/g)	He Henry Const. (mol/g bar)	Ne Henry Const. (mol/g bar)	Ar Henry Const. (mol/g bar)	median He Henry Const. (mol/g bar)	He Henry const. 75% (mol/g bar)	He Henry const. 25% (mol/g bar)	median Ne Henry Const. (mol/g bar)	Ne Henry const. 75% (mol/g bar)	Ne Henry const. 25% (mol/g bar)	median Ar Henry Const. (mol/g bar)	Ar Henry const. 75% (mol/g bar)	Ar Henry const. 25% (mol/g bar)	P (kbar)	T (°C)	duration (hr)	PHe	PNe	PAr	Note
yellow garnet																																	
		CS_NG_EXP35																															
	4.78	6.0E+05	2.0E-14	1.8E-14	6.6E-16	1.9E-15	1.4E-15	1.3E-15	8.9E-09	8.4E-09	3.0E-10	8.6E-10	6.1E-10	6.2E-10	2.0E-11	6.7E-13	1.4E-12											1.33	625	65.5	0.44	0.44	0.44	
	26.94	3.4E+06	5.6E-14	1.7E-14	9.2E-16	1.8E-15	4.9E-15	1.3E-15	4.5E-09	2.0E-09	7.4E-11	1.5E-10	3.9E-10	1.7E-10	1.0E-11	1.7E-13	8.8E-13											1.33	625	65.5	0.44	0.44	0.44	
	16.80	2.1E+06	3.2E-14	1.6E-14	-8.2E-16	2.2E-15	1.6E-15	1.3E-15	4.1E-09	2.5E-09	-1.1E-10	2.9E-10	2.0E-10	1.8E-10	9.3E-12	-2.4E-13	4.6E-13											1.33	625	65.5	0.44	0.44	0.44	
	10.76	1.4E+06	5.9E-14	1.7E-14	3.4E-15	1.8E-15	1.9E-15	1.3E-15	1.2E-08	5.1E-09	6.8E-10	4.3E-10	3.9E-10	2.9E-10	2.7E-11	1.5E-12	8.7E-13											1.33	625	65.5	0.44	0.44	0.44	
	10.87	1.4E+06	4.9E-14	1.6E-14	1.6E-15	1.9E-15	8.2E-16	1.3E-15	9.7E-09	4.6E-09	3.2E-10	3.9E-10	1.6E-10	2.6E-10	2.2E-11	7.1E-13	3.7E-13											1.33	625	65.5	0.44	0.44	0.44	
	7.70	9.7E+05	3.8E-15	1.6E-14	3.6E-16	1.8E-15	7.0E-16	1.3E-15	1.1E-09	4.6E-09	9.9E-11	5.0E-10	2.0E-10	3.7E-10	2.4E-12	2.2E-13	4.4E-13											1.33	625	65.5	0.44	0.44	0.44	
	0.35	4.4E+04	6.0E-15	1.6E-14	-4.3E-16	1.8E-15	-3.4E-16	1.3E-15	3.7E-08	1.0E-07	-2.6E-09	1.1E-08	-2.1E-09	8.1E-09	8.3E-11	-6.0E-12	-4.8E-12											1.33	625	65.5	0.44	0.44	0.44	
																		2.01E-11	2.43E-11	9.72E-12	NA	NA	NA	NA	NA	NA							
green cz																																	
		EHPV_NG_EXP68																															
	1.50	8.9E+04	7.0E-16	7.3E-16	-1.3E-15	2.3E-15	-2.1E-15	4.3E-15	1.3E-09	1.5E-09	-2.4E-09	4.6E-09	-4.1E-09	8.4E-09	3.4E-12	-6.0E-12	-1.0E-11											1.20	1050	60.0	0.40	0.40	0.40	
	3.94	2.3E+05	6.8E-16	7.4E-16	2.3E-15	2.3E-15	-1.3E-15	6.2E-15	5.0E-10	5.7E-10	1.7E-09	1.8E-09	-9.9E-10	4.6E-09	1.3E-12	4.3E-12	-2.5E-12											1.20	1050	60.0	0.40	0.40	0.40	
	8.17	1.0E+06	-7.3E-16	8.3E-16	4.9E-15	2.4E-15	2.8E-15	4.3E-15	-1.2E-10	1.5E-10	8.2E-10	4.8E-10	4.7E-10	7.3E-10	-3.1E-13	2.1E-12	1.2E-12											1.20	1050	60.0	0.40	0.40	0.40	
																		1.25E-12	2.30E-12	4.71E-13	NA	NA	NA	NA	NA	NA	1.20	1050	60.0	0.40	0.40	0.40	
red cz																																	
		EHPV_NG_EXP68																															
	2.03	2.6E+05	2.8E-15	7.7E-16	1.9E-15	2.4E-15	-2.1E-15	4.4E-15	1.9E-09	8.1E-10	1.3E-09	1.6E-09	-1.4E-09	3.0E-09	4.7E-12	3.2E-12	-3.6E-12											1.20	1050	60.0	0.40	0.40	0.40	
	7.38	9.3E+05	8.8E-15	1.0E-15	4.9E-15	2.4E-15	-2.8E-15	4.5E-15	1.6E-09	5.7E-10	9.1E-10	5.3E-10	-5.3E-10	8.5E-10	4.1E-12	2.3E-12	-1.3E-12											1.20	1050	60.0	0.40	0.40	0.40	
	8.22	1.0E+06	1.4E-14	7.8E-16	-2.1E-15	2.6E-15	1.0E-14	4.3E-15	2.3E-09	7.6E-10	-3.6E-10	4.5E-10	1.7E-09	9.1E-10	5.7E-12	-8.9E-13	4.4E-12											1.20	1050	60.0	0.40	0.40	0.40	
	9.25	1.2E+06	1.5E-14	8.9E-16	2.8E-15	2.4E-15	5.3E-15	4.4E-15	2.2E-09	7.2E-10	4.2E-10	3.8E-10	7.8E-10	7.0E-10	5.4E-12	1.1E-12	1.9E-12											1.20	1050	60.0	0.40	0.40	0.40	
																		5.05E-12	5.45E-12	4.55E-12	NA	NA	NA	NA	NA	NA	1.20	1050	60.0	0.40	0.40	0.40	
ysz 3																																	
		EHPV_NG_EXP68																															
	3.82	4.8E+05	-6.3E-17	7.6E-16	2.3E-15	2.6E-15	6.9E-15	4.3E-15	-2.3E-11	2.7E-10	8.3E-10	9.8E-10	2.5E-09	1.7E-09	-5.4E-14	2.0E-12	5.9E-12											1.26	1075	39.8	0.42	0.42	0.42	
	5.01	6.3E+05	4.1E-16	8.2E-16	3.6E-15	2.4E-15	5.6E-15	4.3E-15	1.1E-10	2.3E-10	9.7E-10	7.4E-10	1.5E-09	1.3E-09	2.7E-13	2.3E-12	3.7E-12											1.26	1075	39.8	0.42	0.42	0.42	
	6.89	8.7E+05	2.1E-15	7.3E-16	4.6E-15	2.7E-15	7.2E-15	4.7E-15	4.3E-10	2.0E-10	9.1E-10	6.2E-10	1.4E-09	1.0E-09	1.0E-12	2.2E-12	3.4E-12											1.26	1075	39.8	0.42	0.42	0.42	
	8.67	1.1E+06	1.2E-15	8.2E-16	9.8E-16	2.5E-15	1.2E-14	4.8E-15	1.8E-10	1.4E-10	1.5E-10	4.0E-10	1.8E-09	9.7E-10	4.4E-13	3.7E-13	4.4E-12											1.26	1075	39.8	0.42	0.42	0.42	
	4.21	5.3E+05	2.7E-15	7.4E-16	4.1E-15	2.5E-15	5.7E-15	4.4E-15	8.6E-10	3.7E-10	1.4E-09	9.4E-10	1.9E-09	1.6E-09	2.1E-12	3.2E-12	4.4E-12											1.26	1075	39.8	0.42	0.42	0.42	
	0.18	2.2E+04	3.4E-17	7.4E-16	2.4E-15	2.3E-15	4.8E-15	4.4E-15	2.6E-10	5.8E-09	1.9E-08	1.9E-08	3.8E-08	3.7E-08	6.3E-13	4.5E-11	9.0E-11											1.26	1075	39.8	0.42	0.42	0.42	
	0.56	7.1E+04	1.1E-15	7.5E-16	3.9E-15	2.3E-15	6.2E-15	4.5E-15	2.7E-09	2.0E-09	9.6E-09	6.5E-09	1.5E-08	1.2E-08	6.4E-12	2.3E-11	3.6E-11											1.26	1075	39.8	0.42	0.42	0.42	
																		6.26E-13	1.54E-12	3.52E-13	NA	NA	NA	NA	NA	NA	1.26	1075	39.8	0.42	0.42	0.42	Ne, Ar surface?
ysz 4																																	
		EHPV_NG_EXP68																															
	5.60	7.0E+05	1.0E-15	8.6E-16	1.6E-15	2.3E-15	-3.5E-15	4.3E-15	2.5E-10	2.3E-10	3.9E-10	5.8E-10	-8.5E-10	1.1E-09	5.9E-13	9.4E-13	-2.0E-12											1.26	1075	39.8	0.42	0.42	0.42	
	7.05	8.9E+05	1.4E-15	7.5E-16	4.4E-15	2.4E-15	1.8E-15	4.4E-15	2.8E-10	1.7E-10	8.5E-10	5.5E-10	3.6E-10	8.6E-10	6.6E-13	2.0E-12	8.5E-13											1.26	1075	39.8	0.42	0.42	0.42	
	8.46	1.1E+06	1.2E-15	7.6E-16	-5.1E-16	2.3E-15	5.3E-15	4.3E-15	2.0E-10	1.4E-10	-8.3E-11	3.8E-10	8.6E-10	7.5E-10	4.7E-13	-2.0E-13	2.1E-12											1.26	1075	39.8	0.42	0.42	0.42	
	3.05	3.8E+05	-3.0E-18	7.4E-16	-8.6E-16	2.4E-15	-5.0E-15	4.5E-15	-1.4E-12	3.3E-10	-3.9E-10	1.1E-09	-2.3E-09	2.2E-09	-3.2E-15	-9.2E-13	-5.4E-12											1.26	1075	39.8	0.42	0.42	0.42	
	7.93	1.0E+06	6.5E-16	7.6E-16	-8.4E-16	2.6E-15	1.0E-15	4.5E-15	1.1E-10	1.4E-10	-1.4E-10	4.5E-10	1.7E-10	7.9E-10	2.7E-13	-3.5E-13	4.1E-13											1.26	1075	39.8	0.42	0.42	0.42	
	0.98	1.2E+05	2.2E-16	7.9E-16	3.4E-15	2.3E-15	2.6E-15	4.3E-15	3.1E-10	1.1E-09	4.7E-09	3.6E-09	3.6E-09	6.1E-09	7.4E-13	1.1E-11	8.6E-12											1.26	1075	39.8	0.42	0.42	0.42	
	0.84	1.1E+05	-9.5E-16	7.8E-16	3.5E-15	2.4E-15	-5.5E-16	4.3E-15	-1.4E-09	1.4E-09	5.8E-09	4.3E-09	-9.0E-10	7.0E-09	-3.7E-12	1.4E-11	-2.1E-12											1.26	1075	39.8	0.42	0.42	0.42	
	0.75	9.5E+04	3.8E-16	8.1E-16	8.2E-16	2.4E-15	6.7E-15	4.5E-15	7.0E-10	1.5E-09	1.5E-09	4.5E-09	1.2E-08	9.2E-09	1.7E-12	3.6E-12	2.9E-11											1.26	1075	39.8	0.42	0.42	0.42	
	12.19	1.5E+06	1.0E-15	7.4E-16	3.6E-15	2.3E-15	1.5E-14	4.3E-15	1.1E-10	9.2E-11	4.0E-10	3.0E-10	1.6E-09	7.3E-10	2.7E-13	9.6E-13	3.9E-12											1.26	1075	39.8	0.42	0.42	0.42	
																		4.70E-13	6.60E-13	2.69E-13	NA	NA	NA	NA	NA	NA	1.26	1075	39.8	0.42	0.42	0.42	Ne, Ar surface?
san carlos olivine																																	
		EHPV_NG_EXP45																															
	12.21	3.8E+05	7.8E-15	9.6E-16	-7.8E-15	2.7E-14	-2.7E-16	6.1E-16	6.1E-09	2.1E-09	-6.1E-09	2.1E-08	-2.1E-10	4.8E-10	3.6E-12	NA	NA											1.69	900	24.0	1.69	0.00	0.00	
	18.97	6.0E+05	6.2E-15	9.6E-16	-2.7E-14	2.6E-14	6.3E-16	6.2E-16	3.1E-09	1.1E-09	-1.4E-08	1.4E-08	3.2E-10	3.3E-10	1.9E-12	NA	NA											1.69	900	24.0	1.69	0.00	0.00	
	6.53	2.1E+05	1.8E-15	9.6E-16	3.5E-14	2.6E-14	-9.7E-17	7.0E-16	2.7E-09	1.6E-09	5.1E-08	4.2E-08	-1.4E-10	1.0E-09	1.6E-12	NA	NA											1.69	900	24.0	1.69	0.00	0.00	
	10.37	6.2E+05	5.4E-15	9.3E-16	-2.4E-14	2.7E-14	2.0E-15	6.2E-16	2.6E-09	9.7E-10	-1.2E-08	1.4E-08	9.9E-10	4.4E-10	1.5E-12	NA	NA											1.69	900	24.0	1.69	0.00	0.00	
	8.26	1.0E+06	5.4E-15	1.0E-15	-2.6E-14	2.7E-14	-7.9E-17	6.1E-16	1.5E-09	5.9E-10	-7.6E-09	8.2E-09	-2.3E-11	1.8E-10	9.1E-13	NA	NA											1.69	900	24.0	1.69	0.00	0.00	
	16.77	1.0E+06	7.7E-15	9.4E-16	1.7E-14	2.7E-14	-3.0E-17	6.1E-16	2.3E-09	8.2E-10	5.1E-09	8.2E-09	-9.0E-12	1.8E-10	1.4E-12	NA	NA											1.69	900	24.0	1.69	0.00	0.00	
	30.26	9.5E+05	1.0E-13	1.1E-15	4.8E-14	2.8E-14	9.6E-16	6.1E-16	3.3E-08	1.1E-08	1.5E-08	1.0E-08	3.0E-10	2.2E-10	1.9E-11	NA	NA											1.69	900	24.0	1.69	0.00	0.00	not used
	12.80	4.0E+05	3.5E-15	9.5E-16	-5.5E-15	2.6E-14	-4.6E-16	6.0E-16	2.6E-09	1.1E-09	-4.1E-09	2.0E-08	-3.4E-10	4.6E-10	1.5E-12	NA	NA											1.69	900	24.0	1.69	0.00	0.00	
	16.23	2.9E+05	2.7E-15	9.4E-16	2.0E-14	2.6E-14	1.9E-16	6.3E-16	2.8E-09	1.4E-09	2.1E-08	2.8E-08	2.0E-10	6.6E-10	1.7E-12	NA	NA											1.69	900	24.0	1.69	0.00	0.00	
	15.82	5.0E+05	5.5E-15	9.3E-16	-7.3E-15	2.7E-14	-6.5E-16	7.2E-16	3.3E-09	1.2E-09	-4.4E-09	1.6E-08	-3.9E-10	4.5E-10	2.0E-12	NA	NA											1.69	900	24.0	1.69	0.00	0.00	
	15.55	4.9E+05	2.2E-15	9.4E-16	-1.6E-14	2.7E-14	4.5E-16	6.1E-16	1.4E-09	7.3E-10	-1.0E-08	1.7E-08	2.8E-10	3.9E-10	8.1E-13	NA	NA											1.69	900	24.0	1.69	0.00	0.00	
	14.71	8.7E+05	7.4E-15	1.0E-15	-1.7E-14	2.7E-14	-3.6E-16	6.5E-16	2.5E-09	9.1E-10	-5.9E-09	9.4E-09	-1.2E-10	2.3E-10	1.5E-12	NA	NA											1.69	900	24.0	1.69	0.00	0.00	
raster line	3.98	7.8E+05	7.6E-15	9.6E-16	4.9E-14	2.7E-14	8.0E-16	6.5E-16	2.9E-09	1.0E-09	1.9E-08	1.2E-08	3.1E-10	2.7E-10	1.7E-12	NA	NA											1.69	900	24.0	1.69	0.00	0.00	
																		1.56E-12	1.77E-12	1.47E-12	NA	NA	NA	NA	NA	NA	1.69	900	24.0	1.69	0.00	0.00	
		EHPV_NG_EXP46																															
	8.16	1.0E+06	2.1E-14	9.2E-16	3.4E-14	2.6E-14	9.3E-16	6.2E-16	6.0E-09	2.0E-09	9.9E-09	8.4E-09	2.7E-10	2.0E-10	5.9E-12	NA	NA											1.02	900	24.0	1.02	0.00	0.00	
	7.17	9.0E+05	1.9E-14	9.6E-16	2.1E-15	2.7E-14	8.9E-16	6.0E-16	6.4E-09	2.1E-09	7.1E-10	8.9E-09	3.0E-10	2.2E-10	6.3E-12	NA	NA											1.02	900	24.0	1.02	0.00	0.00	
	8.86	2.8E+05	2.9E-15	9.6E-16	-3.4E-14	2.6E-14	-7.6E-16	7.0E-16	3.2E-09	1.5E-09	-3.6E-08	3.1E-08	-8.2E-10	8.0E-10	3.1E-12	NA	NA											1.02	900	24.0	1.02	0.00	0.00	
	8.11	4.8E+05	8.0E-15	9.4E-16	2.0E-14	2.7E-14	5.6E-16	6.3E-16	5.0E-09	1.7E-09	1.3E-08	1.7E-08	3.5E-10	4.1E-10	4.9E-12	NA	NA											1.02	900	24.0	1.02	0.00	0.00	
	4.80	2.9E+05	1.1E-14	9.4E-16	-1.5E-14	2.7E-14	4.5E-16	6.4E-16	1.1E-08	3.8E-09	-1.6E-08	2.9E-08	4.7E-10	6.9E-10	1.1E-11	NA	NA											1.02	900	24.0	1.02	0.00	0.00	
	2.59	1.5E+05	6.7E-15	9.3E-16	2.7E-14	2.7E-14	6.4E-16	6.0E-16	1.3E-08	4.7E-09	5.3E-08	5.5E-08	1.2E-09	1.2E-09	1.3E-11	NA	NA											1.02	900	24.0	1.02	0.00	0.00	
	2.58	1.5E+05	4.2E-15	9.3E-16	-1.8E-14	2.7E-14	-3.2E-16	6.1E-16	8.2E-09	3.2E-09	-3.5E-08	5.3E-08	-6.3E-10	1.2E-09	8.0E-12	NA	NA											1.02	900	24.0	1.02	0.00	0.00	
	5.32	1.7E+05	6.1E-15	9.4E-16	5.5E-14	2.7E-14	-4.3E-16	6.5E-16	1.1E-08	4.0E-09	9.8E-08	5.9E-08	-7.7E-10	1.2E-09	1.1E-11	NA	NA											1.02	900	24.0	1.02	0.00	0.00	
	13.47	1.7E+06	2.7E-14	9.8E-16	-2.0E-14	2.7E-14	5.4E-16	6.1E-16	4.8E-09	1.6E-09	-3.6E-09	4.9E-09	9.5E-11	1.1E-10	4.7E-12	NA	NA											1.02	900	24.0	1.02	0.00	0.00	
	13.84	8.2E+05	2.2E-14	9.3E-16	-3.5E-15	2.7E-14	1.2E-15	6.0E-16	8.0E-09	2.7E-09	-1.3E-09	9.8E-09	4.5E-10	2.6E-10	7.9E-12	NA	NA											1.02	900	24.0	1.02	0.00	0.00	
	17.68	5.6E+05	6.3E-15	9.3E-16	-2.2E-14	2.6E-14	7.1E-16	6.1E-16	3.4E-09	1.2E-09	-1.2E-08	1.5E-08	3.8E-10	3.5E-10	3.3E-12	NA	NA											1.02	900	24.0	1.02	0.00	0.00	
	5.00	6.3E+05	2.4E-14	9.8E-16	8.5E-15	2.7E-14	-2.8E-17	6.1E-16	1.1E-08	3.8E-09	4.1E-09	1.3E-08	-1.3E-11	2.9E-10	1.1E-11	NA	NA											1.02	900	24.0	1.02	0.00	0.00	
	2.02	2.5E+05	6.0E-15	1.0E-15	3.7E-15	2.6E-14	1.0E-16	6.3E-16	7.1E-09	2.6E-09	4.3E-09	3.1E-08	1.2E-10	7.4E-10	6.9E-12	NA	NA											1.02	900	24.0	1.02	0.00	0.00	
	2.22	2.8E+05	9.9E-15	9.5E-16	2.4E-15	2.7E-14	2.9E-16	6.1E-16	1.1E-08	3.6E-09	2.6E-09	2.9E-08	3.1E-10	6.7E-10	1.0E-11	NA	NA											1.02	900	24.0	1.02	0.00	0.00	
																		7.40E-12	1.05 8E-11	5.138E-12	NA	NA	NA	NA	NA	NA	1.02	900	24.0	1.02	0.00	0.00	
		EHPV_NG_EXP47																															
	19.68	2.5E+06	6.3E-15	1.1E-15	4.1E-15	2.2E-14	3.2E-15	6.0E-16	7.7E-10	2.8E-10	4.9E-10	2.6E-09	3.8E-10	1.5E-10	1.5E-12	NA	NA											0.51	900	24.0	0.51	0.00	0.00	
	18.19	2.3E+06	1.7E-15	1.0E-15	-1.8E-14	2.2E-14	-2.9E-17	5.3E-16	2.2E-10	1.5E-10	-2.3E-09	2.9E-09	-3.7E-12	6.9E-11	4.4E-13	NA	NA											0.51	900	24.0	0.51	0.00	0.00	
	17.34	2.2E+06	7.5E-15	1.0E-15	1.5E-14	2.2E-14	4.3E-16	5.2E-16	1.0E-09	3.7E-10	2.1E-09	3.1E-09	5.8E-11	7.4E-11	2.0E-12	NA	NA											0.51	900	24.0	0.51	0.00	0.00	
	14.28	1.8E+06	3.0E-15	1.0E-15	-5.6E-14	2.4E-14	1.1E-15	5.1E-16	4.9E-10	2.4E-10	-9.4E-09	5.0E-09	1.8E-10	1.0E-10	9.7E-13	NA	NA											0.51	900	24.0	0.51	0.00	0.00	
	41.02	5.2E+06	5.1E-15	1.0E-15	1.5E-15	2.2E-14	1.6E-15	6.4E-16	3.0E-10	1.2E-10	8.8E-11	1.3E-09	9.2E-11	4.8E-11	5.9E-13	NA	NA											0.51	900	24.0	0.51	0.00	0.00	
	7.63	9.6E+05	1.2E-15	1.1E-15	1.1E-14	2.2E-14	2.9E-16	5.2E-16	3.7E-10	3.5E-10	3.4E-09	6.9E-09	9.1E-11	1.6E-10	7.2E-13	NA	NA											0.51	900	24.0	0.51	0.00	0.00	
	14.28	1.8E+06	4.1E-15	1.0E-15	-2.6E-14	2.2E-14	-3.3E-16	5.3E-16	6.8E-10	2.8E-10	-4.4E-09	3.9E-09	-5.6E-11	9.1E-11	1.3E-12	NA	NA											0.51	900	24.0	0.51	0.00	0.00	
	28.83	3.6E+06	7.7E-15	1.2E-15	-3.8E-14	2.5E-14	8.8E-16	5.1E-16	6.4E-10	2.3E-10	-3.2E-09	2.3E-09	7.3E-11	4.9E-11	1.3E-12	NA	NA											0.51	900	24.0	0.51	0.00	0.00	
	24.88	3.1E+06	3.6E-15	1.1E-15	4.1E-14	2.3E-14	5.4E-16	5.2E-16	3.5E-10	1.5E-10	3.9E-09	2.5E-09	5.1E-11	5.3E-11	6.8E-13	NA	NA											0.51	900	24.0	0.51	0.00	0.00	
raster line	11.15	1.9E+06	5.9E-15	1.0E-15	1.1E-14	2.2E-14	1.3E-15	5.5E-16	9.3E-10	3.5E-10	1.7E-09	3.6E-09	2.0E-10	1.1E-10	1.8E-12	NA	NA											0.51	900	24.0	0.51	0.00	0.00	
raster line	9.18	1.8E+06	3.2E-15	1.3E-15	2.0E-14	2.2E-14	2.2E-15	6.3E-16	5.2E-10	2.7E-10	3.3E-09	3.8E-09	3.6E-10	1.6E-10	1.0E-12	NA	NA											0.51	900	24.0	0.51	0.00	0.00	
																		1.03E-12	1.42E-12	7.001E-13	NA	NA	NA	NA	NA	NA	0.51	900	24.0	0.51	0.00	0.00	
		EHPV_NG_EXP48																															
	15.57	2.0E+06	9.7E-15	1.1E-15	-1.6E-14	2.2E-14	1.9E-15	5.9E-16	1.5E-09	5.2E-10	-2.4E-09	3.4E-09	2.8E-10	1.3E-10	6.2E-12	NA	NA											0.24	900	24.0	0.24	0.00	0.00	
	15.42	1.9E+06	4.5E-15	1.0E-15	-5.7E-15	2.4E-14	-1.2E-16	7.5E-16	6.9E-10	2.8E-10	-8.7E-10	3.7E-09	-1.9E-11	1.2E-10	2.9E-12	NA	NA											0.24	900	24.0	0.24	0.00	0.00	
	7.92	1.0E+06	6.5E-15	1.1E-15	5.1E-14	2.3E-14	1.6E-15	5.1E-16	2.0E-09	7.3E-10	1.5E-08	8.5E-09	4.7E-10	2.2E-10	8.2E-12	NA	NA											0.24	900	24.0	0.24	0.00	0.00	
	7.99	1.0E+06	2.5E-15	1.0E-15	-9.0E-15	2.2E-14	1.9E-15	5.2E-16	7.3E-10	3.9E-10	-2.7E-09	6.6E-09	5.5E-10	2.4E-10	3.1E-12	NA	NA											0.24	900	24.0	0.24	0.00	0.00	

	24.58	3.1E+06	5.3E-15	1.0E-15	-2.3E-15	2.2E-14	3.3E-15	6.5E-16	5.1E-10	2.0E-10	-2.3E-10	2.1E-09	3.2E-10	1.2E-10	2.1E-12	NA	NA									0.24	900	24.0	0.24	0.00	0.00	
	13.89	1.7E+06	2.9E-15	1.0E-15	1.9E-14	2.2E-14	9.2E-16	5.3E-16	5.0E-10	2.4E-10	3.2E-09	3.9E-09	1.6E-10	1.0E-10	2.1E-12	NA	NA									0.24	900	24.0	0.24	0.00	0.00	
	33.58	4.2E+06	7.2E-15	1.3E-15	-4.2E-14	2.2E-14	2.0E-15	6.5E-16	5.1E-10	1.9E-10	-3.0E-09	1.8E-09	1.4E-10	6.6E-11	2.1E-12	NA	NA									0.24	900	24.0	0.24	0.00	0.00	
	28.84	3.6E+06	5.8E-15	1.1E-15	-2.7E-17	2.2E-14	-6.1E-16	6.2E-16	4.8E-10	1.8E-10	-2.2E-12	1.8E-09	-5.1E-11	5.4E-11	2.0E-12	NA	NA									0.24	900	24.0	0.24	0.00	0.00	
	26.86	3.4E+06	7.4E-15	1.0E-15	-1.6E-14	2.2E-14	8.4E-17	6.1E-16	6.6E-10	2.4E-10	-1.4E-09	2.0E-09	7.5E-12	5.4E-11	2.8E-12	NA	NA									0.24	900	24.0	0.24	0.00	0.00	
raster line	9.05	1.8E+06	2.5E-15	1.1E-15	-9.2E-15	2.2E-14	2.7E-15	6.0E-16	4.2E-10	2.3E-10	-1.5E-09	3.7E-09	4.5E-10	1.8E-10	1.8E-12	NA	NA									0.24	900	24.0	0.24	0.00	0.00	
raster line	13.27	2.5E+06	5.2E-15	1.0E-15	-1.6E-14	2.2E-14	6.1E-16	7.0E-16	6.2E-10	2.4E-10	-2.0E-09	2.8E-09	7.4E-11	8.8E-11	2.6E-12	NA	NA									0.24	900	24.0	0.24	0.00	0.00	
																		2.60E-12	2.973E-12	2.093E-12	NA	NA	NA	NA	NA	NA	0.24	900	24.0	0.24	0.00	0.00	
		EHPV_NG_EXP49																															
	29.53	3.7E+06	9.3E-14	7.4E-16	5.0E-14	1.8E-14	5.8E-16	4.0E-16	7.5E-09	2.5E-09	4.0E-09	2.0E-09	4.7E-11	3.6E-11	6.8E-11	NA	NA									0.11	900	24.0	0.11	0.00	0.00	not used
	16.34	2.1E+06	8.3E-15	7.3E-16	5.0E-14	1.7E-14	7.7E-16	3.9E-16	1.2E-09	4.2E-10	7.2E-09	3.4E-09	1.1E-10	6.8E-11	1.1E-11	NA	NA									0.11	900	24.0	0.11	0.00	0.00	
	16.85	2.1E+06	6.4E-15	7.2E-16	4.9E-14	1.7E-14	-6.8E-17	3.7E-16	9.0E-10	3.1E-10	6.9E-09	3.3E-09	-9.6E-12	5.3E-11	8.2E-12	NA	NA									0.11	900	24.0	0.11	0.00	0.00	
	15.44	1.9E+06	5.0E-15	7.2E-16	7.7E-15	1.7E-14	-1.3E-16	3.8E-16	7.8E-10	2.8E-10	1.2E-09	2.6E-09	-2.0E-11	5.9E-11	7.1E-12	NA	NA									0.11	900	24.0	0.11	0.00	0.00	
	27.13	3.4E+06	7.0E-15	7.3E-16	-1.8E-14	1.8E-14	-1.4E-15	4.7E-16	6.2E-10	2.1E-10	-1.6E-09	1.6E-09	-1.2E-10	5.7E-11	5.6E-12	NA	NA									0.11	900	24.0	0.11	0.00	0.00	
	5.75	7.2E+05	2.3E-15	7.5E-16	2.1E-14	1.7E-14	-9.8E-16	3.7E-16	9.6E-10	4.4E-10	8.6E-09	7.6E-09	-4.0E-10	2.0E-10	8.7E-12	NA	NA									0.11	900	24.0	0.11	0.00	0.00	
	7.59	9.5E+05	3.1E-15	7.2E-16	-4.3E-15	1.7E-14	3.0E-16	3.8E-16	9.7E-10	3.9E-10	-1.4E-09	5.4E-09	9.3E-11	1.2E-10	8.8E-12	NA	NA									0.11	900	24.0	0.11	0.00	0.00	
	22.95	2.9E+06	3.0E-15	7.0E-16	-1.2E-14	1.9E-14	5.2E-17	3.9E-16	3.1E-10	1.3E-10	-1.2E-09	2.0E-09	5.4E-12	4.0E-11	2.8E-12	NA	NA									0.11	900	24.0	0.11	0.00	0.00	
	22.46	2.8E+06	3.7E-15	7.0E-16	2.7E-14	1.7E-14	1.4E-15	3.9E-16	3.9E-10	1.5E-10	2.9E-09	2.1E-09	1.5E-10	6.4E-11	3.6E-12	NA	NA									0.11	900	24.0	0.11	0.00	0.00	
	30.25	3.8E+06	4.9E-15	7.0E-16	1.7E-14	1.7E-14	-9.3E-16	3.7E-16	3.9E-10	1.4E-10	1.3E-09	1.4E-09	-7.3E-11	3.8E-11	3.5E-12	NA	NA									0.11	900	24.0	0.11	0.00	0.00	
	19.60	2.5E+06	4.3E-15	7.1E-16	6.9E-15	1.9E-14	1.3E-15	4.4E-16	5.3E-10	1.9E-10	8.4E-10	2.3E-09	1.6E-10	7.6E-11	4.8E-12	NA	NA									0.11	900	24.0	0.11	0.00	0.00	
raster line	13.72	3.4E+06	4.6E-15	7.3E-16	-1.2E-14	1.8E-14	5.0E-16	3.8E-16	4.0E-10	1.5E-10	-1.0E-09	1.6E-09	4.4E-11	3.6E-11	3.7E-12	NA	NA									0.11	900	24.0	0.11	0.00	0.00	
raster line	12.46	2.9E+06	3.8E-15	7.5E-16	-1.4E-14	2.0E-14	9.8E-16	3.9E-16	3.9E-10	1.5E-10	-1.4E-09	2.1E-09	1.0E-10	5.2E-11	3.6E-12	NA	NA									0.11	900	24.0	0.11	0.00	0.00	
																		5.20E-12	8.331E-12	3.566E-12	NA	NA	NA	NA	NA	NA	0.11	900	24.0	0.11	0.00	0.00	
		EHPV_NG_EXP50																															
	24.51	3.1E+06	1.0E-15	7.3E-16	-2.5E-14	1.7E-14	3.7E-18	4.4E-16	9.7E-11	7.8E-11	-2.4E-09	1.8E-09	3.6E-13	4.3E-11	1.8E-12	NA	NA									0.06	900	24.0	0.06	0.00	0.00	
	35.64	4.5E+06	2.0E-15	8.4E-16	1.1E-15	1.7E-14	6.9E-16	3.8E-16	1.3E-10	7.2E-11	7.1E-11	1.1E-09	4.6E-11	2.9E-11	2.5E-12	NA	NA									0.06	900	24.0	0.06	0.00	0.00	
	34.22	4.3E+06	3.5E-15	7.2E-16	-1.5E-15	1.7E-14	8.4E-16	3.6E-16	2.5E-10	9.6E-11	-1.0E-10	1.2E-09	5.9E-11	3.2E-11	4.5E-12	NA	NA									0.06	900	24.0	0.06	0.00	0.00	
	33.74	4.2E+06	1.1E-15	7.4E-16	1.9E-14	1.7E-14	7.6E-16	3.8E-16	7.8E-11	5.8E-11	1.4E-09	1.3E-09	5.3E-11	3.2E-11	1.4E-12	NA	NA									0.06	900	24.0	0.06	0.00	0.00	
	32.68	4.1E+06	4.0E-15	7.4E-16	1.9E-14	1.7E-14	2.9E-15	3.6E-16	2.9E-10	1.1E-10	1.4E-09	1.3E-09	2.1E-10	8.3E-11	5.3E-12	NA	NA									0.06	900	24.0	0.06	0.00	0.00	
	30.88	3.9E+06	2.7E-15	7.1E-16	-3.0E-15	1.7E-14	4.8E-16	3.9E-16	2.1E-10	8.8E-11	-2.3E-10	1.3E-09	3.7E-11	3.2E-11	3.8E-12	NA	NA									0.06	900	24.0	0.06	0.00	0.00	
	30.32	3.8E+06	3.3E-15	7.1E-16	2.2E-14	1.7E-14	5.4E-16	3.8E-16	2.6E-10	1.0E-10	1.8E-09	1.4E-09	4.2E-11	3.3E-11	4.7E-12	NA	NA									0.06	900	24.0	0.06	0.00	0.00	
	29.33	3.7E+06	1.5E-15	8.3E-16	1.4E-14	1.8E-14	-4.3E-16	3.9E-16	1.2E-10	7.8E-11	1.1E-09	1.5E-09	-3.5E-11	3.3E-11	2.2E-12	NA	NA									0.06	900	24.0	0.06	0.00	0.00	
raster line	12.34	3.4E+06	1.7E-15	7.0E-16	3.0E-14	1.7E-14	8.2E-16	3.7E-16	1.5E-10	7.8E-11	2.7E-09	1.7E-09	7.2E-11	4.0E-11	2.7E-12	NA	NA									0.06	900	24.0	0.06	0.00	0.00	
raster line	7.93	2.6E+06	1.3E-15	7.2E-16	4.8E-14	1.8E-14	3.1E-16	4.2E-16	1.5E-10	9.7E-11	5.5E-09	2.7E-09	3.5E-11	5.0E-11	2.8E-12	NA	NA									0.06	900	24.0	0.06	0.00	0.00	
raster line	8.65	2.6E+06	3.1E-15	7.1E-16	-1.5E-14	1.7E-14	-6.6E-16	3.7E-16	3.7E-10	1.5E-10	-1.7E-09	2.1E-09	-7.8E-11	5.1E-11	6.7E-12	NA	NA									0.06	900	24.0	0.06	0.00	0.00	
																		2.80E-12	4.573E-12	2.333E-12	NA	NA	NA	NA	NA	NA	0.06	900	24.0	0.06	0.00	0.00	
		EHPV_NG_EXP51																															
	16.47	2.1E+06	4.0E-14	1.0E-15	5.5E-15	2.7E-14	1.0E-15	6.1E-16	5.8E-09	1.9E-09	7.9E-10	3.8E-09	1.5E-10	1.0E-10	7.3E-12	NA	NA									0.80	900	24.0	0.80	0.00	0.00	
	16.95	1.0E+06	2.4E-15	9.6E-16	2.2E-14	2.7E-14	-1.5E-16	6.2E-16	7.3E-10	3.7E-10	6.6E-09	8.3E-09	-4.6E-11	1.8E-10	9.1E-13	NA	NA									0.80	900	24.0	0.80	0.00	0.00	
	18.15	1.1E+06	1.2E-14	9.3E-16	3.2E-14	2.7E-14	1.3E-15	6.4E-16	3.2E-09	1.1E-09	8.9E-09	8.0E-09	3.5E-10	2.1E-10	4.0E-12	NA	NA									0.80	900	24.0	0.80	0.00	0.00	
	15.37	9.1E+05	2.5E-15	9.6E-16	1.2E-14	2.7E-14	4.5E-16	6.0E-16	8.2E-10	4.1E-10	3.9E-09	9.0E-09	1.5E-10	2.0E-10	1.0E-12	NA	NA									0.80	900	24.0	0.80	0.00	0.00	
	8.43	1.1E+06	5.1E-15	9.3E-16	-2.6E-14	2.7E-14	-3.2E-16	6.2E-16	1.4E-09	5.4E-10	-7.3E-09	7.9E-09	-9.1E-11	1.8E-10	1.8E-12	NA	NA									0.80	900	24.0	0.80	0.00	0.00	
	22.32	1.3E+06	2.6E-15	9.4E-16	-1.3E-14	2.6E-14	9.0E-16	6.0E-16	5.8E-10	2.8E-10	-3.0E-09	6.0E-09	2.0E-10	1.5E-10	7.2E-13	NA	NA									0.80	900	24.0	0.80	0.00	0.00	
	13.68	1.7E+06	3.7E-15	9.4E-16	-2.1E-14	2.7E-14	-4.4E-16	6.0E-16	5.4E-10	2.7E-10	-3.6E-09	4.8E-09	-7.6E-11	1.1E-10	8.0E-13	NA	NA									0.80	900	24.0	0.80	0.00	0.00	
	21.08	2.6E+06	5.3E-15	1.1E-15	-7.6E-15	2.6E-14	1.2E-15	6.6E-16	6.0E-10	2.3E-10	-8.6E-10	3.0E-09	1.3E-10	8.7E-11	7.4E-13	NA	NA									0.80	900	24.0	0.80	0.00	0.00	
	12.63	1.6E+06	5.4E-15	9.4E-16	-4.5E-15	2.6E-14	-4.2E-16	6.3E-16	1.0E-09	3.8E-10	-8.5E-10	5.0E-09	-7.9E-11	1.2E-10	1.3E-12	NA	NA									0.80	900	24.0	0.80	0.00	0.00	
	6.26	7.9E+05	4.6E-15	9.3E-16	-6.1E-15	2.6E-14	-6.7E-16	6.0E-16	1.8E-09	6.8E-10	-2.3E-09	1.0E-08	-2.5E-10	2.4E-10	2.2E-12	NA	NA									0.80	900	24.0	0.80	0.00	0.00	
raster line	6.91	1.6E+06	2.1E-14	9.9E-16	2.0E-14	2.7E-14	-1.1E-16	6.0E-16	4.1E-09	1.4E-09	3.8E-09	5.4E-09	-2.1E-11	1.2E-10	5.1E-12	NA	NA									0.80	900	24.0	0.80	0.00	0.00	
raster line	7.26	1.1E+06	5.6E-15	9.3E-16	8.5E-15	2.7E-14	-4.6E-16	6.1E-16	1.6E-09	5.8E-10	2.4E-09	7.5E-09	-1.3E-10	1.7E-10	2.0E-12	NA	NA									0.80	900	24.0	0.80	0.00	0.00	
																		1.53E-12	2.661E-12	8.806E-13	NA	NA	NA	NA	NA	NA	0.80	900	24.0	0.80	0.00	0.00	
		EHPV_NG_EXP63																															
	12.60	1.6E+06	3.3E-15	1.5E-15	-1.1E-15	2.3E-15	6.9E-16	1.4E-16	6.2E-10	3.4E-10	-2.1E-10	4.5E-10	1.3E-10	5.0E-11	9.0E-13	NA	NA									0.68	900	29.5	0.68	0.00	0.00	
	13.66	1.7E+06	2.4E-15	1.4E-15	3.4E-15	2.2E-15	8.6E-16	1.4E-16	4.2E-10	2.9E-10	5.9E-10	4.3E-10	1.5E-10	5.5E-11	6.2E-13	NA	NA									0.68	900	29.5	0.68	0.00	0.00	
	12.23	1.5E+06	-2.5E-16	1.5E-15	-2.7E-15	2.2E-15	5.7E-16	1.4E-16	4.4E-11	2.2E-10	3.6E-10	4.6E-10	1.1E-10	4.5E-11	-7.1E-14	NA	NA									0.68	900	29.5	0.68	0.00	0.00	
	30.52	3.8E+06	3.9E-15	1.5E-15	2.9E-15	2.1E-15	7.8E-16	1.4E-16	3.1E-10	1.5E-10	2.2E-10	1.8E-10	6.1E-11	2.3E-11	4.5E-13	NA	NA									0.68	900	29.5	0.68	0.00	0.00	
	25.14	3.2E+06	4.6E-15	1.4E-15	2.0E-15	2.2E-15	8.6E-16	1.4E-16	4.3E-10	2.0E-10	1.9E-10	2.2E-10	8.1E-11	3.0E-11	6.4E-13	NA	NA									0.68	900	29.5	0.68	0.00	0.00	
	32.34	1.9E+06	1.8E-15	1.4E-15	2.6E-15	2.1E-15	1.6E-16	1.3E-16	2.8E-10	2.4E-10	4.1E-10	3.6E-10	2.4E-11	2.2E-11	4.1E-13	NA	NA									0.68	900	29.5	0.68	0.00	0.00	
																		5.36E-13	6.31E-13	4.196E-13	NA	NA	NA	NA	NA	NA	0.68	900	29.5	0.68	0.00	0.00	
		EHPV_NG_EXP64																															
	34.78	4.4E+06	1.5E-14	1.4E-15	7.7E-17	2.1E-15	4.4E-16	1.4E-16	9.9E-10	3.4E-10	5.3E-12	1.5E-10	3.0E-11	1.4E-11	9.0E-13	NA	NA									1.11	900	37.0	1.11	0.00	0.00	
	21.32	2.7E+06	1.0E-14	1.5E-15	1.8E-15	2.2E-15	4.7E-16	1.4E-16	1.2E-09	4.2E-10	2.0E-10	2.5E-10	5.3E-11	2.4E-11	1.1E-12	NA	NA									1.11	900	37.0	1.11	0.00	0.00	
	29.02	3.6E+06	9.0E-15	1.5E-15	1.1E-15	2.2E-15	3.0E-16	1.4E-16	7.4E-10	2.7E-10	8.7E-11	1.9E-10	2.5E-11	1.4E-11	6.7E-13	NA	NA									1.11	900	37.0	1.11	0.00	0.00	
	15.56	2.0E+06	5.3E-15	1.4E-15	4.3E-15	2.1E-15	2.1E-16	1.4E-16	8.1E-10	3.5E-10	6.6E-10	3.9E-10	3.2E-11	2.3E-11	7.3E-13	NA	NA									1.11	900	37.0	1.11	0.00	0.00	
	28.21	3.5E+06	1.7E-14	1.4E-15	-4.7E-16	2.1E-15	3.0E-16	1.5E-16	1.4E-09	4.8E-10	-4.0E-11	1.8E-10	2.5E-11	1.5E-11	1.3E-12	NA	NA									1.11	900	37.0	1.11	0.00	0.00	
	9.65	1.2E+06	1.3E-14	1.4E-15	7.3E-16	2.1E-15	1.9E-16	1.3E-16	3.3E-09	1.1E-09	1.8E-10	5.3E-10	4.8E-11	3.7E-11	2.9E-12	NA	NA									1.11	900	37.0	1.11	0.00	0.00	
																		9.73E-13	1.215E-12	7.732E-13	NA	NA	NA	NA	NA	NA	1.11	900	37.0	1.11	0.00	0.00	
		EHPV_NG_EXP65																															
	33.03	4.2E+06	6.1E-15	1.4E-15	2.8E-15	2.2E-15	1.5E-14	1.9E-16	4.4E-10	1.8E-10	2.0E-10	1.7E-10	1.1E-09	3.6E-10	1.3E-12	5.8E-13	3.2E-12									1.03	1000	96.0	0.34	0.34	0.34	
	17.35	2.2E+06	2.7E-15	1.4E-15	4.9E-16	2.2E-15	2.6E-14	1.9E-16	3.7E-10	2.3E-10	6.8E-11	3.0E-10	3.6E-09	1.2E-09	1.1E-12	2.0E-13	1.1E-11									1.03	1000	96.0	0.34	0.34	0.34	
	8.39	1.1E+06	4.7E-15	1.6E-15	-2.6E-15	2.2E-15	1.6E-14	1.8E-16	1.3E-09	6.2E-10	-7.3E-10	6.8E-10	4.7E-09	1.5E-09	3.9E-12	-2.1E-12	1.4E-11									1.03	1000	96.0	0.34	0.34	0.34	
	2.74	3.4E+05	-5.0E-16	1.4E-15	2.5E-15	2.1E-15	2.2E-14	1.9E-16	-4.3E-10	1.3E-09	2.2E-09	2.0E-09	1.9E-08	6.4E-09	-1.3E-12	6.4E-12	5.7E-11									1.03	1000	96.0	0.34	0.34	0.34	
	0.62	7.8E+04	9.6E-16	1.4E-15	2.3E-16	2.2E-15	1.9E-14	1.7E-16	3.7E-09	5.6E-09	8.8E-10	8.6E-09	7.3E-08	2.4E-08	1.1E-11	2.6E-12	2.1E-10									1.03	1000	96.0	0.34	0.34	0.34	not used for He_{HC}
	0.29	3.6E+04	1.6E-15	1.4E-15	8.9E-16	2.1E-15	1.8E-14	1.6E-16	1.3E-08	1.2E-08	7.3E-09	1.8E-08	1.5E-07	5.0E-08	3.9E-11	2.1E-11	4.4E-10									1.03	1000	96.0	0.34	0.34	0.34	not used for He_{HC}
	0.20	2.5E+04	-3.9E-16	1.4E-15	-3.4E-16	2.1E-15	1.9E-14	2.0E-16	-4.4E-09	1.7E-08	-4.0E-09	2.5E-08	2.2E-07	7.4E-08	-1.4E-11	-1.2E-11	6.5E-10									1.03	1000	96.0	0.34	0.34	0.34	not used for He_{HC}
	0.04	5.6E+03	-1.6E-15	1.4E-15	1.8E-15	2.1E-15	1.6E-14	1.7E-16	-8.7E-08	8.1E-08	9.7E-08	1.2E-07	8.7E-07	2.9E-07	-2.5E-10	2.8E-10	2.5E-09									1.03	1000	96.0	0.34	0.34	0.34	not used for He_{HC}
	0.02	2.1E+03	1.0E-16	1.4E-15	-2.3E-15	2.2E-15	1.4E-14	1.4E-16	1.4E-08	2.0E-07	-3.2E-07	3.2E-07	2.0E-06	6.6E-07	4.2E-11	-9.3E-10	5.8E-09									1.03	1000	96.0	0.34	0.34	0.34	not used for He_{HC}
	0.02	2.3E+03	-6.5E-16	1.4E-15	2.7E-15	2.1E-15	1.3E-14	1.3E-16	-8.5E-08	1.9E-07	3.5E-07	3.0E-07	1.8E-06	5.8E-07	-2.5E-10	1.0E-09	5.1E-09									1.03	1000	96.0	0.34	0.34	0.34	not used for He_{HC}
																		1.27E-12	3.871E-12	1.074E-12	NA	NA	NA	NA	NA	NA	1.03	1000	96.0	0.34	0.34	0.34	
		EHPV_NG_EXP69																															
	20.67	2.6E+06	7.0E-15	1.5E-15	2.1E-15	2.1E-15	8.2E-14	2.8E-16	8.1E-10	3.2E-10	2.4E-10	2.6E-10	9.5E-09	3.1E-09	1.8E-12	5.4E-13	2.1E-11									1.33	1000	65.5	0.44	0.44	0.44	
	20.67	2.6E+06	1.5E-14	1.4E-15	3.6E-16	2.1E-15	9.8E-14	2.9E-16	1.7E-09	5.9E-10	4.2E-11	2.5E-10	1.1E-08	3.7E-09	3.9E-12	9.4E-14	2.6E-11									1.33	1000	65.5	0.44	0.44	0.44	
	8.04	1.0E+06	3.1E-15	1.4E-15	-4.3E-16	2.2E-15	1.0E-13	3.6E-16	9.1E-10	5.2E-10	-1.3E-10	6.4E-10	3.1E-08	1.0E-08	2.0E-12	-2.8E-13	6.9E-11									1.33	1000	65.5	0.44	0.44	0.44	
	0.41	5.1E+04	1.9E-15	1.5E-15	-1.6E-15	2.1E-15	9.8E-14	2.1E-16	1.1E-08	9.5E-09	-9.6E-09	1.3E-08	5.8E-07	1.9E-07	2.5E-11	-2.2E-11	1.3E-09									1.33	1000	65.5	0.44	0.44	0.44	not used for He_{HC}
	0.27	3.3E+04	1.4E-16	1.4E-15	-7.1E-16	2.1E-15	1.1E-13	1.4E-16	1.2E-09	1.3E-08	-6.4E-09	1.9E-08	1.0E-06	3.3E-07	2.8E-12	-1.4E-11	2.3E-09									1.33	1000	65.5	0.44	0.44	0.44	not used for He_{HC}
	13.94	1.8E+06	6.8E-15	1.4E-15	-2.6E-15	2.1E-15	1.3E-13	5.2E-16	1.2E-09	4.6E-10	-4.4E-10	3.9E-10	2.2E-08	7.3E-09	2.6E-12	-9.9E-13	5.0E-11									1.33	1000	65.5	0.44	0.44	0.44	
	29.52	3.7E+06	1.3E-14	1.5E-15	-1.2E-15	2.2E-15	1.3E-13	2.3E-16	1.1E-09	3.7E-10	-9.6E-11	1.8E-10	1.0E-08	3.4E-09	2.4E-12	-2.2E-13	2.3E-11									1.33	1000	65.5	0.44	0.44	0.44	
	0.18	2.3E+04	-7.3E-16	1.4E-15	6.0E-16	2.1E-15	1.2E-13	4.1E-16	-9.6E-09	1.9E-08	7.9E-09	2.8E-08	1.6E-06	5.2E-07	-2.2E-11	1.8E-11	3.6E-09									1.33	1000	65.5	0.44	0.44	0.44	not used for He_{HC}
	0.04	4.5E+03	3.6E-17	1.4E-15	9.3E-16	2.1E-15	8.8E-14	1.3E-16	2.4E-09	9.4E-08	6.2E-08	1.4E-07	5.9E-06	1.9E-06	5.5E-12	1.4E-10	1.3E-08									1.33	1000	65.5	0.44	0.44	0.44	not used for He_{HC}
																		2.38E-12	2.64E-12	2.044E-12	NA	NA	NA	NA	NA	NA	1.33	1000	65.5	0.44	0.44	0.44	
corundum																																	
		EHPV_NG_EXP25																															
line raster	1.13	2.2E+05	3.5E-13	1.7E-14	8.9E-16	1.7E-15	3.9E-15	2.0E-16	4.0E-07	1.3E-07	1.0E-09	2.0E-09	4.5E-09	1.5E-09	2.5E-10	NA	NA									1.58	973	12.0	1.58	0.00	0.00	
line raster	1.21	2.4E+05	6.2E-14	1.6E-14	-1.3E-15	1.9E-15	2.0E-15	1.8E-16	6.5E-08	2.7E-08	-1.4E-09	2.0E-09	2.1E-09	7.2E-10	4.1E-11	NA	NA									1.58	973	12.0	1.58	0.00	0.00	
line raster	1.16	2.3E+05	5.5E-14	1.6E-14	-9.0E-16	1.8E-15	6.1E-16	1.8E-16	6.0E-08	2.6E-08	-9.6E-10	2.0E-09	6.6E-10	2.9E-10	3.8E-11	NA	NA									1.58	973	12.0	1.58	0.00	0.00	
line raster	1.08	2.3E+05	4.9E-14	1.6E-14	3.4E-15	1.5E-15	2.3E-16	1.9E-16	5.4E-

spot	4.86	1.5E+05	3.8E-15	1.0E-15	2.1E-14	2.2E-14	-4.2E-16	6.0E-16	6.2E-09	2.6E-09	3.4E-08	3.8E-08	-6.9E-10	1.0E-09	3.7E-12	NA	NA											1.68	715	92.0	1.68	0.00	0.00	
spot	3.26	1.9E+05	4.6E-15	1.0E-15	-1.7E-14	2.2E-14	-3.3E-16	5.3E-16	5.9E-09	2.4E-09	-2.3E-08	2.9E-08	-4.3E-10	7.0E-10	3.5E-12	NA	NA											1.68	715	92.0	1.68	0.00	0.00	
spot	6.92	4.1E+05	1.4E-14	1.1E-15	1.3E-15	2.2E-14	-2.3E-17	6.2E-16	8.7E-09	3.0E-09	7.6E-10	1.3E-08	-1.4E-11	3.8E-10	5.2E-12	NA	NA											1.68	715	92.0	1.68	0.00	0.00	
spot	2.27	1.4E+05	5.0E-15	1.0E-15	-1.2E-14	2.2E-14	1.8E-16	6.1E-16	9.2E-09	3.6E-09	-2.2E-08	4.1E-08	3.4E-10	1.1E-09	5.5E-12	NA	NA											1.68	715	92.0	1.68	0.00	0.00	
spot	1.54	1.9E+05	1.5E-14	1.0E-15	-3.1E-15	2.3E-14	5.0E-16	6.1E-16	1.9E-08	6.5E-09	-4.0E-09	2.9E-08	6.5E-10	8.2E-10	1.1E-11	NA	NA											1.68	715	92.0	1.68	0.00	0.00	
																		5.47E-12	7.986E-12	4.067E-12	NA	NA	NA	NA	NA	NA		1.68	715	92.0	1.68	0.00	0.00	
	EHPV_NG_EXP61																																	
spot	0.53	3.2E+04	1.8E-14	8.0E-16	-1.5E-14	1.7E-14	1.2E-15	3.6E-16	1.5E-07	4.8E-08	-1.2E-07	1.4E-07	9.2E-09	4.2E-09	9.9E-11	NA	NA											1.47	900	24.0	1.47	0.00	0.00	
spot	1.11	6.6E+04	6.8E-13	2.6E-15	3.0E-14	1.7E-14	2.8E-15	4.2E-16	2.6E-06	8.6E-07	1.1E-07	7.6E-08	1.0E-08	3.8E-09	1.8E-09	NA	NA											1.47	900	24.0	1.47	0.00	0.00	
spot	0.61	3.6E+04	3.3E-15	7.0E-16	-1.9E-14	1.7E-14	5.3E-16	3.9E-16	2.3E-08	8.9E-09	-1.3E-07	1.2E-07	3.7E-09	2.9E-09	1.5E-11	NA	NA											1.47	900	24.0	1.47	0.00	0.00	
spot	1.37	8.1E+04	7.6E-15	7.5E-16	2.5E-14	1.8E-14	1.0E-16	3.7E-16	2.3E-08	8.1E-09	7.8E-08	6.0E-08	3.1E-10	1.1E-09	1.6E-11	NA	NA											1.47	900	24.0	1.47	0.00	0.00	
spot	2.65	1.6E+05	4.1E-15	7.2E-16	-2.0E-14	1.8E-14	-3.9E-16	3.7E-16	6.6E-09	2.5E-09	-3.1E-08	3.1E-08	-6.1E-10	6.2E-10	4.5E-12	NA	NA											1.47	900	24.0	1.47	0.00	0.00	
spot	1.45	8.6E+04	1.2E-14	7.6E-16	9.8E-15	1.9E-14	-1.7E-16	3.6E-16	3.5E-08	1.2E-08	2.8E-08	5.6E-08	-5.0E-10	1.1E-09	2.3E-11	NA	NA											1.47	900	24.0	1.47	0.00	0.00	
spot	0.70	4.1E+04	4.9E-15	6.9E-16	7.3E-14	1.8E-14	1.9E-15	4.8E-16	3.0E-08	1.1E-08	4.4E-07	1.8E-07	1.2E-08	4.8E-09	2.0E-11	NA	NA											1.47	900	24.0	1.47	0.00	0.00	
spot	0.22	1.3E+04	4.9E-15	7.2E-16	8.5E-15	1.7E-14	1.3E-16	3.9E-16	9.2E-08	3.3E-08	1.6E-07	3.3E-07	2.5E-09	7.5E-09	6.3E-11	NA	NA											1.47	900	24.0	1.47	0.00	0.00	
																		2.02E-11	4.32E-11	1.57E-11	NA	NA	NA	NA	NA	NA		1.47	900	24.0	1.47	0.00	0.00	
	EHPV_NG_EXP64																																	
	2.99	3.8E+05	3.3E-16	1.5E-15	1.6E-15	2.3E-15	3.0E-16	1.3E-16	2.2E-10	1.0E-09	1.1E-09	1.6E-09	2.0E-10	1.1E-10	2.0E-13	NA	NA											1.11	900	24.0	1.11	0.00	0.00	
	11.45	1.4E+06	2.8E-15	1.4E-15	3.1E-15	2.2E-15	1.6E-16	1.4E-16	4.8E-10	2.9E-10	5.4E-10	4.2E-10	2.8E-11	2.5E-11	4.3E-13	NA	NA											1.11	900	24.0	1.11	0.00	0.00	
	14.42	1.8E+06	1.4E-15	1.4E-15	5.1E-15	2.1E-15	6.4E-16	1.4E-16	1.9E-10	2.0E-10	7.1E-10	3.7E-10	8.9E-11	3.5E-11	1.7E-13	NA	NA											1.11	900	24.0	1.11	0.00	0.00	
	10.33	1.3E+06	-6.8E-16	1.4E-15	3.2E-15	2.2E-15	4.3E-16	1.4E-16	-1.3E-10	2.8E-10	6.2E-10	4.7E-10	8.2E-11	3.8E-11	-1.2E-13	NA	NA											1.11	900	24.0	1.11	0.00	0.00	
	13.94	1.8E+06	2.1E-15	1.5E-15	5.5E-15	2.1E-15	6.1E-16	1.4E-16	3.1E-10	2.3E-10	7.9E-10	4.0E-10	8.7E-11	3.5E-11	2.8E-13	NA	NA											1.11	900	24.0	1.11	0.00	0.00	
	14.57	1.8E+06	2.7E-15	1.5E-15	6.1E-15	2.2E-15	7.4E-16	1.4E-16	3.7E-10	2.4E-10	8.3E-10	4.0E-10	1.0E-10	3.8E-11	3.3E-13	NA	NA											1.11	900	24.0	1.11	0.00	0.00	
																		2.37E-13	3.20E-13	1.76E-13	NA	NA	NA	NA	NA	NA		1.11	900	24.0	1.11	0.00	0.00	
	EHPV_NG_EXP69																																	
	4.88	6.1E+05	2.5E-15	1.5E-15	1.1E-15	2.2E-15	3.1E-16	1.4E-16	1.0E-09	6.8E-10	4.6E-10	9.1E-10	1.2E-10	6.9E-11	2.3E-12	1.0E-12	2.8E-13											1.33	1000	65.5	0.44	0.44	0.44	
	9.48	1.2E+06	-6.2E-16	1.4E-15	3.6E-15	2.2E-15	2.5E-16	1.4E-16	-1.3E-10	3.0E-10	7.6E-10	5.2E-10	5.2E-11	3.4E-11	-2.9E-13	6.9E-13	1.2E-13											1.33	1000	65.5	0.44	0.44	0.44	
	10.36	1.3E+06	-1.4E-15	1.5E-15	3.3E-15	2.2E-15	6.2E-16	1.4E-16	-2.6E-10	3.0E-10	6.3E-10	4.7E-10	1.2E-10	4.8E-11	-5.9E-13	6.8E-13	2.7E-13											1.33	1000	65.5	0.44	0.44	0.44	
	0.07	8.5E+03	-9.7E-16	1.5E-15	3.3E-15	2.1E-15	6.8E-17	1.3E-16	-2.8E-08	4.4E-08	9.6E-08	7.0E-08	2.0E-09	4.0E-09	-6.4E-11	1.0E-10	4.5E-12											1.33	1000	65.5	0.44	0.44	0.44	not used for He_{4C}
	0.02	2.4E+03	-1.5E-15	1.4E-15	4.7E-15	2.1E-15	3.8E-17	1.4E-16	-1.5E-07	1.5E-07	4.8E-07	2.7E-07	3.9E-09	1.4E-08	-3.5E-10	3.5E-10	8.9E-12											1.33	1000	65.5	0.44	0.44	0.44	not used for He_{4C}
																		-2.94E-13	1.01E-12	-4.42E-13	NA	NA	NA	NA	NA	NA		1.33	1000	65.5	0.44	0.44	0.44	Ar, Ne ?
labradorite																																		
	CS_NG_EXP12																																	
	5.62	7.1E+05	1.3E-14	2.9E-15	1.3E-15	3.9E-15	6.2E-16	3.8E-16	6.8E-09	2.0E-09	6.5E-10	2.0E-09	3.2E-10	2.1E-10	5.2E-12	NA	NA											1.30	600	41.0	1.30	0.00	0.00	
	16.51	2.1E+06	8.8E-14	3.2E-15	6.4E-15	3.5E-15	3.2E-15	3.9E-16	1.5E-08	3.1E-09	1.1E-09	6.5E-10	5.6E-10	1.3E-10	1.2E-11	NA	NA											1.30	600	41.0	1.30	0.00	0.00	
	22.47	2.8E+06	1.6E-13	2.9E-15	5.8E-15	4.0E-15	3.1E-15	4.0E-16	2.0E-08	4.1E-09	7.5E-10	5.4E-10	4.0E-10	9.6E-11	1.6E-11	NA	NA											1.30	600	41.0	1.30	0.00	0.00	
	7.82	9.8E+05	3.2E-14	2.8E-15	8.0E-15	3.7E-15	1.3E-15	3.8E-16	1.2E-08	2.6E-09	2.9E-09	1.5E-09	4.7E-10	1.7E-10	9.2E-12	NA	NA											1.30	600	41.0	1.30	0.00	0.00	
	3.09	3.9E+05	1.2E-14	2.9E-15	6.8E-15	3.7E-15	3.8E-16	4.1E-16	1.1E-08	3.5E-09	6.4E-09	3.7E-09	3.6E-10	3.9E-10	8.5E-12	NA	NA											1.30	600	41.0	1.30	0.00	0.00	
	22.82	2.9E+06	1.5E-13	2.8E-15	6.0E-15	3.8E-15	4.2E-15	3.9E-16	2.0E-08	3.9E-09	7.6E-10	5.1E-10	5.3E-10	1.2E-10	1.5E-11	NA	NA											1.30	600	41.0	1.30	0.00	0.00	
	16.82	2.1E+06	1.1E-13	3.3E-15	1.9E-14	3.7E-15	2.5E-15	3.8E-16	2.0E-08	4.0E-09	3.2E-09	9.0E-10	4.3E-10	1.1E-10	1.5E-11	NA	NA											1.30	600	41.0	1.30	0.00	0.00	
	8.34	1.0E+06	4.2E-14	3.2E-15	1.2E-14	3.9E-15	3.3E-15	3.8E-16	1.4E-08	3.1E-09	4.3E-09	1.6E-09	1.1E-09	2.6E-10	1.1E-11	NA	NA											1.30	600	41.0	1.30	0.00	0.00	
																		1.15E-11	1.508E-11	9.048E-12	NA	NA	NA	NA	NA	NA		1.30	600	41.0	1.30	0.00	0.00	
	EHPV_NG_EXP45																																	
	17.57	2.2E+06	2.0E-13	3.9E-15	-6.0E-16	9.5E-16	3.9E-15	6.4E-16	3.4E-08	1.1E-08	-9.9E-11	1.6E-10	6.4E-10	2.4E-10	2.0E-11	NA	NA											1.69	900	24.0	1.69	0.00	0.00	
	13.16	7.8E+05	8.3E-14	3.3E-15	3.0E-15	8.0E-16	1.6E-15	6.3E-16	3.9E-08	1.3E-08	1.4E-09	5.9E-10	7.3E-10	3.8E-10	2.3E-11	NA	NA											1.69	900	24.0	1.69	0.00	0.00	
	13.72	8.1E+05	6.8E-14	3.0E-15	3.6E-15	7.4E-16	1.4E-15	6.3E-16	3.0E-08	1.0E-08	1.6E-09	6.3E-10	6.3E-10	3.5E-10	1.8E-11	NA	NA											1.69	900	24.0	1.69	0.00	0.00	
	7.35	4.4E+05	2.1E-14	2.8E-15	1.0E-15	7.7E-16	6.1E-16	6.3E-16	1.7E-08	6.2E-09	8.6E-10	7.0E-10	5.1E-10	5.5E-10	1.0E-11	NA	NA											1.69	900	24.0	1.69	0.00	0.00	
	7.30	4.3E+05	6.6E-15	2.6E-15	-2.5E-16	8.0E-16	6.1E-16	6.2E-16	5.5E-09	2.9E-09	-2.1E-10	6.7E-10	5.1E-10	5.5E-10	3.3E-12	NA	NA											1.69	900	24.0	1.69	0.00	0.00	
	19.63	1.2E+06	1.3E-13	2.9E-15	2.5E-15	7.5E-16	1.3E-15	6.3E-16	3.9E-08	1.3E-08	7.7E-10	3.5E-10	3.9E-10	2.3E-10	2.3E-11	NA	NA											1.69	900	24.0	1.69	0.00	0.00	
	24.97	1.5E+06	6.1E-14	2.7E-15	3.4E-16	9.4E-16	1.7E-15	6.2E-16	1.5E-08	5.0E-09	8.3E-11	2.3E-10	4.1E-10	2.0E-10	8.9E-12	NA	NA											1.69	900	24.0	1.69	0.00	0.00	
	5.73	7.2E+05	3.3E-14	2.8E-15	2.9E-15	7.6E-16	1.1E-15	6.2E-16	1.7E-08	5.7E-09	1.5E-09	6.2E-10	5.5E-10	3.6E-10	9.9E-12	NA	NA											1.69	900	24.0	1.69	0.00	0.00	
	13.67	8.1E+05	2.1E-14	2.8E-15	2.9E-15	7.9E-16	1.3E-15	6.2E-16	9.6E-09	3.4E-09	1.3E-09	5.5E-10	5.9E-10	3.4E-10	5.7E-12	NA	NA											1.69	900	24.0	1.69	0.00	0.00	
																		1.03E-11	1.988E-11	8.898E-12	NA	NA	NA	NA	NA	NA		1.69	900	24.0	1.69	0.00	0.00	
	EHPV_NG_EXP46																																	
	13.08	7.8E+05	7.0E-16	6.6E-15	-4.0E-15	3.7E-14	2.9E-15	9.6E-15	3.3E-10	3.1E-09	-1.9E-09	1.7E-08	1.3E-09	4.5E-09	3.2E-13	NA	NA											1.02	900	24.0	1.02	0.00	0.00	
	23.16	1.4E+06	6.0E-14	1.3E-14	-2.2E-14	3.7E-14	2.9E-14	1.1E-14	1.6E-08	6.2E-09	-5.7E-09	9.9E-09	7.7E-09	3.8E-09	1.6E-11	NA	NA											1.02	900	24.0	1.02	0.00	0.00	
	21.81	1.3E+06	1.2E-14	6.8E-15	2.3E-14	3.7E-14	1.1E-16	9.7E-15	3.2E-09	2.2E-09	6.5E-09	1.1E-08	3.2E-11	2.7E-09	3.2E-12	NA	NA											1.02	900	24.0	1.02	0.00	0.00	
	32.31	1.0E+06	3.0E-14	6.6E-15	-3.0E-15	3.7E-14	8.0E-15	9.6E-15	1.1E-08	4.1E-09	-1.1E-09	1.3E-08	2.9E-09	3.6E-09	1.1E-11	NA	NA											1.02	900	24.0	1.02	0.00	0.00	
	31.22	9.8E+05	2.3E-14	6.7E-15	3.8E-14	3.7E-14	-1.2E-16	9.8E-15	8.6E-09	3.8E-09	1.4E-08	1.5E-08	-4.5E-11	3.6E-09	8.4E-12	NA	NA											1.02	900	24.0	1.02	0.00	0.00	
	28.39	3.6E+06	2.0E-14	6.5E-15	-2.6E-14	3.6E-14	-9.3E-16	9.6E-15	2.0E-09	9.5E-10	-2.7E-09	3.8E-09	-9.5E-11	9.8E-10	2.0E-12	NA	NA											1.02	900	24.0	1.02	0.00	0.00	
	57.37	1.8E+06	2.5E-14	6.9E-15	3.9E-14	3.7E-14	1.5E-15	1.0E-14	5.0E-09	2.2E-09	7.8E-09	7.8E-09	3.0E-10	2.0E-09	4.9E-12	NA	NA											1.02	900	24.0	1.02	0.00	0.00	
																		4.89E-12	9.527E-12	2.585E-12	NA	NA	NA	NA	NA	NA		1.02	900	24.0	1.02	0.00	0.00	
	EHPV_NG_EXP47																																	
	13.50	8.0E+05	4.3E-15	2.6E-15	1.1E-15	8.3E-16	6.5E-16	6.2E-16	1.9E-09	1.4E-09	5.1E-10	4.1E-10	3.0E-10	3.0E-10	3.8E-12	NA	NA											0.51	900	24.0	0.51	0.00	0.00	
	10.73	1.3E+06	8.2E-15	2.6E-15	1.4E-15	7.7E-16	8.1E-16	6.2E-16	2.2E-09	1.0E-09	3.7E-10	2.4E-10	2.2E-10	1.8E-10	4.3E-12	NA	NA											0.51	900	24.0	0.51	0.00	0.00	
	19.09	2.4E+06	2.1E-14	2.6E-15	2.6E-15	8.7E-16	1.7E-15	6.3E-16	3.2E-09	1.1E-09	4.0E-10	1.9E-10	2.6E-10	1.3E-10	6.2E-12	NA	NA											0.51	900	24.0	0.51	0.00	0.00	
	14.54	1.8E+06	1.7E-14	2.7E-15	4.1E-15	8.6E-16	1.0E-15	6.2E-16	3.4E-09	1.3E-09	8.2E-10	3.2E-10	2.1E-10	1.4E-10	6.7E-12	NA	NA											0.51	900	24.0	0.51	0.00	0.00	
	30.90	3.9E+06	8.5E-14	2.7E-15	3.4E-15	8.1E-16	2.7E-15	6.2E-16	7.9E-09	2.6E-09	3.2E-10	1.3E-10	2.5E-10	1.0E-10	1.6E-11	NA	NA											0.51	900	24.0	0.51	0.00	0.00	
	10.92	1.4E+06	5.3E-15	2.8E-15	7.3E-16	8.2E-16	9.1E-16	6.3E-16	1.4E-09	8.7E-10	1.9E-10	2.3E-10	2.4E-10	1.8E-10	2.8E-12	NA	NA											0.51	900	24.0	0.51	0.00	0.00	
	17.05	2.1E+06	2.5E-14	2.8E-15	2.7E-15	9.6E-16	1.8E-15	6.3E-16	4.3E-09	1.5E-09	4.6E-10	2.2E-10	3.0E-10	1.5E-10	8.4E-12	NA	NA											0.51	900	24.0	0.51	0.00	0.00	
																		6.25E-12	7.532E-12	4.083E-12	NA	NA	NA	NA	NA	NA		0.51	900	24.0	0.51	0.00	0.00	
	EHPV_NG_EXP48																																	
	32.78	1.0E+06	5.9E-14	6.5E-15	4.6E-14	3.6E-14	7.3E-15	9.7E-15	2.1E-08	7.2E-09	1.6E-08	1.4E-08	2.6E-09	3.5E-09	8.6E-11	NA	NA											0.24	900	24.0	0.24	0.00	0.00	high He?
	31.11	1.8E+06	7.7E-14	6.6E-15	-5.3E-15	3.6E-14	1.1E-14	9.9E-15	1.5E-08	5.2E-09	-1.0E-09	7.1E-09	2.2E-09	2.1E-09	6.3E-11	NA	NA											0.24	900	24.0	0.24	0.00	0.00	high He?
	29.46	1.7E+06	8.7E-14	6.6E-15	2.2E-14	3.6E-14	1.0E-14	9.6E-15	1.8E-08	6.1E-09	4.5E-09	7.6E-09	2.2E-09	2.1E-09	7.5E-11	NA	NA											0.24	900	24.0	0.24	0.00	0.00	high He?
	26.47	1.6E+06	1.8E-13	8.5E-15	5.5E-14	3.6E-14	1.7E-14	1.0E-14	4.2E-08	1.4E-08	1.3E-08	9.4E-09	3.9E-09	2.6E-09	1.7E-10	NA	NA											0.24	900	24.0	0.24	0.00	0.00	high He?
	27.13	1.6E+06	1.2E-13	7.6E-15	-4.8E-14	3.9E-14	1.5E-14	9.6E-15	2.7E-08	9.2E-09	-1.1E-08	9.4E-09	3.4E-09	2.4E-09	1.1E-10	NA	NA											0.24	900	24.0	0.24	0.00	0.00	high He?
																		8.61E-11	1.146E-10	7.492E-11	NA	NA	NA	NA	NA	NA		0.24	900	24.0	0.24	0.00	0.00	
	EHPV_NG_EXP49																																	
	15.38	1.9E+06	2.1E-14	2.6E-15	7.0E-15	9.9E-16	1.5E-15	6.2E-16	3.9E-09	1.4E-09	1.3E-09	4.7E-10	2.8E-10	1.5E-10	3.6E-11	NA	NA											0.11	900	24.0	0.11	0.00	0.00	
	10.03	1.3E+06	2.6E-15	2.6E-15	1.4E-15	8.4E-16	1.5E-15	6.2E-16	7.6E-10	8.0E-10	4.1E-10	2.8E-10	4.3E-10	2.3E-10	6.9E-12	NA	NA											0.11	900	24.0	0.11	0.00	0.00	
	11.07	1.4E+06	2.1E-15	2.7E-15	3.1E-15	9.8E-16	1.4E-15	6.2E-16	5.6E-10	7.3E-10	8.1E-10	3.7E-10	3.6E-10	2.0E-10	5.1E-12	NA	NA											0.11	900	24.0	0.11	0.00	0.00	
	11.94	1.5E+06	4.7E-15	2.7E-15	4.2E-15	9.4E-16	1.7E-15	6.2E-16	1.1E-09	7.4E-10	1.0E-09	4.0E-10	4.1E-10	2.0E-10	1.0E-11	NA	NA											0.11	900	24.0	0.11	0.00	0.00	
	10.41	1.3E+06	2.1E-15	2.6E-15	5.0E-15	7.7E-16	1.3E-15	6.2E-16	5.7E-10	7.6E-10	1.4E-09	5.1E-10	3.7E-10	2.1E-10	5.2E-12	NA	NA											0.11	900	24.0	0.11	0.00	0.00	
																		6.88E-12	1.027E-11	5.218E-12	NA	NA	NA	NA	NA	NA		0.11	900	24.0	0.11	0.00	0.00	
	EHPV_NG_EXP51																																	
	18.99	2.4E+06	1.2E-13	2.8E-15	5.3E-15	7.8E-16	3.2E-15	6.3E-16	1.8E-08	5.9E-09	8.0E-10	2.9E-10	4.8E-10	1.9E-10	2.2E-11	NA	NA											0.80	900	24.0	0.80	0.00	0.00	
	18.51	2.3E+06	9.8E-14	2.7E-15	4.7E-15	7.9E-16	3.3E-15	6.3E-16	1.5E-08	5.1E-09	7.4E-10	2.7E-10	5.1E-10	1.9E-10	1.9E-11	NA	NA											0.80	900	24.0	0.80	0.00	0.00	
	18.51	2.3E+06	6.1E-14	2.7E-15	3.0E-15	9.2E-16	2.3E-15	6.2E-16	9.6E-09	3.2E-09	4.7E-10	2.1E-10	3.6E-10	1.5E-10	1.2E-11	NA	NA											0.80	900	24.0	0.80	0.00	0.00	
	9.37	1.2E+06	8.2E-14	2.8E-15	6.5E-15	8.3E-16	2.1E-15	6.2E-16	2.5E-08	8.4E-09	2.0E-09	7.1E-10	6.5E-10	2.9E-10	3.2E-11	NA	NA											0.80	900	24.0	0.80	0.00	0.00	
	4.99	6.3E+05	1.3E-14	2.6E-15	3.0E-15	7.7E-16	1.4E-15	6.2E-16	7.7E-09	3.0E-09	1.8E-09	7.3E-10	8.3E-10	4.5E-10	9.7E-12	NA	NA											0.80	900	24.0	0.80	0.00	0.00	
	5.43	6.8E+05	2.6E-14	2.7E-15	5.6E-15	8.3E-16	1.5E-15	6.2E-16	1.4E-08	4.8E-09	3.0E-09	1.1E-09	8.0E-10	4.2E-10	1.7E-11	NA	NA											0.80	900	24.0	0.80	0.00	0.00	
	5.17	6.5E+05	1.3E-14	2.6E-15	8.2E-16	7.9E-16	1.4E-15	6.2E-16	7.2E-09	2.8E-09	4.6E-10	4.7E-10	7.8E-10	4.3E-10	9.0E-12	NA	NA											0.80	900	24.0	0.80	0.00	0.00	
																		1.72E-11	2.076E-11	1.083E-11	NA	NA	NA	NA	NA	NA		0.80	900	24.0	0.80	0.00	0.00	
	EHPV_NG_EXP65																																	
	5.71	3.4E+05	4.4E-15	2.7E-15	5.7E-15	8.1E-16	2.0E-15	6.2E-16	4.7E-09	3.3E-09	6.1E-09	2.2E-09	2.1E-09	9.6E-10	1.4E-11	1.8E-11	6.1E-12											1.03	1000	96.0	0.34	0.34	0.34	
	11.71	7.0E+05	1.4E-14	2.9E-15	7.4E-15	8.7E-16	2.2E-15	6.2E-16	7.4E-09	2.9E-09	3.8E-09	1.3E-09	1.1E-09	5.0E-10	2.1E-11	1.1E-11	3.3E-12											1.03	1000	96.0	0.34	0.34	0.34	
	21.27	1.3E+06	1.7E-14	2.8E-15	1.2E-14	1.0E-15	4.6E-15	6.2E-16	4.9E-09	1.8E-09	3.3E-09	1.1E-09	1.3E-09	4.7E-10	1.4E-11	9.7E-12	3.8E-12											1.03	1000	96.0	0.34	0.34	0.34	
	5.53	7.0E+05	7.0E-15	2.7E-15	8.8E-15	7.4E-16

	14.48	1.8E+06	2.9E-14	2.6E-15	1.3E-14	7.4E-16	5.1E-15	6.4E-16	5.8E-09	2.0E-09	2.6E-09	8.6E-10	1.0E-09	3.6E-10	1.7E-11	7.5E-12	3.0E-12										1.03	1000	96.0	0.34	0.34	0.34	
	3.49	4.4E+05	1.1E-14	2.6E-15	4.0E-15	1.0E-15	3.7E-15	6.3E-16	9.3E-09	3.8E-09	3.3E-09	1.4E-09	3.1E-09	1.1E-09	2.7E-11	9.6E-12	8.9E-12										1.03	1000	96.0	0.34	0.34	0.34	
	1.87	2.3E+05	8.8E-15	2.7E-15	2.3E-15	9.4E-16	2.3E-15	6.2E-16	1.4E-08	6.2E-09	3.6E-09	1.9E-09	3.6E-09	1.5E-09	4.0E-11	1.0E-11	1.0E-11										1.03	1000	96.0	0.34	0.34	0.34	
	0.32	4.1E+04	1.3E-14	2.7E-15	3.5E-15	9.9E-16	3.7E-15	6.2E-16	1.2E-07	4.6E-08	3.2E-08	1.4E-08	3.3E-08	1.2E-08	3.4E-10	9.2E-11	9.6E-11										1.03	1000	96.0	0.34	0.34	0.34	not used for He_{HC}
	0.15	1.9E+04	3.0E-15	2.7E-15	1.5E-15	8.7E-16	2.6E-16	6.2E-16	5.7E-08	5.5E-08	2.9E-08	1.9E-08	4.9E-09	1.2E-08	1.7E-10	8.4E-11	1.4E-11										1.03	1000	96.0	0.34	0.34	0.34	not used for He_{HC}
	0.10	1.3E+04	7.8E-16	2.6E-15	3.0E-16	1.0E-15	2.3E-16	6.2E-16	2.2E-08	7.5E-08	8.4E-09	2.9E-08	6.5E-09	1.8E-08	6.5E-11	2.4E-11	1.9E-11										1.03	1000	96.0	0.34	0.34	0.34	not used for He_{HC}
		EHPV_NG_EXP66																1.68E-11	2.142E-11	1.368E-11	*8.63E-12*	*1.31E-11*	*5.76E-12*	*4.62E-12*	*6.32E-12*	*3.137E-12*	1.03	1000	96.0	0.34	0.34	0.34	
	3.89	4.9E+05	1.2E-13	3.0E-15	9.9E-14	1.6E-15	8.2E-14	6.3E-16	8.9E-08	2.9E-08	7.3E-08	2.4E-08	6.1E-08	2.0E-08	2.3E-10	1.9E-10	1.5E-10										1.18	1050	168.0	0.39	0.39	0.39	He profile?
	4.71	2.8E+05	5.4E-14	2.8E-15	4.1E-14	1.2E-15	3.8E-14	6.6E-16	7.0E-08	2.3E-08	5.4E-08	1.8E-08	5.0E-08	1.6E-08	1.8E-10	1.4E-10	1.3E-10										1.18	1050	168.0	0.39	0.39	0.39	He profile?
	1.06	6.3E+04	4.8E-14	2.7E-15	3.3E-14	8.0E-16	3.1E-14	6.3E-16	2.8E-07	9.3E-08	1.9E-07	6.3E-08	1.8E-07	6.0E-08	7.0E-10	4.8E-10	4.6E-10										1.18	1050	168.0	0.39	0.39	0.39	He profile?
	0.52	3.1E+04	1.7E-14	3.0E-15	1.7E-14	1.5E-15	1.4E-14	6.4E-16	2.0E-07	7.4E-08	2.0E-07	6.8E-08	1.6E-07	5.3E-08	5.0E-10	5.1E-10	4.1E-10										1.18	1050	168.0	0.39	0.39	0.39	He profile?
	13.64	8.1E+05	4.3E-14	2.7E-15	3.4E-14	1.1E-15	3.4E-14	6.2E-16	1.9E-08	6.5E-09	1.5E-08	5.1E-09	1.5E-08	5.1E-09	4.9E-11	3.9E-11	3.9E-11										1.18	1050	168.0	0.39	0.39	0.39	He profile?
	11.18	6.6E+05	5.1E-14	2.8E-15	4.0E-14	1.3E-15	3.3E-14	6.8E-16	2.8E-08	9.3E-09	2.2E-08	7.2E-09	1.8E-08	6.0E-09	7.0E-11	5.5E-11	4.6E-11										1.18	1050	168.0	0.39	0.39	0.39	He profile?
	6.49	3.9E+05	4.1E-14	2.7E-15	3.3E-14	7.5E-16	3.3E-14	6.4E-16	3.8E-08	1.3E-08	3.1E-08	1.0E-08	3.1E-08	1.0E-08	9.7E-11	8.0E-11	7.8E-11										1.18	1050	168.0	0.39	0.39	0.39	He profile?
	4.84	2.9E+05	4.7E-14	2.7E-15	3.7E-14	9.9E-16	3.3E-14	6.2E-16	5.9E-08	2.0E-08	4.7E-08	1.6E-08	4.1E-08	1.4E-08	1.5E-10	1.2E-10	1.1E-10										1.18	1050	168.0	0.39	0.39	0.39	He profile?
	2.12	1.3E+05	3.9E-14	2.7E-15	3.1E-14	1.8E-15	3.1E-14	6.5E-16	1.1E-07	3.8E-08	8.9E-08	3.0E-08	8.9E-08	2.9E-08	2.8E-10	2.3E-10	2.3E-10										1.18	1050	168.0	0.39	0.39	0.39	He profile?
	0.61	3.6E+04	3.9E-14	2.6E-15	3.2E-14	1.1E-15	2.9E-14	6.3E-16	3.9E-07	1.3E-07	3.2E-07	1.1E-07	3.0E-07	9.8E-08	1.0E-09	8.1E-10	7.5E-10										1.18	1050	168.0	0.39	0.39	0.39	He profile?
k-feldspar																		NA	NA	NA	NA	NA	NA	NA	NA	NA	1.18	1050	168.0	0.39	0.39	0.39	high He?
		CS_NG_EXP12																															
	6.01	3.6E+05	1.9E-13	8.0E-15	-1.4E-14	5.2E-15	-4.0E-15	2.8E-15	2.1E-07	6.8E-08	-1.5E-08	7.6E-09	-4.3E-09	3.3E-09	1.6E-10	NA	NA										1.30	600	41.0	1.30	0.00	0.00	
	16.96	1.0E+06	6.6E-13	7.5E-15	-1.8E-14	5.2E-15	1.4E-14	2.8E-15	2.5E-07	8.3E-08	-6.7E-09	3.0E-09	5.5E-09	2.1E-09	1.9E-10	NA	NA										1.30	600	41.0	1.30	0.00	0.00	
	17.27	5.4E+05	1.6E-14	3.1E-14	-1.0E-14	5.3E-15	3.0E-15	2.8E-15	1.2E-08	2.2E-08	-7.1E-09	4.4E-09	2.1E-09	2.1E-09	8.9E-12	NA	NA										1.30	600	41.0	1.30	0.00	0.00	
																		1.76E-10	1.85E-10	1.67E-10	NA	NA	NA	NA	NA	NA	1.30	600	41.0	1.30	0.00	0.00	
		EHPV_NG_EXP21																															
	1.69	3.4E+05	2.4E-13	1.8E-14	9.3E-16	5.6E-16	4.9E-16	1.6E-16	2.7E-07	9.0E-08	1.0E-09	7.2E-10	5.5E-10	2.6E-10	1.7E-10	NA	NA										1.58	1000	10.0	1.58	0.00	0.00	
	3.18	6.4E+05	4.7E-13	1.8E-14	3.0E-15	6.9E-16	1.1E-15	1.6E-16	2.8E-07	9.4E-08	1.8E-09	7.3E-10	6.7E-10	2.4E-10	1.8E-10	NA	NA										1.58	1000	10.0	1.58	0.00	0.00	
	3.94	7.8E+05	6.5E-13	1.8E-14	1.2E-15	5.6E-16	1.7E-15	1.6E-16	3.2E-07	1.1E-07	5.7E-10	3.3E-10	8.5E-10	2.9E-10	2.0E-10	NA	NA										1.58	1000	10.0	1.58	0.00	0.00	
	2.99	5.9E+05	8.5E-13	1.8E-14	2.6E-16	5.3E-16	3.5E-15	1.7E-16	5.5E-07	1.8E-07	1.7E-10	3.5E-10	2.3E-09	7.6E-10	3.5E-10	NA	NA										1.58	1000	10.0	1.58	0.00	0.00	
																		1.90E-10	2.39E-10	1.76E-10	NA	NA	NA	NA	NA	NA	1.58	1000	10.0	1.58	0.00	0.00	
		EHPV_NG_EXP63																															
	1.28	1.6E+05	2.1E-16	1.7E-14	4.0E-16	1.8E-15	-2.8E-16	1.3E-15	5.1E-10	4.0E-08	9.5E-10	4.2E-09	-6.7E-10	3.1E-09	7.5E-13	NA	NA										0.68	900	29.5	0.68	0.00	0.00	not used for He_{HC}
	8.38	5.0E+05	9.6E-14	1.8E-14	2.9E-15	2.0E-15	2.6E-15	1.3E-15	7.4E-08	2.8E-08	2.3E-09	1.7E-09	2.0E-09	1.2E-09	1.1E-10	NA	NA										0.68	900	29.5	0.68	0.00	0.00	
	5.17	3.1E+05	2.7E-14	1.6E-14	1.0E-15	1.8E-15	6.9E-16	1.3E-15	3.3E-08	2.3E-08	1.3E-09	2.3E-09	8.6E-10	1.7E-09	4.9E-11	NA	NA										0.68	900	29.5	0.68	0.00	0.00	
	5.35	3.2E+05	4.8E-14	1.7E-14	-1.8E-15	1.8E-15	9.0E-16	1.3E-15	5.8E-08	2.8E-08	-2.2E-09	2.3E-09	1.1E-09	1.6E-09	8.6E-11	NA	NA										0.68	900	29.5	0.68	0.00	0.00	
	7.28	4.3E+05	9.2E-14	1.7E-14	9.9E-16	1.9E-15	2.2E-15	1.3E-15	8.2E-08	3.1E-08	8.8E-10	1.7E-09	2.0E-09	1.3E-09	1.2E-10	NA	NA										0.68	900	29.5	0.68	0.00	0.00	
	8.99	1.1E+06	3.2E-13	1.8E-14	-1.0E-16	1.9E-15	5.9E-15	1.3E-15	1.1E-07	3.6E-08	-3.5E-11	6.5E-10	2.0E-09	8.0E-10	1.6E-10	NA	NA										0.68	900	29.5	0.68	0.00	0.00	
	22.17	7.0E+05	3.1E-13	1.6E-14	-1.6E-15	1.9E-15	7.4E-15	1.3E-15	1.7E-07	5.7E-08	-8.7E-10	1.1E-09	4.1E-09	1.5E-09	2.5E-10	NA	NA										0.68	900	29.5	0.68	0.00	0.00	
	17.75	5.6E+05	2.5E-13	1.6E-14	-8.0E-16	2.0E-15	6.1E-15	1.3E-15	1.7E-07	5.9E-08	-5.5E-10	1.4E-09	4.2E-09	1.7E-09	2.6E-10	NA	NA										0.68	900	29.5	0.68	0.00	0.00	
	14.87	1.9E+06	9.0E-13	2.0E-14	1.8E-15	2.1E-15	2.1E-14	1.3E-15	1.9E-07	6.1E-08	3.6E-10	4.5E-10	4.4E-09	1.5E-09	2.7E-10	NA	NA										0.68	900	29.5	0.68	0.00	0.00	
	2.86	1.7E+05	2.2E-14	1.7E-14	-1.2E-15	1.8E-15	2.9E-17	1.3E-15	4.9E-08	4.1E-08	-2.6E-09	4.1E-09	6.6E-11	3.0E-09	7.2E-11	NA	NA										0.68	900	29.5	0.68	0.00	0.00	
	0.07	4.0E+03	3.4E-15	1.6E-14	-7.2E-16	1.9E-15	-4.8E-16	1.3E-15	3.3E-07	1.6E-06	-7.0E-08	1.8E-07	-4.6E-08	1.3E-07	4.9E-10	NA	NA										0.68	900	29.5	0.68	0.00	0.00	
																		1.40E-10	2.55E-10	9.17E-11	NA	NA	NA	NA	NA	NA	0.68	900	29.5	0.68	0.00	0.00	
		EHPV_NG_EXP64																															
	14.92	8.9E+05	4.5E-13	1.7E-14	1.8E-16	1.9E-15	5.3E-15	1.3E-15	2.0E-07	6.5E-08	7.8E-11	8.1E-10	2.3E-09	9.5E-10	1.8E-10	NA	NA										1.11	900	37.0	1.11	0.00	0.00	
	21.41	6.7E+05	7.7E-13	2.3E-14	-2.1E-15	1.9E-15	7.6E-15	1.3E-15	4.4E-07	1.5E-07	-1.2E-09	1.2E-09	4.4E-09	1.6E-09	4.0E-10	NA	NA										1.11	900	37.0	1.11	0.00	0.00	
	7.17	9.0E+05	7.0E-13	1.7E-14	-8.7E-16	1.8E-15	5.2E-15	1.3E-15	3.0E-07	9.9E-08	-3.7E-10	7.7E-10	2.2E-09	9.2E-10	2.7E-10	NA	NA										1.11	900	37.0	1.11	0.00	0.00	
	28.23	8.9E+05	2.5E-12	2.1E-14	1.8E-15	1.7E-15	1.8E-14	1.3E-15	1.1E-06	3.6E-07	7.6E-10	8.0E-10	7.7E-09	2.6E-09	9.7E-10	NA	NA										1.11	900	37.0	1.11	0.00	0.00	not used for He_{HC}
	18.31	5.8E+05	1.2E-12	1.8E-14	-6.9E-16	1.8E-15	8.6E-15	1.3E-15	7.9E-07	2.6E-07	-4.6E-10	1.2E-09	5.7E-09	2.1E-09	7.1E-10	NA	NA										1.11	900	37.0	1.11	0.00	0.00	
	15.74	4.9E+05	3.4E-13	1.7E-14	1.4E-15	1.8E-15	4.1E-15	1.3E-15	2.6E-07	8.8E-08	1.1E-09	1.4E-09	3.2E-09	1.5E-09	2.4E-10	NA	NA										1.11	900	37.0	1.11	0.00	0.00	
	11.38	6.8E+05	3.6E-13	1.7E-14	4.0E-16	1.8E-15	4.2E-15	1.3E-15	2.1E-07	6.9E-08	2.3E-10	1.0E-09	2.4E-09	1.1E-09	1.9E-10	NA	NA										1.11	900	37.0	1.11	0.00	0.00	
	9.07	5.4E+05	2.9E-13	1.7E-14	1.7E-15	1.8E-15	2.7E-15	1.3E-15	2.1E-07	7.0E-08	1.2E-09	1.3E-09	1.9E-09	1.1E-09	1.9E-10	NA	NA										1.11	900	37.0	1.11	0.00	0.00	
	3.49	4.4E+05	3.2E-13	1.6E-14	8.6E-16	1.9E-15	1.3E-15	1.3E-15	2.8E-07	9.2E-08	7.5E-10	1.7E-09	1.1E-09	1.2E-09	2.5E-10	NA	NA										1.11	900	37.0	1.11	0.00	0.00	
	2.87	3.6E+05	2.2E-13	1.6E-14	1.3E-15	1.7E-15	7.7E-16	1.3E-15	2.3E-07	7.9E-08	1.4E-09	1.9E-09	8.2E-10	1.4E-09	2.1E-10	NA	NA										1.11	900	37.0	1.11	0.00	0.00	
																		2.37E-10	2.69E-10	2.69E-10	NA	NA	NA	NA	NA	NA	1.11	900	37.0	1.11	0.00	0.00	
		EHPV_NG_EXP66																															
	16.22	9.6E+05	8.6E-14	1.7E-14	7.1E-14	2.3E-15	7.0E-15	1.3E-15	3.4E-08	1.3E-08	2.8E-08	9.4E-09	2.8E-09	1.1E-09	8.7E-11	7.2E-11	7.2E-12										1.18	1050	168.0	0.39	0.39	0.39	
	17.21	1.0E+06	1.0E-13	1.6E-14	6.7E-14	2.4E-15	6.4E-15	1.3E-15	3.8E-08	1.4E-08	2.5E-08	8.4E-09	2.4E-09	9.4E-10	9.7E-11	6.5E-11	6.2E-12										1.18	1050	168.0	0.39	0.39	0.39	
	27.66	8.7E+05	1.9E-13	1.6E-14	1.3E-13	3.6E-15	2.7E-14	1.3E-15	8.5E-08	2.9E-08	5.7E-08	1.9E-08	1.2E-08	3.9E-09	2.2E-10	1.5E-10	3.0E-11										1.18	1050	168.0	0.39	0.39	0.39	
	6.26	7.9E+05	6.6E-14	1.6E-14	6.1E-14	2.5E-15	7.9E-15	1.3E-15	3.2E-08	1.3E-08	3.0E-08	9.9E-09	3.8E-09	1.4E-09	8.2E-11	7.7E-11	9.8E-12										1.18	1050	168.0	0.39	0.39	0.39	
	8.16	1.0E+06	1.0E-13	1.6E-14	6.9E-14	2.2E-15	7.6E-15	1.3E-15	3.8E-08	1.4E-08	2.6E-08	8.6E-09	2.9E-09	1.1E-09	9.6E-11	6.7E-11	7.4E-12										1.18	1050	168.0	0.39	0.39	0.39	
	14.46	1.8E+06	3.2E-13	1.8E-14	1.5E-13	3.2E-15	1.5E-14	1.3E-15	6.7E-08	2.3E-08	3.2E-08	1.1E-08	3.2E-09	1.1E-09	1.7E-10	8.3E-11	8.2E-12										1.18	1050	168.0	0.39	0.39	0.39	
	20.94	2.6E+06	5.6E-13	2.0E-14	3.1E-13	2.2E-15	5.5E-14	1.4E-15	8.2E-08	2.7E-08	4.5E-08	1.5E-08	8.1E-09	2.7E-09	2.1E-10	1.1E-10	2.1E-11										1.18	1050	168.0	0.39	0.39	0.39	
	3.85	4.8E+05	3.9E-14	1.6E-14	3.2E-14	2.7E-15	7.0E-15	1.3E-15	3.1E-08	1.7E-08	2.6E-08	8.7E-09	5.6E-09	2.1E-09	7.8E-11	6.6E-11	1.4E-11										1.18	1050	168.0	0.39	0.39	0.39	
	11.51	1.4E+06	1.8E-13	1.7E-14	1.2E-13	4.1E-15	1.3E-14	1.3E-15	4.7E-08	1.6E-08	3.3E-08	1.1E-08	3.6E-09	1.2E-09	1.2E-10	8.4E-11	9.2E-12										1.18	1050	168.0	0.39	0.39	0.39	
	5.49	6.9E+05	4.6E-14	1.6E-14	5.4E-14	2.1E-15	8.9E-15	1.3E-15	2.6E-08	1.3E-08	3.0E-08	1.0E-08	5.0E-09	1.8E-09	6.6E-11	7.7E-11	1.3E-11										1.18	1050	168.0	0.39	0.39	0.39	
	0.08	1.0E+04	2.5E-14	1.7E-14	3.2E-15	1.8E-15	1.8E-15	1.3E-15	9.4E-07	7.1E-07	1.2E-07	7.9E-08	6.9E-08	5.4E-08	2.4E-09	3.1E-10	1.8E-10										1.18	1050	168.0	0.39	0.39	0.39	not used for He_{HC}
	0.00	2.9E+02	1.1E-14	1.6E-14	3.5E-15	1.8E-15	8.6E-16	1.3E-15	1.5E-05	2.2E-05	4.7E-06	2.8E-06	1.1E-06	1.8E-06	3.8E-08	1.2E-08	2.9E-09										1.18	1050	168.0	0.39	0.39	0.39	not used for He_{HC}
																		9.66E-11	1.58E-10	8.30E-11	7.71E-11	8.36E-11	6.80E-11	9.52E-12	1.39E-11	7.57E-12	1.18	1050	168.0	0.39	0.39	0.39	Ne, Ar profile?
scapolite																																	
		CS_NG_EXP9																															
	8.60	2.7E+05	8.4E-13	7.2E-14	5.0E-14	4.3E-14	1.6E-15	9.1E-16	1.2E-06	4.1E-07	7.1E-08	6.6E-08	2.2E-09	1.5E-09	8.9E-10	NA	NA										1.35	750	39.0	1.35	0.00	0.00	
	12.85	4.0E+05	1.4E-12	7.3E-14	2.2E-14	5.9E-14	1.6E-15	8.4E-16	1.3E-06	4.4E-07	2.1E-08	5.7E-08	1.5E-09	9.4E-10	9.7E-10	NA	NA										1.35	750	39.0	1.35	0.00	0.00	
	14.85	4.7E+05	1.8E-12	8.8E-14	-3.8E-14	4.3E-14	1.5E-15	9.0E-16	1.5E-06	5.1E-07	-3.1E-08	3.7E-08	1.2E-09	8.5E-10	1.1E-09	NA	NA										1.35	750	39.0	1.35	0.00	0.00	
	4.07	1.3E+05	3.3E-13	7.5E-14	8.2E-15	4.0E-14	-4.5E-16	8.5E-16	1.0E-06	4.0E-07	2.5E-08	1.2E-07	-1.4E-09	2.6E-09	7.4E-10	NA	NA										1.35	750	39.0	1.35	0.00	0.00	
	2.50	1.5E+05	4.0E-13	7.1E-14	6.9E-14	4.0E-14	1.1E-15	8.6E-16	1.0E-06	3.9E-07	1.8E-07	1.2E-07	2.8E-09	2.4E-09	7.7E-10	NA	NA										1.35	750	39.0	1.35	0.00	0.00	
	5.73	3.4E+05	1.0E-12	7.3E-14	4.4E-14	4.5E-14	3.5E-16	9.0E-16	1.2E-06	3.9E-07	5.0E-08	5.3E-08	3.9E-10	1.0E-09	8.5E-10	NA	NA										1.35	750	39.0	1.35	0.00	0.00	
	6.62	2.1E+05	6.5E-13	7.7E-14	6.9E-15	4.2E-14	2.4E-16	8.5E-16	1.2E-06	4.2E-07	1.3E-08	7.7E-08	4.4E-10	1.6E-09	8.9E-10	NA	NA										1.35	750	39.0	1.35	0.00	0.00	
	3.59	1.1E+05	2.9E-13	7.5E-14	-1.6E-14	4.0E-14	5.6E-16	8.7E-16	1.0E-06	4.2E-07	-5.4E-08	1.4E-07	1.9E-09	3.0E-09	7.4E-10	NA	NA										1.35	750	39.0	1.35	0.00	0.00	
																		8.71E-10	9.12E-10	7.66E-10	NA	NA	NA	NA	NA	NA	1.35	750	39.0	1.35	0.00	0.00	
		EHPV_NG_EXP56																															
	4.53	1.4E+05	7.8E-14	3.6E-14	7.9E-14	9.8E-14	-1.3E-14	2.8E-14	2.1E-07	1.2E-07	2.1E-07	2.8E-07	-3.6E-08	7.6E-08	6.5E-10	6.7E-10	-1.1E-10										0.97	650	48.0	0.32	0.32	0.32	
	14.37	8.5E+05	7.0E-13	3.9E-14	1.3E-13	9.0E-14	2.8E-14	2.8E-14	3.1E-07	1.1E-07	5.9E-08	4.5E-08	1.2E-08	1.3E-08	9.8E-10	1.8E-10	3.9E-11										0.97	650	48.0	0.32	0.32	0.32	
	10.80	1.4E+06	1.2E-12	3.5E-14	1.7E-13	9.6E-14	1.8E-14	2.8E-14	3.3E-07	1.1E-07	4.8E-08	3.1E-08	5.2E-09	8.1E-09	1.0E-09	1.5E-10	1.6E-11										0.97	650	48.0	0.32	0.32	0.32	
	7.06	4.2E+05	3.4E-13	3.4E-14	1.6E-13	1.2E-13	7.3E-15	3.0E-14	3.1E-07	1.1E-07	1.4E-07	1.2E-07	6.7E-09	2.8E-08	9.7E-10	4.5E-10	2.1E-11										0.97	650	48.0	0.32	0.32	0.32	
	10.21	6.1E+05	4.7E-13	3.4E-14	3.2E-13	9.6E-14	9.1E-15	2.8E-14	3.0E-07	1.0E-07	2.0E-07	9.1E-08	5.7E-09	1.8E-08	9.3E-10	6.3E-10	1.8E-11										0.97	650	48.0	0.32	0.32	0.32	
	5.42	6.8E+05	5.0E-13	3.5E-14	4.0E-15	1.1E-13	8.8E-15	3.2E-14	2.8E-07	9.5E-08	2.3E-09	6.1E-08	5.0E-09	1.8E-08	8.8E-10	7.1E-12	1.5E-11										0.97	650	48.0	0.32	0.32	0.32	
	12.25	7.3E+05	6.2E-13	3.6E-14	1.1E-13	9.9E-14	1.6E-14	3.0E-14	3.3E-07	1.1E-07	5.9E-08	5.6E-08	8.4E-09	1.6E-08	1.0E-09	1.8E-10	2.6E-11										0.97	650	48.0	0.32	0.32	0.32	
	2.70	5.8E+05	3.8E-13	3.6E-14	1.6E-13	9.1E-14	1.1E-14	2.9E-14	2.5E-07	8.6E-08	1.1E-07	7.0E-08	7.3E-09	1.9E-08	7.8E-10	3.3E-10	2.3E-11										0.97	650	48.0	0.32	0.32	0.32	
																		9.47E-10	9.89E-10	8.54E-10	NA	NA	NA	NA	NA	NA	0.97	650	48.0	0.32	0.32	0.32	
		EHPV_NG_EXP58																															
	1.83	5.8E+04	1.7E-13	6.0E-15	-4.9E-14	2.7E-14	-3.7E-14	2.0E-14	1.2E-06	3.8E-07	-3.3E-07	2.1E-07	-2.4E-07	1.6E-07	6.8E-10	NA	NA										1.68	715	92.0	1.68	0.00	0.00	
	2.74	8.6E+04	2.9E-13	5.7E-15	-2.8E-14	2.7E-14	3.6E-14	2.8E-14	1.3E-06	4.3E-07	-1.3E-07	1.3E-07	1.6E-07	1.3E-07	7.7E-10	NA	NA										1.68	715	92.0	1.68	0.00	0.00	
	8.55	2.7E+05	1.1E-12	6.5E-15	-3.4E-14	2.8E-14	9.1E-14	2.1E-14	1.6E-06	5.3E-07	-4.9E-08	4.4E-08	1.3E-07	5.2E-08	9.5E-10	NA	NA										1.68	715	92.0	1.68	0.00	0.00

	11.61	3.6E+05	4.2E-13	3.3E-15	9.6E-14	5.8E-15	4.5E-15	8.9E-16	4.4E-07	1.5E-07	1.0E-07	3.4E-08	4.7E-09	1.8E-09	1.0E-09	2.3E-10	1.1E-11									1.30	775	65.0	0.43	0.43	0.43	
	6.36	2.0E+05	1.9E-13	1.3E-15	4.8E-14	3.8E-15	2.2E-15	9.6E-16	3.6E-07	1.2E-07	9.3E-08	3.2E-08	4.2E-09	2.3E-09	8.4E-10	2.1E-10	9.7E-12									1.30	775	65.0	0.43	0.43	0.43	
	1.32	7.8E+04	5.8E-14	1.7E-15	2.0E-14	3.2E-15	8.5E-15	8.9E-16	2.9E-07	9.5E-08	9.8E-08	3.6E-08	4.2E-08	1.5E-08	6.6E-10	2.3E-10	9.7E-11									1.30	775	65.0	0.43	0.43	0.43	
	1.21	7.2E+04	5.1E-14	1.4E-15	5.1E-15	3.1E-15	4.1E-15	8.9E-16	2.7E-07	9.1E-08	2.7E-08	1.9E-08	2.2E-08	8.6E-09	6.3E-10	6.3E-11	5.0E-11									1.30	775	65.0	0.43	0.43	0.43	
	4.83	2.9E+05	2.8E-13	3.6E-15	1.0E-13	5.8E-15	6.2E-15	1.0E-15	3.7E-07	1.2E-07	1.3E-07	4.5E-08	8.3E-09	3.1E-09	8.5E-10	3.1E-10	1.9E-11									1.30	775	65.0	0.43	0.43	0.43	
	2.75	1.6E+05	1.4E-13	1.7E-15	3.8E-14	5.1E-15	2.5E-15	9.2E-16	3.4E-07	1.1E-07	8.9E-08	3.2E-08	5.9E-09	2.9E-09	7.7E-10	2.1E-10	1.4E-11									1.30	775	65.0	0.43	0.43	0.43	
	2.28	1.4E+05	9.9E-14	1.5E-15	2.7E-14	4.0E-15	6.4E-16	9.2E-16	2.8E-07	9.3E-08	7.6E-08	2.8E-08	1.8E-09	2.7E-09	6.5E-10	1.8E-10	4.2E-12									1.30	775	65.0	0.43	0.43	0.43	
	3.22	1.9E+05	1.7E-13	2.1E-15	4.9E-14	2.9E-15	7.6E-15	9.8E-16	3.5E-07	1.1E-07	9.9E-08	3.3E-08	1.5E-08	5.4E-09	8.0E-10	2.3E-10	3.5E-11									1.30	775	65.0	0.43	0.43	0.43	
	3.29	2.0E+05	1.7E-13	2.3E-15	3.4E-14	4.1E-15	5.3E-15	8.9E-16	3.4E-07	1.1E-07	6.7E-08	2.3E-08	1.0E-08	3.8E-09	7.9E-10	1.5E-10	2.4E-11									1.30	775	65.0	0.43	0.43	0.43	
	8.14	4.8E+05	5.0E-13	4.3E-15	6.9E-14	8.8E-15	5.4E-15	9.1E-16	4.0E-07	1.3E-07	5.5E-08	1.9E-08	4.3E-09	1.6E-09	9.2E-10	1.3E-10	9.9E-12									1.30	775	65.0	0.43	0.43	0.43	
																		7.94E-10	8.47E-10	6.91E-10	2.10E-10	2.28E-10	1.59E-10	1.65E-11	3.23E-11	1.02E-11	1.30	775	65.0	0.43	0.43	0.43	Ar lower limit
prehnite																																	
	CS_NG_EXP17																																
	7.39	4.4E+05	1.3E-12	7.1E-15	-2.2E-15	3.6E-14	1.9E-15	9.6E-15	1.0E-06	3.4E-07	-1.7E-09	2.7E-08	1.4E-09	7.4E-09	7.2E-10	NA	NA									1.57	375	46.0	1.42	0.00	0.00	
	7.32	4.3E+05	1.6E-12	8.3E-15	2.1E-14	3.6E-14	8.6E-15	9.7E-15	1.3E-06	4.1E-07	1.6E-08	2.8E-08	6.7E-09	7.9E-09	8.8E-10	NA	NA									1.57	375	46.0	1.42	0.00	0.00	
	3.73	2.2E+05	6.7E-13	8.9E-15	2.6E-14	3.6E-14	6.7E-15	9.6E-15	1.0E-06	3.4E-07	4.0E-08	5.6E-08	1.0E-08	1.5E-08	7.2E-10	NA	NA									1.57	375	46.0	1.42	0.00	0.00	
	2.49	1.5E+05	4.7E-13	7.2E-15	-2.3E-14	3.5E-14	-2.0E-15	9.7E-15	1.1E-06	3.6E-07	-5.4E-08	8.3E-08	-4.6E-09	2.2E-08	7.7E-10	NA	NA									1.57	375	46.0	1.42	0.00	0.00	
	2.68	1.6E+05	5.1E-13	8.2E-15	-3.2E-15	3.6E-14	-4.9E-15	9.6E-15	1.1E-06	3.6E-07	-6.9E-09	7.6E-08	-1.1E-08	2.1E-08	7.6E-10	NA	NA									1.57	375	46.0	1.42	0.00	0.00	
	1.67	9.9E+04	3.1E-13	6.7E-15	8.5E-15	3.6E-14	2.5E-15	9.5E-15	1.1E-06	3.5E-07	2.9E-08	1.2E-07	8.6E-09	3.3E-08	7.4E-10	NA	NA									1.57	375	46.0	1.42	0.00	0.00	
																		7.52E-10	7.23E-10	7.23E-10	NA	NA	NA	NA	NA	NA	1.57	375	46.0	1.42	0.00	0.00	
	CS_NG_EXP18																																
	12.72	7.6E+05	2.1E-14	1.2E-15	2.7E-15	2.6E-15	1.2E-14	9.5E-16	9.4E-09	3.1E-09	1.2E-09	1.2E-09	5.3E-09	1.8E-09	NA	NA	3.7E-12									1.57	350	48.0	0.00	0.00	1.42	He detected?
	6.53	3.9E+05	1.7E-14	1.2E-15	-2.5E-15	2.5E-15	1.1E-14	8.7E-16	1.5E-08	5.0E-09	-2.2E-09	2.3E-09	9.4E-09	3.2E-09	NA	NA	6.6E-12									1.57	350	48.0	0.00	0.00	1.42	He detected?
	3.41	2.0E+05	1.4E-14	1.2E-15	-4.1E-15	2.6E-15	8.6E-15	9.2E-16	2.3E-08	7.8E-09	-6.9E-09	5.0E-09	1.4E-08	5.0E-09	NA	NA	1.0E-11									1.57	350	48.0	0.00	0.00	1.42	He detected?
	1.70	1.0E+05	4.1E-15	1.3E-15	-1.7E-15	2.5E-15	3.8E-15	1.1E-15	1.4E-08	6.3E-09	-5.5E-09	8.7E-09	1.3E-08	5.5E-09	NA	NA	9.1E-12									1.57	350	48.0	0.00	0.00	1.42	He detected?
	0.86	5.1E+04	3.5E-15	1.2E-15	-1.7E-15	2.4E-15	4.6E-15	9.2E-16	2.3E-08	1.1E-08	-1.1E-08	1.7E-08	3.1E-08	1.2E-08	NA	NA	2.2E-11									1.57	350	48.0	0.00	0.00	1.42	He detected?
	0.77	9.7E+04	5.4E-15	1.2E-15	5.0E-16	2.6E-15	1.2E-14	1.1E-15	1.9E-08	7.5E-09	1.8E-09	9.1E-09	4.1E-08	1.4E-08	NA	NA	2.9E-11									1.57	350	48.0	0.00	0.00	1.42	He detected?
	0.57	7.2E+04	3.2E-15	1.2E-15	5.1E-15	2.5E-15	1.2E-14	9.3E-16	1.5E-08	7.7E-09	2.4E-08	1.4E-08	5.6E-08	1.9E-08	NA	NA	4.0E-11									1.57	350	48.0	0.00	0.00	1.42	He detected?
	1.08	1.4E+05	4.7E-15	1.2E-15	-6.5E-16	2.6E-15	1.4E-14	9.3E-16	1.2E-08	4.9E-09	-1.6E-09	6.6E-09	3.6E-08	1.2E-08	NA	NA	2.5E-11									1.57	350	48.0	0.00	0.00	1.42	He detected?
	2.00	2.5E+05	1.1E-14	1.3E-15	9.3E-16	2.4E-15	1.1E-14	8.7E-16	1.5E-08	5.3E-09	1.3E-09	3.3E-09	1.5E-08	5.2E-09	NA	NA	1.1E-11									1.57	350	48.0	0.00	0.00	1.42	He detected?
	3.05	3.8E+05	2.1E-14	1.3E-15	1.5E-15	2.5E-15	2.1E-14	1.0E-15	1.8E-08	6.2E-09	1.3E-09	2.3E-09	1.9E-08	6.2E-09	NA	NA	1.3E-11									1.57	350	48.0	0.00	0.00	1.42	He detected?
																		NA	NA	NA	NA	NA	NA	4.00E-11	NA	NA	1.57	350	48.0	0.00	0.00	1.42	Ar lower limit
	CS_NG_EXP25																																
	3.04	1.8E+05	1.2E-13	2.2E-15	5.6E-14	3.5E-15	-6.0E-15	2.1E-14	2.3E-07	7.6E-08	1.0E-07	3.5E-08	-1.1E-08	4.0E-08	1.4E-09	6.3E-10	-6.7E-11									0.50	350	48.0	0.17	0.17	0.17	
	8.48	1.1E+06	5.2E-13	2.9E-15	1.0E-13	6.9E-15	3.0E-14	2.0E-14	1.7E-07	5.5E-08	3.3E-08	1.1E-08	9.6E-09	7.1E-09	1.0E-09	2.0E-10	5.8E-11									0.50	350	48.0	0.17	0.17	0.17	
	4.67	5.9E+05	3.3E-13	1.5E-15	1.5E-13	6.8E-15	1.4E-14	2.0E-14	1.9E-07	6.4E-08	8.5E-08	2.8E-08	7.9E-09	1.2E-08	1.2E-09	5.1E-10	4.8E-11									0.50	350	48.0	0.17	0.17	0.17	
	2.36	3.0E+05	1.7E-13	1.8E-15	9.4E-14	4.1E-15	-1.0E-14	1.9E-14	1.9E-07	6.4E-08	1.1E-07	3.6E-08	-1.1E-08	2.2E-08	1.2E-09	6.4E-10	-6.9E-11									0.50	350	48.0	0.17	0.17	0.17	
	5.10	6.4E+05	3.7E-13	1.8E-15	1.2E-13	7.9E-15	-2.4E-15	1.9E-14	2.0E-07	6.5E-08	6.3E-08	2.1E-08	-1.3E-09	1.0E-08	1.2E-09	3.8E-10	-7.8E-12									0.50	350	48.0	0.17	0.17	0.17	
	1.51	1.9E+05	1.2E-13	1.8E-15	8.6E-14	6.4E-15	-5.4E-16	2.1E-14	2.2E-07	7.2E-08	1.5E-07	5.2E-08	-9.6E-10	3.7E-08	1.3E-09	9.2E-10	-5.7E-12									0.50	350	48.0	0.17	0.17	0.17	
	1.77	2.2E+05	1.1E-13	1.6E-15	8.7E-14	3.3E-15	3.0E-15	1.9E-14	1.7E-07	5.7E-08	1.3E-07	4.4E-08	4.5E-09	3.0E-08	1.0E-09	7.9E-10	2.7E-11									0.50	350	48.0	0.17	0.17	0.17	
	1.72	2.2E+05	2.4E-13	2.4E-15	9.8E-14	7.5E-15	1.0E-15	2.0E-14	3.8E-07	1.2E-07	1.5E-07	5.2E-08	1.6E-09	3.1E-08	2.3E-09	9.2E-10	9.4E-12									0.50	350	48.0	0.17	0.17	0.17	
																		1.17E-09	1.32E-09	1.13E-09	**1.28E-09**	**1.69E-09**	**1.10E-09**	NA	NA	NA	0.50	350	48.0	0.17	0.17	0.17	
	CS_NG_EXP27																																
	3.83	2.3E+05	4.9E-13	4.9E-15	1.9E-13	2.8E-14	4.7E-14	9.2E-14	7.2E-07	2.4E-07	2.8E-07	1.0E-07	7.1E-08	1.4E-07	1.6E-09	6.3E-10	1.6E-10									1.34	500	25.8	0.45	0.45	0.45	
	14.06	8.3E+05	1.1E-12	4.0E-15	1.6E-13	3.6E-14	7.0E-14	9.1E-14	4.4E-07	1.4E-07	6.6E-08	2.6E-08	2.8E-08	3.8E-08	9.8E-10	1.5E-10	6.3E-11									1.34	500	25.8	0.45	0.45	0.45	
	1.46	1.8E+05	4.1E-13	3.5E-15	1.5E-13	2.3E-14	3.8E-16	9.2E-14	7.6E-07	2.5E-07	2.9E-07	1.0E-07	7.0E-10	1.7E-07	1.7E-09	6.4E-10	1.6E-12									1.34	500	25.8	0.45	0.45	0.45	
	2.92	3.7E+05	7.6E-13	3.8E-15	2.6E-13	2.6E-14	3.9E-14	9.1E-14	7.0E-07	2.3E-07	2.4E-07	8.4E-08	3.6E-08	8.5E-08	1.6E-09	5.5E-10	8.0E-11									1.34	500	25.8	0.45	0.45	0.45	
	2.60	3.3E+05	7.6E-13	3.7E-15	3.8E-13	3.4E-14	-7.3E-16	9.3E-14	7.9E-07	2.6E-07	4.0E-07	1.4E-07	-7.6E-10	9.7E-08	1.8E-09	8.9E-10	-1.7E-12									1.34	500	25.8	0.45	0.45	0.45	
	5.52	6.9E+05	1.3E-12	7.2E-15	4.6E-13	3.9E-14	-1.3E-13	9.1E-14	6.2E-07	2.0E-07	2.3E-07	7.7E-08	-6.1E-08	4.9E-08	1.4E-09	5.1E-10	-1.4E-10									1.34	500	25.8	0.45	0.45	0.45	
	7.89	9.9E+05	1.6E-12	5.4E-15	6.6E-13	4.9E-14	3.7E-14	9.1E-14	5.5E-07	1.8E-07	2.3E-07	7.7E-08	1.3E-08	3.1E-08	1.2E-09	5.1E-10	2.9E-11									1.34	500	25.8	0.45	0.45	0.45	
	10.08	1.3E+06	1.9E-12	5.0E-15	4.6E-13	2.7E-14	1.5E-14	9.3E-14	5.0E-07	1.6E-07	1.2E-07	4.1E-08	3.9E-09	2.5E-08	1.1E-09	2.8E-10	8.8E-12									1.34	500	25.8	0.45	0.45	0.45	
	7.42	9.3E+05	1.6E-12	4.0E-15	5.4E-13	2.9E-14	1.4E-15	9.2E-14	5.7E-07	1.9E-07	1.9E-07	6.5E-08	5.0E-10	3.3E-08	1.3E-09	4.4E-10	1.1E-12									1.34	500	25.8	0.45	0.45	0.45	
	9.80	1.2E+06	1.8E-12	6.1E-15	5.2E-13	2.6E-14	-5.5E-14	9.1E-14	5.0E-07	1.7E-07	1.4E-07	4.7E-08	-1.5E-08	2.6E-08	1.1E-09	3.2E-10	-3.4E-11									1.34	500	25.8	0.45	0.45	0.45	
																		1.80E-09	**1.90E-09**	**1.74E-09**	**8.65E-10**	**1.05E-09**	**6.85E-10**	NA	NA	NA	1.34	500	25.8	0.45	0.45	0.45	
	CS_NG_EXP29																																
	22.47	7.1E+05	7.3E-13	7.4E-15	1.6E-15	6.6E-16	-1.1E-15	1.9E-15	3.5E-07	1.2E-07	7.6E-10	4.0E-10	-5.4E-10	9.2E-10	5.1E-10	NA	NA									0.68	350	29.5	0.68	0.00	0.00	
	8.33	2.6E+05	3.2E-13	6.9E-15	3.4E-15	5.3E-16	-9.3E-16	1.9E-15	4.1E-07	1.4E-07	4.4E-09	1.6E-09	-1.2E-09	2.5E-09	6.1E-10	NA	NA									0.68	350	29.5	0.68	0.00	0.00	
	2.67	8.4E+04	1.0E-13	4.4E-15	4.1E-16	6.0E-16	-1.2E-15	1.9E-15	4.1E-07	1.4E-07	1.7E-09	2.5E-09	-5.0E-09	7.8E-09	6.0E-10	NA	NA									0.68	350	29.5	0.68	0.00	0.00	
	11.25	3.5E+05	4.0E-13	4.4E-15	-1.1E-16	6.7E-16	-1.1E-15	1.9E-15	3.9E-07	1.3E-07	-1.1E-10	6.5E-10	-1.1E-09	1.8E-09	5.7E-10	NA	NA									0.68	350	29.5	0.68	0.00	0.00	
	30.44	9.6E+05	7.1E-13	8.5E-15	1.6E-15	5.9E-16	-1.6E-15	1.9E-15	2.5E-07	8.4E-08	5.7E-10	2.8E-10	-5.6E-10	6.9E-10	3.7E-10	NA	NA									0.68	350	29.5	0.68	0.00	0.00	
	26.85	8.4E+05	6.9E-13	6.0E-15	1.7E-15	6.3E-16	-1.6E-15	1.9E-15	2.8E-07	9.1E-08	6.8E-10	3.4E-10	-6.3E-10	7.9E-10	4.1E-10	NA	NA									0.68	350	29.5	0.68	0.00	0.00	
	14.51	4.6E+05	5.3E-13	5.1E-15	6.5E-16	6.2E-16	-6.9E-16	1.9E-15	3.9E-07	1.3E-07	4.9E-10	4.9E-10	-5.1E-10	1.4E-09	5.8E-10	NA	NA									0.68	350	29.5	0.68	0.00	0.00	
																		6.80E-10	**7.45E-10**	**6.10E-10**	NA	NA	NA	NA	NA	NA	0.68	350	29.5	0.68	0.00	0.00	
	CS_NG_EXP30																																
	3.16	5.6E+04	1.5E-13	5.2E-15	-4.2E-16	5.4E-16	-3.0E-16	1.9E-15	9.2E-07	3.1E-07	-2.5E-09	3.4E-09	-1.8E-09	1.1E-08	8.3E-10	NA	NA									1.11	350	37.0	1.11	0.00	0.00	
	3.68	1.2E+05	3.4E-13	5.7E-15	6.7E-16	5.8E-16	1.2E-15	1.9E-15	9.8E-07	3.2E-07	2.0E-09	1.8E-09	3.6E-09	5.7E-09	8.9E-10	NA	NA									1.11	350	37.0	1.11	0.00	0.00	
	9.27	2.9E+05	6.6E-13	5.2E-15	-9.0E-17	5.3E-16	-5.8E-16	1.9E-15	7.7E-07	2.5E-07	-1.0E-10	6.2E-10	-6.8E-10	2.2E-09	6.9E-10	NA	NA									1.11	350	37.0	1.11	0.00	0.00	
	14.14	4.4E+05	8.1E-13	7.4E-15	-1.0E-15	5.5E-16	-8.9E-16	1.9E-15	6.2E-07	2.0E-07	-7.9E-10	4.9E-10	-6.8E-10	1.5E-09	5.6E-10	NA	NA									1.11	350	37.0	1.11	0.00	0.00	
	18.15	5.7E+05	9.5E-13	5.2E-15	7.0E-16	5.8E-16	-1.2E-15	1.9E-15	5.6E-07	1.9E-07	4.1E-10	3.7E-10	-7.4E-10	1.1E-09	5.1E-10	NA	NA									1.11	350	37.0	1.11	0.00	0.00	
	6.63	2.1E+05	5.5E-13	5.0E-15	-1.6E-16	6.0E-16	-5.6E-16	1.9E-15	8.9E-07	3.0E-07	-2.5E-10	9.8E-10	-9.2E-10	3.1E-09	8.1E-10	NA	NA									1.11	350	37.0	1.11	0.00	0.00	
	9.76	3.1E+05	7.7E-13	7.6E-15	-6.8E-17	5.9E-16	-1.0E-15	1.9E-15	8.5E-07	2.8E-07	-7.5E-11	6.5E-10	-1.1E-09	2.1E-09	7.6E-10	NA	NA									1.11	350	37.0	1.11	0.00	0.00	
																		9.93E-10	**1.45E-09**	**9.10E-10**	NA	NA	NA	NA	NA	NA	1.11	350	37.0	1.11	0.00	0.00	
	EHPV_NG_EXP52																																
	3.24	1.9E+05	2.3E-14	6.0E-15	-3.9E-14	2.7E-14	-4.6E-15	1.8E-14	4.0E-08	1.7E-08	-6.9E-08	5.3E-08	-8.0E-09	3.2E-08	2.8E-11	NA	NA									1.57	435	46.0	1.42	0.00	0.00	
	6.46	3.8E+05	9.1E-15	5.5E-15	3.6E-14	2.7E-14	5.8E-15	1.9E-14	8.1E-09	5.6E-09	3.2E-08	2.6E-08	5.1E-09	1.6E-08	5.7E-12	NA	NA									1.57	435	46.0	1.42	0.00	0.00	
	1.93	1.1E+05	8.8E-15	5.6E-15	5.0E-14	2.7E-14	6.9E-15	1.8E-14	2.6E-08	1.9E-08	1.5E-07	9.3E-08	2.0E-08	5.5E-08	1.8E-11	NA	NA									1.57	435	46.0	1.42	0.00	0.00	
	5.70	3.4E+05	2.1E-14	5.5E-15	-1.0E-15	2.7E-14	-7.7E-15	1.8E-14	2.1E-08	8.9E-09	-1.0E-09	2.7E-08	-7.8E-09	1.9E-08	1.5E-11	NA	NA									1.57	435	46.0	1.42	0.00	0.00	
	9.98	5.9E+05	3.0E-14	5.6E-15	1.6E-14	2.7E-14	4.8E-15	1.8E-14	1.7E-08	6.4E-09	8.9E-09	1.6E-08	2.8E-09	1.1E-08	1.2E-11	NA	NA									1.57	435	46.0	1.42	0.00	0.00	
	2.62	3.3E+05	3.6E-14	5.5E-15	-2.3E-14	2.7E-14	2.6E-15	1.9E-14	3.7E-08	1.3E-08	-2.4E-08	2.9E-08	2.6E-09	1.9E-08	2.6E-11	NA	NA									1.57	435	46.0	1.42	0.00	0.00	
	1.28	1.6E+05	2.0E-14	5.6E-15	1.8E-14	2.8E-14	2.1E-15	1.8E-14	4.1E-08	1.8E-08	3.8E-08	5.9E-08	4.4E-09	3.9E-08	2.9E-11	NA	NA									1.57	435	46.0	1.42	0.00	0.00	
	5.37	6.7E+05	5.3E-14	5.6E-15	9.0E-14	2.8E-14	9.5E-16	1.8E-14	2.6E-08	9.2E-09	4.5E-08	2.1E-08	4.8E-10	9.2E-09	1.9E-11	NA	NA									1.57	435	46.0	1.42	0.00	0.00	
																		1.83E-11	2.23E-11	1.34E-11	NA	NA	NA	NA	NA	NA	1.57	435	46.0	1.42	0.00	0.00	low He?

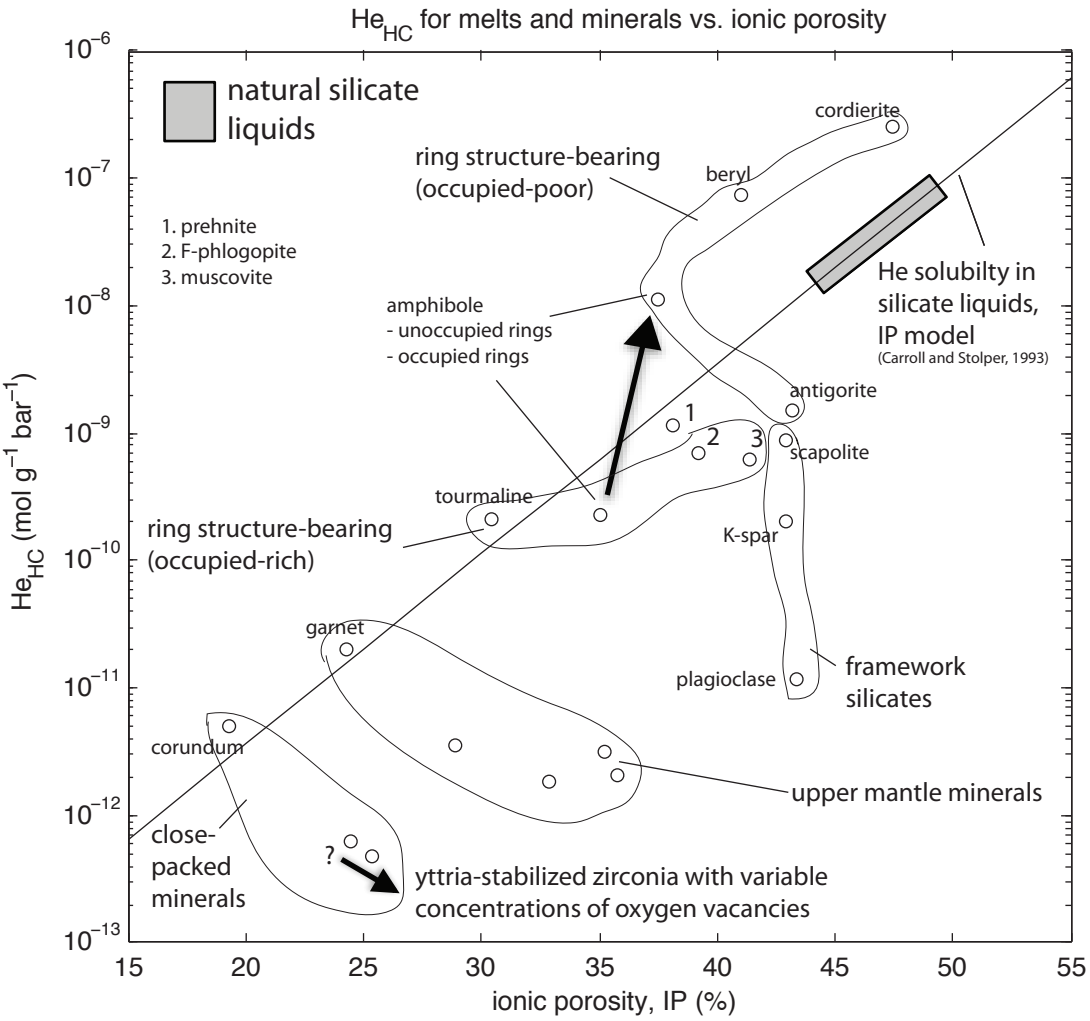

Appendix Figure 1:

Helium solubility data normalized to helium fugacity (Henry's constant, He_{HC}) plotted as a function of ionic porosity for a range of minerals. Mineral names are given in smaller type and grouped into similar structural types by drawn-in fields. Fields are named with larger type. A wide range of He_{HC} values have been measured, greatly surpassing the range measured in natural silicate liquids. Mantle minerals and close-packed minerals have low He_{HC}, and no correlation is present between IP and He_{HC}. Yttria-stabilized zirconia with high and variable concentrations of oxygen vacancies have similarly low He_{HC} (arrow with question mark). Framework silicates have intermediate He_{HC}, and no correlation is present between He_{HC} and IP. Ring structure-bearing minerals where the ring structures are mostly occupied have lower He_{HC} compared to ring structure-bearing minerals where the ring structures are mostly unoccupied. The larger arrow gives the vector associated with associated with the openning the ring structure porosity in amphibole. This vector is steep compared to the melt He_{HC} model, underlining the favorability of ring structure environments for noble gase. Overall, there is a broad correlation between He_{HC} and IP across all minerals, suggesting porosity does facilitate the dissolution of noble gases, but the specific topology of the porosity appears more as evidenced by inter-amphibole comparisons.

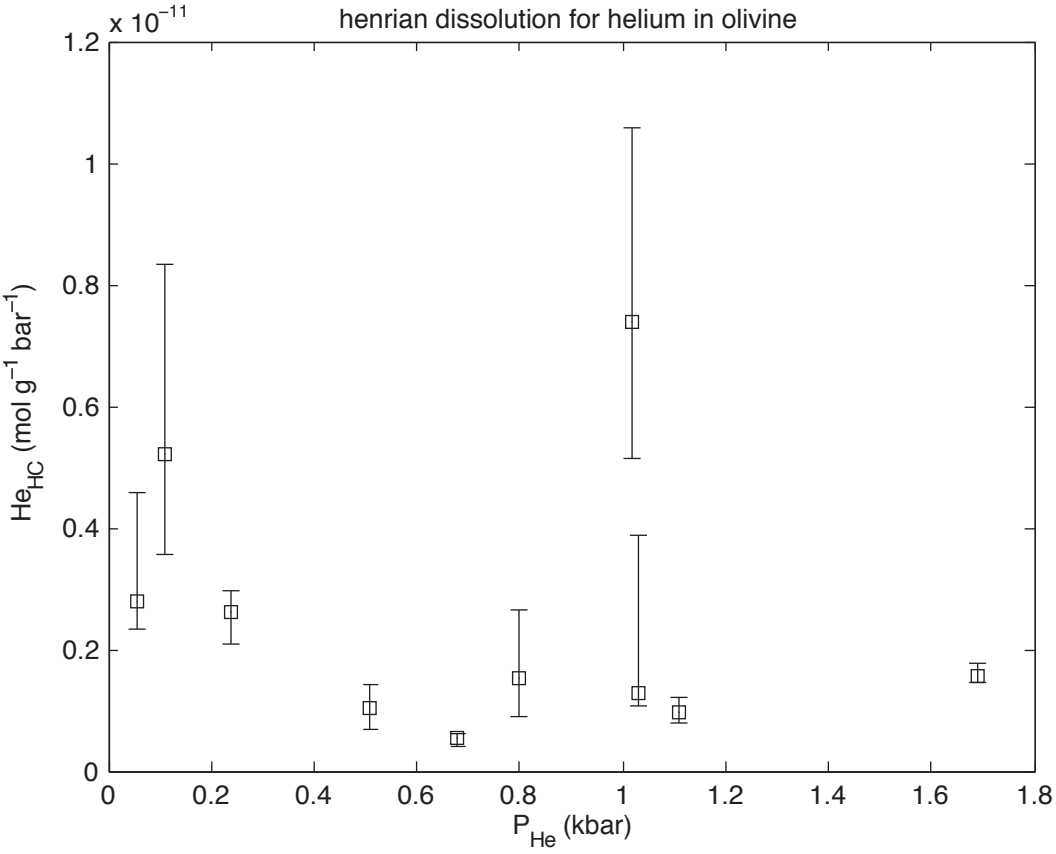

Appendix Figure 2:

Helium solubility data normalized to helium fugacity (Henry's constant) plotted as a function of helium fugacity. Henry's constants do not change with helium fugacity, indicating Henrian solution behavior over the range of fugacity explored. Lower fugacity experiments are required to verify that the same solution mechanisms that control solubility between 50 and 2000 bar He fugacity also control solubilty under mantle conditions. The high He_{HC} centered near 1 kbar is likely an outlier.

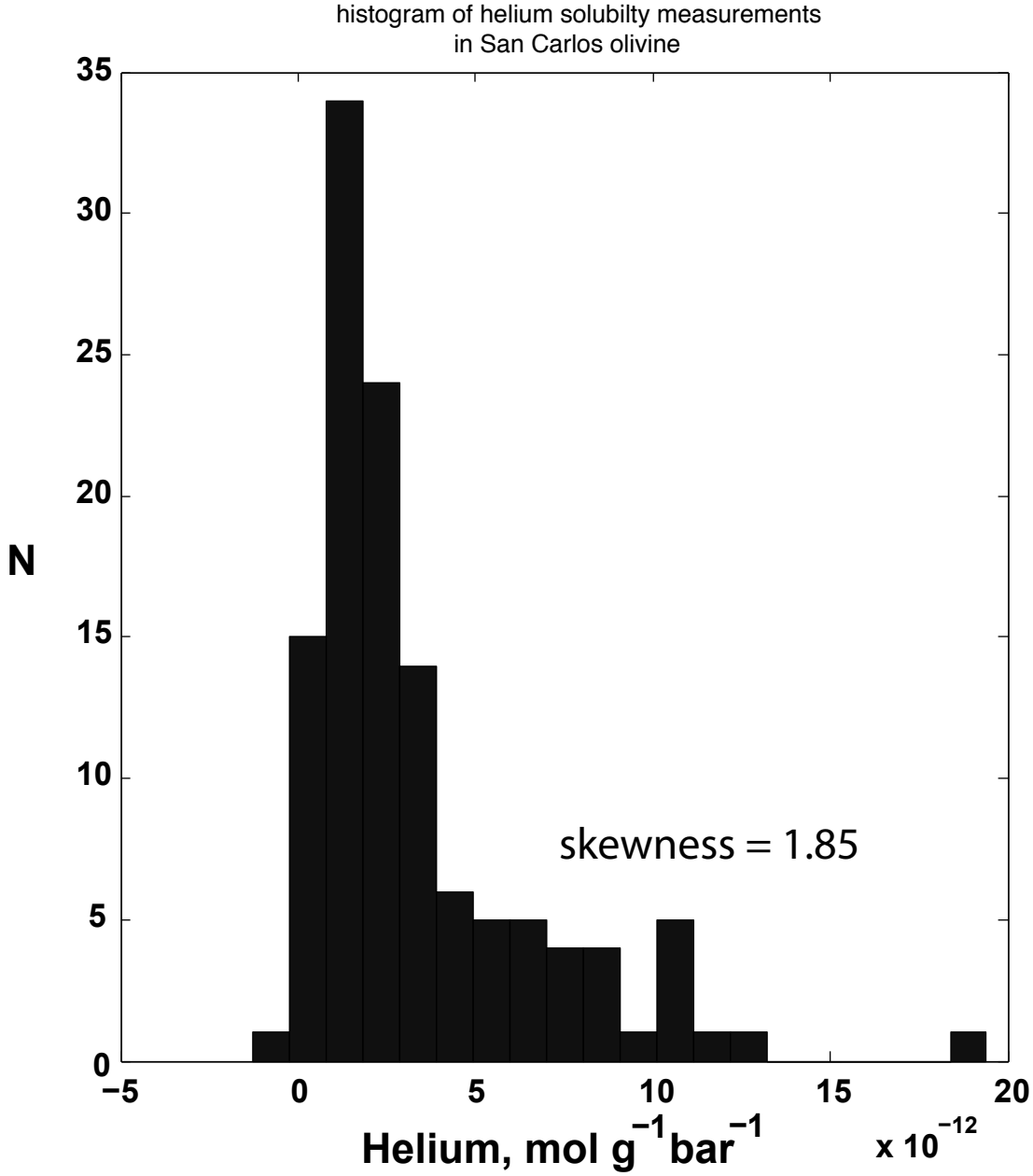

Appendix Figure 3:

Helium solubility data normalized to helium fugacity (Henry's constant, He_{HC}) for San Carlos olivine plotted as a histogram. Data show a strong peak centered near 10^{-12} mol g^{-1} bar^{-1} but the distribution is skewed to higher values. This suggests that small amounts of a material with higher helium solubility was variably incorporated to the analyzed material.

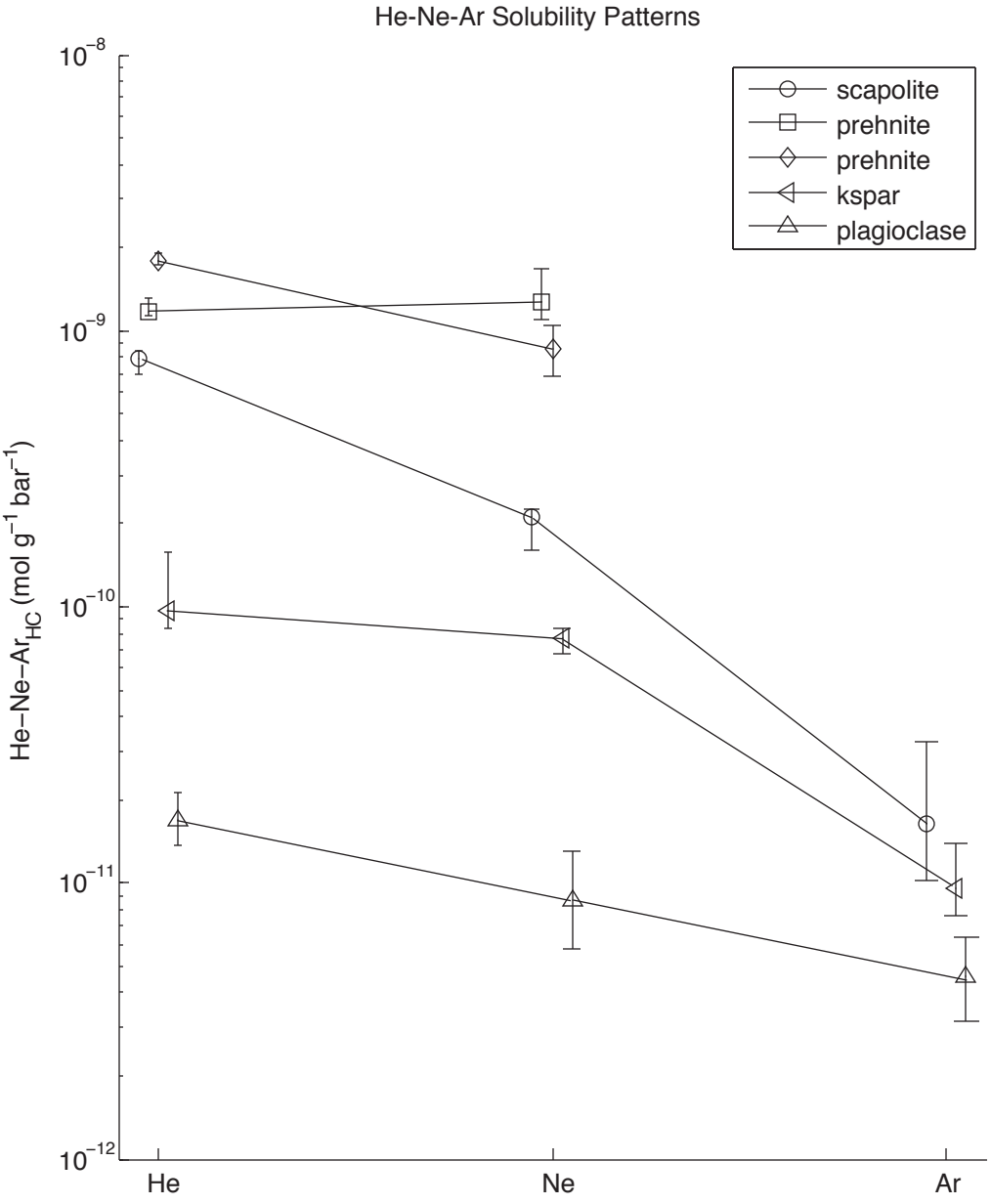

Appendix Figure 4:

Patterns of He-Ne-Ar solubility in a variety of minerals. No mineral investigated to data shows a clear preference for larger radii noble gases, but Ar solubility is generally within a factor of 10 of He solubility.

Appendix 2: Future Directions on Noble Gas Recycling

Appendix 2, Future Directions on Noble Gas Recycling:

This appendix focuses on developing a framework for quantifying how noble gases are incorporated into slabs during hydrothermal alteration and released from slabs during prograde metamorphism associated with subduction. The ultimate goal is to develop the application of noble gases as tracers of fluids in subduction zones and volatile element recycling. Below I discuss noble gas transport through subduction zones and highlight areas where additional study is needed.

1.0 Motivation

Oceanic lithosphere (slabs) is returned to the mantle via subduction. During their transit from ridge to trench, oceanic slabs continuously interact with hydrothermal fluids. The hydrothermal fluids introduced into the oceanic slab act as an exchange medium between Earth's surface and interior and stabilize a variety of hydrous minerals in the slab. Hydrothermally altered materials are transported deeper into Earth's interior upon subduction, where they are exposed to progressively higher temperatures and pressures. The reactions associated with hydrothermal alteration are generally exothermic. As temperatures and pressures rise in the subducted slab, the stability of hydrous minerals decreases, leading to dehydration. The fluids driven off of the slab rise into overlying lithologies following their buoyancy and are largely returned to the atmosphere via magmatism. Slab fluids ultimately affect a wide spectrum of geological phenomena, including mantle viscosity, growth of continents, volcanic eruptions, and mass exchange between Earth's interior and exterior.

Here, we consider the development of noble gases as tracers of fluid in subduction zones. Noble gases are a group of unreactive elements with regular variations in physical properties (i.e. radius, polarizability, compressibility). Because of this regularity, processes such as absorption (volume solubility), adsorption (surface solubility), degassing, and diffusion should impart regular elemental fractionations that can be observed in natural samples, similar to how rare earth elements are utilized. Physical mixing between different geochemical reservoirs can be traced by homogenization of their isotopic differences. Fractionations associated with recent degassing can be corrected for using noble gas radiogenic systems (e.g., Honda and McDougall, 1998). These properties make noble gases a potentially information-rich, robust tracer of subduction fluids. The strength of noble gases as a tracer is highlighted by comparison with hydrogen and carbon (other elements that readily partition into fluid phases), which are both mono-element, di-isotopic systems, making the deconvolution of separate processes difficult.

The following discussion is divided into three sections. The first section explores the controls on the uptake of noble gases into hydrothermally altered sections of slabs. The second section explores the controls on the release of noble gases from subducting slabs. Combined, the uptake and release of noble gases determines the composition and mass of recycled noble gases as well as the noble gases released into the mantle wedge. The final section focuses on the composition of noble gases in the mantle and how this can be used to place constraints on the time-integrated flux of recycled noble gases.

2.0 Noble Gas Uptake:

The extent and nature of hydrothermal alteration in slabs links with many aspects of Earth science and remains a topic of intense study. Interactions of seawater with oceanic crust act to modify the chemistry of the oceans, introduce fluids into subduction zones, support microbial communities, and recycle volatile elements into the mantle. Generally, lithologies closest to the surface are pervasively altered at relatively low temperatures and authigenic sediments are commonplace (Alt et al., 1984; Alt et al., 1986). Deeper alteration into the dikes, gabbros and lithospheric mantle is highly heterogeneous and more localized to zones of high fluid permeability (e.g. faults or shear zones) (Alt et al., 1996; Dick et al., 2000; Wilson et al., 2006). The extent of deeper alteration is largely affected the intensity and location of magmatic activity, and hence, spreading rate (Wilson et al., 1996). High temperature and low water/rock ratio assemblages are more common deeper into the slab. Extremely deep hydrothermal alteration is limited by the thermal stability of hydrous minerals. Thus, the conditions (temperature, pressure, water/rock ratio, rock chemistry) of alteration are expected to vary widely throughout a slab and between different subduction zones. Variations in the conditions of alteration should be reflected in the abundances of noble gases present in the altered rock. The effects of temperature, pressure, water/rock ratio, and rock chemistry on noble gas uptake are explored below.

2.1 Basic Theory and Background:

The uptake of noble gases into slab materials is essentially a trace element partitioning problem, where a noble gas atom is partitioned between the fluid phase (either aqueous fluid or supercritical fluid) and solid material. The partition coefficient for a noble gas between any two phases can be determined by ratioing the solubility of

that noble gas in the two phases of interest under the same conditions. The equilibrium concentration of a noble gas in a solid phase can be determined by multiplying the appropriate partition coefficient by the concentration of that noble gas dissolved into the corresponding aqueous liquid or fluid. For hydrothermal alteration of oceanic lithospere, the abundance of a given noble gas in the reacting fluid can, to a first order, be taken as equal to the abundance of that noble gas in seawater (Kennedy, 1988; Winckler et al., 2000). The concentration and elemental pattern of noble gases emanating from hydrothermal vents are similar to those measured in ambient seawater, indicating little uptake and fractionation of these noble gases by the interacting solids. There is good evidence that phase-separation commonly occurs in hydrothermal systems, resulting from either the boiling of an aqueous fluid or two-phase separation of a super-critical fluid and saline brine during heating (Kennedy, 1988; Wincker et al., 2000). In both cases, the noble gases readily partition into the lower density phase. Upon cooling, the low density, noble gas-rich phase will condense (the degree of enrichment depends on the extent of boiling or nature of the two-phase separation), but the elemental pattern in the condensed phases will be unaffected.

2.2 Temperature and Pressure

To date, our experimental work has focused on determining the solubility of noble gases in mineral lattices (Jackson et al., 2013a, Chapter 3, Appendix 1). No large temperature or pressure dependencies for volume solubility in minerals have been measured, indicting the temperature and pressure dependencies of the aqueous fluid will dominate changes in partitioning behavior between mineral lattices and fluids.

The temperature and pressure dependencies of noble gas abundances in aqueous fluids are large and complex (Potter and Clynne, 1978; Crovetto et al., 1982), and consequently, pressure and temperature must be considered when evaluating the uptake of noble gases into slab. Essentially, conditions with low noble gas solubility in aqueous fluids will be more conducive to the uptake of noble gases into solids. At low temperature (<100˚C), noble gas solubility in aqueous fluids decreases with increasing temperature. Whereas, at higher temperature, noble gas solubility increases up to the critical point (374˚C, 2.16 kbar). Fugacity-solubility relationships for noble gases in H_2O-rich supercritical fluids have not been studied, but experimental work on hydrogen (both H_2 and noble gases are non-polar species with similar solublities in aqueous fluids) solubility in H_2O-rich supercritical fluids suggests that noble gas solubility closely approximates ideal behavior above the critical point up to moderate pressures (~500 bar) (Kishima and Sakai, 1984). Thus, under this pressure and temperature regime, noble gas fugacity can be calculated as the mole fraction of the gas multiplied the total pressure of the system. This assumption breaks down at lower temperature, higher pressure conditions, particularly for heavier noble gases, which may be common during the alteration of deeper slab materials (e.g. hydration of slab mantle). Under these conditions, noble gas fugacity is expected to be substantially greater than the ideal approximation and should be calculated using a Redlich-Kwong equation of state in the absence directly applicable experimental data.

Mineral surfaces and grain boundaries offer alternative environments for noble gas uptake. Adsorption (uptake onto the mineral surface) has been studied experimentally. Work to date shows that elemental patterns associated with adsorption

can be complicated, i.e. neither monotonically increasing nor decreasing with noble gas radius, and adsorptive affinities can vary widely from material to material (Fanale and Cannon, 1971; Podosek et al., 1981; Yang and Anders, 1982; Marrocchi et al., 2005; Bazan et al., 2011). A general preference, however, for heavier noble gases in shales is observed, which may be the most direct analog to oceanic sediments experimentally studied to date. Temperature dependencies on adsorption are strong, with higher temperatures favoring a lower adsorbed component (logarithm of adsorbed concentration is negatively correlated to inverse temperature, defining the enthalpy of adsorption). At the low temperatures associated with the formation of seafloor sediments and alteration of basaltic extrusives, adsorption appears to strongly influence the budget of noble gases, evidenced by the strong enrichment of heavy noble gases relative to lighter noble gases in oceanic sediments (e.g. Matsuda and Nagao, 1986). At higher temperatures, adsorptive affinities decrease, and if a fluid phase is still present, adsorbed noble gases will readily partition back into the fluid and volume solubility may dominate bulk solubility. Rather than losing originally adsorbed noble gases with increases in temperature, it is also possible that originally adsorbed noble gases become trapped or fixed (e.g. mineral growth acts to incorporate adsorbed noble gases within a mineral interior) (Podosek et al., 1981), making these gases more robust to loss at elevated temperature.

Grain boundaries provide relatively open structures that may be favorable locations for noble gas uptake. The mass fraction of grain boundaries in a rock, however, is very low. For grain boundaries to constitute a major reservoir for noble gases, grain size must be very small and the mineral volume – grain boundary partition coefficient must be extremely low. A single study focused on noble gas dissolution onto grain

boundaries has been completed (Baxter et al., 2007). Results from this study suggest Ar and He are similarly soluble in grain boundaries and basaltic liquids. Thus, in mantle systems, where noble gases are relatively insoluble in the minerals present (Jackson et al., 2013b, Appendix 1), grain boundaries may contain ~50% of noble gases. However, in systems where the volume solubility of noble gases in minerals is relatively high, i.e. hydrothermally altered slabs (Jackson et al., 2013, Chapter 3, Appendix 1), grain boundaries are not likely to be significant reservoirs of noble gases, unless grain sizes approach micron-scale diameters or if cpx-cpx grain boundaries are poor analogs for geological systems in general. More work is needed on different types of grain boundaries over a wide range of temperatures and pressures to confirm this speculation.

2.3 Water/Rock Ratio

The ratio of water to rock during hydrothermal alternation is not constant across the slab and is expected to affect the uptake of noble gases into the slab. In very high water/rock ratio systems, the relative abundance of water ensures that the concentration of noble gases in the reacting fluid will be essentially equivalent to their concentration in seawater, fixing the concentration of noble gases absorbed and adsorbed under equilibrium conditions. In very low water/rock ratio systems, the elements that are not incorporated into the minerals that form during reaction between fluid and rock will become enriched in the fluid, increasing their activity or fugacity. Experimental work to date suggests noble gases are likely to be incompatible with the rock during hydrothermal alteration (Jackson et al., 2013, Chapter 3, Appendix 1) and are thus candidates for this type of behavior.

In the extreme case, where all the fluid is consumed during reactions with the rock or where seawater is retained as a trapped component in the rock (i.e. closed-system interactions), the abundance of noble gases in the slab will be equal to the initial abundance of noble gases in the fluid. Measurements of drill cores indicate that the oceanic crust contains sufficient microporosity to dominate the budget of noble gases input into subduction zones, provided the mircopores are filled with seawater (Jarrard, 2003). The extrusive lithologies can contain more than several percent microporosity. Microporosity decreases with depth and time in oceanic crust, following the precipitation of low temperature alteration phases in the micropores, but a finite amount of mircoporosity remains present throughout the crust (Carlson, 2010). Only a few cores of the sheeted dikes have been completed, but microporosities of 0.5-2% have been reported (Wilson et al., 2006). Deeper gabbroic sections still retain small amounts of microporosity, but measurements are variable, and likely biased upwards due to fracturing upon decompression. Nonetheless, the median of microporosity measurements of gabbros in 735B is 0.2% (Ildefonse and Pezard, 2001).

The fate of fluids initially hosted in mircopores during subduction is unclear, but it is likely that some of these fluids are incorporated into the host rock during prograde metamorphism associated with the early stages of subuduction (Peacock, 1990). The high pressures and low permeability of green and blue schist facies rocks favor noble gases partitioning into slab solids during the early stages of subduction.

2.4 Rock Chemistry

The stable assemblage and mode of minerals in a rock is determined by the chemistry of the system, pressure, and temperature. The mode of minerals present in the rock define the bulk partition coefficient for noble gases in the rock-fluid system, influencing the uptake of noble gases into the slab. Ultimately, it is desirable to quantify the solubility (absorption and adsorption) of noble gases in all of the phases potentially present within a slab and combine this information with their mode within a specific slab to identify which lithologies have the highest capacity to incorporate noble gases and predict elemental fractionations for a given pressure and temperature. The slab can be divided into three broadly distinct chemical layers, 1) the sediments, 2) basaltic crust, 3) and lithospheric mantle. Each layer is altered under distinct, but variable, conditions to characteristic mineral assemblages, meaning that each layer has a unique propensity for recycling noble gases. Most of our understanding of alteration of slab lithologies and alteration comes from drill cores, exhumed slabs, and seismic studies (e.g. Alt et al., 1996; Bebout, 1996; Carlson, 2003).

Sediment thickness on the ocean floor is highly variable and correlated with productivity in the water column and proximity to continental sediment sources (Divins et al., 2003). Composition varies range between clay-rich, carbonate-rich, or silicic (Plank and Langmuir, 1998). The extrusive sections of the crust are dominated by ~500 m of pillow basalts which are pervasively altered at low temperatures and high water/rock ratios. Under these conditions clays, oxides, calcite and sulfides are common alteration products (Alt and Honnorez, 1984). The pillow basalts are fed by the underlying sheeted dikes. The sheeted dikes are also pervasively altered, with up to 50% replacement of igneous minerals by secondary minerals (Hole 504B). Hydrothermal

veins of highly altered materials are common, with near-complete replacement of igneous minerals. Alteration halos typically surround the hydrothermal veins. Amphibole is a common alteration product, primarily replacing clinopyroxene, in higher temperature sections altered sheeted dikes (>300˚C). Zeolite, secondary plagioclase, chlorite, epidote, and anhydrate commonly replace plagioclase. Olivine is replaced by serpentine, chlorite, talc, quartz, and various oxides (Vanko et al., 1996).

Intrusive rocks underlie the sheeted dikes. These rocks are predominantly gabbros, including ferro-gabbros, but more exotic lithologies, such as troctolites and dunites, are also observed. These different rock types are altered across a wide range in temperatures (Hole 735B Hole 1256D) (Dick et al., 2000, Wilson et al., 2006). High-temperature assemblages (700-1000˚C) are dominated by amphibole and secondary plagioclase and are associated with shear zones, presumably related to increased permeability. Mid-temperature assemblages (250-400˚C) are dominated by amphibole and chlorite. Prehnite and epidote are also produced in this regime. Low-temperature (<300˚C) assemblages are also located within the intrusive lithologies of oceanic crust. These assemblages are dominated by chlorite, smectite clays, carbonates, and sulfides. Only a few drill cores have extend into the intrusive sections of oceanic crust, but it appears that alteration is less pervasive, with approximately 10-20% replacement of igneous mineral common, albeit with considerable local variability. It should be noted that 735B is drilled into tectonically exposed gabbros. The pervasive, low temperature alteration observed in 735B is likely not representative of typical gabbros. Hole 1256D successfully drilled into in-sequence gabbros. The gabbros of 1256D are altered at high

to mid-range temperatures and did now show evidence for the low temperature assemblages observed in 504B.

Drill cores have not penetrated beyond the MOHO, leaving the hydration properties of the slab mantle section poorly known. Some insight into the hydrating reactions comes from slow spreading ridges, where mantle rocks are exposed at the seafloor to vast amount of seawater by extensional faulting. These rocks readily alter to serpentinites at low temperatures (<500˚C). Lizardite and crysotile dominate the hydrothermal assemblage (mid- and low-temperature polymorphs of serpentine, respectively) for mantle rocks, while antigorite is less abundant. In addition to serpentine, hydration of ultramafic rocks at low temperature invariably leads to the production of minor amounts of other minerals. Dunite hydrates to produce serpentine and minor amounts of brucite, given the stoichiometry of serpentine and olivine. A more opx-rich ultramafic rock hydrates to produce serpentine and talc. Divalent iron dissolved into olivine and pyroxene is not stable in serpentine following its lattice geometry and is oxidized to stabilize magnetite (Sleep et al., 2004), which precipitates as a ubiquitous secondary phase. Aluminum and calcium act to stabilize amphibole and chlorite (Schmidt and Poli, 1998). Serpentine contains approximately 13 wt. % H_2O, allowing hydrated mantle to transport large amounts of water into subduction zones. Given the stability of serpentine to high pressure and high capacity to dissolve H_2O, it has been suggested that hydrated mantle controls the flux of recycled water in cold subduction zones (Van Keken et al., 2011). The high pressure stability may also favor relatively large amounts of noble gases being recycled by hydrated lithospheric mantle.

2.5 Analysis of Noble Gases in Altered Oceanic Crust and Mantle:

The ground truth for studying the uptake of noble gases by the slab comes from the measurement of noble gases in slab materials. Experiments and theory are needed to provide a framework to interpret the natural observations and to direct where observational efforts should be concentrated. Below I summarize the current state of observations of noble gases in altered slab materials and other applicable metamorphic rocks.

Ocean sediments and altered basaltic extrusives are monotonically enriched in heavier noble gases compared to lighter noble gases and are relatively rich in noble gases (Dymond and Hogan, 1978; Matsuda and Nagao, 1986; Staudacher and Allegre, 1988). The enrichment of heavy noble gases in sediments is in excess of the enrichment observed in seawater, suggesting a second process is needed to further enrich heavy noble gases in sediments. Experiments have shown that Kr and Xe strongly adsorb to pelitic sediments at low temperature and that Xe adsorption is greater than Kr (Fanale and Cannon, 1971; Podosek et al., 1981). This can be extrapolated to suggest adsorption favors heavier noble gases, perhaps reflecting their greater polarizability. Additional work on lighter noble gases, different materials, and aqueous systems are required to confirm this extrapolation. Our experiments on noble gas absorption by minerals do not show preferential affinity for heavier noble gases (Jackson et al., 2013a, Chapter 3, Appendix 1). Thus, the heavy noble gas enrichment is consistent with adsorption + burial by mineral growth controlling the noble gas contents in sediments and altered basaltic extrusives. Limited work has been completed to document the full spectrum of noble gas contents in deeper basaltic lithologies. Results to date suggest that deeper basaltic lithologies have noble gas elemental patterns more similar to seawater, i.e. not

systemically enriched in heavier noble gases (Kumagai et al., 2003). Helium and Ne isotopes and elemental abundances have been measured on gabbros from 735B (slow-spreading ridge, tectonically exposed gabbro) (Moreira et al., 2003). Neon abundances are similar to those measured in altered extrusive basalts, and neon isotopic compositions are essentially atmospheric, neglecting several samples with low Ne abundances. More work is clearly needed to fully document the composition and distribution of noble gases in oceanic crust, particularly for in-place intrusive lithologies.

Data regarding noble gases in subduction-related serpentinite and prograde hydrated mantle have recently been reported by Kendrick and co-workers (Kendrick et al., 2011; Kendrick et al., 2013). Both seafloor and antigorite serpentinites have been measured for Ne-Xe. The results are broadly consistent with small excesses of heavy noble gases relative to seawater, but these excesses are muted compared to sediments and altered exstruvie oceanic crust. Abundances are variable, but Ar abundances in seafloor sepentinites are ~10× greater than those measured in altered oceanic crust. This comparison is suspect, however, as the serpentinites exposed on the seafloor are not direct analogs for serpentinites formed at depth within the slab. Nonetheless, prograde serpentinites (antigorite schists) and dehydrated serpentinites (harzburgites) have Ar abundances 10-100× lower than the seafloor serpentinites, and the protoliths to these rocks may be a more direct analog for typical slab serpentinite. The Ar-Kr-Xe patterns of different metamorphic grade serpentinites are broadly similar despite a wide range in abundance, which provides some constraint on the mechanisms for noble gas loss (i.e. no large elemental fractionations associated with noble gas loss). The Ne/Ar ratio of serpentinites, however, appears to increase with increasing grade.

2.6 Summary of Noble Gas Uptake:

Many parameters affect how noble gases are incorporated into slabs and the concentration of noble gases transported into subduction zones. At temperatures associated with oceanic sediments and extrusive crust, adsorption likely controls the abundance of noble gases. At higher temperatures associated with alteration of the sheeted dikes and gabbros, noble gas uptake into the slab is likely controlled by absorption, given the temperature dependences on adsorption. Experimental measurements of adsorption and absorption by hydrothermal minerals remain sparse and preclude predicting the relative affinity of different lithologies for noble gases. Work from this thesis suggests noble gases are most strongly absorbed by ring structure-bearing minerals, which are present throughout the slab. More work is needed to document the full spectrum of noble gas solubility in these minerals. Temperature and pressure have strong effects on noble gas solubility in hydrous fluids and are expected to vary spatially and temporally throughout the slab. The effects of salts, CO_2, pressure, temperature, particularly above the critical point, on noble gas solubility in seawater fluids are not well documented. Rock chemistry has a first order effect on determining the stable assemblage of minerals in an altered rock, and the major alteration phases change as a function of depth in a slab. Correspondingly, each horizon within a slab will have a different propensity to incorporate noble gases. A significant amount of noble gases are likely present within fluid-filled microporosity of slabs. These fluids have the capacity to dominate the budget of recycled noble gases, depending of the timing of their release and the degree to which they incorporated into the slab solids.

Additional experimental measurements of noble gas solubility in minerals will clarify the propensity of each slab lithology to incorporate and fractionate noble gases. These data, in combination with field measurements of noble gases in different slab materials, will yield insight into the conditions and processes associated with noble gas uptake into slabs.

3.0 Noble Gas Loss

The loss of noble gases from the slab during subduction can be considered separately from the uptake and transport of noble gases into a subduction zone. Noble gases are trace elements, and so their abundance does not affect the physical or chemical properties of the host system. As a result, models can focus on percent loss and relative fractionations of noble gases associated with devolatilization (ignore the initial abundances of noble gases in slab solids) and maintain usefulness.

Noble gases prefer fluids compared to minerals, and so their fate during suduction will largely be determined by the fate of fluids in subduction zones (Smye et al., 2013). Consequently, it is useful to examine how water is lost from the slab at different stages of subduction.

From the trench to ~45 km depth, fluid lost from the slab rises into the accretionary prism and forearc. Fluids released into the accretionary prism or forearc do not contribute to noble gas recycling. The loss of noble gases from the slab during subduction starts with the expulsion of pore waters during compaction of the sediments. Compaction is largely complete by ~5 km depth, but a small fraction of porosity remains open to deeper depths (Moore and Vrolijk, 1992). Additional fluids are produced at

shallow depths by the conversion of expandable clays (i.e. smectites) to illite (an inter-layer deficient mica) in the sediments and upper extrusives (~200˚C, Moore and Vrolijk, 1992). The relative fluid loss from the sediments to the forearc and accretionary prism is large. Combined, sediment pore waters and sediment structural water make up 50% of the water transported into subduction zones, ignoring any flux associated with hydrated mantle (Jarrard, 2003). In the forearc, these fluids help to stabilize serpentine. Serpentine is buoyant and weak, giving rise to serpentine mud volcanoes in forearc arc terrenes. Serpentinites in forearc mud volcanoes have been shown to be rich in noble gases (Kendrick et al,. 2013), with abundance patterns similar to seawater.

By 45 km depth, it is estimated that 98% of water initially associated with the sedimentary layer (structural and pore waters) has been lost (Jarrard, 2003). Field observations have been used to estimate that 81% of water initially hosted in the extrusive sections of oceanic crust (primarily hosted by low temperature assemblages) has been lost by 45 km depth (Bebout, 1995). The loss of these fluids likely also represents a massive loss of noble gases from the subducting slab. At equilibrium, any noble gases adsorbed onto minerals surfaces will have partitioned into the fluid given temperatures associated with the slab at <45 km depth.

The kinetics of equilibrating absorbed noble gases in clays and micas with fluids at low temperatures (<400˚C) are not known but are expected be relatively slow compared to the adsorbed component. It is possible that absorbed noble gases will equilibrate with the fluid if exchange kinetics are sufficiently rapid. In this case, it is likely that majority of noble gases hosted in the sediments will partition into the fluid, given the incompatibility of noble gases in solids. At low porosities (i.e. low water/rock

ratios), the release of fractionated noble gases into a fluid may be sufficient to affect the concentration of noble gases in the fluid phase. In this case, the abundance of noble gases that partition into the minerals will reflect, to a degree, the fractionated signature of noble gases in the sediments prior to noble gas loss. It is also possible that the temperature-time path of sediments is such that there is only partial loss of noble gases to the fluid (sluggish kinetics associated with noble gas loss). In this scenario, a larger amount of noble gases will remain retained in the solids and these noble gases will be elementally fractionated following their respective diffusivities. Following this, even though the sediments and extrusives lose large amounts of fluids to the accretionary prism and forearc, these lithologies may still contribute significantly to noble gas recycling if a small, but finite, fraction of fluid is retained deep into subduction or if volume diffusion kinetics are sluggish. The fluid may either remain free in the slab or be consumed in subsequent closed-system by prograde reactions.

As the slab descends deeper into the subduction zone, it experiences progressively higher pressures and temperatures. Beyond ~45 km depth, fluids released by the slab will ascend into the mantle and will contribute to arc magma genesis (Bebout, 1991; Bebout, 1995). Thermal structure modeling of subducting slabs indicate that all slab lithologies experience some dehydration at depths shallower than arc magma genesis (Hacker, 2008), ~100 km depth (Gill, 1981), providing the opportunity for noble gas loss to the mantle wedge and elemental fractionation within the slab. Dehydration of mafic crustal lithologies in hot subduction zones is nearly complete prior to ~100 km depth. Some liberated water may be resorbed by lawsonite, phengite, talc, or chlorite at high pressure and temperature (Hacker, 2008; Grove et al., 2006). If this resorbtion occurs as a closed

or near-closed system or if the fluid remains trapped in the subducting slab because permeability is low, then noble gases can be effectively transported deeper. If the fluid is not trapped or consumed by the host rock, then it will migrate to lower pressures, transporting its compliment of noble gases as well. As the fluid rises, it will interact with the minerals it encounters, imparting noble gases with seawater isotopic signatures to some degree. If this reacted material is entrained downwards with the subducting slab (Cagnioncle et al., 2007), this process offers another mechanism for noble gas recycling. The elemental pattern of recycled noble gases associated with the entrained material will be a function of the initial noble gas composition of the fluid, the kinetics of exchange of noble gases between the minerals and migrating fluid, and the partitioning of the noble gases between the fluid and minerals.

Noble gas abundances have been measured in partially serpentinized peridotite inferred to be exhumed from the mantle wedge (~100 km depth, Sumino et al., 2010). The elemental patterns of noble gases in these peridotites are similar to seawater, although perhaps slightly depleted in Ne. This type of observation can potentially provide a constraint regarding the source of noble gases released into the mantle wedge and the transport of noble gases from the slab into the mantle wedge.

Ultimately, a large portion of the fluid released from the slab is incorporated into magmas that rise buoyantly and eventually erupt in the arc. The noble gases that are incorporated into the erupted lavas are not recycled. The noble gas elemental and isotopic compositions of the parental arc magmas potentially provide an additional constraint regarding the materials responsible for fluxing the mantle wedge and the fluid migration process. However, unambiguous determinations of noble gas compositions in

parental magmas are difficult because atmospheric contamination (noble gases in the atmosphere and seawater are isotopically identical), crustal assimilation, and degassing all combine to obscure the true magmatic compositional values. Some work has been done to this end for arc and backarc magmatic products (Patterson et al. 1994; Bach and Niedermann, 1998; Ikeda et al., 1998; Honda et al., 1993). The results of these studies are suggestive of seawater-derived heavier noble gases strongly affecting the composition of subduction-related magmas, but contamination and primitive elemental patterns have not been fully and unambiguously resolved.

3.1 Summary of Noble Gas Loss

The majority of fluids initially hosted in the slab are lost to the accretionary prism and forearc. It can be inferred that the majority of noble gases initially hosted in the slab are also lost to at this stage. Fluids that remain trapped in residual pore space and slab minerals transport noble gases deeper into subduction zones. A large percent of hydrous minerals in the crust are destabilized at pressures and temperatures less than those associated with arc magmatism, and correspondingly, a large percent of crust-hosted noble gases are lost via volcanism, particularly in hot subduction zones. Several mechanisms exist that can facilitate the transport of initially crust-hosted noble gases deeper into the mantle, and during transport there are opportunities for noble gases to be elementally fractionated by both equilibrium and kinetic processes. Hydrated mantle offers a separate pathway for noble gas transport through subduction zones. Given the stability of serpentine to high pressures, hydrated mantle has the potential to efficiently transport noble gases to depth beyond arc magma genesis.

4.0 An Integrated Noble Gas Recycling Constraint

The noble gases that are transported past the point of magma genesis in arcs and backarc are fluxed into ambient mantle where they mix with mantle noble gases. This mixing is recorded as a homogenization of atmospheric and mantle noble gas isotopic signatures and a homogenization of the elemental patterns associated with the recycled noble gases and mantle noble gases. Thus, the isotopic composition and elemental pattern of noble gases in the mantle constrains the composition of recycled noble gases.

The He-Xe elemental pattern of the depleted mantle has been established (Moreira et al., 1998; Holland and Ballentine, 2006). The pattern is similar to seawater for Ar-Xe, but slightly enriched in heavier noble gases, including a stark depletion in Xe. The similarity in Ar-Xe elemental patterns between seawater and the mantle led Holland and Ballentine (2006) to conclude that recycled noble gases with a pattern similar to seawater, but slightly enriched in heavier noble gases, control the depleted mantle Ar-Xe budget. This observation potentially provides a constraint on the time-integrated flux of recycled noble gases.

Isotopic arguments support the notion that noble gas recycling strongly influences the budget of Ar-Xe in the mantle. The non-radiogenic isotopic composition of the depleted mantle Ar-Xe is similar to the atmosphere, and distinct from primordial sources (at least for Kr and Xe), once corrected for atmospheric contamination (Holland and Ballentine, 2006; Holland et al., 2009, Raquin and Moreira, 2009; Mukhopadhyay, 2012; Tucker et al., 2012). High precision measurements of Xe isotopes imply ~85% of Xe in the depleted mantle is associated with a recycled component (Holland and Ballentine,

2006; Holland et al., 2009, Raquin and Moreira, 2009; Mukhopadhyay, 2012; Tucker et al., 2012). Similarly, high precision measurements of Kr isotopes imply a substantial fraction of Kr (exact percentages not calculated but >25 and <75% are reasonable limits for discussion purposes here) in the depleted mantle is associated with a recycled component (Holland et al., 2009). Unambiguously defining the percentage of non-radiogenic Ar in the mantle is impossible because non-radiogenic Ar is isotopically homogenous throughout the mantle and atmosphere (Raquin and Moreira, 2009; Mukhopadhyay, 2012). Thus, non-radiogenic Ar isotopes are consistent with either 1) complete homogenization of Ar via recycling, i.e. ~100% of non-radiogenic Ar in the mantle associated with a recycled component, or 2) initially homogenous accretion of Ar, making non-radiogenic Ar insensitive to recycling. Of all the noble gases retained in the atmosphere, Ne is most starkly different between the atmosphere and mantle for its non-radiogenic composition ($^{20}Ne/^{22}Ne$ = 9.8, 12.5, and >13 for the atmosphere, depleted mantle, and high $^{3}He/^{4}He$ mantle, respectively) (Ballentine et al., 2005; Yokochi and Marty, 2004; Mukhopadhyay, 2012). Of the potential primordial sources of Ne in the mantle, the solar nebula has the highest associated $^{20}Ne/^{22}Ne$ ratio (13.8) (Grimberg et al., 2006), and taking this as an upper limit of Earth's mantle initial $^{20}Ne/^{22}Ne$, this implies <30% of Ne in the depleted mantle and <20% of Ne in the high $^{3}He/^{4}He$ source is associated with a recycled component. These percentages for Ne are upper limits because it is possible that the initial $^{20}Ne/^{22}Ne$ ratio of the mantle was a mixture of solar and chondritic sources, and thus, lower than 13.8.

Percentages of each noble gas associated with recycling in the mantle can be converted into concentrations using the known concentration of He in the mantle and

various elemental ratios (concentration and ratios from Holland and Ballentine, 2006). Figure 1 plots the potential field of recycled noble gas elemental patterns normalized to seawater and ^{130}Xe. The field is large, primarily reflecting the inability to place a firm lower limit on the percent of recycled, non-radiogenic Ne and Ar. In the absence of a firm lower limit, we assume a lower limit for Ne and Ar of 1% recycled.

Evaluating the limits on the recycled noble gas field, it is clear that Xe is preferentially recycled compared to Kr and Ar, even after accounting for the fact that heavier noble gases are more soluble in seawater compared to lighter noble gases (Potter and Clynne, 1978; Crovetto et al., 1982). If a full 30% of mantle Ne is attributed to a recycled component, i.e. the initial $^{20}Ne/^{22}Ne$ ratio of the depleted mantle dominated by solar nebula Ne (13.8), this implies Ne is preferentially recycled compared to all other noble gases and that the integrated Ne-Xe recycling pattern is "U-shaped." Shales with a "U-shaped" Ne-Xe pattern are rare but have been observed (Podosek, 1981; Bernatowicz et al., 1984). Unaltered basalts commonly display "U-shaped" Ne-Xe patterns (Type 2 pattern of Ozima and Alexander (1976)), but the noble gases contained in these materials are primarily of mantle origin and do not factor into this recycling budget. The overwhelming majority of Ne-Xe abundance patterns associated with hydrothermally altered slab materials closely follow a seawater abundance pattern or are monotonicically enriched in heavy noble gases relative seawater (Dymond and Hogan, 1978; Matsuda and Nagao, 1986; Staudacher and Allegre, 1988; Kumagi et al., 2003; Kendrick et al., 2011). If these materials fully capture the range of Ne-Xe abundace pattens in slabs prior to subduction, then a "U-shaped" Ne-Xe integrated recycling pattern would require preferential retention of Ne of compared to Ar-Xe during noble gas loss from the slab.

Moreover, the Ar-Xe pattern of the slab must remain in favor of the heavier Xe despite sufficient loss to impart the elevated Ne abundance. It is not obvious what process could lead to the preferential retention of Ne while not also leading to the preferential retention of Ar and Kr relative to Xe. The noble gases are a group of elements with regularly varying physical properties from lighter to heavier noble gases. A "U-shaped" Ne-Xe pattern likely requires a confluence of two or more processes.

An alternative hypothesis is that heavier noble gases are monotonically enriched in the integrated recycling pattern. This hypothesis is supported by the elemental abundance measurements of Ar-Xe in the depleted mantle (Holland and Ballentine, 2006). A monotonically heavy noble gas enriched recycling pattern could be explained by a combination of the Ne-Xe pattern of noble gases input to subduction zones monotonically favoring heavier noble gases, which is observed (Dymond and Hogan, 1978; Matsuda and Nagao, 1986; Staudacher and Allegre, 1988; Kendrick et al., 2011), or by kinetic fractionations associated with loss of noble gases to fluids leaving the slab (preferential retention of slower diffusing, heavier noble gases in the slab). Measurements of noble gas solubility in minerals (absorption) do not show a preference for heavier noble gases (Heber et al., 2007, Jackson et al., 2013b, Chapter 3, Appendix 1). A monotonically enriched noble gas recycling pattern is favored over a "U-shaped" pattern because of the simplicity of the associated processes and support from multiple observations.

Taking a monotonically enriched integrated noble gas recycling pattern as the favored hypothesis, we can now evaluate the implications of this pattern. If >10% of Ne in the mantle is attributed to recycling, a monotonically increasing Ne-Xe integrated

noble gas recycling pattern is not maintained. This then implies that an upper limit of 10% for the amount of recycled Ne in the mantle. A monotonically enriched integrated noble gas recycling pattern implies that non-radiogenic Ne the depleted mantle was initially a blend of solar and meteoritic sources. If true, the mixing relationships between solar nebula and chondritic sources suggest the initial Ar, Kr and Xe signatures of the depleted mantle were controlled by meteoritic sources. This latter suggestion is supported by the Kr signature of well gases affected by noble gases sourced from the depleted mantle (Holland et al., 2009).

The goal is to develop this final section (4.0 An Integrated Noble Gas Recycling Constraint) into a manuscript in this coming summer. A best estimate of the integrated pattern of recycled noble gases will provide a target and additional context for future research on noble gas recycling. For example, our work on noble gas solubility in slab minerals (Jackson et al., 2013a, Chapter 3, Appendix 1) demonstrates that volume solubility does not act to preferentially recycle heavier noble gases. Additional processes appear required to explain the integrated pattern of recycled noble gases. We have initiated a collaboration to numerically model how noble gases are fractionated during slab devolatilization. A best estimate of the integrated pattern of recycled noble gases is crucial to evaluating the outputs of these models. This manuscript will further develop the implications of a monotonically enriched noble gas recycling pattern (e.g. implications for other types of volatiles elements and slab devolatilization processes) and the uncertainties associated with the approach taken here to develop the recycling pattern.

5.0 Conclusions

The study of noble gas recycling is at an early stage. Historically, deconvolving the composition of mantle-derived noble gases (particularly Kr and Xe) from atmospheric contamination has been impossible due to the ubiquitous nature of atmospheric contamination and low gas contents of mantle-derived samples. Developments in noble gas mass spectrometric methods now allow for the precise measurement of very small gas quantities. Recent noble gas studies of mantle-derived materials have solidified the importance recycling in determining the composition of noble gases in the mantle (e.g. Mukhopadhyay, 2012; Tucker et al., 2012). Parallel efforts in experimentally and numerically studying the behavior of noble gases in subduction and slab environments are now required.

I have outlined a series of factors that have the potential to affect the uptake and loss of noble gases from slabs. To evaluate the significance of these different factors for noble gas recycling, experimental data, in conjunction with numerical modeling, are needed. Noble gas adsorption, absorption, and diffusivity measurements in slabs minerals will be particularly useful to this end. The solubility of noble gases in high pressure, hydrous fluids is also a critical area to study. Under slab dehydration conditions, the activities of noble gases, particularly heavier noble gases, in fluids likely deviate positively from ideal behavior. This behavior, in turn, should affect the elemental fractionations associated with the loss of noble gases from the slab during dehydration.

The results of modeling noble gases during uptake into the slab and loss during subduction must be evaluated in the context of measurements of natural samples. To this end, additional measurements of the full spectrum of noble gas abundances in slab materials are required. Specifically, it should be a high priority to document the spatial

and temporal variability of noble gas abundances in slabs, particularly for the deeper lithologies affected by hydrothermal alteration.

The exchange of fluids between Earth's exterior and interior is a fundamental process, linking to volcanism, earthquakes, mantle convection, and the formation and maintenance of habitable planet. The study of noble gas recycling offers a new, and potentially powerful, way to trace fluid cycling. Future geochemical, experimental, and numerical efforts can combine to realize this potential.

Figure Captions:

Figure 1: Pattern of recycled noble gases in depleted mantle as constrained by isotopic compositions. The absolute abundance of recycled noble gas *i* is normalized to the abundance of ^{130}Xe and the $i/^{130}$Xe ratio in seawater. In this normalization scheme, a seawater abundance pattern plots as a horizontal line with a value of unity. The upper and lower dashed lines represent the upper and lower limits, respectively, on the abundance of recycled noble gas for element *i*. For all possible scenarios, ^{130}Xe is more abundant than ^{36}Ar or ^{84}Kr, even after accounting for the preferential dissolution of heavier noble gases in seawater. Considering the upper limit scenario, a "U-shaped" abundance pattern is possible, i.e. a full 30% of ^{22}Ne in the depleted mantle is recycled and the ^{20}Ne/^{22}Ne ratio of the depleted mantle was initially set by the solar nebula (13.8). This scenario is considered unlikely in light of the abundance patterns of noble gases in altered sections of slabs and the expectation that noble gases will be regularly fractionated during loss from the slab. We favor a monotonically increasing pattern for the abundance of recycled noble gases because it is supported by the elemental patterns

of noble gases in the depleted mantle, the elemental patterns of noble gases in altered sections of slabs, and the expectation that noble gases will be regularly fractionated during loss from the slab. Given this pattern, ~7% of ^{22}Ne, ~75% ^{36}Ar, and ~70% ^{84}Kr, and 85% of ^{130}Xe is associated with a recycled component in the depleted mantle.

References:

Alt, J., Honnorez, J., 1984. Alteration of the upper oceanic crust, DSDP site 417: mineralogy and chemistry. Contributions to Mineralogy and Petrology 87, 149-169.

Alt, J.C., 1996. Hydrothermal alteration of a section of upper oceanic crust in the eastern equatorial Pacific: A synthesis of results from Site 504 (DSDP Legs 69, 70, and 83, and ODP Legs 111, 137, 140, and 148). Proceedings of the Ocean Drilling Program. Scientific results, 417.

Alt, J.C., Honnorez, J., Laverne, C., Emmermann, R., 1986. Hydrothermal alteration of a 1 km section through the upper oceanic crust, deep sea drilling project Hole 504B – mineralogy, chemistry, and evolution of seawater-basalt interactions. Journal of Geophysical Research-Solid Earth and Planets 91, 309-335.

Bach, W., Niedermann, S., 1998. Atmospheric noble gases in volcanic glasses from the southern Lau Basin: origin from the subducting slab? Earth and planetary science letters 160, 297-309.

Ballentine, C.J., Marty, B., Lollar, B.S., Cassidy, M., 2005. Neon isotopes constrain convection and volatile origin in the Earth's mantle. Nature 433, 33-38.

Baxter, E.F., Asimow, P.D., Farley, K.A., 2007. Grain boundary partitioning of Ar and He. Geochimica Et Cosmochimica Acta 71, 434-451.

Bazan, R., Bastos-Neto, M., Moeller, A., Dreisbach, F., Staudt, R., 2011. Adsorption equilibria of O_2, Ar, Kr and Xe on activated carbon and zeolites: single component and mixture data. Adsorption 17, 371-383.

Bebout, G.E., 1995. The impact of subduction-zone metamorphism on mantle-ocean chemical cycling. Chemical Geology 126, 191-218.

Bebout, G.E., 1996. Volatile transfer and recycling at convergent margins: mass-balance and insights from high-P/T metamorphic rocks. Geophysical Monograph Series 96, 179-193.

Bernatowicz, T., Podosek, F., Honda, M., Kramer, F., 1984. The atmospheric inventory of xenon and noble gases in shales: the plastic bag experiment. Journal of Geophysical Research: Solid Earth (1978–2012) 89, 4597-4611.

Cagnioncle, A.M., Parmentier, E., Elkins-Tanton, L.T., 2007. Effect of solid flow above a subducting slab on water distribution and melting at convergent plate boundaries. Journal of Geophysical Research: Solid Earth (1978–2012) 112.

Carlson, R., 2010. How crack porosity and shape control seismic velocities in the upper oceanic crust: Modeling downhole logs from Holes 504B and 1256D. Geochemistry, Geophysics, Geosystems 11.

Carlson, R.L., 2003. Bound water content of the lower oceanic crust estimated from modal analyses and seismic velocities of oceanic diabase and gabbro. Geophysical Research Letters 30.

Crovetto, R., Fernández-Prini, R., Japas, M.L., 1982. Solubilities of inert gases and methane in H_2O and in D_2O in the temperature range of 300 to 600 K. The Journal of Chemical Physics 76, 1077-1086.

Dick, H.J.B., Natland, J.H., Alt, J.C., Bach, W., Bideau, D., Gee, J.S., Haggas, S., Hertogen, J.G.H., Hirth, G., Holm, P.M., Ildefonse, B., Iturrino, G.J., John, B.E., Kelley, D.S., Kikawa, E., Kingdon, A., LeRoux, P.J., Maeda, J., Meyer, P.S., Miller, D.J., Naslund, H.R., Niu, Y.L., Robinson, P.T., Snow, J., Stephen, R.A., Trimby, P.W., Worm, H.U., Yoshinobu, A., 2000. A long in situ section of the lower ocean crust: results of ODP Leg 176 drilling at the Southwest Indian Ridge. Earth and Planetary Science Letters 179, 31-51.

Divins, D., 2003. Total Sediment Thickness of the World's Oceans and Marginal Seas. NOAA National Geophysical Data Center, Bolder, CO

Dymond, J., Hogan, L., 1978. Factors controlling the noble gas abundance patterns of deep-sea basalts. Earth and Planetary Science Letters 38, 117-128.

Fanale, F.P., Cannon, W.A., 1971. Physical adsorption of rare gas on terrigenous sediments. Earth and Planetary Science Letters 11, 362-368.

Grimberg, A., Baur, H., Bochsler, P., Buehler, F., Burnett, D.S., Hays, C.C., Heber, V.S., Jurewicz, A.J.G., Wieler, R., 2006. Solar wind neon from Genesis: Implications for the lunar noble gas record. Science 314, 1133-1135.

Grove, T.L., Chatterjee, N., Parman, S.W., Medard E., 2006. The influence of H_2Oon mantle wedge melting. Earth and Planetary Science Letters 249, 79-89.

Hacker, B.R., 2008. H_2O subduction beyond arcs. Geochemistry Geophysics Geosystems 9, 24.

Holland, G., Ballentine, C.J., 2006. Seawater subduction controls the heavy noble gas composition of the mantle. Nature 441, 186-191.

Holland, G., Cassidy, M., Ballentine, C.J., 2009. Meteorite Kr in Earth's Mantle Suggests a Late Accretionary Source for the Atmosphere. Science 326, 1522-1525.

Honda, M., McDougall, I., 1998. Primordial helium and neon in the Earth - a speculation on early degassing. Geophysical Research Letters 25.

Honda, M., Patterson, D.B., McDougall, I., Falloon, T.J., 1993. Noble gases in submarine pillow basalt glasses from the Lau Basin: Detection of a solar component in backarc basin basalts. Earth and Planetary Science Letters 120, 135-148.

Ikeda, Y., Nagao, K., Stern, R.J., Yuasa, M., Newman, S., 1998. Noble gases in pillow basalt glasses from the northern Mariana Trough back-arc basin. Island Arc 7, 471-478.

Ildefonse, B., Pezard, P., 2001. Electrical properties of slow-spreading ridge gabbros from ODP Site 735, Southwest Indian Ridge. Tectonophysics 330, 69-92.

Jackson, C.R.M., Parman, S., Kelley, S.P., Cooper, R.F., 2013a. Noble gas transport into the mantle facilitated by high solubility in amphibole. Nature Geoscience 6, 562-565.

Jackson, C.R.M., Parman, S.W., Kelley, S.P., Cooper, R.F., 2013b. Constraints on light noble gas partitioning at the conditions of spinel-peridotite melting. Earth and Planetary Science Letters 384, 178-187.

Jarrard, R.D., 2003. Subduction fluxes of water, carbon dioxide, chlorine, and potassium. Geochemistry Geophysics Geosystems 4.

Kendrick, M.A., Honda, M., Pettke, T., Scambelluri, M., Phillips, D., Giuliani, A., 2013. Subduction zone fluxes of halogens and noble gases in seafloor and forearc serpentinites. Earth and Planetary Science Letters 365, 86-96.

Kendrick, M.A., Scambelluri, M., Honda, M., Phillips, D., 2011. High abundances of noble gas and chlorine delivered to the mantle by serpentinite subduction. Nature Geoscience 4, 807-812.

Kennedy, B., 1988. Noble gases in vent water from the Juan de Fuca Ridge. Geochimica et Cosmochimica Acta 52, 1929-1935.

Kishima, N., Sakai, H., 1984. Fugacity-concentration relationship of dilute hydrogen in water at elevated temperature and pressure. Earth and Planetary Science Letters 67, 79-86.

Kumagai, H., Dick, H.J.B., Kaneoka, I., 2003. Noble gas signatures of abyssal gabbros and peridotites at an Indian Ocean core complex. Geochemistry Geophysics Geosystems 4.

Marrocchi, Y., Razafitianamaharavo, A., Michot, L.J., Marty, B., 2005. Low-pressure adsorption of Ar, Kr, and Xe on carbonaceous materials (kerogen and carbon blacks), ferrihydrite, and montmorillonite: Implications for the trapping of noble gases onto meteoritic matter. Geochimica et cosmochimica acta 69, 2419-2430.

Matsuda, J., Nagao, K., 1986. Noble gas abudances in a deep-sea sediment core for eastern equatorial Pacific. Geochemical Journal 20, 71-80.

Moore, J.C., Vrolijk, P., 1992. Fluids in accretionary prisms. Reviews of Geophysics 30, 113-135.

Moreira, M., Blusztajn, J., Curtice, J., Hart, S., Dick, H., Kurz, M.D., 2003. He and Ne isotopes in oceanic crust: implications for noble gas recycling in the mantle. Earth and Planetary Science Letters 216, 635-643.

Moreira, M., Kunz, J., Allegre, C., 1998. Rare gas systematics in popping rock: Isotopic and elemental compositions in the upper mantle. Science 279, 1178-1181.

Mukhopadhyay, S., 2012. Early differentiation and volatile accretion recorded in deep-mantle neon and xenon. Nature 486.

Patterson, D., Honda, M., McDougall, I., 1994. Noble gases in mafic phenocrysts and xenoliths from New Zealand. Geochimica et Cosmochimica Acta 58, 4411-4427.

Peacock, S.A., 1990. Fluid processes in subduction zones. Science 248, 329-337.

Peto, M.K., Mukhopadhyay, S., Kelley, K.A., 2013. Heterogeneities from the first 100 million years recorded in deep mantle noble gases from the Northern Lau Back-arc Basin. Earth and Planetary Science Letters 369, 13-23.

Plank, T., Langmuir, C.H., 1998. The chemical composition of subducting sediment and its consequences for the crust and mantle. Chemical Geology 145, 325-394.

Podosek, F.A., Bernatowicz, T.J., Kramer, F.E., 1981. Adsorption of xenon and krypton on shales. Geochimica Et Cosmochimica Acta 45, 2401-2415.

Podosek, F.A., Honda, M., Ozima, M., 1980. Sedimentary noble gases. Geochimica Et Cosmochimica Acta 44, 1875-1884.

Potter, R.W., Clynne, M.A., 1978. Solublity of the noble gases He, Ne, Ar, Kr, and Xe in water up to the critical point. Journal of Solution Chemistry 7, 837-844.

Raquin, A., Moreira, M., 2009. Atmospheric $^{38}Ar/^{36}Ar$ in the mantle: Implications for the nature of the terrestrial parent bodies. Earth and Planetary Science Letters 287, 551-558.

Schmidt, M.W., Poli, S., 1998. Experimentally based water budgets for dehydrating slabs and consequences for arc magma generation. Earth and Planetary Science Letters 163, 361-379.

Seyfried Jr, W.E., Bischoff, J.L., 1979. Low temperature basalt alteration by sea water: an experimental study at 70°C and 150°C. Geochimica et Cosmochimica Acta 43, 1937-1947.

Sleep, N., Meibom, A., Fridriksson, T., Coleman, R., Bird, D., 2004. H2-rich fluids from serpentinization: geochemical and biotic implications. Proceedings of the National Academy of Sciences of the United States of America 101, 12818-12823.

Smith, S.P., Kennedy, B.M., 1983. The solubility of noble gases in water and in NaCl brine. Geochimica Et Cosmochimica Acta 47, 503-515.

Smye, A.J., Warren, C.J., Bickle, M.J., 2013. The signature of devolatisation: Extraneous ^{40}Ar systematics in high-pressure metamorphic rocks. Geochimica et Cosmochimica Acta 113, 94-112.

Staudacher, T., Allegre, C.J., 1988. Recycling of oceanic crust and sediments: the noble gas subduction barrier. Earth and Planetary Science Letters 89, 173-183.

Tucker, J.M., Mukhopadhyay, S., Schilling, J.G., 2012. The heavy noble gas composition of the depleted MORB mantle (DMM) and its implications for the preservation of heterogeneities in the mantle. Earth and Planetary Science Letters 355, 244-254.

van Keken, P.E., Hacker, B.R., Syracuse, E.M., Abers, G.A., 2011. Subduction factory: 4. Depth-dependent flux of H_2O from subducting slabs worldwide. Journal of Geophysical Research-Solid Earth 116.

Vanko, D.A., Laverne, C., Tartarotti, P., Alt, J.C., 1996. Chemistry and origin of secondary minerals from the deep sheeted dikes cored during Leg 148 (Hole 504B), Proceedings of Ocean Drilling Program Scientific Results. National Science Foundatino, pp. 71-86.

Wilson, D.S., Teagle, D.A.H., Alt, J.C., Banerjee, N.R., Umino, S., Miyashita, S., Acton, G.D., Anma, R., Barr, S.R., Belghoul, A., Carlut, J., Christie, D.M., Coggon, R.M., Cooper, K.M., Cordier, C., Crispini, L., Durand, S.R., Einaudi, F., Galli, L., Gao, Y., Geldmacher, J., Gilbert, L.A., Hayman, N.W., Herrero-Bervera, E., Hirano, N., Holter, S., Ingle, S., Jiang, S., Kalberkamp, U., Kerneklian, M., Koepke, J., Laverne, C., Vasquez, H.L.L., Maclennan, J., Morgan, S., Neo, N., Nichols, H.J., Park, S.-H., Reichow, M.K., Sakuyama, T., Sano, T., Sandwell, R., Scheibner, B., Smith-Duque, C.E., Swift, S.A., Tartarotti, P., Tikku, A.A., Tominaga, M., Veloso, E.A., Yamasaki, T., Yamazaki, S., Ziegler, C., 2006. Drilling to Gabbro in Intact Ocean Crust. Science 312, 1016-1020.

Winckler, G., Kipfer, R., Aeschbach–Hertig, W., Botz, R., Schmidt, M., Schuler, S., Bayer, R., 2000. Sub sea floor boiling of Red Sea Brines: New indication from noble gas data. Geochimica et Cosmochimica Acta 64, 1567-1575.

Yang, J., Anders, E., 1982. Sorption of noble gases by solids, with reference to meteorites. III. Sulfides, spinels, and other substances; on the origin of planetary gases. Geochimica et Cosmochimica Acta 46, 877-892.

Yokochi, R., Marty, B., 2004. A determination of the neon isotopic composition of the deep mantle. Earth and Planetary Science Letters 225, 77-88.

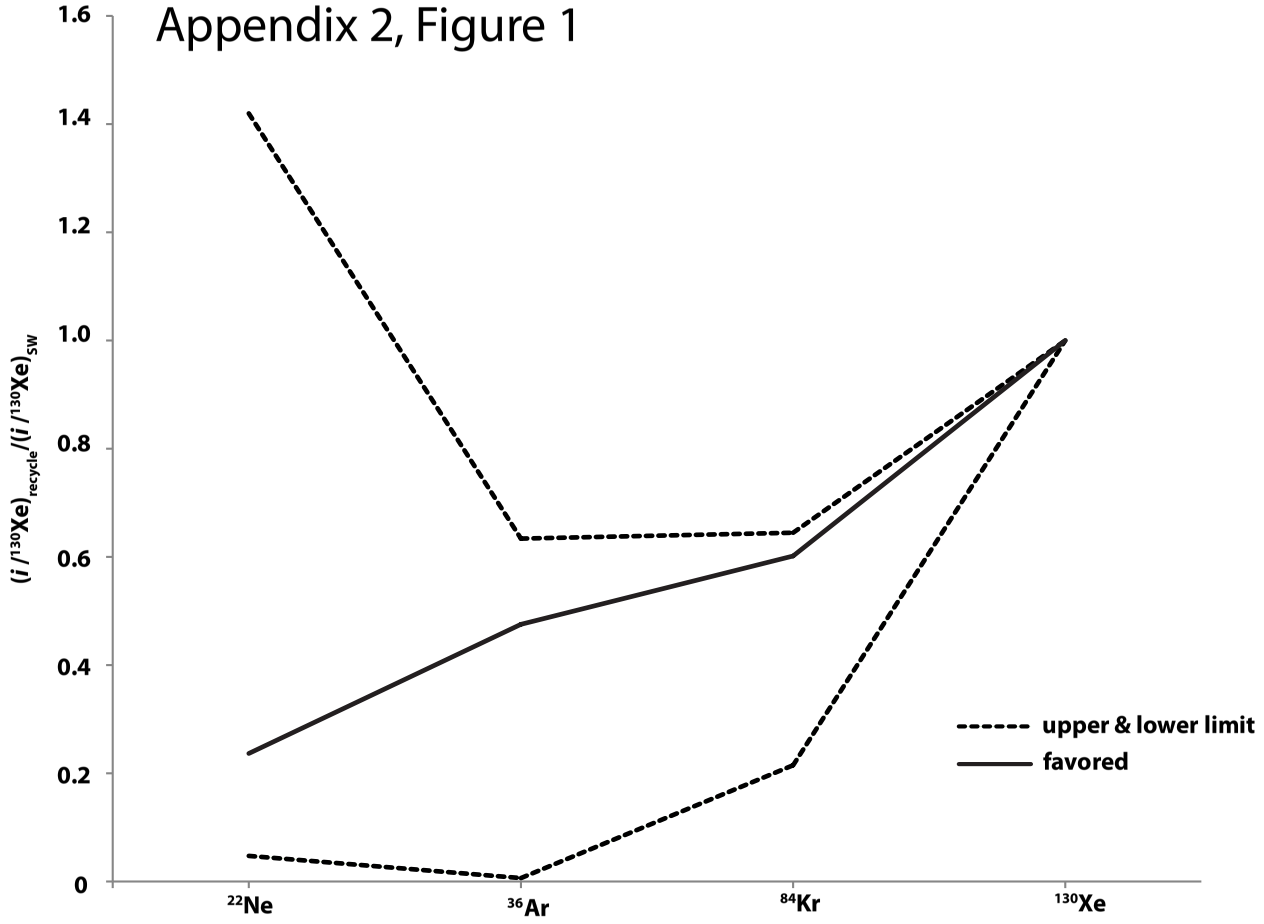
Appendix 2, Figure 1
1.6
1.4
1.2
1.0
0.8
0.6
0.4
0.2
0
$(i/^{130}Xe)_{recycle}/(i/^{130}Xe)_{SW}$
^{22}Ne
^{36}Ar
^{84}Kr
^{130}Xe
upper & lower limit
favored